Electromagnetic and Light Scattering XII

Conference Proceedings

June 28 – July 2, 2010
University of Helsinki, Finland

Editors: Karri Muinonen, Antti Penttilä, Hannakaisa Lindqvist,
Timo Nousiainen, and Gorden Videen

The conference is sponsored by

Department of Physics,
University of Helsinki

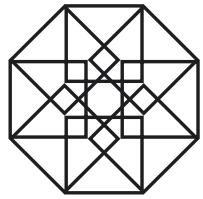

The Federation Of Finnish
Learned Societies

Vaisala Group

U.S. Army International Technology
Center-Atlantic, Research Division
(USAITC-A)

U.S. Office of Naval Research Global,
Conference Support Program (ONR-CSP)

Preface

It is a pleasure to welcome scattering researchers from around the world to ELS XII in Helsinki, Finland, June 28 - July 2, 2010. ELS XII concentrates on theoretical, observational, computational, and experimental aspects of light scattering by particles with varying sizes, shapes, and optical properties, as well as aspects of multiple scattering by complex media composed of such particles.

The ELS conference series originated when the Conference on Light Scattering by Nonspherical Particles (Amsterdam 1995, Helsinki 1997, and New York 1998) merged with the Workshop on Electromagnetic and Light Scattering (Bremen 1996, Moscow 1997, Bremen 1998). The first joint conference, considered fourth in the ELS series, was held in Vigo (1999), followed by Halifax (2000), Gainesville (2002), Bremen (2003), Salobreña (2005), St. Petersburg (2006), Bodrum (2007), and Hatfield (2008).

In astronomy, ELS XII gathers together researchers working on light scattering by solar-system dust such as that on the surfaces of asteroids and in the comae of comets, as well as researchers working on scattering by interstellar and circumstellar dust. In meteorology and atmospheric physics, researchers attending ELS XII study scattering by terrestrial aerosol and ice particles. In material sciences, scattering by nanoparticles is among the key topics of ELS XII, challenging even the validity of classical electromagnetism described by the Maxwell equations. ELS XII is strikingly cross-disciplinary and also addresses research in, for example, remote sensing, biology, medicine, and geophysics. Reaching the 12th conference in the ELS series, novel theoretical, computational, and experimental methods are being vigorously developed around the globe.

Light and shape mark the nature in Finland. Complex shapes are exemplified by the trees in the forests, the lake districts with broken shore lines, as well as the archipelago and broken coast line of the Baltic Sea. Light is locally of particular significance: during the winter, there is commonly lack of light; whereas, during the summer, there is plenty of light day and night.

The Conference Proceedings of Electromagnetic and Light Scattering XII at hand include the 85 articles that have been accepted for publication after a peer-review process organized in March 1 – June 15, 2010. I would like to thank the Scientific Organizing Committee, the Local Organizing Committee, the Sponsors, and all the authors and reviewers of the conference articles for their invaluable contributions to ELS XII.

Karri Muinonen
ELS XII
Scientific Organizing Committee, Chair

SCIENTIFIC ORGANIZING COMMITTEE (SOC)

Chair: Karri Muinonen (University of Helsinki & Finnish Geodetic Institute)
Vice-chair: Timo Nousiainen (University of Helsinki)
Edward Bowell (Lowell Observatory)
Alberto Cellino (Torino Astronomical Observatory)
James Hough (University of Hertfordshire)
Joop Hovenier (University of Amsterdam)
Hiroshi Kimura (Kobe University)
Gerrit de Leeuw (University of Helsinki)
Anny-Chantal Levasseur-Regourd (Université Pierre & Marie Curie)
Daniel Mackowski (Auburn University)
Pinar Mengüc (University of Kentucky)
Michael Mishchenko (NASA Goddard Institute for Space Studies)
Fernando Moreno (Institute for Astrophysics of Andalucia)
Jouni Peltoniemi (Finnish Geodetic Institute)
Yurij Shkuratov (Kharkov National University)
Wenbo Sun (NASA Langley Research Center)
Gorden Videen (Army Research Laboratory)
Nikolai Voshchinnikov (St. Petersburg State University)
Thomas Wriedt (University of Bremen)
Evgenij Zubko (University of Helsinki)

LOCAL ORGANIZING COMMITTEE (LOC)

Chair: Antti Penttilä
Hannakaisa Lindqvist
Päivi Mauno
Karri Muinonen
Timo Nousiainen
Dagmara Oszkiewicz
Mark Paton
Tuomo Pieniluoma
Jani Tyynelä
Evgenij Zubko

The local organizing committee members are from the main sponsoring organization, the Department of Physics, University of Helsinki (P.O. Box 64, FI-00014 University of Helsinki, Finland).

Contents

Conference articles

Monte Carlo simulation of light scattering from diatom frustules of *Gomphoneis sp.*

G. A. Ahmed*

Optoelectronics and Photonics Research Laboratory, Department of Physics, Tezpur University, Tezpur 784028, Assam, India.

Monte Carlo simulation of the light scattering pattern from diatom frustules of the species *Gomphoneis* was attempted by implementing Mie theory in conjunction with a subroutine which accounts for size distribution among the diatoms. A biotechnical procedure was followed in preparing the samples of diatom frustules which were used as samples for scattering measurements required for validating the simulations.

INTRODUCTION

In recent years, a tremendous amount of research has been done to understand the nature of electromagnetic scattering by spherical and nonspherical particles [1-3]. In addition to experimental and theoretical studies on light scattering by particulate matter, several groups have tried to simulate light propagation in scattering media [4-8]. Such Monte Carlo methods of solving the light scattering problems due to particulate matter have been proving to be a very successful tool in verifying experimental observations obtained by use of the different investigating instruments as well as lending support and improving the current theoretical models.

In this work we report the development of a program coded in C language for Monte Carlo simulation of light scattering from diatom frustules of *Gomphoneis species* and comparison of these simulations with experimental observations and theoretical predictions. The technique involved generation of light scattering intensity values as a function of scattering angle for a particular size and shape of diatom frustules. In case of simulation, the scattering intensity at each angle was represented by average of non-uniform random values generated by Monte Carlo method and computed on the basis of Mie theory. A normal size distribution was considered on the basis of images obtained by scanning electron microscope. The experimental observations of scattered light intensity from the diatom frustules were obtained using a designed and fabricated laser-based setup incorporating sixteen silicon detectors to monitor the scattered light [9].

DIATOMS

Diatoms are a group of single celled photosynthetic micro alga found in both fresh water and marine environment. Diatoms are unicellular structures with the protoplasts enclosed in an amorphous silica cell wall called frustules, consisting of two valves joined together by a girdle.

* Gazi A. Ahmed (gazi@tezu.ernet.in)

These structures in the diatom frustule range from micrometer to nanometer scales. These naturally synthesized 3D nanostructured materials are of great importance in recent research in nanotechnology from various points of view, which includes its morphology, mechanical properties, optical, and electrical properties. Researchers are reporting the potential application of diatom frustules in optoelectronics, biophotonics, gas sensor, filtration and targeted drug delivery. Out of the over 200 000 species of these photosynthetic algae with world wide distribution, our work here focuses on the light scattering properties from the particular *Gomphoneis species* of diatoms which is found locally in water in Assam, India. A sample (20 ml) of water containing diatoms was centrifuged at 6000 rpm for 15 minutes to allow sedimentation of the heavy diatom particles. The precipitate was suspended in 1 ml of distilled water and washed. The "WC" media proposed by Guillard and Lorenzen (1972) was used with slight modifications to culture the diatoms using the prepared sample as inoculum [10]. The solid culture plates were incubated at 22°C under white fluorescent light in a B.O.D. incubator (Narang Scientific Works, New Delhi) for 14 days. For the liquid culture, all the growth nutrients were dissolved in 1000 ml of sterile water and the media was autoclaved before inoculation with environmental samples.

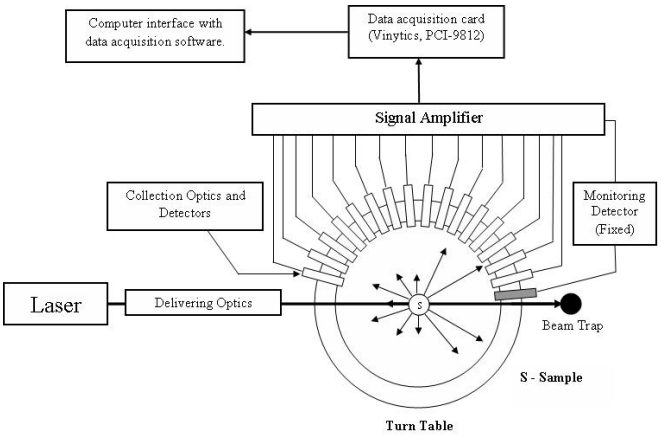

Figure 1. Experimental setup.

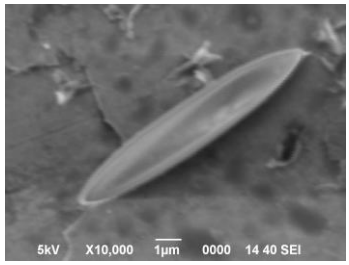

Figure 2. SEM micrograph of *Gomphoneis sp.*

EXPERIMENTS AND SIMULATION

The schematic diagram of the experimental setup is shown in Fig. 1. The setup consisted of a laser source, controlled sample holders, photodetector arrangements, data acquisition systems, and associated instrumentation. In this experiment we used a He-Ne laser source with 632.8 nm wavelength and an output power of 2 mW. The diameter of the beam cross-section was 2 mm and the distance between the source and the scattering centre was 250 mm. The laser light was scattered by a sample of fresh water diatoms suspended in water and placed at the scattering centre by a mechanical arrangement. The scattered light intensity was sensed by 16 static Si detectors (BPW34) having large sensitive area (7.5 mm^2) mounted on a circular disc and were connected to a high gain, low noise amplifier circuit. The amplified

signals were interfaced to a dedicated data acquisition system (Vinytics, PCI-9812) for data recording. The whole array of 16 detectors could be rotated simultaneously about an axis perpendicular to the plane of the circular disc. Readings were in steps of 1° from an angle of 10° to 170° and each detector was separated from the next one by an angle of 10°.

The simulation process involved the generation of uniform random numbers and then forcing the uniform random numbers into a non-uniform pattern governed by Mie-theory (using it as a probability distribution function) by using the Inverse transformation method. Fig. 3 gives the algorithm for such a process. The photons in the simulation program were shared unequally among the diatoms of different size which were governed by a normal size distribution function. Finally, this simulated plot for the phase function of the Mueller matrix was compared with the experimental and theoretical plots.

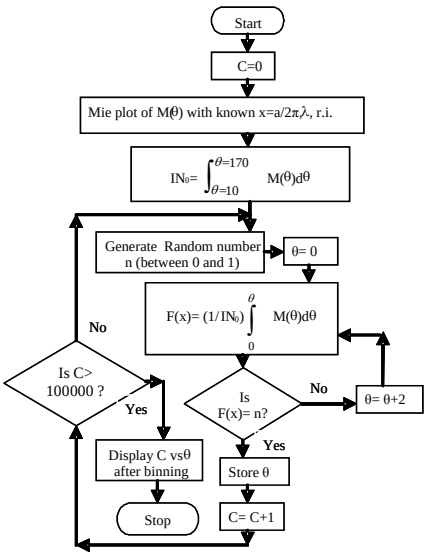

Figure 3. Simulation flowchart.

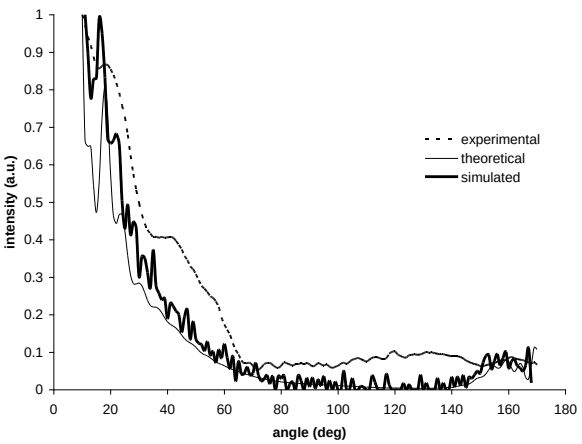

Figure 4. Plot of intensity vs. angle.

RESULTS AND DISCUSSION

Figure 4 shows the simulated plot superposed on the experimental and theoretical plot (Mie theory) obtained for diatom frustules of *Gomphoneis species* with a length of around 7 μm. Normal size distribution with a standard deviation of 5 % was considered for simulation. The simulation results are fairly consistent with the theoretical predictions for the diatoms. However, there is a noticeable deviation of both the simulated and theoretical plots from the experimental plot. One of the reasons for this discrepancy is because of the inadequacy of Mie theory in case of diatom structures with a very high asphericity aspect ratio. Moreover, the non-uniformity of the surface of these diatom frustules also plays a role in this discrepancy. Yet, it can be seen from Fig. 4 that the simulated plot tends more towards the experimental

results in comparison to the theoretical plot especially in the forward scattering region between 10° and 60°.

Although it is difficult to simulate for diatoms with very complex structures using current theories alone, a combination of different techniques will be tried in the future for further investigations of more complex diatoms.

REFERENCES

[1] C.F. Bohren and D.R. Huffman. *Absorption and Scattering of Light by Small Particles*. New York: Wiley (1983).

[2] M.I. Mishchenko, J.W. Hovenier, and L.D. Travis (eds). *Light Scattering by Nonspherical Particles: Theory, Measurements, and Applications*. San Diego, California: Academic Press (2000).

[3] M.I. Mishchenko, L.D. Travis, and A.A. Lacis. *Scattering absorption and emission of light by small particles*. Cambridge University Press (2002).

[4] H.T. Chuah and H.S. Tan. A Monte Carlo Backscatter model for radar backscatterer from a half space random medium. IEEE Trans. Geosci. Remote Sens. **27** (1998).

[5] S. Bartel and A.H. Hielscher. Monte Carlo simulations of the diffuse backscattering Mueller matrix for highly scattering media. Appl. Opt. **39** (2000).

[6] B.D. Cameron et al. Measurement and calculation of the two- dimensional backscattering Mueller matrix of a turbid medium. Optics Letters **23**(7) (1998).

[7] L.H. Wang, S.L. Jacques, and L. Zheng. MCML-Monte Carlo modeling of light transport in multilayered tissues. Comput. Methods Programs Biomed. **47** (1995).

[8] B. Kaplan, G. Ledanois, and B. Drevillon. Mueller matrix of dense polystyrene latex sphere suspensions: Measurements and Monte Carlo simulation. Appl. Opt. **40** (2001).

[9] A. Gogoi, A.K. Buragohain, A. Choudhury, and G.A. Ahmed. Laboratory measurements of light scattering by tropical fresh water diatoms. Journal of Quantitative Spectroscopy & Radiative Transfer **110** (2009).

[10] R.R.L. Guillard and C.J. Lorenzen. Yellow-Green algae with chlorophyllide c. Journal of Phycology **8** (1972).

Mie theory applications to study response of metallic nanospheres in a nanocomposite medium

S. Benghorieb[1,2], R. Saoudi[1], and A. V. Tishchenko[*,1]

[1]*Hubert Curien Laboratory, University Jean Monnet, 18 rue Benoit Lauras, 42000 Saint Etienne, France.*
[2]*Microsystems and Instrumentation Laboratory, University Mentouri, route d'Ain El Bey, Constantine 25000, Alger.*

In this work we present two Mie theory applications for electromagnetic wave scattering by a sphere. The first concerns the change in the refractive index of a dielectric matrix in the presence of metal nanospheres. We develop on the basis of Mie formalism a novel technique to determine the effective index of a composite nanostructure. The second application concerns the extraction of the plasmon field on a metal nanosphere placed in a dielectric matrix. We present some results on effective index variation as well as on the plasmon field distribution.

INTRODUCTION

The refractive index of a material is the key parameter that determines its main optical properties. The possibility to control its variations is, therefore, of interest in many applications in photonics and optoelectronics. Modification of the refractive index can provide new optical properties of absorption, dispersion, and transmission. This helps building a new optical response related to created index changes. We are interested in the index changes produced by metal particles in a dielectric as the effects of surface plasmons are prominent in the spectrum. This allows for manufacturing selective filters and for control of colors. Theories dealing with material index changes produced by metal particles are relatively less developed and reliable. The only rigorous theory in this field is developed by Mie (1908), but his method is not directly applicable to the index calculation. The electrostatic approach (Maxwell-Garnett, 1904) allows for index calculation but it is limited by the case of small particles (~ 10 nm). The aim of our work is to fill this gap by further developing the Mie theory to determine the modified index of dielectric matrix in the presence of metallic nanoparticles

The interaction of light with spherical metal particles reveals a particular behavior, namely, a large field located on the particle surface. This effect is due to a collective oscillation of free electrons on the metal surface excited by the incident light. Many numerical methods have been developed to model this effect. But all these classical approaches describe all fields in the vicinity of the sphere, while our approach, based on the Mie formulation, is capable to filter the resonant plasmon field.

* Corresponding author: Alexandre V. Tishchenko (alexandre.tishchenko@univ-st-etienne.fr)

RESULTS AND DISCUSSION

Calculating the change in index of a dielectric matrix in the presence of metal nanospheres using the Mie theory, we present some results for silver particles in SiO_2 matrix and gold particles in TiO_2 matrix. First, we treat the case of a single sphere. Figure 1 represents spectral dependence of the real and imaginary parts of the index change of SiO_2 in the presence of silver nanoparticles of variable size (10 nm to 30 nm). The curves are normalized to the concentration of silver particles.

Absorption and dispersion in the matrix depend strongly on the particle size. Absorption increases with the size of particles. The plasmon resonance moves towards large wavelengths with growth of the particle size. We also note an increase of the width of resonance peak with the particle size. This offers a possibility of using such objects as spatially and spectrally selective optical filters. The same tendency, with the size and the wavelength, is observed for the real part of the index change in the dielectric. This helps to understand and predict how the electromagnetic wavefront is disturbed in the vicinity of silver nanoparticle and then calculate the resulting phaseshift. To this end, the refractive index perturbation by the spherical particle can be defined from the real part of matrix element $S(0)$ [1]. The index change spectral behavior is similar to that known for the Lorentz model but the fundamental difference is that here we consider the resonance with surface plasmons.

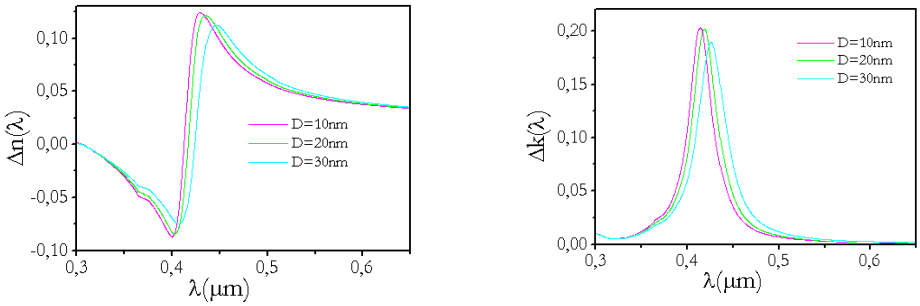

Figure 1. Real and imaginary parts of SiO_2 refractive index variations in presence of silver nanospheres of diameter D=10, 20, 30 nm.

EXTRACTION OF THE PLASMON FIELD FROM THE MIE SCATTERING

The scattered field near the sphere can be expressed as the sum of a singular part that defines the plasmon field and a regular part representing all other fields [2]:

$$\mathbf{E}(\mathbf{r},\omega)=\frac{\omega_p \mathbf{E}_p(\mathbf{r})}{\omega-\omega_p}+\sum_{n=0}^{\infty}\mathbf{E}_n(\mathbf{r})\left(\frac{\omega-\omega_p}{\omega_p}\right)^n, \qquad (1)$$

where ω_p is the resonance frequency, $\mathbf{E}_p(\mathbf{r})$ is the plasmon electric field, and $\mathbf{E}_n(\mathbf{r})$ are power moments of the regular part of the electric field. To calculate the plasmon field, we

extract first the frequency of the plasmon resonance. Note that the latter represents the singular term in Eq. (1). To this end, we use numerical approach developed in [2].

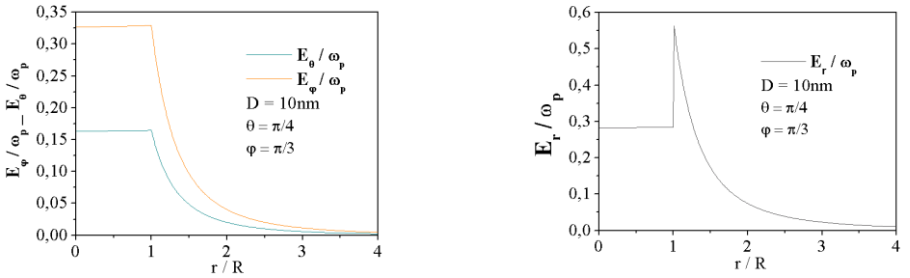

Figure 2. Component modulus a) radial, b) polar of the plasmon field of an Au nanosphere of diameter D = 10 nm embedded in a TiO_2 matrix.

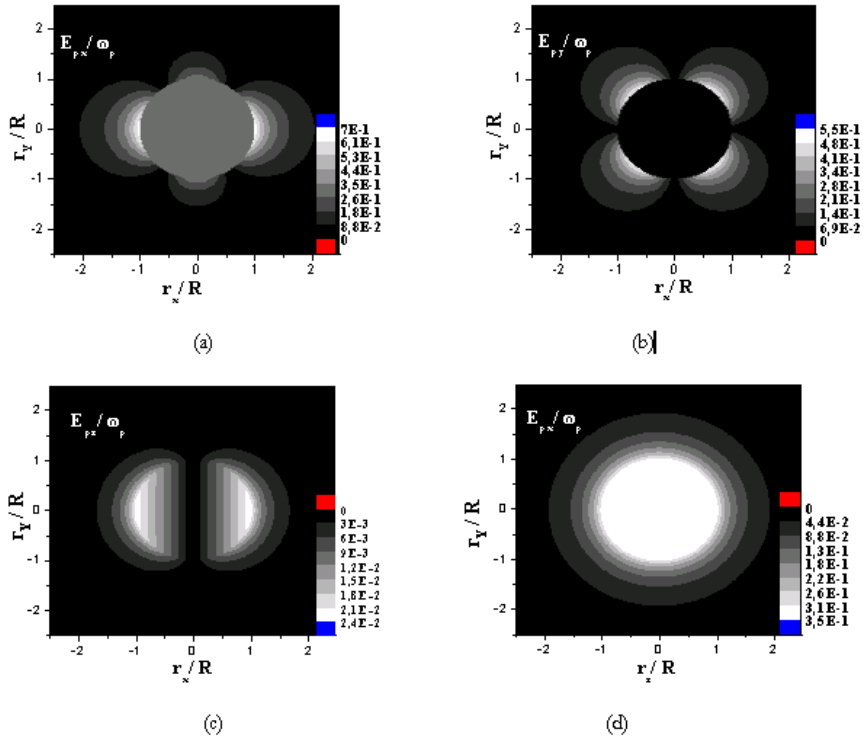

Figure 3. The plasmon electric field distribution on an Au nanosphere (D = 10 nm) in a TiO_2 matrix: a) E_{xp}, b) E_{yp}, c) E_{zp} in plane xOy, d) E_{xp} in plane yOz.

Plasmon-field calculation in spherical coordinates

In this section, we present our first results for Au nanospheres of diameter D = 10 nm in a titanium dioxide matrix. The incidence is along the z axis, polarisation is along the x axis. The direction in which the field components are calculated is taken at angles $\theta = \pi/4$ and

$\varphi = \pi/3$. We represent the moduli of three field components E_r, E_θ, E_φ in spherical coordinates. Figure 2 shows the radial and polar electric field components. The field is uniform inside the metal sphere. A strong plasmon field is concentrated at the surface of the particle and decreases exponentially with distance from the interface. In this respect, it is quite different from the field given by the dipole approximation in the quasi-static limit (the small size of the sphere).

Plasmon-field calculation in Cartesian coordinates

Figure 3 shows the distribution of the plasmon field of a gold nanosphere of diameter D = 10 nm in the xOy plane. Both components E_{px} and E_{py} (Fig. 4a, b) are homogeneous in the metal. Contrary to the dipole field, component E_{pz} did not vanish though it is very small (Fig. 3c). The interference of plasmons turning around the sphere leads to the null value of field E_{py} at four points. The electric field in the interior of the particle coincides with the incident wave polarization (Fig. 3d) and is very homogeneous because of small particle size. Such angular behaviour is similar to that given by the quasi-static approximation.

CONCLUSIONS

The possibility of determining the effective index of a composite material and extract the plasmon field on a metal nanosphere by the Mie scattering on a sphere offers perspectives for study of optical properties of metallic nanoparticles and composite media. This approach is capable to predict and explain the disturbances (absorption, phase shift, dispersion) that can undergo a plane electromagnetic wave when it crosses a composite medium. It applies to a wide class of particles and matrices.

The numerical results show that the plasmon field is localized near the metal/dielectric interface. The presented method demonstrates its capability to extract the exact plasmon field independently of all other fields around the sphere.

REFERENCES

[1] A. García-Valenzuela, R. G. Barrera, C. Sánchez-Pérez, A. Reyes Coronado, and E. R. Méndez. Coherent reflection of light from a turbid suspension of particles in an internal-reflection configuration: Theory versus experiment. Opt. Express **13** (2005).

[2] A. V. Tishchenko, M. Hamdoun, and O. Parriaux. Two-dimensional coupled mode equation for grating waveguide excitation by a focused beam. Opt. and Quantum Electron. **35** (2003).

Retrieval of particle parameters with the neural network using multi-angle light-scattering data

V. Berdnik[1], O. Gritsai[2], and V. Loiko[*,2]

[1]*Techniques of Hydrogeological Investigation S.A., Kazan, 420015 Russia.*
[2]*Institute of Physics of the NASB, Nezavisimosti ave. 68, Minsk, 220072 Belarus.*

A method to retrieve radius and refractive index of spherical homogeneous non-absorbing particles by multi-angle scattering is proposed. It is based on formation of the noise resistant functionals of intensity, which are invariant relative to linear homogeneous transformations of an intensity-based signal, and approximation of the retrieved parameters' dependence on the functionals by a feed-forward neural network. The method allows reducing retrieval errors in the region of small sizes and refractive indices of particles close to unity.

INTRODUCTION

The problem of retrieval of disperse particle characteristics often arises in science and engineering. Efforts of researchers to solve this problem have led to the evolution of numerous methods. The choice of the method depends on particle characteristics and measurement conditions. Among the choices are light-scattering methods that are fast and noninvasive [1].

The problem of particle parameter retrieval belongs to one type of inverse problems. In recent years, the neural-network method is widely used to solve the inverse light scattering problems [2, 3]. In the neural-network method, the main computer time is spent in training the network. Once trained, the network determines the particle characteristics very quickly. Large stability to random errors can be achieved. These are the advantages of the method. In the present paper, the feed-forward neural network is used to retrieve parameters of homogeneous spherical particles using multi-angle scattering data.

CONSTRUCTION AND TRAINING OF A NEURAL NETWORK

We consider a problem of retrieval of a particle radius R and relative refractive index n by the intensity of light scattered in the interval of angles from 10^o up to 60^o. This range of angles is available for measurements in a new generation of scanning flow cytometers [4]. The particle is illuminated by a non-polarized beam of light. The wavelength λ of the incident light in a medium is equal to 0.476 μm. The particle radius ranges from 0.6 μm to 13.6 μm, the relative refractive index ranges from 1.015 to 1.28. To retrieve the particle parameters the feed-forward neural network is used [5].

An element of the neural network is a neuron, which calculates the weighted sum of signals entered as its input and transforms the results according to a non-linear function.

* Corresponding author: Valery Loiko (loiko@dragon.bas-net.by)

Using the redistribution system, the signals from the outputs of neurons of the first layer are passed to inputs of the neurons of the second layer. The neurons of the second layer process the signal in the same manner as the first one and pass the signal to the input of the neuron of the next layer. The output signal of the *N*-layer neuron network of forward propagation is:

$$y_l^{out} = F\left(\sum_k w_{lk}^N y_k^N = \cdots F\left(\sum_j w_{tj}^2 y_j^2 = F\left(\sum_i w_{ji}^1 y_i^1 = y_i^{in}\right)\right)\right). \quad (1)$$

Here y_i^1, y_j^2, … , y_k^N are the signals at inputs of the 1st, 2nd , …, *N*th layer of the neural network, w_{ji}^1, w_{ji}^2,…, w_{lk}^N are the weight coefficients of the neurons of the 1st, 2nd , …, *N*th layer of the neural network; *F*(x) is the neuron activation function [5].

Usually, vectors of input signals for each layer contain the permanent unit signal y_0^n, where n = 1, 2, 3. It is supposed that all neurons have an identical activation function. We use the continuous function which is obtained from the function given in [6]:

$$F(x) = \frac{1}{x_{\max} - x_{\min}}\left(\sqrt{\beta + (x - x_{\min})^2} - \sqrt{\beta + (x - x_{\max})^2}\right), \quad (2)$$

where $x_{\min}$, $x_{\max}$, and β are parameters.

Simplicity and an opportunity to change the form of the activation function in a wide range are advantages of Eq. (2). We used the function $F(x)$ at $x_{\min}$ = -1, $x_{\max}$ =1, and β = 0.1. From Eq. (2), it is easy to obtain an expression for derivative of function $F(x)$, which is used at the neural-network training:

$$F'(x) = \frac{1}{x_{\max} - x_{\min}}\left(\frac{x - x_{\min}}{\sqrt{\beta + (x - x_{\min})^2}} - \frac{x - x_{\max}}{\sqrt{\beta + (x - x_{\max})^2}}\right). \quad (3)$$

To train the neural network, it is necessary to find weight coefficients of the neurons of all layers using the least-squares minimization method. It is better to minimize relative errors of measurements than the absolute ones, as the particle parameters can vary in a wide range. It leads to a problem of the minimization of a square-law form at training of the neural network for determination of radius

$$\Phi = \frac{1}{2}\sum_{\alpha=1}^{N_B}\left(\frac{y^{out}\left(w_{ji}^1, \ldots, w_k^N, y_{i\alpha}^{in}\right)}{R_\alpha} - 1\right)^2 \quad (4)$$

and relative refractive index

$$\Phi = \frac{1}{2}\sum_{\alpha=1}^{N_B}\left(\frac{y^{out}\left(w_{ji}^{1},...,w_{k}^{N},y_{i\alpha}^{in}\right)-1}{n_\alpha - 1}-1\right)^2, \quad (5)$$

respectively. Here α = 1, 2, …, N_B, and N_B is the number of samples in the training database.

After transformations of Eqs. (4) and (5), we can write

$$\Phi = \frac{1}{2}\sum_{\alpha=1}^{N_B}\frac{1}{s_\alpha^2}\left(y^{out}\left(w_{j}^{1},...,w_{lk}^{N},y_{i\alpha}^{in}\right)- p_{n\alpha}\right)^2. \quad (6)$$

Here $p_{n\alpha}$ is the normalized value of parameter $\sigma_\alpha = R_\alpha - a_R$ in training of the neural network at the radius determination and parameter $s_\alpha = n_\alpha - a_n$ - b_n in training of the neural network at the relative-refractive-index determination. To solve the optimization problem Eq. (6), the limited memory BFGS method [7] was used.

Calculations show that the criterion function $\Phi\left(w_{ji}^{1},...,w_{lk}^{N},y_{i\alpha}^{in}\right)$ has many minima, where values are approximately the same. In such conditions, searching of a global minimum can take vast amounts of time. Therefore, we found three (or four) local minima, starting from the point with coordinates chosen by the random-number generator from the interval [-1, 1]. We used the minimum providing the minimal value of the criterion function.

ESTIMATION OF ERRORS OF PARTICLE PARAMETERS RETRIEVAL

In training the neural network, we used the book of problems containing 10^4 samples randomly chosen from the range of considered parameters. If the set of samples is insufficiently representative, the stability of the neural network to input data changes is low. The neural network well trained on the samples from the book of problems can give significant errors on the other samples. We verified the work of the neural network using 10^4 samples which were different from the samples used in the neural-network training. To increase the stability of the neural network, the amount of the neurons of the internal network layers was decreased and random noise in the input data was introduced.

The correlation dependences of the original values of parameters R and n and the retrieved values of R_e and n_e were obtained. The values of R_e and n_e were calculated using the three-layer neural network with 10 neurons in the internal layer. Comparison with the results obtained with the neural networks trained with the minimal absolute error revealed that the proposed technique enables the parameter retrieval error in the interval of small sizes and close to unity relative refractive indices to be essentially reduced.

The mean relative error of radius retrieval was estimated as follows:

$$\delta R = \frac{1}{A}\sum_{\alpha=1}^{A}\left|1-\frac{R_{e\alpha}}{R_\alpha}\right|, \quad (7)$$

where $R_{e\alpha}$ are the retrieved values of radius; R_α is the original value of radius.

To evaluate the error of the relative refractive index retrieval the quantity was used

$$\delta n = \frac{1}{A}\sum_{\alpha=1}^{A}\left|1-\frac{n_{e\alpha}-1}{n_\alpha-1}\right|. \quad (8)$$

Here $n_{e\alpha}$ are the retrieved values of relative refractive index; n_α is the original value of relative refractive index.

CONCLUSION

A method to retrieve radius and relative refractive index of non-absorbing homogeneous spherical particles by light scattered in the range of angles 10^o – 60^o is proposed. It is based on the construction of the scattered intensity signal, which is invariant with respect to the linear homogeneous transformations, and on the approximation of the dependence of the retrieved parameters on the signal functionals by the neural network of forward propagation.

To verify the proposed technique, experimental data [4] on angular dependences of scattered light obtained by the scanning flow cytometry were used. We retrieved the particle parameters by the neural network and by the least-squares method. The relative deviation of parameters found with the neural network and the least-squares method does not exceed 4.3 % for radii and 3.8 % for refractive index.

REFERENCES

[1] R. Xu. *Particle characterization: light scattering methods*. Kluwer Academic Publishers, Dordrecht (2000).

[2] Z. Ulanowski et al. Application of neural networks to the inverse light scattering problem for spheres. Appl. Opt. **37** (1998).

[3] V. V. Berdnik and V. A. Loiko. Retrieval of size and refractive index of spherical particles by multiangle light scattering. Appl. Opt. **48** (2009).

[4] V. Maltsev and K Semyanov. *Characterization of Bio-Particles from Light Scattering*. VSP, Utrecht (2004).

[5] S. Haykin. *Neural Networks – A Comprehensive Foundation*. Prentice Hall (1999).

[6] X.-P. Zhang. Thresholding neural network for adaptive noise reduction. IEEE Transactions on Neural Networks **12** (2001).

[7] D. Liu and J. Nocedal. On the limited memory BFGS method for large scale optimization. Math. Prog. B **45** (1989).

Holographic imaging of particles

M. J. Berg[*,1,2] and G. Videen[1]

[1] *US Army Research Laboratory, 2800 Powder Mill Road, Adelphi, MD 20783-1197 USA.*
[2] *Department of Physics and Astronomy, Mississippi State University, Mississippi State, MS 39762 USA.*

This work describes the imaging of particles using in-line holography. Single particles are confined in an electrodynamic trap and illuminated by a focused laser beam. A CCD camera is used to record the resulting hologram from which an image of the particle is reconstructed computationally. Examples involving a single glass microsphere and multiple Tunisian sand particles are presented.

INTRODUCTION

The *in situ* characterization of small particles is a persistent objective in applied electromagnetic scattering. Countless examples of measurements and theoretical modeling of the scattering patterns of single and multiple particles can be found in the literature. A typical goal of such work is to infer information relating to the particles' physical form, such as size and shape, by analyzing the angular structure of the scattering patterns. This inference has proved to be very difficult in practice, except for the simplest of cases.

Ideally, one would prefer to image particles directly, thus eliminating the complexity and ambiguity associated with interpretation of the scattering patterns. However, for micrometer sized particles, *in situ* imaging using conventional geometrical optics is not feasible due to the variability of particle position, optical aberrations, diffraction, and the limited numerical aperture of the imaging system. Holography is an alternative that can provide particle images while being free of these limitations. This work will present an apparatus to measure single and multiple-particle holograms and demonstrate the computational reconstruction of particle images from the holograms.

HOLOGRAPHIC IMAGING

In the context of this work, holography is the measurement of the *interference* between the light illuminating a particle and the particle's far-field scattered wave. This interference pattern constitutes a system of fringes measured by the detector, the specific structure of which is controlled by the local relative phase between the illuminating and scattered waves across the detector face. Consequently, the hologram is as complicated as the associated scattering pattern. However, unlike the scattering pattern, a simple computational operation can be performed to render an image of the particle. In short, the hologram is regarded as a transmission diffraction grating and the Fresnel-Kirchhoff (FK) integral is used to calculate its near-field diffraction pattern under plane-wave illumination. This calculation can be done rapidly since the FK integral is evaluated using fast Fourier transforms. The reconstruction

*Corresponding author: Matthew J. Berg (mberg81@gmail.com)

is done in a plane that is parallel to the hologram; if the plane corresponds to the plane containing the particle during the measurement, the resulting diffraction pattern produces an image of the particle [1]. Otherwise, a blurred image results. The resolution of the image is ultimately limited by the pixel size of the CCD and the wavelength [1]. It is for this reason that computer-based holographic image-reconstruction is a relatively new technology; large CCD arrays with sufficiently small pixels have only recently become economical and widely available.

APPARATUS AND MEASUREMENTS

Fig. 1 shows a picture (a) and the corresponding diagram (b) of the apparatus used to measure single-particle holograms. The design is based on the so-called in-line configuration, where the particle, optical components, and detector are all co-linearly arranged. The light source is a 70 ns pulsed Nd:YAG laser, frequency doubled to 532 nm. This light passes through a Glan-Thompson (GT) polarizer to ensure linear polarization of the light before being focused by lens L_1 onto a 50 μm diameter high-power pinhole. An iris (I) is used to block all but the primary lobe of the pinhole diffraction pattern from reaching a second lens (L_2). This short focal-length lens brings the lobe to a tight waist at a location near the trapping volume of a spherical-void electrodynamic levitator (SVEL). A particle confined in this volume is illuminated by the light diverging from the waist; hence, the waist effectively acts as a virtual point source producing a spherical wave. This wave continues to expand until it reaches the CCD detector along with the scattered light from the particle. The resulting interference pattern between these waves across the CCD constitutes the hologram.

By using a short focal-length lens to form a virtual source near the particle, the light illuminating the particle is more intense than it would be if only the pinhole was used for illumination. This results in a relative amplification of the particle's scattered wave at the CCD face, which enhances the interference structure of the hologram leading to improved particle-image quality. Using a pulsed laser permits the investigation of particle systems in motion. This is especially useful for aerosol applications where particles may be delivered to the apparatus in a flowing stream.

The in-line configuration used to form the hologram is traditionally problematic since the reconstruction process produces both a real and virtual image [1]. These twin images overlap in the reconstruction plane; if one is in focus, the other is blurred and diminishes the quality of the focused image. Using the computational techniques of Xu et al., the influence of the out-of-focus twin image is suppressed in the reconstruction stage [2]. The advantage of the in-line configuration, however, is that it typically requires the least number of optical components. This is important when imaging micrometer-sized particles because ambient dust, which is of similar size and inevitably collects on these surfaces, will contribute to the hologram leading to noise and ambiguity upon reconstruction.

Fig. 2 shows two examples of the particle holograms and their corresponding reconstructed particle-images. One can see in these plots that the technique is successful in imaging particles as small as 20 μm and as large as 300 μm. Modifications to the optical apparatus are planned that are intended to improve the resolution of the imaging process. The ultimate goal of these modifications is to image particle with nominal sizes from one to ten microns,

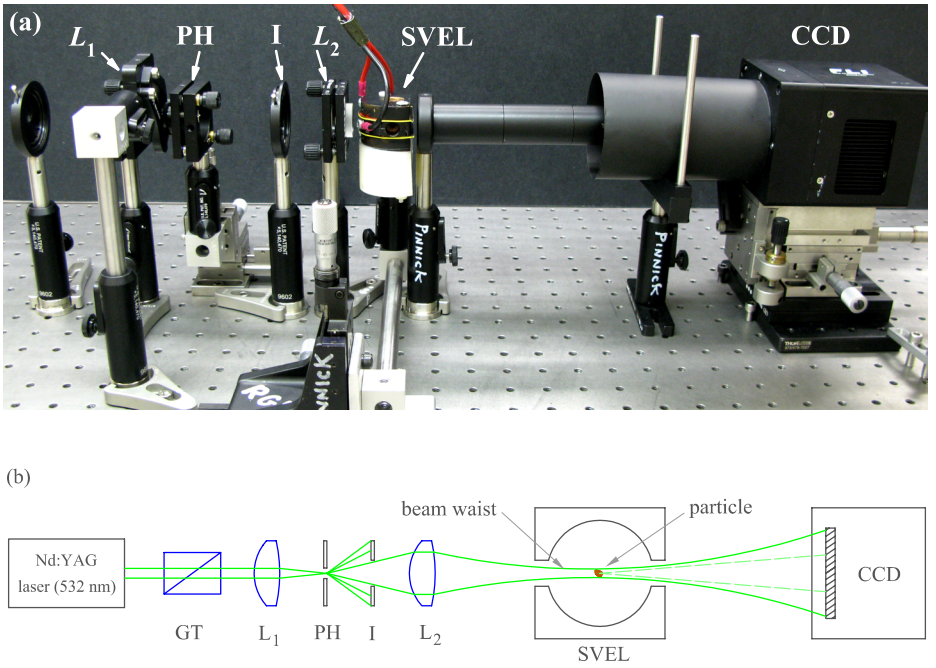

Figure 1. Holographic imaging apparatus (a) and corresponding diagram (b).

which covers much of the size range of environmental aerosols.

ACKNOWLEDGMENTS

This work is supported by a National Research Council Postdoctoral Fellowship, funded by the US Defense Threat Reduction Agency, contract no. DAAD17-03-0070. The authors are thankful for the advice given by Drs. Y.-L. Pan and Dave Ligon.

REFERENCES

[1] T. Kreis, *Handbook of holographic interferometry: Optical and digital methods*. Wiley-VCH, Weinheim (2005).

[2] W. Xu, M.H. Jericho, I.A. Meinertzhagen and H.J. Kreuzer. Digital in-line holography of microspheres. Appl. Opt. **41** (2002).

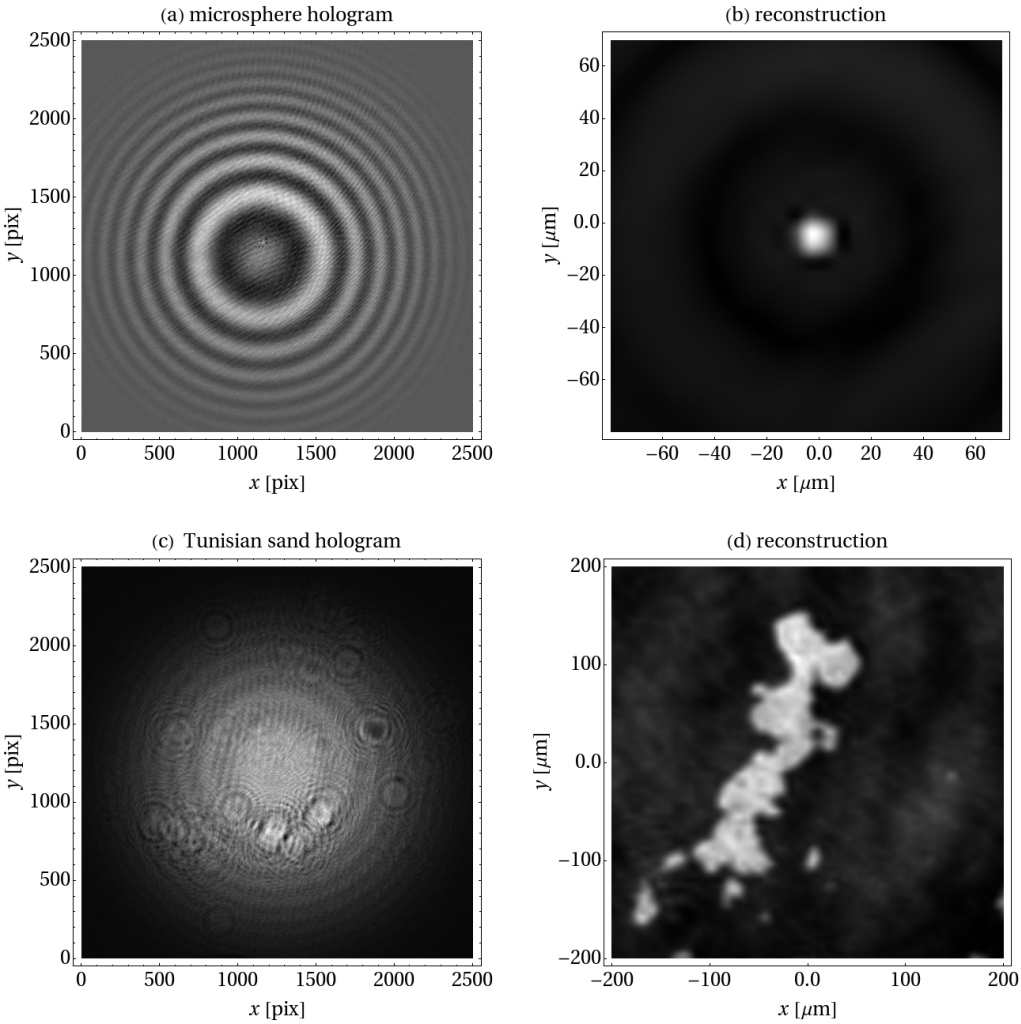

Figure 2. Particle holograms and their reconstructed images. Plot (a) shows the hologram produced by a single 20 µm diameter glass microsphere trapped in the SVEL. The image of this particle reconstructed from the hologram in (a) is shown in (b). The hologram in (c) corresponds to a sample of Tunisian sand particles sprinkled onto a glass slide and placed at the location of the SVEL in Fig. 1. This is done because the sand is too large to be suspended in the SVEL. The reconstructed images of these particles is shown in (d), where one can clearly see the clustered, nonspherical nature of the particles.

Light scattering by large faceted particles

A. Borovoi* and N. Kustova

V.E. Zuev Institute of Atmospheric Optics, Academician Zuev sq. 1, Tomsk 634021 Russia.

The problem of calculation of the scattering matrices for large faceted particles within the framework of physical optics is split into three steps. First, we find the matrix in the geometric optics approximation. Second, we calculate the so-called Fraunhofer diffraction matrix. And, finally, the matrix desired is found as an integral transform of the geometric optics matrix by means of the Fraunhofer matrix.

INTRODUCTION

The problem of light scattering by large, as compared with the incident wavelength λ, non-spherical particles, i.e. $a >> \lambda$ where a is a characteristic particle size, is successfully solved on the basis of the Maxwell equations if the size parameter $\rho = a/\lambda$ does not exceed, the value of about 10 (see e.g. [1]). The opposite case $\rho >> 1$ is conventionally calculated by use of geometric optics, in particular, by means of the ray-tracing technique [2]. To fill the gap of the intermediate case of $\rho \approx 10$, physical optics is an obvious and rather simple instrument [3-6]. However the physical-optics approximations are often restricted by taking into account only diffraction near the forward-scattering direction, which is produced by particle projections or shadows (e.g., [7]).

In the case of large faceted particles like atmospheric ice crystals, the problem of light scattering within the framework of physical optics can be analytically reduced to a simple extension of the geometric-optics solution that is the topic of this presentation.

GEOMETRIC-OPTICS AND PHYSICAL-OPTICS SCATTERED WAVES

In general, a solution for any electromagnetic wave scattered by a particle is defined by a superposition of the incident $\mathbf{E}^0$ and scattered $\mathbf{E}^s$ waves

$$\mathbf{E} = \mathbf{E}^0 + \mathbf{E}^s \tag{1}$$

at any spatial point $\mathbf{r}$. At large distances from the particle, the scattered wave $\mathbf{E}^s$ is conventionally considered on the scattering direction sphere $\mathbf{n}$ ($|\mathbf{n}| = 1$) as the function $\mathbf{E}^s(\mathbf{n})$. In

* Corresponding author: Anatoli Borovoi (borovoi@iao.ru)

the near zone, i.e. at a distance $r << ka^2$ where $k = 2\pi/\lambda$ is the wavenumber, the scattered wave for a large faceted particle becomes strictly a superposition of discrete plane-parallel beams leaving the particle at various propagation directions

$$\mathbf{E}^s = \sum_{j=0}^{\infty} \mathbf{E}_j^s \,. \tag{2}$$

Here every beam $\mathbf{E}_j^s(\mathbf{r})$ is characterized by its transversal size and shape, polarization and propagation direction $\mathbf{n}_j$. At large distance from the particle $r >> a$, the beam propagation directions $\mathbf{n}_j$ become equivalent to the scattering directions, and the scattered wave on the scattering direction sphere $\mathbf{n}$ is reduced to a singular function. This singular function is strictly the superpositions of the Dirac delta-functions $\delta(\mathbf{n} - \mathbf{n}_j)$. Fig. 1 shows an example of the functions calculated for a fixed particle orientation. Note that the superposition of Eq. (2) includes not only the beams produced by an arbitrary number of reflections and refractions on the particle facets but also a shadow-forming beam (see e.g. [6, 8]). Appearance of the shadow-forming beam follows immediately from the superposition of Eq. (1) by subtraction of the incident wave from the total one. The shadow-forming beam propagates in the incident direction $\mathbf{n}_0$ and its transversal shape corresponds to the particle projection.

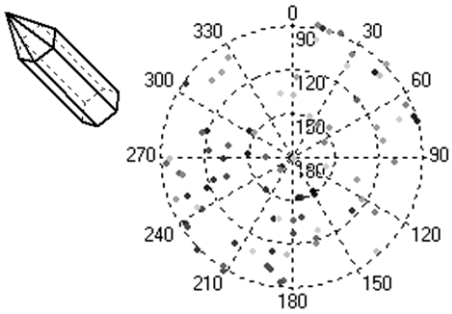

Figure 1. Phase function for a bullet ice crystal of a fixed orientation. The brightness of the dots is proportional to energy of the beams.

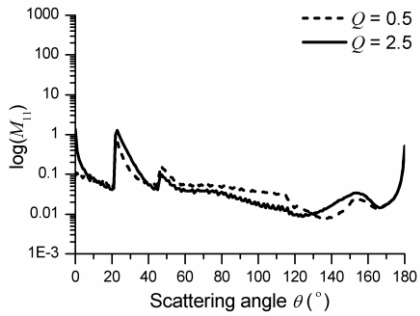

Figure 2. Phase functions for randomly oriented hexagonal ice plate and column (Q=diameter/length).

When the singular functions like those shown in Fig. 1 are averaged over particle orientations the δ-function singularities are smoothed in the majority of directions $\mathbf{n}$ resulting in some regular functions as shown in Fig. 2. Nevertheless some singularities still are left at certain directions manifesting themselves in Fig. 2 as sharp peaks. Note that the appearance of singularities is typical for the majority of functions obtained within the framework of geometric optics.

The superpositions of Eqs. (1) and (2) remain valid at arbitrary distances from the particle. As a result, in the wave zone $r >> ka^2$ every dot in Fig. 1 should be smeared into a Fraunhofer diffraction spot. In other words, the δ-functions $\delta(\mathbf{n} - \mathbf{n}_j)$ should be replaced by

the Fraunhofer diffraction functions $F_j(\mathbf{n}-\mathbf{n}_j)$ obeying the same normalization $\int F_j(\mathbf{n})d\mathbf{n}=1$. Similar replacements should also take place for any values averaged over an arbitrary probability distribution of particle orientations like the curves in Fig. 2. In general, we find the Mueller scattering matrices of the physical optics approach $\mathbf{M}_P$ become the following integral transform of the geometric optics matrix $\mathbf{M}_G$

$$\mathbf{M}_P(\mathbf{n},\mathbf{n}_0)=\int \mathbf{F}(\mathbf{n},\mathbf{n}')\mathbf{M}_G(\mathbf{n}',\mathbf{n}_0)d\mathbf{n}', \tag{3}$$

where the matrix $\mathbf{F}$ takes into account the Fraunhofer diffraction of the near-zone plane-parallel beams along with their interference on the scattering direction sphere $\mathbf{n}$.

SPECULAR (ONCE-REFLECTED) SCATTERING

For a large faceted particle with random orientation, the light once–reflected by its facets can be calculated analytically. In our recent paper [9], we have considered the general case of an arbitrary distribution of such a particle over its orientation. In particular, if the normal $\mathbf{N}$ to a particle facet is distributed as $p(\mathbf{N})$, the average specular intensity $I_G(\mathbf{n})$ produced by reflection from this facet is described by the following equation

$$I_G(\mathbf{n})=(s/4)R\left(\mathbf{n}\cdot\frac{\mathbf{n}-\mathbf{n}_0}{|\mathbf{n}-\mathbf{n}_0|}\right)p\left(\frac{\mathbf{n}-\mathbf{n}_0}{|\mathbf{n}-\mathbf{n}_0|}\right), \tag{4}$$

where s is the facet area and R is the Fresnel reflection coefficient.

For convex particles, the total specular scattering intensity is just a sum of intensities obtained by means of Eq. (4) for all facets. Then, if a facet can be approximately replaced by a circle, there is an analytical equation for the Fraunhofer diffraction functions (see Eq. (16) of Ref. [9]). And, finally, 2D-convolution of the geometric optics value of Eq. (4) with the diffraction function $\mathbf{F}$ results in the specular phase function in the physical optics approximation. This result is a simplified case of the general equation (3).

BACKSCATTERING BY HEXAGONAL ICE CRYSTALS

The proper geometric optics values for the case of ice hexagonal crystals were studied in details in our previous paper [10]. In particular, we proved that there are four types of photon trajectories that make contributions to backscattering. Unlike the abovementioned problem of specular scattering, this calculation is more complicated since we have to take into account the singularity appearing in the geometric optics approximation at the strict backward direction. We overcome these difficulties by cumbersome numerical calculations. The results obtained will be presented at the conference.

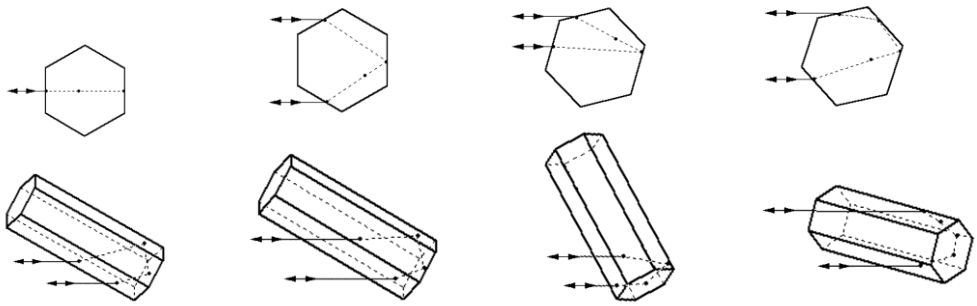

Figure 3. Four types of photon trajectories making main contribution to backscattering.

REFERENCES

[1] M.I. Mishchenko, L.D. Travis and A.A. Lacis. *Scattering, absorption, and emission of light by small particles.* Cambridge University Press, Cambridge (2002).

[2] K.N. Liou. *An introduction to atmospheric radiation.* Academic Press, San Diego (2002).

[3] K. Muinonen. Scattering of light by crystals: a modified Kirchhoff approximation. Appl. Opt. **28** (1989).

[4] P. Yang and K.N. Liou. Geometric-optics-integral-equation method for light scattering by nonspherical ice crystals. Appl. Opt. **35** (1996).

[5] P. Yang and K.N. Liou. Light scattering by hexagonal ice crystals: solutions by a ray-by-ray integration algorithm. JOSA A **14** (1997).

[6] A.G. Borovoi and I.A. Grishin. Scattering matrices for large ice crystal particles. JOSA A **20** (2003).

[7] M.I. Mishchenko and A. Macke. Incorporation of physical optics effects and computation of the Legendre expansion for ray-tracing phase functions involving δ-function transmission. J. Geophys. Res. **103** (1998).

[8] A.G. Borovoi. Multiple scattering of short waves by uncorrelated and correlated scatterers. In: *Light Scattering Reviews* (vol. 1). A.A. Kokhanovsky (ed.). Springer-Praxis (2006).

[9] A. Borovoi and N. Kustova. Specular scattering by preferentially oriented ice crystals. Appl. Opt. **48** (2009).

[10] A.G. Borovoi, N.V. Kustova, and U.G. Oppel. Light backscattering by hexagonal ice crystal particles in the geometrical optics approximation. Opt. Engin. **44**(7) (2005).

A new three-parameter H,G_1,G_2 magnitude phase function for asteroids

A. Cellino*[,1], I. Belskaya[2], M. Delbò[3], A.-C. Levasseur-Regourd[4], K. Muinonen[5,6], A. Penttilä[5], and E. F. Tedesco[7]

[1]*INAF-Osservatorio Astronomico di Torino, strada Osservatorio 20, 10025 Pino Torinese, Italy.*
[2]*Astronomical Institute of Kharkiv National University, 35 Sumska street, 61035 Kharkiv, Ukraine.*
[3]*UMR 6202 Lab. Cassiopée, Obs. de la Côte d'Azur, BP 4229, 06304 Nice Cedex 4, France.*
[4]*UPMC Univ. Paris 06, UMR 7620, BP3, 91371 Verrières, France.*
[5]*Department of Physics, P.O. Box 64, FI-00014 U. Helsinki, Finland.*
[6]*Finnish Geodetic Institute, Geodeetinrinne 2, P.O. Box 15, FI-02431 Masala, Finland.*
[7]*Planetary Science Institute, 1700 E. Fort Lowell, Suite 106, Tucson, AZ 85719-2395, U.S.A.*

We have developed a new three-parameter H,G_1,G_2 magnitude phase function for asteroids. The phase function is aimed at replacing the currently adopted two-parameter H,G phase function. We show that H,G_1,G_2 produces better fits of available magnitude - phase curves of well-observed asteroids. We show also that the new system can be conveniently reduced to a two-parameter H,G_{12} magnitude phase function, which allows us to derive better estimates of the absolute magnitudes of asteroids for which poorly-sampled magnitude phase curves are available.

INTRODUCTION

Apparent position, motion, and brightness are the three basic pieces of information one can immediately derive for an asteroid based on a remote observation using an optical telescope. Measurements of position and motion are used to derive the orbits of the objects. From knowledge on the orbits, one can derive the corresponding distances of the object from the observer and from the Sun at any given epoch of observation. Based on this, it is possible to convert available measurements of apparent brightness into information on the intrinsic brightness of the object. On one hand, this operation consists of simply converting measurements of apparent brightness at a given epoch of observation into corresponding estimates of the brightness that would have been measured, if the object had been located at a fixed distance (usually assumed to be equal to 1 Astronomical Unit) from both the Sun and the observer. This can be easily done based on the trivial r^{-2} and Δ^{-2} dependence of the brightness, where r and Δ are the distances from the object to the Sun and to the observer, respectively. On the other hand, a more difficult problem is due to the fact that asteroids can be observed in a variety of illumination conditions, and the resulting brightness depends on these conditions. In particular, asteroids are brighter when seen close to the heliocentric opposition, that is when the so-called *phase angle*, namely the angle between the directions to the Sun and to the observer as seen from the asteroid, approaches zero. For increasing values of the phase angle, the objects tend to become increasingly fainter (using astronomical terminology, their magnitude increases). The change of magnitude as a function of phase angle is usually represented by the so-called phase curves. The increase of magnitude for

*Corresponding author: Alberto Cellino (cellino@oato.inaf.it)

increasing phase angle generally follows a nearly linear trend in a wide interval of phase angles, but close to opposition, at phase angles less than about $10°$, a non-linear brightness surge, usually named the *opposition effect*, takes place.

Based on the above considerations, the *absolute magnitude* of an asteroid is defined as the apparent brightness in standard V light that would be measured if the object was observed at a unit distance from both the Sun and the observer and at zero phase angle. Here, we do not deal with further complications due to fact that the objects are not spherical and then exhibit a periodic variation of brightness due to their rotation. The main point here is that the absolute magnitude is a very important parameter, since it is directly related to the size of an object and to its albedo (reflectance), which are fundamental physical properties.

Due to its importance from the point of view of physical studies for asteroids, the derivation of the absolute magnitude must be considered as a very important and delicate task. For this reason, the development of suitable magnitude phase functions is of outstanding importance for asteroid science. To address this issue, the International Astronomical Union (IAU) adopted in 1985 the so-called H,G system. The two parameters have the following meaning: H corresponds to the mean brightness, in Johnson V magnitude, at zero-degree phase angle, and corresponds thus to the absolute magnitude as defined above; G is the so-called slope parameter, which describes the general behavior of magnitude-phase curves. In practical terms, the slope parameter has been derived only for a tiny fraction of the known asteroids. This is due to the fact that, in general, only a handful of photometric observations, obtained at only a few phase angles, are available for any given asteroid, and this is insufficient to derive both H and G. In these cases, an assumed value of G, usually 0.15, is adopted [1]. Currently, all major catalogues of H values, with the only one notable exception of the AstDys database maintained at the University of Pisa, trace their values to the Minor Planet Center's database. Unfortunately, the accuracy of these values usually turns out to be poor, probably due to low-quality photometry used to obtain the H (and in a few cases, the G) values. As a consequence, asteroid V-band magnitudes predicted from the available H,G values are usually affected by significant errors. In particular, the objects tend to be very often significantly fainter than predicted [2, 3].

In this paper, we briefly summarize some recent results we have obtained concerning the development of a new three-parameter magnitude phase function that aims at replacing the two-parameter phase function that is currently adopted by IAU. An extensive explanation of our procedures and results is given in[4].

FROM H,G TO H,G_1,G_2

The H,G magnitude phase function was developed from efforts by several authors to model light-scattering phenomena in planetary regoliths. It has the following form for the reduced observed magnitude V:

$$V(\alpha) = H - 2.5\log_{10}[(1-G)\Phi_1(\alpha) + G\Phi_2(\alpha)], \quad (1)$$

where α is the phase angle, and $\Phi_1(\alpha)$ and $\Phi_2(\alpha)$ are two basis functions normalized at unity for $\alpha = 0°$. According to Eq. (1), the magnitude phase curve (hereinafter, simply "phase curve") of an object is described as the partitioning of the Φ_1 and Φ_2 functions in the ratio $(1-G) : G$. In turn, the slope parameter G is scaled in such a way that it is close to 0 for steep phase curves, and close to 1 for shallow phase curves, but values outside this

interval are not excluded *a priori*.

The explicit mathematical expressions for $\Phi_1(\alpha)$ and $\Phi_2(\alpha)$ can be found in [1, 4]. These two functions constituted the state of the art at the time of development of this photometric system. Their forms were suggested by theoretical models of light scattering that at that time did not include yet the phenomenon of coherent backscattering.

The H,G phase function still does a reasonably good job in fitting phase curves for many asteroids, especially in the region from $\sim 10^\circ$ to $\sim 60^\circ$. However, there are now some high-quality phase curves for which this is not really true, especially at phase angles in the region of the opposition brightness surge.

As a consequence of a thorough exercise to optimize $\Phi_1(\alpha)$ and $\Phi_2(\alpha)$ using stochastic optimization methods, we concluded that no "minor" revision of the H,G phase function can lead to a substantial improvement of the best fit to high-quality photometric phase data. This seems to be due to the intrinsic limits imposed by the choice of a linear two-parameter system using fixed basis functions. Therefore, we were obliged to conclude that a better fit of high-quality photometric data can only be obtained by adding an additional parameter to the photometric phase function. This is what we call our new H,G_1,G_2 magnitude phase function.

In the H,G_1,G_2 magnitude system for asteroids, the reduced observed magnitudes can be obtained from

$$\begin{aligned} 10^{-0.4V(\alpha)} &= a_1\Phi_1(\alpha) + a_2\Phi_2(\alpha) + a_3\Phi_3(\alpha) \\ &= 10^{-0.4H}[G_1\Phi_1(\alpha) + G_2\Phi_2(\alpha) + (1 - G_1 - G_2)\Phi_3(\alpha)], \end{aligned} \tag{2}$$

where the absolute magnitude H and the coefficients G_1 and G_2 are

$$H = -2.5\log_{10}(a_1 + a_2 + a_3), \quad G_1 = \frac{a_1}{a_1 + a_2 + a_3}, \quad G_2 = \frac{a_2}{a_1 + a_2 + a_3}. \tag{3}$$

The coefficients a_1, a_2, and a_3 are estimated from the observations by using the linear least-squares method. Thereafter, H,G_1, and G_2 follow from Eq. (3). As for the three basis functions, they must trivially satisfy the condition $\Phi_1(0) = \Phi_2(0) = \Phi_3(0) = 1$. Our idea was to construct a magnitude phase function consisting of an opposition-effect function Φ_3 and two linear basis functions Φ_1 and Φ_2. The derivation of their final explicit mathematical form by means of the stochastic optimization method is thoroughly explained in [4].

The results of this exercise were quite positive. In practically all analyzed cases of our sample, we obtained best-fit curves better, in terms of residuals, with respect to the corresponding H,G solutions. In several cases, the resulting best fits were significantly better. Again, all plots and Tables are given in [4]. The proposed three-parameter magnitude phase function is therefore much better in reproducing the behavior exhibited by well-observed, real objects. Such a conclusion might appear, however, as a speculative exercise in practice, if we think that for the vast majority of asteroids only a handful of (often poor) photometric data are available. In this situation, applying a three-parameter magnitude phase function would seem *a priori* a sterile exercise. Fortunately, the situation seems much different. The reason is that we found that, by considering the whole set of observed objects in our sample, a correlation exists between our derived G_1 and G_2 parameters. This fact can then be exploited, to express G_1 and G_2 as functions of a single G_{12} parameter, keeping the basis functions Φ_1, Φ_2, and Φ_3 fixed. It is then possible to fit the data by using a new two-parameter magnitude phase function that we call the H,G_{12} phase function. Once G_{12} is

determined, the parameters of the three-parameter system H,G_1 and G_2 can be computed correspondingly.

In this way, we found a satisfactory fit of asteroid phase curves even when only a small number of observations are available (by artificially removing large numbers of observations from the phase curves in our sample). Some preliminary tests of the predictive power of the H,G_{12} approach are given in [4]. Figure 1 shows the nonlinear least-squares fit using the H,G_{12} phase function to the observations of asteroids (24) Themis and (44) Nysa. We obtain the following best-fit parameter values with 3-σ error estimates: for Themis, $H = 7.12 \pm 0.04$ mag, $G_{12} = 0.7 \pm 0.2$, $G_1 = 0.7 \pm 0.2$, and $G_2 = 0.1 \pm 0.1$; for Nysa, $H = 6.90 \pm 0.04$ mag, $G_{12} = 0.07 \pm 0.08$, $G_1 = 0.01 \pm 0.06$, and $G_2 = 0.69 \pm 0.07$.

The next step of our analysis will be precisely to investigate in more details the performances of this method in different situations that can be encountered in practice, including those that will correspond to the forthcoming Gaia and Pan-STARRS sky surveys. Taking into account the significant errors that affect the absolute magnitudes in current asteroid catalogs, we think that our proposed H,G_1,G_2 phase function can be an extremely useful tool to derive accurate absolute magnitudes from the huge amount of new data we can expect to come from the new-generation sky surveys from the ground and from space.

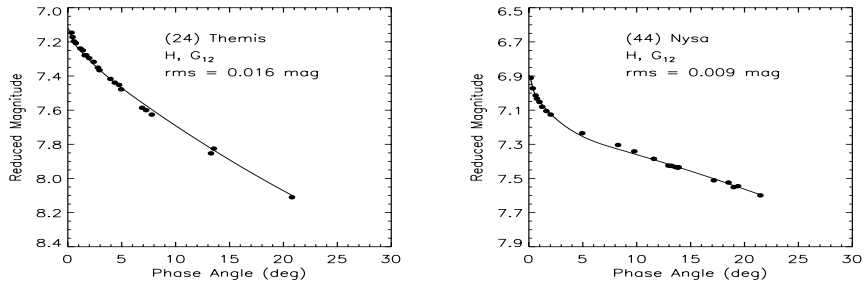

Figure 1. Nonlinear least-squares fits (solid lines) to the phase curves of the C-class asteroid (24) Themis (left; observations by Harris et al. [5]) and the E-class asteroid (44) Nysa (right; observations by Harris et al. [6]) using the two-parameter H, G_{12} magnitude phase function.

REFERENCES

[1] E.L.G. Bowell et al. Application of photometric models to asteroids. In: *Asteroids II*, T. Gehrels, M.T. Matthews, and R.P. Binzel (eds.). University of Arizona Press (1989).

[2] A. Parker, Z. Ivezić, M. Jurić, R. Lupton, M.D. Sekora, and A. Kovalski. The size distributions of asteroid families in the SDSS Moving Object Catalog 4. Icarus **198** (2008).

[3] A. Cellino, A. Dell'Oro, and E.F. Tedesco. Asteroid families: Current situation. Planet. Space Sci. **57** (2009).

[4] K. Muinonen, I.N. Belskaya, A. Cellino, M. Delbò, A.-C. Levasseur-Regourd, A. Penttilä, and E.F. Tedesco. A Three-Parameter Magnitude Phase Function for Asteroids. Icarus (in press) (2010).

[5] A.W. Harris et al. Photoelectric observation of asteroids 3, 24, 60, 261, 863. Icarus **77** (1989).

[6] A.W. Harris et al. Phase relations of high albedo asteroids: the unusual opposition brightening of 44 Nysa and 64 Angelina. Icarus **81** (1989).

The need for a first-order quasi-Lorentz transformation

D. Censor*

Dept. of Electrical and Comp. Engineering, Ben-Gurion University, Beer Sheva, 84105, Israel.

Solving electromagnetic scattering problems involving non-uniformly moving objects requires an approximate but consistent extension of Einstein's Special Relativity theory which originally is valid for constant velocities only. For moderately varying velocities, a quasi-Lorentz transformation is presented. The conditions for form-invariance of the Maxwell equations, the so-called "principle of relativity", are shown to hold for a broad class of motional modes and time scales. An example of scattering by a harmonically oscillating mirror is given. The present extended abstract is an overview of the full draft [1], where the derivations and formulas are given explicitly.

INTRODUCTION AND RATIONALE

Einstein's Special Relativity (SR) theory [2] is based on the invariance of c, the speed of light in free space (vacuum), for all inertial observers. The other postulate is the so-called "principle of relativity" (PR) for the Maxwell equations (ME). From the invariance of c follow [2] the spatial and temporal Lorentz Transformations (LT) (Eq. 1 in [1]), involving inertial reference systems $\mathbf{\Gamma}$ and $\mathbf{\Gamma}'$ and their associated space-time coordinates $\mathbf{r}, t$, and $\mathbf{r}', t'$, respectively.

Henceforth, inverse formulas will be referred to by an asterisk on the initial equation number, e.g., Eq. 1* (in [1]). Typically, inverse transformations are derived by solving the initial formulas for the sought variables. Formally, they follow by interchanging primed and unprimed symbols where $\mathbf{v}' = -\mathbf{v}$.

So far the LT (Eq. 1 in [1]) is restricted to constant velocities $\mathbf{v}$. If we try to formulate a systematic model for varying velocities, at least one reference frame ceases to be inertial. We cannot claim that such an approximate model is applicable to arbitrarily large velocities. Therefore, for varying velocities, the model will be restricted to a first order approximation in the normalized velocity $\beta = v/c$. Furthermore, for the model to be simple and tractable, the effects of the varying velocities are viewed as kinematical only, i.e., no attempt will be made to incorporate acceleration into media properties and/or the ME. For sufficiently small accelerations, this seems to provide a reasonable theoretical framework.

A very suggestive methodology for generalizing the problem to varying velocities is to approximate an inhomogeneously moving reference frame as a sequence of systems moving with different local/instantaneous velocities $\bar{\mathbf{v}} = \bar{\mathbf{v}}(\bar{\mathbf{r}}, \bar{t})$, instead of the continuously changing $\mathbf{v} = \mathbf{v}(\mathbf{r}, t)$. The velocity $\bar{\mathbf{v}}$ is assumed to be valid for a limited span of space-time in the vicinity of the world event $\bar{\mathbf{r}}, \bar{t}$. When the discrepancy becomes too large, the

* Corresponding author: Daniel Censor (censor@ee.bgu.ac.il)

velocity is updated. Thus, the continuous change of $\mathbf{v} = \mathbf{v}(\mathbf{r}, t)$ is replaced by a sequence of discrete constant velocities.

As a multi-scale method, this is plausible for systems, where the velocity changes slowly and monotonically over space and time regions large in comparison to other system parameters. However, this assumption holds only for a restricted class of configurations. It does not hold, for example, in the case of a wave emitted by oscillating antennas or scatterers. Intuitively one expects the antenna motion to cause a Doppler effect which during the mechanical cycle creates higher and lower frequencies. The results would then be akin to a frequency modulated carrier wave of frequency ω, creating sidebands of frequencies $\omega \pm n\Omega$, with Ω corresponding to the mechanical frequency. This is a result that cannot be displayed when the local instantaneous $\overline{\mathbf{v}}$ is employed, because for each incremental change of $\overline{\mathbf{v}}$ a different Doppler frequency shift is created, and the resulting continuous spectrum does not merge into the expected discrete sideband frequencies.

Our goal is to find a first-order quasi-Lorentz transformation (QLT) that will satisfactorily deal with scattering by objects moving at varying velocities.

FIRST-ORDER QUASI-LORENTZ TRANSFORMATION

The first-order SR is derived by keeping in the LT and ME only the first-order terms in β. For varying velocities we use a space-time dependent velocity $\mathbf{v}(\mathbf{r}, t)$. Thus, the differential first-order QLT is *postulated* as

$$d\mathbf{r}' = d\mathbf{r} - \mathbf{v}(\mathbf{r}, t)dt, dt' = dt - \mathbf{v}(\mathbf{r}, t) \cdot d\mathbf{r} / c^2 \tag{8a-b}$$

The corresponding integral forms are only valid when it is possible to return to the initial differential formula (Eq. 8). This prescribes that the line integrals be determined by the integration end points. Otherwise, the Leibniz rule for differentiation of integrals is not applicable. Hence the velocity field must be conservative.

THE PRINCIPLE OF RELATIVITY

Einstein [2] postulated PR, namely the form-invariance of ME. Thus, in Γ the ME are given by

$$\partial_{\mathbf{r}} \times \mathbf{E} = -\partial_t \mathbf{B}, \partial_{\mathbf{r}} \times \mathbf{H} = \partial_t \mathbf{D}, \partial_{\mathbf{r}} \cdot \mathbf{D} = 0, \partial_{\mathbf{r}} \cdot \mathbf{B} = 0 \tag{12a-d}$$

with fields that are space and time dependent, e.g., $\mathbf{E} = \mathbf{E}(\mathbf{r}, t)$. According to PR, in another inertial system Γ', the form-invariance of ME (Eq. 12) is preserved. Thus, the fields are $\mathbf{E}' = \mathbf{E}'(\mathbf{r}', t')$ etc. in terms of the appropriate native coordinates in Γ'.

The PR *statement* associating Eq. 12, Eq. 12*, is incomplete unless the LT relating the fields is provided, facilitating the derivation of the Field Transformation (FT) formulas. Here

we need the FT only to order β. The chain rule of calculus is applied, specifying an LT for the differential operators (Eq. 14 in [1]). Substituting Eq. 14 (in [1]) in the inverse ME (Eq. 12*) and collecting terms, Eq. 12 is obtained subject to the FT to the first order in β,

$$\mathbf{E}' = \mathbf{E} + \mathbf{v}\times\mathbf{B}, \mathbf{B}' = \mathbf{B} - \mathbf{v}\times\mathbf{E}/c^2, \mathbf{D}' = \mathbf{D} + \mathbf{v}\times\mathbf{H}/c^2, \mathbf{H}' = \mathbf{H} - \mathbf{v}\times\mathbf{D}. \quad (20a\text{-}d)$$

MAXWELL-EQUATIONS FORM INVARIANCE FOR VARYING VELOCITIES

To the first order in β, application of the chain rule for varying velocity $\mathbf{v} = \mathbf{v}(\mathbf{r}, t)$ to Eq. 12d* yields Eq. 12d, and similarly for Eq. 12c* and Eq. 12c, respectively. For the vector equations 12a*, 12a, and 12b*, 12b, this holds only if the wave angular frequency is much smaller than the typical velocity variation

$$\partial_t \mathbf{v} \ll \omega\mathbf{v} \quad (25)$$

In cases where Eq. 25 holds, the FT in Eq. 20 apply by replacing the constant $\mathbf{v}$ with $\mathbf{v} = \mathbf{v}(\mathbf{r}, t)$.

PLANE-WAVE TRANSFORMATIONS

Plane waves are characterized by constant vector amplitudes, with the space and time variation delegated to appropriate scalar phase exponential $e^{i\theta}$. Hence the FT (Eq. 20) are applied to the constant vector amplitudes, and the phase is a relativistic scalar invariant

$$\theta = \mathbf{k}\cdot\mathbf{r} - \omega t = \theta' = \mathbf{k}'\cdot\mathbf{r}' - \omega' t' \quad (28)$$

leading to the SR Fresnel drag and Doppler shift formulas, respectively. To first order in β

$$\mathbf{k}' = \mathbf{k} - \mathbf{v}\omega/c^2, \omega' = \omega - \mathbf{v}\cdot\mathbf{k} \quad (30a\text{-}b)$$

Replacing Eq. 28 by

$$d\theta = \mathbf{k}\cdot d\mathbf{r} - \omega dt = d\theta' = \mathbf{k}'\cdot d\mathbf{r}' - \omega' dt' \quad (31)$$

and substituting the QLT Eq. 8 yields Eq. 30 with space-time dependent parameters.

SCATTERING BY A PLANE OSCILLATING MIRROR

A simple example of a harmonic plane wave normally incident on a plane oscillating mirror is analyzed. Free space (vacuum), normal incidence, and a perfect mirror are assumed. The mirror is at rest in $\mathbf{\Gamma}'$ at $z' = 0$, moving harmonically with respect to the origin of $\mathbf{\Gamma}$.

The incident wave is given in $\mathbf{\Gamma}$ by

$$\mathbf{E} = \hat{\mathbf{x}} E_0 e^{i\theta}, \mathbf{H} = \hat{\mathbf{y}} H_0 e^{i\theta}, E_0 / H_0 = (\mu_0 / \varepsilon_0)^{1/2} = Z, \theta = kz - \omega t . \tag{37}$$

In $\mathbf{\Gamma}'$, where in terms of order β_0 we may use either t or t', the phase is given by

$$\begin{aligned} \theta' &= \int d\theta' = \int_{z_0'}^{z'} k'(t') d\underset{\sim}{z}' - \int_{t_0'}^{t'} \omega'(\underset{\sim}{t}') d\underset{\sim}{t}' = k'z' - \omega t' + (\omega\beta_0 / \Omega)\sin\Omega t' \\ k' &= k - (\omega v_0 / c^2)\cos\Omega t = kP,\ P = 1 - \beta_0 \cos\Omega t = 1 - \beta_0 \cos\Omega t' \end{aligned} \tag{38a-b}$$

The amplitudes are transformed according to

$$\begin{aligned} &\mathbf{E}' = \hat{\mathbf{x}} E_0' e^{i\theta'} = E_0 \hat{\mathbf{x}} P e^{i\theta'}, \mathbf{H}' = \hat{\mathbf{y}} H_0' e^{i\theta'} = H_0 \hat{\mathbf{y}} P e^{i\theta'} \\ &E_0' / E_0 = H_0' / H_0 = P, E_0' / H_0' = Z \end{aligned} \tag{39}$$

At the mirror location $z' = 0$, the fields are time-varying in accordance with

$$M = P e^{-i\omega t' + i\xi_0 \sin\Omega t'}, \xi_0 = \omega\zeta_0 / c = \omega\beta_0 / \Omega , \tag{40a}$$

vindicating the assertion above that, at the oscillating mirror, we have a new spectrum.

In order to calculate the reflected wave and transform it back from $\mathbf{\Gamma}'$ to $\mathbf{\Gamma}$, we first need to represent the spectrum as a superposition of time-harmonic signals. Expanding the exponential in Eq. 40a in a series involving Bessel functions, we get

$$\begin{aligned} M &= P e^{-i\omega t'} \Sigma_n J_n e^{in\Omega t'} = P \Sigma_n J_n e^{-i\omega_n' t'} \\ \omega_n' &= \omega - n\Omega, \Sigma_n = \Sigma_{n=-\infty}^{n=\infty}, J_n = J_n(\xi_0) \end{aligned} \tag{40b}$$

Finally, the reflected wave, constituting a superposition of harmonic plane waves, is

$$\begin{aligned} &\mathbf{E}' = \hat{\mathbf{x}} E_0 \Sigma_n I_n e^{i\theta_n'}, \mathbf{H}' = \hat{\mathbf{y}} H_0 \Sigma_n I_n e^{i\theta_n'}, \theta_n' = k_n' z' - \omega_n' t' \\ &I_n = (J_n - \beta_0 (J_{n-1} + J_{n+1}) / 2) = (1 - \beta_0 n / \xi_0) J_n = (1 - n\Omega / \omega) J_n \end{aligned} \tag{39b}$$

REFERENCES

[1] http://www.ee.bgu.ac.il/~censor/quasi-lorentz.pdf

[2] A. Einstein, "Zur Elektrodynamik bewegter Körper", *Ann. Phys. (Lpz.)*, Vol. 17, 891-921, 1905; English translation: "On the Electrodynamics of moving bodies", *The Principle of Relativity*, Dover.

Benchmark of convolution and deconvolution models: implications for planetary opposition surges

E. Déau*,[1], A. Brahic[2], L. Dones[3], and C.C. Porco[4]

[1]*Jet Propulsion Laboratory, NASA/CalTech, 4800 Oak Grove Drive Pasadena CA 91109, U.S.A.*
[2]*Université Denis Diderot, Laboratoire AIM, 10 rue A. Domon et L. Duquet, 75205 Paris, France.*
[3]*Southwest Research Institute, 1050 Walnut Street, Suite 300, Boulder CO 80302, U.S.A.*
[4]*CICLOPS, 3100 Walnut Street, Suite A535, Boulder CO 80303, U.S.A.*

We benchmark several convolution and deconvolution models on phase curves at small phase angles (0.005°-1°). These curves were provided by several NASA missions (Clementine/UVVIS, Galileo/SSI and Cassini/ISS) when the Sun had different angular radii ($\alpha_\odot$=0.266°, 0.051°, 0.028°). For the smallest phase angles, the brightness of the objects (Moon, Europa and the Saturn's rings) exhibits a strong flattening below the angular size of the Sun. However, the brightness continues to increase below $\alpha_\odot$ before finally flattening at $0.4\alpha_\odot$. These behaviors are consistent with the convolution models tested.

INTRODUCTION

When the observer and the source of light are aligned, a strong surge called the opposition effect is observed in the phase curves of astronomical objects [1]. Although observed since the 19th century, the opposition effect is not understood and the causes which provoke it are still a matter of debate [1]. Several theoretical models have proposed to explain the shape of the surge by different mechanisms [2, 3]. Because the Sun is not a point-like light source for Solar System objects, it is therefore necessary to deconvolve the data or to convolve the theoretical models. Both approaches are tested on phase curves at small phase angles.

OPPOSITION DATA

We use the opposition data of the Moon observed by Clementine/UVVIS [4], Europa seen by Galileo/SSI [5] and the Saturn's rings observed by Cassini/ISS in 2005 [6].

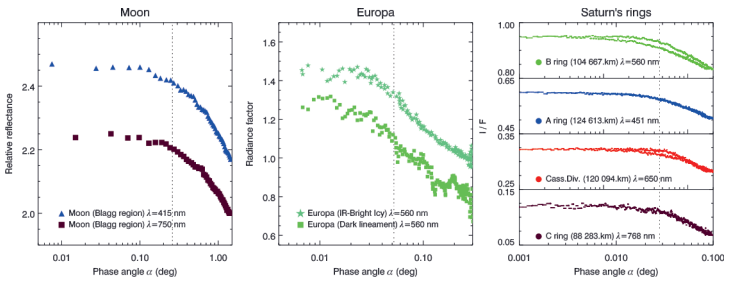

Figure 1. Phase curves of the Moon, Europa and the Saturn's rings from images of Clementine, Galileo and Cassini. Vertical dotted lines correspond to solar angular radii.

*Corresponding author: Estelle Deau (estelle.deau@jpl.nasa.gov)

CONVOLUTION MODELS

We tested two convolution models. The first one is the limb darkening function of [7]: $W(\mu') = a_\lambda + b_\lambda \mu' + c_\lambda \left[1 - \mu' \cdot \log\left(1 + 1/\mu'\right)\right]$, where $\mu' = \cos\theta'$ and θ' varies from 0 to the Sun's angular radius $\alpha_\odot$. a_λ, b_λ and c_λ are coefficients that depend on the wavelength. It has been used in the past to be convolved with a theoretical opposition effect function of [8]. The normalized convolution of the linear-exponential function of [9] $r_{linexp}(\alpha) = I_b + I_s \cdot \alpha + I_p \cdot \exp\left(-\alpha/2w\right)$ to the limb darkening function is:

$$r_{pw}(\alpha) = \frac{\int_0^{\alpha_\odot} d\theta' \int_0^{2\pi} d\phi' \sin\theta' r_{linexp}(\alpha) \cdot W(\cos\theta') \cos\theta_0(\Omega')}{\int_0^{\alpha_\odot} d\theta' \int_0^{2\pi} d\phi' \sin\theta' W(\cos\theta') \cos\theta_0(\Omega')}. \quad (1)$$

The angles θ_0, Ω' and ϕ' are fully described in [8]. The second limb darkening function tested here is the one-parameter solar limb-darkening model of [10]: $I_\lambda(\hat{r}) = (1 - \hat{r}^2)^{\beta_\lambda}$ where $I_\lambda(\hat{r})$ is the normalized limb-darkened solar intensity, $\hat{r}$ is the normalized radial coordinate of the solar disk, and β_λ is a wavelength-dependent constant. We fitted the linear exponential function to the data and computed r_{hm} by using:

$$r_{hm}(\alpha) = \frac{\int r_{linexp}(\alpha, \Omega) I_\lambda(\Omega) d\Omega}{\int I_\lambda(\Omega) d\Omega} \quad (2)$$

where $I_\lambda(\Omega)$ is the limb-darkened solar intensity, $\alpha(\Omega)$ is the phase angle, and the integrations were made over the solid angle $d\Omega$ of the solar disk.

As a result, both convolution models tested here give a good agreement with the data and between themselves (Fig. 2).

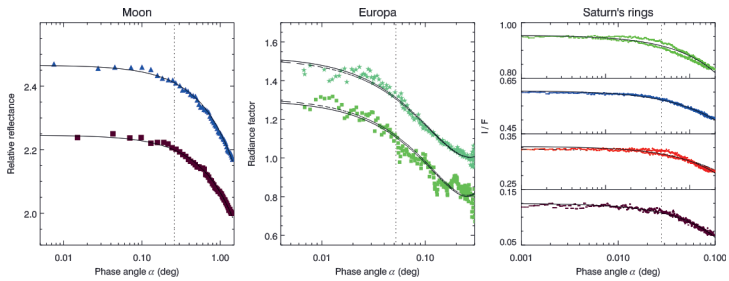

Figure 2. Phase curves of the Moon, Europa and the Saturn's rings fitted with the model of [7] in solid curves and the model of [10] in dashed curves.

DECONVOLUTION MODEL

We performed previously a convolution of the linear-exponential function to several limb darkening functions. However, this refinement does not provide information about the behavior of the brightness if the Sun were a point-like source, because the linear-exponential function intrinsically flattens as $\alpha \to 0$ (see dashed curve in Fig. 3). Few models that deconvolve phase curves exist so we use a simple model. The deconvolution model of [11] uses the logarithmic function of [12] because it does not flatten at small phase angles and

assumes a logarithmic increase of the data below the light source's angular size, as for larger phase angles:

$$r_{log}(\alpha) = a_0 + a_1 \cdot \ln(\alpha) \quad (3)$$

This assumption is consistent with the recent laboratory measurements of [13] at small phase angles (0.008^o –1.51^o), that did not show any flattening of the phase curves (Fig. 3). This is because [13] increase the laser separation distance from 25 meters to 40 meters to obtain the smallest phase angles and then, artificially decrease the angular size of their light source.

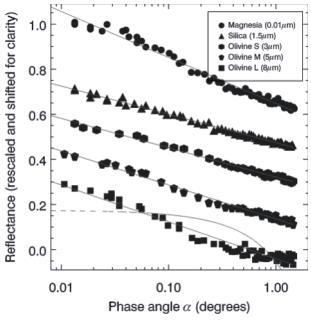

Figure 3. Laboratory phase curves of [13] at very small phase angles

DISCUSSION

Morphology of the surge before and after the deconvolution

With the convolution and deconvolution models, the behavior of the surge appears to be more clear. The flattening of the phase curves is progressive and effective at approximately $0.4\alpha_{\odot}$. This value is found either with the phase curves (Fig. 4) or either by looking at the derivative of the convolved linear-exponential function fitted to the data. The deconvolution model suggests a logarithmic trend for the brightness for α near 0^o.

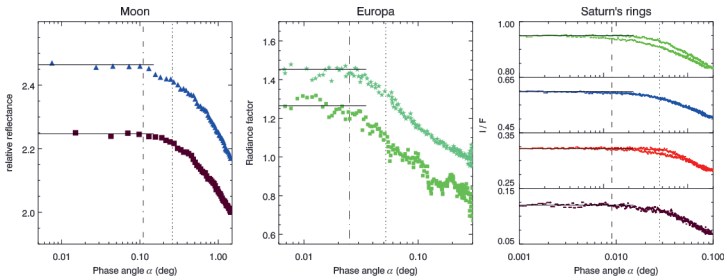

Figure 4. Phase curves of the Moon, Europa and the Saturn's rings fitted with several logarithmic functions of [12]. Vertical dotted lines correspond to α of effective flattening.

Implication for the surge of planetary surfaces

We tested the influence of the solar angular size by representing in Fig. 5 the convolved and deconvolved angular width of the surge as a function of the distance from the Sun (in Astronomical Units) for various Solar System objects [11]. The convolved HWHMs follow a power-law function with the heliocentric distance while the deconvolved HWHMs are independent of the distance from the Sun (see Fig. 5). With the deconvolved HWHMs, Solar System objects seem to be grouped by their albedo. This could be a consequence of the opposition effect mechanisms, since they are albedo-dependent [2, 3].

CONCLUSION

To better understand the behavior of the brightness near the solar angular radius, we (1) convolved the theoretical models and (2) deconvolved the data. The first approach shows a

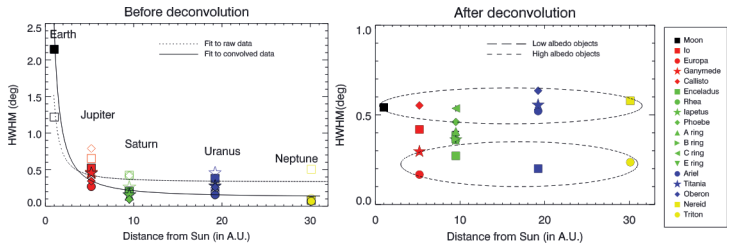

Figure 5. Angular width of the surge before and after the deconvolution for various rings and satellites of the Solar System from the study of [11].

good agreement between the two convolution models used and the second approach finds an agreement between a simple deconvolution model and some laboratory measurements.

Acknowledgments: This study is performed at Jet Propulsion Laboratory (JPL), under contract with NASA and is funded by the NASA Postdoct. Program led by OakRidge Associated Universities.

REFERENCES

[1] P. Helfenstein et al. The lunar opposition effect. Icarus **128** (1997).

[2] B. Hapke. Bidirectional Reflectance Spectroscopy 5. The coherent backscatter opposition effect and anisotropic scattering. Icarus **157** (2002).

[3] M. I. Mishchenko. The angular width of the coherent back-scatter opposition effect - an application to icy outer planet satellites. Astrophys. and Space Sci. **194** (1992).

[4] Yu. G. Shkuratov et al. Opposition effect from Clementine data and mechanisms of backscatter. Icarus **141** (1999).

[5] P. Helfenstein et al. Galileo observations of Europa's opposition effect. Icarus **135** (1998).

[6] E. Déau, et al. Sunshine on the rings: the opposition effect seen at high resolution with Cassini-ISS. BAAS **38** (2006).

[7] A. K. Pierce and J. H. Waddell. Analysis of limb darkening observations. Memoirs of the Royal Astron. Soc. **63** (1961).

[8] Y. Kawata and W. M. Irvine. Models of Saturn's rings which satisfy the optical observations. In: *Exploration of the planetary system* (1974).

[9] S. Kaasalainen et al. Comparative study on opposition effect of icy Solar System objects. JQSRT **70** (2001).

[10] D. Hestroffer and C. Magnan. Wavelength dependency of the Solar limb darkening. Astr. and Astrophys. **333** (1998).

[11] E. Déau et al. The opposition effect in the outer Solar system: A comparative study of the phase function morphology. Planet. and Space Sci. **57** (2009).

[12] M. S. Bobrov. Physical properties of Saturn's rings. In: *Surfaces and Interiors of Planets and Satellites* A. Dollfus (ed.) (1970).

[13] V. Psarev et al. Photometry of particulate surfaces at extremely small phase angles. JQSRT **106** (2007).

Numerically-exact computer modeling of light scattering by random absorbing media

J. M. Dlugach[*,1], M. I. Mishchenko[2], and L. Liu[2]

[1]*Main Astronomical Observatory of the National Academy of Sciences of Ukraine, 03680, Kyiv, Ukraine.*
[2]*NASA Goddard Institute for Space Studies, NY 10025, New York, U.S.A.*

We employ the superposition *T*-matrix method to perform computations of electromagnetic scattering by a volume of discrete random medium densely filled with spherical particles with the real part of the refractive index m_R = 1.31, 1.5 and the imaginary part m_I = 0, 0.01, 0.1, 0.3. Our computations show that increasing the value of m_I can both decrease and increase manifestations of the coherent backscattering (CB) effect, dependent on the values of the particle packing density and the real part of the refractive index.

INTRODUCTION

In our previous publications [1–3], by using the numerically-exact solution of the Maxwell equations we have studied electromagnetic scattering by a volume of statistically homogeneous discrete random medium of various sizes, consisting of different numbers of non-absorbing particles. In particular, we have shown that all backscattering effects predicted by the low-density theory of CB (see, e.g., [4] and references therein) also take place in the case of a densely packed medium. In this paper, we extend our numerically-exact computer modeling to the case of a medium composed of absorbing particles and analyze the effect of absorption on scattering characteristics of a medium composed of different numbers of particles with different refractive indices. Note that earlier in [5], on the basis of computations performed for m_R = 1.32 and particle packing density $\tilde{\rho}$ = 22%, it was concluded that increasing absorption diminishes such optical effects as depolarization and CB.

METHODOLOGY

Our model of particulate random medium is a spherical volume of radius *R* filled with *N* identical non-overlapping spherical particles of radius *r*. The size parameter of the volume is kR, and the particle size parameter is kr, where k is the wave number. To model the complete randomness of particle positions within the spherical volume, we follow the approach adopted in [1–3]. This approach yields an infinite continuous set of random realizations of the scattering volume and allows us to use the highly efficient orientation-averaging technique afforded by the superposition *T*-matrix method [6]. The latter

* Corresponding author: Janna Dlugach (dl@mao.kiev.ua)

represents a direct, numerically-exact computer solver of the macroscopic Maxwell equations for a multi-sphere group (see, e.g., [7]).

We assume that the random particulate volume is illuminated by a quasi-monochromatic beam of light and is observed from a distant point. Using the scattering plane for reference allows us to define the relation between the Stokes parameters of the incident ("inc") and scattered ("sca") light in terms of the normalized scattering matrix of the entire volume [4, 8]:

$$\begin{bmatrix} I^{sca} \\ Q^{sca} \\ U^{sca} \\ V^{sca} \end{bmatrix} \propto \begin{bmatrix} a_1(\theta) & b_1(\theta) & 0 & 0 \\ b_1(\theta & a_2(\theta) & 0 & 0 \\ 0 & 0 & a_3(\theta) & b_2(\theta) \\ 0 & 0 & -b_2(\theta) & a_4(\theta) \end{bmatrix} \begin{bmatrix} I^{inc} \\ Q^{inc} \\ U^{inc} \\ V^{inc} \end{bmatrix}, \quad (1)$$

where θ is the scattering angle. The zeros denote scattering matrix elements negligibly small (in the absolute sense) relative to the other elements at the same scattering angle.

Elements of the scattering matrix define specific properties of the scattered light corresponding to different states of polarization of the incident light. If the incident light is unpolarized, then the element $a_1(\theta)$, called the phase function, describes the angular distribution of the scattered intensity, while the ratio $-b_1(\theta)/a_1(\theta)$ gives the corresponding degree of linear polarization. If the incident light is polarized linearly in the scattering plane, then the linear polarization ratio $\mu_L=(a_1(\theta) - a_2(\theta))/(a_1(\theta) + 2b_1(\theta) + a_2(\theta))$. If the incident light is polarized circularly in the counterclockwise direction when looking in the direction of propagation, then the circular polarization ratio $\mu_C = (a_1(\theta) + a_4(\theta))/(a_1(\theta) - a_4(\theta))$.

NUMERICAL RESULTS

Some of the results of our extensive computations are presented in Figs. 1 and 2. Here, we limit ourselves to analyzing only the data obtained in the range of large scattering angles $150° \le \theta \le 180°$. The computations have been performed for a scattering volume of the size parameter $kR = 30$ filled with spherical particles with a complex refractive index $m = m_R + im_I$, where $m_R = 1.31$ (Fig. 1), 1.5 (Fig. 2), and $m_I = 0$, 0.01, 0.1, 0.3. The values of the particle size parameter were adopted to be $kr = 2$ ($m_R = 1.31$) and $kr = 1.76$ ($m_R = 1.5$). The point is that in [2, 3] we have obtained that just for these values of kr the single scattering polarization has a wide horizontal "shelf" of near-zero values extending from $\theta = 150°$ up to 180°. But with growing N, the polarization $-b_1(\theta)/a_1(\theta)$ develops a pronounced minimum caused by the increasing contribution of multiple scattering. Such behavior of polarization is caused by the effect of CB, and the question is how the absorption can influence the behavior of the negative branch of polarization. In the case of $m_R = 1.31$, the number of constituent particles N was varied from 100 up to 400 what corresponds the variation of the packing density $\tilde{\rho}$ from 3.6% up to 14.6%, and for $m_R = 1.5$, N varies from 100 ($\tilde{\rho} = 2.4\%$) up to 600 ($\tilde{\rho} = 14.5\%$).

From Fig. 1 we see that in the range $\theta > 170°$ the backscattering peak in the normalized scattered intensity $a_1(\theta)/a_1(180°)$, caused by the effect of CB, decreases with increasing the absorption, and the angular widths of these peaks increase with increasing absorption. A somewhat different situation is seen in Fig. 2. Specifically, in the case of $N = 100$ ($\tilde{\rho} = 2.4\%$), increasing m_I from 0 up to 0.1 results in increasing intensity backscattering peak and decreasing its angular width. Then, when $m_I = 0.3$, the backscattering peak decreases and practically does not differ from that in the case of $m_I = 0$, 0.01. In the case of N=600 ($\tilde{\rho} = 14.5\%$), the intensity backscattering peak decreases with increasing absorption monotonously. Besides, note that when $m_I = 0.3$ the backscattering enhancement is still sufficiently strong for both values of N, which is indicative of a significant contribution of multiple scattering for $m_R = 1.5$ even in the case of such strong absorption.

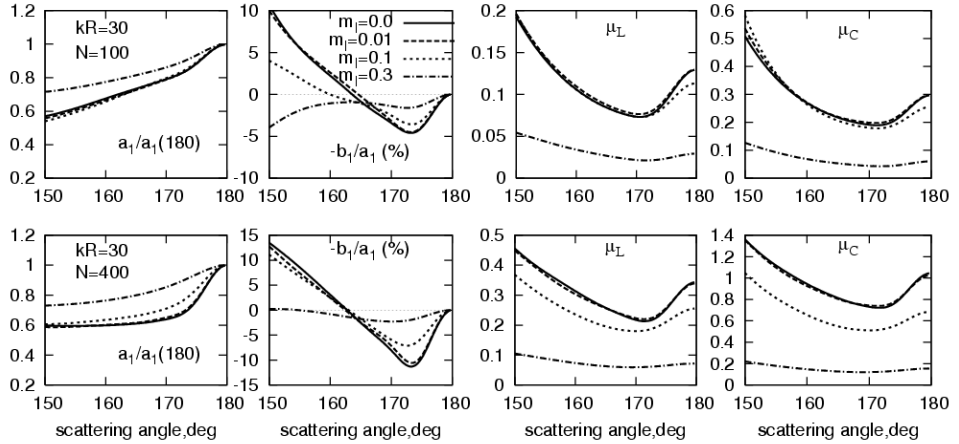

Figure 1. Scattering characteristics of a $kR = 30$ scattering volume randomly filled with N identical spherical particles of $kr = 2.0$, $m_R = 1.31$, and $0 \le m_I \le 0.3$. The upper row: N=100 (the packing density $\tilde{\rho} = 3.6\%$), the bottom row: N=400 ($\tilde{\rho} = 14.6\%$).

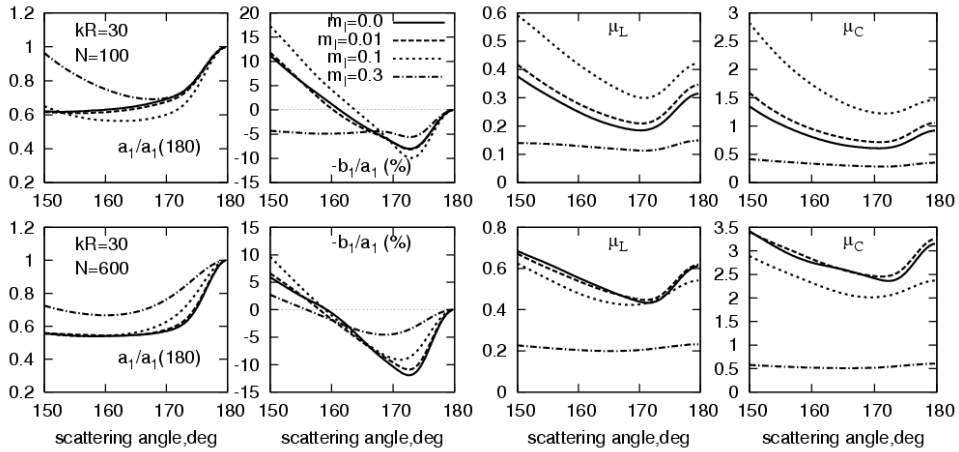

Figure 2. Scattering characteristics of a $kR = 30$ scattering volume randomly filled with N identical spherical particles of $kr = 1.76$, $m_R = 1.5$, and $0 \le m_I \le 0.3$. In the upper row, N = 100 (the packing density $\tilde{\rho} = 2.4\%$). In the bottom row, N=600 ($\tilde{\rho} = 14.5\%$).

In the case of $m_R = 1.31$ (Fig. 1), the minimum of polarization $-b_1(\theta)/a_1(\theta)$ monotonously decreases with increasing m_I, and when $m_I = 0.3$, the curve of polarization changes its shape. Note that for $N = 100$, the asymmetry of the polarization curve increases with increasing m_I up to 0.1, but if $N = 400$ then the position of the inversion point does not change. Fig. 2 demonstrates that in the case of $m_R = 1.5$ and $N = 100$, the behavior of the value of minimum polarization (similar for the behavior of the intensity) is not monotonous with increasing absorption. Firstly, increasing m_I from 0 up to 0.1 results in increasing the maximum absolute value of negative polarization, and, when $m_I = 0.3$, the absolute value of negative polarization decreases. For the case of $N = 600$, the depth of the polarization minimum decreases monotonously with increasing absorption.

Finally, from Fig. 1 we see that increasing absorption monotonously diminishes the values of the linear μ_L and the circular μ_C polarization ratios, and when $m_I = 0.3$, depolarization of the medium approaches zero. Again, the results of computations of μ_L and μ_C performed for $m_R = 1.5$ and $N = 100$ and shown in Fig. 2, demonstrate a significant increase of these values with increasing m_I from 0 up to 0.1.

Thus, we can conclude that increasing absorption can both enhance and suppress manifestations of the CB effect depending on the particle packing density and the real part of the refractive index. It is necessary to note that in [9] it has been shown that absorbing Rayleigh scatterers can yield more pronounced enhancement factors and polarization surges than nonabsorbing Rayleigh scatterers.

REFERENCES

[1] M.I. Mishchenko, L. Liu, D.W. Mackowski et al. Multiple scattering by random particulate media: exact 3D results. Opt Express **15** (2007).

[2] M.I. Mishchenko, J.M. Dlugach, L. Liu et al. Direct solutions of the Maxwell equations explain opposition phenomena observed for high-albedo solar system objects. Astrophys J. **705** (2009).

[3] M.I. Mishchenko, J.M. Dlugach, and L. Liu. Azimuthal asymmetry of the coherent backscattering cone: exact theoretical results. Phys Rev A **80** (2009).

[4] M.I. Mishchenko, L.D. Travis, and A.A. Lacis. *Multiple scattering of light by particles: radiative transfer and coherent backscattering*. Cambridge Univ Press, Cambridge (2006).

[5] M.I. Mishchenko, L. Liu, and J.W. Hovenier. Effects of absorption on multiple scattering by random particulate media: exact results. Opt Express **15** (2007).

[6] D.W. Mackowski and M.I. Mishchenko. Calculation of the T-matrix and the scattering matrix for the ensembles of spheres. J Opt Soc Am A **13** (1996).

[7] M.I. Mishchenko, L.D. Travis, and A. A. Lacis. *Scattering, absorption and emission of light by small particles*. Cambridge Univ Press, Cambridge (2002).

[8] J.W. Hovenier, C. van der Mee, and H. Domke. *Transfer of polarized light in planetary atmospheres – basic concepts and practical methods*. Springer, Berlin (2004).

[9] K. Muinonen. Coherent backscattering of light by complex random media of spherical scatterers: numerical solution. Waves Random Media **14** (2004).

Numerical simulations of light scattering characteristics of ice fractal particles

J. M. Dlugach[*,1], M. I. Mishchenko[2], and D. W. Mackowski[3]

[1]*Main Astronomical Observatory of the National Academy of Sciences of Ukraine, 03680, Kyiv, Ukraine.*
[2]*NASA Goddard Institute for Space Studies, NY 10025, New York, U.S.A.*
[3]*Department of Mechanical Engineering, Auburn University, AL 36849, U.S.A.*

For the model of a vertically and horizontally homogeneous slab of an arbitrary optical thickness composed of fractal aggregates of small spherical ice monomers, generated by applying three different approaches, we analyze the results of computations of the backscattering circular polarization ratio. The computations are performed for the refractive index $m = 1.78 + i0.003$ by using the superposition T-matrix and vector radiative transfer codes.

INTRODUCTION

Scattering of electromagnetic waves by media composed of ice fractal particles is the subject of utmost importance to the discipline of remote sensing of the Earth and other solar system objects. In particular, the knowledge of scattering properties of such media is needed for the interpretation of radar observations of terrestrial ice sheets [1], Galilean satellites of Jupiter [2], and Saturn's rings [3]. To solve this problem it is necessary, in the first place, to calculate the single scattering characteristics of fractal aggregate particles, and various techniques have been developed for this purpose over many years (see [4]). In recent years, the numerically-exact superposition T-matrix method [5] has been extensively applied to the computations of scattering by multi-sphere clusters (see, e.g., [6]). It is obvious that when performing such computations the model of aggregate structure must be adopted, and it should be expected that scattering characteristics of clusters can be affected in some way by their morphology. The question is that of how strong these effects can be.

In this paper, for a slab composed of fractal aggregates of small spherical ice monomers, generated by applying several procedures, we investigate the influence of the cluster morphology on the behavior of the circular backscattering polarization ratio which may contain information on microphysical properties of the scattering medium [3].

ICE CLUSTER MODELS AND COMPUTATIONAL TECHNIQUES

Let the scattering medium be a plane-parallel slab composed of randomly distributed, independently scattering aggregate particles built of spherical monomers. The slab is illuminated

* Corresponding author: Janna Dlugach (dl@mao.kiev.ua)

by a parallel beam of light, with (θ_0, φ_0) and (θ, φ) specifying the directions of incidence and reflection. The first step in computations of the single-scattering characteristics of the medium composed of fractal-like clusters is generating monomer positions in a fractal aggregate. As an initial model of aggregates we adopt fractal clusters which can be described by the following statistical scaling law [4]:

$$N_{\mathrm{S}} = k_0 \left(\frac{R_g}{r} \right)^{D_{\mathrm{f}}}, \tag{1}$$

where r is the monomer radius, $1 \leq D_{\mathrm{f}} \leq 3$ is the fractal dimension, k_0 is the fractal prefactor, N_{S} is the number of monomers in the aggregate, and R_{g}, called the radius of gyration, is a measure of the overall aggregate radius. Parameters N_{S}, D_{f}, and k_0 specify the morphology of a fractal aggregate.

We apply the following algorithms to generate monomer positions in fractal aggregates.

A) The cluster–cluster aggregation procedure [7]. The basic idea of this method is to generate a sequence of random sphere positions subject to the constraint that the positions, at any point in the sequence, identically satisfy Eq. (1) for given k_0 and D_{f} and that each monomer touches at least one other monomer.

B) The original diffusion-limited aggregation (DLA) method [8] in which the generation procedure starts with a pair of spheres in contact for pre-set k_0 and D_{f} values and adds a single monomer at a time. Compared to the cluster–cluster aggregation procedure, the DLA algorithm is less realistic, but it can be used for a wider range of the values of the fractal parameters. Note that the overall shape of fractals generated by using both the cluster-cluster and DLA algorithms is nearly spherical.

C) The approach which gives the possibility to generate clusters of spheroidal overall shape. Specifically, it generates fractals composed of spherical monomers that lie randomly within the surface of a spheroid, subject to the constraints that no two spheres overlap and that each sphere contacts with at least one neighbour. In the case of unit monomers, the monomer packing density p is defined as

$$p = \frac{N_S}{ER^3}, \tag{2}$$

where E is the aspect ratio, R is the axial radius of the spheroid, and $E > 1$ represents a prolate spheroid. Note that such fractals are not described by Eq. (1).

To compute the elements of the single-scattering matrix for the generated fractals, we use the superposition T-matrix method [5] and the corresponding FORTRAN code which is publicly available online*. Then the obtained single-scattering characteristics of aggregate particles are used to compute the elements of the diffuse Stokes reflection matrix. In the case of a semi-infinite homogeneous slab we employ a vector radiative-transfer code based on the numerical solution of the Ambarzumian's nonlinear integral equation [9], and for a finite slab

* ftp://ftp.eng.aubum.edu/pub/dmckwski/scatcodes/index.html

we use a numerically exact computer code based on the invariant imbedding technique [10]. The circular polarization ratio is derived from Eqs. (14.3.21)–(14.3.25) and (14.5.15) of [11].

NUMERICAL RESULTS AND DISCUSSION

In Fig. 1, we depict the computed dependences of the backscattering circular polarization ratio μ_C on the angle $B = \pi/2 - \theta$. The computations are performed for a plane-parallel homogeneous slab of optical thickness $\tau = 2$ (three bottom curves) and a semi-infinite slab (three top curves) composed of fractal ice aggregates with the refractive index $m = 1.78 + i0.003$ which corresponds to weakly contaminated water ice at a wavelength of 12.6 cm. The monomer packing density p is fixed at 0.2, the monomer radius $r = 1$ cm, the fractal dimension $D_f = 2.5$, and the overall cluster radius R is varied in the range $4 \le R \le 10$ cm. Similarly [12], to obtain the single-scattering characteristics, we generate an ensemble of ten fractal-parameter-equivalent realizations of an aggregate, compute the single-scattering characteristics for each realization, and then average them over the ensemble. The necessity to perform such averaging was discussed in [12].

The top row shows the results of computations performed for slabs composed of aggregates generated by employing the three procedures described above. First of all, we see that for $\tau = 2$, the angular dependence of μ_C on B decreases significantly with increasing R, but it increases with increasing τ. One can see that when using the cluster-cluster and DLA algorithms, for the same values of τ the values of μ_C do not practically depend on the aggre-

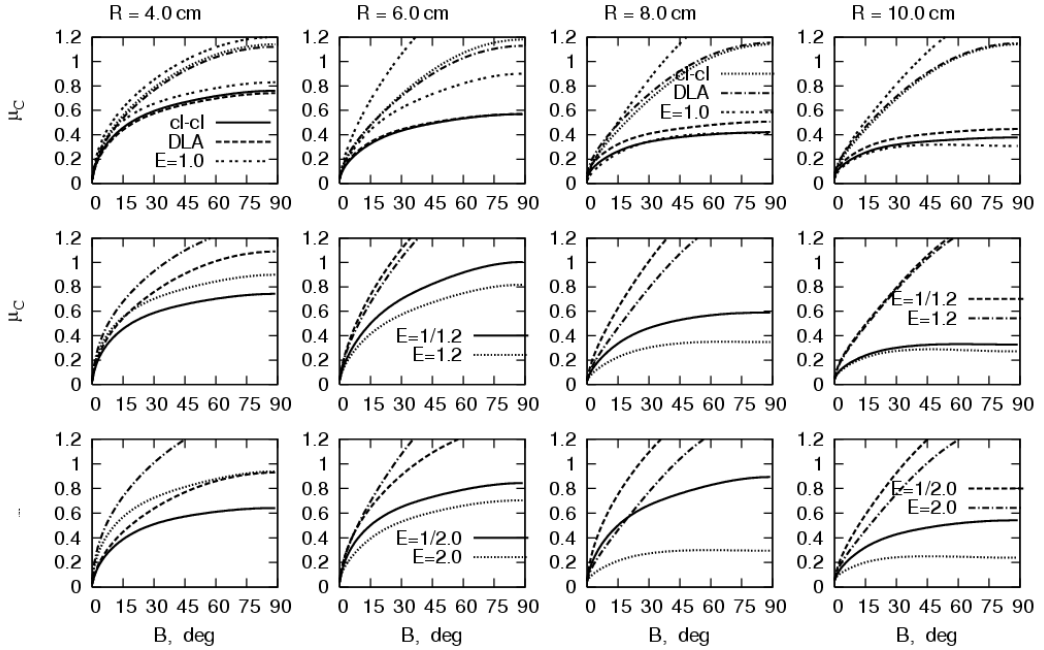

Figure 1. Angular dependence of the backscattering circular polarization ratio. Different curves correspond to the results of computations performed for a layer of two values of the optical thickness (τ = 2 and semi-infinite) and varying cluster structure.

gate generating procedure, the dependence increases weakly with increasing R. Our computations performed for $D_f = 3$ (not presented here) show that the difference in the values of μ_C due to the difference in the aggregate structure produced by employing such procedures, substantially increases with increasing D_f. As regards the case of clusters described by Eq. (2) for E = 1, τ = 2, R = 4, 6 cm, a significant difference in the values of μ_C obtained by using this approach and the cluster-cluster or the DLA procedures is seen. This difference increases with increasing R from 4 cm up to 6 cm, but with further increasing R it starts to decrease noticeably. The numerical results obtained for aggregates of prolate (E > 1) and oblate (E < 1) spheroidal overall shapes are depicted in the middle (E = 1.2, 1/1.2) and bottom (E = 2, 1/2) rows. One can see that with the exception of the case of R = 10 cm, E = 1.2, 1/1.2, for the slabs composed of fractals of the overall oblate and prolate spheroidal shapes, the values of μ_C differ from each other.

Thus, the results of our computations show that, for the slabs composed of aggregates generated by the cluster-cluster and the DLA procedure, the values of the backscattering polarization ratio differ from each other very weakly. In the case of using Eq. (2), the dependence of μ_C on aggregate structure can be significant.

REFERENCES

[1] E. Rignot. Backscatter model for the unusual radar properties of the Greenland Ice Sheet. J. Geophys. Res. **100** (1995).

[2] S. J. Ostro. Planetary radar astronomy. Rev. Mod. Phys. **65** (1993).

[3] P. D. Nicholson et al. Radar imaging of Saturn's rings. Icarus **177** (2005).

[4] C.M. Sorensen. Light scattering by fractal aggregates: a review. Aerosol Sci. Technol. **35** (2001).

[5] D.W. Mackowski and M.I. Mishchenko. Calculation of the *T*-matrix and the scattering matrix for the ensembles of spheres. J. Opt. Soc. Am. A **13** (1996).

[6] M.I. Mishchenko, G. Videen, V.A. Babenko et al. Comprehensive *T*-matrix reference database: A 2007–2009 update. JQSRT **111** (2010).

[7] D.W. Mackowski. A simplified model to predict the effects of aggregation on the absorption properties of soot particles. JQSRT **100** (2006).

[8] D.W. Mackowski. Electrostatistics analysis of radiative absorption by sphere clusters in the Rayleigh limit: application to soot particles. Appl. Opt. **34** (1995).

[9] W.A. de Rooij. *Reflection and transmission of polarized light by planetary atmospheres*. Ph.D. thesis. Free University, Amsterdam (1985).

[10] M.I. Mishchenko. The fast invariant imbedding method for polarized light: computational aspects and numerical results for Rayleigh scattering. JQSRT **43** (1990).

[11] M.I. Mishchenko, L.D. Travis, and A.A. Lacis. *Multiple scattering of light by particles: radiative transfer and coherent backscattering*. Cambridge Univ Press, Cambridge (2006).

[12] M.I. Mishchenko and J.M. Dlugach. Radar polarimetry of Saturn's rings: modeling ring particles as fractal aggregates built of small ice monomers. JQSRT **110** (2009).

Analysis of the extreme transmission effect via discrete sources method

Y. Eremin[*,1], E. Eremina[2], N. Grishina[1], and T. Wriedt[3]

[1]*Moscow Lomonosov State University, Vorobyov's Hills, 119991 Moscow, Russia.*
[2]*University of Bremen, Badgasteiner str.3, 28359 Bremen, Germany.*
[3]*Institute of Materials' science, Badgasteiner str.3, 28359 Bremen, Germany.*

The Discrete Sources Method (DSM) has been adjusted to model polarized light transmission through metal film deposited on a glass prism with nano-sized inhomogeneity. A correlation between Extreme Transmission Effect (ETE) and Surface Plasmon Resonance (SPR) has been investigated. The distribution of the scattered intensity in the peak of ETE has been analyzed.

INTRODUCTION

The discovery of enhanced optical transmission through sub-wavelength holes in noble metal film has attracted considerable interest to this optical phenomenon [1]. Different groups of researchers worldwide have recently examined the transmission properties of sub-wavelength apertures. But the most of them considered normal incidence of an exciting plane wave on the film surface. At the same time, there are multiple practical applications involving an evanescent wave scattering in nano-optics and biophotonics [2-3]. Using evanescent waves allows in particular avoiding the problem of filtering of the scattered light from the refracted one behind the film.

Extreme Transmission Effect (ETE) through a nano-sized hole in noble metal film deposited on a glass prism has been reported in [4]. Later it was found that the ETE also occurs with other types of the film inhomogeneities [5]. The ETE arises in the region of evanescent waves behind the angle of total internal reflection. It demonstrates a sharp (by an order of magnitude) increase in the total scattering cross section compared to the normal incidence of the wave on the film. In this case, the diameter of an inhomogeneity is much smaller than the diffraction limit. A specific feature of this effect is that it is independent of the inhomogeneity shape, diameter and material, the film thickness, and the filling of the external half-space; it can only be determined by the film material.

In this paper, we consider a correlation between ETE and Surface Plasmon Resonance (SPR) [6]. The Discrete Sources Method [3] has been adjusted to model polarized light transmission through metal film deposited on a glass prism with nano-sized inhomogeneity. The distribution of the scattered intensity in the peak of ETE has been analyzed.

* Corresponding author: Yuri Eremin (eremin@cs.msu.ru)

The Discrete Sources Method

The model presented here is based on the Discrete Sources Method (DSM), which seems to be one of the most flexible techniques for scattering problems treatment. The advantage of the DSM is that it is a semi-analytical meshless method and it does not require any integration procedures. By use of this technique, the scattered field everywhere outside an axial-symmetric inhomogeneity is constructed as a finite linear combination of the fields resulting from multipoles distributed over the axis of symmetry inside the inhomogeneity. The DSM solution satisfies the Maxwell equations, required conditions at infinity, and transmission conditions enforced at the layered interfaces. The Green Tensor of a layered plane interface is employed to account for the complete interaction of the inhomogeneity with a stratified interface analytically. While most of the conditions of the boundary-valued scattering problem are satisfied analytically, the unknown discrete sources amplitudes are determined from transmission conditions enforced at the inhomogeneity's surface only [3]. One of the most attractive features of the DSM implementation consists in a flexible choice of the discrete sources system that is used for the approximation of the solution. Besides, the DSM enables to employ different numbers of basic functions for scattered and internal field representation that gives an opportunity to examine the obstacle with high refractive indices.

DSM numerical scheme is based on the axial symmetry of the scattering problem geometry (inhomogeneity plus interface). While the multipoles generating the fields are distributed over the axis of symmetry inside the inhomogeneity, the DSM solution including Weyl-Sommerfeld integrals accepts the form of finite Fourier series with respect to the azimuth angle. Exciting evanescent wave impinging the inhomogeneity from prism surface is resolved in Fourier series with respect to the azimuth angle. This leads to the reducing surface approximation to a set of one-dimensional approximating problems enforced at the inhomogeneity's meridian. To fit the transmission conditions we use generalized point-matching technique distributing the matching points over the meridian. It provides reduction of the sizes of linear systems to be solved and thus leads to a reduction of the computation time and memory storage. Multipoles' amplitudes are determined as pseudo-solutions over-determined systems of the linear equations. To ensure the full rank a rectangular matrix of the over-determined systems regularization procedure is applied. We use complex shift of spectrum of the extended rectangular matrix, which enables to get normal pseudo-solution.

The DSM numerical scheme allows considering of all incident angles and both polarization P and S at once. The DSM computer model controls convergence and stability of the results by a posterior evaluation of the surface residual at the inhomogeneity surface in least square norm. Besides, the corresponding far field pattern is represented as a finite linear combination of elementary functions allowing fast computer analysis of the intensity distribution and objective response [4].

NUMERICAL RESULTS

Let us consider the scattering of a P/S polarized plane wave propagating from glass (LASF46A) prism with a refractive index n_p=1.904, on Si (n=4.37-0.08j) sphere, D=49 nm, immersed in Au (n_f=0.18-3.26j) film of thickness d=50 nm. We analyze the scattered inten-

sity in the incident plane versus scattering angle and Scattered Cross Sections (SCSs) in upper and lower hemispheres versus incident angle with respect to the normal to the plane interfaces.

Figure 1 demonstrates the SCS in μm² units for P/S polarized incidences versus incident angle. In this particular case the critical angle behind which the evanescent wave appears is θ_c=31.68°. One can see the close correlation between the SPR (minimum value of the reflection coefficient from prism-film-air media) and ETE. Minimum value of scattering appears at the incident angle of 32.5° and the maximum at 33.7°.

Figure 2 shows the distribution of the scattered intensity in the incident plane. Data for normal incidence - 180° demonstrate symmetry with respect to 0-180° plane. For the oblique incidences maximal values are achieved in the incident and specular directions.

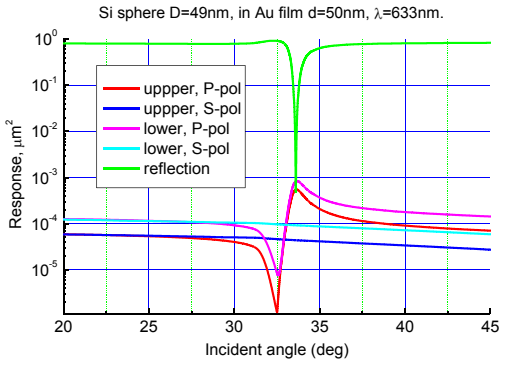

Figure 1.

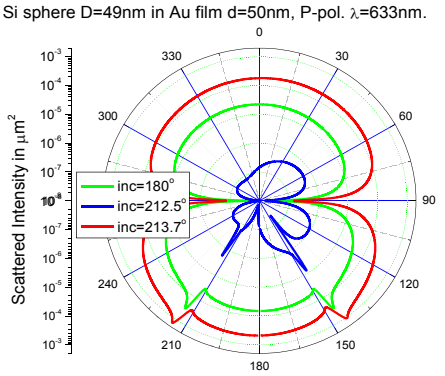

Figure 2.

ACKNOWLEDGEMENTS

Authors would like to acknowledge support of this work by the Russian Foundation for Basic Research (Project 09-01-00318).

REFERENCES

[1] R. Wannemacher. Plasmon-supported transmission of light through nanometric holes in metallic thin films. Opt. Comm. **195** (2001).

[2] I. Abdulhalim, M. Zourov, and A. Lakhtakia. Surface Plasmon Resonance for Biosensing: A Multi Review. Electromagnetics. **28** (2008).

[3] Yu.A. Eremin and A.G. Sveshnikov. Mathematical models in nanooptics and biophotonics problems on the base of Discrete Sources Method. Comput. Maths. Math. Phys. **47** (2007).

[4] E. Eremina, Y. Eremin, N. Grishina, and T. Wriedt. Analysis of light scattering in the evanescent waves area by a cylindrical nanohole in a noble-metal film. Opt. Comm. **281** (2008).

[5] E. Eremina, Y. Eremin, N. Grishina, and T. Wriedt. Analysis of Extreme Light Transmission Through a Nanohole in a Metal Film Based on Discrete Sources Method. J. Comput. Theor. Nanoscience **6** (2009).

[6] N. Grishina, Yu.A. Eremin, and A.G. Sveshnikov. Analysis of the effect of an extremal energy leakage through a conducting film with a nano-sized inset. Optics and Spectroscopy **106** (2009).

[7] S. Maier. *Plasmonics: Fundamentals and Applications*. Springer. 2007.

Modeling aspects of computer analysis of light scattering from red blood cells

E. Eremina*

University of Bremen, Badgasteiner str. 3, 28359 Bremen, Germany.

Biological particles play important roles in all aspects of our life. Studying their features and behavior is of interest for a wide variety of applications, from engineering to medicine. Among other biological particles, the human red blood cell attracts special attention due to its importance for human health. In this paper modeling aspects of computer simulations of light scattering from red blood cells and some numerical methods suitable for such modeling are discussed. Recent calculation results based on an improved numerical scheme of the Discrete Sources Method are presented in comparison with results of the Discrete Dipole Approximation.

INTRODUCTION

In recent years, biological particles and their features have been studied intensively for multiple applications, from climate science to medicine. The investigation of light scattering by biological particles is considered to be an effective technique for obtaining information about their properties. This is supported by a considerable amount of modeling methods that can be applied to the theoretical study of light-scattering problems. In an ideal case the results of numerical modeling can be applied for the interpretation of measured results [1].

Human blood cells are intensively studied due to their importance for human health. Among other blood cells the Red Blood Cell (RBC, erythrocyte) attracts considerable attention due to its functions in blood and relatively simple internal structure. Biologically, the RBC is responsible for oxygen delivery over the body and change in its optical properties is a marker for certain diseases (e.g. anemia). The last fact makes its study of interest for medical diagnostic applications. In most mammals, mature RBCs lack a nucleus and organelles, typical for other cells. It makes it a convenient object for modeling methods.

MODELLING ASPECTS AND METHODS

Despite the fact the RBC has no internal structure, its complicated biconcave shape causes difficulties for modeling. In earlier works the RBC has been approached as a sphere and in some works, an equivolume sphere. Later it has been suggested to use the shape of a flat disk or oblate spheroid. Recently, it has been shown that simplified approximations that do not account for erythrocyte biconcavity in some cases deliver totally different results [2]. In the last years several shape models to approach the realistic biconcave shape have been

* Elena Eremina (eremina@iwt.uni-bremen.de)

suggested: Fung model, Skalak model, Lu model, Cassini-based model. Their short description is collected e.g. in [3].

In recent years different numerical methods have been applied to model the light scattering by biconcave shape models of the RBC. One of them is the Finite Difference Time Domain (FDTD) [4]. The method provides a discrete reformulation of Maxwell's equations in their differential form. It restricts the electromagnetic field problem with its open boundary problem to a simply connected and bounded space containing the region of interest. The computational domain is decomposed into a finite number of volume elements. Due to this fact the FDTD is well suitable for parallelization that helps to reduce the time of calculations. Parallelization was successfully used for calculation of RBC [4,5].

The Discrete Dipole Approximation (DDA) is another effective method for calculation of light scattering by biconcave RBCs [6]. The idea of DDA is based on a volume discretization of the investigated object. The scatterer is approximated by a lattice of dipoles, whose number depends on object shape, size, refractive index, wavelength etc. The scattering characteristics are calculated as a superposition of the dipole's fields. The main restriction of the DDA is its complexity for computation due to the growing number of dipoles used. The main challenge for DDA application consists in the low relative refractive index of RBC (1.03-1.06). The latter circumstance makes it possible to start an iterative procedure from the Born approximation, which provides reasonable values for the dipoles' polarisation. In the last years DDA has been compared to FDTD [7].

Another method suitable for modeling of biconcave RBCs is the Discrete Sources Method (DSM) [8]. The main advantage of the DSM is that it is a semi-analytical meshless method and it does not require any integration procedure. By use of this technique the scattered field everywhere outside an axially symmetric obstacle is constructed as a finite linear combination of the fields of Discrete Sources (DS) (multipoles) deposited in a complex plane adjoined to the symmetry axis of the RBC. This procedure is presented in [2] in details. The DSM solution is built to satisfy Maxwell's equations and conditions at infinity. While the most conditions of the scattering problem are satisfied analytically the unknown amplitudes of the DS are determined from transmission conditions enforced at the obstacle surface. One of the most attractive features of the DSM implementation consists in a flexible choice of the DS, which are used for the construction of the approximate solution. Besides, the DSM enables the employment of different numbers of DS used for the scattered and the internal field representation, which provides an opportunity to examine the obstacle with high refractive indices as well.

The DSM numerical scheme makes use of the axial symmetry of an obstacle's geometry and is especially suitable for biconcave shapes. Due to the multipoles' deposition in a complex plane, the DSM solution accepts the form of a finite Fourier series with respect to the azimuth angle. It allows a reduction of the surface approximation problem over the whole surface to a set of one-dimensional approximating problems enforced at the particles' meridian. To fit the transmission conditions, the generalized point-matching technique is used. It provides a considerable reduction of the sizes of linear systems and leads to a decrease of the computation time and memory storage used. The multipoles' amplitudes are determined as pseudo-solutions of over-determined systems of the linear equations. To ensure the full rank of a rectangular matrix in the over-determined system, a regularization procedure is applied.

In the last years, different shape models for RBCs have been used for light-scattering calculations based on the DSM [2,9]. The investigation of the RBC parameters on the light-scattering characteristics has been presented in [10]. The results of the DSM have been compared to results of some other numerical methods [3]. Recently it has been compared with DDA [11]. Comparison with DDA demonstrated that for RBC calculations under large scattering angles in respect to the rotational axis, DSM meets some difficulties, which are caused by a large number of Fourier harmonics needed to construct the solution. At the same time the DSM numerical scheme allows calculation of all incident angles and both polarization P and S at once, which is advantageous compared to DDA. Besides, the DSM based computer model controls convergence and stability of the results by a posterior evaluation of the surface residual at the particle surface in least-square norm [8].

NUMERICAL RESULTS

In the last months the DSM code has been improved by use of the Tikhonov's regularization in least square sense with a spectral shift in a complex plane. Due to this improvement it is now able to overcome the numerical instability observed previously.

In the following figures the results of a comparison between the DSM and DDA are presented for the element $S_{11}(\theta)$ of the Mueller Matrix [5]. For this demonstration the Fung model of the RBC [4] with a diameter D=6 μm has been taken. The wavelength is λ=496 nm (in water), the RBC refractive index is n=1.06, and the incident angle is 90°. In Fig. 1 the results based on the unmodified version of the DSM code in comparison with the results of DDA are presented (see [11]). Fig. 2 shows the same results, but for the modified DSM code. From these results it is obvious, that the modified version delivers much more stable results, which show good congruence with DDA compared to the old version.

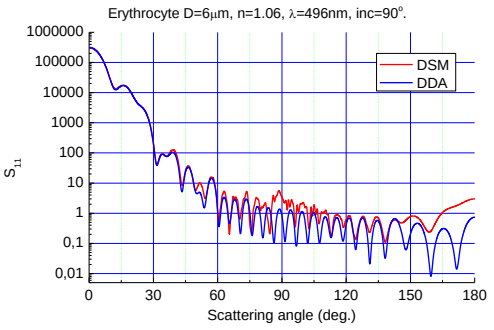

Figure 1.

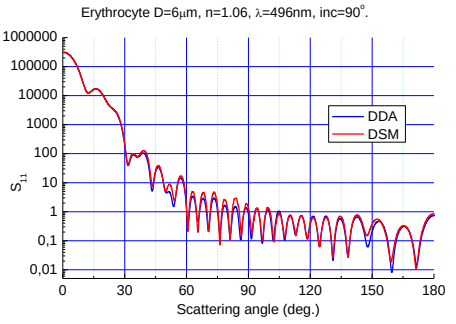

Figure 2.

ACKNOWLEDGEMENTS

The author would like to acknowledge support of this work by the Deutsche Forschungsgemeinschaft (ER 553/1-1).

REFERENCES

[1] V.P. Maltsev and K.A. Semyanov. *Characterisation of Bio-Particles from Light Scattering*. Inverse and Ill-Posed Problems Series. VSP, Utrecht (2004).

[2] E. Eremina, Y. Eremin, and T. Wriedt. Analysis of light scattering by different shape models of erythrocyte based on Discrete Sources Method. Opt. Comm. **244** (2005).

[3] T. Wriedt, J. Hellmers, E. Eremina, and R. Schuh. Light scattering by single erythrocyte: Comparison of different methods. JQSRT **100**(1-3) (2006).

[4] J.Q. Lu, P. Yang and X.H. Hu. Simulations of light scattering from a biconcave red blood cell using the finite-difference time-domain method. J. Biomed. Opt. **10**(2) (2005).

[5] R.S. Brock, X.-H. Hu, P. Yang, and J.Q. Lu. Evaluation of a parallel FDTD code and application to modeling of light scattering by deformed red blood cells. Optics Express **13**(14) (2005).

[6] M.A. Yurkin, K.A. Semyanov, P.A. Tarasov, A.V. Chernyshev, A.G. Hoekstra, and V.P. Maltsev. Experimental and theoretical study of light scattering by individual mature red blood cells by use of scanning flow cytometry and a discrete dipole approximation. Applied Optics **44**(25) (2005).

[7] M.A. Yurkin, A.G. Hoekstra, R.S. Brock, and J.Q. Lu. Systematic comparison of the discrete dipole approximation and the finite difference time domain method for large dielectric scatterers. Optics Express **15**(26) (2007).

[8] Yu. Eremin. The method of discrete sources in electromagnetic scattering by axially symmetric structures. J. Commun. Technology and Electronics **45**(Suppl. 2) (2000).

[9] E. Eremina, J. Hellmers, Y. Eremin, and T. Wriedt. Different shape models for erythrocyte. Light scattering analysis based on the Discrete Sources Method. JQSRT **102** (2006).

[10] E. Eremina. Light scattering by an erythrocyte based on Discrete Sources Method: shape and refractive index influence. JQSRT **110** (2009).

[11] K.V. Gilev, E. Eremina, M.A. Yurkin, and V.P. Maltsev. Comparison of the discrete dipole approximation and the discrete source method for simulation of light scattering by red blood cells. Optics Express **18**(6) (2010).

New studies on scattering properties of four kinds of soot

M. Francis[*,1], J.-B. Renard[1], E. Hadamcik[2], B. Couté[1], B. Gaubicher[1], and M. Jeannot[1]

[1]*L Laboratoire de Physique et Chimie de l'Environnement et de l'Espace / Université d'Orléans, 3A avenue de la recherche scientifique, F-45071 Orléans cedex 2, France.*
[2]*UMPC Univ. Paris 06, LATMOS-IPSL, BP3, F-91371 Verrières le Buisson cedex, France.*

New polarization curves as a function of the scattering angle are studied with PROGRA2 instruments (Propriétés Optiques des Grains Astronomiques et Atmosphériques) for 4 different kinds of soot, levitating in a cloud and deposited on a surface. The smallest agglomerates of few μm produce higher polarization values than the full set of agglomerates. The small agglomerates and the packed particles on a surface have the higher polarization. These results need more studies. These curves will be used for detection of soot in the stratosphere by remote sensing measurements.

INTRODUCTION

It is now known that soot is present in stratosphere, and it can have a direct effect on the atmospheric chemistry and, through radiative transfer, on climate [1]. Reference scattering curves for soot are necessary to identify their types from remote sensing measurements in particular using balloon-born radiometer MicroRADIBAL [2]. Models using the Mie theory failed to give the optical properties of soot because of their fractal irregular shape [3]. An experimental database of the optical properties of soot made in a laboratory is then necessary. Preliminary studies on light scattering with some kinds of soot have already been done [1]. Here we present new measurements for the polarization produced by four types of soot obtained by the PROGRA2 experiment. New cameras used by PROGRA2 are more sensitive, so the optical properties of the smaller particles are easier to detect.

The studied samples have an unknown imaginary part of the index, complicating the explanation of the polarization degrees. Previous studies on polarization by deposited particles have been made by Shkuratov et al. 2006 [4], where the imaginary part of index was known.

MEASUREMENT SYSTEM WITH PROGRA2-VIS AND DATA ANALYSIS

PROGRA2 instruments are imaging polarimeters with two randomly polarized lasers at 632.8 nm and 543.5 nm. The laser beam carried by optical fibres illuminates the particles. Light scattered by samples at a given scattering angles is split between the parallel and perpendicular component by a beam splitter cube. The cube is followed by the detectors: two CCD cameras providing 25 images per second. PROGRA2-vis observes the levitating parti-

* Corresponding author: Mirvatte Francis (mirvatt@hotmail.com)

cles lifted by a small injection of nitrogen in a vial. The incident laser beam and the vial rotate and the detection system is fixed. The size of the agglomerates having diameters greater than 20 μm can be determined by images recorded by the instrument. PROGRA2-surf performed measurement for deposited particles on a surface. More details of the PROGRA2 are presented in Renard et al. [5] and in Hadamcik et al. [6].

The degree of linear polarization P of the scattered light can be given

$$P = \frac{I_{per} - I_{par}}{I_{per} + I_{par}} , \quad (1)$$

where I_{per} and I_{par} are the scattered intensities polarized perpendicular and parallel to the scattering plane, respectively.

The imaging system allows sorting out the polarization values per different grain size classes to estimate the effect of size on the polarization for a given sample.

SCATTERING CURVES FOR SOOT

Studied samples

Two of the studied samples are produced from an incomplete combustion of a liquid solvent: Toluene (C_7H_8). The two others are produced from a solid polymer; Polymethyl Methacrylate or PMMA ($C_5H_8O_2$). Table 1 shows information about the studied samples. The global equivalent ratio is defined as the ratio between the mass ratio of fuel to air during the experiment, and the mass ratio of fuel to air at stoichiometry [6].

Table 1. Detailed info about the four samples.

Name	Ventilation flow rate (m^3/h)	Global equivalence ratio	Primary particle diameter (nm)	Fractal dimension	Soot density (g/cm^3)
Toluene1	450	0.01	52	1.86	1.46
Toluene2	100	0.06	70	1.81	1.46
PMMA1	450	0.06	42	1.78	1.52
PMMA2	50	0.49	56	1.74	1.52

Levitating and deposited samples

Figure 1 presents the dependence of linear polarization on the scattering angle at λ =632.8 nm for levitating agglomerates of soot. The amplitude of positive polarization branches are obtained with toluene1, followed by a similar behavior of the polarization produced by toluene2 and PMMA1. The lowest amplitude of the polarization is obtained with PMMA2. All the amplitudes of polarization are obtained for scattering angles between 80° and 90°.

The angular profile of linear polarization produced by the smallest agglomerates of a few μm in diameter can be retrieved by using images recorded after 30 seconds of the nitrogen injection. Fig. 2 shows the polarization curves of such particles. An obviously larger difference is noticed between the polarization amplitude obtained with the smallest agglomerates and those obtained with the full set of agglomerates. As we can see in the Fig. 2, the two samples issued with low flow ventilation rate PMMA1 and toluene1 produce the highest polarization curves and show similar behavior to each other. The two other samples, PMMA2 and toluene2, having lower flow ventilation rate than the others, produce lower polarization curves for the small agglomerates. When the ventilation flow rate decreases, the global equivalent ratio increases, and the fractal dimension decreases [7]. This could be an explanation for the impact of the ventilation flow rate on the polarization values.

It is interesting to check the dependence of polarization on the diameter of the agglomerate after averaging the data over size intervals of 50 μm, following a power law fit. The imaging system allows identifying polarization produced by particles larger than 20 μm in diameter. Fig. 3 shows an example given at 70° scattering angle, obtained with the sample Toluene1. The polarization increases with the diameter, and large fluffy absorbing particles produce higher polarization [6].

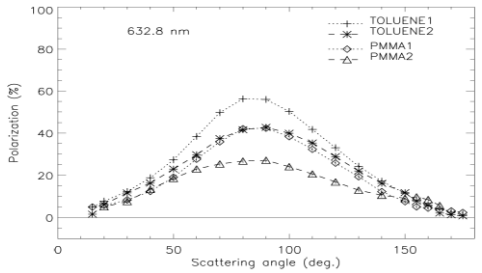

Figure 1. Polarization curves for the agglomerates for levitating samples.

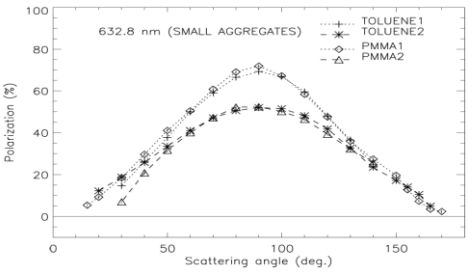

Figure 2. Polarization curves for the small agglomerates for levitating samples.

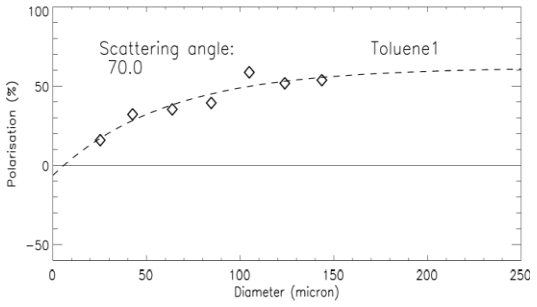

Figure 3. Dependence of polarization on size after averaging the data over 50 μm size intervals.

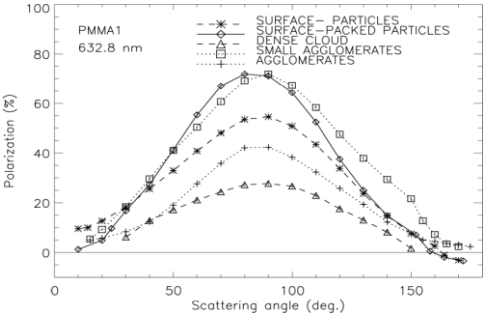

Figure 4. Polarization curves for the PMMA1 sample measured in different conditions.

Figure 4 shows a comparison of amplitudes of positive polarization branches for the same sample, PMMA1, in different conditions. The highest amplitudes of polarization are

obtained with the two curves produced by the smallest agglomerates and with the packed particles on a surface. The amplitude for both of these curves is about 72 %. A negative polarization is noticed for the packed samples on a surface at large scattering angles. Deposited particles produce lower polarization curves than the packed ones and greater than the one obtained with lifted agglomerates. The lowest polarization amplitude is given by a dense cloud of particles; more studies are needed and are in progress to give an explanation for this result.

CONCLUSIONS

Smallest agglomerates in a range of few μm in diameter present a higher amplitude of polarization than those obtained with the full set of agglomerates. The polarizations produced by small agglomerates mainly depend on the flow ventilation factor used during the incomplete combustion. Smallest agglomerates and packed particles on a surface give the highest amplitude of polarization. The lowest amplitudes are produced by a dense cloud of levitating agglomerates; further studies are needed to explain this result.

The new version of PROGRA2 using more sensitive cameras allows to detect agglomerates having low brightness. New measurements with other kinds of soot will be studied. Finally the data will be added to the PROGRA2 data base (http://www.icare.univ-lille1.fr/progra2/). In particular, they will be used to identify the type of the grains of soot detected in the stratosphere with MicroRADIBAL.

REFERENCES

[1] J.-B. Renard et al. Optical proprieties of randomly distributed soot: improved polarimetric and intensity scattering functions. Appl Opt. **44**(4) (2005).

[2] C. Brogniez et al. PSC microphysical properties measured by microRadibal instrument on January 25, 2000 above Esrange and modeling interpretation. J. Geophys. Res **108**(D6) (2003).

[3] S. Klusek et al. Compendium of scattering matrix element profiles for soot agglomerates. JQRST **79-80** (2003).

[4] Yu. Shkuratov et al. Comparative studies of the reflectance and degree of linear polarization of particulate surfaces and independently scattering particles. J. Quant. Spectrosc. Radiat. Transfer **100** (2006).

[5] J.-B. Renard et al. Light scattering by dust particles in microgravity: Polarization and brightness imaging with the new version of the PROGRA2 instrument. Appl. Opt. **41** (2002).

[6] E. Hadamcik et al. Light scattering by agglomerates: Interconnecting size and absorption effects (PROGRA^2 experiment). JQSRT **110**(14–16) (2009).

[7] F.-X. Ouf et al. Characterization of Soot Particles in the Plumes of Over-Ventilated Diffusion Flames. Combustion Science and Technolog. **180**(4) (2008).

Thermal performances of nanoscale-gap thermophotovoltaic energy conversion devices

M. Francoeur[1], M. P. Mengüç[*,1,2], and R. Vaillon[3]

[1]*Radiative Transfer Laboratory, Department of Mechanical Engineering, University of Kentucky, Lexington, KY 40506-0503, USA.*
[2]*Özyeğin University, Altunizade, 34662 Istanbul, Turkey.*
[3]*Université de Lyon, CNRS, INSA-Lyon, UCBL, CETHIL, UMR5008, F-69621, Villeurbanne, France.*

The thermal effects on the performances of $In_{0.18}Ga_{0.82}Sb$ based nanoscale-gap thermophotovoltaic (nano-TPV) energy conversion devices are analyzed via the solution of the coupled near-field thermal radiation, charge and heat transport problem. The results suggest that the performances are quite low due to excessive heating of the p-n junction converting radiation into electricity. This problem could be circumvented by designing nanostructures selectively emitting thermal radiation in the near-field.

INTRODUCTION

In thermophotovoltaic (TPV) energy conversion, a heat source is employed to maintain a radiator at a specified temperature, which in turns emits thermal radiation toward a cell generating electricity. In order to potentially improve the power output and conversion efficiency of TPV systems, Whale and Cravalho [1] proposed to separate the radiator and TPV cells by a sub-wavelength vacuum gap. At sub-wavelength distances, radiation heat transfer is in the near-field regime, such that the energy exchanges can exceed the values predicted for blackbodies. For thermal radiation temperatures, the near-field effects become dominant when the bodies are separated by few tens of nanometers. Therefore, a TPV system using the near-field effects of thermal radiation is referred hereafter as a nanoscale-gap TPV (nano-TPV) device. While the studies available in the literature have clearly shown that the near-field effects of thermal radiation can substantially improve the electrical power output of TPV systems [1-3], some important questions about the feasibility of nano-TPV energy conversion are still unanswered. In this work, we aim to study the energy required for maintaining the TPV cells at room temperature via the analysis of the thermal effects in nano-TPV devices. For purpose of comparison with the literature, we study systems based on $In_{0.18}Ga_{0.82}Sb$ cells [3].

* Corresponding author: M.P. Mengüç (pinar.menguc@ozyegin.edu.tr)

EVALUATION OF NANO-TPV SYSTEM PERFORMANCES

As shown in Fig. 1, a bulk radiator (tungsten W, T_0 = 2000 K) and a TPV cell ($In_{0.18}Ga_{0.82}Sb$, bandgap E_g of 0.56 eV at 300 K) are separated by a sub-wavelength vacuum gap of length d_c. The TPV cell consists of a single p-n junction, where the thicknesses of the p-doped and n-doped regions are given by t_p = 0.4 μm and t_n = 10 μm [3]. As the TPV cell is likely to heat up from various sources (absorption by the free carriers and the lattice, non-radiative recombination and thermalization [4]), a thermal management system is used to maintain the p-n junction around room temperature. The cooling system is modeled as a convective boundary with a fixed temperature T_∞ = 293 K and a heat transfer coefficient h_∞.

The performances of the nano-TPV device are evaluated through the solution of the coupled near-field thermal radiation, charge and heat transport problem. The mathematical details as well as the modeling of the optical, electrical and thermophysical properties are given in reference [4].

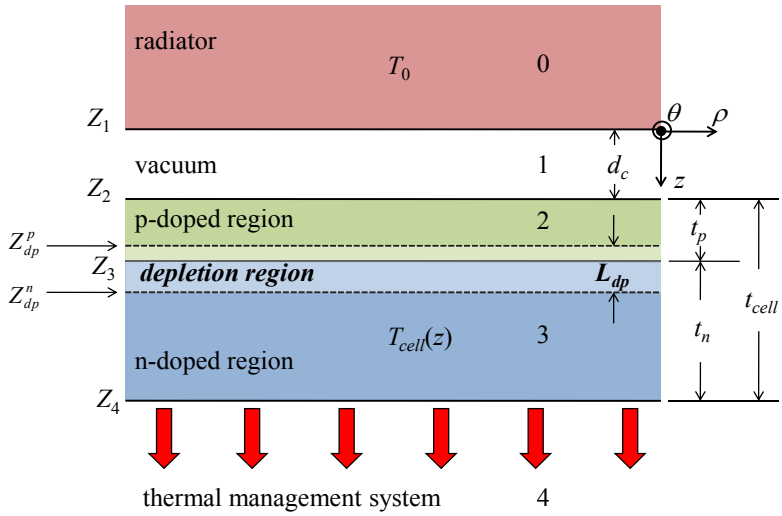

Figure 1. Schematic representation of the nano-TPV power generation system under study.

When the temperature of the cell is varied artificially (i.e., the energy equation is not solved), it can be observed in Fig. 2(a) that thermal radiation absorption increases slightly as the temperature of the cell increases mostly due to the fact that E_g decreases. On the other hand, the electrical power output P_m decreases significantly when T_{cell} increases, regardless of the gap d_c. For example, the conversion efficiency η_c is 24.8% when d_c = 20 nm and T_{cell} = 300 K, a value that drops to 3.23% when T_{cell} = 500 K.

Figure 2(b) shows that the short-circuit current J_{sc} slightly varies with T_{cell}, while the open-circuit voltage V_{oc} significantly decreases with increasing T_{cell} (due to an increasing dark current), thus explaining the low P_m and η_c values reported above.

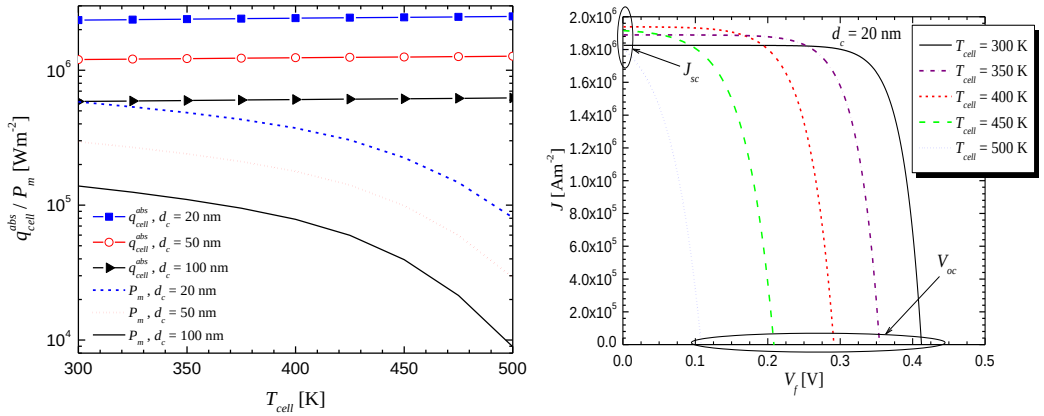

Figure 2. (a) Radiation absorbed by the cell and electrical power output as a function of T_{cell} and d_c. (b) J-V characteristic for d_c = 20 nm as a function of T_{cell}.

Figure 3(a) shows averaged cell temperature $T_{cell,avg}$ as a function of the heat transfer coefficient h_∞ for various gaps d_c. The values of h_∞ needed to maintain the TPV cell around 300 K are quite high. Indeed, for a gap d_c of 5 μm, a h_∞ value of 10^4 Wm^{-2}K^{-1} is required to maintain the p-n junction around room temperature, while a h_∞ of 10^5 Wm^{-2}K^{-1} is needed for gaps d_c of 100 nm, 50 nm, and 20 nm. Generally speaking, heat transfer coefficients h_∞ up to 10^3 Wm^{-2}K^{-1} can be achieved via free convection, while h_∞ up to about 2×10^4 Wm^{-2}K^{-1} can be reached by forced convection; heat transfer coefficients above this threshold are possible via convection involving phase change. The results of Fig. 3(a) should not be surprising, since radiation with energy E exceeding the bandgap E_g largely contributes to heat generation in the p-n junction. The use of a bulk radiator in the near-field provides a broadband enhancement of the flux, which contributes simultaneously to increase the electrical power output and to increase heat generation within the p-n junction.

The electrical power output is presented in Fig. 3(b) as a function of d_c and the heat transfer coefficient h_∞. As expected, the performances of the nano-TPV devices are significantly affected by the thermal boundary condition imposed at Z_4. For example, when d_c = 20 nm, the conversion efficiency η_c is 25.4% when $h_\infty = 10^6$ Wm^{-2}K^{-1} ($T_{cell,avg}$ = 294 K), and this value drops to 6.9% when $h_\infty = 5\times10^3$ Wm^{-2}K^{-1} ($T_{cell,avg}$ = 466 K).

CONCLUSIONS

The results presented in this work suggest that the performances of the nano-TPV devices proposed so far in the literature are quite low. A potential way to avoid excessive heating of the cell is to design nanostructures selectively emitting thermal radiation in the near field. The performance of the nano-TPV device discussed here could be analyzed further as a function of the doping levels, the configuration of the cell, the thicknesses of the p- and n-doped re-

gions, and the relative proportion of GaSb and InSb. Finally, the impacts of using radiators made of thin films of W should be investigated in a future research effort.

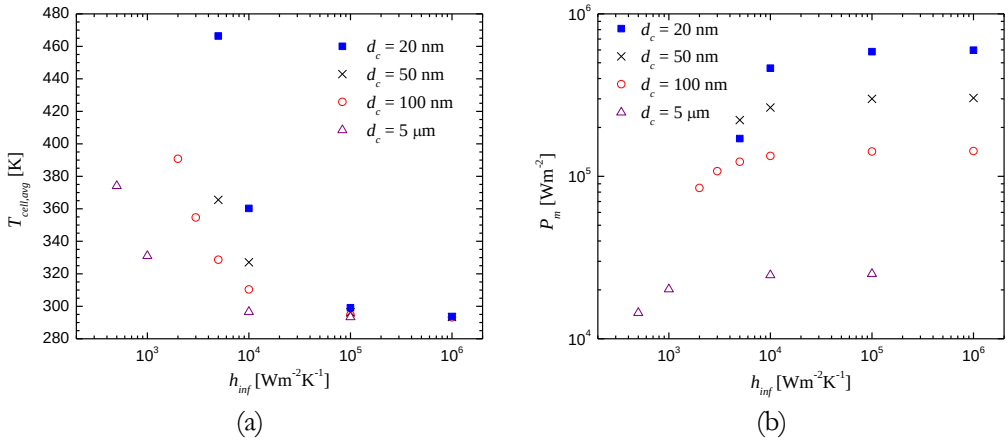

Figure 3. (a) Averaged cell temperature $T_{cell,avg}$ as a function of d_c and h_∞. (b) Electrical power output P_m as a function of d_c and h_∞.

ACKNOWLEDGEMENTS

This work is partially sponsored by the U.S. Department of Energy Grant No. DE-FG02-07ER46375 and the Kentucky Science and Engineering Foundation Grant No. KSEF-1718-RDE-011. Partial support for M.P.M. is received from a Marie Curie International Reintegration Grant (IRG) (NF-RAD 239382) through FP7-PEOPLE-IRG-2008) and by TUBITAK 1001 grant (109M170) at Özyeğin University, Istanbul.

REFERENCES

[1] M.D. Whale and E. Cravalho. Modeling and performance of microscale thermophotovoltaic energy conversion devices. IEEE Trans. Energy Convers. **17** (2002).

[2] M. Laroche, R. Carminati, and J.-J. Greffet. Near-field thermophotovoltaic energy conversion. J. Appl. Phys. **100** (2006).

[3] K. Park, S. Basu, W.P. King, and Z.M. Zhang. Performance analysis of near-field thermophotovoltaic devices considering absorption distribution. J. Quant. Spectrosc. Radiat. Transfer. **109** (2008).

[4] M. Francoeur. Near-field radiative transfer: Thermal radiation, thermophotovoltaic power generation and optical characterization. Ph.D. Dissertation, University of Kentucky (2010).

Development of a software package for the analysis of electromagnetic scattering from small particles

A. Gogoi[*,1], P. Rajkhowa[2], A. Choudhury[1], and G. A. Ahmed[1]

[1]*Optoelectronics and Photonics Research Laboratory, Department of Physics, School of Science and Technology, Tezpur University, Tezpur 784028, Assam, India.*
[2]*Computer Center, Tezpur University, Tezpur 784028, Assam, India.*

An integrated software package incorporated with a graphical user interface (GUI) was developed for modeling electromagnetic scattering from virtual small particles and also yield characteristic properties of real particles from experimental data. Its interactive features enable the user to observe the changes in output scattering properties in real time. In addition to its ease of use, it has high computational accuracy, efficiency, reliability and adaptability.

INTRODUCTION

The light scattering behavior of isolated spherical and nonspherical particles (ice particles, aerosols and hydrosols) where the particle size ranges from micrometer to nanometer is a subject of intensive research in the fields of remote sensing, climatology, radiative transfer, environmental science, astrophysics etc. The intensity of light scattered by a particle (or ensemble of particles) is a function of the angle between the incident and scattered radiation, size (and dispersion of sizes) of particles, shape (and dispersion of shapes) of particles, optical properties of particles (refractive index, permittivity, absorption), particle orientation, incident wavelength, polarization of the incident wave, density, structure of aggregates (fluffy, fractal, dense, etc.), and quality of particle surfaces (roughness, buffing, etc.). It is very important to study the angular scattering dependency of small particulate matter as such results contain information by which the particle may often be classified or even identified and helps for better understanding of radiation transfer through a medium containing the scatterer. Various theoretical approaches which involve computational techniques are used to explain experimentally observed light scattering patterns due to particulate matter. Some of these techniques are Mie theory, separation of variables (SVM) method, Ray optics or geometrical optics approximation, Waterman's T-matrix method, finite difference time domain (FDTD) method, discrete dipole approximation (DDA) etc. [1, 2]. Usually the solutions of these light scattering theories are very complex, hard to visualize and sometimes it becomes difficult to extract the physical characteristics of the scattering system from these solutions. However the recent rapid growth in the high performance computing systems, helped in developing efficient and accurate computer programs to simulate light scattering problems. Integration of such high performance computer programs with an interactive Graphical User Interface (GUI) makes the interaction between a user and a computer program very easy and helps the researchers to observe the results in near real time and verify their own techniques [3].

* Corresponding author: Ankur Gogoi (ankurgogoi@gmail.com)

In this contribution, an efficient and reliable software package named TUSCAT is developed on java platform and presented to simulate and display the plane wave scattering from small particles. The package uses and involves a user friendly GUI in order to enable the users to enter the required input parameters for light scattering calculations and observe the results more intuitively. The numerical results of the scattering matrix elements and the efficiencies can also be saved in a user defined data file. The computational programs behind TUSCAT are based on Mie theory for spherical particles and T-matrix theory for nonspherical particles (cylindrical and spheroids). Moreover, another very important facility for comparing experimental results from some unknown particle with theoretical results was also incorporated in the software so as to provide an analytical tool for light scattering experiments from monodisperse and polydisperse particles.

DESCRIPTION OF THE GRAPHICAL USER INTERFACE (GUI)

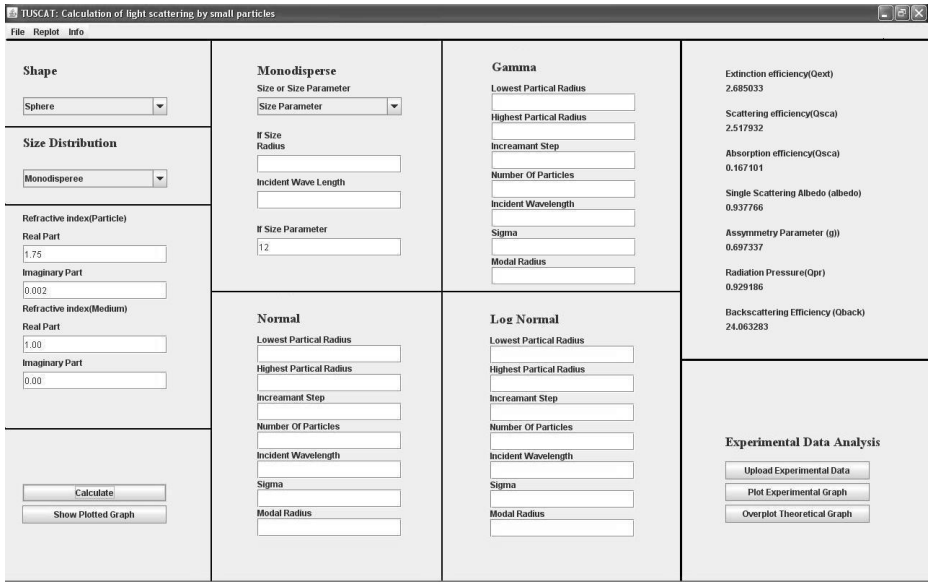

Figure 1. Screenshot of the GUI of the developed software package.

TUSCAT incorporates a user friendly GUI programmed in java (JDK 1.5). Fig. 1 shows a screenshot of the control panel of the GUI when calculations were done for a spherical particle of size parameter 12.0 and refractive index $1.75+i0.002$. The medium refractive index was taken to be $1.0+i0.0$. At the top of the window, a menu bar is used to save the calculated scattering matrix elements and the efficiencies and give initial information of the software. On the left hand side of the GUI, drop down menus are used to select the shape of the particles and size distribution of the particles. Complex refractive index of the particle and the medium can be given at the appropriate boxes below these dropdown menus. The theoretical calculations are initiated when the 'Calculate' button is pressed and similarly when 'Show plotted graph' button is pressed the software generated plots for different scattering matrix elements are shown as shown in Fig. 2. At the middle of the GUI four rectangular panels are provided to allow the user for entering the input parameters for the desired size distribution.

It is worth mentioning that only one of these rectangular panels is activated against the respective selection of the required size distribution in the size distribution drop down menu. On the right hand side of the GUI, the calculated values of extinction, scattering, absorption and backscattering efficiencies, single scattering albedo, asymmetry parameter and radiation pressure are displayed in their respective panels. At the bottom right of the GUI, the most important part of TUSCAT i.e. panel for experimental data analysis is placed. This facility can be used to compare the plots for the experimental data from an unknown scattering particle with the superimposed plots for theoretical data generated by varying the input parameters, to find the characteristic properties of that particle.

For nonspherical particles, the input boxes are slightly modified in the control panel and the plots for the scattering matrix elements are displayed in a similar plotting window.

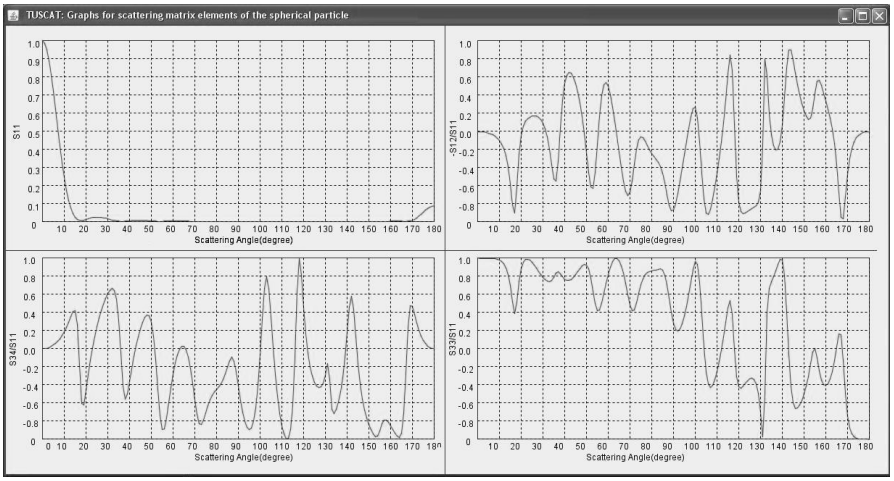

Figure 2. Screenshot of the plotting window.

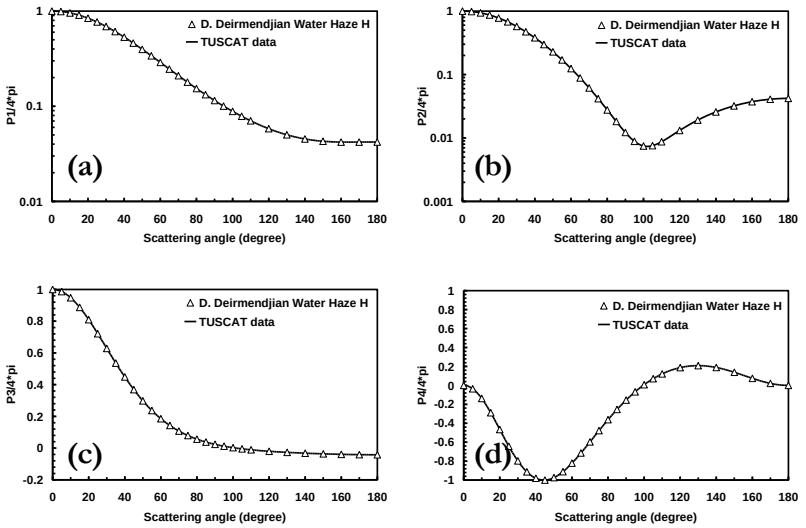

Figure 3. Normalized graphs of (a) $P_1/4\pi$, (b) $P_2/4\pi$, (c) $P_3/4\pi$ and (d) $P_4/4\pi$ as a function of scattering angle for Water haze H (as described by D. Deirmendjian [4]).

RESULTS AND DISCUSSION

TUSCAT was tested several times to optimize its performance and accuracy. The results for scattering efficiencies, radiation pressure, single scattering albedo, asymmetry parameter and the scattering matrix elements for different input parameters agree qualitatively well with the available computer programs and sources in the literature. For checking the accuracy of our program we used it to give the normalized values of $P_1(\theta)/4\pi$, $P_2(\theta)/4\pi$, $P_3(\theta)/4\pi$ and $P_4(\theta)/4\pi$ and compare the results with the normalized benchmark results (Table T.29) of D. Deirmendjian [4] for an ensemble of gamma distributed particles (Water haze H) having refractive index $1.322+i0.00001$, total number of particles 100 cm^{-3}, modal radius 0.1 μm, alpha 2, gamma 1 at 1.19 μm incident wavelength. It was observed that graphs for both the results tally within acceptable limits of deviation as shown in Fig. 3 (a)-(d) ensuring the efficiency and reliability of TUSCAT.

CONCLUSION

An interactive software package, TUSCAT was developed as an analytical tool for modeling light scattering properties of small particles and for the analysis of the experimental results from some unknown scatterer. The GUI associated with the software enables the user to visualize the effect of changing input parameters on the resulting scattering patterns in near real time. Works are in progress to improve the software package for the calculation of light scattering properties of other nonspherical shapes like Chebyshev particles, star shaped etc.

Acknowledgements: The work was supported by a Senior Research Fellowship (Physics) of the Council of Scientific and Industrial Research, India under sanction number 09/796/(0013)/2009/ EMR-I.

REFERENCES

[1] M.I. Mishchenko, J.W. Hovenier, and L.D. Travis. *Light Scattering by Nonspherical Particles: Theory, Measurements, and Applications*. San Diego, California: Academic Press (2000).

[2] N.V. Voshchinnikov, V.B. Il'in, Th. Henning, B. Michel, and V.G. Farafonov. Extinction and Polarization of Radiation by Absorbing Spheroids: Shape/Size Effects and Some Benchmarks. JQSRT **65** (2000).

[3] D. Ko. Kasper and C. Kimani. Toussaint Jr. A simple GUI for modeling the optical properties of single metal nanoparticles. JQSRT **110** (2009).

[4] D. Deirmendjian. *Electromagnetic Scattering on Spherical Polydispersions*. Elsevier, New York (1969).

Comparison of different TIRM schemes based on the DSM

N. Grishina[*,1], E. Eremina[2], Y. Eremin[1], and T. Wriedt[3]

[1]*Moscow Lomonosov State University, Vorobyov's Hills, 119991 Moscow, Russia.*
[2]*University of Bremen, Badgasteiner str.3, 28359 Bremen, Germany.*
[3]*Institute of Materials' science, Badgasteiner str.3, 28359 Bremen, Germany.*

Total Internal Reflection Microscopy (TIRM) is an effective technique to measure weak interactions between colloidal particles in solution and a flat surface. In this paper, the Discrete Sources Method (DSM) has been applied to model different TIRM measuring schemes to find the most appropriate one for the determination of the distance between the particle and flat surface. It has been found that placing the collector beneath the prism gives a considerable advantage as compared to the conventional TIRM design.

INTRODUCTION

Total Internal Reflection Microscopy (TIRM) is an effective modern technique to measure weak interactions between colloidal particles in solution and a flat surface with high resolution up to 1nm [1]. The high sensitivity of TIRM is due to the use of the Brownian fluctuations of a free colloidal particle for obtaining the interaction potential. Another advantage of TIRM is that it is appropriate for measurements close to the surfaces. Recently, TIRM has been applied to measure van der Waals, Casimir, magnetic, depletion, and electrostatic forces [2].

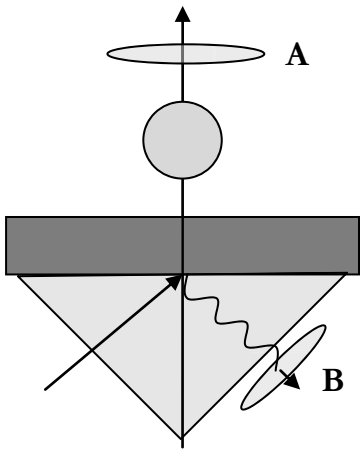

Figure 1. Model geometry: objective placement for the cases of conventional setup (A) and alternative setup (B).

In the beginning of TIRM measurements, the reconstruction of the interaction potential was based on the simple assumption that the intensity of the field scattered by a particle is

* Corresponding author: Natalia Grishina (ngrishina@inbox.ru)

proportional to the intensity of an evanescent exciting field in the particle domain. Later measurements showed deviation from the behaviour predicted by the simple model. Recently, the simple assumption has been corrected by using the rigorous scattering model based on the Discrete Sources Method (DSM) [3]. It has been proved that the use of the DSM model allows reconstruction of the potential with high precision [4].

In TIRM setups, the colloidal particle is situated above the glass prism. The laser beam propagating from the prism to the surface with an angle slightly above the angle of total internal reflection generates an evanescent field in the area above the prism. In conventional TIRM schemes the scattered light is collected by objective placed above the particle in the far zone (Fig. 1A). Recently, it has been suggested to place the light collector in the area beneath the glass prism. In this case, the collecting objective is oriented toward the beam which is reflected from the prism surface (Fig. 1B). To reduce the intensity of the reflected beam the effect of Plasmon Resonance (PR) in a thin gold film, deposited on the prism surface, can be employed [5]. In the present work, DSM has been applied to model and compare the efficiency of both of the suggested TIRM schemes. The direct comparison allows choosing the scheme that is more appropriate for the determination of the distance between particle and film.

Discrete Sources Method

In this section, we start with the mathematical statement of the polarized light scattering problem. Consider a glass prism occupying a half-space D_1, where $z<0$, with a metal film of thickness d occupying D_f, where $d>z>0$, on the prism. An axially symmetric penetrable particle with interior domain D_i and smooth boundary ∂D is deposited above the film in the domain D_0, where $z>d$. Introduce a Cartesian coordinate system $Oxyz$ by choosing its origin O at the prism surface Σ_0 and the z-axis coincides with the axis of symmetry of the particle and is directed into the domain D_0. We assume that the exciting field $\{\mathbf{E}^0, \mathbf{H}^0\}$ is a linearly polarized plane wave propagating inside the glass prism at an angle θ_1 with respect to the z-axis. Then, the mathematical statement of the scattering problem includes:

- the Maxwell equations, in $D_{1,f,i,0}$;
- transmission conditions at the prism, film $\Sigma_{0,f}$, and particle ∂D surfaces;
- the radiation conditions in $D_{1,0}$ and attenuation condition in D_i at infinity.

The solution of the boundary value problem (BVP) is constructed following the DSM requirements [3]. First, the diffraction problem of the plane wave $\{\mathbf{E}^0, \mathbf{H}^0\}$ on the layered plane interface is solved. The resulting field $\{\mathbf{E}^0_\zeta, \mathbf{H}^0_\zeta\}, \zeta = 0,1,f$ satisfies the transmission condition at $\Sigma_{0,f}$. Then, we construct an approximate solution of the BVP for the scattered field $\{\mathbf{E}^s_\zeta, \mathbf{H}^s_\zeta\}$ in the domains D_ζ, $\zeta = 0, f, 1$ and the total field inside the particle D_i. According to the DSM scheme, the electromagnetic fields are represented as a finite linear combination of multipole fields that satisfy analytically the following: the Maxwell equations

in the domains $D_{0,1,f}$ as well as the infinity conditions and the transmission conditions at the plane interfaces $\Sigma_{0,f}$. Thus, the scattering problem is reduced to the problem of approximating the exciting field on the particle surface ∂D. The amplitudes of Discrete Sources (DS) are to be determined from the transmission conditions at the particle surface ∂D

$$\mathbf{n}\times(\mathbf{E}_i-\mathbf{E}_0^s)=\mathbf{n}\times\mathbf{E}_0^0,\ \mathbf{n}\times(\mathbf{H}_i-\mathbf{H}_0^s)=\mathbf{n}\times\mathbf{H}_0^0 \qquad (1)$$

Here $\mathbf{n}$ is the normal to ∂D, and $\{\mathbf{E}_i,\mathbf{H}_i\}$ is the internal field.

To construct the fields of dipoles and multipoles that analytically satisfy the transmission conditions at the plane interfaces $\Sigma_{0,f}$, the Green's tensor for a stratified interface is used. Since the scattering problem geometry is axially symmetric with respect to the z-axis and the multipoles are distributed along the axis of symmetry, fulfilling the transmission conditions at the surface ∂D can be reduced to the sequential solution of the transmission problems for the Fourier harmonics of the fields involved in (1). So, instead of matching the fields on the scattering surface, we can match their Fourier harmonics, thus reducing the approximation problem on the surface to a set of problems enforced at the particle surface generatrix $\Im$. The one-dimensional problems are solved by the Generalized Point Matching Technique. In this approach, the Fourier harmonics of the DSM amplitudes are determined by solving over-determined linear systems and computing a normal pseudo-solution.

The approximate solution converges to the exact one since the systems of the fields of the dipoles and multipoles are complete. As DSM is a direct method, it allows solving the scattering problem for the entire set of incident angles θ_1 and both polarizations (*P* and *S*) at once. Besides, the numerical scheme provides an opportunity to control the convergence of the approximate solution by posterior error estimation [3].

After the amplitudes of the DSM are determined, one can compute the far field pattern of the scattered field in the far zone of $D_{1,0}$ as

$$\mathbf{E}_{0,1}^s(\mathbf{r})\Big/\left|\mathbf{E}^0(0)\right|=\frac{\exp\{jk_{0,1}r\}}{r}\mathbf{F}_{0,1}(\theta,\varphi)+O\left(r^{-2}\right),\ r\to\infty \qquad (2)$$

Here, $\mathbf{F}_{0,1}^{P,S}(\theta,\varphi)$ is a far field pattern at the unit sphere corresponding to *P*/*S* polarized excitation. It is represented by finite linear combinations of elementary functions. This circumstance ensures fast and effective computer analysis of the scattering characteristics in the far zone.

Presently, we consider the scattered intensity in $D_{0,1}$, $I_{0,1}^{P,S}(\theta_1,\theta,\varphi)=\left|\mathbf{F}_{0,1}^{P,S}(\theta_1,\theta,\varphi)\right|^2$, and the objective response $\sigma_{0,1}^{P,S}(\theta_1)=\int\limits_{\Omega_{0,1}} I_{0,1}^{P,S}(\theta_1,\theta,\varphi)d\omega$. Here the solid angles correspond to collectors deposited above or beneath the prism.

NUMERICAL RESULTS

Below some numerical results are presented. In Fig. 2, the objective response versus the particle-film distance is presented for the particle of diameter D=350 nm, for collectors deposited above the prism (conventional setup) and beneath the prism. From direct comparison, it is obvious that the interpretation of the measuring results for the standard scheme is complicated due to the non-monotonic behaviour of the curves for both polarizations. Unlike the conventional setup, the objective response of the scattered light observed beneath the prism behaves monotonically and should be easier to analyse. In Fig. 3, the intensity of the scattered light from the particle D=350 nm is presented in polar coordinates in the plane of the incident wave for two particle-film distances, which correspond to the positions of the local minima and maxima of the intensity curve for P polarization above the prism. These distances provide almost the same values of the collector's response for the conventional TIRM setup (see Fig. 2).

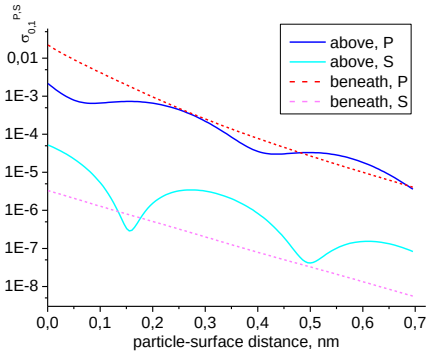

Figure 2. Objective response vs. the particle-film distance for the particle D=350 nm, collectors deposited above and beneath the prism. P and S polarizations.

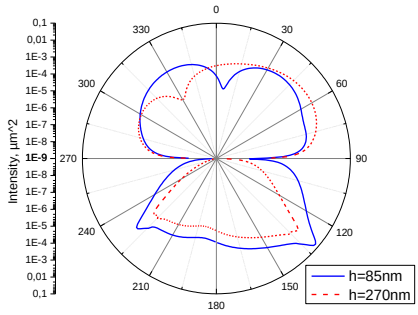

Figure 3. Intensity of the scattered light for the particle D=350 nm in the plane of incidence, two particle-film distances. P polarization.

REFERENCES

[1] D. C. Prieve. Measurement of colloidal forces with TIRM. Adv. Colloid. Interfac. Sci. 82 (1999).

[2] C. Hertlein, L. Helden, A. Gambassi, S.Dietrich, and C. Bechinger. Direct measurement of critical Casimir forces. Nature 451 (2008).

[3] Y. Eremin. The Method of Discrete Sources in electromagnetic scattering by axially symmetric structures. J. Commun. Technology and Electronics **45**(S2) (2000).

[4] L. Helden, E. Eremina, Y. Eremin, N. Riefler, C. Hertlein, C. Bechinger, and T. Wriedt. Single particle evanescent light scattering simulations for total internal reflection microscopy. Appl. Optics **45** (2006).

[5] H. Raether. *Surface Plasmon on Smooth and Rough Surfaces and on Gratings* (ch. 2). Springer, Berlin (1998).

Circular polarization of light scattered by a non-central region of a comet

D. Guirado*, F. Moreno, and O. Muñoz

Instituto de Astrofísica de Andalucía (CSIC), Glorieta de la Astronomía s/n 18008, Granada.

A Monte-Carlo model of radiative transfer in comets has been developed. It calculates the four Stokes parameters of the light scattered by particles in the coma. By applying this model, non-negligible values of the DCP were obtained just by assuming conditions of multiple scattering by spherical optically inactive particles, and considering only light coming from a non-central small region of the coma of the comet. The calculated values are one or two orders of magnitude below the observed, but the mechanism fits all other features of the observations.

INTRODUCTION

A non-zero degree of circular polarization (hereafter DCP), has been observed in light scattered by Comets Halley [1, 2, 3], Hale-Bopp [4, 5], C/1999 S4 (LINEAR) [6] and C/2001 Q4 (NEAT) [7]. The DCP is of the order of 1 % in Halley's observations, and of the order 0.1 % for the others that were observed in the 1990s and 2000s with better precision. Some other remarkable features of the observations are the following:

1. The DCP approaches zero when the aperture of the diaphragm increases in Halley's observations [2, 3].
2. For precise observations (all but Halley's), the DCP approaches zero when looking at the nuclear region of the comet.
3. In all cases, the observed DCP for a certain region of the comet is highly variable in time (day-to-day and even minute-to-minute).
4. In most cases, both positive and negative values of the DCP are obtained, except for two exceptions: observations of Hale-Bopp by Rosenbush et al. [5], where all obtained values were negative, and observations of Comet C/1999 S4 (LINEAR) [6]. For the latter case, all observed values were positive for the largest scattering angle (119.1°). Then both positive and negative values appeared at intermediate values of θ, becoming finally mostly negative at $\theta = 57.9°$.

Several mechanisms that may give rise to circular polarization in astrophysical environments have been historically proposed: *Alignment of non-spherical particles* [8], *Asymmetrical particles in random orientation* [9], *Optical activity* [6, 7] and *Multiple scattering* [2, 6]. As previous attempts to reproduce the observations of DCP by all mechanisms listed above were unsuccessful, we tried another one: local observation of a non-central region of the comet.

*Corresponding author: Daniel Guirado (dani@iaa.es)

FEASIBILITY OF THE MECHANISM

From now on, let us make two assumptions: the coma of the comet is spherical, and the source emits natural light (as solar light when considering wavelength bands as wide as those used in the observations [11]).

To be valid, the mechanism should explain all features of the observations listed above:

1. Opening the diaphragm means taking into account photons coming from other parts of the comet, with values of the Stokes parameter V, that may partially compensate those of the photons coming from the original region. Then, the DCP tends to zero.
2. By looking at the nuclear region of the comet, the scattering system becomes azimuthally symmetrical around the direction of the incident light, which makes the DCP to vanish [10].
3. The minute-to-minute variation of the DCP only occurs for the case of Halley, so it might be due to the lack of precision of those observations. For the other observations we find a day-to-day variation, which may be caused by the rotation and translation of the comet, and the variations that occur in its coma due to the thermal changes of its surface.
4. The predominant sign of the observed DCP might be due to symmetry reasons, related to the scattering angle. In particular, there might be a change of sign around $\theta = 90°$. This idea matches the observations: all negative values of the DCP observed by Rosenbush et al. [5] were obtained at one single scattering angle ($\theta = 134°$), but a change of sign might occur for $\theta < 90°$. In fact, it occurs in Comet C/1999 S4 when it moves from $119.1°$ to $57.9°$.

Let us assume reciprocity and mirror symmetry. Then, after applying to an incident packet of photons one single scattering event and a rotation of the scattering plane to write the Stokes parameters in the meridional plane of observation, the Stokes parameters of the outgoing light will be proportional to $(F_{11}, F_{12}\cos 2i_{rot}, -F_{12}\sin 2i_{rot}, 0)^t$, where (F_{ij}) is the scattering matrix, i_{rot} is the rotation angle, and t means transpose. As $V = 0$, then $DCP = 0$. This means that multiple scattering is necessary to produce a non-zero DCP.

DESCRIPTION OF THE RADIATIVE-TRANSFER MODEL

Let us represent a comet by a spherical cloud of dust, with a totally absorbent spherical solid shell of radius R_N in its center. The dust grains are assumed to be spherical optically inactive particles. The cloud extends to infinity but its particle number density distribution varies as $\frac{1}{R^2}$ with the distance R to the center. Packets of photons with Stokes parameters (1,0,0,0) are launched from a far plane-parallel source, their paths are tracked, and their Stokes parameters are recorded when they escape to infinity, along with the directions of escape (θ, φ). Some more details about the model can be found in [12].

RESULTS AND DISCUSSION

Let us consider a comet that is illuminated by a source in the direction and sense of axis Z. Scattered light is emitted from all regions of the comet in all directions. We focus only on packets of photons coming from a non-central small zone defined by a cone centered at $(\theta_{loc}, \varphi_{loc}) = (60°, 0°)$ with a width of $10°$.

Fig. 1 shows the results for $\tau_N = 2.5$ with $r_{max} = 200$ µm (left side), and $r_{max} = 2$ mm (right side). The rest of the input parameters are defined in the paragraph above and in Table 1. We just present results for $-90° \leq \varphi \leq 90°$ because the best statistics was achieved for those angles.

Table 1. Common input parameters for all radiative transfer calculations in the present work.

R_N	5 km
Kind of particles	spheres
Size distribution type	power-law, exponent=-3.5
r_{min}	0.05 µm
Refractive index	$1.6 + i0.001$
Wavelength	0.5 µm
Number of packets of photons launched	10^8

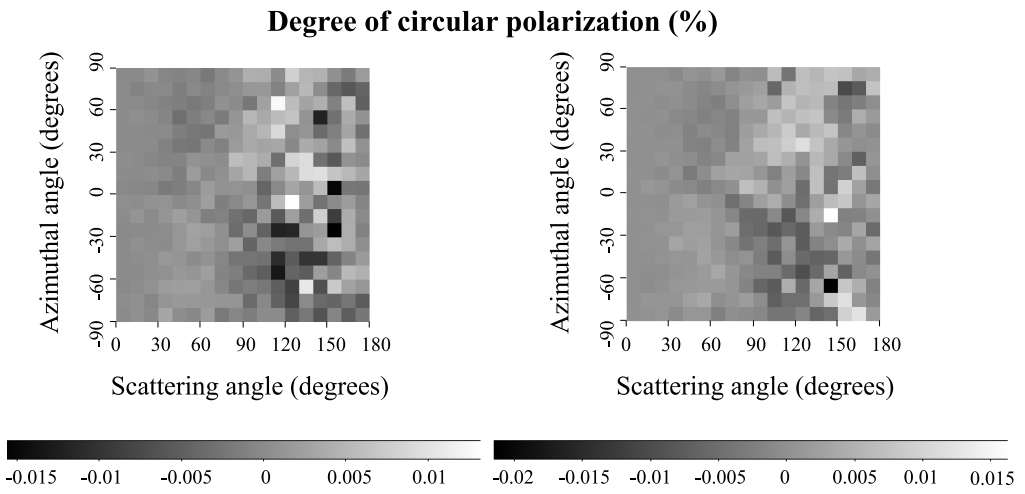

Figure 1. Results for the calculations of the DCP with our radiative transfer model by using parameters given in Table 1, $\tau_N = 2.5$ and two values of r_{max}: 200 µm for the left panel, and 2 mm for the right one.

We find three main features in the results presented in Fig. 1:

1. The upper and lower parts of both panels are color-complementary. If a certain DCP appears by any means for a certain scattering direction (θ, φ), the opposite value must be found when observing from $(\theta, -\varphi)$ because of the symmetry of the system.
2. A significant increase of the maximum DCP occurs when increasing r_{max}. This means that large particles make a very significant contribution to the DCP, especially considering that they are the least abundant (see Table 1).
3. The calculated values of the DCP are about one or two orders of magnitude below those of the observations.

We would like to remark that multiple scattering in the coma of a comet matches all features of the observed DCP, except for the order of magnitude of the calculated values.

Any other kind of grains (in size, shape or composition) may yield higher calculated values of the DCP.

REFERENCES

[1] A.V. Morozhenko, N.N. Kiselev, and A.L. Gural'Chuck. On the circular polarization of comet Halley head. Kinematica i Fizika Nebesnykh Tel **3** (1987).

[2] K. Metz and R. Haefner. Circular polarization near the nucleus of comet P/Halley. Astronomy and Astrophysics **187** (1987).

[3] A. Dollfus and J.-L. Suchail. Polarimetry of grains in the coma of P/Halley. I - Observations. Astronomy and Astrophysics **187** (1987).

[4] N. Manset and P. Bastien. Polarimetric observations of comets C/1995 O1 Hale-Bopp and C/1996 B2 Hyakutake. Icarus **145** (2000).

[5] V.K. Rosenbush, N.M. Shakhovskoj, and A.E. Rosenbush. Polarimetry of comet Hale-Bopp: linear and circular polarization, stellar occultation. Earth Moon and Planets **78** (1999).

[6] V. Rosenbush, L. Kolokolova, A. Lazarian, N. Shakhovskoy, and N. Kiselev. Circular polarization in comets: observations of comet C/1999 S4 (LINEAR) and tentative interpretation. Icarus **186** (2007).

[7] V. Rosenbush, N. Kiselev, N. Shakhovskoy, S. Kolesnikov, and V. Breus. Circular and linear polarization of comet C/2001 Q4 (NEAT). Why circular polarization in comets is predominantly left-handed? In: *X Conference on Electromagnetic & Light Scattering by Non-Spherical Particles*. Bodrum, Turkey (2007).

[8] A.Z. Dolginov and I.G. Mitrofanov. Orientation of cometary dust and polarization observations of comets. Soviet Astronomy **19** (1976).

[9] D. Guirado, F. Moreno, and J.W. Hovenier. Circular polarization of light scattered by randomly built aggregates. In: *X Conference on Electromagnetic & Light Scattering by Non-Spherical Particles*. Bodrum, Turkey (2007).

[10] D. Guirado, F. Moreno, and M.I. Mishchenko. A new mechanism possibly explaining the circular polarization of light scattered in comets: asymmetry of the comet itself. In: *XI Conference on Electromagnetic & Light Scattering by Non-Spherical Particles*. Hertfordshire, UK (2008).

[11] J.C. del Toro Iniesta. *Introduction to Spectropolarimetry*. Cambridge University Press, UK (2003).

[12] F. Moreno, O. Muñoz, J.J. López-Moreno, A. Molina, and J.L. Ortiz. A Monte Carlo code to compute energy fluxes in cometary nuclei. Icarus **156** (2002).

Observations and laboratory simulations of asteroids by polarization measurements

E. Hadamcik*[,1], A.C. Levasseur-Regourd[1], J.-B. Renard[2], J. Lasue[3], and A. K. Sen[4]

[1]*UPMC Univ. Paris 06, LATMOS/IPSL, 11 Bld d'Alembert, 78280 Guyancourt, France.*
[2]*LPC2E/CNRS, 3A Avenue de la recherche scientifique,45071 Orléans cedex, France.*
[3]*LPI, 3600 Bay Area Bld, Houston, TX 77058-113 USA.*
[4]*Assam Univ., Silchar 788001, India.*

We present polarization observations of C-type asteroids and of (21) Lutetia, one of the targets of the Rosetta mission. The (21) Lutetia phase curves are compared to C-type and M-type asteroid phase curves. In a second part of the work, we use powdered meteorites to compare their polarization at two wavelengths to those observed for different asteroids, e.g., (21) Lutetia and (2867) Steins (the second asteroid observed by Rosetta).

INTRODUCTION

Sunlight scattered by asteroidal surfaces is partially linearly polarized. The polarization depends on the physical properties of the dust particles and on the geometry and wavelength of the observations. The polarization phase curves (hereafter PPC) are typical of irregular particles with a bell-shaped positive branch and a shallow negative branch. Except for a small number of mostly near-Earth objects, the asteroidal observations are limited to relatively small phase angles. The PPC parameters allow a classification into various types [1,2], which are similar to the spectral classification. They also provide information on, e.g., the bulk surface albedo by the slope at inversion and a two-parameter empirical function [3, 4].

To better document the database in the red wavelength domain and, more recently, in three other domains (green, red, and infrared), low-albedo asteroids have been observed at Observatoire de Haute-Provence, France (OHP). At the same time, (21) Lutetia, which is a target of the Rosetta mission (flyby 2010 July 10) and still has a controversial type, was also observed. Supplementary observations have been obtained at IUCAA Girawali Observatory (IGO) near Pune in India.

Some meteorites are fragments of asteroids ejected during collisions or fragmentation. Some of them are related to their parent body (or to an asteroidal type). Powdered meteorites deposited on a surface can be thus used as regolith analogs of their parent body. Such work is in progress with the PROGRA2 experiment (http://www.icare.univ-lille1.fr/progra2), and we present a study of an aubrite meteorite as an analog of (2867) Steins, an E-type asteroid [5].

* Corresponding author: Edith Hadamcik (edith.hadamcik@latmos.ipsl.fr)

OBSERVATIONS

The two telescopes, the 0.80-m one at OHP and the 2-m one at IGO, are in a Cassegrain configuration. Four polaroid filters are placed on a rotating wheel at OHP, whereas a half-wave plate with a Wollaston is used at IGO. BVRI filters are used.

C-type asteroids

Figure 1 presents the data points and trigonometric fits in blue-green and red wavelength domains. The polarization value increases with wavelength in the two phase-angle regions in both the negative and positive branches. Table 1 gives the parameters of the PPC. The bulk surface albedo is estimated with coefficients from [3]. An albedo of 0.08 ± 0.01 is derived from slope and P_{min}.

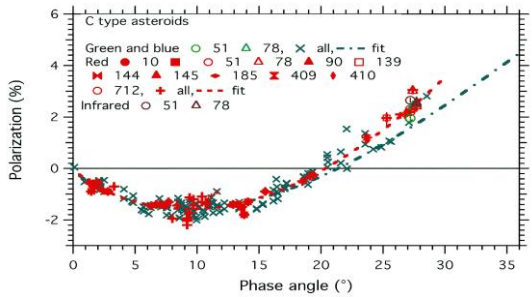

Figure 1. C-type asteroid polarization phase curves. Our observations are indicated by the asteroid number, other observations by crosses.

Table 1. Minimum polarization P_{min}, phase angles at minimum polarization α_{min} and at inversion α_0, and slope h at inversion for C-type asteroids.

Filters	α_{min} (°)	P_{min} (%)	α_0 (°)	h (% per deg)
Blue-green	9 ± 1	-1.6 ± 0.1	21.5 ± 0.5	0.23 ± 0.01
Red	9± 1	-1.6 ± 0.1	20.3 ± 1.0	0.28 ± 0.03

(21) Lutetia and M-type asteroids

Figure 2a presents the data points and a trigonometric fit for each wavelength range for (21) Lutetia. The negative branch becomes more pronounced as the wavelength increases. The inversion angle seems to be identical in the two domains. Figure 2b presents the synthetic data from the literature and fits in B-V (grouped together) and R domains. A possible dichotomy between M-type asteroids is noticed [8]. (21) Lutetia seems to belong to the new W type, which shows a deeper negative branch. The deeper negative branch is also shown by C-type asteroids; nevertheless, the wavelength behavior seems to be different for (21) Lutetia.

Our new observations of (21) Lutetia have allowed us to obtain phase curves for longer wavelengths than the classical blue-green and confirm the more pronounced negative branch with increasing wavelength [9]. The estimated bulk albedo is (0.12 ± 0.02) %.

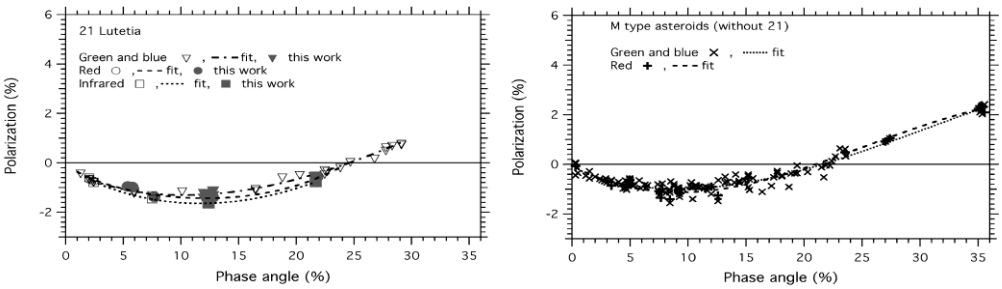

Figure 2. (21) Lutetia and M-type asteroid synthetic PPC. Our observations indicated by filled symbols, other observations by open symbols.

Table 2. Minimum polarization P_{min}, phase angles at minimum polarization α_{min} and at inversion α_0, and slope h at inversion for (21) Lutetia and M-type asteroids.

	Filters	α_{min} (°)	P_{min} (%)	α_0 (°)	h (% per deg)
21 Lutetia	Blue-green	10 ± 1	-1.31 ± 0.04	24.6 ± 1.0	0.17 ± 0.01
	Red	12 ± 2	-1.43 ± 0.06	24.5 ± 2.0	0.28 ± 0.03
	Infrared	12 ± 2	-1.64 ± 0.08	26 ± 2	--
M-type	Blue-green	9 ± 1	-0.99± 0.05	21 ± 1	0.14 ± 0.01
	Red	9 ± 3	-1.13 ± 0.06	21 ± 2	0.16 ± 0.01

LABORATORY SIMULATIONS

Powdered meteorites of different classes are tentatively used as analogs to retrieve polarization phase curves. For example, aubrite meteorites are estimated to originate from E-type asteroids. This was confirmed by the first results obtained by the observations of (2867) Steins from Rosetta. An aubrite sample (ALHA 78113,82) from the Antarctic Working Group was studied in a coordinated work [8]. The E-type asteroids data corresponding to (44) Nysa, (64) Angelina, (214) Aschera, (620) Drakonia, (2867) Steins, and 1998 WT_{24} are used to build synthetic PPC through R and V filters (Fig. 3). P_{max} is estimated to be about 1.6% with a very small difference between green and red wavelengths. The slope at inversion is (0.3 ± 0.1)% per degree.

The observations are compared to laboratory measurements on deposited grains for two size distributions with sizes $s < 125$ μm and 125 μm $< s <$ 250 μm with the PROGRA²-surf instrument (Fig. 4a). From micro-gravity measurements with the PROGRA²-vis instrument, the variation of P_{max} as a function of size of the grains is deduced for lifted grains (Fig. 4b). When the grains are on a surface a similar decrease is noticed [9]. The values for deposited grains are included in Fig. 4b for an average size measured on SEM images for the two samples. For P_{max} of about 2 %, an average size smaller than 50 μm can be suspected for the (2867) Steins surface.

For (21) Lutetia analogs, CV3 and CO3 meteorites have been suggested as an alternative to a metal-rich surface. The laboratory work is in progress.

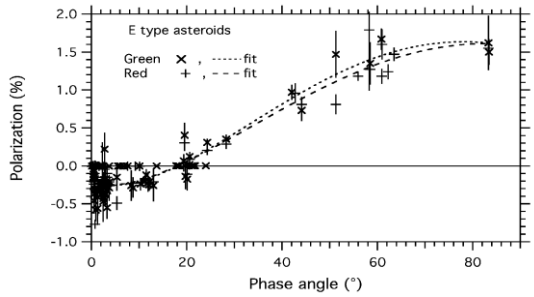

Figure 3. E-type asteroid (44, 64, 214, 620, 2867, 1998 WT_{24}) polarization phase curves.

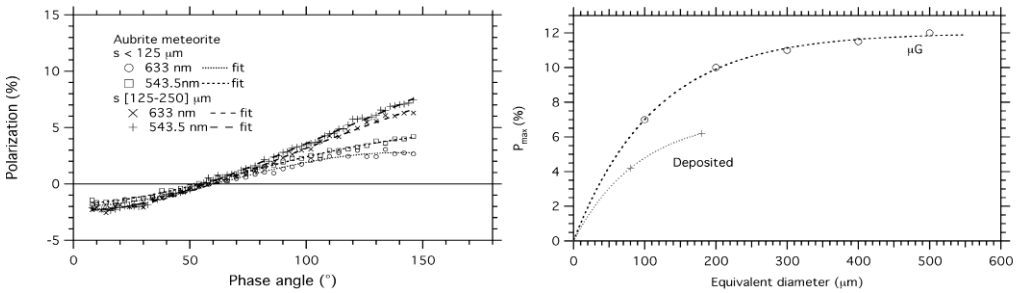

Figure 4. a) Aubrite meteorite polarization phase curves. b) P_{max} vs. grain size (s).

REFERENCES

[1] B. Goidet-Devel, J.-B. Renard, and A.C. Levasseur-Regourd. Polarization of asteroids. Synthetic curves and characteristic parameters. PSS **43** (1995).

[2] A. Penttilä, K. Lumme, E. Hadamcik, and A.C. Levasseur-Regourd. Statistical analysis of asteroidal and cometary polarization phase curves. A&A **432** (2005).

[3] A. Cellino, R. Gil-Hutton, E.F. Tedesco, M. DiMartino, and A. Brunini. Polarimetric observations of small asteroids: preliminary results. Icarus **138** (1999).

[4] K. Muinonen, A. Penttilä, A. Cellino et al. Asteroid photometric and polarimetric phase curves: Joint linear exponential modeling. Metoritics Planet Sci. **44** (2009).

[5] A.C. Levasseur-Regourd, J.-B. Renard, and E. Hadamcik. Laboratory light scattering experiments on Meteorites, in preparation for the Rosetta mission. BAAS, DPS **41** (2009).

[6] R. Gil-Hutton. Polarimetry of M-type asteroids. A&A **464** (2007).

[7] I.N. Belskaya, A.C. Levasseur-Regourd, A. Cellino et al. Polarimetry of main belt asteroids: wavelength dependence. Icarus **199** (2009).

[8] L. McFadden et al. Coordinated laboratory studies of meteorites supporting Rosetta mission's asteroid flyby target: 2867 Steins. LPSC **40.2287** (2009).

[9] E. Hadamcik, J.-B. Renard, A.C. Levasseur-Regourd, J. Lasue, G. Alcouffe, and M. Francis. Light scattering by agglomerates: Interconnecting size and absorption effects (PROGRA^2 experiment). JQSRT **110** (2009).

ScattPort light-scattering internet information portal: present state and further development

J. Hellmers[*,1], G. Berg[1,2], J. Thomaschewski[2], and T. Wriedt[3]

[1]*University of Bremen, FB04, Badgasteiner Str. 3, 28359 Bremen, Germany.*
[2]*University of Applied Sciences Emden/Leer, Constantiaplatz 4, 26723 Emden, Germany.*
[3]*Institute of Materials Science, Badgasteiner Str. 3, 28359 Bremen, Germany.*

The internet portal ScattPort not only offers varying information on the topic of light scattering, like upcoming conferences, open positions, and a comprehensive list of computer programs. Additionally, it can serve as a communication platform for scientists. It is going to be improved within a recent, DFG-funded project. Here, we would like to outline the aim of the project and to invite the light-scattering community to join our efforts for improving the online information source.

SCATTPORT: PRESENT STATE

In March 2009, the light-scattering information portal ScattPort [1], the development of which is funded by the German Research Foundation DFG, went online in its actual form (see Fig. 1). Since then the access numbers show a steadily increasing interest in the pages: in one year, they went up nearly 100%, with an average of about 3000 visits per month and 2000 hits per day.

ScattPort offers various pieces of information in regard to the topic of light scattering – like latest news, upcoming conferences, vacant positions, lists of related webpages and homepages of scientists working on the field of light scattering, etc. Another focus is on a sorted list of available software for the simulation of light scattering. This list contains more than 250 programs. Additionally, a search option based on a recently developed categorization scheme for light-scattering software helps interested users to find fitting codes for their scientific problems [2].

A key characteristic of the technical realization of the ScattPort website is the usage of a Content Management System (CMS). Here the open source software Joomla [3] was applied. Using a CMS not only simplifies the daily administration of the webpages and their contents. It additionally allows the integration of registered users worldwide into the publishing process. Interested scientists can apply for a login-account for the CMS which enables them to publish their own information online in a very simple way. Special knowledge about HTML is not necessary. On the other side, a CMS like Joomla puts the internet presentation in a more or less 'rigid frame' – which can have negative side effects on the usability.

* Corresponding author: Jens Hellmers (hellmers@iwt.uni-bremen.de)

Therefore the next step within the ongoing development of ScattPort is to improve its attractiveness for the users. The idea is to apply the latest knowledge about user-friendly interfaces (see below), as well as the implementation of new contents according to the users demands. Additionally, new functions are planned to be added to the existing ones offering, for example, a 'Wiki' function that will allow for establishing a comprehensive encyclopedia around the topic of light scattering.

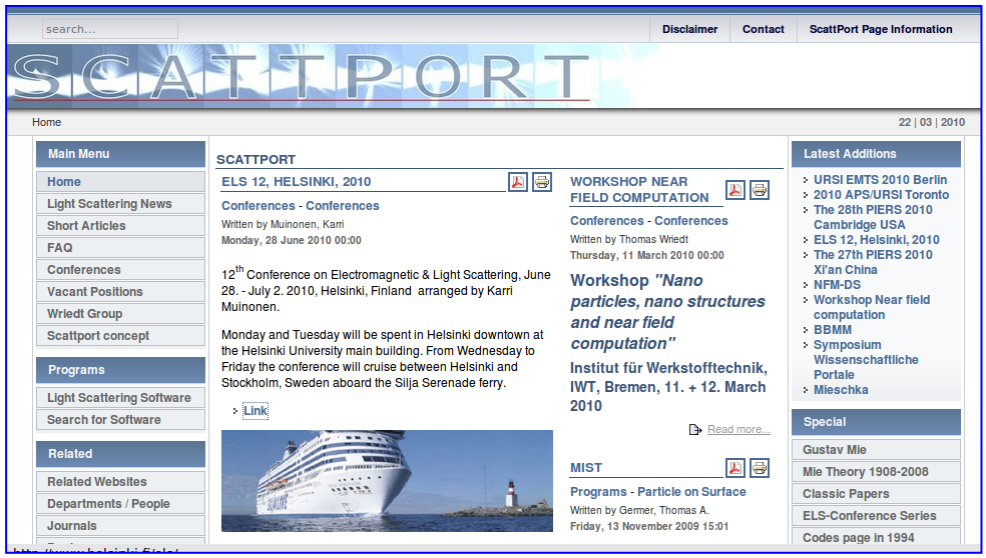

Figure 1. Screenshot of the ScattPort Internet Information Portal.

USABILITY

Definition of Usability

J. Nielsen defines usability as follows: *"Usability is a quality attribute that assesses how easy user interfaces are to use. The word "usability" also refers to methods for improving ease-of-use during the design process."* [4].

It consists of five quality components:

- Learnability: How easy is it for users to accomplish basic tasks the first time they encounter the design?
- Efficiency: Once users have learned the design, how quickly can they perform tasks?
- Memorability: When users return to the design after a period of not using it, how easily can they reestablish proficiency?
- Errors: How many errors do users make, how severe are these errors, and how easily can they recover from the errors?
- Satisfaction: How pleasant is it to use the design?

Importance of Usability

In the first few seconds, users decide if a website is good or bad. The greatest factor for this decision is the way the information is presented. If a website is difficult to use, people leave or close it. If users cannot find the answers to their questions or encounter errors on the website, they leave it, too. Therefore, usability is necessary for the handling of a website. For a scientific internet presence this is especially important: when users cannot find the needed information, they cannot discuss it either.

Improving the Usability

A user connects the interaction with a system always with certain targets. From this several tasks can be defined, which give a degree for the usability. The degree of the usability consists of effectiveness, efficiency and satisfaction (ISO 9241 Part 11). To get a high standard of usability the process of the Usability Engineering has to be used [5].

Usability Engineering is an evolution process and there are many methods for studying usability. The most common are *user testing* and the *interview-methods*. Attention should be paid to get hold of some *representative users*. The aim is to create a design which has a high standard of functionality.

Application to ScattPort

As a good usability is a key factor for the attractiveness of internet pages it is planned to overhaul the ScattPort Information Portal following the latest developments in usability engineering as drafted above. For this, we plan a survey at ELS XII. This survey will allow learning more about the users of the portal, how they use the portal, the specific information they look for and their opinions and impressions about the portal.

The survey will concentrate on the following questions:

- Were users able to find the information they were looking for?
- How satisfied are users with the portal?
- What experiences did users make with the portal or similar sites?
- What do users like best and least about the portal?
- What frustrations or issues have users had with the portal?
- Do users have any ideas or suggestions for improvements?

Additionally the survey can be used to allow users to rate or rank the current features of the portal.

CALL FOR PARTICIPATION

We would like to invite the light scattering community to join our efforts for improving the ScattPort light scattering information portal. For the ELS XII conference, we will prepare a questionnaire to ask for opinions, critics, suggestions, and demands. Please feel free to provide us with any comments.

ACKNOWLEDGEMENT

We would like to acknowledge funding of this project by German Research Foundation DFG (INST 1216/1-2).

REFERENCES

[1] ScattPort. http://www.scattport.org.

[2] J. Hellmers and T. Wriedt. New approaches for a light scattering Internet information portal and categorization schemes for light scattering software. JQSRT **110** (2009).

[3] Joomla! http://www.joomla.org.

[4] J. Nielsen and R. Molich. Heuristic evaluation of user interfaces. In: *Proceedings of the SIGCHI conference on Human factors in computing systems: Empowering people*. J.C. Chew, J.C. Carrasco and J. Carrasco Chew (eds). Addison-Wesley, New York (1990).

[5] F. Sarodnick and H. Brau. *Methoden der Usability Evaluation. Wissenschaftliche Grundlagen und praktische Anwendung*. Huber, Bern (2006).

Light scattering by horizontally oriented particles: Symmetry properties of the phase matrix

J. W. Hovenier*,[1] and O. Muñoz[2]

[1]*Astronomical Institute ``Anton Pannekoek'', University of Amsterdam, P.O. Box 94249, 1090GE Amsterdam, The Netherlands.*
[2]*Inst. de Astrof. de Andalucía, CSIC, Glorieta de la Astronomía s/n, 18080 Granada, Spain.*

Using elementary symmetry considerations ,we present seven symmetry relations for the phase matrix of horizontally oriented particles. These relations have a wide range of validity and hold for all directions of incident and scattered electromagnetic radiation.

INTRODUCTION

We consider light scattering by a small volume element in a medium containing independently scattering particles that are horizontally oriented. Examples of such particles are various types of hydrometeors, like snow flakes and ice crystals. Suppose the volume element is located at the origin of a coordinate system with axes x, y, and z (see Fig. 1). We call the x, y plane the horizontal plane and the positive z-axis the local vertical. The matrix transforming the Stokes parameters of the incident beam into those of the scattered beam is the phase matrix. Here the meridian planes of both beams are used as a plane of reference for the Stokes parameters.

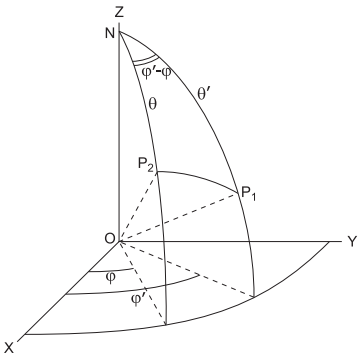

Figure 1. Scattering by a local volume-element at O. Points N, P_1 and P_2 are located on a unit sphere. The direction of the incident light is OP_1 and that of the scattered light is OP_2.

The phase matrix of a volume element plays a key role in studies of light scattering. It occurs, for instance, as the kernel in the equation of radiative transfer [1, 2, 3, 4, 5, 6, 7]. The phase matrix depends, in general, on the angles θ' and φ' of the incident beam and θ and φ of the scattered beam. The azimuthal angles are measured clockwise from the positive x-axis when looking in the direction of the upward vertical. If there is rotational symmetry

*Corresponding author: J.W. Hovenier (J.W.Hovenier@uva.nl)

about the local vertical the azimuth dependence reduces to the difference $\varphi - \varphi'$. Making the Stokes parameters I, Q, U and V of a beam of light the elements of a Stokes vector, **I**, the scattering process can be written as

$$\mathbf{I}^s(u,\varphi) = c\mathbf{Z}(u,u',\varphi-\varphi')\mathbf{I}^i(u',\varphi') \tag{1}$$

where the superscripts s and i refer to the scattered and incident beam, respectively, $u = -\cos\theta$ and $u' = -\cos\theta'$, c is a scalar that can be used for normalization purposes, and $\mathbf{Z}(u,u',\varphi-\varphi')$ is the phase matrix of the volume element.

Quite general symmetry relations for the phase matrix of collections of particles that are randomly oriented in three-dimensional space have been presented earlier [1]. The main purpose of this contribution is to investigate, by means of elementary symmetry arguments, which symmetry relations hold for the phase matrix of horizontally oriented particles.

We consider particles having a plane of symmetry. Such particles are identical to their mirror particles. As an example, we first consider collections of hexagonal plates with two broad flat sides in the horizontal plane, but with random orientation in that plane.

SYMMETRY RELATIONS

Reciprocity

The reciprocity principle corresponds to invariance of the ratio cause/effect under inversion of time. This amounts to changing u' into $-u$ and u into $-u'$, as well as interchanging φ and φ' (see Fig. 1). The result is the reciprocity relation

$$\mathbf{Z}(-u',-u,\varphi'-\varphi) = \mathbf{P}\tilde{\mathbf{Z}}(u,u',\varphi-\varphi')\mathbf{P}, \tag{2}$$

where **P** is the 4×4 diagonal matrix (1,1,-1,1) and a tilde above a matrix stands for the transposed matrix.

Eq. (2) is well known from the theory for scattering by randomly oriented particles [1, 3]. Since reciprocity holds, under certain conditions, for each individual particle in arbitrary orientation the validity of Eq. (2) does not depend on the orientation of the particles [8, 9]. Sufficient conditions for reciprocity are that the dielectric, permeability and conductivity tensors of the particles are symmetric and magnetic fields can be ignored. We shall henceforth assume that reciprocity holds for all particles considered in this work.

Mirror symmetry

It is clear that we have mirror symmetry with respect to the meridian plane of incidence. Referring to Fig. 2, it is readily seen that, if an incident beam i_1 gives rise (among others) to a scattered beam r_1, then the incident beam i_2, which is the mirror image of i_1 with respect to the meridian plane of incidence, gives rise (among others) to the beam of scattered light r_2, which is the mirror image of r_1 with respect to the meridian plane of incidence. Now i_1 and i_2 differ in the signs of their third and fourth Stokes parameters and so do r_1 and r_2. Furthermore, we have $\varphi_2 - \varphi_0 = \varphi_0 - \varphi_1$. Using Eq. (1) first for r_1 and then for r_2, we find the following mirror symmetry relation for the phase matrix

$$\mathbf{Z}(u, u', \varphi' - \varphi) = \mathbf{PQZ}(u, u', \varphi - \varphi')\mathbf{QP}, \tag{3}$$

where **Q** is the 4×4 matrix diag (1,1,1,-1), so that **PQ** = **QP** = diag (1,1,-1,-1). An interesting corollary of Eq. (3) is that, if a Fourier-series expansion is used to handle the azimuth dependence of the phase matrix, the 2×2 submatrices in the upper left corner and the lower right corner contain only cosine terms and in general an azimuth independent term, whereas the other two 2×2 submatrices possess only sine terms or vanish.

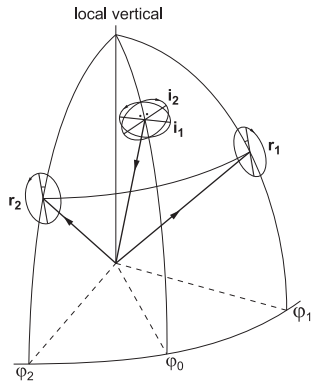

Figure 2. Illustration of the mirror symmetry relation for the phase matrix. If the incident beam i_1 gives rise (among others) to the beam of scattered light r_1, then the incident beam i_2, which is the mirror image of i_1 with respect to the plane of incidence, gives rise (among others) to the beam of scattered light r_2, which is the mirror image of r_1 with respect to the plane of incidence. The position angles of the polarization ellipses of the incident light (dots) and scattered light (small arcs) are also indicated, as well as the sense in which the four polarization ellipses are traced. [After Hovenier, [10]]

Rotational symmetry

We have assumed rotational symmetry about the vertical (azimuthal symmetry). Therefore, simultaneous rotation of the meridian planes of incidence and scattering about the vertical, through any angle, gives no new symmetry relation. However, rotation of the horizontal plane, together with the directions of the incident and scattered light, about a horizontal axis over an angle π gives physically the same scattering problem, but the sign of the azimuth difference must be switched [1]. This yields the symmetry relation

$$\mathbf{Z}(-u, -u', \varphi' - \varphi) = \mathbf{Z}(u, u', \varphi - \varphi'). \tag{4}$$

Combinations

By combining the three fundamental symmetry equations Eq. (2), Eq. (3), and Eq. (4) we find

$$\mathbf{Z}(-u', -u, \varphi - \varphi') = \mathbf{Q}\tilde{\mathbf{Z}}(u, u', \varphi - \varphi')\mathbf{Q}. \tag{5}$$

$$\mathbf{Z}(u', u, \varphi - \varphi') = \mathbf{P}\tilde{\mathbf{Z}}(u, u', \varphi - \varphi')\mathbf{P}. \tag{6}$$

$$\mathbf{Z}(-u, -u', \varphi - \varphi') = \mathbf{PQZ}(u, u', \varphi - \varphi')\mathbf{QP}. \tag{7}$$

and

$$\mathbf{Z}(u', u, \varphi' - \varphi) = \mathbf{Q}\tilde{\mathbf{Z}}(u, u', \varphi - \varphi')\mathbf{Q}. \tag{8}$$

CONCLUSIONS

Using symmetry arguments, we have found seven symmetry relations for the phase matrix of horizontally oriented hexagonal plates. It is, however, directly clear from the symmetry arguments that these relations must hold for many other kinds of horizontally oriented particles. These include hexagonal columns with their long axes randomly oriented in a horizontal plane and randomly rotated about their long axes. As long as the particles and their orientation distribution are such that the three fundamental symmetry relations Eq. (2), Eq. (3), and Eq. (4) hold, all seven symmetry relations are valid. A more extensive treatment of the topic of this abstract is given in [11].

REFERENCES

[1] J.W. Hovenier. Symmetry relationships for scattering of polarized light in a slab of randomly oriented particles. J. Atmos. Sci. **26** (1969).

[2] J.W. Hovenier, C.V.M. van der Mee, and H. Domke. *Transfer of polarized light in planetary atmospheres: basic concepts and practical methods*. Kluwer, Springer, Dordrecht. Berlin (2004).

[3] H.C. van de Hulst. *Multiple Light Scattering. Tables, Formulas and Applications*. Academic Press, San Diego (1980).

[4] M.I. Mishchenko. Multiple scattering of polarized light in anisotropic plane-parallel media. Transp. Theory and Statist. Phys. **19** (1990).

[5] M.I. Mishchenko, J.W. Hovenier, and L.D. Travis. *Light Scattering by Nonspherical Particles: Theory, Measurements, and Applications*. Academic Press, San Diego (2000).

[6] M.I. Mishchenko, L.D. Travis, and A.A. Lacis. *Scattering, Absorption, and Emission of Light by Small Particles*. Cambridge University Press, Cambridge (2002).

[7] M.I. Mishchenko, L.D. Travis, and A.A. Lacis. *Multiple Scattering of Light by Particles: Radiative Transfer and Coherent Backscattering*. Cambridge University Press, Cambridge (2006).

[8] D.S. Saxon. Tensor scattering matrix for the electromagnetic field. Phys. Rev. **100** (1995).

[9] M.I. Mishchenko. Transfer of polarized infrared radiation in optically anisotropic media: application to horizontally oriented ice crystals: comment. J. Opt. Soc. Am. A **11** (1994).

[10] J.W. Hovenier. Principles of symmetry for polarization studies of planets. Astron. Atrophys. **7** (1970).

[11] J.W. Hovenier and O. Muñoz. Symmetry relations for the phase matrix of horizontally oriented particles. JQRST (submitted) (2010).

Extinction by stratified interstellar dust grains

M. A. Iatì*[,1], C. Cecchi-Pestellini[2], A. Cacciola[3], R. Saija[3], P. Denti[3], and F. Borghese[3]

[1]*Istituto per i Processi Chimico-Fisici, CNR, Viale F. Stagno d'Alcontres 37, I-98158 Messina.*
[2]*Osservatorio Astronomico di Cagliari, Strada n.54, Loc. Poggio dei Pini, I-09012 Capoterra.*
[3]*Dipartimento di Fisica della Materia e Ingegneria Elettronica, Università di Messina, Viale F. Stagno d'Alcontres 31, I-98166 Messina, Italy.*

We compute the optical properties of spherical dust grains composed of hollow silicate cores coated with two carbonaceous layers, the inner layer of mostly graphitic sp^2 carbon and the outer layer of sp^3 polymeric amorphous carbon, and explore the consequences on modelled interstellar extinction curves. A family of curves is created by varying the thicknesses of the sp^2 and the sp^3 layers. The average galactic extinction curve is well matched by one of this family of computed curves.

INTRODUCTION

Dust is almost everywhere in interstellar space, from the expanding envelopes of mass-losing stars where it is formed, to warm gas cooling behind supernova shocks. At least on large scales, the dust and gas are well mixed, with the density of dust tending to be proportional to the density of gas. Although very familiar to the astronomers, the nature of interstellar dust is still elusive after almost 100 years from its discovery.

Various models have been proposed for interstellar dust which may be summarized in three broad classes: (i) the silicate-graphite model [1] (the so-called MRN model) with major upgrades providing the optical constants for "astronomical" silicates [2] and graphites [3], and the natural extension to include a population of small grains, filling the size range between 5 nm (the previous MRN lower limit) and 0.3 nm, the size of large molecules [4] --- these molecules, basically free-flying or stacked PAHs, are described by means of two Drude profiles [5]; (ii) the silicate core carbonaceous-mantle model (e.g., [6, 7, 8]); and (iii) the composite model, which assumes the dust to be low-density aggregates of small silicate and carbonaceous particles ([9], and more recently [10]). While differing in details, all these model categories have certain properties in common, as they also share certain problems. Each model exploits a different (to some extent arbitrary) form for the size distribution of grains, with several free parameters to be determined by fitting the model predictions to the observations. Attempts to determine the optimum size distributions from observational constraints alone have been put forward in the last decade, using the maximum entropy method [11], and regularization techniques [10]. This opens the possibility of determining effective size distributions of grains for individual lines of sight.

Here we adopt a description similar to the one proposed by Jones et al.[7]. Details of the model can be found in Iatì et al.[12]. Carbon atoms and ions are assumed to be deposited on dust grains, partially hydrogenated, and retained on the surface. The newly deposited hydrogen-rich carbon is dominated by the sp^3 bonding. Under the influence of the interstellar radiation field, this aliphatic carbon loses hydrogen and becomes more

*Corresponding author: Maria Antonia Iatì (iati@me.cnr.it)

graphitic and aromatic, and is dominated by the sp^2 bonding. The optical properties of these two carbonaceous materials are quite different; for example, the sp^2 material absorbs strongly in the visible, while the sp^3 polymeric material does not. Thus, in this model there are two main types of mantle, an inner layer of older sp^2 material, and an outer layer of more recently deposited sp^3 material.

COMPUTATIONAL APPROACH, MODEL, AND RESULTS

To calculate the optical properties of stratified spheres, we use the extension of the Mie theory to radially non-homogeneous spheres by Wyatt[13]. To preserve the continuity of the refractive index and its radial derivative between two contiguous layers (of refractive indexes n_1 and n_2), a thin transition zone of thickness Δr is placed at the interface. In this zone the refractive index, n varies as a function of δr, the distance from the base of the lower layer, as $n^2(\delta r) = n_1^2 + \left(3s^2 - 2s^3\right) \times \left(n_2^2 - n_1^2\right)$, with $s = \delta r/\Delta r$. The introduction of a transition layer of appropriate thickness may also account for the fact that the upper layer is actually formed by successive deposition of carbon atoms. It is reasonable to think that the first deposited atoms are adsorbed at the surface of the internal layer thus giving origin to a smooth transition from the properties of the internal layer to those of the external layer in formation.

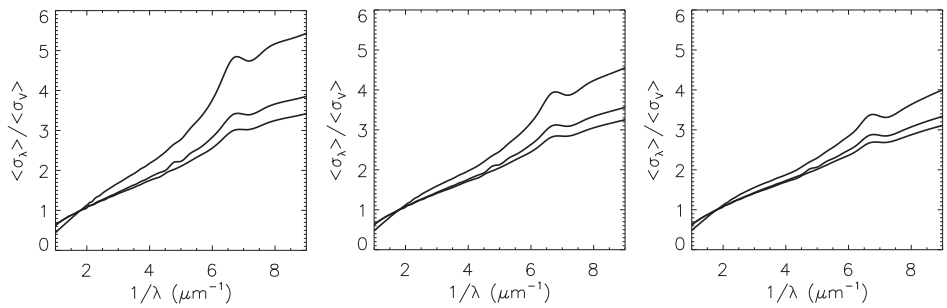

Figure 1. Normalized size-averaged extinction cross section as a function of the wave number. The size distribution is the MRN power-law $a^{-3.5}$. The lower and upper limits of the size spectrum are $a = 5$ and 1000 nm, respectively. The mantle thickness is $w = 2$ nm. The (inner) sp^2 layer has a thickness $w_{sp^2} = 0$ left, 1 central, and 2 nm right panel. In each panel the core vacuum volume fraction is 0, 1/3, and 2/3 (bottom to top).

In our model grain there are 3 concentric components: the silicate shell, the sp^2 layer and the sp^3 layer. Optical constants for the adopted materials are taken from [2], [14] (sample BE), and [15], respectively. To simulate porosity, silicate cores may present a central void, whose volume is a fixed fraction (f_V) of the total core volume, irrespective of the core size. To illustrate the results, we consider a size distribution for the silicate cores given by a power-law $a^{-3.5}$ with $a = 5$ and 1000 nm the lower and upper limits of the distribution, respectively. In Fig. 1 we show the size averaged extinction cross section normalized to its value in the visible. We keep fixed the mantle thickness to $w = 2$ nm over the whole range of grain sizes to simulate mantle accretion in the interstellar medium (e.g., [16]). The increase in the central void volume increases the relative (to the visible) extinction in the UV while, as expected, the UV extinction decreases with increasing sp^2 mantle fraction.

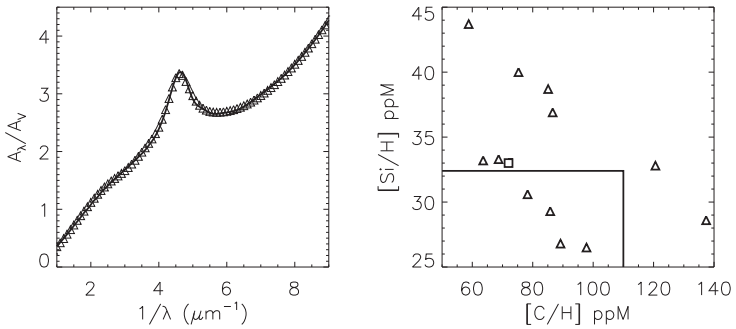

Figure 2. Left panel: model AGE (solid line) compared to the one (triangles) derived by Fitzpatrick and Massa[17]. Right panel: Si and C masses (ppM) locked in grains as functions of the mantle thickness and core vacuum fraction (triangles). The square represents the pair of values derived by the AGE best-fit. Models within the box satisfy the constraints on both Si and C masses.

There is a remarkable variety of IR-through-UV extinction curves. Several decades of work utilizing pair method extinction curves spanning the near-IR through UV spectral domain have provided a good estimate of the average wavelength dependence of the extinction in the Milky Way, summarized in an average galactic extinction (AGE) profile [17]. We fitted the AGE (see Fig. 2, left panel) with two separate populations of grains: core-mantle grains described above, and a collection of single and stacked PAHs summarized through a double Lorentz profile to include both the convolution of individual $\pi \rightarrow \pi^\star$ transitions, as well as the tail of the giant resonance associated with the $\sigma + \pi$ electron plasmon centred at wavelengths shortwards of the Lyman edge. The fit to the AGE by the adopted model is excellent. However, distinct populations of small ($5 \leq a \leq 13$ nm) and large ($80 \leq a \leq 440$ nm) grains are required to achieve this fit: continuous size distributions fail to reproduce the AGE (cf. Fig.1 e.g., the small bump near 6.2 μm^{-1} not present in the AGE). We exploit an MRN-like power-law for the size distribution with $q = 3.53$. The fitting technique then determines $w = 1.2$ nm, $f_V = 0.5$, and $f_{sp^2} = 0.97$. The resulting masses in silicates and carbon are [Si/H] = 33 and [C/H] = 72 ppM. To explore the best dependence on the elemental mass, we generate 12 additional models keeping the mantle thickness and the core vacuum fraction fixed, and derive the corresponding best fit to the AGE and the mass budget. Results are reported in the right panel of Fig. 2. As evident from the figure, the Si mass and the C mass appear to be anti-correlated. Adopting a Si solar abundance of 32.4 ppM [18] and a mean C abundance of 110 ppM [19], we find that there is a wide range of parameters consistent with the mass constraints in the diffuse interstellar medium.

DISCUSSION AND CONCLUSIONS

The interstellar extinction curve may be attributed to a population of layered grains of silicate cores with carbonaceous mantles, as an alternative to the more conventional grain model of separate populations of each materials. Varying the sp^2/sp^3 ratio within the layers generates a family of interstellar extinction curves. The variation of dust optical properties is compatible with a scenario in which carbon is deposited slowly on the surfaces of silicate cores.

The solid carbon is also processed by the interstellar radiation so that its optical properties change with time. The computed interstellar extinction curve for this model thus evolves in time. The variety of observed extinction curves may be interpreted (at least, in part) as due to evolutionary changes of interstellar dust.

REFERENCES

[1] J.S. Mathis, W. Rumpl, and K.H. Nordsieck. The size distribution of interstellar grains. ApJ **217** (1977).

[2] B.T. Draine and H.M. Lee. Optical properties of interstellar graphite and silicate grains. ApJ **285** (1984).

[3] B.T. Draine and N. Anderson. Temperature fluctuations and infrared emission from interstellar grains. ApJ **292** (1985).

[4] J.C. Weingartner and B.T. Draine. Dust grain-size distributions and extinction in the Milky Way, Large Magellanic Cloud, and Small Magellanic Cloud. ApJ **548** (2001).

[5] B.T. Draine and A. Li. Infrared emission from interstellar dust. IV. The silicate-graphite-PAH model in the post-*Spitzer* era. ApJ **657** (2007).

[6] F.-X Desert, F. Boulanger, and J.L. Puget. Interstellar dust models for extinction and emission. A&A **237** (1990).

[7] A.P. Jones, W.W. Duley, and D.A. Williams. The structure and evolution of hydrogenated amorphous carbon grains and mantles in the interstellar medium. QJRAS **31** (1990).

[8] A. Li and J.M. Greenberg. A unified model of interstellar dust. A&A **323** (1997).

[9] J.S. Mathis and G. Whiffen. Composite interstellar grains. ApJ **341** (1989).

[10] V. Zubko, E. Dwek, and R.G. Arendt. Interstellar dust models consistent with extinction, emission, and abundance constraints. ApJ **610** (2004).

[11] G.C. Clayton, M.J. Wolff, U.J. Sofia, K.D. Gordon, and K.A. Misselt. Dust grain size distributions from MRN to MEM. ApJ **588** (2003).

[12] M.A. Iatì, R. Saija, F. Borghese, P. Denti, C. Cecchi-Pestellini, and D.A. Williams. Stratified dust grains in the interstellar medium — I. An accurate computational method for calculating their optical properties. MNRAS **384** (2008).

[13] P.J. Wyatt. Scattering of electromagnetic plane waves from inhomogeneous spherically symmetric objects. Phys Rev **127** (1962).

[14] F. Rouleau and P.G. Martin. Shape and clustering effects on the optical properties of amorphous carbon. ApJ **377** (1991).

[15] N.H. Ashok, P.L.H. Varaprasad, and J.R. Birch. Polyehtylene $(C_2H_4)_n$. In: *Handbook of Optical Constants of Solids*, E.D. Palik (ed.), Academic Press (1991).

[16] D.C. Whittet. *Dust in the Galactic Environment*. Institute of Physics Publishing, Bristol (2002).

[17] E.L. Fitzpatrick and D. Massa. An analysis of the shapes of interstellar extinction curves. V. The IR-through-UV curve morphology. ApJ **663** (2007).

[18] M. Asplund, N. Grevesse, A.J. Suaval, and P. Scott. The Chemical Composition of the Sun. ARA&A **47** (2009).

[19] J.S. Mathis. Properties of interstellar dust. J. Geophys. Res. **105** (2000).

Theoretical and computational aspects of the SVM, EBCM, and PMM methods in light scattering by small particles

V. B. Il'in*[,1,2,3], V. G. Farafonov[2], and A. A. Vinokurov[2,3]

[1]*St. Petersburg University, Universitetskij pr. 28, St. Petersburg, 198504 Russia.*
[2]*State University of Aerospace Instrument., Bol. Morskaya 67, St. Petersburg, 190000 Russia.*
[3]*Pulkovo Observatory, Pulkovskoe chaussee 65/1, St. Petersburg, 196140 Russia.*

We consider the generalized separation of variables, extended boundary condition, and generalized point-matching methods that apply single expansions of the electromagnetic fields in terms of wave functions to solve the light-scattering problem. We consider especially theoretical studies related to analysis of infinite linear systems, questions of field-expansion convergence, and the Rayleigh hypothesis. The passage from the infinite systems to truncated ones used in calculations will be discussed, and numerical solutions provided by the methods will be compared.

INTRODUCTION

The behavior of the electromagnetic (EM) fields $\vec{E}, \vec{H}$ in any medium is governed by the macroscopic Maxwell equations. In the light scattering (LS) theory one usually considers time-harmonic fields $\vec{E}(\vec{r},t) = \vec{E}(\vec{r})\, e^{-i\omega t}$, where ω is the radiation frequency [1]. So, for most of the media the Maxwell equations transform into

$$\Delta\vec{E}(\vec{r}) + k^2(\vec{r})\,\vec{E}(\vec{r}) = 0, \quad \vec{\nabla}\cdot\vec{E}(\vec{r}) = 0, \tag{1}$$

where $k(\vec{r})$ is the wavenumber in the medium, and similar equations for the magnetic field $\vec{H}(\vec{r})$ related to the electric one as $\vec{H}(\vec{r}) = (i\mu(\vec{r})k_0)^{-1}\,\vec{\nabla}\times\vec{E}(\vec{r})$, where $\mu(\vec{r})$ is the magnetic permeability, k_0 the wavenumber in vacuum.

The boundary conditions to Eqs. (1) are provided by continuity of the tangential components of the fields at any interface, which gives for a scatterer with the surface $\partial\Gamma$

$$\left.\begin{aligned}(\vec{E}^{\rm inc}(\vec{r}) + \vec{E}^{\rm sca}(\vec{r}) - \vec{E}^{\rm int}(\vec{r}))\times\vec{n}(\vec{r}) = 0,\\ (\vec{H}^{\rm inc}(\vec{r}) + \vec{H}^{\rm sca}(\vec{r}) - \vec{H}^{\rm int}(\vec{r}))\times\vec{n}(\vec{r}) = 0,\end{aligned}\right\}_{\vec{r}\in\partial\Gamma} \tag{2}$$

where $\vec{E}^{\rm inc}, \vec{H}^{\rm inc}$, $\vec{E}^{\rm sca}, \vec{H}^{\rm sca}$, and $\vec{E}^{\rm int}, \vec{H}^{\rm int}$ are the fields of incident, scattered, and internal radiation, respectively, $\vec{n}(\vec{r})$ is the outward normal to $\partial\Gamma$. There is also the well-known radiation condition at infinity for the scattered field.

Various methods are used to solve the LS problem for non-spherical scatterers (see, e.g., the reviews [1, 3]). One often applies the separation of variables (SVM), extended boundary condition (EBCM), and point-matching (PMM) methods based on the same single expansions of the EM fields in terms of vector wave functions $\vec{F}_\nu(\vec{r})$

$$\vec{E}(\vec{r}) = \sum_\nu \alpha_\nu\,\vec{F}_\nu(\vec{r}), \quad \vec{H}(\vec{r}) = \sum_\nu \beta_\nu\,\vec{F}_\nu(\vec{r}), \tag{3}$$

*Corresponding author: Vladimir Il'in (ilin55@yandex.ru)

where α_ν, β_ν are some coefficients.

METHODS UNDER CONSIDERATION

Generalized SVM approach

Here one usually substitutes the expansions (3) in the boundary conditions (2), multiplies these conditions by the angular part of different index wave functions and integrates the results over the scatterer surface $\partial\Gamma$ (see, e.g., [1, 4]). As a result one gets a set of linear algebraic equations relative to unknown coefficients of the external ($\alpha_\nu^{\rm sca}$) and internal ($\alpha_\nu^{\rm int}$) field expansions

$$\left\{ \begin{array}{l} A\,\vec{x}^{\,\rm sca} + B\,\vec{x}^{\,\rm int} = E\,\vec{x}^{\,\rm inc}, \\ C\,\vec{x}^{\,\rm sca} + D\,\vec{x}^{\,\rm int} = F\,\vec{x}^{\,\rm inc}, \end{array} \right. \tag{4}$$

where $A, B, ..., F$ are matrices whose elements are integrals of the wave functions and their derivatives, $\vec{x}^{\,\rm sca,int} = \{\alpha_\nu^{\rm sca,int}\}_{\nu=1}^{\infty}$, and $\vec{x}^{\,\rm inc}$ is a vector of the known coefficients of the incident field expansion. Solution to the system (4) gives the unknown coefficients which allows one to calculate any optical properties of a scatterer [4]. We consider the *generalized* SVM when the approach is applied to particles of arbitrary shape (see for more details [4]).

Standard EBCM approach

In this case a surface integral formulation of the LS problem arisen from the Stratton-Chu formula is utilized (see, e.g., [5])

$$\vec{\nabla} \times \int_S \vec{n}(\vec{r}\,') \times \vec{E}^{\,\rm int}(\vec{r}\,')\, g(\vec{r}, \vec{r}\,')\, {\rm d}s' - \frac{1}{ik_0\varepsilon}\vec{\nabla} \times \vec{\nabla} \times \tag{5}$$

$$\int_S \vec{n}(\vec{r}\,') \times \vec{H}^{\,\rm int}(\vec{r}\,')\, g(\vec{r}, \vec{r}\,')\, {\rm d}s' = \left\{ \begin{array}{l} -\vec{E}^{\,\rm inc}(\vec{r}), \;\; \vec{r} \in \Gamma_-, \\ \vec{E}^{\,\rm sca}(\vec{r}), \;\; \vec{r} \in \Gamma_+, \end{array} \right.$$

where $g(\vec{r}, \vec{r}\,')$ is the free space Green function, Γ_- and Γ_+ mean the interior and exterior of a scatterer, respectively, ε is the dielectric permittivity. The field expansions (3) and the known Green function expansion in terms of some wave functions are substituted in the extended boundary conditions (5). Linear independence of the basis functions allows one to equal the expansion coefficients for each function $\vec{F}_\nu$ (see for more details [4]). So, the equations (5) give two matrix equations relative to the unknown expansion coefficients

$$\left\{ \begin{array}{rcl} Q_{\rm S}\,\vec{x}^{\,\rm int} & = & \vec{x}^{\,\rm inc}, \\ \vec{x}^{\,\rm sca} + Q_{\rm R}\,\vec{x}^{\,\rm int} & = & 0, \end{array} \right. \tag{6}$$

where the matrices $Q_{\rm R}, Q_{\rm S}$ have the elements being integrals of the wave functions and their derivatives. The EBCM suggested by Barber [6] and used by us [4] and Waterman's null-field method discussed in [1] are practically the same.

Integral generalized PMM approach

In the PMM one considers a residual δ describing fulfillment of the boundary conditions (2) in a set of points $\{\vec{r}_s\}_{s=1}^{M}$ on the scatterer surface $\partial\Gamma$

$$\delta = \sum_{s=1}^{M} \left\{ \left| \left(\vec{E}^{\rm inc} + \vec{E}^{\rm sca} - \vec{E}^{\rm int} \right) \times \vec{n} \right|^2 + \left| \left(\vec{H}^{\rm inc} + \vec{H}^{\rm sca} - \vec{H}^{\rm int} \right) \times \vec{n} \right|^2 \right\}_{\vec{r}=\vec{r}_s \in \partial\Gamma} . \tag{7}$$

The first N (in the generalized PMM $N < M$) terms of the field expansions (3) are substituted in Eq. (7) and the residual is minimized in the least-square sense. The derivatives of the residual with respect to the unknown coefficients $\alpha_\nu^{\rm sca}, \alpha_\nu^{\rm int}$ for $\nu = 1, 2, ..., N$ are made equal to 0, which gives $2N$ linear algebraic equations relative to these coefficients. As a result, one gets a system like (4) but with other matrix elements [1, 4]. Replacing summation in Eq. (7) with integration provides more accurate results for smaller M being now the number of knots [7]. So, hereafter we discuss such an *integral generalized* PMM. In our theoretical analysis below this approach is considered for the case of $N = \infty$.

DISCUSSION OF THE METHODS

In computations one always deals with truncated expansions of the EM fields. They can be considered as approximations to the infinite expansions giving the exact values. We discuss theoretical aspects related to the infinite expansions (3), the infinite linear systems (4),(6) and a passage from them to truncated systems as well as some numerical results. Generally, we try to follow and extend the fundamental review [1, 2].

Convergence of infinite field expansions

This point is considered by analyzing singularities of the analytic continuations of the EM fields [8]. We discuss the role played by the expansion convergence in the methods under consideration and concern the Rayleigh hypothesis problem by debating a recent review [9].

Investigations of infinite linear systems

This aspect has not yet been discussed in the literature on the EBCM and generalized SVM. We investigate the infinite systems (4) and (6) arisen in these methods and find the condition of their solvability that involves distances to singularities of analytic continuations of the EM fields. We also explain the connection between the pattern equation method (see [10] and references therein) and the EBCM, which allows us to make important conclusions for the far-field zone. Though equivalence of the EBCM and generalized SVM was generally shown in [11], we demonstrate equivalence of the infinite systems arisen in all the methods under consideration in a more strict way.

Infinite system truncation and numerical comparison of methods

Our passage to truncated systems is based on a proof that infinite systems are regular in terms of [12]. Then they must have the only solution that can be found by the expansion

truncation method. Using a homogeneous set of our generalized SVM, EBCM, integral generalized PMM codes, we confront results of calculations with the theoretical predictions. We also compare these numerical solutions for scatterers of different shape and structure. Special attention is paid to the behavior of the truncated system condition numbers.

REVIEW OF APPLICATIONS OF THE METHODS

Finally, keeping in mind the above discussion, we give a review of works on development and application of the SVM, EBCM and PMM approaches. We mainly concentrate on the SVM and PMM as works on the EBCM are well reviewed (see [13] and references therein) and discuss the use of different (spherical, cylindrical, spheroidal, and ellipsoidal) bases in treatment of homogeneous and layered scatterers and their systems.

Acknowledgements: The work was supported by the grants NSh 1318.2008.2, NTP 2.1.1/665 and RFFI 10-02-00593.

REFERENCES

[1] F.M. Kahnert. Numerical methods in electromagnetic scattering theory. JQSRT **79**–**80** (2003).

[2] F.M. Kahnert. Electromagnetic scattering by nonspherical particles: recent advances. JQSRT (in press) (2010).

[3] M.I. Mishchenko, J.W. Hovenier, and L.D. Travis. *Light scattering by nonspherical particles*. Acad. Press (2000).

[4] V.G. Farafonov and V.B. Il'in. Single light scattering: computational methods. In: *Light scattering reviews*. A.A. Kokhanovsky (ed.). Springer-Praxis (2006).

[5] D. Colton and R. Kress. *Integral equation methods in scattering theory*. J.Wiley & Sons (1983).

[6] P. Barber and C. Yeh. Scattering of electromagnetic waves by arbitrarily shaped dielectric bodies. Appl. Opt. **14** (1975).

[7] V.G. Farafonov and V.B. Il'in. Scattering of light by axially symmetric particles: modification of the point-matching method. Opt. Spectrosc. **100** (2006).

[8] V.F. Apel'tsin and A.G. Kyurkchan. *Analytical properties of wave fields*. Moscow Univ. (1990), in Russian.

[9] J. Wauer and T. Rother. Considerations of Rayleigh's hypothesis. Opt. Comm. **282** (2009).

[10] A.G. Kyurkchan and N.I. Smirnova. The pattern equation method based on the Wilcox representation. J. Commun. Technol. Electr. **53** (2008).

[11] K. Schmidt, T. Rother, and J. Wauer. The equivalence of applying the extended boundary condition and the continuity conditions for solving electromagnetic problems. Opt. Comm. **150** (1998).

[12] L.V. Kantorovich and V.I. Krylov. *Approximate methods of higher analysis*. P.Noordhoff (1958).

[13] M.I. Mishchenko, N.T. Zakharova, G. Videen, N.G. Khlebtsov, and T. Wriedt. Comprehensive T-matrix reference database: a 2007–2009 update. J. Quant. Spectr. Rad. Transf. **111** (2010).

Black carbon aerosol optics in chemical data assimilation and climate forcing studies

M. Kahnert*

Swedish Meteorological and Hydrological Institute, Folkborgsvägen 1, 601 76 Norrköping, Sweden.

Optical properties of freshly emitted black carbon aerosols are computed with a numerically exact method for fractal aggregates. Computations are performed for 14 bands in the wavelength range 0.2−12.195 µm. The results are integrated into the aerosol optical observation operator of the Multiple-scale Atmospheric Transport and CHemistry modelling system MATCH. 3D-fields of ensemble-averaged aerosol optical properties computed with MATCH are coupled to radiative transfer calculations to assess the regional radiative forcing effect of black carbon over Europe. The results indicate that the forcing estimates obtained with the aggregate model can be up to a factor of 2 higher than corresponding estimates obtained with the homogeneous sphere approximation, which is still commonly employed in chemical transport and climate modelling.

INTRODUCTION

The authors of the most recent IPCC report have identified the direct interaction of electromagnetic radiation with aerosols as one of the major sources of uncertainty in assessing the radiative energy balance of the atmosphere [1]. Most aerosol species counteract the positive forcing of greenhouse gases. However, black carbon (BC) originating from soot and biomass burning emissions has been identified as the second most important primary cause for global warming after CO_2 [2]. BC global forcing estimates range between 0.4 to 1.2 W/m^2, which is as much as 55 % of the forcing of CO_2, and more than the forcing caused by all other anthropogenic greenhouse gases combined [1]. BC aerosols increase the energy in the atmosphere, reduce the radiative flux at the surface, and increase the radiative forcing at the top-of-the-atmosphere. BC is a short-lived warming agent, so emission reductions would have an immediate effect to slow down global warming. Therefore the radiative impact of this aerosol species is of considerable interest for both researchers and policy makers.

The trend in modern climate modelling is to build Earth system models in which aerosol fields are treated dynamically by coupling a chemical transport model (CTM) to an atmosphere-ocean circulation model. The treatment of aerosol optical properties in such a model needs to be geared to the output of the CTM. This usually requires that all computations need to be based on volume-equivalent size comparisons.

Elevated concentrations of BC in ambient air are also a public health concern, as they can give rise to increased morbidity and mortality. Air pollution modelling relies on the use of a CTM, which one usually constrains by use of chemical data assimilation of both in situ and satellite observations of aerosols. Assimilation of remote sensing observations relies,

*Michael Kahnert (michael.kahnert@smhi.se)

again, on coupling an aerosol optics model to the output of the CTM. This paper deals with computations of BC optical properties suitable for chemical data assimilation and Earth system climate modelling.

PHYSICAL PROPERTIES OF FRESHLY EMITTED BC

According to a recent critical review of available measurements, the refractive index and mass density of BC aerosols encountered in the atmosphere vary within a range that is considerably smaller than previously assumed [3]. The variation of the refractive index of atmospheric BC can be mainly explained by varying amounts of void fractions in the carbonaceous material, and to a much lesser extent by a variation in the sp^2/sp^3 electronic structure. The measurements in Ref. [4] are reasonably representative for atmospheric BC and agree well with void-fraction simulations of the refractive index [3]. The mass density is around 1.8 g/cm^3. Both measurements and modelling studies agree in that the fractal dimension of the BC aggregates lies around 1.82, and the fractal prefactor can be assumed to be around 1.27 [5]. Fractal dimensions larger than 2 are not representative for fresh BC aerosols. They are more typical for aged BC aggregates. The radius of the primary monomers, of which the aggregates are composed, varies between 10-25 nm. In this range the mass absorption cross section of BC aggregates is not sensitive to the monomer size. However, our sensitivity studies indicate that a monomer radius of 25 nm yields the most reasonable results for the single-scattering albedo.

Model geometries were computed by the random cluster generation algorithm written by Mackowski [6]. Figure 1 shows a model aggregate consisting of 1000 monomers.

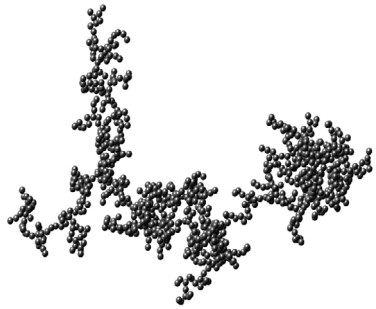

Figure 1. Black carbon model aggregate consisting of 1000 monomers.

OPTICAL PROPERTIES OF BC AGGREGATES

We tested two superposition T-matrix codes, one written by Mackowski and Mishchenko [7] and another written by Xu and Gustafson [8]. The latter offers, in addition to an exact solver, a fast approximate solution method based on limiting the interaction among the monomers. However, we found that the approximate method was not sufficiently accurate for our purposes. The exact method in Ref. [8] gave results that agreed well with those obtained with the exact method described in Ref. [7], and the computation times were

comparable. For the broadband computations, we employed the code by Mackowski and Mishchenko [7].

Computations were performed for aggregates consisting of up to 1000 monomers, and for 16 wavelengths in the range between 0.2 µm−12.195 µm. The spectral range and division points were tailored to the most recent version of the radiation model employed in the Integrated Forecasting System (IFS), which is the global numerical weather prediction model operated at the European Centre for Medium Range Weather Forecast (ECMWF). The new global Earth system climate model EC-EARTH currently developed at ECMWF is based on IFS. As an example, Fig. 2 shows results for a wavelength of 440 nm. Corresponding results for volume-equivalent spheres are also shown.

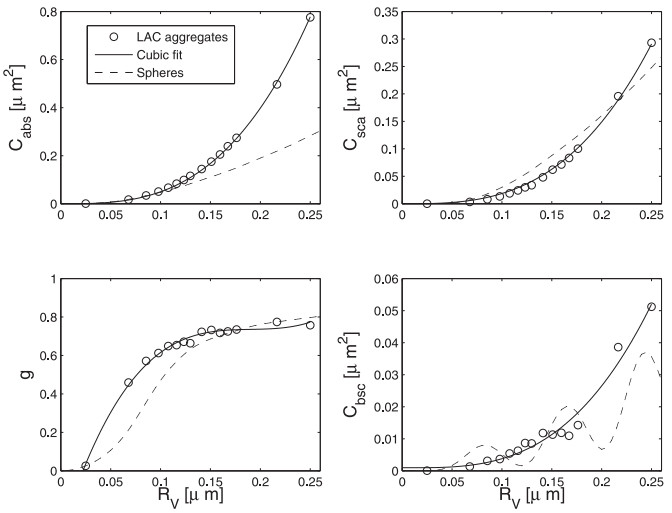

Figure 2. Optical properties as a function of volume-equivalent radius R_V at λ=440 nm.

The use of the homogeneous sphere approximation (HSA) is still common practice in climate research and chemical transport modelling. As can be seen in Fig. 2, over a large part of the size range the HSA strongly underestimates absorption, overestimates total scattering, and underestimates the asymmetry parameter (overestimated side-scattering).

We included the computed optical properties into the optical observation operator of the Multiple-scale Atmospheric Transport and CHemistry modelling system (MATCH) [9], which is a regional CTM. The optical properties of all aerosol components other than BC are computed with the HSA. The optical properties computed with MATCH are coupled to the radiative transfer model DISORT [10] to compute spectral radiative net flux F_λ. By repeating the computations in the absence of BC, one obtains a spectral reference net flux F_λ^0, from which one obtains the spectral radiative forcing effect $\Delta F_\lambda = F_\lambda - F_\lambda^0$. As an example, Fig. 3 shows ΔF_{440} at a wavelength of 440 nm. In this case, we have an aerosol layer at altitudes up to 2−3 km. The BC aerosols give rise to a positive radiative forcing above the aerosol layer, and a negative forcing at the surface, as expected. At the top of the atmosphere, the forcing effect estimated with the aggregate model is twice as high as that computed with the HSA.

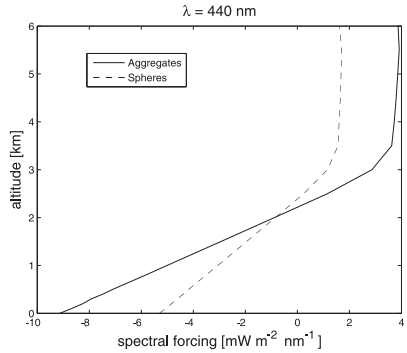

Figure 3. BC radiative forcing as a function of altitude at a latitude of 48.2° N and a longitude of 2.3° E, computed with MATCH and DISORT for 25 July 2006. The solid and dashed lines represent results obtained with the aggregate model and the HSA, respectively.

Acknowledgments: The author is grateful to D. Mackowski for providing his program for aggregated-particle generation. B. Å. S. Gustafson, D. Mackowski, M. Mishchenko, and Y. Xu are acknowledged for making their electromagnetic scattering programs publicly available.

REFERENCES

[1] P. Forster et al. Changes in atmospheric constituents and in radiative forcing. In: *Climate Change 2007: The Physical Science Basis*. S. Solomon et al. (eds.). Cambridge University Press, Cambridge (2007).

[2] V. Ramanathan and G. Carmichael. Global and regional climate changes due to black carbon. Nature Geoscience **1** (2008).

[3] T. C. Bond and R. W. Bergstrom. Light absorption by carbonaceous particles: An investigative review. Aerosol Sci. Technol. **40** (2006).

[4] H. Chang and T. T. Charalampopoulos. Determination of the wavelength dependence of refractive indices of flame soot. Proc. R. Soc. Lond. A **430** (1990).

[5] C. M. Sorensen and G. M. Roberts. The prefactor of fractal aggregates. J. Colloid. Interface Sci. **186** (1997).

[6] D. W. Mackowski. Calculation of total cross sections of multiple-sphere clusters. J. Opt. Soc. Am. A **11** (1994).

[7] D. W. Mackowski and M. I. Mishchenko. Calculation of the T matrix and the scattering matrix for ensembles of spheres. J. Opt. Soc. Am. A **13** (1996).

[8] Y. Xu and B. Å. S. Gustafson. A generalized multiparticle Mie solution: further experimental verification. J. Quant. Spectrosc. Radiat. Transfer **70** (2001).

[9] C. Andersson, J. Langner, and R. Bergström. Interannual variation and trends in air pollution over Europe due to climate variability during 1958-2001 simulated with a regional CTM coupled to the ERA40 reanalysis. Tellus **59B** (2007).

[10] K. Stamnes, S.-C. Tsay, W. Wiscombe, and K. Jayaweera. Numerically stable algorithm for discrete-ordinate-method radiative transfer in multiple scattering and emitting layered media. Appl. Opt. **27** (1988).

Measurements of circular depolarization of light scattered from single ice particles

A. Kiselev[*,1], T. Clauss[1], P. H. Kaye[2], E. Hirst[2], R. Greenaway[2], J. Ulanowski[2], E. Hesse[2], and M. Schnaiter[3]

[1]*Leibniz - Institute for Tropospheric Research, Permoserstr. 15, 04318 Leipzig, Germany.*
[2]*University of Hertfordshire, Centre for Atmospheric and Instrumentation Research, Hatfield, Hertfordshire, AOL10 9AB, United Kingdom.*
[3]*Karlsruhe Institute of Technology, P.O. box 3640, 76021 Karlsruhe, Germany.*

A novel small ice detector LISA was used to measure the circular depolarization ratio δ_C for light scattered from water droplets, just-frozen droplets and pristine ice crystals into near-backward direction. For hexagonal plates the values of δ_C were found to be very high compared to those for the columns and frozen droplets. For liquid droplets, the measured values of δ_C have shown a good agreement with the Mie calculations.

INTRODUCTION

Due to importance of ice phase for the radiative and microphysical properties of clouds, the in-situ characterization of single ice particles in clouds and in the laboratory has been receiving an increased attention in the past years. This characterization is often done optically, e.g., by detecting the light scattered by single particles or visualizing the ice crystals directly. The conventional light scattering methods do not provide the required information about the shape and orientation of ice crystals, and the imaging methods suffer from the resolution constraints and high detection limit. Therefore, some alternative approaches are necessary. The Leipzig Ice Scattering Apparatus (LISA) is a modification of the Small Ice Detector (SID3) [1] built by University of Hertfordshire to study the nucleation and growth of ice crystals in the Leipzig Aerosol and Cloud Interaction Simulator (LACIS) [2]. In October 2009 LISA took part in the experiment at the AIDA cloud chamber [3,4] at the Karlsruhe Institute of Technology within the framework of the Virtual Institute on Aerosol-Cloud Interaction (VI-ACI) of the Helmholtz Association. During this experiment, the ice formation on mineral dust and soot coated with secondary organic aerosol (SOA) was studied. The variability of growth processes in the AIDA chamber allowed measuring the scattering patterns and circular depolarization of light scattered by ice crystals of different shapes from almost spherical just-frozen droplets to pristine ice crystals like hexagonal plates or columns. Here we report some selected results of these measurements.

* Corresponding author: Alexei Kiselev (kiselev@tropos.de)

EXPERIMENT

The optical layout of LISA is shown in Fig. 1. LISA is capable of capturing high-resolution two dimensional light-scattering patterns from single particles in an angular range of 9° to 25° in the near-forward direction with a gated intensified CCD camera (780 x 582 pixels). The size, shape, and orientation of the observed particles can be deduced by comparing recorded images with the scattering patterns calculated for particles of known shape and orientation [5] or measured with ice analog crystals [6]. As opposed to other SID3 instruments, LISA is also capable of measuring the circular depolarization ratio δ_C in near-backward direction (scattering angle from 166° to 172°). This is done by registering the cross-polarized components of backscattered light after sending it through a quarter wave plate (QWP), installed in front of a polarizing beam splitter cube (see Fig.1). In this way δ_C is defined as

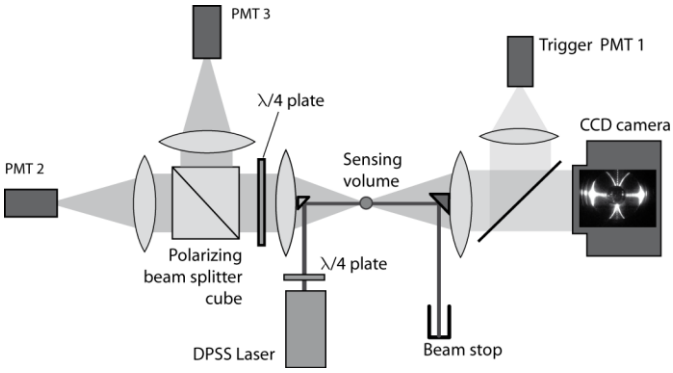

Figure 1. Schematic of LISA instrument (top view). Ice particles are crossing the sensing volume perpendicular to the drawing plane. The laser beam (λ = 532 nm) is circularly polarized to avoid polarization-dependent variations in the scattering patterns.

$$\delta_C = \frac{I_s + V_s}{I_s - V_s},$$

where I_s and V_s are the first and the last components of the Stokes vector of the scattered light.

Ice crystals were nucleated and grown in the AIDA chamber as described in [3]. Under the varying conditions inside the chamber (temperature, pressure, and ice saturation) the evolution of the ice crystals' population was characterized with the help of in-situ optical instrumentation available at AIDA or by drawing a sample flow from the chamber [4]. In this experiment, LISA was operating alongside with several other ex-situ single-particle optical detectors (WELAS, PHIPS, SID3, NIXE-CAPS, CPI).

RESULTS AND DISCUSSION

With LISA, we were able to measure δ_C for several distinct classes of particles: liquid droplets, frozen droplets, hexagonal plates, and columns (Figs. 2 and 3). The shape and orientation of ice crystals was deduced from visual examination of scattering pattern and comparison with the exemplary patterns [5,6]. For water droplets, the diameter could be assessed by comparing the number of rings with Mie calculations. In all cases, the populations of several hundreds of particles were evaluated.

The distributions of δ_C for water drops were found to be in a good agreement with Mie calculations. However, the ice crystals originating from the heterogeneous freezing of

droplets have shown a distinctly higher values of δ_C than expected for liquid droplets of almost the same size (Figs. 2b and 2c). Also the broadness of the distribution is evidently larger, which might be attributed to the variability of the slightly aspherical shape that droplets acquire when freezing.

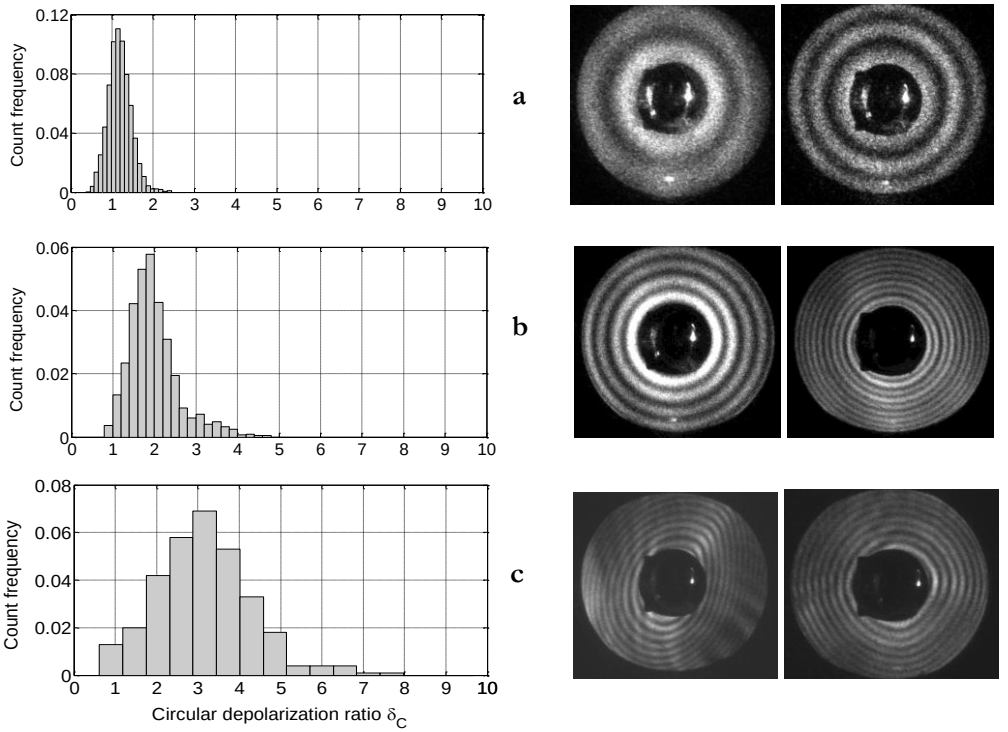

Figure 2. Scattering patterns (right) and histograms of δ_C (left) for liquid and frozen droplets. (a) liquid droplets with size from 3 μm to 15 μm; (b) liquid droplets with size from 10 μm to 26 μm; (c) just-frozen droplets, size in the range 15 μm – 27 μm.

To investigate the orientation dependence of δ_C for columns, we have divided the evaluated column-like ice crystals into two populations: one, with the main axis oriented exactly perpendicular to the illuminating laser beam (no curvature of the main feature on the scattering pattern can be established, Fig. 3a), and second, with the main axis tilted with respect to the exact perpendicular plane (the main bright feature on the scattering pattern clearly curved, see Fig. 3b). No significant difference of the δ_C values have been found for these two populations.

The highest values of δ_C were observed for the hexagonal plates with the main facet oriented perpendicular to the laser beam. In this case only scattering patterns showing straight rays of the six-pointed "star" were hand-selected for the evaluation (see Fig. 3c). The size assessment of the pristine ice crystals from the scattering patterns was not possible. To achieve this, and also to get a better understanding of the circular depolarization results, a model calculations of scattering by single ice crystals in a fixed orientation will be necessary. That we are going to address in the near future.

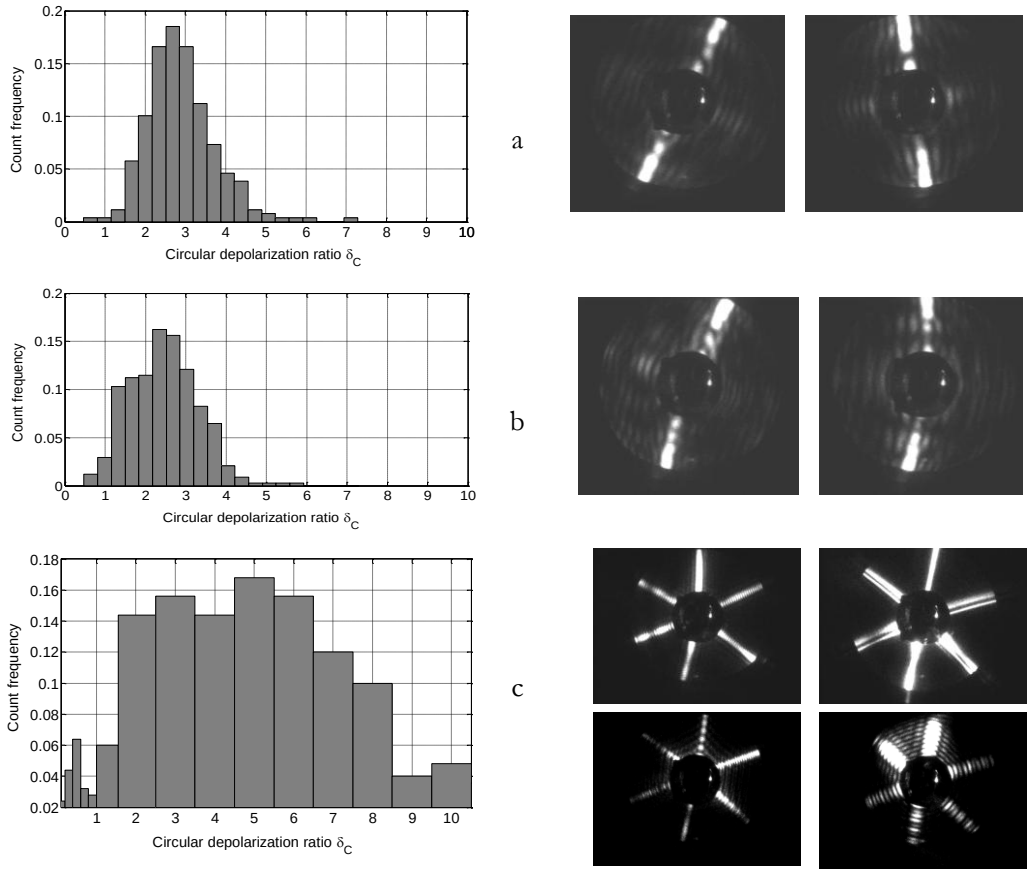

Figure 3. Scattering patterns (right) and histograms of δ_C (left) for pristine ice crystals. (a) columns oriented perpendicular to the laser beam; (b) columns tilted with respect to the laser beam; (c) hexagonal plates oriented perpendicular to the laser beam.

REFERENCES

[1] P.H. Kaye et al. Classifying atmospheric ice crystals by spatial light scattering. Optics Letters **33** (2008).

[2] F. Stratmann et al. Laboratory studies and numerical simulations of cloud droplet formation under realistic supersaturation conditions. J. Atmos. Ocean. Tech. **21** (2004).

[3] O. Möhler et al. Experimental investigation of homogeneous freezing of sulphuric acid particles in the aerosol chamber AIDA. Atmos. Chem. Phys. **3** (2003).

[4] R. Wagner et al. A review of optical measurements at the aerosol and cloud chamber AIDA. JQSRT **110** (2009).

[5] A.J.M. Clarke et al. A 3D implementation of ray tracing combined with diffraction on facets: Verification and a potential application. JQSRT **100** (2006).

[6] J. Ulanowski et al. Light scattering by complex ice-analogue crystals. JQSRT **100** (2006).

Phase-angle variations in absorption bands as a manifestation of the coherent-backscattering effect

L. Kolokolova[*,1], V. Tishkovets[2], and B. Buratti[3]

[1]*Department of Astronomy, University of Maryland, College Park, MD, USA.*
[2]*Institute of Radioastronomy, Kharkiv, Ukraine.*
[3]*Jet Propulsion Laboratory, Pasadena, CA, USA.*

We have found systematic variations in the depth of the absorption bands in the spectra of Saturn's icy satellites and showed that these variations likely resulted from the coherent-backscattering effect (CBE). Our computer modeling of the CBE reproduces the observed spectral variations and also shows that they are strongly affected by the size and packing of particles. The variations in the absorption bands produced by the CBE not only allow us to improve interpretation of the spectra but also provide a promising approach to study size and packing of the regolith and dust particles.

INTRODUCTION

The coherent-backscattering effect (CBE) results from the interference of the light that experiences multiple scattering in the medium and has the same but opposite optical path, i.e., was scattered by the same particles but in the opposite order. The most well known manifestation of the CBE is a steep brightness spike observed at small phase angles for numerous dusty environments, including planetary rings and icy cosmic bodies. Since the CBE spike is formed by multiply scattered light, it is more pronounced if more opportunities for multiple scattering occur, e.g., in the case of less absorbing particles. Strong dependence of the CBE on absorption was confirmed by numerous theoretical and laboratory simulations (see, e.g., [1-5]). Since the steepness of the CBE spike depends on the absorption, it should be different for the wavelengths within and outside of the absorption bands. As a result, the depth of the absorption bands should be different at different phase angles. We study this effect observationally and theoretically and provide recommendations for its application.

MANIFESTATION OF COHERENT BACKSCATTERING EFFECT IN THE SPECTRA OF ICY BODIES

The coherent-backscattering effect is especially pronounced for high albedo bodies such as Saturn's rings [6], icy satellites of the outer planets [7-10], Kuiper-belt objects (KBOs) [11], and E-type asteroids [12]. As it was mentioned above, it manifests itself in a steep photometric spike at the phase angles smaller than 3°. It is more pronounced for the high-albedo bodies and the steepness of the spike increases with increasing albedo [7]. Thus, one can expect that, at the wavelengths where the body is brighter, the CBE spike is steeper than at the wavelength where the body is darker. The different steepness affects the difference between the brightness of the object within and outside the absorption bands and, thus, results in a different depth of the bands at different phase angles. Such an effect has been already noticed for Saturn's rings [13]; however, [13] could not provide any explanation of this effect

* Corresponding author: Ludmilla Kolokolova (ludmilla@astro.umd.edu)

and neglected it in the interpretation of the data. The effect of CBE on the photometric data taken in different spectral bands was discussed in [8] for satellites of Uranus; however, [8] did not have the data within absorption bands and the effect of the CBE on the spectra was not analyzed there.

Cassini VIMS spectra of icy satellites of Saturn

A great opportunity to study spectral variations with phase angle appeared when the data for icy satellites of Saturn were taken by the instrument VIMS (Visual and Infrared Mapping Spectrometer, see [14]). VIMS provided the spectra in a broad range of wavelengths, including the near infrared where the deep water ice absorption bands are located. Due to the high spatial resolution provided by VIMS, the spectra for the same surface features can be selected, thus eliminating an effect of rotational variations of albedo. Besides, VIMS data have been analyzed to check the phase dependence of brightness, and a strong opposition spike whose steepness and width are consistent with the CBE was found [10]. Here we focus on the data for the leading hemisphere of Rhea as they are characterized by the best signal-to-noise ratio. The expected effect of changing the depth of the absorption bands with the phase angle is clearly seen in the spectra of Rhea (Fig. 1). For example, the difference in the depth for the 2 μm ice band is 12% for the phase angles 0.05° and 1.5° with the accuracy of the measurements about 1%.

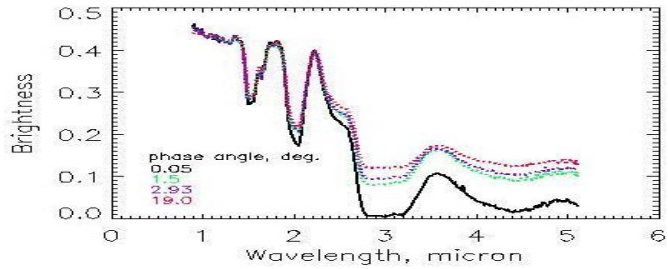

Figure 1. Spectra for Rhea taken at several phase angles (indicated in the plot) at a similar orbital longitude. The spectra were shifted to match the continuum at the short wavelengths. The units of brightness are the ratio of the measured intensity to the solar flux at the heliocentric distance of Saturn. For a grayscale image, the absorption bands for smaller phase angles are deeper.

Computer simulations of the CBE effects in the spectra

To check if CBE can be responsible for the observed phase angle variations in the spectra of Rhea, we modeled the spectra using the approach to CBE developed in [15-16]. At this approach the CBE is considered as the weak localization of the electromagnetic waves scattered by a layer of discrete random medium. A solution of the weak localization problem was presented in [16]; it is based on a transformation of an exact system of integral equations into a system of linear algebraic equations which can be solved readily. Comparisons of the theoretical results with benchmark numerical data for a medium composed of non-absorbing Rayleigh scatterers as well as with experimental data for a medium composed of wavelength-sized particles have shown that this approximation can be expected to give a good accuracy.

Using this technique we simulated the spectra for semi-infinite layer of water ice spheres of different size and packing [17]. We considered three packing factors ξ = 0.05, 0.1, and 0.2

(that corresponds to the porosity 95%, 90%, and 80%), and two particle radii, r=0.25 and 0.5 μm, that can be typical for the icy satellites of Saturn [18]. The optical constants of water ice were taken from [19]. The results (Fig. 2) show that the theoretical modeling produces the same tendencies that were observed for Rhea: the depth of the band gets smaller with increasing phase angle and the faster change in the depth happens at smaller phase angles. The rate of the change and the shape of the bands are strongly affected by the particle size and packing. The trend most close to the observational data (compare the vertical separation between the spectra in Figs. 1 and 2) is demonstrated by particles of r=0.5 μm and ξ = 0.2.

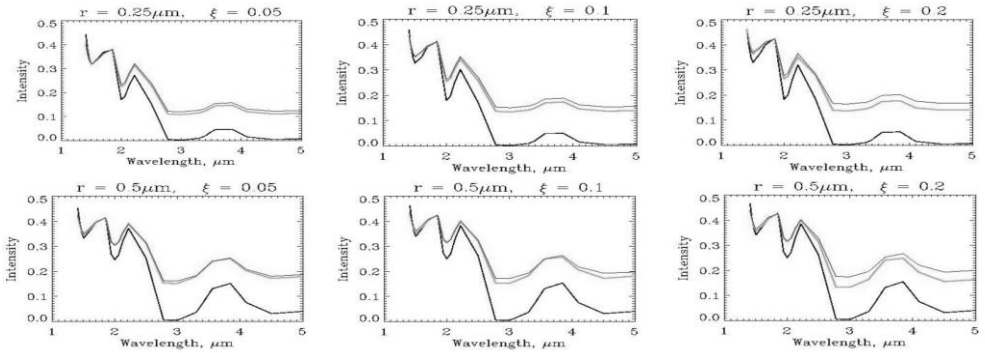

Figure 2. Computer modeling of Rhea's spectra. The radius of particles and their packing are indicated on the top of each figure. The results are for the phase angle 0.05° (the deepest absorption band), 1.5° (next deepest band) and 19° (the most shallow absorption band). As in Fig. 1, the spectra were shifted to match at the shortest wavelength.

CONCLUSIONS

Coherent backscattering affects not only the photometric (and polarimetric) characteristics of high-albedo objects, but also their spectra at small phase angles. The depth of the absorption bands and their shape are different at different phase angles, reflecting the dependence of the steepness of the CBE photometric spike on the absorption of the material.

The phase angle dependence of the spectra should be a common phenomenon for high-albedo cosmic bodies: planetary rings, satellites of the outer planets, KBOs, E-type asteroids, etc., and should be a part of any interpretation of their spectra. Neglecting the phase angle variations of the absorption bands at a comparative analysis of spectral data obtained at different phase angles can result in misinterpretation of the spectra, leading to erroneous conclusions about compositional and particle size differences of icy bodies. Particularly, ignoring this effect provides misleading conclusions regarding composition and relative abundance of water ice on the surface of the bodies.

Studies of the spectral manifestations of CBE not only improve our understanding of the formation of absorption bands, but also can be used as a new remote sensing technique for the characterization of surfaces and dust particles. The advantage of this method is that it does not require a detailed phase angle trend and, thus, does not need multiple observations. The spectra at 2–3 phase angles are sufficient so that the future modeling allows extracting information about the size and packing of regolith or ring particles. We can say that the role of the range of phase angles is replaced here by the role of the range of wavelengths. This makes the method especially convenient at studies of very

distant objects, e.g. KBOs, whose phase angle changes slowly and within a very narrow range.

REFERENCES

[1] A. Etemad et al. Weak localization of photons: Termination of coherent random walks by absorption and confined geometry. Phys. Rev. Lett. **59** (1987).

[2] Yu. Shkuratov et al. The Opposition Effect and Negative Polarization of Structural Analogs for Planetary Regoliths. Icarus **159** (2002).

[3] K. Muinonen et al. Asteroid Photometric and Polarimetric Phase Effects. In: *Asteroids III*. Tucson, Univ. Arizona Press (2002).

[4] M. Mishchenko, L. Travis, and A. Lacis. Multiple Scattering of Light by Particles. Cambridge, Cambridge Univ. Press (2006).

[5] B. Hapke et al. A quantitative test of the ability of models based on the equation of radiative transfer to predict the bidirectional reflectance of a well-characterized medium. Icarus **199** (2009).

[6] A. Cook, F. Franklin, and F. Palluconi. Saturn's Rings- A Survey. Icarus **18** (1973).

[7] V. Rosenbush et al. Photometric and Polarimetric Opposition Phenomena Exhibited by Solar System Bodies. In: *Optics of Cosmic Dust*. Dordrecht: Kluwer (2002).

[8] V. Avramchuk, V. Rosenbush, and T. Bul'ba. Photometric study of the major satellites of Uranus. Solar System Research **41** (2007).

[9] I. Kulyk. Saturnian icy satellites: Disk-integrated observations of the brightness opposition surge at low phase angles. Planet Space Sci. **56** (2008).

[10] B. Buratti et al. Opposition Surges of the Satellites of Saturn from the Cassini Visual Infrared Mapping Spectrometer (VIMS). In: *40th Lunar and Planetary Science Conference* #1738 (2009).

[11] B. Schaefer et al. The Diverse Solar Phase Curves of Distant Icy Bodies II. The Cause of the Opposition Surges and Their Correlations. Astron. J. **137** (2009).

[12] A. W. Harris et al. Phase relations of high albedo asteroids - The unusual opposition brightening of 44 Nysa and 64 Angelina. Icarus **81** (1989).

[13] F. Poulet et al. Compositions of Saturn's rings A, B, and C from high resolution near-infrared spectroscopic observations. Astron. Astrophys. **412** (2003).

[14] R. Brown et al. The Cassini Visual and Infrared Mapping Spectrometer (VIMS) Investigation. Space Sc. Rev. **115** (2004).

[15] V. Tishkovets and M. Mishchenko. Coherent backscattering of light by a layer of discrete random medium. JQSRT **86** (2004).

[16] V. Tishkovets and M. Mishchenko. Approximate calculation of coherent backscattering for semi-infinite discrete random media. JQSRT **110** (2009).

[17] L. Kolokolova, B. Buratti, and V. Tishkovets. Impact of coherent backscattering on the spectra of icy satellites of Saturn and the implications of its effects for remote sensing. Astroph. J. Let. **711** (2010).

[18] S. Newman et al. Water Ice Crystallinity and Grain Sizes on Dione. In: *AGU Fall Meeting* P43A-05 (2007).

[19] S. G. Warren. Optical constants of ice from the ultraviolet to the microwave. Applied Optics. **23** (1984).

Observations and calculations of two-dimensional angular optical scattering patterns of a levitated bi-sphere

U. K. Krieger* and P. Meier

Institute for Atmospheric and Climate Science, ETH Zurich, 8092 Zurich, Switzerland.

We use single bi-sphere particles levitated in an electrodynamic balance to record two-dimensional angular scattering patterns at different angles of the coordinate system of the aggregate relative to the incident laser beam. Due to Brownian motion, the particle covers the whole set of possible angles with time and allows to select patterns with high symmetry for analysis. These are qualitatively compared to numerical calculations. An experimental procedure is proposed for studying restructuring effects occurring in mixed particles upon evaporation.

INTRODUCTION

Our interest in measuring two-dimensional angular optical scattering (TAOS) patterns of single aggregate particles made out of spheres originate from previous work [1], where we were using optical resonance spectroscopy for sizing evaporating solid, non-spherical particles. We observed that the shift of optical resonances with time, when the particle is solid, exhibits distinct discontinuities which we ascribed to sudden rearrangements processes within the evaporating solid. While this explanation is plausible, it warrants a more detailed investigation. A simple aggregate built from polystyrene latex microspheres and a solid with sufficient high vapor pressure could provide a model system for studying such processes. Besides optical resonance spectroscopy, analyzing the TAOS patterns with the help of numerical simulations should allow a more detailed analysis of the rearrangements taking place in aggregate particles upon evaporation.

Here we present a test of the basic concept by measuring the simplest aggregate particle possible, a bi-sphere, and compare the observed TAOS patterns with calculated ones using the code developed by Mackowski [2].

Our experimental setup resembles in a lot of aspects the one used in the pioneering work of Bottiger et al. [3], but the analysis of the scattered light differs in one essential aspect. Namely, instead of recording rotational averaged scattering matrices, we record the TAOS pattern for a fixed, distinct orientation. Previously, Holler et al. [4] have done similar experiments for sphere clusters consisting of multiple spheres, but they observed these clusters in an aerosol flow, while we levitate a single cluster and observe the same cluster for a prolonged period of time. This allows us to study the scattering at different angles between the coordinate system of the cluster and the incoming laser beam.

EXPERIMENTAL

The experimental setup has been described elsewhere in [5]. Briefly, Fig. 1 shows a schematic of the experimental setup. A particle is levitated in an electrodynamic balance with CCD1 recording a microscopic image of the particle illuminated with a weakly focused laser beam from below. CCD2 is a fast, progressive scan CCD (60 fps, shutter speed: 1/250 s) to record

*Corresponding author: Ulrich K. Krieger (ulrich.krieger@env.ethz.ch)

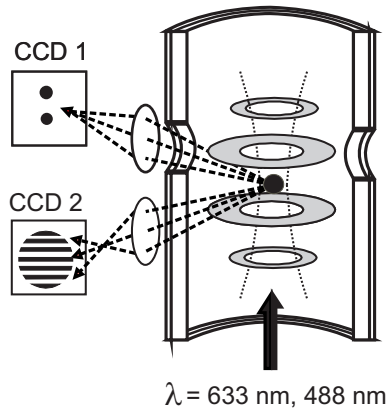

Figure 1. Schematic of the experimental setup. CCD1 records a microscopic image of the particle, CCD2 records the TAOS pattern due to scattered laser light with a wavelength of either 633 nm or 488 nm.

the corresponding TAOS pattern. The observed angles range approximately from 85° to 95° in both, polar and azimuthal angle, but no effort was made for these test experiments to calibrate the angles using the scattering of a single sphere of known radius and refractive index. A single-particle generator (Hewlett-Packard 51633A ink jet cartridge) is used to inject a single liquid droplet (volume 140 pl) from solutions made from suspensions of polystyrene latex particles purchased from Polyscience, Inc., diluted with MilliQ water. The number of primary particles within the droplet follows Poisson statistics and depends on the concentration of the suspension. The water evaporates and leaves an aggregate of spheres levitated in the electrodynamic balance. By adjusting the concentration of the suspension, the probability for obtaining a single sphere, a bi-sphere or tri-sphere may be optimized. By replacing the water with a dilute aqueous solution of, for example, a low-vapor-pressure dicarboxylic acid and subsequent drying of the particle in the electrodynamic balance, mixed particles consisting of polystyrene spheres and crystalline dicarboxylic acid may be produced. Upon evaporation of the dicarboxylic acid, restructuring of the remaining polystyrene spheres is expected to occur.

The particle is subject to rotational Brownian motion while trapped in the center of the electrodynamic balance [6]. In addition, with larger particles (radius > 5 µm), slight asymmetries in the balance together with the anisotropic polarizability of the bi-sphere particles induce an almost stationary rotation of the particle around one of the axes of symmetry. We observed a typical timescale of this motion of about 1 round per 10 seconds. If this effect is undesirable, the electrodynamic balance can be switched to a quasi-electrostatic mode, which allows the free Brownian motion about all axes [6]. For a particle of 5-µm radius, rotational Brownian motion leads to a mean rotation of 22 degrees per second. When movies of the Brownian motion are recorded with CCD1 and CCD2, single frames can be selected showing high symmetry because the polar and azimuthal angles of the aggregate are parallel or perpendicular to the plane of polarization of the illuminating laser beam. Two examples are shown in Fig. 2.

RESULTS

The upper row in Fig. 2 shows the experimental TAOS pattern in panel (a), the corresponding TAOS calculations [2] in panel (b) and the microscopic image of the particle in panel (c). The particle is a bi-sphere cluster with the nominal radii of the single spheres being 5.0 µm. The lower row shows the same particle but in a different orientation: (d) is again the measured TAOS pattern, (e) shows the calculated TAOS pattern and (f) the microscopic image. The microscopic images clearly reveal the orientation of the bi-sphere perpendicular to the line of view of CCD1 by showing 4 separated glare spots in the upper row image panel (c). Note that the glare spots seem to form at the corners of a square, as expected for a bi-sphere consisting of two spheres with the same radius. When rotated by 90° only 2 glare spots are visible as seen in the lower row image panel (f). These orientations yield distinct TAOS patterns, the one in the lower row (d) almost resembling the typical Mie pattern of a single sphere.

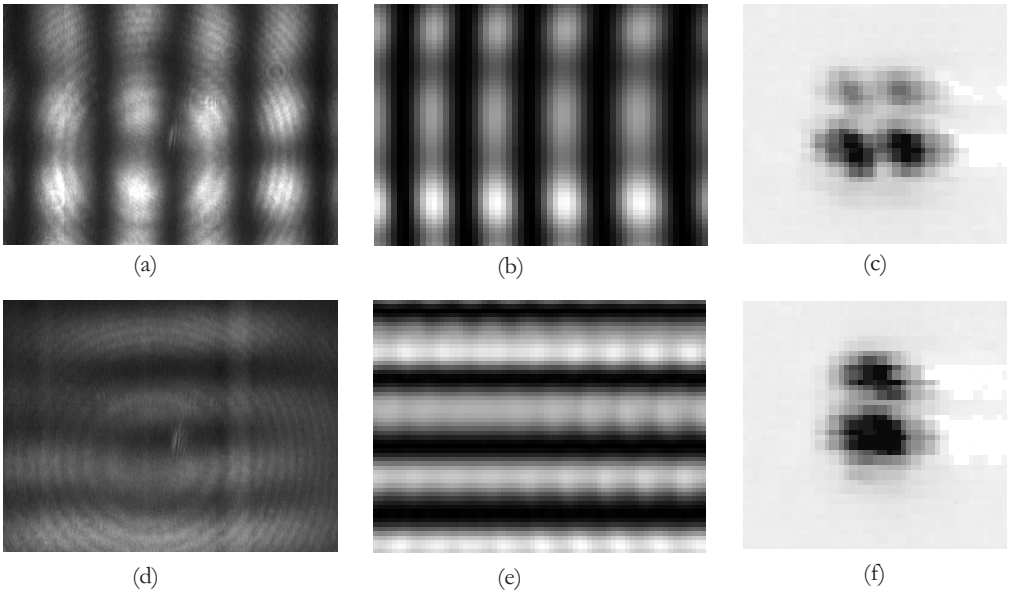

Figure 2. Observed (a, d) and calculated TAOS patterns (b, e) with microscopic images of a bi-sphere particle with single-sphere radii of 5.0 µm. Incident laser wavelength 488 nm.

A randomly picked TAOS pattern shows typically some distortion relative to the patterns shown in Fig. 2. Two examples are shown in Fig. 3. We do not know azimuthal and polar angles a priori and did not try to find these angles through comparison with calculations. But, in principle, comparison with a number of calculations performed over a sufficiently narrow grid should allow to estimate the angles of the laser beam relative to the bi-sphere coordinate system.

CONCLUSIONS AND OUTLOOK

Our setup allows us to measure the TAOS patterns of single, levitated aggregate sphere particles. Characterization of the particles is possible by comparing the observed and cal-

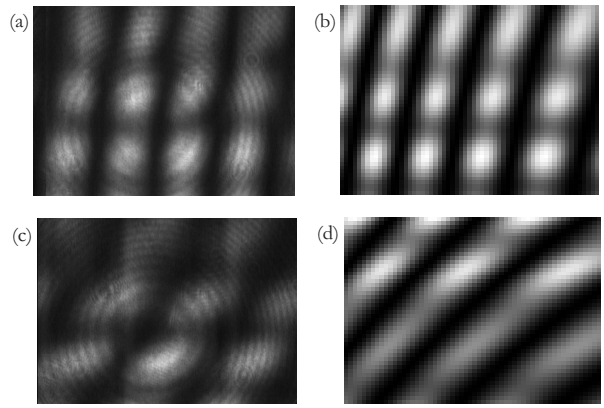

Figure 3. Observed TAOS patterns (a) and (c) which appear to be tilted relative to the ones shown in Fig. 2. Patterns originate from scattering of the same particle as in Fig. 2. For comparison, panels (b) and (d) show calculated TAOS patterns with angles α, β [2] of 0°, 15° and 0°, 45°, respectively.

culated TAOS patterns. In the future, we intend to study mixed particles, composites of polystyrene spheres and crystalline succinic acid, with the succinic acid crystallites evaporating slowly with time. This should allow us to analyze the restructuring of the composite particle by comparing its TAOS patterns with the corresponding calculations.

REFERENCES

[1] A.A. Zardini, and U.K. Krieger. Evaporation kinetics of a non-spherical, levitated aerosol particle using optical resonance spectroscopy for precision sizing. Opt. Express **17** (2009).

[2] D. Mackowski. *SCSMFO.FOR: Calculation of the Scattering Properties for a Cluster of Spheres*. User guide accompanying the SCSMFO.FOR code (1999).

[3] J.R. Bottiger, E.S. Fry and R.C. Thompson. Phase Matrix Measurements for Electromagnetic Scattering by Sphere Aggregates. In: *Light Scattering by Irregularly Shaped Particles*. D.W. Schuerman (ed.). Plenum Press, N.Y. (1979).

[4] S. Holler, J.-C. Auger, B. Stout, Y. Pan, J.R. Bottiger, R.C. Chang, and G. Videen. Observations and calculations of light scattering from clusters of spheres. Appl. Opt. **39** (2000).

[5] C. Braun and U.K. Krieger. Two-dimensional angular light-scattering in aqueous NaCl single aerosol particles during deliquescence and efflorescence. Opt. Express **8** (2001).

[6] U.K. Krieger and A.A. Zardini. Using dynamic light scattering to characterize mixed phase single particles levitated in a quasi-electrostatic balance. Faraday Discuss. **137** (2008).

Simulation of electromagnetic scattering characteristics of particles with anisotropic surface impedance

A. G. Kyurkchan* and D. B. Demin

Moscow Technical University of Communication and Informatics, Aviamotornaya Street 8A, Moscow, 111024, Russia.

The pattern equation method has been extended to solve the scattering problems of electromagnetic waves on particles with anisotropic surface impedance. The scattering characteristics of axially symmetrical scatterers with artificially soft and hard surfaces and with complicated structures of curves of conductivity on their surfaces are investigated. The comparisons to the results obtained using other methods are discussed.

INTRODUCTION

In this paper, we consider scattering of electromagnetic waves on particles with anisotropic surface impedance. In this case, the surface impedance in the impedance boundary condition, known as Leontovich's boundary condition, is given by a tensor with the components corresponding to appropriate directions of anisotropy.

We extended the pattern equation method (PEM) to solve the abovementioned problem. The PEM has already been applied to solve problems of electromagnetic wave scattering on impedance and dielectric scatterers [1-3]. The PEM is one of the most effective methods for solving scattering problems of electromagnetic waves. It has been earlier established [1-3] that the rate of convergence of the PEM's numerical algorithm is mainly governed by the scatterer size and weakly depends on its geometry.

Under the boundary value problem, we consider the scattering problem of plane waves for axisymmetric scatterers. We investigate the scattering characteristics of these scatterers with artificially soft and hard surfaces [4] using special values of anisotropic impedance. Also, we simulate scattering of circularly polarized plane waves on particles with boundary conditions which correspond to complicated structures of curves of conductivity [5].

PROBLEM STATEMENT

Let us consider the problem of electromagnetic scattering of incident primary monochromatic ($e^{i\omega t}$) field $\vec{E}^0$, $\vec{H}^0$ by an arbitrarily shaped 3D compact obstacle bounded by surface S. Let the following impedance boundary condition be met at S:

$$\left(\vec{n}\times\vec{E}\right)_S = \hat{Z}\left[\vec{n}\times\left(\vec{n}\times\vec{H}\right)\right]_S, \qquad (1)$$

* Corresponding author: Alexander G. Kyurkchan (kyurkchan@yandex.ru)

where $\vec{n}$ is the outward unit normal to S; $\hat{Z}$ is a tensor of surface impedance (an anisotropic surface impedance) which is

$$\hat{Z} = \begin{bmatrix} Z_l & Z_{l\varphi} \\ Z_{\varphi l} & Z_\varphi \end{bmatrix} \tag{2}$$

for axially symmetrical bodies; $\vec{E} = \vec{E}^0 + \vec{E}^1$, $\vec{H} = \vec{H}^0 + \vec{H}^1$ is the total field; $\vec{E}^1, \vec{H}^1$ is the secondary (diffracted) field, which satisfies the system of homogeneous Maxwell equations elsewhere outside S and the Sommerfeld radiation condition at infinity.

The component Z_l of tensor $\hat{Z}$ corresponds to the direction of the unit vector $\vec{i}_l$ which is tangential to S and perpendicular to the unit vectors $\vec{i}_\varphi$ (unit vector of a spherical coordinate system (r, θ, φ)) and $\vec{n}$. Thus, the vectors $\vec{i}_l$, $\vec{i}_\varphi$, and $\vec{n}$ form a right-handed orthogonal system.

REDUCTION OF BOUNDARY-VALUE PROBLEM TO SYSTEM OF ALGEBRAIC EQUATIONS

According to the PEM standard scheme [1-3], the initial boundary-value problem for the Maxwell equations is reduced to an infinite system of linear algebraic equations with respect to the unknown coefficients a_{nm}, b_{nm} of expansion of the scattering patterns $\vec{F}^E$, $\vec{F}^H$ of electric and magnetic fields in terms of vector angular spherical harmonics, which compose the orthogonal basis in the spherical coordinates (r, θ, φ).

For the diffracted field $\vec{E}^1, \vec{H}^1$ in the far zone, the following asymptotic relations are met

$$\vec{E}^1, \vec{H}^1 = \frac{\exp(-ikr)}{r} \vec{F}^{E,H}(\theta, \varphi) + O\left(1/(kr)^2\right).$$

Then, using the integral representations for the field $\vec{E}^1, \vec{H}^1$, which could be obtained from the Maxwell equations, and decompositions of these fields in terms of vector spherical harmonics, we have the following system of PEM:

$$\begin{cases} a_{nm} = a_{nm}^0 + \sum\limits_{q=1}^{\infty} \sum\limits_{p=-q}^{q} \left(G_{nm,qp}^{11} a_{qp} + G_{nm,qp}^{12} b_{qp} \right), \\ b_{nm} = b_{nm}^0 + \sum\limits_{q=1}^{\infty} \sum\limits_{p=-q}^{q} \left(G_{nm,qp}^{21} a_{qp} + G_{nm,qp}^{22} b_{qp} \right), \end{cases} \quad n = 1,2,..., \quad |m| \le n, \tag{3}$$

where

$$a_{nm}^{0} = a_{nm}^{00} + a_{nm}^{\tilde{z}0}; \quad b_{nm}^{0} = b_{nm}^{00} + b_{nm}^{\tilde{z}0}; \quad G_{nm,qp}^{ij} = G_{nm,qp}^{0ij} + G_{nm,qp}^{\tilde{z}ij}; \ i, j = 1,2. \qquad (4)$$

In Eq. (4), the coefficients with the additional superscript "0" correspond to the perfect conductor ($\hat{Z} = 0$), and the ones marked by "$\tilde{z}$" designate additional terms caused by the anisotropic impedance $\hat{Z}$. The coefficients a_{nm}^{0}, b_{nm}^{0} are determined by the incident wave. These coefficients and the matrix elements $G_{nm,qp}^{ij}$, $i, j = 1,2$ in (3) are represented in surface integrals on S, and they are similar to those published in [1-3].

The verification of applicability of the numerical algorithm of PEM has been made earlier (see, for example, [1-3]).

NUMERICAL RESULTS

Consider examples of searching for the scattering patterns for the following axially symmetric scatterers: sphere and spheroid. The z-axis was chosen as the symmetry axis of the scatterers. In all examples, the incident field is a plane wave propagating along the z-axis.

In Fig. 1, the scattering patterns of E-field (with the polarization of the vector $\vec{E}^{0}$ along the *x*-axis) are shown for the prolate spheroid with the parameters: $ka = 10$ (small semiaxis) and $kc = 20$ (large semiaxis). Curve 1 corresponds to the scattering pattern $|F_{\theta}^{E}|$ (in the $\varphi = 0$ plane) of perfectly conducting scatterer ($\hat{Z} = 0$), and curves 2 and 3 correspond to the patterns $|F_{\theta}^{E}|$ (in the $\varphi = 0$ plane) and $|F_{\varphi}^{E}|$ (in the perpendicular plane) for scatterer with artificially soft surface. The value of anisotropic impedance $\hat{Z}$ of artificially soft surfaces for electromagnetic waves is defined as follows: $|Z_l| = \infty$, $Z_{l\varphi} = Z_{\varphi l} = Z_{\varphi} = 0$. The value of anisotropic impedance $\hat{Z}$ of artificially hard surfaces is defined as follows: $|Z_{\varphi}| = \infty$, $Z_l = Z_{l\varphi} = Z_{\varphi l} = 0$ (see [4]). In our calculations, infinity is replaced by the number equal to $1000\zeta_0$ (ζ_0 is the wave impedance of the vacuum). From Fig. 1, it is clear that the patterns $|F_{\theta}^{E}|$ and $|F_{\varphi}^{E}|$ for soft particle almost coincide with the pattern $|F_{\theta}^{E}|$ of perfect conductor for scattering angles corresponding to the illuminated part of the surface. The same result was observed for the artificially hard particle.

In our second example, we consider scattering of a plane wave with circular polarization (left-handed) by a sphere and a prolate spheroid. In Fig. 2, we plot the normalized scattering patterns of particles. Here $Z_{l\varphi} = -\nu(\theta) Z_{\varphi}$, $Z_l = -\nu(\theta) Z_{\varphi l}$, and $\nu(\theta) = i0.025\sin^2\theta$ that correspond to spiral curves of conductivity on the scatterer with the angle of rise $\psi(\theta)$, $\nu(\theta) = \mathrm{tg}\psi(\theta)$ [5]. The radii of the spheres are equal to $ka = 0.9$ (curve 1), $ka = 1$ (curve 2), $ka = 1.1$ (curve 3). The parameters of the spheroid are as follows: $ka = 0.65$, $kc = 1.6$ (curve 4), that is, the sizes of the particles there are less than the wavelength of the incident field. From Fig. 2, it is visible that, under axial incidence of the circularly-polarized plane

wave on particles with spiral curves of conductivity, full absorption is observed, coinciding with the result given in [5]. Let us note that, when $ka > 1.1$, backward scattering grows.

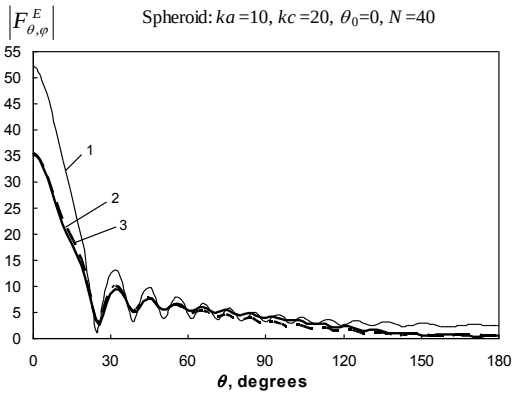

Figure 1. The scattering pattern for a spheroid.

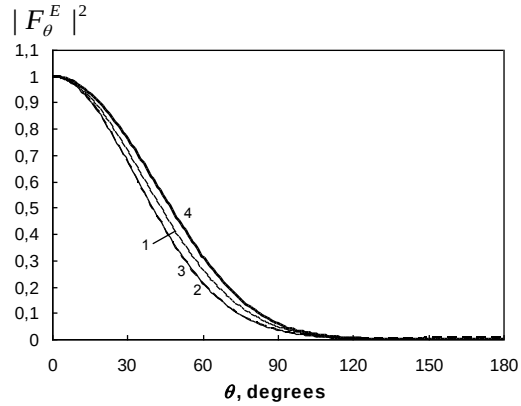

Figure 2. The scattering pattern for a sphere and a spheroid.

CONCLUSION

Thus, we have demonstrated that impedance conditions with anisotropic impedance are applicable in the simulation of scattering characteristics of particles with artificially hard and soft surfaces, and with complicated structures of curves of perfect conductivity.

ACKNOWLEDGMENTS

This work was supported by Russian Foundation for Basic Research, Project no. 09-02-00126.

REFERENCES

[1] A.G. Kyurkchan. Solution of vector scattering problems by the pattern equation method. Journ Comm Tech and Electron. **45** (2000).

[2] A.G. Kyurkchan and D.B. Demin. Electromagnetic wave diffraction from impedance scatterers with piecewise - smooth boundaries. Journ Comm Tech and Electron. **47** (2002).

[3] A. Kyurkchan and D. Demin. Pattern equation method for solving problems of diffraction of electromagnetic waves by axially dielectric scatterers. JQSRT **89** (2004).

[4] P-S. Kildal. Artificially Soft and Hard Surfaces in Electromagnetics. IEEE Transactions on Antennas and Propagation **38**(10) (1990).

[5] E.N. Korshunova, A.N. Sivov, and A.D. Shatrov. Journ Comm Tech and Electron. **45** (2000).

Solving diffraction problems by the *T*-matrix and the pattern equations methods

A. G. Kyurkchan* and N. I. Smirnova

Chair of probability theory and applied mathematics, Moscow Technical University of Communications and Informatics, Aviamotornaya str. 8a 111024 Moscow.

T-matrix method is compared to the pattern equation method. It is shown that the pattern equation method allows analytical averaging of particle orientation, as well as the *T*-matrix method. However, the pattern equation method is applicable to diffraction problems for a broader class of particle geometry and gives higher accuracy than the *T*-matrix method.

INTRODUCTION

The *T*-matrix method (TMM), proposed by Waterman more than forty years ago [1], is currently commonly used for solving wave diffraction problems arising in optics, radio physics, radio astronomy, etc. [2, 3]. *T* matrix interrelates incident and scattered wave spherical basis expansion coefficients. As such, *T* matrix depends only on physical and geometric characteristics of a scatterer and is absolutely independent on propagation and polarization directions of the incident and scattered fields [2, 3].

The pattern equation method, for the first time proposed in paper [4], also allows obtaining the solution of the diffraction problem in the form similar to TMM, but it is applicable at significantly less stringent restrictions on scatterer geometry. Therefore, it is of interest to compare these two methods.

TMM AND PEM ALGORITHMS

In paper [5], it is shown that TMM is correct only if the scatterer geometry belongs to the class of Rayleigh bodies, i.e. such bodies that all wave field analytic continuation singularities are located inside of the sphere inscribed in a scatterer. Such class of geometries is particularly narrow.

PEM allows to obtain the rigorous diffraction problem solution (i.e. theoretically with any given accuracy) for so called weakly non-convex bodies [4]. All convex bodies are part of this class.

Let us perform a more detailed comparison of both methods. Consider two-dimensional diffraction problem on a scatterer with Dirichlet boundary condition for simplicity. As is well known, the scattered field cylindrical harmonic expansion

* Corresponding author: Alexander Kyurkchan (kyurkchan@yandex.ru)

$u^1(\vec{r}) = \sum_{n=-\infty}^{\infty} c_n H_n^{(2)}(kr) e^{in\varphi}$ coefficients c_n are related to the incident field (plane wave, propagating at angle φ_0 to the OX axis) expansion coefficients a_n by the following formula

$$\overline{c} = T\overline{a}\,, \tag{1}$$

where $T = QH^{-1}$, and

$$a_n = -(-i)^n e^{-in\varphi_0}\,, \tag{2}$$

$$Q_{nm} = \int_0^{2\pi} J_n(k\rho(\varphi)) e^{i(m-n)\varphi} d\varphi, \quad H_{nm} = \int_0^{2\pi} H_n^{(2)}(k\rho(\varphi')) e^{i(m-n)\varphi'} d\varphi'\,. \tag{3}$$

In PEM, similar to Eq. (1) formula is given by:

$$\overline{c} = (I - G)^{-1}\overline{c}^0, \tag{4}$$

where I is the identity matrix and matrix G and vector $\overline{c}^0$ elements are given by [4]:

$$G_{nm} = \frac{1}{4}\int_0^{2\pi} J_n(k\rho(\varphi))\left[ik\rho(\varphi) H_m^{(2)\prime}(k\rho) + m\frac{\rho'(\varphi)}{\rho(\varphi)} H_m^{(2)}(k\rho)\right] e^{i(m-n)\varphi} d\varphi\,, \tag{5}$$

$$c_n^0 = \frac{k}{4}\int_0^{2\pi} J_n(k\rho(\varphi))\left[\rho(\varphi)\cos(\varphi-\varphi_0) + \rho'(\varphi)\sin(\varphi-\varphi_0)\right] e^{-ik\rho(\varphi)\cos(\varphi-\varphi_0) - in\varphi} d\varphi\,. \tag{6}$$

Obviously, although values c_n^0 are not incident wave cylindrical basis expansion coefficients, but similarly to a_n coefficients in TMM, they depend (functionally) on the incident plane wave angle φ_0 only. As can be seen from Eqs. (5) and (6), in order to find vector $\overline{c}$ in PEM, it is necessary to invert the matrix with much more complex element formulas than in TMM. However, the inverted matrix $(I-G)^{-1}$ is already essentially a T matrix that links vector $\overline{c}^0$, characterizing the incident wave, to the scattered wave coefficients $\overline{c}$, while in TMM, in order to obtain T matrix, it is still necessary to perform matrix Q and H^{-1} multiplication (although those matrices are significantly more simple). Therefore, it is of interest to compare the computation speed and accuracy for both methods.

NUMERICAL RESULTS

As an example, let us consider the diffraction problem for a plane wave with incident angle $\varphi_0 = 0$ on Rayleigh ellipse with semiaxes $ka = 8,\ kc = 11$. We calculate the scattering pattern as:

$$g(\varphi) = \sum_{n=-\infty}^{\infty} c_n i^n e^{in\varphi} . \qquad (7)$$

Let us denote $g_N(\varphi)$ - the scattering pattern, obtained by solving the truncated system (when its size is equal to $2N+1 \times 2N+1$). We calculate the difference between the patterns at different N as $\Delta g^{\max}_{N_1,N_2} = \max\left|g_{N_1}(\varphi) - g_{N_2}(\varphi)\right|$. If $\Delta g^{\max}_{N_1,N_2} < 10^{-6}$, i.e. at least 7 significant digits are agreeing in the patterns, we consider that adequate accuracy is achieved and there is no point to increase N any more. Additionally, we assess the graphic overlap of patterns.

The calculated values of $\Delta g^{\max}_{N_1,N_2}$ at different N_1, N_2 for PEM and TMM are given in Table 1.

Table 1.

	PEM	TMM
$\Delta g^{\max}_{10,15}$	$4.7334279 \cdot 10^{-1}$	$4.7133309 \cdot 10^{-1}$
$\Delta g^{\max}_{15,20}$	$6.0765886 \cdot 10^{-4}$	$1.1055532 \cdot 10^{-2}$
$\Delta g^{\max}_{20,25}$	$3.3979730 \cdot 10^{-7}$	$1.7063574 \cdot 10^{-4}$
$\Delta g^{\max}_{25,30}$	$2.4759473 \cdot 10^{-11}$	$1.6644684 \cdot 10^{-6}$
$\Delta g^{\max}_{30,35}$	$8.3348103 \cdot 10^{-14}$	$3.2701861 \cdot 10^{-6}$

As it shows, the PEM has much higher convergence rate and allows obtaining twice as good accuracy than TMM. In PEM, we have reached the desired accuracy of 10^{-6} already at $N = 20$, whereas TMM did not obtain the desired accuracy at all. The highest possible accuracy, which PEM provides for a given scatterer, is $8.3348103 \cdot 10^{-14}$, but TMM achieves only $1.6644684 \cdot 10^{-6}$. As it can be seen, at $N > 35$ for PEM and at $N > 25$ for TMM, the accuracy begins to decrease. This is caused by the increase of special function calculation error, which eventually leads to the failure of the algorithm (see [5]).

Let us now compare the computation time. At $N = 20$, the computation time of PEM is 10.779 seconds and TMM is 9.224 seconds. At $N = 35$, the computation time of PEM is 50.136 seconds and TMM is 21.502 seconds.

We can see that, at smaller N values, the computation time is about the same for both methods, but as N increases, the computation time for PEM becomes significantly longer. The explanation is that in the case of TMM we calculate $(2N+1)^2$ times a rather simple integral Eq. (3), whereas in the case of PEM we calculate $(2N+1)^2$ times a much more complicated integral Eq. (5) plus $2N+1$ times integral Eq. (6). However, during the first 10

seconds using PEM, we obtained the accuracy of 10^{-10}, while using TMM for the same time we obtained only 10^{-5}.

As already mentioned above, the applicability of PEM (any weak non-convex bodies) is much broader than the applicability of TMM (only Rayleigh bodies). This is another major advantage of PEM. Some examples illustrating inapplicability of TMM to non- Rayleigh geometries can be found in [5].

Let us now consider the particle irradiated by a plane wave, incident at random angles φ_0. We can calculate scattering characteristics of the particle averaged by irradiation angles. For example, the single-particle scattering cross section $\langle C_{sca} \rangle$, averaged over the ensemble of random orientations, can be calculated in the *T*-matrix method as [2] $\langle C_{sca} \rangle = \sum_n \sum_m |T_{nm}|^2$ (see also Eq. (1) and Eq. (7)). Similarly, as follows from the equations (4) and (7), in the method of pattern equations the same value can be calculated as $\langle C_{sca} \rangle = \sum_n \sum_m \sum_p |(I-G)^{-1}_{nm}| C_{mp}$, where $C_{mp} = \frac{1}{2\pi} \int_0^{2\pi} c_m^0 c_p^{0*} d\varphi_0$. Our simulations show that equal accuracy of the $\langle C_{sca} \rangle$ requires twice as much computation time using the pattern equation method, relative to the *T*-matrix method.

To summarize, the comparison of PEM and TMM clearly demonstrates that PEM is unconditionally superior to TMM in terms of accuracy and applicability. The price for this is some increase of computation time. The averaging of scattering characteristics by orientation of the particle is similarly simple in both PEM and TMM.

ACKNOWLEDGEMENTS

This work was supported by the Russian foundation of basic researches, project № 09-02-00126.

REFERENCES

[1] P.C. Waterman. Matrix formulation of electromagnetic scattering. Proc. IEEE **53** (1965).

[2] M.I. Mishchenko, L.D. Travis, and A.A. Lacis. *Scattering, absorption and emission of light by small particles*. Cambridge: Cambridge University Press (2002).

[3] M.I. Mishchenko, G. Videen, V.A. Babenko, N.G. Khlebtsov, and T. Wriedt. T-matrix theory of electromagnetic scattering by particles and its applications: A comprehensive reference database. JQSRT **88** (2004).

[4] A.G. Kyurkchan. A new integral equation in the diffraction theory. Soviet Physics Doklady **37** (1992).

[5] A.G. Kyurkchan and N.I. Smirnova. Solution of diffraction problems by null field and T-matrix methods with accounting for wave field analytical continuation singularities. In: *Proceedings of the International Conference "Days on Diffraction 2009"* (2009).

Diffraction of a plane wave on a grating consisting of impedance bodies of revolution

A.G. Kyurkchan and S. A. Manenkov*

Moscow Technical University of Communications and Informatics. 111024, Aviamotornaya, 8A, Moscow, Russia.

The three-dimensional problem of plane electromagnetic wave scattering on a grating consisting of coaxial impedance bodies of revolution is considered. An infinite system of integral equations, to which the initial problem is reduced, is derived. An efficient algorithm for the calculation of the periodic Green's function is offered. The angular dependence of the scattering pattern is obtained.

INTRODUCTION

The paper considers diffraction of a plane electromagnetic wave on an infinite periodic grating consisting of impedance bodies of revolution located at one axis. To solve the problem, we use a modified null field method (MNFM), which has previously been successfully applied in [1, 2]. The null field method (NFM), often named in the literature also as a method of *T*-matrix [3], has been offered for the first time by Waterman [4]. The basis for the method is a certain relation (see below) which is satisfied everywhere inside the scatterer. If we require that this relation is fulfilled on some closed surface inside the scatterer, the initial boundary problem is reduced to the integral equation of the first kind relative to an unknown current distributed on the surface of the body. In [1, 2], it has been shown that the integral equation has the solution corresponding to the boundary problem, if and only if the surface (designated in these works with the letter Σ) on which the condition of the null field is fulfilled, covers the set of singularities of analytical continuation of the diffracted field inside the scatterer. Besides, it is shown that, for the development of high-speed and stable algorithms, the surface Σ should be constructed by means of analytical deformation of the surface of the scatterer [5].

Notice that, in solving the considered problem, we face the development of an efficient algorithm for the calculation of the periodic Green's function. We calculate the Green's function by the method analogous to the approach proposed in [6], which considered the problem of diffraction on a body in a circular waveguide.

DERIVATION OF THE MAIN RELATIONS

Consider a grating consisting of identical coaxial impedance bodies of revolution. We assume that the grating has a period d. Introduce a Cartesian coordinate system and direct the z-

* Corresponding author: Alexander G. Kyurkchan (kyurkchan@yandex.ru)

axis along the axis of the grating. Denote by S_0 the surface of the central element of the grating. We suppose that the structure is irradiated by the plane wave:

$$\vec{E}^0 = \vec{p}_0 \exp(-ikr(\sin\theta_0 \sin\theta\cos(\varphi-\varphi_0) + \cos\theta_0 \cos\theta)), \quad (1)$$

where (r,θ,φ) are the spherical coordinates, k is the wave number, and θ_0, φ_0 are the incidence angles of the plane wave. The diffracted field outside the grating obeys the homogeneous Maxwell equations and also satisfies the Floquet periodic conditions:

$$\vec{E}^1(\rho,\varphi,z+d) = \vec{E}^1(\rho,\varphi,z)\exp(-i\kappa), \quad (2)$$

where $\kappa = kd\cos\theta_0$ is the Floquet parameter and (ρ,φ,z) are the cylindrical coordinates. The formulas for the magnetic field are similar. The diffracted field also obeys the radiation condition at infinity. On the surface of each element of the grating, the impedance boundary condition

$$\vec{n}\times\vec{E} = Z_0\,\vec{n}\times(\vec{n}\times\vec{H}) \quad (3)$$

is satisfied. Here $\vec{n}$ is the outward normal and Z_0 is the impedance.

Let us apply MNFM. For this aim, we construct the auxiliary surface Σ_0 which is located inside the original surface S_0 of the central element of the grating. If the equation of the surface S_0 in the spherical coordinate system has the form $r = r(\theta)$, the auxiliary surface is defined by the equations: $x = r_\Sigma \sin\theta_\Sigma \cos\varphi$, $y = r_\Sigma \sin\theta_\Sigma \sin\varphi$, $z = r_\Sigma \cos\theta_\Sigma$, where [5]

$$\theta_\Sigma = \arg\xi(\tau), \quad r_\Sigma = |\xi(\tau)|, \quad \xi(\tau) = r(\tau+i\delta)\exp(i\tau-\delta), \quad (4)$$

In formulas (4) δ is a positive parameter responsible for the degree of deformation of the contour of the body axial cross section and $\tau\in[0,\pi]$. The choice of the parameter δ is detailed in [1, 2, 5]. In accordance with MNFM we state the following condition at the auxiliary surface Σ_0:

$$\vec{n}\times\int_{S_0}\left[-i\varsigma\left(-(\vec{J},\nabla' G)\nabla G + k^2\vec{J}G\right) + kZ_0\left(\nabla G\times(\vec{n}'\times\vec{J})\right)\right]ds' = -\vec{n}\times\vec{E}^0, \quad (5)$$

where $\vec{r}\in\Sigma_0$, $\vec{J}$ is the unknown current on the surface S_0 of the central element of the grating, and ς is the wave impedance. This equation is solvable only on condition that the surface Σ_0 covers the set of the singularities of the analytical continuation of the diffracted field inside S_0. The function G in Eq. (5) is the periodic Green's function:

$$G(\vec{r},\vec{r}') = \sum_{s=-\infty}^{\infty} G_0(R_s)\exp(-is\kappa), \text{ where}$$

$$G_0(R_s) = \frac{\exp(-ikR_s)}{4\pi kR_s},\ R_s = \sqrt{\rho^2+\rho'^2-2\rho\rho'\cos\psi+(z-z'-sd)^2},\ \psi=\varphi-\varphi'. \quad (6)$$

Expand the unknown current $\vec{J}$ and the Green's function into the Fourier series:

$$\vec{J}(t,\varphi) = \sum_{n=-\infty}^{\infty} \vec{I}_n(t)\exp(in\varphi), \quad (7)$$

$$G(r,\theta,r',\theta',\varphi-\varphi') = \sum_{m=-\infty}^{\infty} S_m(r,\theta,r',\theta')\exp(im(\varphi-\varphi')). \quad (8)$$

Then we define $\vec{I}_m(t) = I_m^1(t)\frac{r'(t)}{r(t)}\vec{i}_r + I_m^1(t)\vec{i}_\theta + I_m^2(t)\vec{i}_\varphi$, where $\vec{i}_r$, $\vec{i}_\theta$, $\vec{i}_\varphi$ the unit vectors of the spherical coordinates and the prime denotes the derivative by the corresponding argument. Using formulas (5) – (8), one can obtain the following system of integral equations:

$$\begin{cases} \int_0^\pi K_m^{11}(\tau,t)I_m^1(t)dt + \int_0^\pi K_m^{12}(\tau,t)I_m^2(t)dt = B_m^1(\tau), \\ \int_0^\pi K_m^{21}(\tau,t)I_m^1(t)dt + \int_0^\pi K_m^{22}(\tau,t)I_m^2(t)dt = B_m^2(\tau), \end{cases} \quad (9)$$

where $m = 0,\pm1,\pm2,\ldots$, $\tau\in[0,\pi]$. The kernels of this system are expressed by the coefficients S_m and their derivatives. Note that the system (9) is solved by the collocation technique [1, 2, 5].

NUMERICAL RESULTS

To test the method, we consider the problem of wave scattering by a grating consisting of closely-spaced superellipsoids of revolution. The axial cross-section of the superellipsoid is defined by the equation

$$\left(\frac{x}{a}\right)^{2l} + \left(\frac{z}{c}\right)^{2l} = 1.$$

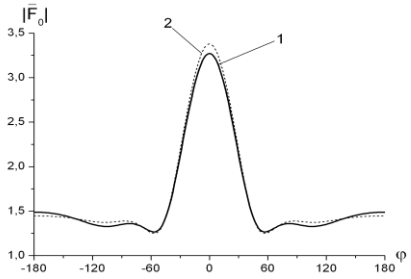

Figure 1.

For large values of the parameter l and small distances between the scatterers, the problem of such a geometry is only slightly different from the two-dimensional problem of scattering by an infinite circular cylinder (it is assumed that the plane wave is incident perpendicular to

the axis z and the electric vector is parallel to the axis of the structure). As is well known, this problem has an analytical solution. In Fig. 1, the distribution of the pattern $\vec{F}_0(\theta_0, \varphi)$ of zero mode of the grating is presented. In cylindrical coordinates, the pattern is defined by the formula

$$\vec{E}^1 \simeq -\frac{i\pi}{2kd}\sqrt{\frac{2}{\pi}}e^{i\pi/4}\sum_{s=-\infty}^{\infty}\vec{F}_0(\theta_s,\varphi)\frac{\exp(-iv_s\rho - iw_s z)}{\sqrt{v_s\rho}}, \qquad (10)$$

where $w_s = (\kappa + 2\pi s)/d$, $v_s = \sqrt{k^2 - w_s^2}$, $\theta_s = \arccos(w_s)$. The sign of square root is chosen so that its imaginary part is not positive. The parameters of the problem are the following: $ka = 2.5;\quad kc = 5;\quad l = 10$, period of the grating $kd = 10.1$, $\varphi_0 = 0$, $\theta_0 = \pi/2$, $\vec{p}_0 = \vec{i}_z$. Curve 1 in Fig. 1 demonstrates the dependence of the pattern for the grating consisting of the superellipsoids and curve 2 corresponds to the case of scattering by the infinite circular cylinder with radius $ka = 2.5$. One can see rather small differences between the dependences.

Acknowledgments: This work was supported by Russian Foundation for Basic Research, Project no. 09-02-00126.

REFERENCES

[1] A.G. Kyurkchan and N.I. Smirnova. Generalization of the method of extended boundary conditions. J. of Commun. Technol. and Electron. **53**(7) (2008).

[2] A.G. Kyurkchan and N.I. Smirnova. Solution of diffraction problems by null field and T-matrix methods with accounting for wave field analytical continuation singularities. In: *Proceedings of the International Conference "Days on Diffraction 2009"* (2009).

[3] M.I. Mishchenko, G. Videen, V.A. Babenko, N.G. Khlebtsov, and T. Wriedt. T-matrix theory of electromagnetic scattering by particles and its applications: A comprehensive reference database. JQSRT **88** (2004).

[4] P.C. Waterman. Matrix formulation of electromagnetic scattering. Proc. IEEE. **53** (1965).

[5] A.P. Anyutin, A.G. Kyurkchan, S.A. Manenkov, and S.A. Minaev. About 3D solution of diffraction problems by MMDS. JQSRT **100** (2006).

[6] S.A. Manenkov. Diffraction of a mode of a circular dielectric waveguide by a compact obstacle located inside the waveguide. J. Commun. Technol. Electron. **53**(7) (2006).

Light scattering by cometary dust

A.C. Levasseur-Regourd*

UPMC, LATMOS, BC 102, Université Paris 6, 4 place Jussieu, 75252 Paris Cedex 05, France.

Observations of sunlight scattered by cometary dust particles provide clues to their properties. Interpretation of the variations of its linear polarization, through laboratory and numerical simulations, suggests that dust particles might be built of both very fluffy aggregates and more compact grains, with significant amount of rather transparent silicates and absorbing materials.

INTRODUCTION

Cometary dust

Dust particles, which may consist in compact grains as well as in aggregates, are everywhere in the Solar System, on cometary nuclei, in cometary comae, tails and trails, as well as in the interplanetary dust cloud, in planetary atmospheres, on asteroidal surfaces, on trans-neptunian objects, and on the surfaces of planets and moons. While a limited amount of information on cometary dust is available from a few in-situ missions (i.e. Giotto, Vega, Deep-Space 1, Deep Impact) and one sample return mission (Stardust), clues to the bulk properties of the dust mainly stem from remote observations, i.e. spectroscopy that provides information on the composition and study of the characteristics of the solar scattered light that provides information on the bulk properties (e.g. morphology, structure, size distribution, and tentatively albedo). This latter approach, reviewed in [1], may provide evidence on the physical processes that allowed the formation and evolution of the dust.

Relevance of polarization measurements

Solar light scattered by low-density particulate media, e.g. cometary comae and dust tails, is partially linearly polarized. The degree of linear polarization, thereafter called P, is the ratio of the difference to the sum of the polarized brightness components respectively perpendicular and parallel to the scattering plane. It is a very convenient quantity, since it is normalized and depends neither on the distances to the Sun (while the brightness does not follow a R^{-2} law with solar distance R) and to the observer, nor on the dust spatial density. It only varies with the phase angle α (or scattering angle) and the wavelength λ of the observations, and with the properties of the scattering medium. It thus reveals changes in dust properties from changes in polarization in different regions of the coma observed at the same time for identical α and λ, as well as different classes of comets from their polarization properties, even while they are studied at different distances to the Sun and to the observer. It may nevertheless be added that observations of the light scattered by comets requires some attention, since comets are usually faint extended objects and since dust observations have to be done through narrow filters to avoid depolarization from cometary gaseous emissions.

* Anny-Chantal Levasseur-Regourd (Anny-Chantal.Levasseur@aerov.jussieu.fr)

MAIN TRENDS IN COMETARY OBSERVATIONS

Changes within cometary comae

The variation of the linear polarization of the dust inside comet 1P/Halley coma had been monitored from the OPE experiment on board the Giotto spacecraft, as shown in Fig 1 [2]. In addition, the average dust geometric albedo and density of the particles have been estimated to be about respectively 0.04 and 100 kg m^{-3} in the inner coma [3]. Since then, polarization images have been obtained from remote observations of various comets [see e.g. 4-6]. Significant variations are pointed out, especially for active comets, with often two types of features: i) a circum-nucleus halo with a lower polarization, ii) fan-shaped features with a higher polarization corresponding to some jet-like features. Also, radial averages of the polarization reach an asymptote for increasing nucleus distance, leading to the determination of whole coma polarization from polarimetric images.

Phase angle dependence

The dependence (for a fixed wavelength) of the whole coma polarization upon the phase angle, $P_\lambda(\alpha)$, is monitored through the changing geometry for an Earth-based observer. It provides smooth polarization phase curves (see e.g. Fig. 2), with a shallow negative branch near the backscattering region, an inversion region near 20° and a wide positive branch. Such curves are typical of scattering by irregular particles with sizes greater than the observational wavelength, i.e. a few μm. Data suggest the existence of at least two classes of comets, corresponding to different properties of the dust particles: comets with a low maximum in polarization (in the 0.10 to 0.15 range), comets with a high maximum in polarization (in the 0.25 to 0.30 range), and comet C/1999 O1 Hale-Bopp, the polarization of which was the highest ever measured [7]. The maximum in polarization is high whenever a silicate emission feature is detected near 11 μm and may increase after an outburst.

Wavelength dependence

The dependence (for a fixed phase angle greater than about 30°) of the whole coma polarization upon the wavelength, $P_\alpha(\lambda)$, presents a quasi-linear trend, at least in the visible domain [5,8]. Some exceptions have been noticed in the innermost coma of comet 1P/Halley (see Fig. 1) and during some disruption events. They reveal drastic changes in the physical properties of the dust freshly ejected, possibly from the subsurface of the nucleus.

LABORATORY AND NUMERICAL SIMULATIONS

Constraints on the properties of the dust are provided by the above-mentioned phase and wavelength dependences. However, some empirical laws, documented for light scattering by surfaces (e.g. albedo - slope at inversion relation), are not necessarily acceptable for optically thin dust clouds; besides the uniqueness of the results through straightforward Mie theory is hardly proven for light scattering by irregular particles with a size parameter above 1. Interpretation of the observed variations of the polarization thus stems from simulations

with so-called analogue particles, generally considered to correspond to a realistic composition and morphology of the cometary dust.

Laboratory simulations have been initiated in the sixties, with purpose-built particles for microwave experiments. More recently, measurements in jet streams and steady-state gas flow, which provide the whole Mueller matrix at 632.8 nm and are most appropriate for particles below 1 μm, have been successfully performed [9]. We have, since the mid-nineties, developed the PROGRA² experiment, which provides brightness and polarization measurements on dust samples at 543.5 and 632.8 nm for phase angles in the 6° to 165° range, as reviewed in detail in [10]. Measurements are feasible on low-density clouds of particles of about 1 μm or much more enclosed in a vial; small or fluffy particles are lifted in N_2 draught, while the larger or more compact particles are levitating in microgravity conditions during parabolic flight campaigns, in order to avoid sedimentation and orientation of the dust. A wide variety of samples are used, including series with one parameter changing (e.g. size of the grains, particles size, structure, absorption) and specific cometary analogues. As far as cometary measurements are concerned, excellent matches have been obtained with porous aggregates of sub-μm (MgSiO + FeSiO + C) grains and compact Mg-silicates [e.g. 11].

Numerical simulations have been initiated, after the comet Halley return, of spheres with realistic sizes distribution or more irregular grains. More recently, numerous simulations have been developed with porous aggregates of grains, using DDA, T-Matrix or Ray-tracing codes [e.g. 12,13]. We have initiated simulations for spheroids of astronomical silicates and more absorbing organics and fractal aggregates thereof (BCCA & BPCA, 256 grains) leading to a limited number of free parameters (slope s of the size distribution a^s, minimal and maximal equivalent radius a, silicates/organics ratio) [14]. For comet Hale-Bopp and a fit in two colours, both compact and fluffy particles are required, s is about -3, a is in the 0.1-20 μm range and there are 40 to 65 % silicates in mass and 60 to 35% in organics. As illustrated on Fig. 2, there is an excellent agreement between the fits and the observational data in other colours [15,16].

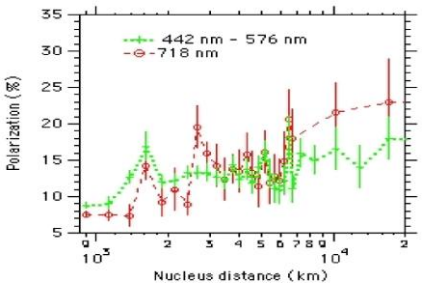

Figure 1. Changes in polarization with nucleus distance along Giotto trajectory within Halley coma, at 73° phase angle.

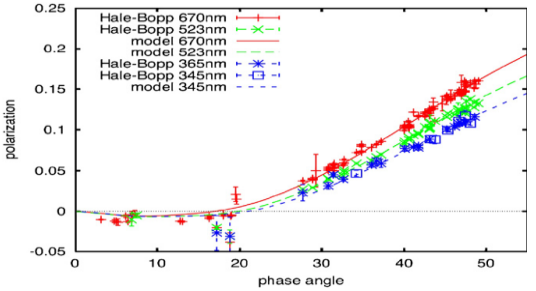

Figure 2. $P_\lambda(\alpha)$ data for Hale-Bopp, compared fits (from blue and red data) with compact grains and fluffy aggregates [15].

The similarities found between the conclusions of such simulations and the ground truth provided by Stardust samples [17] demonstrates the relevance of light-scattering observations.

REFERENCES

[1] L. Kolokolova et al. Physical properties of cometary dust from light scattering and thermal emission. In: *Comets II*. M. Festou et al. (eds.). Univ. Arizona Press (2004).

[2] A.C. Levasseur-Regourd et al. Similarities between in situ measurements of local dust scattering and dust flux impact data within the coma of 1P/Halley. Astron. Astrophys. **348** (1999).

[3] M. Fulle et al. In-situ dust measurements from within the coma of 1P/Halley. Astron. J. **119** (2000).

[4] E. Hadamcik and A.C. Levasseur-Regourd. Imaging polarimetry of cometary dust: different comets and phase angles. JQSRT **79** (2003).

[5] E. Hadamcik and A.C. Levasseur-Regourd. Dust evolution of comet C/1995 O1 by imaging polarimetric observations. Astron. Astrophys. **403** (2003).

[6] R. Furusho et al. Imaging polarimetry of comet 9P/Tempel 1 before and after the Deep impact. Icarus **191** (2007).

[7] A.C. Levasseur-Regourd. Polarization of light scattered by cometary dust particles: observations and tentative interpretations. Space Science Rev. **90** (1999).

[8] A.C. Levasseur-Regourd and E. Hadamcik. Light scattering by irregular dust particles in the solar system. JQSRT **79** (2003).

[9] H. Volten et al. Experimental light scattering by fluffy aggregates of magnesiosilica, ferrosilica, and alumina cosmic dust analogs. Astron. Astrophys. **470** (2007).

[10] E. Hadamcik et al. Laboratory measurements of the light scattered by clouds of solid particles by an imaging technique. In: *Light scattering review 4*. A.A. Kokhanovsky (ed.). Springer (2009).

[11] E. Hadamcik et al. Light scattering by fluffy Mg-Fe-SiO and C mixtures as cometary analogs. Icarus **190** (2007).

[12] E.P. Petrova et al. Polarization of light scattered by solar system bodies and the aggregate model of dust particles. Sol. Syst. Res. **38** (2004).

[13] H. Kimura et al. Light scattering by cometary dust numerically simulated with aggregate particles consisting of identical spheres. Astron. Astrophys. **449** (2006).

[14] J. Lasue and A.C. Levasseur-Regourd. Porous aggregates of irregular sub-micron sized grains to reproduce cometary dust light scattering observations. JQSRT **100** (2006).

[15] A.C. Levasseur-Regourd, T. Mukai, J. Lasue, and Y. Okada. Physical properties of cometary and interplanetary dust. Plan. Space Sci. **55** (2007).

[16] J. Lasue et al. Cometary dust properties retrieved from polarization observations. Icarus **199** (2009).

[17] F. Hörz et al. Impact features on Stardust. Science **314** (2006).

Light scattering by porous volcanic ash particles

H. Lindqvist*[,1], T. Nousiainen[1], E. Zubko[1], and O. Muñoz[2]

[1]*Department of Physics, University of Helsinki, P.O. Box 48, FI-00014 Finland.*
[2]*Instituto de Astrofísica de Andalucía, CSIC, c/ Camino Bajo de Huétor 50, 18080 Granada, Spain.*

Single-scattering properties of volcanic ash particles are evaluated theoretically using a novel shape model for porous particles with cratery surfaces. Preliminary discrete-dipole approximation computations reveal that light scattering by the model particles produces large-scale features comparable to the measured properties of real volcanic ash particles. The effect of internal porosity is also investigated, and it turns out that internal porosity generally promotes positive polarization and decreases the depolarization ratio.

INTRODUCTION

After a volcanic eruption, the smallest ash particles can remain in the atmosphere for days to months [1], affecting the radiation balance on Earth. Airborne volcanic ash particles also pose a major threat to aviation and would therefore be essential to distinguish and identify by remote sensing and radar techniques.

Quantitative assessment of the radiative impact of volcanic ash clouds requires accurate knowledge of the optical behavior of single ash particles, in size comparable to or larger than the wavelength. Inspired by SEM images (Scanning Electron Microscope) and the light-scattering measurements of such particles [2], we have developed a sophisticated shape model for porous particles with vesicular surfaces. Using this model and the discrete-dipole approximation (DDA) [3], we are able to compute the single-scattering properties of small volcanic ash particles and study the effects of porosity on their scattering. Because the sizes of the measured volcanic ash particles range from submicron to a few millimeters [2], DDA cannot cover the entire range of size parameters at visible wavelengths. Nevertheless, the measurements act as a valuable qualitative reference to which we can compare whether our shape model seems plausible for volcanic ash in terms of scattering.

VOLCANIC ASH PARTICLES

SEM images of volcanic ash (an example in Fig. 1a) present a variety of irregular shapes which can be roughly categorized as vesicular (hereafter porous ash particles) or non-vesicular, depending on their composition and the way they were formed [4]. Vesicles are empty cavities formed by gas bubbles that escape when the volcanic melt is cooled to glass. In this work we focus on the modeling of porous ash particles.

*Corresponding author: Hannakaisa Lindqvist (hannakaisa.lindqvist@helsinki.fi)

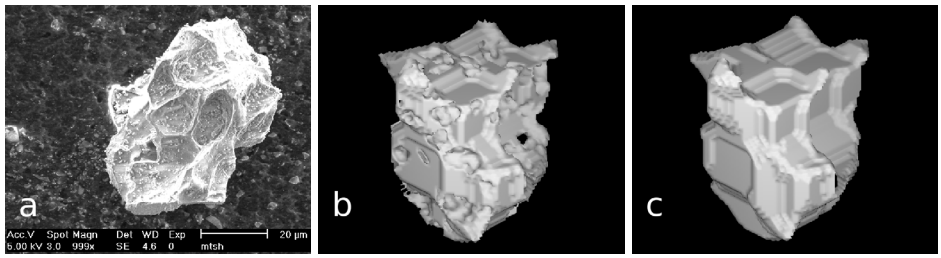

Figure 1. a) SEM image of a volcanic dust particle. b) Porous model shape. c) Compact shape.

Shape model

A shape model for porous volcanic ash particles (Fig. 1b) is constructed using the following five steps illustrated in Fig. 2: a) creating a cluster of spheres, b) calculating the concave hull for the cluster, c) replacing the spheres with Gaussian random spheres, d) finding the volume constrained between the Gaussian particles and the concave hull, and finally, e) peeling extra dipoles away from the surface.

The first phase utilizes a generic ballistic clustering algorithm. The radii of the spheres r follow a power-law distribution

$$n(r) = \frac{2r_1 r_2}{r_2^2 - r_1^2} r^{-3}, \tag{1}$$

where r_1 and r_2 are the minimum and maximum radii, respectively. Our sample shape in Fig. 1b is made using 200 spheres and $r_2 = 2r_1$. In the second phase, a generating sphere of radius $r_{\rm g}$ is rolled around the particle: the inner surface formed by the sphere defines the concave hull, as explained in more detail by [5]. Here we have set $r_g = r_2$. After this, the spheres of the ballistic cluster are replaced with Gaussian random spheres, which are statistically deformed spheres fully defined by two parameters: the standard deviation of radial distance σ and the power-law index ν [6], in these studies set to $\sigma = 0.2$ and $\nu = 4.0$. The porous particle itself is then composed of the volume in between the Gaussian random spheres and the concave hull. A compact version of the particle can be created by filling the cavities occupied by air. Finally, unnatural overhangs are reduced by flaying and smoothing the particle several times. In the case of porous particles, this procedure also exposes the internal structure and results in random-sized and shaped craters on the surface, as depicted in Fig. 1b. Next to it, Fig. 1c shows the compact version of the shape. The packing density of the porous shape is 0.77 when compared to the compact particle.

PRELIMINARY RESULTS

Light scattering by small volcanic ash particles is computed using DDA. While assessing the impact of porosity on scattering, the dimensions of the particle are kept constant. For the compact shape, the equal-volume-sphere size parameters are in these preliminary studies set to $x_{\rm eq} = 4$ and 8. Since the measured refractive indices of different volcanic ash samples

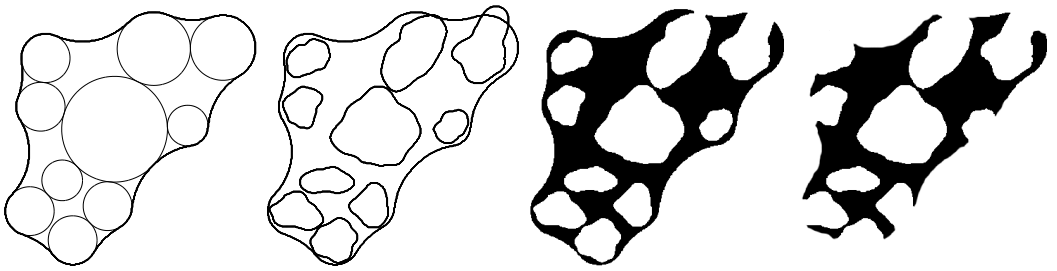

Figure 2. A two-dimensional sketch on the shape model for porous volcanic ash particles. The phases are explained in the text.

vary, as reviewed in [2], we use $m = 1.6 + 0.001\mathrm{i}$ that has real and imaginary parts somewhat higher than plain silicates to roughly account for possible absorbing constituents in the samples. The DDA computations are averaged over 242 orientations to mimic randomly oriented particles.

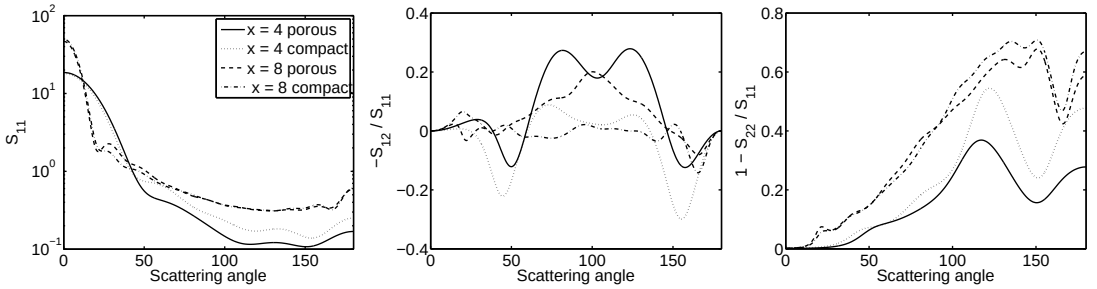

Figure 3. Light scattering results for porous and compact particles with $x = 4$ and 8. The porous shape acts as a model for small volcanic ash particles.

The first results presented in Fig. 3 show that porosity does affect light scattering, for example by promoting positive degree of linear polarization on intermediate scattering angles and decreasing depolarization ratio from 100 degrees scattering angle to backscattering. The effects of porosity on scattering are dependent on whether the outer dimensions or the volume of the particle are kept constant during the study. This makes it challenging to unambiguously distinguish the origin of the discrepancies in scattering. We will look into this by analysing the size dependency of scattering for both particle types and by comparing the size-integrated results. Also, particles with another type of porosity will be taken into account by simulating a shape with fewer but larger holes in the material.

Considering the modeling of the measured optical properties of volcanic ash presented in [2], the results of the porous particles are qualitatively encouraging: the large-scale characteristics of the measurements, including featureless sidescattering in intensity and generally positive polarization, are seen especially in the case of the larger porous particles. Although the results presented here for intensity, degree of linear polarization, and depolarization ratio show smaller-scale variations that are not seen in the measurements, it is expected that these deviations will disappear when calculating the scattering properties of an ensemble of

model particles. Next, the study will be continued further by averaging the scattering results obtained for several sizes and different sample shapes.

ACKNOWLEDGEMENTS

This work has been partially funded by the Academy of Finland (contracts 125180 and 121482).

REFERENCES

[1] W.I. Rose, G.J.S. Bluth, D.J. Schneider, G.G.J. Ernst, C.M. Riley, L.J. Henderson, and R.J. McGimsey. Observations of volcanic clouds in their first few days of atmospheric residence: the 1992 eruptions of Crater Peak, Mount Spurr Volcano, Alaska. J. Geology **109** (2001).

[2] O. Muñoz, H. Volten, J.W. Hovenier, B. Veihelmann, W.J. van der Zande, L.B.F.M. Waters, and W.I. Rose. Scattering matrices of volcanic ash particles of Mount St. Helens, Redoubt, and Mount Spurr Volcanoes. JGR **109** (2004).

[3] M.A. Yurkin and A.G. Hoekstra. User manual for the discrete dipole approximation code Amsterdam DDA (2006).

[4] C.M. Riley, W.I. Rose, and G.J.S. Bluth. Quantitative shape measurements of distal volcanic ash. JGR **108** (2003).

[5] H. Lindqvist, K. Muinonen, and T. Nousiainen. Light scattering by coated Gaussian and aggregate particles. JQSRT **9** (2009).

[6] K. Muinonen, T. Nousiainen, P. Fast, K. Lumme, and J.I. Peltoniemi, Light scattering by Gaussian random particles: ray optics approximation. JQSRT **55**(5) (1996).

Ice crystal classification based on silhouettes

H. Lindqvist*[,1], K. Muinonen[1,2], and T. Nousiainen[1]

[1]*Department of Physics, University of Helsinki, P.O. box 48, FI-00014 Finland.*
[2]*Finnish Geodetic Institute, P.O. Box 15, FI-02431 Masala, Finland.*

An automatic classification system for ice crystals is being developed based on shape parameters derived from crystal silhouette perimeters. As a test set, we use a small sample of crystal silhouettes captured by a cloud particle imager in cirrus clouds. Preliminary results show that the chosen parameters are suitable for separating single and aggregate crystals, and further, dividing these into plates, plate aggregates, single rosettes, and rosette aggregates. Columns and bullets remain as one unseparated group. The results are encouraging for future studies on larger observational data sets, but also offer a method for testing ice-crystal shape models against images of real ice crystals.

INTRODUCTION

Tropospheric cirrus clouds have a considerable effect on the radiation balance of the Earth. The radiative impact depends largely on the single-scattering properties of individual ice crystals, which in turn depend on the sizes and shapes, i.e. habits, of the crystals. This makes determining the habit distribution a critical factor for assessing ice-cloud radiative impacts. Since these clouds are found in 6-10 km height, observing single ice crystals is challenging and usually carried out using a cloud particle imager (CPI) attached to an airplane. CPI images reveal that large ice crystals possess shapes varying from single hexagonal columns, bullets, and plates to regular and irregular aggregates of these crystals [1]. The presence and proportion of each shape in an ice cloud depend on the prevailing meteorological conditions and, therefore, may vary between clouds. With an automatic classification system, the ice-crystal shape distribution of a cirrus cloud can be obtained efficiently. Classification also reveals valuable information on the ratio of cross-sectional area to the maximum dimension of the crystals: maximum dimension is used for defining crystal size; whereas, cross-sectional area determines the extinction cross section, a key parameter in radiative transfer considerations.

SILHOUETTE SHAPE CLASSIFICATION

CPI images of ice crystals present, in fact, silhouettes of crystals, as demonstrated in Fig. 1. They are taken by illuminating the crystal with a laser beam while the crystal is located in between the camera and the light source. Interpretation of silhouettes is challenging because three-dimensional shapes of real ice crystals cannot be unambiguously derived from CPI images without assumptions. For instance, single columns, bullets, and plates can produce exactly similar silhouettes when photographed directly from the top. Other complicating issues are the limited resolution and laser diffraction patterns on the images.

First step in the classification is to detach the perimeters of the crystals from the CPI images. Then, the extracted perimeters of crystals are discretized into 360 points using

*Corresponding author: Hannakaisa Lindqvist (hannakaisa.lindqvist@helsinki.fi)

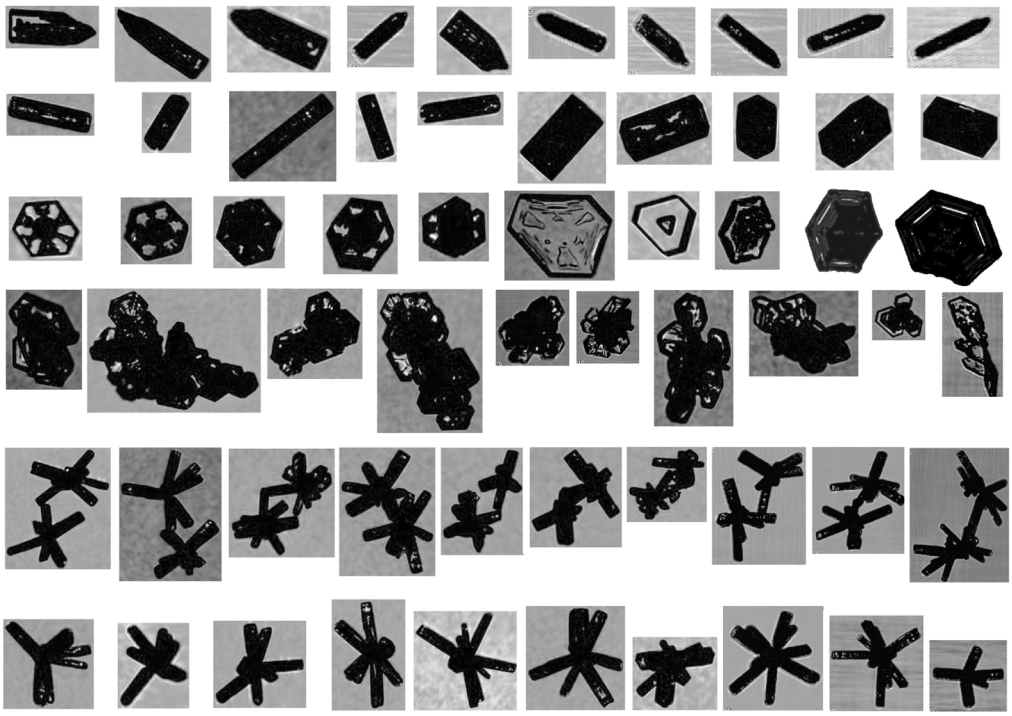

Figure 1. Sample ice crystal silhouettes. From top row to bottom: bullets, columns, plates, plate aggregates, column or bullet rosette aggregates, and column or bullet rosettes.

cubic splines so that the distance of two adjacent points along the perimeter is constant. The total length of the perimeter is then normalized to 360 degrees. This allows us to define an invariant angle γ, which corresponds to a certain proportion of the entire length of the perimeter, for instance $\gamma = 90$ degrees equals to 25 % of the total length of the perimeter. Angles are measured along the perimeter because this simplifies the treatment of non-starlike silhouettes.

In the next phase, certain shape parameters are calculated from the perimeter. The chosen parameters characterize the crystals in different ways and can be, therefore, useful in classification. The parameters considered are the following:

- Ratio A of the area inside the perimeter to the area of the convex hull.
- Aspect ratio. This is calculated as the ratio of the maximum length between two perimeter points to the maximum perpendicular width.
- Ratio R of the original length of the perimeter squared to the area inside the perimeter.
- Average of the length of the line segment $\bar{d}(\gamma)$ and its autocovariance $\mathrm{cov}(d(\gamma, \varphi))$ (cf. [2]): $d(\gamma)$ is the distance of two perimeter points separated by an invariant angle γ, $\bar{d}(\gamma)$ is the average over the perimeter, and $\mathrm{cov}(d(\gamma, \varphi))$ measures the correlation of two line segment lengths separated by an invariant angle φ. Here we have used $\gamma = 30$, 90, and 180 degrees, and $\varphi = 0$, 30, 90, and 180 degrees for the invariant angles, which results in 15 parameters.

- Average of the angle between the surface normal vectors $\bar{\alpha}(\gamma)$ and its autocovariance $\mathrm{cov}(\alpha(\gamma, \varphi))$: $\alpha(\gamma)$ is the angle measured between two surface normals of the perimeter points separated by γ. The invariant angles have values of $\gamma = 5$, 10, 30, 90, and 180 degrees, and $\varphi = 0$, 10, 30, 90, and 180 degrees, which leads to 30 parameters.

The classification itself includes two phases: first, we divide the crystals into compact and aggregate particles and then do the classification separately for both types. Compact and aggregate particles are separated according to parameter A, since it is equal or close to unity when considering compact crystal shapes, i.e. single plates, columns, or bullets. Thus, the value for compact particles is set to $A \geq 0.95$; other shapes are considered as aggregates.

In the second classification phase, we utilize different parameters for compact and aggregate crystals. Compact crystals are characterized by aspect ratio and parameter R; whereas for aggregates, we use A, aspect ratio, $\bar{d}$, $\mathrm{cov}(d)$, $\bar{\alpha}$, and $\mathrm{cov}(\alpha)$. Then, principal components analysis (PCA) is applied to the parameters to better distinguish the differences between the crystal properties. PCA transforms the input data vectors to a coordinate system where most of the information included in the input parameters is shown in fewer dimensions, defined by the most significant principal components. The outcome of PCA can then be used as a basis for classification.

PRELIMINARY RESULTS

As a test set we use altogether 60 CPI images, including both single and aggregated bullet, column, and plate crystals, 10 of each as shown in Fig. 1 on separate rows. The crystals in the images are identifiable and yet representative of their class, for instance the images of bullets and columns show varying aspect ratios and orientations.

The first results of the silhouette classification reveal that the division into compact and aggregate crystals based on the criterion $A \geq 0.95$ works perfectly for this test set, resulting in 30 compact and 30 aggregate crystals. For these separate groups, further results of the classification utilizing PCA are presented in Fig. 2, which shows the crystals in the coordinate system of the two most significant principal components of each data set. In the case of compact shapes, the plate-like crystals form a very dense group easy to identify; whereas, the bullets and columns tend to overlap. This means that the chosen parameters are not ideal for separating these two types of shapes. Also, some of the column-like crystals are close to the plates, which can be explained by looking at the test images: the columns with small aspect ratios do resemble the shape of the plate crystals in reality, as well.

The aggregate crystals divide into three distinguishable areas in the principal components space. According to Fig. 2, the single rosettes form a dense group indicating that the chosen parameters yield quite similar results to the rosettes, regardless of the observable differences among the silhouettes. This seems to apply to the rosette aggregates, as well. The plate aggregates, however, are distributed more widely. This can be due to the large variation in the number of the plates in the aggregates, which could be a useful feature in further classification and shape analyses.

CONCLUSION

The novel classification system for ice-crystal silhouettes proves to be efficient in separating the crystals of the test set: only single bullets and columns remain inseparable with the

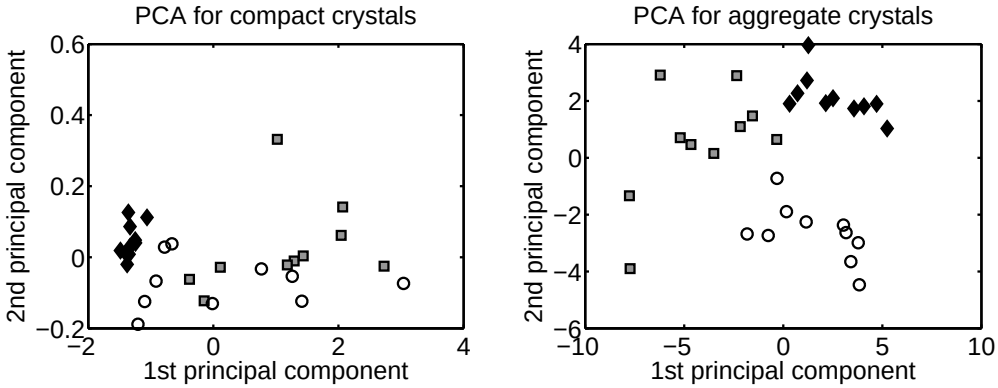

Figure 2. Compact (left) and aggregate (right) ice crystals in a coordinate system of two most significant principal components. For compact crystals, the squares, circles, and diamonds correspond to bullets, columns, and plates, and in the case of aggregate crystals, to plate aggregates, rosette aggregates, and single rosettes, respectively.

shape parameters used here. The next steps of the study are to develop new and improve the existing parameters used in PCA, and to apply an algorithm for classifying the PCA results automatically, for instance the nearest neighbor –algorithm. With this, the statistical reliability of the classification results can be assessed. Moreover, the classification needs to be tested for a larger data set that includes more irregularly shaped crystals. Applying the classification tool to the crystal silhouettes previously classified as irregulars or unclassifiable, can indeed reveal interesting common features among the crystals.

In addition to real CPI data, the classification system presented here can be applied to simulated crystal shapes. By generating synthetic silhouettes from model crystals and deriving the shape parameters it is possible to verify that model shapes statistically resemble the corresponding, real ice crystal shapes.

Finally, an intriguing and relevant question is that how do the single-scattering properties change between the classes and whether there is notable variation in the scattering characteristics inside a class. For this study, the models for ice crystals need to be improved to obtain a wider and more realistic view on the collection of shapes of naturally occurring ice crystals.

Acknowledgments: The authors wish to acknowledge Greg McFarquhar for providing the CPI data, Hanne Hakkarainen and Risto Makkonen for their contributions in ice-crystal image processing, and Antti Penttilä for advice in statistical matters. This work has been funded by the Academy of Finland (contracts 125180 and 127461).

REFERENCES

[1] J. Um and G. M. McFarquhar. Single-scattering properties of aggregates of plates. Q. J. R. Meteorol. Soc. **135** (2009).

[2] K. Muinonen. Inversion of small-particle silhouettes for Gaussian-sphere parameters. In: *9th Conference on Electromagnetic and Light Scattering by Nonspherical Particles: Theory, Measurements, and Applications*. N. Voshchinnikov (ed.) (2006).

Light scattering by a disperse layer of closely packed two-layered spherical particles

V. Loiko[*,1] and V. Berdnik[2]

[1]*Institute of Physics, Nezavisimosti ave. 68, Minsk, 220072 Belarus.*
[2]*Técnicas de Investigacion Hidrogeologica C.A. Kazan, Russia.*

Light scattering by a layer of closely packed two-layered non-absorbing spherical particles (core-shell particles) is investigated. The interference approximation is used to take into account collective scattering effects. The darkening effect and spectral dependence of the scattering coefficient are considered under this approximation.

INTRODUCTION

Light scattering by natural and artificial media with a high concentration of particles has drawn the attention of researchers recently [1]. For a strict description of scattering in densely packed media it is necessary to use the theory of multiple scattering of waves (MSW) [2]. Because of the complexity and cumbersomeness of the mathematical apparatus of the MSW theory, complete solutions are obtained in rare instances. The effects caused by ordered arrangements of optically soft particles in large concentrations are referred to such instances. In the present work the interference approximation is used to study light scattering by a system of spherical particles of the core-shell type.

ELEMENTARY VOLUME CHARACTERISTICS FOR A MEDIUM WITH SPHERICAL PARTICLES

In accordance with the interference approximation, expressions for differential scattering and extinction coefficients for a medium consisting of identical spherical particles can be written in the form:

$$\sigma_h(\gamma) = w\sigma_{0l}\, p_l(\gamma) S_3(\gamma, w), \tag{1}$$

$$\sigma_h = w\sigma_{0l} u, \tag{2}$$

$$\varepsilon_h = w\left(\varepsilon_{0l} - \sigma_{0l} + \sigma_{0l} u\right), \tag{3}$$

$$u = \int_0^{\pi} p_l(\gamma) S_3(\gamma, w) \sin\gamma d\gamma, \tag{4}$$

* Corresponding author: Valery Loiko (loiko@dragon.bas-net.by)

where $w = Nv/V$ is the volume concentration of the particles; N is the number of particles with volume $v = \frac{4}{3}\pi R^3$, contained in volume V of the medium; R is the particle radius; $\sigma_h(\gamma)$ is the differential scattering coefficient of a medium with a volume concentration w of particles; γ is the scattering angle; $\sigma_{0l} = \Sigma_s/v$; $\varepsilon_{0l} = \alpha_{0l} + \sigma_{0l} = \Sigma_e/v$; $\alpha_0 = \Sigma_a / v$; Σ_a, Σ_s and Σ_e are the absorption, scattering and extinction cross sections of an individual particle; and $p_l(\gamma)$ is the phase function of an individual particle normalised by the condition $\int_0^\pi p_l(\gamma)\sin\gamma d\gamma = 1$.

The structure factor $S_3(\gamma,w)$ takes into account the effect of light interference occurring in a system of correlated particles:

$$S_3(\gamma, w) = 1 + 4\pi n \int_0^\infty [g(r, w) - 1] \frac{\sin zr}{zr} r^2 dr . \quad (5)$$

Here n is the number of particles in the unit volume; $g(r,w)$ is the radial distribution function characterizing the spatial arrangement of particles, $z = 4x\sin\gamma/2$.

For a system with a hard sphere potential, the structure factor can be calculated under the Percus-Yevick approximation [3,4]:

$$S_3(\gamma, w) = \left(1 - 24n \int_0^1 g(r, w) \frac{\sin zr}{zr} r^2 dr \right)^{-1}, \quad (6)$$

where

$$g(r, w) = \begin{cases} -a - b\frac{r}{2R} - c\left(\frac{r}{2R}\right)^3, r \le 2R \\ 0, r > 2R \end{cases}, \quad (7)$$

$$a = \frac{(1 + 2w)^2}{(1 - w)^4}, \quad (8)$$

$$b = -6w\frac{(1 + 0.5w)^2}{(1 - w)^4}, \quad (9)$$

$$c = 0.5w\frac{(1 + 2w)^2}{(1 - w)^4}. \quad (10)$$

Thus the optical properties of the medium of closely packed particles are defined by the phase function of a separate particle $p_l(\gamma)$ and the structure factor $S_3(\gamma, w)$. To calculate scattering characteristics of particles, the algorithms described in [5] were used.

CHARACTERIZATION OF ENSEMBLE OF SPHERICAL HOMOGENEOUS PARTICLES AND ENSEMBLE OF TWO-LAYERED SPHERICAL PARTICLES

The deviation of parameter u from unity characterises the degree of particles interaction. For spherical homogeneous particles, increasing the concentration decreases the value u monotonically. The spectral dependence of parameter u is not monotonic. The dependence of parameter u on relative wavelength $\lambda_r = \lambda/R$ and concentration of homogeneous spherical particles with refractive index n_0 = 1.1 is presented in Fig.1. As seen from the figure, the spectral dependence has a maximum in the range λ_r = 3 – 5 which shifts to small wavelengths with increase of particles concentration. The magnitude of maximum increases as well.

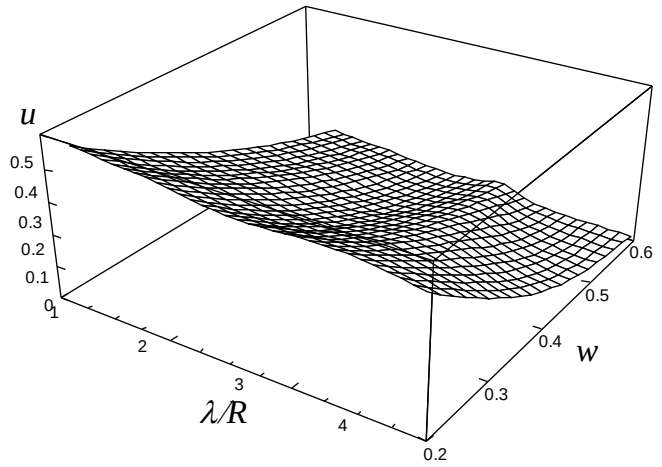

Figure 1. Dependence of $u(\lambda/R, w)$ for homogeneous particles. Radius of particle R=0.3 μm, relative refractive index of particle n_0 = 1.1.

The intensity of the forward-scattered light decreases with increasing volume concentration w. In the case of large concentrations of particles, the phase function has a characteristic maximum at non-zero scattering angles. The position of such a maximum is shifted to larger angles with increasing volume concentration w and to smaller angles with increasing size of particles. At some values of particle concentration the asymmetry parameter $g = \int_{-1}^{1} p(\mu)\mu d\mu$ can be less or equal to zero.

For a medium containing two-layered particles, the dependence of $u(\lambda/R, w)$ differs essentially from that displayed above for ensembles of homogeneous particles. Values of parameter u can be more than 1 at certain ratios of refractive indices of core and shell even at small volume concentration. They attain magnitude 2.5 (see Fig. 2) at volume concentration w = 0.6. Simulations reveal that the asymmetry parameter attains essentially smaller negative values, than in the case of homogeneous particles.

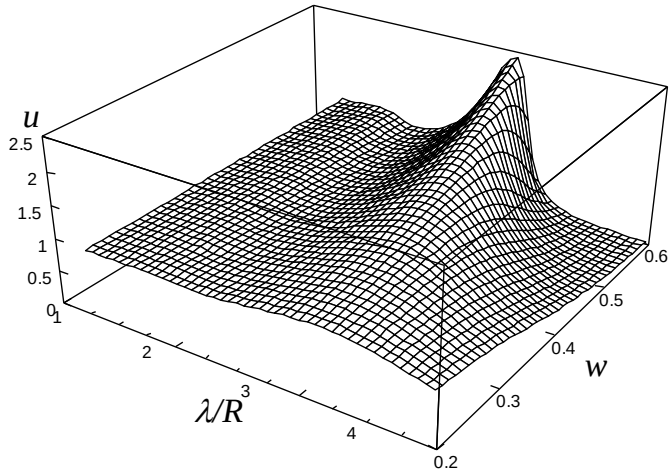

Figure 2. Dependence of $u(\lambda/R, w)$ for ensemble of two-layered particles. Radius of core *R*c = 0.18 μm, refractive index of core n_c = 1.10843, radius of shell *R* = 0.3 μm, refractive index of shell *n*=0.96364.

CONCLUSION

Light scattering from a layer with closely packed homogeneous and two-layered spherical, non-absorbing particles has been investigated. To model light scattering, the interference approximation and algorithms for light scattering by homogeneous and two-layered particles were used. Simulations disclosed that in a layer of two-layered particles the darkening effect (the optical thickness increasing with the volume concentration) can be implemented. This effect is considered in the details. The developed model can be used to describe the light scattering in liquated glasses, porous glasses and structures, etc.

REFERENCES

[1] V. Loiko and V. Berdnik. Light scattering in a disperse layer with partially ordered soft particles. In: *Wave scattering in complex media: from theory to applications*. B. Tiggelen and S. Skipetrov (eds.). Kluwer (2003).

[2] V. Twersky. Multiple scattering of waves and optical phenomena. JOSA **52** (1962).

[3] J. Percus and G. Yevick. Analysis of classical statistical mechanics by means of collective coordinates. Phys. Rev. **110** (1958).

[4] J. Ziman. *Models of disorder*. University Press, Cambridge (1979).

[5] V. Babenko et al. *Electromagnetic scattering in disperse media*. Springer, Berlin (2003).

Interaction of nanoparticles on a substrate with an AFM probe: DDA-SI formulation

V. L. Y. Loke* and M. P. Mengüç

School of Engineering, Özyeğin University, Kuşbakışı Cad. No:2, Altunizade 34662, Istanbul, Turkey.

Motivated by the need for a modeling tool for nanostructures interacting with a substrate and an AFM probe, we developed a MATLAB implementation of the discrete dipole approximation with surface interactions (DDA-SI). The method is applied to investigate the near-field coupling between particles on the surface and an AFM probe. The results presented here explore the effects of a number of physical, geometrical and material properties that can eventually assist nanolithography, particularly in defining the parameters for nano-writing.

INTRODUCTION

Atomic force microscopes (AFMs) are used to image surfaces with nanometric structures. They can also be used as nanolithographic tools, i.e., to write on a surface by means of melting nanoparticles or the substrate itself [1]. Following from our initial work with free-space-dependent scattering formulations presented for two-particle [2,3] and particle-probe [4] systems, we study the field intensity profiles resulting from near-field coupling of a system comprising an AFM probe, a particle and a surface (Fig 1).

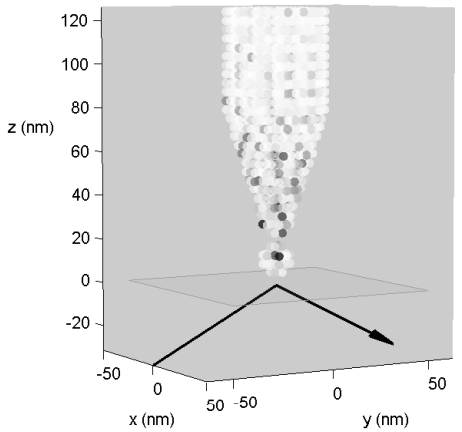

Figure 1. Dipole model of an AFM probe and a particle on a surface. The incident TM plane wave from below the surface is internally reflected; an evanescent wave exists above the surface. The darkness of each dipole is plotted proportionally to the field intensity.

* Corresponding author: Vincent L. Y. Loke (Vincent.Loke@ozyegin.edu.tr)

Our model is based on the discrete dipole approximation (DDA) [5, 6] and its subsequent development that account for surface interactions (Fig. 2). The model does not account for the effect of radiative emission but it is part of the scope of our ongoing development to account for all relevant phenomena in AFM nano-engineering.

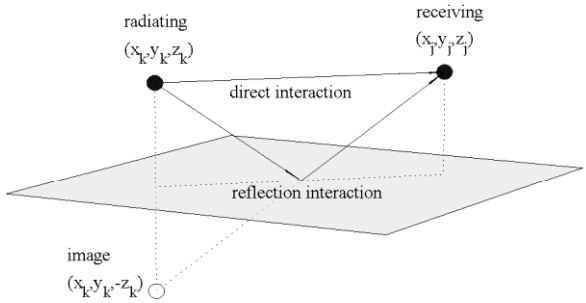

Figure 2. Direct and reflected dipole interactions.

MODELING METHODOLOGY

DDA is widely used to model light scattering from arbitrarily shaped mesoscopic and nanoscale objects in free space. DDA has also been extended to include surface effects of a homogeneous substrate (as per DDSURF [7]) and later for filmed surfaces (DDFILM [8]); our MATLAB implementation is called DDA-SI. The surface interaction involves decomposing spherical waves into cylindrical and planar components [9] which expand in parallel and perpendicular to the surface respectively (Fig. 3); the latter is multiplied by Fresnel reflection coefficients, accounting for the fraction of light reflecting of the plane surface.

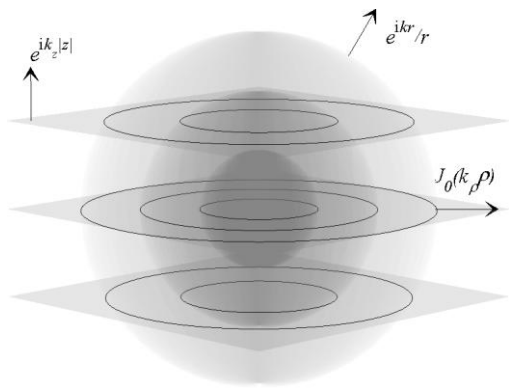

Figure 3. The spherical wave decomposed into cylindrical and planar components.

The system of equations, whose derivation is explained in [7,9], is

$$\sum_{k=1}^{N}\left(\mathbf{B}_j + k_0^2\mathbf{G}_{jk} + \mathbf{S}_{jk} + \frac{k_1^2 - k_2^2}{k_1^2 + k_2^2}k_0^2\mathbf{G}_{1,jk},\right)\mathbf{P}_k = \mathbf{E}_{inc,j}, \qquad (1)$$

where the terms $\mathbf{B}_j + k_0^2 \mathbf{G}_{jk}$ are equivalent to the free-space interaction matrix $\mathbf{A}_{jk}$ defined in [6] and the other terms account for surface reflection interaction [7]; $\mathbf{B}_j$ is the reciprocal of the dipole polarizability [6], $\mathbf{G}_{jk}$ is the dyadic Green's function of the electric field from a radiating dipole, $\mathbf{S}_{jk}$ contains the essential integrals which comprise Bessel or Hankel functions, evaluated using contour integrals [9] and $\mathbf{G}_{I,jk}$ is the image dyadic Green's function of the field from an image dipole [7]. The linear equations are solved using the generalized minimal residual method (*gmres* function in MATLAB).

RESULTS AND DISCUSSION

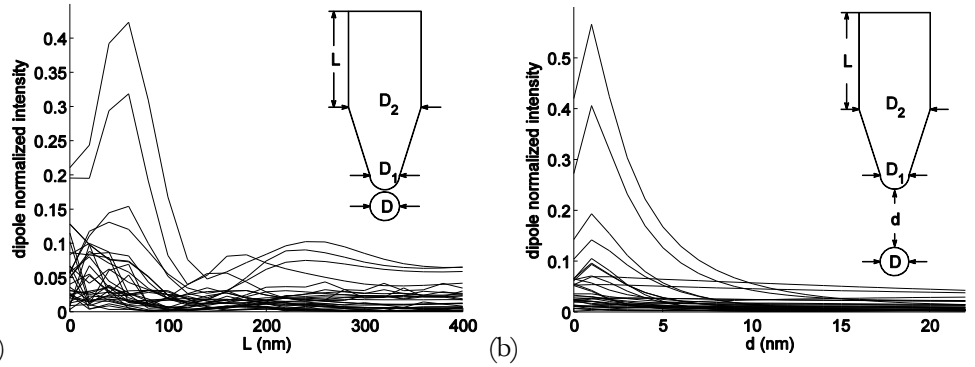

Figure 4. Field intensity of the 32 dipoles that make up a sphere on the surface as a function of the AFM probe a) shaft length, *L* (const. *d*=2 nm) b) vertical separation, *d*, between the tip and sphere (const. *L*=60 nm). In both cases, *D*=20, D_1=20 and D_2=50 nm.

The MATLAB implementation of the Sommerfeld Identities was tested against that of [9] which was written in FORTRAN, and the DDA-SI implementation was benchmarked against [10]. Satisfied with the results, we modeled the AFM probe configuration in Fig. 1, illuminated with either TE or TM polarized evanescent waves above the surface. The TE wave has just a component in the *x*-direction; whereas, the TM wave has both *y* and *z* components. As expected, the coupling is stronger in the latter case, which has contributions from the vertical component of the incident evanescent field. The results of the dipole field intensities are shown in Fig 4 and Fig. 5.

Fig. 4a shows the effect of the shaft length on the field intensity; as the shaft gets longer, the reflective effects from the flat top of the truncated shaft, peaking at around *L*=60 nm, diminishes. However, the effect of the truncated shaft can be exploited to increase near-field coupling. Varying the separation between the AFM probe tip and the particle, we see that the field intensity peaks at *d* = 1 nm (Fig. 4b). Fig. 5 shows that, for a particular AFM probe-tip separation, there is a corresponding resonance frequency. We continue to investigate the coupling dependence on other parameters and with multi-particle configurations. Although other physical phenomena such as radiative transfer, emission and perhaps Casimir and opti-

cal forces need to be considered in order to attain a complete model, the field intensity in the material is a major factor for determining the parameters for melting a particle onto a substrate, e.g., in the nano-writing process.

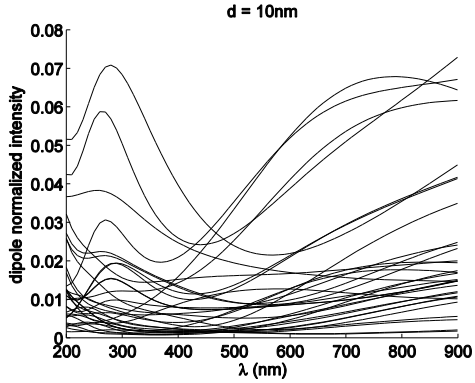

Figure 5. Resonance effect of the AFM probe at a given tip and particle separation.

REFERENCES

[1] E.A. Hawes, J.T. Hastings, C. Crofcheck, and M.P. Mengüç. Spatially selective melting and evaporation of nanosized gold particles. Opt. Lett. **33**(12) (2008).

[2] Z. Ivezic and M.P. Mengüç. An investigation of dependent/independent scattering regimes for soot particles using discrete dipole approximation. IJHMT **39**(7) (1996).

[3] Z. Ivezic, M.P. Mengüç, and T.G. Knauer. A procedure to determine the onset of soot agglomeration from multiwavelength experiments. JQSRT **57**(6) (1997).

[4] F. N. Dönmezer, M. P. Mengüç, and T. Okutucu. Dependent absorption and scattering by interacting nanoparticles. In: *RAD-10, Sixth International Symposium on Radiative Transfer*. Antalya, Turkey (2010).

[5] E. M. Purcell and C. R. Pennypacker. Scattering and absorption of light by nonspherical dielectric grains. Astrophys. J. **186** (1973).

[6] B. T. Draine and P. J. Flatau. Discrete-dipole approximation for scattering calculations. J. Opt. Soc. Am. A **11**(4) (1994).

[7] R. Schmehl, B. M. Nebeker, and E. D. Hirleman. Discrete-dipole approximation for scattering by features on surfaces by means of a two-dimensional fast Fourier transform technique. J. Opt. Soc. Am. A. **14**(11) (1997).

[8] H. Zhang and E. D. Hirleman. Prediction of light scattering from particles on a filmed surface using discrete-dipole approximation. Proceedings of SPIE **4692** (2002).

[9] G. J. Burke and A. J. Poggio. *Numerical electromagnetics code (NEC-4) - method of moments, part I: program description – theory*. Rep. UCID-18834, Lawrence Livermore Laboratory (1981).

[10] M. A.Taubenblatt and T. K.Tran. Calculation of light scattering from particles and structures on a surface by the coupled-dipole method. J. Opt. Soc. Am. A **10**(5) (1993).

Modelling of high-numerical-aperture imaging of complex scatterers using T-matrix method

V. L. Y. Loke[1,2], T. A. Nieminen[1,*], N. R. Heckenberg[1], and H. Rubinsztein-Dunlop[1]

[1] *The Univ. of Queensland, Quantum Science Lab., Sch. of Math. and Phys., QLD 4072, Australia.*
[2] *Özyeğin University, School of Engineering, Altunizade, Istanbul, Turkey.*

A high-numerical-aperture objective used for imaging can be represented by a T-matrix. Thus, it is possible to model the imaging of complex objects that can be themselves modelling using the T-matrix method. Polarization filtering can be included.

INTRODUCTION

The imaging of microscopic objects is a commonly performed optical task using a standard optical instrument, the optical microscope. An elementary treatment of microscopy is included in the typical optics course or textbook, so it would be reasonable to assume that the calculation or modelling of image formation is straightforward. However, the usual treatment of the problem is based on a number of simplifying assumptions, such as the paraxial and scalar approximations [1]. While it is possible to reduce the number of approximations, for example by using nonparaxial 3D vectorial transfer functions [2], the treatment of complex objects, where multiple scattering within the object being imaged is important, such as will be the case for thick objects, or polarization effects are important, remains an outstanding problem, especially for high-numerical-aperture imaging (e.g., beyond NA ≈ 1 for water- or oil-immersion objectives, or NA ≈ 0.75 in air).

We will consider a simple treatment of high-numerical-aperture vectorial imaging, with full polarization effects, of an arbitrary complex object. We will assume that an existing method can be used for calculating the field scattered from the object of interest, at an arbitrary point in space. We will assume that this information is available in the form of a T-matrix of the object; in principle, this can be obtained using whatever method of choice is used for the actual scattering calculation [3, 4].

Note that knowledge of the scattered field does not immediately allow us to determine the image captured by the objective lens of a microscope, which has a limited field of view and is focused on a given horizontal plane that intersects the particle. It is necessary to first determine what part of the scattered field of the object being imaged is collected and focussed. Here, we present a method, using the T-matrix formulation, for reproducing the image seen through a high numerical aperture microscope imaging system, motivated by our recent experimental work on polarization imaging of microscopic vaterite spherulites [5].

METHOD

The fields of the incident ($\mathbf{E}_{inc}$) and scattered ($\mathbf{E}_{sca}$) light for an illuminated particle can be represented in terms of vector spherical wave functions (VSWFs) [6, 3, 4, 7]:

*Corresponding author: Timo Nieminen (timo@physics.uq.edu.au)

$$\mathbf{E}_{\text{inc}} = \sum_{n=1}^{\infty} \sum_{m=-n}^{n} a_{nm}\mathbf{M}_{nm}^{(3)}(kr) + b_{nm}\mathbf{N}_{nm}^{(3)}(kr), \tag{1}$$

$$\mathbf{E}_{\text{sca}} = \sum_{n=1}^{\infty} \sum_{m=-n}^{n} p_{nm}\mathbf{M}_{nm}^{(1)}(kr) + q_{nm}\mathbf{N}_{nm}^{(1)}(kr). \tag{2}$$

where $\mathbf{M}_{nm}^{(3)}$ and $\mathbf{N}_{nm}^{(3)}$ are regular VSWFs, $\mathbf{M}_{nm}^{(1)}$ and $\mathbf{N}_{nm}^{(1)}$ are the outward-propagating VSWFs, n and m are radial and azimuthal mode indices respectively and the coefficients of the incident and scattered fields are related by the T-matrix [6, 3, 4]:

$$\begin{bmatrix} p_{nm} \\ q_{nm} \end{bmatrix} = \mathbf{T} \begin{bmatrix} a_{nm} \\ b_{nm} \end{bmatrix}. \tag{3}$$

The light scattering properties of the particle, for a given wavelength, are expressed in the T-matrix.

The same formalism can be used to represent the effect of the imaging objective. In this case, our coefficients a_{nm} and b_{nm} are the coefficients of the total outgoing field from the object (that is, the sum of the outgoing portion of the incident field, which could, for example, be a plane wave or a focussed beam, and the scattered field), and p_{nm} and q_{nm} are the part of this outgoing field collected by the objective.

Firstly, we calculate the scattering coefficient as per the canonical T-matrix method using (3). We used the T-matrix for the object (here, this is a vaterite sphere, and we calculate the T-matrix using a hybrid FDTD/T-matrix method [8]).

We then cycle through all the azimuthal and radial modes (m and n) incident on the objective, one at a time, finding the spherical wave spectrum of the collected field using over-determined least-squares point-matching [3]. The objective is in the far-field of the light from the object, and the only parameter needed to represent the objective is the angles over which light enters (determined from the numerical aperture). The size of the region being viewed determines the series truncation: $n = N_{max} \approx x$, where x is the "size parameter" or the viewed area. The effective radius of this area is that, measured from the focal point of the objective, required to enclose the object. For a sub-resolution object, the resolution limit should be used as the effective size. Each iteration yields a column of the T-matrix describing the objective. For a simple rotationally symmetric objective, there will be no coupling to different values of m, as usual for the T-matrix for axisymmetric objects [6, 3, 9].

If a polarizer is included in the objective system, e.g., for viewing a sample through crossed polarizers, there will be coupling between different angular momenta, and the usual optimisation for axisymmetric particles can no longer be used. However, this coupling is highly restricted, and only a limited subset of angular momenta are available, so it is still possible to optimise this calculation, as described in the following section.

In effect, we use a double T-matrix method, involving using the pre-calculated T-matrix of the scatterer in free space, and a T-matrix representing the effect of the objective (and polarizer, if included). The T-matrix for the objective does not depend on the object being imaged, and can be calculated independently, and the same T-matrix used for the imaging of a variety of objects.

Effect of polarizer

The VSWFs expansions used in (1) and (2) to represent the electromagnetic fields are in spherical polar coordinates. The filter can be represented as a matrix applied to the outgoing field, in spherical coordinates. The radial component ($\mathbf{E}_r$) can be ignored as it approaches zero in far-field; thus, the filter matrix dimensions will be 2×2. For our derivation of the filter matrix, the beam is linearly polarized in the x-direction and propagates in the $+z$-direction. The cross-polarization filter sits flat on the horizontal plane and it filters out the y-component of the $\mathbf{E}$-field.

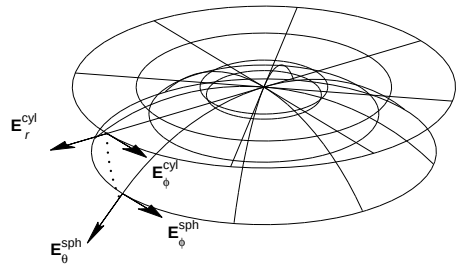

Figure 1. Projecting the E-field vectors from the spherical to the cylindrical coordinate system.

Consider the x-component of the filtered $\mathbf{E}$-field expressed in cylindrical coordinates,

$$\mathbf{E}_x = \mathbf{E}_r^{(cyl)} \cos\phi_{cyl} - \mathbf{E}_\phi^{(cyl)} \sin\phi_{cyl}, \tag{4}$$

and $\mathbf{E}_y = 0$. Since the fields are calculated in spherical coordinates, we project the spherical components onto the cylindrical plane (figure 1) such that $\mathbf{E}_\phi^{(sph)} \rightarrow \mathbf{E}_\theta^{(cyl)}$ and $\mathbf{E}_\theta^{(sph)} \rightarrow \mathbf{E}_r^{(cyl)}$, when substituted in (4), the field components expressed in spherical coordinates and in matrix form is

$$\begin{bmatrix} \mathbf{E}_x \\ 0 \end{bmatrix} = \begin{bmatrix} \cos\phi & -\sin\phi \\ 0 & 0 \end{bmatrix} \begin{bmatrix} \mathbf{E}_\theta \\ \mathbf{E}_\phi \end{bmatrix}, \tag{5}$$

bearing in mind that $\phi_{sph} = \phi_{cyl}$. Now, converting back to spherical coordinates,

$$\begin{bmatrix} \mathbf{E}'_\theta \\ \mathbf{E}'_\phi \end{bmatrix} = \begin{bmatrix} \cos\phi & \sin\phi \\ -\sin\phi & \cos\phi \end{bmatrix} \begin{bmatrix} \cos\phi & -\sin\phi \\ 0 & 0 \end{bmatrix} \begin{bmatrix} \mathbf{E}_\theta \\ \mathbf{E}_\phi \end{bmatrix}, \tag{6}$$

we obtain the filter matrix in the spherical coordinate system,

$$\begin{bmatrix} \mathbf{E}'_\theta \\ \mathbf{E}'_\phi \end{bmatrix} = \begin{bmatrix} \cos^2\phi & -\cos\phi\sin\phi \\ -\cos\phi\sin\phi & \sin^2\phi \end{bmatrix} \begin{bmatrix} \mathbf{E}_\theta \\ \mathbf{E}_\phi \end{bmatrix}. \tag{7}$$

RESULTS AND DISCUSSION

The method was tested using an object composed of four square slabs, shown on the left in figure 2, with resolution consistent with the Rayleigh criterion and polarization effects. On the right, figure 2 shows calculated images of a vaterite microsphere compared with experimental results [5].

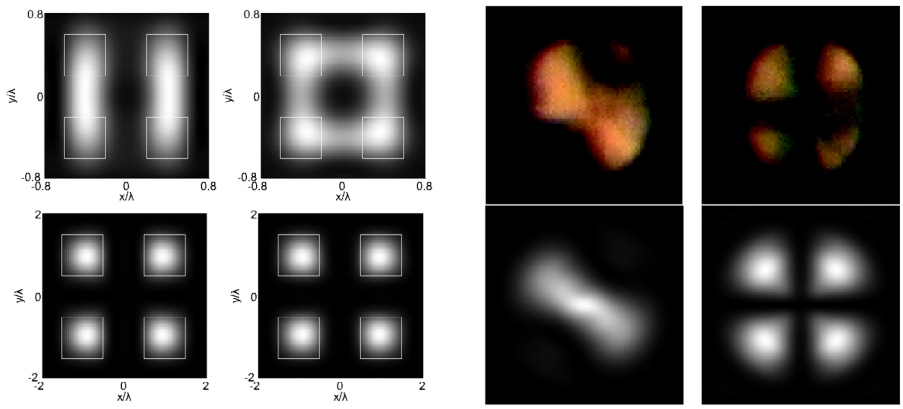

Figure 2. **Left:** Imaging of four square objects. Squares in the top row are 0.4λ across, and in the bottom row, 1λ. The illumination plane-polarized in the up--down direction in the left column, and circularly polarized on the right. **Right:** Experimental (top) and calculated (bottom) images of vaterite microspheres as seen through crossed polarizers.

Overall, it can be seen that the method works, even for complex objects that strongly affect the polarization of the light. By exploiting the mirror symmetry of the polarizer when solving the linear system resulting from the point-matching, the calculation of the T-matrix of the imaging system took a matter of minutes on a high-end desktop PC.

Although it is possible to include interaction (i.e., multiple scattering) between the objective and the object, e.g., iteratively, we have not done so here since the large distance between them, and the design of the objective to limit reflection (or back-scattering) makes this unnecessary for imaging applications.

REFERENCES

[1] C. J. R. Sheppard. The optics of microscopy. J. Opt. A **9** (2007).

[2] M. R. Arnison and C. J. R. Sheppard. A 3D vectorial optical transfer function suitable for arbitrary pupil functions. Opt. Commun. bf 211 (2002).

[3] T. A. Nieminen, H. Rubinsztein-Dunlop, and N. R. Heckenberg. Calculation of the *T*-matrix: general considerations and application of the point-matching method. J. Quant. Spectrosc. Radiat. Transfer **79--80** (2003).

[4] F. M. Kahnert. Numerical methods in electromagnetic scattering theory. J. Quant. Spectrosc. Radiat. Transfer **79--80** (2003).

[5] S. J. Parkin et al. Highly birefringent vaterite microspheres: production, characterization and applications for optical micromanipulation. Opt. Express **17** (2009).

[6] P. C. Waterman. Symmetry, unitarity, and geometry in electromagnetic scattering. Phys. Rev. D **3** (1971).

[7] T. A. Nieminen, H. Rubinsztein-Dunlop, and N. R. Heckenberg. Multipole expansion of strongly focussed laser beams. J. Quant. Spectrosc. Radiat. Transfer **79--80** (2003).

[8] V. L. Y. Loke et al. FDFD/T-matrix hybrid method. J. Quant. Spectrosc. Radiat. Transfer **106** (2007).

[9] M. I. Mishchenko. Light scattering by randomly oriented axially symmetric particles. J. Opt. Soc. Am. A **8** (1991).

Light scattering by dust particles in the solar system with assessments of both direct and inverse problems

K. Lumme*

Department of Physics, University of Helsinki, P.O. Box 64, FI-00014 Finland.

We analyze both the intensity and linear polarization of cosmic dust particles by using the physically exact fixed cluster *T*-matrix method for aggregates of spheres and DDA for aggregates of Gaussian random spheres. We study both the spherical geometry (in cometary comae) and cylindrical slabs (for regoliths) up to 1024 monomers with size parameters less than ~3. It is straightforward to produce the observed linear polarization in both geometries while the typically convex opposition spike seems to require the regolith geometry.

INTRODUCTION

The nonlinear brightening and linear polarization, particularly the negative branch, close to the opposition geometry of a large number of atmosphereless bodies in the solar system are issues which have been known for decades. The quantitative explanation with measurable physical parameters is lacking to a rather large extent. The coherent backscattering (CB) mechanism seems to be the leading factor at small phase angles α, because CB simultaneously explains both the increase of the brightness and the negative branch. However, the actual shape of the brightness increase still needs some clarification. In most cases the observed shape is convex (second derivative positive at $\alpha=0^o$, while almost all the existing computations of CB with various aggregate parameters produce concave shapes.

Often some adjustable parameters that produce nice formal fits to the data are assumed without any real physical meaning. These solutions are rarely unique. Because of the complexity of the problem the real inversion at this point seems rather hopeless. We can, however, find reasonable constraints for some of the key parameters.

AGGREGATE GEOMETRIES

We assume for all the aggregates that every monomer has a touching neighbor. This does not need to be actually true because some electrostatic forces can produce some separation. Our computations show that if the separation is less than about 10% of the radii the results are fairly insensitive to this. The key parameters in our aggregates are: the size and size distribution of the monomers, the particle packing algorithm and the packing density *pD*. The best source to evaluate some of these are several images of the cosmic dust particles (CDP) on the internet with the accurate scale bars. From these images we have been able to conclude that the monomers are rather round. The radii r seem to lay in the interval from 0.08 μm to 0.22

* Kari Lumme (Kari.Lumme@helsinki.fi)

μm and the size distribution is rather close to a lognormal distribution. Naturally we must take this information with a special caution if applied to the whole population of the CDPs.

We first consider packing of spheres with an arbitrary size distribution. A popular packing code for aggregates is either the ballistic particle-cluster aggregation (PC) or the ballistic cluster-cluster aggregation (CC). The PC code produces aggregates with roughly the same *pD*. The other code we have used randomly selects a monomer from a binomial distribution. Here we insert a new one as a touching neighbor if it does not intersect the others. With one parameter we can create quite different *pD*s. To estimate quantitatively *pD* we need a reference volume. This volume is often taken as a sphere with a minimum radius that confines all the packed monomers. This is not a good choice because it underestimates *pD* for elongated aggregates. Instead, we use the convex hull (CH) for which ready codes exist on the internet.

For nonspherical monomers we can pack general ellipsoids, standard and spherocylinders, Gaussian random spheres (GRS) and convex polyhedra. For these monomers the parameter space increases considerably and systematical light-scattering studies have to wait.

LIGHT SCATTERING METHODS

There are two widely used methods to do light scattering of aggregates. First, the superposition *T* matrix (CTM) [1] and, second, some of the several versions of the discrete dipole approximation (DDA) [2] are used. The original CTM uses an analytical orientation averaging but as recently shown [3], the fixed orientation technique (FCTM) deserves some obvious benefits over the standard CTM. Particularly, with this version, the number of monomers can be greatly increased. A highly efficient numerical integration technique which suits both the CTM and the DDA methods, called *cubature,* was recently found by Penttilä [4].

Both CTM and DDA have their pros and cons. If very accurate results are required close to the backscattering then the CTM method is superior. If the monomer shape is of key importance then, of course, the DDA method is the only possibility. Also, if we are interested in a large number *n* of rather small spherical monomers, then DDA is the only choice.

LIGHT SCATTERING BY COMETARY DUST

The cometary dust particles have been modeled by PC and CC aggregates. The number of free parameters even with some simplifying assumptions is so large that a unique inversion of the good observational polarization data in the interval $0^\circ<\alpha<120^\circ$ is quite impossible.

We have scanned the realistic range of the real part m_R of the refractive index in the range from 1.5 to 1.8. The imaginary part m_I seems to have a small effect if it is less than about 0.01. Only as an exercise, we have studied two models based on the PC and CC geometries (Fig. 1). In the former we assume a collection of aggregates of 256 equal-sized monomers and numerically integrate the results in the range $0.75<x<2.5$ where x is the size parameter and follows a power law with one parameter γ. Assuming $m_I=0.01$ leaves only γ and m_R to be solved. A very extensive data collection for cometary polarization is provided

with the *Database of comet polarimetry**. Of these the data in the red filter is most extensive and can be used to obtain the two free parameters. We can see that the fit is very good indeed and the free parameters come out as m_R=1.68 and γ=2.73. The same kind of fits can also be done to the data in different colors.

The other case we studied is a CC aggregate (Fig. 1). We assumed 16 sub-clusters with 32 equal-sized monomers in each. The 16 values for the radii were taken randomly from a power law in the same range as above. We used eight realizations and took the mean of those. This model leaves only one parameter, m_R, to be determined for which we got 1.63. The fit is also very good. These exercises clearly indicate how difficult it is to obtain unique solutions.

To see the effect of nonsphericity on the results we have packed 128 lognormally distributed monomer GRSs with our code and used DDA with the cubature orientation averaging to compute an example. In Fig. 2 we compare these results to those of a PC aggregate with spherical monomers. We assumed here that m_R =1.6, m_I =0.01.

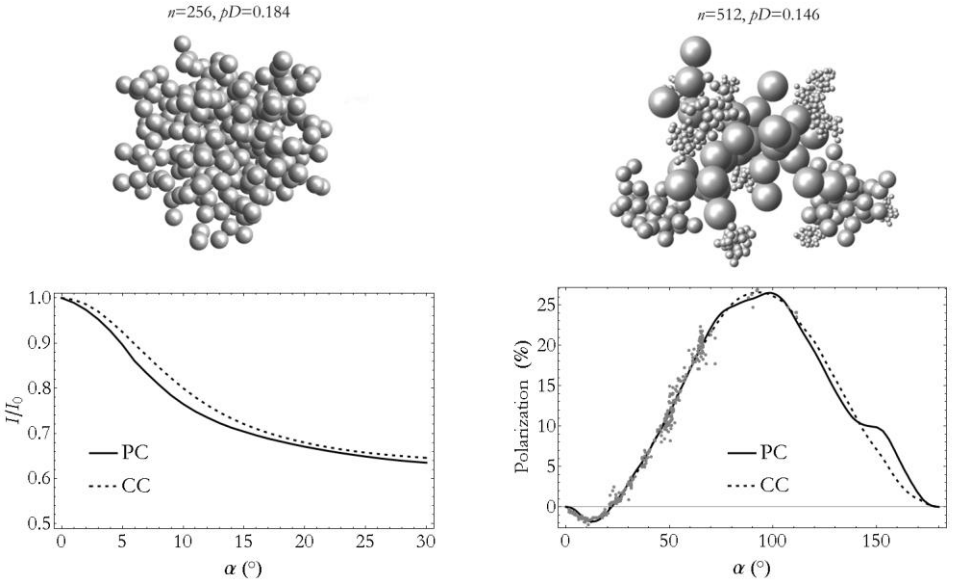

Figure 1. Intensities and polarizations are computed of PC (top left) and CC (top right) aggregates and compared to the red filter data of cometary polarization. For details, see text.

LIGHT SCATTERING BY REGOLITHS

With current methods it is impossible to model the horizontally very large regoliths. We do this approximately by using cylindrical slabs with the size parameter radius R_x>>1 using FCTM in the range 0º<α<20º. One of our exercises is shown in Fig. 3. We integrate the computations over the angle of incidence *i* in the range 0º<*i*<20º. Comparison to a PC aggregate with equal constituents shows that the intensity spike is stronger for the slab, al-

* Available on the internet at the Small Bodies Node (http://sbn.pds.nasa.gov/).

though not yet clearly convex as required by observed data. The linear polarization is more asymmetric than those of the PC results.

With DDA code ADDA it is possible to analyze slabs up to R_x ~100 and height H_x ~20 which we will do in near future. We think that the regolith structure could best be described as random heterogeneous medium in submicron scale where CB is mainly responsible for the intensity and polarization behavior at the small phase angle observations. The sub millimeter scale can still cause some effects due to the mutual shadowing and surface roughness.

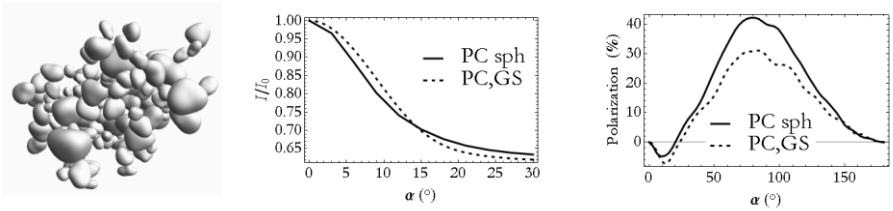

Figure 2. Normalized intensities and linear polarization are shown for PC aggregates of log-normally distributed spherical 128 monomers (not shown) and Gaussian spheres (GS).

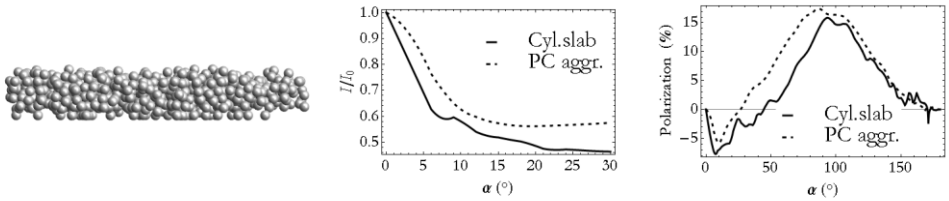

Figure 3. Normalized intensities and linear polarization for a PC aggregate and an extended cylindrical slab to model a regolith. In both cases we have equal sized monomers of x=1.75 and m=1.6+ i 0.001. The radius (in size parameters) of the slab is 53 and the height 20. Note particularly a stronger opposition spike and more asymmetric negative polarization.

Acknowledgements: This work would not have been possible without the help provided by Antti Penttilä.

REFERENCES

[1] D. W. Mackowski and M. I. Mishchenko. Calculation of the T-matrix and the scattering matrix for the ensembles of spheres. J. Opt. Soc. Am. A **13** (1996).

[2] A. Penttilä, E. Zubko, K. Lumme, K. Muinonen, M.A. Yurkin, B. Draine, J. Rahola, A. G. Hoekstra, and Y. Shkuratov. Comparison between discrete dipole implementations and exact techniques. JQRST **106** (2007).

[3] Y. Okada. Efficient numerical orientation averaging of light scattering properties with a quasi-Monte-Carlo method. JQSRT **109** (2008).

[4] A. Penttilä and K. Lumme. Cubature orientation averaging scheme. In: *Proceedings of the ELS'XII in Helsinki* (2010).

T-matrix approach to calculating circular polarization of aggregates made of optically active (chiral) materials and its applications to cometary dust observations

D. W. Mackowski*,[1], L. Kolokolova[2], and W. Sparks[3]

[1]*Department of Mechanical Engineering, Auburn University, Auburn, AL, USA.*
[2]*Department of Astronomy, University of Maryland, College Park, MD, USA.*
[3]*Space Telescope Science Institute, Baltimore, MD, USA.*

Optical activity is a typical property of the biological materials where left-handed aminoacids and right-handed carbohydrates dominate (so called homochirality). Observationally, optically active materials reveal themselves through the circular polarization in the light they scatter. Thus, circular polarization produced by the optically active particles can serve as a biomarker. This and other applications stimulated a development of the T-matrix code presented in this paper. It allows us to calculate the scattering matrix, and, specifically circular polarization, of the light scattered by aggregated optically active particles. The code can be used for modeling the light scattering by biological objects (e.g., colonies of bacteria, blood cells) and for interpretation of the circular polarization produced by the cosmic dust that contains (pre)biological organic molecules, e.g., comet dust or planetary aerosols.

INTRODUCTION

Many complex organic molecules exist in two forms that are identical except that they pose chirality, i.e., are mirror images of each other. A unique characteristic of life is the homochirality of biological molecules, i.e., predominance of one of the mirror forms of the organic molecules. This characteristic may be manifested on a macroscopic scale through the optical activity of the chiral molecules and, hence, the presence of circular polarization (CP) in the light they scatter. Recently a unique set of data on circular polarization in comets has been accumulated [1]. Characteristics of the cometary CP, specifically a domination of the left-handed polarization in all observed comets, favor the idea that this is evidence of homochiral organics in comet dust similar to that found in meteorites. We have also explored remote-sensing capabilities of circular polarization in the laboratory, studying light scattering from astrobiologically relevant micro-organisms and setting these in the context of abiotic minerals [2]. We have found a dependence of the CP on the dichroism of the materials that results in greater circular polarization in absorption bands.

Theoretical and computational tools are needed to confirm whether the presence of chiral organics can produce the observed characteristics of comet circular polarization and explain the results of our laboratory measurements. A well-known solution exists for an isolated, optically active sphere [3], yet a single sphere model for complex comet dust particles or colonies of bacteria is both unrealistic and incapable of explaining recent results.

Comet dust is known to possess an aggregated structure, and such a structure is also plausible for a variety of biological particles. To better account for the non–spherical na-

*Corresponding author: Daniel Mackowski (mackodw@auburn.edu)

ture of such particles, we have developed a T-matrix code to predict light scattering and absorption by aggregates of optically active spheres. We anticipate that this code will be applicable to a variety of astrobiological problems, including the search for materials containing molecules of prebiological and biological origin in comets, planets, extrasolar planets, and protoplanetary nebulae as well as for studying biological particles in the Earth atmosphere and in the laboratory.

FORMULATION OF THE T-MATRIX CODE FOR OPTICALLY ACTIVE MULTIPLE SPHERES

The existing T-matrix code to calculate light scattering by aggregates assumes that the monomer particles are optically isotropic spheres [4]. However, it is relatively simple to extend the formulation to include aggregates of optically active spheres.

As is the case for isotropic spheres, the electric fields incident on, and scattered by, an optically active sphere can be represented by expansions of regular and outgoing vector wave harmonics (VWH), respectively, which appear as

$$\mathbf{E}_{inc}(\mathbf{r}) = \sum_{n=1} \sum_{m=-n}^{n} \sum_{p=1}^{2} f_{mnp}\, \mathbf{N}^{(1)}_{mnp}(\mathrm{k}\,\mathbf{r}), \tag{1}$$

$$\mathbf{E}_{sca}(\mathbf{r}) = \sum_{n=1} \sum_{m=-n}^{n} \sum_{p=1}^{2} a_{mnp}\, \mathbf{N}^{(3)}_{mnp}(\mathrm{k}\,\mathbf{r}), \tag{2}$$

in which f and a denote the incident-field and scattered-field expansion coefficients, and (m, n, p) denote the degree, order, and mode (TM or TE) of the harmonic. Unlike the isotropic case, however, the optically active sphere results in a coupling of TE and TM modes between the incident and scattered field coefficients for a given harmonic order [3]. That is, the Mie relation for the active sphere appears as

$$a_{mnp} = \sum_{q=1}^{2} \overline{a}_{n;\,pq}\, f_{mnq}, \tag{3}$$

in which the coefficients $\overline{a}$ will be functions of the sphere size parameter ka and the left and right refractive indices.

The modified Mie relation for the active sphere can be incorporated directly into the formulation for a cluster of N_p spheres, and results in the following interaction equations for the sphere scattering coefficients,

$$a^i_{mnp} - \sum_{p'=1}^{2} \overline{a}^i_{n;pp'} \sum_{\substack{j=1 \\ j\neq i}}^{N_p} \sum_{l=1}^{L_j} \sum_{k=-l}^{l} \sum_{q=1}^{2} H^{i-j}_{mnp'\,klq}\, a^j_{klq} = \sum_{p'=1}^{2} \overline{a}^i_{n;pp'}\, f^i_{mnp'}. \tag{4}$$

Above, H^{i-j} is an outgoing harmonic translation matrix, and depends solely on the distance and direction between the origins i and j. Following the procedures developed in [4], a T matrix for the cluster of active spheres can be obtained from the solution of the interaction equations, and the orientation–averaged scattering-matrix elements can be analytically determined from operations on the T matrix.

TESTS AND APPLICATIONS OF THE T-MATRIX CODE FOR OPTICALLY ACTIVE AGGREGATES

A number of consistency checks have been applied to test the veracity of the solution for clusters of optically active spheres. The solution identically satisfy energy conservation (extinction = absorption + scattering) and conforms to equivalent rotations of the cluster and the incident field. In addition, the solution provides a detailed prediction of the electric field in the near-field zones – both within and exterior to the spheres – and this can be used to check the continuity conditions at the surfaces of the spheres. Also, for a single sphere, the solution reduces to the solution from [3] and for isotropic material it provides the standard multi-sphere case from [4].

The results of illustrative test calculations are presented in Fig. 1. Shown are values of the circular polarization ratio S_{14}/S_{11}, as a function of scattering angle, for random–oriented aggregates. For these calculations we set the radius of the monomers to 0.1 μm, which is typical of cometary particles [5], and the incident wavelength is $\lambda = 0.6$ μm which corresponds to the comet red filter. Values of refractive index correspond to $\mathsf{m}_\mathrm{R} = 1.55 + 0.0006004\mathsf{i}$ and $\mathsf{m}_\mathrm{L} = 1.5500338 + 0.0006000\mathsf{i}$ (R and L refering to left-handed and right-handed, respectively), which are typical for the amino-acids discovered in the Murchison meteorite [6]. According to [7], the specific rotation angle for them is about 100°, which corresponds to a difference in refractive index for left-handed and right-handed circular polarization of 3×10^{-6}. In our calculations, 10 % of the material is assumed to be optically active.

Two models of aggregates are used in the calculations of Fig. 1, being a fractal–like aggregate with $D_f = 1.8$ and $k_0 = 2.2$ that is characteristic of aggregates formed from cluster–cluster diffusion processes, and clusters of spheres packed randomly and uniformly into a spherical boundary with a volume fraction of 0.5. This latter form would correspond to aggregates formed from evaporation of the liquid phase from droplets of liquid–solid suspensions. Aggregates were generated using a Monte-Carlo method, and the curves represent averages of 20 different realizations of each aggregate for a fixed sphere number N_p. To identically cancel out effects due to random L and R rotation in the aggregate structures – and thereby focus entirely on circular polarization due to optical activity – half of these realizations were mirror images of the other half. Also shown in both plots are the polarization ratios for the single monomer sphere.

The calculation results shown in Fig. 1 are not intended to fit any observational or laboratory data. However, we do see in them some encouraging outcomes. Specifically, the angular change of CP for fractal aggregates (Fig. 1, left) is similar to that observed in comets [1], namely within the range of phase angles $20-120°$ (scattering angles $160-60°$) CP increases almost linearly. Though the values of CP are approximately one order of magnitude smaller than the observed ones (there CP reached 0.4 % at the scattering angle 60°), at all angles, except the forward scattering area, the results show increase in the CP with the increase of the number of monomers. We expect that for larger aggregates we may reach higher values of CP. The current models of the cometary dust require domination of particles of thousands of monomers [8]. For such large aggregates, the CP may be significantly larger.

The results for the packed sphere clusters (Fig. 1, right) also show a general increase of CP with phase angle and with number of monomers. However, the picture is complicated by the resonant structure of the plots. The reason the packed sphere results show the resonance

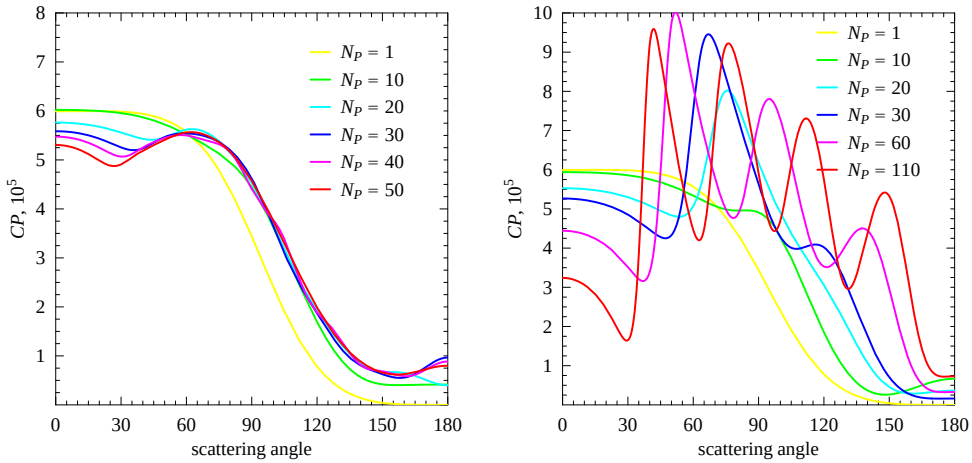

Figure 1. Circular polarization ratios for aggregates of active spheres. Fractal like aggregate (left), and packed–sphere clusters (right).

behavior is because the monomers are forced to fit inside a perfect sphere. This effect would wash out if the enclosing boundary was made random, or when averages were made over different N_p.

One more interesting outcome of our computations is a strong dependence of the CP on the structure of aggregates. It gives us a hope that the new T-matrix code can become a tool to study the structure of cosmic dust particles and planetary aerosols as well as complex biological objects such as cells or microorganisms.

REFERENCES

[1] V. Rosenbush, L. Kolokolova, A. Lazarian, N. Shakhovskoy, and N. Kiselev. Circular polarization in comets: Observations of Comet C/1999 S4 (LINEAR) and tentative interpretation. Icarus **186** (2007).

[2] W.B. Sparks, J.H. Hough, L. Kolokolova, T.A. Germer, F. Chen, S. DasSarma, P. DasSarma, F.T. Robb, N. Manset, I.N. Reid, F.D. Macchetto, and W. Martin. Circular polarization in scattered light as a possible biomarker. JQSRT **110** (2009).

[3] C.F. Bohren. Scattering of electromagnetic waves by an optically active spherical shell. J. Chem. Phys. **62** (1975).

[4] D.W. Mackowski and M.I. Mishchenko, Calculation of the T matrix and the scattering matrix for ensembles of spheres. J. Opt. Soc. Amer. A **13** (1996).

[5] H. Kimura, L. Kolokolova, and I. Mann. Optical properties of cometary dust. Constraints from numerical studies on light scattering by aggregate particles. Astron. Astrophys. **407** (2003).

[6] J.R. Cronin and S. Pizzarello. Amino acids in meteorites. Adv. in Space Research **3** (1983).

[7] S.F. Mason. *Molecular Optical Activity and the Chiral Discriminations*. Cambridge University Press (1982).

[8] L. Kolokolova, H. Kimura, N. Kiselev, and V. Rosenbush. Two different evolutionary types of comets proved by polarimetric and infrared properties of their dust. Astron. Astrophys. **463** (2007).

A T-matrix method based on a plane-wave spectrum

D. W. Mackowski*

Mechanical Engineering Department, Auburn University, AL, 36830, USA.

A computational scheme is proposed to generate a T matrix for an arbitrarily-shaped homogeneous particle. The method models the internal field within the particle as a directional spectrum of plane waves. A system of equations for the plane-wave coefficients is obtained by application of the model to a discrete-dipole representation of the particle.

INTRODUCTION

The work presented here represents a revisiting and re-examination of the discrete-dipole moment method (DDMM) for the calculation of the T matrix of arbitrarily-shaped particles[1]. This method retained the DD representation of the particle as a lattice of dipole elements, yet the distribution of dipole moment within the particle was modeled via an expansion of spherical wave harmonics. In general, the moment method was considerably faster than the corresponding direct DDA-to-T matrix route (DDA for discrete-dipole approximation), the latter of which involves solution of the DDA equations for each order/degree/mode component of a generalized, vector harmonic incident wave expansion. However, the DDMM method, as originally formulated, is difficult to translate into a working code; even though it relies on the DD model of the particle, the method would involve a major modification of the standard DDA codes to implement.

A simpler yet somewhat equivalent approach is outlined here. As opposed to the spherical wave harmonic basis, the dipole distribution within the particle is modeled by a discrete set of plane wave components, with each component corresponding to a specific propagation direction and polarization state. This approach is based on the idea that a regular solution to the Maxwell equations -- which will correspond to the field existing within the modeled particle interior -- can be expressed as an integral over vector plane waves [2]. A plane wave spectrum has been used to represent a Gaussian beam [3], yet the author is not aware of the use of plane wave methods to describe the internal field in the particle scattering problem.

FORMULATION

The analysis begins with the standard discrete-dipole representation of a homogeneous particle. The particle, of refractive index m, is represented as a cubic lattice of N_d dipole elements, with grid spacing $2a$. The scattered field from the entire particle is given by the superposition of fields scattered from each element:

$$\mathbf{E}_{sca,i}(\mathbf{r}) = \sum_{i=1}^{N_d} \sum_{m=-1}^{1} a_m^i \, \mathbf{N}_{m11}^{(3)}(\mathbf{r} - \mathbf{r}_i), \tag{1}$$

in which $\mathbf{N}_{m11}^{(3)}$ is the vector wave harmonic (VWH) of degree m, order 1, and TM mode, and a_m^i denote the sought dipole elements for lattice site i. The interaction equations for

*Daniel Mackowski (mackodw@auburn.edu)

the dipole elements appear as

$$\frac{1}{\overline{a}}\, a_m^i - \sum_{\substack{j=1\\ j\neq i}}^{N_d} \sum_{k=-1}^{1} H_{mk}^{i-j}\, a_k^j = p_{m,\gamma_0}(\mathbf{k}_0)\, f^i(\mathbf{k}_0), \tag{2}$$

in which $\overline{a}$ denotes the dipole polarizability, which is a function of the refractive index m and the dimensionless lattice size $\mathrm{k}\, a = 2\pi a/\lambda$, H^{i-j} is a translation matrix from site j to i, $\mathbf{k}_0$ is a unit vector denoting the direction of the incident plane wave and described by the azimuth and polar angles (α_0, β_0) relative to a target--based frame, p_{m,γ_0} are the plane-wave VWH dipole expansion coefficients (degree m, order 1, and TM mode) for the incident field, with subscript $\gamma_0 = 1, 2$ denoting an incident polarization angle, relative to the $\hat{\mathbf{z}} - \mathbf{k}_0$ plane, of 0 or $\pi/2$, and f^i is the phase factor,

$$f^i(\alpha_0,\ \beta_0) = \exp\left[\mathrm{i}\mathsf{k}((x_i\, \cos\alpha_0 + y_i\, \sin\alpha_0)\sin\beta_0 + z_i\, \cos\beta_0)\right]. \tag{3}$$

Note that a dipole--limit VWH formulation of the DDA equations is employed, in which index m denotes the dipole azimuth degrees $-1, 0, 1$, as opposed to a Cartesian--based dipole-moment formulation; the two formulations are completely equivalent in the end [4, 1].

In general, the number of unknowns in Eq. (2) will scale with $x_V^3 = (\mathrm{k}a_V)^3$, where a_V is a volume-equivalent radius of the particle. The objective of the method proposed here is to reduce the number of unknowns, so that the computational overhead scales with the surface area of the particle as opposed to the volume. The approach taken in [1] was to represent the discrete distribution of dipole elements as a continuous distribution, modeled by an expansion of scalar spherical wave harmonics centered about the particle origin and evaluated for the particle medium. The rationale is that the distribution of dipole elements should satisfy the scalar Helmholtz equation for the particle material, and the spherical wave harmonics form a complete basis for a regular solution to the Helmholtz equation.

The approach taken here is to use a simpler set of basis functions to represent the dipole distribution. Specifically, the distribution of dipole elements are now modeled by a directional spectrum of plane waves, evaluated within the particle medium. This is expressed as

$$a_m^i \approx \sum_{\nu=1}^{M} \sum_{\gamma=1}^{2} \omega_\nu\, p_{m,\gamma}(\mathbf{k}_\nu)\, \hat{f}^i(\mathbf{k}_\nu)\, W_{\nu\gamma,\nu_0\gamma_0}, \tag{4}$$

in which $\mathbf{k}_\nu = (\alpha_\nu, \beta_\nu)$ describes the direction of the plane wave component, ω_ν is a weighting function, W is a matrix which is sought from the analysis, ν_0, γ_0 represents the incident direction and polarization, and $\hat{f}$ is a phase factor evaluated in the particle medium (i.e., wavenumber mk). A logical choice for the distribution of angles and weights is the Gauss quadrature points of a chosen order M_β for $\cos\beta$ and an even distribution of $2M_\beta$ points in α. The total number of directions will then be $M = 2M_\beta^2$

Following the DDMM procedure, a system of equations for W can be obtained by multiplying Eq. (2) by the conjugate of the basis function in Eq. (4) and contracting over all lattice positions. This results in

$$\sum_{\nu'=1}^{M} \sum_{\gamma'=1}^{2} A_{\nu\gamma\,\nu'\gamma'}\, W_{\nu'\gamma'\,\nu_0\gamma_0} = B_{\nu\gamma\,\nu_0\gamma_0} \tag{5}$$

with

$$A_{\nu\gamma\,\nu'\gamma'} = \omega_\nu\,\omega_{\nu'} \sum_{m=-1}^{1}\sum_{k=-1}^{1} \left(p_{m,\gamma}(\mathbf{k}_\nu)\right)^*\, p_{k,\gamma'}(\mathbf{k}_{\nu'}) \times \sum_{i=1}^{N_d} \hat{f}^{i*}(\mathbf{k}_\nu) \left(\frac{1}{a}\,\hat{f}^i(\mathbf{k}_{\nu'})\delta_{m-k} - \sum_{\substack{j=1\\ j\neq i}}^{N_d} H_{mk}^{i-j}\,\hat{f}^j(\mathbf{k}_{\nu'}) \right), \tag{6}$$

$$B_{\nu\gamma\,\nu_0\gamma_0} = \omega_\nu\,\left(p_{m,\gamma}(\mathbf{k}_\nu)\right)^*\, p_{m,\gamma_0}(\mathbf{k}_{\nu_0}) \sum_{i=1}^{N_d} \hat{f}^{i*}(\mathbf{k}_\nu)\, f^i(\mathbf{k}_{\nu_0}). \tag{7}$$

It is computationally simple and efficient to use existing DDA codes to generate the A matrix defined in Eq. (6) [4, 5]. In particular, the FFT convolution scheme can be used to perform the summation over lattice site j, followed by a direct sum over site i. In general, the operation count in generating the A matrix will scale as $M^2 N_d \ln(N_d)$. Standard inversion methods can then be used to obtain the W matrix from the solution of Eq. (5).

Relation to the T matrix

By use of the addition theorem for VWH, the scattered field from the particle, given by Eq. (1), can be represented by a single outgoing VWH expansion centered about the origin of the particle. The expansion coefficients in this representation, for the VWH component of degree/order/mode k, l, q, are given by [1]

$$a_{klp} = \sum_{i=1}^{N_d}\sum_{m=-1}^{1} J_{klq\,m11}^{0-i}\,a_m^i, \tag{8}$$

where J is the regular harmonic translation matrix and L the truncation limit. In the far field, the transverse components of the scattered field in a direction $\mathbf{k}_s$, referenced to the target coordinate frame, will be given by

$$\mathbf{E}_{s,\gamma_s}(\mathbf{k}_s) = \frac{e^{\mathrm{i}k\,r}}{\mathrm{i}kr} \sum_{l=1}^{L}\sum_{k=-l}^{l}\sum_{q=1}^{2} \left(p_{klq,\gamma_s}(\mathbf{k}_s)\right)^*\, a_{klq}, \tag{9}$$

in which p_{klq,γ_s} is the plane-wave VWH coefficient and $\gamma_s = 1$ and 2 would correspond to the θ and ϕ components.

The plane-wave model in Eq. (4) can be substituted directly into Eq. (8) to obtain the VWH form for the scattered field. An alternative approach is to recognize that the plane-wave coefficients p_{klq} and the phase factor f are the eigenvectors and eigenvalues to the translation matrix [6];

$$p_{m11,\gamma}(\mathbf{k})\,f^i(\mathbf{k}) = \sum_{l=1}^{l}\sum_{k=-l}^{l}\sum_{q=1}^{2} J_{m11\,klq}^{i-0}\,p_{klq,\gamma}(\mathbf{k}). \tag{10}$$

By employing the above into Eq. (8) and using the matrix relations developed for the plane-

wave model, the far-field components of electric field will be given by

$$\mathbf{E}_s(\mathbf{k}_s) = \frac{e^{\mathrm{i}k\,r}}{\mathrm{i}k r} \sum_{\nu=1}^{M} \sum_{\gamma=1}^{2} B^*_{\nu\gamma\,\nu_s\gamma_s} W_{\nu\gamma\,\nu_0\gamma_0}$$

$$= \frac{e^{\mathrm{i}k\,r}}{\mathrm{i}k r} \sum_{\nu=1}^{M} \sum_{\gamma=1}^{2} \sum_{\nu'=1}^{M} \sum_{\gamma'=1}^{2} B^*_{\nu\gamma\,\nu_s\gamma_s} A^{-1}_{\nu\gamma\,\nu'\gamma'} B_{\nu'\gamma'\,\nu_0\gamma_0} = \frac{e^{\mathrm{i}k\,r}}{\mathrm{i}k r} S_{\nu_s\gamma_s\,\nu_0\gamma_0}. \quad (11)$$

The matrix S is recognized as a scattering amplitude matrix. The traditional T matrix can be obtained by use of Eq. (10) and the orthogonality relations of the p_{klq} functions. Assuming an integration over direction is accurately represented by the chosen quadrature scheme and weights, the T matrix will be given by

$$T_{mnp\,klq} = \sum_{\nu=1}^{M} \sum_{\gamma=1}^{2} \sum_{\nu'=1}^{M} \sum_{\gamma'=1}^{2} \left(p_{mnp,\gamma}(\mathbf{k}_\nu)\right)^* \, S_{\nu\gamma\,\nu'\gamma'} \, p_{klq,\gamma'}(\mathbf{k}_{\nu'}). \quad (12)$$

Preliminary results and directions

A code has been developed to test the veracity of the proposed method. Preliminary results indicate that the number of polar angles M_β (i.e., the number of quadrature points) needed for accurate agreement with exact DDA results is proportional to x_V. Viewed another way, M_β will be comparable to the VWH order truncation limit L for the T-matrix representation.

The plane-wave form in Eq. (4) offers some unique features when coupled with the DDA procedure. For certain particle shapes, e.g., a rectangular solid, the model becomes a separable function of x, y, and z, and this can reduce considerably the computational overhead in calculation of Eq. (6). It is also relatively simple to implement a surface integral form of the equations -- as opposed to a volume integration -- which will remove the need for a dipole polarizability. These topics, and the results of example calculations, will be presented at the meeting.

REFERENCES

[1] D. W. Mackowski. Discrete dipole moment method for calculation of the T matrix for nonspherical particles. J. Opt. Soc. Amer. A **19** (2002).

[2] A. Doicu, T. Wriedt, and Y. A. Eremin. *Light Scattering by Systems of Particles. Null-Field Method with Discrete Sources: Theory and Programs*. Springer Science+Business Media (2006).

[3] E. E. M. Khaled, S. C. Hill, and P. W. Barber. Scattered and internal intensity of a sphere illuminated with a Gaussian beam. IEEE Trans. Atten. Prop. **41** (1993).

[4] B. T. Draine and P. J. Flatau. Discrete-dipole approximation for scattering calculations. J. Opt. Soc. Amer. A **11** (1994).

[5] M. A. Yurkin and A. G. Hoekstra. The discrete dipole approximation: An overview and recent developments. J. Quant. Spectros. Radiat. Trans. **106** (2007).

[6] K. A. Fuller and D. W. Mackowski. Electromagnetic scattering by compounded spherical particles. In: *Light Scattering by Nonspherical Particles: Theory, Measurements, and Applications*. M. I. Mishchenko, J. W. Hovenier, and L. D. Travis (eds.). Academic Press (2000).

Modeling of radiative impact of a cirrus cloud based on microphysical in-situ measurements

P. Mauno[*,1], T. Nousiainen[1], G. M. McFarquhar[2], M. S. Timlin[3], M. Kahnert[4], and P. Räisänen[5]

[1]*Department of Physics, P.O. Box 48, FI-00014 University of Helsinki, Finland.*
[2]*University of Illinois, Department of Atmospheric Sciences, 105 S. Gregory Street, Urbana, IL 61801-3070, USA.*
[3]*Midwestern Regional Climate Center, 2204 Griffith Drive, Champaign, IL 61820, USA.*
[4]*Swedish Meteorological and Hydrological Institute, Folkborgsvägen 1, S-601 76 Norrköping, Sweden.*
[5]*Finnish Meteorological Institute, P.O. Box 503, 00101 HELSINKI, Finland.*

The shortwave radiative impact of a cirrus cloud observed over Oklahoma is investigated. Single-scattering properties of ice crystals derived based on in-situ measurements of the size and shape distributions of ice crystals are input to the *libradtran* radiative transfer model. The simulated fluxes, especially the shortwave cloud radiative forcing at the top of the atmosphere, depend substantially on assumptions about small ice particles (maximum dimensions less than 120 μm), whose concentrations are highly uncertain.

INTRODUCTION

Tropospheric ice clouds, such as cirrus clouds, are an important component in the Earth-atmosphere system through their role in the redistribution of radiative energy. These clouds are composed of nonspherical and often irregularly shaped ice crystals. The shapes, size distributions, and optical properties of ice crystals are not well known and thus the radiative impact of cirrus clouds is still poorly known.

In this study, the shortwave (SW) radiative impact of an ice cloud is modeled based on in-situ measured size and shape distributions of ice crystals. In particular, the sensitivity of the SW radiative impact to uncertainties in the concentrations and shapes of small ice crystals (hereafter defined as those crystals with maximum dimensions $D < 120$ μm) is investigated.

MEASUREMENTS

Detailed in-situ data were collected by probes installed on the University of North Dakota (UND) Citation aircraft as it flew through cirrus during the Atmospheric Radiation Measurement (ARM) Program's Cloud Intensive Operation Period over the Southern Great Plains (SGP) site in March 2000. In addition, surface measurements of SW radiative fluxes and data from millimeter cloud radar are used in this study.

* Corresponding author: Päivi Mauno (Paivi.Mauno@helsinki.fi)

The UND Citation executed several spiral ascents and descents through cirrus at temperatures between -15 and -50 ˚C. One of these spirals (21:52 to 22:16 GMT on 13 March) is used in this study. The aircraft was equipped with a Forward Scattering Spectrometer Probe (FSSP), a one-dimensional cloud probe (1DC), and a two-dimensional cloud probe (2DC). Although the FSSP is designed for measuring water droplets with $D < 50$ μm, it has also been used to determine size distributions of ice crystals. However, [1] showed that remnants of large ice crystals shattering on the surfaces of this probe dominate its response so that FSSP concentrations should be regarded as a large upper bound. The 1DC (50 μm < D < 120 μm) and 2DC ($D > 120$ μm) may also suffer from shattered artifacts, but are the only available data for this size range. A Cloud Particle Imager (CPI) provided high-resolution (2.3 μm) images of ice crystals to identify ice crystal shape. Ice crystals with $D < 120$ μm have been previously shown to be mainly quasi-spherical [2] and can be represented as quasi-spheres or droxtals. Using an automated habit classification algorithm [3], the size-dependent fraction of large crystals ($D > 120$ μm) in seven categories (columns, plates, bullet rosettes, budding bullet rosettes, spheres, small and large irregulars) is determined at 60-s resolution and applied to all 10-s size distributions derived from the 2DC.

Because of the large uncertainties in the shapes and concentrations of small ice crystals, four alternate representations are used to characterize the small ice crystals: 1) FSSP and 1DC data with droxtal shapes (hereafter referred as droxtal); 2) FSSP and 1DC data with quasi-sphere shapes (quasi); 3) no crystals with $D < 50$ μm and 1DC data for $D > 50$ μm with quasi-sphere shape (quasi50); and 4) no small crystals with D < 120 μm (large). These alternate distributions are used to assess how the uncertainties in the shape and concentration of small crystals impact the radiative properties of the cirrus.

MODELING APPROACH

Size, shape, and wavelength –dependent single-scattering properties of droxtals and large ideal ice crystals are readily available by [4] and [5], respectively. Corresponding calculations for quasi-spherical ice crystals with $D < 120$ μm have been conducted by Timo Nousiainen (unpublished data). The single-scattering properties of individual crystals are combined with the four alternative size-shape distributions to obtain vertical profiles of asymmetry parameter, single-scattering albedo and optical thickness. These profiles are then used as input to the *libradtran* radiative transfer code [6] to compute SW fluxes at the surface and at the top of the atmosphere (TOA).

RESULTS AND DISCUSSION

The modeled SW fluxes at the surface are compared against SW fluxes measured at the SGP Central Facility ([7]). Modeled and measured direct and diffuse downward fluxes at the surface are shown in Fig. 1. Fig. 2 shows the difference between cloud-free and cloudy SW upward flux at the TOA (cloud radiative forcing) based on different assumptions about small ice crystals. Simulated time series are obtained by changing only the solar zenith angle, while keeping the cloud properties fixed to those observed during the flight spiral. It is found that

especially the direct SW fluxes from measurements and calculations differ systematically. One reason could be the spatial separation of about 10 km between the locations of the flight and ground measurement. In addition, the model does not take into account three-dimensional radiative transfer, which may be important due to the inhomogeneity of the cloud.

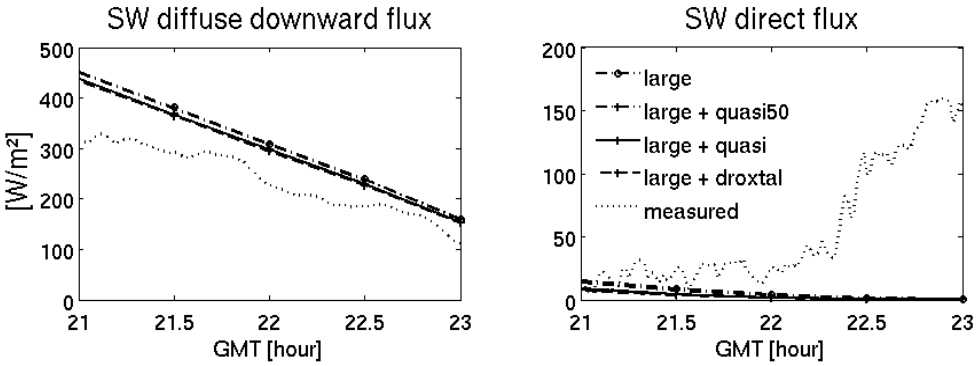

Figure 1. Modeled SW fluxes at the surface based on the alternative size-shape distributions compared against measurements.

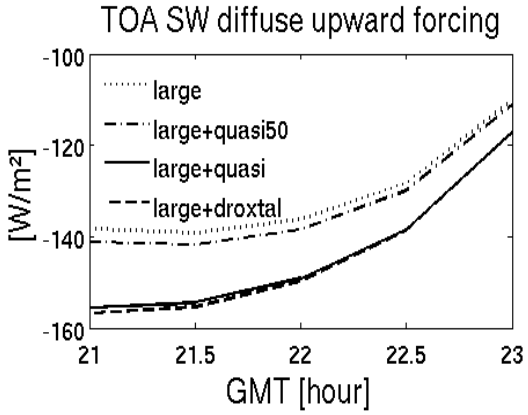

Figure 2. Modeled SW cloud radiative forcing (difference between clear and cloudy-sky upward flux) at the TOA obtained by using different size-shape distributions.

The use of different size-shape distributions does not yield remarkable differences in the SW fluxes at the surface. The use of different shape approximations for small ice crystals (droxtal and quasi-spherical) yields only a few W/m² difference in the diffuse downward flux. A realistic description of the shape of small ice crystals appears also less important than their size distribution for the SW radiative forcing at the TOA. Especially from Fig. 2, it appears that ice crystals with 5 μm < D < 50 μm have larger impacts on the SW fluxes than crystals with 50 μm < D < 120 μm. However, the concentrations for D < 50 μm were measured by an FSSP which greatly overpredicts small crystal concentrations. Hence, the results do not nec-

essarily indicate a large radiative effect of small crystals, but rather the need for reliable and accurate measurements of small crystal concentrations.

CONCLUSIONS

Modeling of the SW radiative impact of cirrus is performed by inputting the optical properties of observed size and shape distributions of ice crystals into a radiative transfer model. It is concluded that accurate information on both the concentrations and shapes of ice crystals is required to accurately model the SW radiative impact of ice clouds. In particular, assumptions about the concentration of small ice crystals are important for the SW upward flux at the TOA. More information is needed on the single-scattering properties of small ice crystals, and, first and foremost, on their concentration.

REFERENCES

[1] G.M. McFarquhar et al. Indirect and Semi-Direct Aerosol Campaign (ISDAC): The impact of arctic aerosols on clouds. Bull. Amer. Meteor. Soc. (submitted) (2010).

[2] T. Nousiainen and G.M. McFarquhar. Light scattering by Quasi-Spherical Ice Crystals. J. Atmos. Sci. **61**(18) (2004).

[3] J. Um and G.M. McFarquhar. Single-scattering properties of aggregates of plates. Q. J. R. Meteorol. Soc. **135** (2009).

[4] P. Yang, B.A. Baum, A.J. Heymsfield, Y.X. Hu, H.-L. Huang, S.-C. Tsay, and S.A. Ackerman. Single scattering properties of droxtals. J. Quant. Spectrosc. Radiat. Transfer **79-80** (2003).

[5] P. Yang, K.N. Liou, K. Wyser, and D. Mitchell. Parametrization of the scattering and absorption properties of individual ice crystals. J. Geophys. Res. **105** (2000).

[6] B. Mayer and A. Kylling. Technical note: The libRadtran software package for radiative transfer calculations – description and examples of use. Atmos. Chem. and Phys. **5** (2005).

[7] Y. Shi and C.N. Long. Best Estimate Radiation Flux Value-Added Procedure: Algorithm Operational Details and Explanations. Atmospheric Radiation Measurement Program Technical Report (ARM-TR) **008** (2002).

Single-scattering by mineral dust particles modeled with spheroids

S. Merikallio[*,1], H. Lindqvist[2], T. Nousiainen[2], and M. Kahnert[3]

[1]*Department of Climate Change, Finnish Meteorological Institute, P.O. box 503, FI-00101 Finland.*
[2]*Department of Physics, University of Helsinki, P.O. box 48, 00014 Finland.*
[3]*Swedish Meteorological and Hydrological Institute, Folkborgsvägen 1, S-60176 Sweden.*

We study how well different mineral dust samples can be modeled using spheroids and whether the best-fit spheroidal shape distributions bear any similarities that would allow us to suggest a generic first-guess shape distribution for dust. Overall, spheroids are found to fit the measurements significantly better than Mie spheres. However, it seems that best-fit shape distributions vary between samples and even between wavelengths considerably, making suggestions for a first-guess shape distribution difficult.

INTRODUCTION

Mineral dust is a very abundant aerosol species in the Earth's atmosphere with a considerable and largely uncertain radiative impact. We are interested in using spheroids to model their radiative impact in a climate model where shape distribution information is not available; thus, finding a generic, accurate shape distribution would be desirable.

MODELING APPROACH

We compare laboratory measurements [1, 2] with scattering matrices calculated from a dust optical database [3]. Measurements exist at wavelengths of 441.6 nm and 632.8 nm. The refractive indices (m) of the samples are not known accurately so, for simulations, we try four different m with $\mathrm{Re}(m) = 1.55$ and 1.7, and $\mathrm{Im}(m) = 0.001$ and 0.01. The shapes include aspect ratios from 1.2 to 2.8 with an increment of 0.2 for both oblate and prolate spheroids. In addition, the special case of spheres is computed.

For comparisons with simulations, the measured F_{11} element needs to be properly normalized. To this end, the measurements are extrapolated using simulated values for scattering angles 0 - 5° and the value measured at 173° for angles of 174 – 180° so that the normalization integral can be applied.

The cost function for assessing the separation between measurements and model is calculated at the measurement points from 5 ° to 170 ° with steps of 5 °, thus excluding 171 °, 172 ° and 173 ° to preserve the angular equality in error analysis.

* Corresponding author: Sini Merikallio (Sini.Merikallio@fmi.fi)

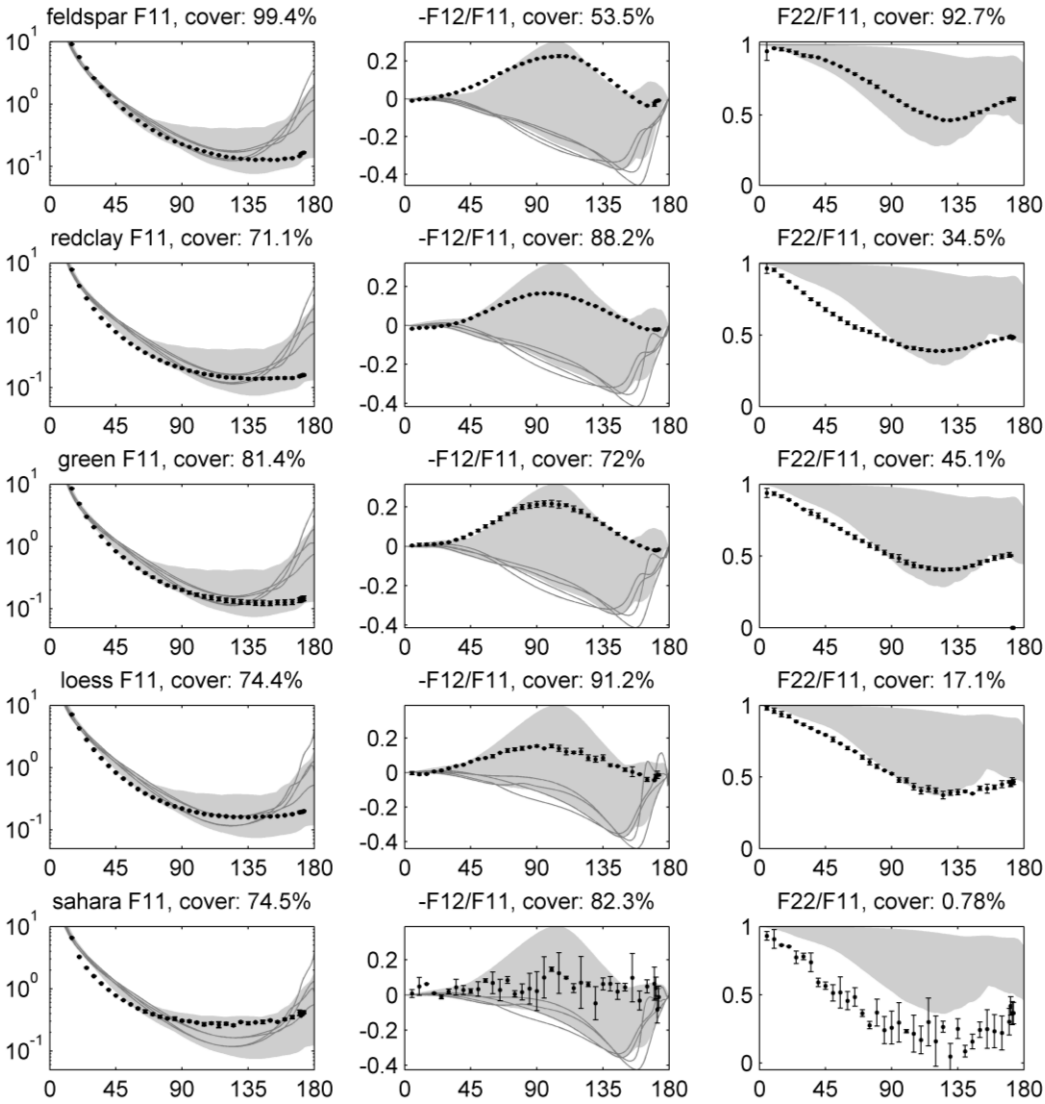

Figure 1. Coverages of measured scattering matrix elements by modeled spheroids at 632.8 nm wavelength for selected matrix elements. Each row corresponds to one sample from smallest (feldspar) to the largest effective radii (Sahara). Measurements are shown with diamonds and error bars, the shaded area indicates the coverage by all different spheroids (shapes and refractive indices) excluding spheres. The Mie spheres are shown with solid lines for each refractive index. Measured F_{11} elements have been normalized using the $n = 3$ shape distribution by [4].

ASSESSING THE OVERALL PERFORMANCE OF SPHEROIDS

The first task is to investigate how well the measured scattering matrix elements can be covered by spheroids of different shapes and refractive indices, since full coverage of measured matrix element by model spheroids is a necessary, but not sufficient, condition for fitting the measurements with simulations. In Fig. 1 three scattering matrix elements have been plotted for each dust sample studied for the wavelength of 632.8 nm. At each measurement point it is seen how much of the measurement error bar falls within the spheroid span, i.e. the relative amount of black dots that fall within the shaded area, and finally averages of these percents are tabulated and shown in subtitles. We believe the poor coverage of the depolarization element F_{22} is caused by smooth-surfaced spheroids being unable to mimic the scattering response of real rough-surfaced particles. This discrepancy is stronger for larger particles.

The coverage percentages averaged over all matrix elements and for the F_{11} element separately are shown in Table 1 for both wavelengths. It can be seen that, overall, the measurements for the samples with smallest particles can be better covered by spheroids than those for the larger ones. Interestingly, loess is covered remarkably well for its size, even comparably to the red clay.

Table 1. Coverages of spheroids for different particles.

	r_{eff} (μm)	441.6 nm, %			632.8 nm, %		
		F_{11}	avg.	std.	F_{11}	avg.	std.
feldspar	1.0	100	**92**	5	99	**89**	19
red clay	1.5	72	**62**	24	71	**58**	24
green clay	1.55	84	**61**	29	82	**63**	19
loess	3.9	76	**55**	35	75	**59**	27
Sahara	8.2	23	**43**	34	75	**48**	29

BEST-FIT SHAPE DISTRIBUTIONS

The suitability of shape distribution parameterization developed by [4] in simulating the mineral dust optical properties is investigated. Optimal shape distributions for spheroids are sought by varying the exponent n of the parametrized shape distribution, computing a cost function for the goodness of agreement, and finding the optimal value for n. In addition, we carry out fitting exercises using a non-linear fitting algorithm for selected cases. The latter method is much more demanding, but allows us to find shape distributions where the weight for each shape is optimal and independent from each other. As the fitting method can return other kinds of shape distributions than the n parametrized shape distribution, it also works as an assessment for the applicability of the first method.

Table 2 summarizes the results for the optimal parametrized shape distributions under different criteria. As the cost functions, we consider χ^2 error for the phase function F_{11}, average χ^2 error for the size independent non-zero phase matrix elements, error below which 80% of points fall (D80), again for both F_{11} and averaged over independent non-zero phase matrix elements, and finally the asymmetry parameter (g) difference.

Obviously, best fits are obtained at different n for different cases. Interestingly, they are often obtained either with the smallest (0) or largest (18) n considered. The F_{11} element, often

the most important, however, is uniformly best modeled with the equiprobable distribution (n=0). Curiously, unlike F_{11}, the asymmetry parameter g is best reached with values of n larger than zero. This may be because the calculation of asymmetry parameter takes into account also the diffraction peak whilst the other criteria only consider angles between 5° and 170 °. One intermediate value of refractive index, namely $m = 1.6 + 0.003i$ is currently being added into our analysis.

From table 2 we see that each row contains multiple refractive indices, implying that inversion of the refractive index from spheroidal simulations is not very robust for mineral dust and may be subject to artifacts arising from the use of simplified model shapes.

Table 2. The best-fit n values of shape distributions [4] using different criteria. The refractive index with which the best-fit value was obtained is indicated by: a = 1.55 + 0.001i; b = 1.55 + 0.01i; c = 1.7 + 0.001i ; and d = 1.7 + 0.01i.

	441.6 nm					632.8 nm				
	F_{11}	avg.	D80 F_{11}	D80 avg.	g	F_{11}	avg.	D80 F_{11}	D80 avg.	g
Feldspar	0 b	3 a	0 ab	0/1 ab	2 a	0 b	2 b	0 c	0 c	9 a
red clay	0 b	18 c	0 a	0 d	1 a	0 b	18 d	0 a	0 d	3 b
green clay	0 b	18 d	0 c	0 c	1 b	0 b	18 d	0 c	1 c	3 b
Loess	0 d	18 c	0 a	0 d	4 c	0 a	0 a	0 b	0 b	18 d
Sahara	0 c	0 c	0 b	0 b	0 c	0 c	0 c	0 b	0 d	0 d

While the spheroidal scheme is superior to that of spheres, its performance is far from perfect especially for samples with larger particles. The optimal shape distributions seem to vary from sample to sample, and also between wavelengths. This suggests the optimal spheroidal shape distribution is not connected to the shapes of the dust particles.

REFERENCES

[1] H. Volten, O. Muñoz, E. Rol, J. F. de Haan, W. Vassen, J. W. Hovenier, K. Muinonen, and T. Nousiainen. Scattering matrices of mineral aerosol particles at 441.6 nm and 632.8 nm. JGR **106**(D15) (2001).

[2] O. Muñoz, H. Volten, J. F. e Haan, W. Vassen, and J. W. Hovenier. Experimental determination of scattering matrices of randomly oriented fly ash and clay particles at 442 and 633 nm. JGR **106**(D19) (2001).

[3] O. Dubovik, A. Sinyuk, T. Lapyonok, B. N. Holben, M. Mishchenko, P. Yang, T. F. Eck, H. Volten, O. Muñoz, B. Veihelmann, W. J. van der Zande, J-F. Leon, M. Sorokin, and I. Slutsker. Application of spheroid models to account for aerosol particle nonsphericity in remote sensing of desert dust. JGR **111**(D11208) (2006).

[4] T. Nousiainen, M. Kahnert, and B. Veihelmann. Light scattering modeling of small feldspar aerosol particles using polyhedral prisms and spheroids. JQSRT **101** (2006).

Monte Carlo simulations of multiple light scattering by large non-spherical particles

M. Mikrenska* and P. Koulev

Institute of Mechanics, Bulgarian Academy of Sciences, Sofia 1113, Bulgaria.

We apply Monte Carlo ray tracing in order to simulate multiple light scattering by ensembles of randomly oriented non-spherical particles with large size parameter. The numerical results obtained show a common tendency for different particle shapes: the degree of polarization decreases when the mean free path decreases.

INTRODUCTION

The single-scattering approximation is the commonly used approach to particle characterization and identification [1-3]. The study of the individual polarization properties at light scattering shows strong dependence of the polarization properties on the shape, size, and refractive index of the scatterers [4-7]. However, multiple scattering is an inherent effect [8] for many natural objects (e.g., atmospheric aerosols and clouds). This effect persists in laboratory measurements as well. Therefore, one should account for multiple-scattering events. Multiple scattering in participating media is generally a complex phenomenon. Theoretical aspects of the general problem of multiple light scattering are presented in [9,10]. Numerical calculations of multiple scattering by spherical particles were reported in [11,12]. The present work is aimed at studying how the multiple scattering affects the polarization properties of an ensemble of particles with non-spherical shape.

In this paper, we extend our previously developed three-dimensional computational model for single light scattering [4-6] to examine the effect of multiple scattering by an ensemble of particles with cubic and rounded cubic shape and sizes larger than the wavelength on the intensity and polarization phase functions.

COMPUTATIONAL MODEL

We consider light scattering of an ensemble of particles randomly and sparsely distributed throughout a finite scattering volume V. The light source is a non–polarized laser. The scattering particles are supposed to be dielectric, homogeneous, transparent or weakly absorbing. They are also assumed to be cubes or rounded cubes with sizes much larger than the wavelength which allows the laws of geometric optics to be applied. The rounded cube is defined as a section of cube and sphere. The roundness parameter is characterized by the degree of roundness defined as:

* Corresponding author: Maya Mikrenska (mikr@imbm.bas.bg)

$$k = \frac{a}{d}, \tag{1}$$

where a is the cube side and d is the diameter of the sphere.

The algorithm for multiple scattering is based on the tracing of paths for a large number of rays in correspondence with geometric-optics laws. Ray tracing is done in three-dimensional geometry. For each ray-particle interaction, we apply a Monte-Carlo algorithm for single scattering by cube [4] or rounded cube [5,6]. At each optical interface, Snel's law determines the possible propagation direction and the changes of light intensities parallel and orthogonal to the scattering plane are calculated by means of Fresnel's formulas. The coefficients in Fresnel's formulas are used as probabilities for the choice of the outcome of the ray – optical interface interaction: reflection or transmission (refraction).

The free path *fp* of the ray at multiple scattering is determined by means of the mean free path *mfp* as follows:

$$fp = -\log(1\text{-}rand)*mfp, \tag{2}$$

where *rand* is a random number, uniformly distributed in [0,1].

When the traced ray leaves the scattering volume V, it is referred to the corresponding phase angle. The contribution of each traced ray is accumulated in angular bins and the final result for the degree of polarization is obtained.

It should be pointed out that the Monte-Carlo computational procedure described is capable of accounting for arbitrary shape, size, and refractive index distribution of the scatterers. The present approach is quite similar to the one developed in [13]. Both algorithms keep track of the phase jumps so that the elliptic polarization is taken into account. However, the averaging over all orientations is different: the cluster in [13] is previously generated, while in the present Monte-Carlo algorithm each ray hits particle with arbitrary orientation. Besides, we do not use facets to approximate rounded parts of the scatterers which might reduce the required computer time and/or memory.

NUMERICAL RESULTS AND DISCUSSION

The computational model is applied to examine multiple light scattering by different ensembles of randomly oriented particles. At first, computer simulations of multiple light scattering by different ensembles of randomly distributed perfect cubes and rounded cubes (roundness parameter k = 1.11) are performed and the effect of the mean free path (i.e., volume fraction of particles) on the intensity and polarization phase function is examined. In all computer simulations the refractive index of the particles is taken to be n = 1.54 which corresponds to crystals of NaCl at the wavelength of 0.63 μm. The refractive index of the surrounding media is n = 1. The scattering particles occupy a spherical region V with diameter D = 1 cm. The number of the traced rays in all numerical experiments is 10^7.

Figure 1a shows calculated values of the polarization phase function for different mean free paths of the rays traced. For comparison, the polarization phase function which corres-

ponds to single scattering by randomly oriented cube is also presented in Fig. 1a. The performed computer simulations show that the specific features of the polarization phase function at single light scattering by cube retain at multiple scattering by ensembles of cubes. The strong negative peak of polarization at backscattering and positive maximum in forward direction typical for single light scattering by cubes retain at multiple scattering by cubes. When the mean free path decreases (i.e. the volume fraction of the scatterers increases), the absolute values of the degree of polarization significantly decrease. The results obtained are quite similar to those reported for clusters of cubes [13].

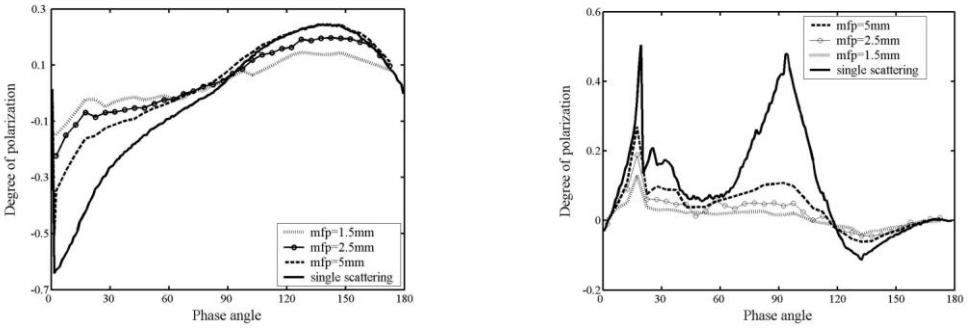

Figure 1. Polarization phase functions for different mean free paths. The scattering particles are cubes **(a)** or rounded cubes with roundness parameter $k = 1.11$ **(b)**. The scatterers with refractive index $n = 1.54$ are randomly distributed within a sphere with diameter of 1 cm.

Similar to the observed tendency for ensembles of perfect cubes, multiple scattering by rounded cubes (Fig. 1b) does not affect the qualitative behavior of the polarization curves, especially, when the mean free paths are relatively large. A decrease in the mean free path also leads to a significant decrease in the absolute values of the degree of polarization. It should be noted that the observed tendency is confirmed by the numerical experiments performed for different degree of roundness.

The second series of numerical experiments is aimed at studying the effect of multiple scattering by randomly distributed cubes on the intensity and polarization phase function. The calculated values of the polarization phase functions of randomly oriented cubic particles for different finite volumes are presented in Fig. 2. The side of the cubes is 20 μm. The volume fraction (packing density) of the particles is $p = 0.1$. For comparison, polarization phase function for semi-infinite medium [13] is also presented.

In conclusion, the results of computer simulations indicate a common tendency for different shapes of the scatterers: For relatively large mean free paths, the main features of the polarization curve retain at multiple scattering but the degree of polarization decreases considerably and tends to zero with a decrease of the mean free path. The computational model is capable of contributing to a more realistic treatment of the observed or laboratory-measured polarization data. Moreover, it allows consideration of mixture of different shapes and optical properties of the scattering particles.

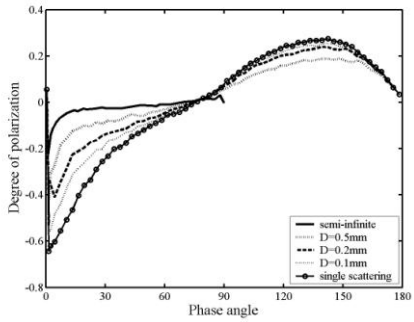

Figure 2. Polarization phase functions for different finite volumes (spheres with diameter *D*) and semi-infinite medium. The scattering particles are cubes with refractive index $n = 1.5$.

REFERENCES

[1] M.I. Mishchenko, J. W. Hovenier, and L. D. Travis (Ed). *Light Scattering by Nonspherical Particles*. Academic Press (2000).

[2] M.I. Mishchenko, L. Travis, and A. Lacis. *Scattering, Absorption and Emission of Light by Small Particles*. Cambridge University Press (2002).

[3] R. Xu. *Particle characterization: Light scattering methods*. Kluwer Academic Publishers (2000).

[4] M. Mikrenska, P. Koulev, and E. Hadamcik. Direct simulation Monte Carlo of light scattering by cube. Compt. rend. Acad. bulg. Sci. **57**(11) (2004).

[5] M. Mikrenska, P. Koulev, J.-B. Renard, E. Hadamcik, and J.-C. Worms. Direct simulation Monte Carlo of light scattering by rounded cubes. Compt. rend. Acad. bulg. Sci. **58**(3) (2005).

[6] M. Mikrenska, P. Koulev, J.-B. Renard, E. Hadamcik, and J.-C. Worms. Direct simulation Monte Carlo ray tracing model of light scattering by a class of real particles and comparison with PROGRA2 experimental results. JQSRT **100** (2006).

[7] M. Mikrenska, P. Koulev, and J.-B. Renard. Determination of the optical extinction of particulate matter by using Monte Carlo simulation of light scattering. Compt. rend. Acad. bulg. Sci. **59**(10) (2006).

[8] X.H. Chen, Q.Liu, and H.L. Wei. The treatment of scattering phase function in the multi-scattering radiative transfer calculation. J. of Light Scattering **19**(3) (2007).

[9] H.C. van de Hulst. *Multiple light scattering*. San Diego: Academic Press (1980).

[10] M.I. Mishchenko, L. D. Travis, and A.A. Lacis. *Multiple scattering of light by particles: radiative transfer and coherent backscattering*. Cambridge University Press (2006).

[11] S. Stefanov, P. Koulev, J.-C.Worms, J.-B. Renard, and E. Hadamcik. Numerical simulation of the scattering of a laser beam introduced in an ensemble of suspended particles. In: *Proc. 9th Nat. Cong. on Theor. and Appl. Mech. 2*. Sofia (2001).

[12] W. Yuehuan, S. Jianqi, and Y. Haitao. Numerical calculation of multiple scattering with the layer model. Particuology **7** (2009).

[13] Y. Grynko, Y. Shkuratov. Ray tracing simulation of light scattering by spherical clusters consisting of particles with different shapes. JQSRT **106**(1–3) (2007).

Light scattering in circumstellar disks

M. Min* and S. V. Jeffers

Astronomical institute, Univ. of Utrecht, P.O. Box 80000, NL-3508 TA Utrecht, The Netherlands.

Planets, asteroids and comets are born in disks of gas and dust surrounding newly formed stars. In these protoplanetary disks, tiny dust grains stick together to form larger bodies. How this happens and at what speed is a question we can address by carefully examining the light scattered and emitted by the dust grains in these disks. Over a timescale of $\sim$ 10 million years, the system evolves into a debris disk, i.e., a disk mainly composed of second-generation dust produced by collisions of larger bodies and outgassing of comets. These debris disks provide a unique view on what might have been the conditions in the early Solar system. Observations of these disks in scattered light provide a way to image the spatial distribution of the dust grains and, at the same time, obtain information on their sizes and structures. In this contribution, we will discuss observations and theoretical modeling of light scattered by dust grains and aggregates in these circumstellar disks. Effects of grain properties as well as effects of the disk geometry on the observables are discussed with a special focus on imaging polarimetry. Also, the computational and observational challenges we face when interpreting observations of the scattering properties of circumstellar dust are discussed.

DUSTY DISKS

It is generally accepted that the origin of grains in circumstellar disks is interstellar dust. Interstellar dust grains are considered to be small and composed of silicate and carbon [1]. In the gas-rich disks around young stars, these grains can coagulate to form larger aggregates. The growth of fluffy aggregates changes the observable signature from both scattered and emitted radiation in particular ways that are qualitatively well understood, though quantitative studies are usually restricted to small aggregates.

When the circumstellar disk evolves into a planetary system, the dust grains we observe are expected to change from the aggregates generally thought to dominate in protoplanetary disks to compact debris dust grains formed from collisions of larger bodies. These compact grains provide their own challenges to dust modelers. For example, effects of surface roughness and complex internal structure are of crucial importance for interpreting observations of scattered light [2]. Below we briefly discuss how scattered light and, in particular, imaging of scattered light, can be used to study the evolution from small grains to larger aggregates and planetesimals all the way to the collisionally formed debris found around main-sequence stars.

SCATTERED LIGHT IMAGING

Imaging protoplanetary disks or debris disks in scattered light is challenging as they are many orders of magnitude fainter than their central stars. The limited spatial resolution of the telescope causes the central star to dominate over the scattered light out to a large distance. There are two methods used to suppress the radiation from the central star: coronographic

*Corresponding author: Michiel Min (M.Min@astro-uu.nl)

imaging, where starlight is blocked by a disk in the optical setup, and polarimetric imaging, where only the scattered light from the star's circumstellar environment is detected.

Coronographic imaging

Coronographic imaging has been successfully used to image numerous circumstellar disks, both protoplanetary and debris disks. The images of protoplanetary disks show rich spatial structure, e.g. spiral arms [3]. The images of debris disks often display ringlike structures, not unlike the Kuiper belt in our Solar system (see, e.g., [4]). The albedo of the circumstellar material around debris disks can be determined from coronographic images combined with the dust's spectral energy distribution. For some debris disks, (e.g., [4]), this results in a relatively low (a few percent) value, consistent with the albedo of some types of asteroids. Additionally, scattered light images provide information on the phase function over quite a large range of scattering angles simultaneously. An example of this is the well-studied debris disk around Fomalhaut. Interestingly, it was found that the grains in this system appear to be dominantly backward scattering[5], which can be explained by very large, rough particles or compact agglomerates[2].

Polarimetric imaging

The physics behind polarimetric imaging is that starlight reflected from circumstellar material becomes linearly polarized. By imaging linearly polarized light, it is possible to clearly discriminate between scattered light from circumstellar environments and unpolarized light from the central star. Already, some polarimetric images of protoplanetary disks are available (see, e.g., [6]). Also, polarimetry has already been used for quite some time to study nearby debris disks (see, e.g., [7]).

MODELS OF DISKS

The observed intensity or polarimetric signal from a circumstellar disk depends foremost on the optical properties of the dust grains in the disk. Many studies analyzing polarimetric measurements today still use spherical particles as their dust grain model (see, e.g., [8]), even though the light-scattering community is well aware of the shortcomings of this particle shape model. Besides the optical properties of the grains, one needs to consider the geometry of the circumstellar disk as well. Gas-rich protoplanetary disks around young stars are optically very thick and, thus, multiple scattering and radiative transfer are essential when modeling these disks.

It is usually assumed that protoplanetary disks are in vertical hydrostatic equilibrium. In order to compute this, one needs to know the temperature structure. For this, the optical properties of the dust grains are needed over a very wide wavelength range. This is one of the key problems in applying advanced particle scattering tools to fully model protoplanetary disks, since most advanced methods cannot provide accurate optical properties all the way from the visual to the millimeter part of the spectrum.

Modeling polarimetric images

As an example of how dust optical properties and disk geometry both influence observables, we focus now on polarimetric imaging. This is a technique gaining in popularity which, when

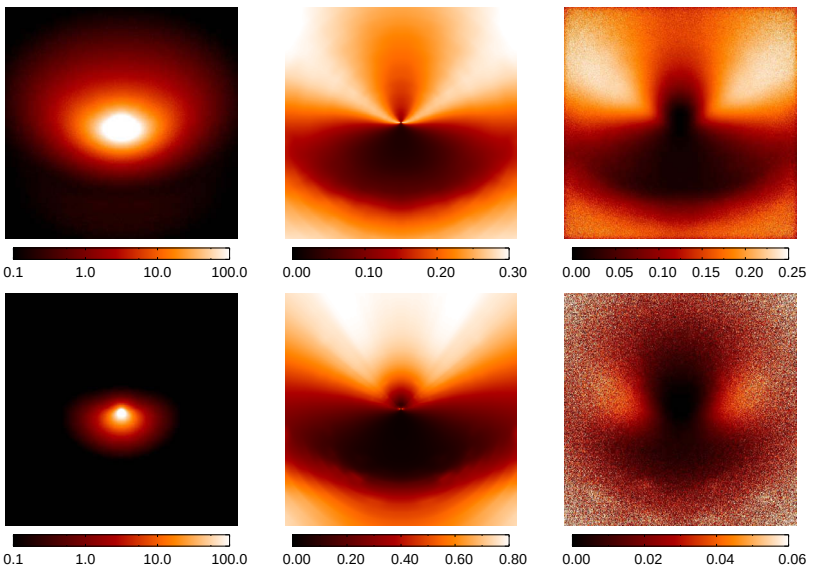

Figure 1. The total intensity (left) and degree of linear polarization (middle, and right) image of a flaring protoplanetary disk with compact grains (upper panels) and fluffy aggregates (lower panels). The size distributions of the grains are chosen such that the spectral energy distribution of the model with compact grains and that of the model with fluffy aggregates are almost identical. The rightmost image is convolved with the response of a 4-m telescope with effects of atmospheric seeing and noise added corresponding to a few hours integration.

properly used, will allow us to lift many degeneracies currently encountered in interpreting disk observations.

The degree of polarization of the light scattered by the circumstellar matter provides additional, independent constraints on the size and shape of the particles in the disk. As an example in the leftmost four panels of Fig. 1, we present model images of two protoplanetary disks. The first model, presented in the upper panels, contains compact particles (computed using the Distribution of Hollow Spheres [9]) with sizes between 0.1 and 1 µm. The second model, presented in the lower panels, contains fluffy aggregates (computed using the Aggregate Polarizability Mixing Rule [10]) with sizes between 0.1 and 10 µm. In both cases, the central star is a Herbig star ($M_\star = 2.5\,M_\odot$, $T_{\rm eff} = 10000\,{\rm K}$) surrounded by a disk with a dust mass of $M_{\rm dust} = 10^{-3}\,M_\odot$. The disk is in vertical hydrostatic equilibrium and extends from the dust evaporation radius out to 200 AU after which the surface density drops exponentially. Both models show a very similar spectral energy distribution, and almost identical infrared emission spectrum. However, it is clear that in polarized light the models can be easily distinguished (also note the difference in absolute scaling of the two polarization images). This is because the two types of grains have very different scattering characteristics.

In the rightmost two panels of Fig. 1, we show the degrees of linear polarization as they would be observed with a 4-meter class telescope from the Earth (i.e., including smearing due to diffraction at the telescope and atmospheric effects). It is clear that the image changes dramatically. Especially, the simulated observation with fluffy aggregates looks quite differ-

ent from the initial model image. This is because for this model the scattering phase function is much more forward peaked so that most radiation is scattered outside the view of the observer. Therefore, the depolarizing effect of the stellar point spread function is much stronger. So although the degree of polarization from the fluffy aggregates is intrinsically much higher than that of the compact grains, the actual observed degree of polarization is much lower. Methods have to be developed to disentangle these effects in order to properly interpret upcoming polarimetric imaging observations.

CONCLUSIONS AND PERSPECTIVE

Scattered light imaging provides a powerful diagnostic tool to study the evolution of protoplanetary to debris disks. With the proper analysis tools, it allows a determination of the sizes and structures of the dust particles and their spatial distribution. The need for optical properties of large complex aggregates and compact grains over a broad wavelength range and with relatively high values of the refractive index challenges the light-scattering community to come up with accurate and efficient computational tools. The additional constraints obtained from the polarimetric images of circumstellar disks are needed to lift the degeneracies of interpreting intensity observations. Examples of current and upcoming polarimeters are ExPo at the 4.2-m WHT, SPHERE at the 8.2-m VLT, and EPICS at the 42-m ELT. Our view on circumstellar dust is going to change dramatically with these new, sensitive polarimetric imagers.

REFERENCES

[1] B. T. Draine, and A. Li. Infrared Emission from Interstellar Dust. IV. The Silicate-Graphite-PAH Model in the Post-Spitzer Era. ApJ **657** (2007)

[2] M. Min, M. Kama, C. Dominik, and L.B.F.M. Waters. The lunar phases of dust grains orbiting Fomalhaut. A&A **509** (2010)

[3] M. Fukagawa et al. Spiral structure in the circumstellar disk around AB Aurigae. ApJ **605** (2004)

[4] P. Kalas, J. Graham, and M.A. Clampin. A planetary system as the origin of structure in Fomalhaut's dust belt. Nature **435** (2005)

[5] J.-B. Le Bouquin, O. Absil, M. Benisty, F. Massi, A. Mérand, and S. Stefl. The spin-orbit alignment of the Fomalhaut planetary system probed by optical long baseline interferometry. A&A **498** (2009)

[6] M.D. Perrin et al. The Case of AB Aurigae's Disk in Polarized Light: Is there Truly a Gap? ApJ **707** (2009)

[7] N.A. Krivova, A.V. Krivov, and I. Mann. The Disk of β Pictoris in the Light of Polarimetric Data. ApJ **539** (2000)

[8] J. Sauter et al. The circumstellar disc in the Bok globule CB 26. A&A **505** (2009)

[9] M. Min, J. W. Hovenier, and A. de Koter. Modeling optical properties of cosmic dust grains using a distribution of hollow spheres. A&A **432** (2005)

[10] M. Min, J. W. Hovenier, L. B. F. M. Waters, and A. de Koter. The infrared emission spectra of compositionally inhomogeneous aggregates composed of irregularly shaped constituents. A&A **489** (2008)

Aerosol remote sensing with the NASA Glory mission

M. I. Mishchenko*, B. Cairns, and L. D. Travis

NASA Goddard Institute for Space Studies, 2880 Broadway, New York, NY 10025, USA.

One of the principal objectives of the NASA Glory mission is to determine the global distribution of detailed aerosol and cloud properties with unprecedented accuracy, thereby facilitating the quantification of the aerosol direct and indirect radiative forcings. This objective will be met by flying the Aerosol Polarimetry Sensor which will collect accurate multi-angle photopolarimetric measurements of the Earth along the satellite ground track within a wide spectral range extending from the visible to the short-wave infrared.

INTRODUCTION

The Earth's climate depends upon the balance between incident solar radiation and the response of the atmosphere and surface via absorption, reflection, and re-radiation. Long-term changes in the composition of the atmosphere can cause global climate change and thereby affect local weather patterns having impact on the quality of human life. The composition of the atmosphere is influenced by both natural and anthropogenic effects, such as the byproducts of modern industrial societies. Over the past century the average temperature at the Earth's surface has increased by approximately 0.7°C. Accurately attributing this increase and the concomitant climate change to either natural events or anthropogenic sources (or both) is of primary importance to the establishment of scientifically and economically effective policy.

Both natural and anthropogenic aerosols are important constituents of the atmosphere affecting global temperature. Although the climate effects of aerosols are believed to be nearly comparable to those of the green-house gases, they remain poorly quantified and represent the largest uncertainty regarding climate change. Numerous recent studies have indicated that the current uncertainties in the aerosol forcings are so large that they preclude the requisite climate model evaluation by comparison with observed global temperature change. These uncertainties must be reduced significantly for uncertainty in climate sensitivity to be adequately constrained. Helping to address this overarching objective is the main purpose of the Aerosol Polarimetry Sensor (APS) on-board the NASA Glory mission, a remote-sensing Earth-orbiting observatory scheduled for launch in November 2010 as part of the A-Train constellation of Earth-orbiting satellites [1].

SCIENTIFIC OBJECTIVES OF THE GLORY APS

The Glory APS is intended to meet the following three scientific objectives:

* Correspondig author: Michael Mishchenko (mmishchenko@giss.nasa.gov)

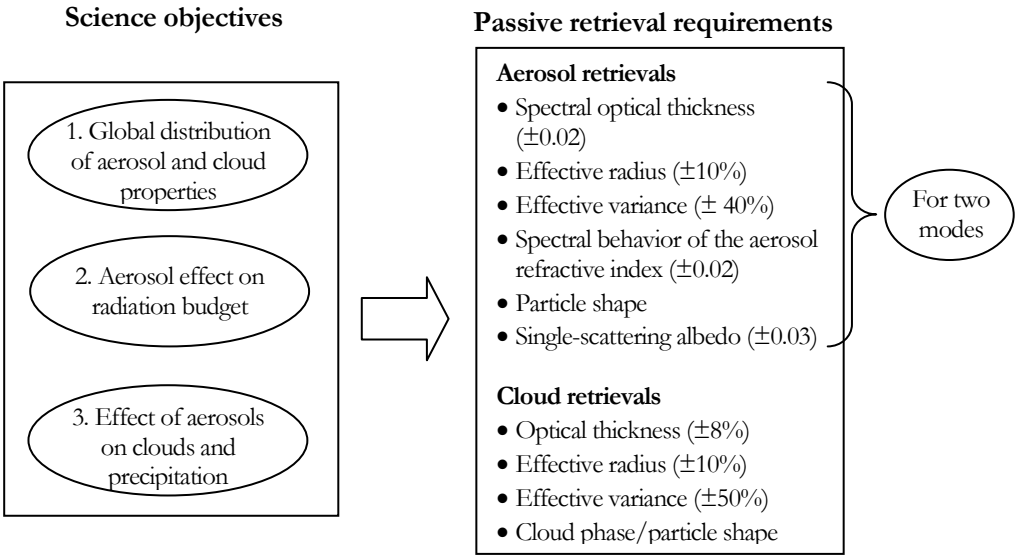

Figure 1. Flowdown of geoscience objectives into specific retrieval requirements for a passive aerosol/cloud satellite instrument [2].

- Facilitate the quantification of the aerosol direct and indirect effects on climate by determining the global distribution of the optical thickness and microphysical properties of natural and anthropogenic aerosols and clouds with much improved accuracy.
- Provide better aerosol representations for use in aerosol assessments by other operational satellite instruments.
- Provide an improved framework for the formulation of future comprehensive satellite missions for aerosol, cloud, and ocean color research.

The left-hand panel of Fig. 1 summarizes the overall scientific objectives of a coordinated and systematic approach for dramatically improving our understanding of aerosol climate impacts and environmental interactions. To achieve these objectives, one needs advanced models coupled with a comprehensive set of accurate constraints in the form of *in situ* measured and remotely retrieved aerosol and cloud distributions and properties. Accordingly, the right-hand panel of Fig. 1 lists the minimal set of aerosol and cloud parameters that must be contributed by a passive satellite instrument in order to facilitate the global quantification of the direct and indirect aerosol effects on climate.

The aerosol measurement requirements include the retrieval of the total column optical thickness (OT) and average column values of the effective radius and effective variance, the real part of the refractive index, and the single-scattering albedo. Since the aerosol population is typically bimodal, all these parameters must be determined for each mode. The refractive index must be determined at multiple wavelengths in a wide spectral range since this is the only means of constraining aerosol chemical composition from space. An integral part of the retrieval procedure must be the detection of nonspherical aerosols such as dust-like and soot particles since nonsphericity can significantly affect the results of optical thickness, refractive index, and size retrievals. The respective minimum cloud measurement requirements include the retrieval of the column cloud OT and the

average column cloud droplet size distribution as well as the determination of the cloud phase and detection of cloud particle nonsphericity.

The criteria for specifying the corresponding measurement accuracy requirements in the right-hand panel of Fig. 1 are dictated by the need to

- detect plausible changes in the direct and indirect aerosol radiative forcings estimated to be possible during the next 20 years; and
- quantify the contribution of these forcings to the planetary energy balance.

APS DESIGN

The unique APS design allows one to take full advantage of the extreme sensitivity of high-accuracy polarization data to aerosol and cloud particle microphysics coupled with the advanced modeling capabilities and thereby ensures the retrieval of all the quantities listed in the right-hand panel of Fig. 1. The flowdown of APS measurement capabilities into the requisite aerosol and cloud retrieval capabilities is summarized in Table 1. The key measurement requirements for the retrieval of aerosol and cloud properties from photopolarimetric data are *high accuracy*, a *broad spectral range*, and observations from *multiple angles*, including a method for reliable and stable *calibration* of the measurements. The APS built for the Glory mission by Raytheon [1] meets these requirements.

The measurement approach required to ensure *high accuracy* in polarimetric observations employs a Wollaston prism. The field stop constrains the APS instantaneous field of view (IFOV) to 8±0.4 mrad which, at the nominal Glory altitude (705 km), yields a geometric IFOV of 5.6 km at nadir. The spatial field is defined by the relay telescope and is collimated prior to the polarization separation provided by the Wollaston prism. This method guarantees that the measured orthogonal polarization states come from the same scene at the same time and allows the required polarimetric accuracy of 0.2% be attained. To measure the Stokes parameters that define the state of linear polarization (I, Q, and U), the APS employs a pair of telescopes with one telescope measuring I and Q and the other telescope measuring I and U. The *broad spectral range* of the APS is provided by dichroic beam splitters and interference filters that define nine spectral channels centered at the wavelengths λ = 410, 443, 555, 670, 865, 910, 1370, 1610 and 2200 nm. Blue enhanced silicon detectors are used in the visible and near-IR channels, while HgCdTe detectors, passively cooled to 160 K, are used in the short-wave IR channels and offer the very high signal-to-noise ratio required to yield a polarimetric accuracy better than 0.3% for typical clear sky scenes over the dark ocean surface.

All spectral channels but the 910- and 1370-nm ones are free of strong gaseous absorption bands. The 1370-nm exception is centered at a major water vapor absorption band and is specifically intended for characterization of thin cirrus clouds and stratospheric aerosols. The locations of the other APS spectral channels are consistent with an optimized aerosol retrieval strategy because they take advantage of several natural circumstances such as the darkness of the ocean at longer wavelengths in the visible and near-infrared, the lower land albedo at shorter visible wavelengths, and the potential for using the 2200-nm band to characterize the land surface contribution at visible wavelengths. The 910-nm band provides information on column water vapor amount.

The ability to view a scene from *multiple angles* is provided by scanning the APS IFOV along the spacecraft ground track with a rotation rate of 40.7 revolutions per minute with angular samples acquired every 8±0.4 mrad, thereby yielding ~250 scattering angles per scene. The polarization-compensated scanner assembly includes a pair of matched mirrors operating in an orthogonal configuration and has been demonstrated to yield instrumental polarization less than 0.05%. The APS viewing angle range at the Earth is from +60° to –80° with respect to nadir. The scanner assembly also allows a set of *calibrators* to be viewed on the side of the scan rotation opposite to the Earth. The APS on-board references provide comprehensive tracking of polarimetric calibration throughout each orbit, while radiometric stability is tracked monthly using observations of the moon to ensure that aerosol and cloud retrieval products are stable over the period of the mission.

Table 1. Flowdown of APS measurement characteristics into specific retrieval capabilities.

Measurement characteristics	Retrieval capacity
Precise and accurate polarimetry (~0.1%)	Particle size distribution, refractive index, shape
Wide scattering angle range for both intensity and polarization	Particle size distribution, refractive index, shape
Multiple (> 30) viewing angles for both intensity and polarization	(i) Particle size distribution, refractive index, shape (ii) Ocean surface roughness
Multiple (> 60) viewing angles for polarization	Cloud particle distribution, refractive index
Multiple (> 30) viewing angles and accurate polarimetry	Aerosol retrievals in cloud-contaminated pixels
Wide spectral range (400–2200 nm) for both intensity and polarization	(i) Separation of submicron and supermicron particles (ii) Spectral refractive index → chemical composition
1370 nm channel for both intensity and polarization	Detection and characterization of thin cirrus clouds and stratospheric aerosols
2200 nm polarization channel	Characterization of the land surface contribution at visible wavelengths
910 nm channel	Column water vapor amount

REFERENCES

[1] M. I. Mishchenko et al. Accurate monitoring of terrestrial aerosols and total solar irradiance: introducing the Glory mission. Bull. Amer. Meteorol. Soc. **88** (2007).

[2] M. I. Mishchenko et al. Monitoring of aerosol forcing of climate from space: analysis of measurement requirements. JQSRT **88** (2004).

Two-dimensional photonic crystals: method of coherent transmission and reflection coefficients computation

A. Miskevich and V. Loiko*

B.I. Stepanov Institute of physics of NAS of Belarus, Nezalezhnastsi ave., 68, Minsk, 220072, Belarus.

A method of two-dimensional (2D) photonic crystal (PC) coherent transmission and reflection coefficients calculation is proposed. It is based on the radial distribution function of an actual PC simulation by blurring the coordination circles of an ideal PC. The computations are performed under the quasi-crystalline approximation of the theory of multiple scattering of waves.

INTRODUCTION

We used the quasicrystalline approximation (QCA) of the theory of multiple scattering of waves to calculate coherent transmittance and reflectance [1-3] of the two-dimensional periodically modulated refractive-index structure, namely photonic crystal (PC) [4]. Using this approximation the spatial arrangement of particles is described by the radial distribution function (RDF) [5], characterizing the probability of particles to be located at a distance R from each other. In partially ordered layers short-range ordering is realized, and RDF tends toward unity at short separation distances (less than ten particle diameters) [3]. In the PCs a long-range ordering of particles is realized. RDF converges toward unity at very large distances between particles, making the problem of numerical calculation of transmittance and reflectance under the quasicrystalline approximation extremely cumbersome. We propose a method of 2D PC radial distribution function simulation, which takes into account long-range ordering of particles and allows for a dramatically simpler scattering solution.

METHOD OF PHOTONIC CRYSTAL RADIAL DISTRIBUTION FUNCTION SIMULATION

We consider the 2D PC with triangular, square, and hexagonal arrangements of identical spherical particles (see Fig. 1). To calculate coherent transmission and reflection coefficients of the PC we use the QCA. This approximation takes into account the spatial distribution of particles in a layer, which determines their optical interaction. The spatial distribution of particles is described by a radial distribution function. It characterizes the probability of finding of particle in space relative to any selected particle [5].

* Corresponding author: Valery A. Loiko (loiko@dragon.bas-net.by)

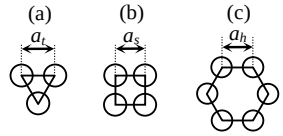

Figure 1. Schematic presentation of unit cells of triangular (a), square (b), and hexagonal (c) lattices. Circles in the lattice sites represent spherical monodisperse particles. a_t, a_s, and a_h are lattice constants for triangular, square and hexagonal lattices, respectively.

To simulate the RDF of an actual PC, we first compute the dependence of the number of particles on distance for the ideal PC. Thereto we select the center of any particle as a coordinate origin and compute relative to it the amount of particle centers as the function of distance *N(R)*. All particle centers located on the same distance *R* from the coordinate origin lie on a coordination sphere [5] (or circle in the case of 2D layer) with radius $R=R_i$. Function $N(R)=N_i$ if $R=R_i$, and $N(R)=0$ if $R \neq R_i$ (N_i is the number of particle centers on the coordination circle with radius R_i). For illustration, we show function *N(R)* for the triangular lattice in Fig. 2.

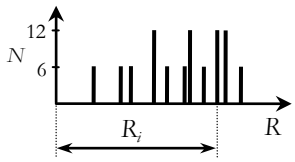

Figure 2. Function showing the number of particles as a function of distance for the triangular lattice. R_i is the radius of the *i*-th coordination circle.

On the basis of the obtained *N(R)* function we simulate the RDF of the actual PC. We use the equation for calculation of the RDF of the simulated photonic crystal:

$$g(u) = \rho_0^{-1} \sum_i \frac{N_i}{2\pi R_i} \frac{1}{\sqrt{2\pi}\sigma} \exp\left(-\frac{(u-R_i)^2}{2\sigma^2} \right). \quad (1)$$

Here $u=R/D$ is dimensionless distance (in particle diameters *D*), ρ_0 is the mean surface numerical concentration (i.e., the ratio of the number of layer particles to the layer area when the area tends to infinity) of particles, N_i is the number of particle centers on the coordination circle with radius R_i (here R_i are determined in particle diameters *D*). We specify parameter σ as a function of distance: $\sigma = \sigma(u)$ that determines the dispersion of the coordination circles radii of the simulated PC and the distance, where the RDF converges to unity. This distance is called the length of correlation (or the correlation length) l_c. The correlation length of a system characterizes the scale of its spatial order. To find the minimal correlation length $l_c^{\min}$ of the PC (i.e. the minimal radius of the coordination circle in which we have to take into account the influence of the particle ordering on light scattering) we estimated the change of its concentration on distance from the coordinate origin. We reveal that $l_c^{\min}$ of the PC is about several tens. We specify $\sigma(u)$ so that the RDF converges to unity with distance

approximately equal to $l_c^{\min}$. We have found that function $\sigma(u) = \sigma_0 u$ can be used to simulate the radial distribution function in a wide range of photonic crystal parameters (σ_0 is the "initial deviation" of radii). It allows us to simulate the RDF with good agreement with the experimental data [6]. The simulated RDF of the PC calculated by the Eq.(1) for the triangular lattice is displayed in Fig. 3. The results are obtained with $\sigma(u) = \sigma_0 u$, $\sigma_0 = 0.01$ and the filling coefficient of a layer (the ratio of particle projections to the area, where they are located) $\eta = 0.5$. The summations in Eq. (1) are implemented over the range of $\pm 10\sigma$ from each u-point.

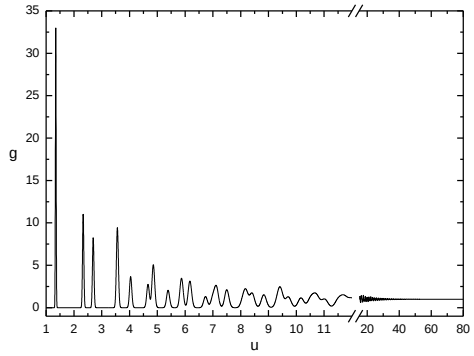

Figure 3. Simulated RDF of PC with the triangular lattice: η=0.5, $\sigma(u) = \sigma_0 u$, σ_0=0.01.

CONCENTRATION DEPENDENCES OF COHERENT TRANSMISSION AND REFLECTION COEFFICIENTS OF PHOTONIC CRYSTAL

We used simulated by Eq. (1) RDFs to calculate coherent transmission T_c and reflection R_c coefficients of PC under the QCA[2,3]. These dependences on size parameter $x=\pi D/\lambda$ (where D is the particle diameter, λ is wavelength of incident light) for PC with the triangular lattice are displayed in Fig. 4 at different filling coefficients η.

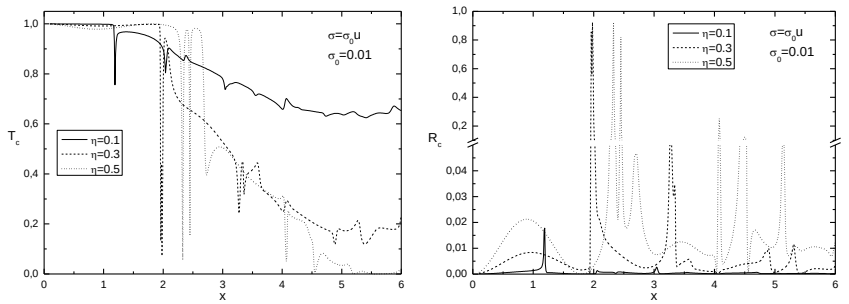

Figure 4. Dependences of coherent transmittance T_c (left) and reflectance R_c (right) of PC with triangular lattice on x at different η. Particles complex refractive index m=1.4+5×10^{-5}i.

The dependences of T_c and R_c for a partially ordered layer with the same filling coefficients and particle refractive indices (as in Fig.4) are displayed in Fig. 5. The data are calcu-

lated under the QCA using the RDF of the partially ordered layer simulated on the base of the Percus-Yevick approximation[3,5]. The data displayed in Figs. 4 and 5 show a dramatic influence of spatial ordering on coherent transmittance and reflectance of the layer. The filling coefficient of the layer has a profound influence (Fig.4) on the location and depth of the photonic band gap (PBG). The displayed data indicate as well, that the PBG occurs even at low concentrations of particles in the PC. The dependencies $T_c(x)$ and $R_c(x)$ of partially ordered layers are smooth.

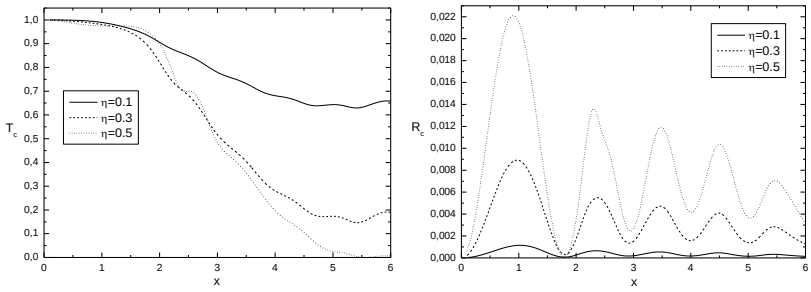

Figure 5. Dependencies of coherent transmittance T_c (left) and reflectance R_c (right) of partially ordered layer on x at different η. Particles complex refractive index $m=1.4+5\times10^{-5}i$.

CONCLUSION

A method for calculation of coherent transmittance and reflectance of a PC is proposed. The obtained radial distribution function is in good agreement with the experimental data. The criterion of correlation length of the PC is derived. Calculation of coherent transmission and reflection coefficients of a PC and partially ordered layer were performed under the QCA. There is a strong difference in the concentration dependencies of transmittance and reflectance of PC and partially ordered layers.

The results can be applied to the design and fabrication of high-efficiency solar cells, highlight-emitting diodes, antireflection layers, extraordinary-transmitting electrodes, etc.

REFERENCES

[1] A. Ishimaru. *Wave Propagation and Scattering in Random Media*. Academic, NY (1978).

[2] K. M. Hong. Multiple scattering of electromagnetic waves by a crowded monolayer of spheres: Application to migration imaging films. J. Opt. Soc. Am. **70** (1980).

[3] V. A. Loiko and A. A. Miskevich. Light propagation through a monolayer of discrete scatterers: analysis of coherent transmission and reflection coefficients. Appl. Opt. **44**(18) (2005).

[4] E. Yablonovitch. Inhibited spontaneous emission in solid-state physics and electronics. Phys. Rev. Lett. **58** (1987).

[5] J. M. Ziman. *Models of Disorder*. Cambridge University (1979).

[6] R. Rengarajan and D. Mittleman. Effect of disorder on the optical properties of colloidal crystals. Phys. Rev. E **71** (2005).

Tunable optical properties of ZnS nanoparticles

M. Moussaoui[1], R. Saoudi[*,1], A. V. Tishchenko[1], and F. Chassagneux[2]

[1]*Université de Lyon, Université Jean Monnet, Laboratoire Hubert Curien CNRS UMR5516,18 Rue du Professeur Benoît Lauras, 42000, Saint-Etienne, France.*

[2]*Université de Lyon, Laboratoire Multimatériaux et Interfaces UMR5615, 43 Bd du 11 novembre 1918, 69622, Lyon France.*

In this study, we synthesized ZnS nanopowders with size ranging from 2 to 200 nm by a simple, low-cost, and mass production chemical method. The nanoparticles were characterised by X-ray powder diffraction (XRD), Atomic force microscopy (AFM), Transmission electron microscopy (TEM), and UV–VIS absorption spectroscopy. From the optical response of ZnS nanoparticles, we estimate the band gap and dielectric permittivity.

INTRODUCTION

When semiconductor particles are reduced in scale to nanometer dimensions, their physical properties differ noticeably from those of the corresponding bulk material and depend on the size and the morphology of the studied structures [1, 2]. The extremely small size of these nanoparticles (NPs) result in quantum confinement of the photogenerated electron-hole pair. When the radius of the particle approaches the Bohr radius of the exciton, the quantum size effect becomes apparent: the energy gap increases with decreasing grain size, which leads to a blueshift of the optical absorption edge with respect to the bulk material [3]. In order to exploit these size-tuneable properties, many works have been devoted to the development of simple methods for synthesizing semiconductor particles of various sizes in a controllable manner [4]. Zinc sulfide (ZnS) is an important direct wide-band-gap (Eg = 3.6 eV at 300 K) semiconductor, which is considered important for applications such as ultraviolet-light-emitting diodes, electroluminescent devices, flat-panel displays, sensors, and injection lasers [5].

In this contribution, ZnS nanoparticles with size ranging from 2 to 200 nm were prepared from an easy and economic chemical method. The synthesis of ZnS NPs was based on the reaction of zinc acetate and thioacetamide. The resulting mixture was heat treated at different temperatures. After the reaction was completed, the resulting product was collected by centrifuging to select a size distribution. The NPs were characterised by X-ray powder diffraction (XRD), atomic force microscopy (AFM), transmission electron microscopy (TEM), and UV–VIS absorption spectroscopy.

To investigate the optimal reaction condition for the fabrication of ZnS NPs, series of experiments have been carried out by changing the experimental parameters. We have observed that the ZnS nanopowder size distribution depends on duration and temperature elaboration.

* Corresponding author: Rachida Saoudi (saoudi@univ-st-etienne.fr)

The XRD pattern of the ZnS NP elaborated at 100°C - 1H is shown in Fig. 1. The spectrum exhibits that ZnS is in pure cubic phase. The three diffraction peaks correspond to (1 1 1), (2 2 0) and (3 1 1) planes, respectively. An average crystallite size of about 3 nm was estimated according to the line width analysis of the (111) diffraction peak based on the Scherrer formula [6].

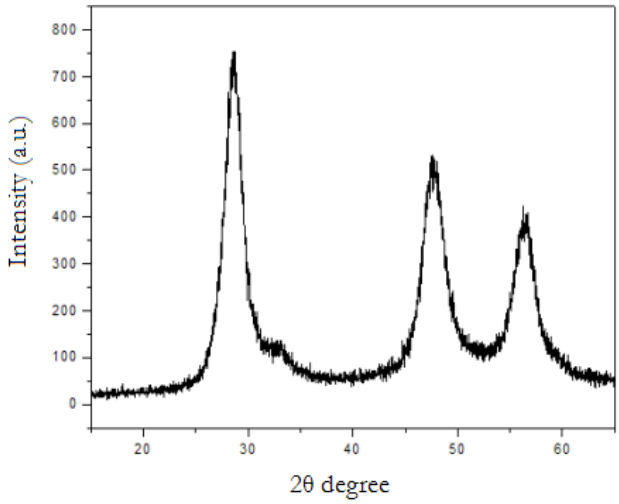

Figure 1. X-ray diffraction pattern of ZnS nanoparticles.

From the AFM picture (Fig. 2) we observe, for the selected scan area, that the ZnS nanoparticles are almost spherical and have diameter ranging from 20 to 100 nm. Fig.3 shows the TEM image of the prepared nanopowders. It can be seen that the majority of the nanoparticles has the average size less than 10 nm and a spherical shape.

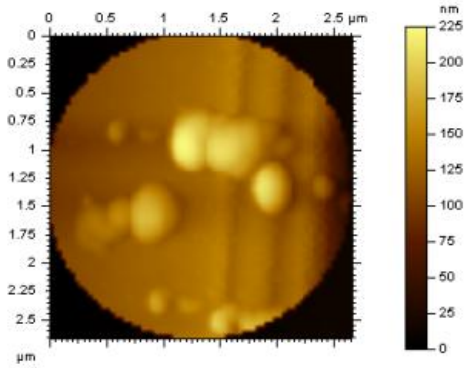

Figure 2. AFM image of the prepared ZnS nanoparticles.

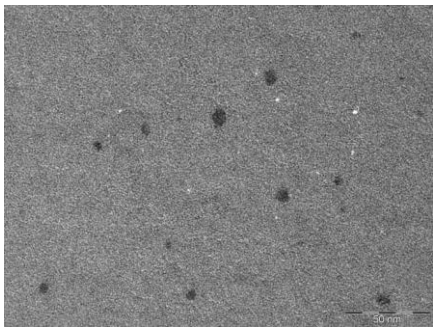

Figure 3. TEM image of the prepared ZnS nanoparticles.

UV-VIS spectra were measured in matched quartz cells of 5 mm path length in lambda 900 spetrophotometer. Fig. 3 is the UV–VIS absorption spectrum of freshly prepared ZnS NPs, which was recorded after the powder sample being dispersed in water. It shows an absorption peak at 323 nm (E = 3.84 eV), which is considerably blue-shifted from 340 nm ($\mathrm{E_g = 3.65\,eV}$) for bulk zinc blende ZnS because of quantum size effect [7].

The resulting estimated average diameter of the nanoparticles is 3 nm, in close agreement with the diameter measured from XRD studies.

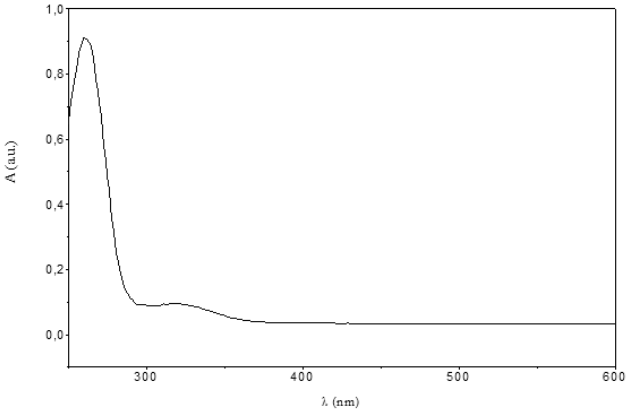

Figure 3. UV–VIS absorption spectrum of the ZnS nanoparticles.

We also studied the dependence of band gap, diameter, and dielectric permittivity of ZnS nanoparticles on treatment parameters (temperature and duration). The direct allowed optical band gap of the ZnS NPs was estimated from the Tauc plot [8] according to the following relation:

$$(\alpha h\upsilon)^2 = \mathrm{C}(\mathrm{h}\upsilon - \mathrm{E_g}) \qquad (1)$$

where α, ν, C, and E_g are the molar absorption coefficient, frequency of light, an arbitrary constant and the band gap of the nanoparticles, respectively. The obtained $\mathrm{E_g}$ was fairly

large (4.97 – 3.84 eV) in comparison with the bulk ZnS value (3.68 eV) corresponding to the ZnS nanoparticle diameters of 2.7 to 10 nm, respectively.

The dielectric permittivity ε of ZnS nanoparticles was also calculated from Wang equation [9]:

$$E_g = E + \left(\frac{\hbar^2 \pi^2}{2R^2}\right) \times \left(\frac{1}{m_e} + \frac{1}{m_h}\right) - \frac{1.786 e^2}{\varepsilon R} \quad (2)$$

where E is the bulk band gap of ZnS (3.68 eV), m_e and m_h are the effective mass of electron and the effective mass of the hole respectively, and R the nanoparticle radius.

The obtained dielectric permittivity value falls in the range of 8.43 10^{-11} to 10.19 10^{-11} C^2 $J^{-1}m^{-1}$ to within a diameter of 1.6 to 2.5 nm. From our experiments we confirm that the estimated permittivity ε increases with the nanoparticle diameter [7, 10].

We also measured the light scattering for different ZnS NPs concentrations in solutions. The results of these measurements permit us to determine the limits in which the optical index of ZnS water dispersed NPs can be measured precisely.

REFERENCES

[1] A. K. Bandyopadhyay. *Nano Materials*. NewAge International (P) Ltd. Publishers (2008).

[2] A. L. Rogach. *Semiconductor Nanocrystal Quantum Dots: Synthesis, Assembly, Spectroscopy and Applications*. Springer-Verlag/Wien (2008).

[3] C. Burda, X. Chen, R. Narayanan, and M. A. El-Sayed, Chemistry and Properties of Nanocrystals of Different Shapes. Chem. Rev. **105** (2005).

[4] G. Schmid. *Nanoparticles from theory to application*. WILEY-VCH Verlag GmbH Co.KGaA (2004).

[5] G. Cao. *Nanostructures and nanomaterials*. Imperial College Press (2004).

[6] B.D. Cullity. *Element of X-ray Diffraction*. A.W.R.C.Inc. Massachchusetts (1967).

[7] A. D. Yoffe. Semiconductor quantum dots and related systems: electronic, optical, luminescence and related properties of low dimensional systems. Advances in Physics **50**(1) (2001).

[8] J.Tauc and A. Menth. States in the gap. Journal of Non-Crystalline Solids **569** (1972).

[9] Y. Wang and N. Herron. Nanometer-Sized Semiconductor Clusters: Materials Synthesis, Quantum Size Effects, and Photophysical properties. J. Phys. Chem. **95** (1991).

[10] V. Turco Liveri. *Controlled Synthesis of Nanoparticles in Microheterogeneous Systems*. Springer (2006).

Laboratory measurements for small particles in single-scattering conditions

O. Muñoz*

Instituto de Astrofísica de Andalucía, CSIC, Glorieta de la Astronomía s/n, 18080 Granada, Spain.

A brief review is presented of the main experimental techniques for studying the effects of nonsphericity on light scattering by small particles in air.

INTRODUCTION

Small particles exist in a wide variety of scenarios ranging from the Earth atmosphere to other planetary and cometary atmospheres in the Solar System, interplanetary medium, reflection nebulae, atmospheres of brown dwarfs, etc. (see Fig. 1). Those small particles play an important role in the radiative balance of the body under study. Light scattering properties of homogeneous spherical particles can be easily computed from Lorenz-Mie theory. However, in the majority of the above mentioned cases, the assumption of spherical particles is highly unrealistic. Some examples of such nonspherical particles are presented in Fig. 2. Prof. van de Hulst published in 1957 his famous book Light scattering by small particles [1]. By that time it was already clear that many atmospheric and cosmic dust particles presented nonspherical shapes. However, limitations in computational resources inhibited reliable computations of light scattering by non-spherical particles. In the 1960's-1970's, the microwave analog method started shedding some light on the scattering behavior of small irregular particles [2, 3]. Meanwhile, first attempts in the visible part of the spectrum were made to experimentally obtain all 16 elements of the 4×4 scattering matrix of irregular particles [4, 5].

Nowadays, even with ever-increasing computer power and sophistication of algorithms, the characterization of small irregular particles from the observed scattered light remains an extremely difficult task due to the complicated morphology of these particles. Consequently, controlled experimental studies of light scattering by irregular dust particles remain a unique and indispensable tool for interpreting space- and ground-based observations. In addition, combination of measurements with powerful simulation methods allows us to evaluate models used to calculate scattering properties of nonspherical particles (e.g. [6--9]). Once the model is tested, we can perform calculations for certain physical properties of the particles or wavelengths for which experiments are highly difficult or not possible at all.

LIGHT SCATTERING EXPERIMENTS

There are various approaches to study the light scattering by irregular mineral particles. The microwave analog experiment is based on the fact that two particles that only differ in size have the same scattering properties if their ratios of size and wavelength are the same. Thus, for this type of measurements a centimeter-sized scattering target with the refractive index and shape of interest is manufactured. Microwave radiation is then scattered by this object

*Corresponding author: Olga Muñoz (olga@iaa.es)

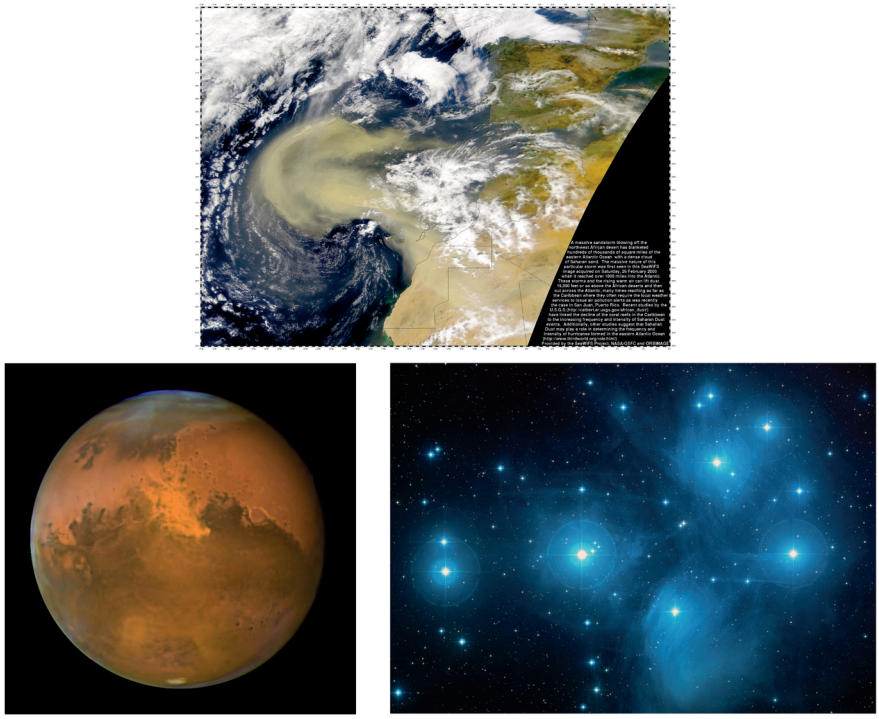

Figure 1. Dust storm sweeps from Africa over the Atlantic (top). Image courtesy Norman Kuring, SeaWifs Project. HST picture of Mars (Bottom left panel), Credit: NASA, ESA, The Hubble Heritage Team (STScI/AURA), J. Bell (Cornell University) and M. Wolff (Space Science Institute); HST image of The Pleiades, one of the nearest examples of a reflection nebula (bottom right panel).

and the results are extrapolated for other wavelengths by keeping the ratio of size and wavelength fixed [2, 3, 10]. The main advantage of this technique is the high control over the shape, size and refractive index of the particle under study. However, the main drawback of microwave measurements is that they can only be performed for one size, shape, and orientation at a time. Therefore, the simulation of a realistic sample of particles in random orientation is almost an impossible task.

Another approach is to let a beam of light be scattered by an ensemble of randomly oriented particles and measure the phase function and/or degree of linear polarization for incident unpolarized light [11--16] , or preferably the full scattering matrix as a function of the scattering angle [4,5,17--23] . The latter approach presents some advantages. For instance, the complete scattering matrix is needed to perform multiple scattering calculations in scattering media such as planetary atmospheres and circumstellar disks. Moreover, measuring all elements of the scattering matrix help us in identifying errors in the electronics or in the alignment of the optics involved in the experiment since all theoretical relationships valid for the elements of the scattering matrix [24] can be applied for tests.

Some measurements performed with various instruments will be presented at the conference to show what can we learn about small irregular particles from laboratory measure-

ments.

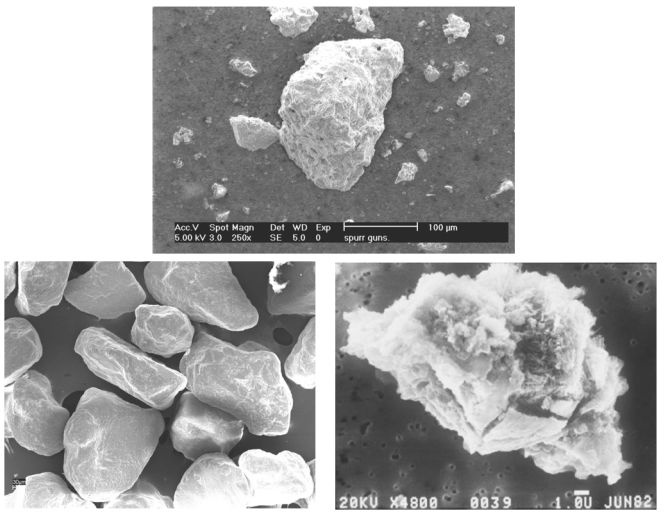

Figure 2. Scanning Electronic Microscope images of different small particles: volcanic ash from Mount Spurr volcano (top panel), desert dust from the Sahara (bottom left panel) (Amsterdam Light Scattering Database), right bottom panel example of an interplanetary dust particle collected at high altitude in the atmosphere of the Earth. Courtesy: NASA/JSC/CDLF.

Acknowledgments: It is a pleasure to thank Joop W. Hovenier for fruitful suggestions on a previous version of this abstract.

REFERENCES

[1] H.C. van de Hulst. *Light scattering by small particles*. Dover Publications, Inc. New York (1957).

[2] J.M. Greenberg, N.E. Pedersen, and J.C. Pedersen. Microwave analog to the scattering of light by nonspherical particles. J. Appl. Phys. **32** (1961).

[3] R. Zerrull and R.H. Giese. Microwave analog studies. In: *Planets, Stars and Nebulae Studied with Photopolarimetry*. T. Gehrels (ed.). Univ. of Arizona Press, Tucson, AZ (1974).

[4] A.C. Holland and G. Gagne. The scattering of polarized light by polydisperse systems of irregular particles. Appl. Opt. **9** (1970).

[5] A.J. Hunt and D.R. Huffman. A new polarization-modulated light scattering instrument. Rev. Sci. Instrum. **44** (1973).

[6] M.I. Mishchenko, L.D. Travis, R.A. Kahn, and R.A. West. Modeling phase functions for dustlike tropospheric aerosols using a shape mixture of randomly oriented polydisperse spheroids. J. Geophys. Res. **102** (1997).

[7] T. Nousiainen, M. Kahnert, and B. Veihelmann. Light scattering modeling of small feldspar aerosol particles using polyhedral prisms and spheroids. JQSRT **101** (2006).

[8] O. Dubovik, A. Sinyak,T. Lapyonok, B.N. Holben, M.I. Mishchenko, P. Ynag, T.F. Eck, H. Volten, O. Muñoz, B. Veihelmann, W. van der Zande, J.-F. Leon, M. Sorokin, and I.

Slukster. Application of spheroid models to account for aerosol particle nonsphericity in remote sensing of desert dust. J. Geophys. Res. **111** (2006).

[9] K. Muinonen, T. Nousiainen, H. Lindqvist, O. Muñoz, and G. Videen. Light scattering by Gaussian particles with internal inclusions and roughened surfaces using ray optics. JQSRT **110** (2009).

[10] B.Å.S. Gustafson. Microwave analog to light scattering measurements. In: *Light Scattering by Nonspherical Particles: Theory, Measurements, and Applications*. M.I. Mishchenko, J.W. Hovenier, and L.D. Travis (eds.). Academic Press, San Diego (2000).

[11] D.L. Jaggard, C. Hill, R.W. Shorthill, R.W. Stuart, M. Glantz, F. Rossworg, B. Taggart, and S. Hammond. Light scattering from particles of regular and irregular shape. Atmos. Environ. **15** (1981).

[12] K. Weiss-Wrana. Optical properties of interplanetary dust — Comparison with light scattering by larger meteoritic and terrestrial grains. Astron. Astrophys. **126** (1983).

[13] R.A. West, L.R. Doose, A.M. Eibl, M.G. Tomasko, and M.I. Mishchenko. Laboratory measurements of mineral dust scattering phase function and linear polarization. J. Geophys. Res. **102** (1997).

[14] D.B. Curtis, B. Meland, M. Aycibin, N. Arnold, V.H. Grassian, M. Young, and P.D. Kleiber. A laboratory investigation of light scattering from representative components of mineral dust aerosol at a wavelength of 550 nm. J. Geophys. Res. **113**(D8) (2008).

[15] A.C. Levasseur-Regourd, M. Cabane, V. Haudebourg, and J.-C. Worms. Light scattering by dust under microgravity conditions. In: *Laboratory Astrophysics and Space Research*. P. Ehrenfreund, C. Krafft, H. Kochan and V. Pirronello (eds.). ASSL, Kluwer Academic Publishers, Dordrecht, The Netherlands (1999).

[16] E. Hadamcik, J.B. Renard, A.C. Levasseur-Regourd, J. Lasue, G. Alcouffe, and M. Francis. Light scattering by agglomerates: Interconnecting size and absorption effects (PROGRA2). JQSRT **110**(14–16) (2009).

[17] R.J. Perry, A.J. Hunt, and D.R. Huffman. Experimental determination of Mueller scattering matrices for nonspherical particles. App. Opt. **17** (1978).

[18] P. Stammes. Light scattering properties of aerosols and the radiation inside a planetary atmosphere. Ph.D. Dissertation, Free University, Amsterdam (1989).

[19] F. Kuik. Single scattering by ensembles of particles with various shapes. Ph. D. Dissertation, Free University, Amsterdam (1992).

[20] J.W. Hovenier. Measuring scattering matrices of small planetary particles at optical wavelengths. In: *Light scattering by nonspherical particles*. M.I. Mishchenko, J.W. Hovenier, and L. D. Travis (eds.). Academic, San Diego, CA (2000).

[21] H. Volten. Light scattering by small planetary particles. An experimental study. Ph. D. Dissertation, Free University, Amsterdam (2001).

[22] H. Volten, O. Muñoz, E. Rol, J.F. de Haan, V. Vassen, J.W. Hovenier, J. Muinonen, and T. Nousianen. Scattering matrices of mineral aerosol particles at 441.6 nm and 632.8 nm. J. Geophys. Res. **106** (2001).

[23] O. Muñoz et al. The new IAA Light scattering apparatus. JQSRT **111** (2010).

[24] J.W. Hovenier, C.V.M. van der Mee and H. Domke. *Transfer of polarized light in planetary atmospheres: Basic concepts and practical methods*. Kluwer Springer, Dordrecht (2004).

Experimental determination of scattering matrices of dust particles at visible wavelengths: IAA light-scattering apparatus

O. Muñoz*, F. Moreno, and D. Guirado

Instituto de Astrofísica de Andalucía, CSIC, Glorieta de la Astronomía s/n, 18080 Granada, Spain.

We present a new laboratory apparatus for measuring the complete scattering matrix as a function of the scattering angle of aerosol particles. The measurements can be performed at the wavelengths of 483, 488, 520, 568, or 647 nm in the scattering angle range from 3° to 177°. The accuracy of the system has been tested by comparison of the measured scattering matrices for water droplets with results of Lorenz-Mie calculations for homogeneous spherical water droplets. The apparatus is devoted to experimentally studying the angle-dependent scattering matrices of dust samples of astrophysical interest. Moreover, there is a great interest in measuring aerosol samples that can affect the radiative balance of the Earth's atmosphere such as desert dust, volcanic ashes, and carbon soot particles.

INTRODUCTION

The study of the scattering behavior of irregular mineral particles is of great importance in many different fields. In particular, irregular dust particles play an important role in the study of the Solar System, especially as far as planetary atmospheres and minor bodies are concerned [1]. If we want to properly interpret space- and ground-based observations we need to know the scattering properties of such irregular mineral particles. For that purpose an experimental apparatus was built in the 1980s in the group of J.W. Hovenier in Amsterdam (see e.g. [2]). In this paper, we present an improved descendant of the Dutch experimental apparatus recently constructed at the Instituto de Astrofísica de Andalucía (IAA) in Granada, Spain [3].

EXPERIMENTAL APPARATUS AND CALIBRATION MEASUREMENTS

In short, to measure the scattering-matrix elements, we use a number of different optical components such as polarizers, a quarter-wave plate, and an electro-optic modulator. These components are used to manipulate the polarization state of light. By using eight different combinations for the orientation angles of the optical components, and assuming reciprocity of the sample, all scattering-matrix elements are obtained as functions of the scattering angle [2]. In the new apparatus, the detectors have been designed so that the blockage of the laser beam at positions close to the forward and backward directions is minimized. This allows us to extend the scattering-angle range of the measurements to 3-177°. Moreover, the accuracy of the measurements at small and large scattering angles has been improved by including in the measuring/reduction process corrections for the background signal. Additionally, we have extended the number of wavelengths of the incident light (λ). In the IAA apparatus, we use a tunable Argon-Krypton laser (483, 488, 520, 568, and 647 nm) as a light source. A detailed description of the instrument and reduction process can be found in [3].

*Corresponding author: Olga Muñoz (olga@iaa.es)

The accuracy and reliability of the instrument is tested by comparing the measured scattering matrices of water droplets at 488 nm, 520 nm, and 647 nm with Lorenz-Mie calculations for a distribution of homogeneous water droplets. For the Lorenz-Mie calculations, we assume a log-normal size distribution as defined by [4]. The refractive index of water is assumed as a fixed parameter at the three studied wavelengths (m=1.33-0.0i). The method to find the best-fitted values for r_g and σ_g that define the log-normal size distribution, is based on the downhill simplex method of Nelder and Mead [5], particularly the FORTRAN implementation described in the Numerical Recipes book [6], subroutine AMOEBA. The method is independently applied to fit the $F_{11}(\theta)$ and $-F_{12}(\theta)/F_{11}(\theta)$ at the 3 studied wavelengths, namely 488, 520, and 647 nm. The averaged values obtained from the best fits for the six studied functions give a value of $\sigma_a = 1.50 \pm 0.04$ and $r_a = 0.80 \pm 0.07$ μm.

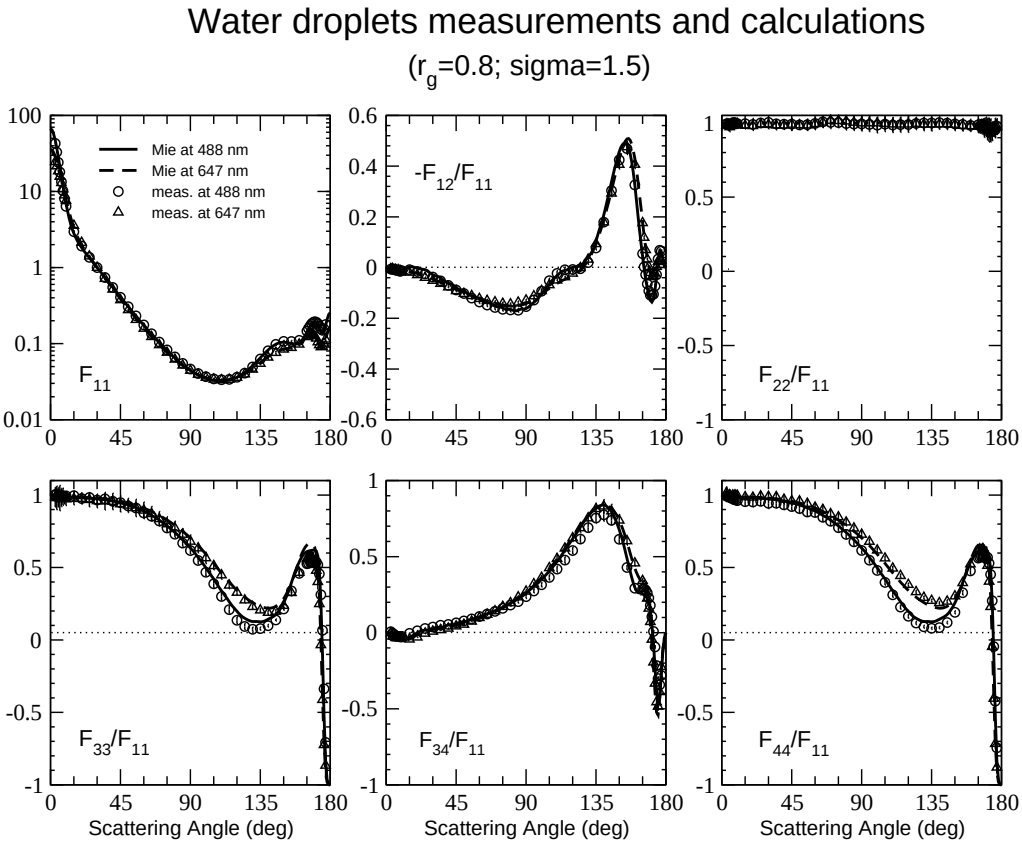

Figure 1. Measured scattering matrix for water droplets at λ=488 nm (circles) and 647 nm (triangles). Solid and dashed lines correspond to results of Lorenz-Mie calculations at 488 nm and 647 nm, respectively, for a log-normal size distribution ($r_g = 0.84$ μm, and σ_g=1.5). Errors are presented by bars that sometimes are not seen because they are smaller than the symbols.

As an example, in Fig. 1, we present the measured and calculated scattering matrices as functions of the scattering angle at $\lambda = 488$ nm and 647 nm. The measured and calculated $F_{11}(\theta)$ are plotted on a logarithmic scale and normalized to 1 at 30°. The other

matrix elements are plotted relative to $F_{11}(\theta)$. We refrain from showing the four element ratios $F_{13}(\theta)/F_{11}(\theta)$, $F_{14}(\theta)/F_{11}(\theta)$, $F_{23}(\theta)/F_{11}(\theta)$, and $F_{24}(\theta)/F_{11}(\theta)$, since we verified that these ratios do not differ from zero by more than the error bars, in accordance with Lorenz-Mie theory. The measurements satisfy the Cloude coherency matrix test (see e.g. [7]) at all measured scattering angles. As shown, the water droplets measurements show an excellent agreement with the Lorenz-Mie computations over the entire angle range at the two presented wavelengths. The experimental data exhibit the typical behavior of a distribution of homogeneous spherical particles, i.e., $F_{22}(\theta)/F_{11}(\theta)$ is equal to unity at all scattering angles. In addition, the $F_{33}(\theta)/F_{11}(\theta)$ and $F_{44}(\theta)/F_{11}(\theta)$ ratios are identical to one another at all scattering angles.

SCATTERING MATRICES FOR A SAMPLE OF WHITE CLAY PARTICLES

As an example of measurements with dust particles, in Fig. 2, we present the measured scattering-matrix elements as a function of the scattering angle of a sample of white clay particles. The measurements are performed at 488 and 647 nm. The scattering matrices fulfill the Cloude coherency matrix test within the experimental errors at all measured scattering angles (see e.g. [7]). The size distribution of the sample has been measured by a Mastersizer 2000, Malvern instruments. The retrieved size distribution parameters based on diffraction are $r_{\text{eff}} = 1.39$ µm and v_{eff}=1.56 [4]. As mentioned above, the measured phase functions are normalized to 1 at 30°. The measured scattering matrix elements present the typical behavior of irregular mineral particles (see e.g. [8] and the Amsterdam Light Scattering Database, www.astro.uva.nl/scatter). The measured $F_{11}(\theta)$ elements present a strong forward peak and almost no structure at side- and backscattering angles. The degree of linear polarization for unpolarized incident light, $-F_{12}(\theta)/F_{11}(\theta)$, presents the typical bell-shape with a maximum around 90° and a negative branch at large scattering angles. The $F_{44}(\theta)/F_{11}(\theta)$ ratios are larger than the $F_{33}(\theta)/F_{11}(\theta)$ at scattering angles larger than 100°, whereas the $F_{22}(\theta)/F_{11}(\theta)$ ratio is different from unity at nearly all measured scattering angles.

When comparing the measurements at the two studied wavelength we observe that the maximum of the degree of linear polarization increases when increasing the wavelength of the incident light, i.e., the smaller the size parameter, the higher the maximum of the degree of linear polarization. Moreover, the measured $F_{22}(\theta)/F_{11}(\theta)$ ratio at 647 nm shows the highest values at almost all measured scattering angles. In contrast, the $F_{33}(\theta)/F_{11}(\theta)$, $F_{34}(\theta)/F_{11}(\theta)$, and $F_{44}(\theta)/F_{11}(\theta)$ ratios do not seem to show any significant differences at the two wavelengths studied. Similar wavelength dependence showed up in the previous measurements performed in Amsterdam with red and green clay particles ([8, 9] and `http://www.astro.uva.nl/scatter`).

REFERENCES

[1] J.W. Hovenier and O. Muñoz. Light scattering in the Solar System: An introductory review. JQSRT **110**(14–16) (2009).

[2] J.W. Hovenier. Measuring scattering matrices of small particles at optical wavelengths. In: *Light scattering by nonspherical particles*. M.I. Mishchenko, J.W. Hovenier and L.D. Travis (eds.). Academic, San Diego, CA (2000).

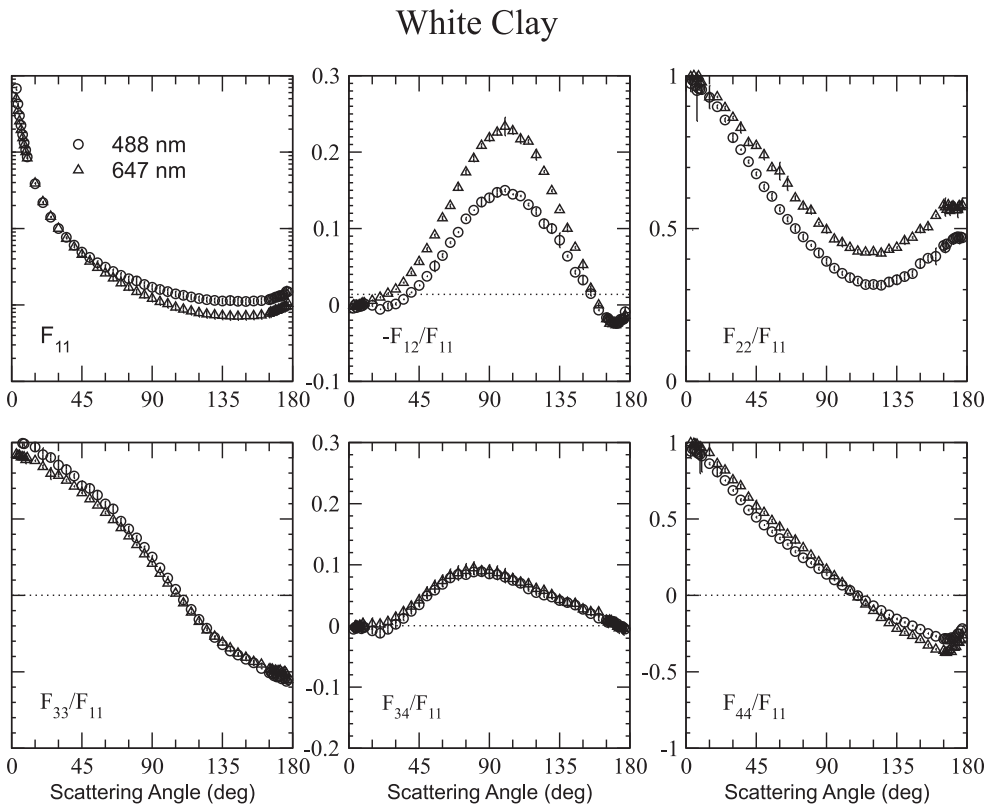

Figure 2. Measured scattering matrix elements for a sample of white clay particles at two different wavelengths 488 nm (circles) and 647 nm (triangles). The measurements are presented together with their error bars. In case no error bars are shown, they are smaller than the symbols.

[3] O. Muñoz et al. The new IAA Light scattering apparatus. JQSRT **111** (2010).

[4] J.E. Hansen, L.D. Travis. Light scattering in planetary atmospheres. Space Sci. Rev. **16**(4) 1974.

[5] A. Nelder and R.A. Mead. A simplex method for function minimization. Computer Journal **7** (1965).

[6] W. Press, S. Teukolsky, W. Vetterling and B. Flannery. *Numerical Recipes in Fortran 77, second edition*. ISBN 0-521-43064-X (1992).

[7] J.W. Hovenier, C.V.M. van der Mee and H. Domke. *Transfer of polarized light in planetary atmospheres : Basic concepts and practical methods*. Kluwer Springer, Dordrecht (2004).

[8] H. Volten, O. Muñoz, E. Rol, J.F. de Haan, V. Vassen, J.W. Hovenier, K. Muinonen and T. Nousiainen. Scattering matrices of mineral aerosol particles at 441.6 nm and 632.8 nm. J. Geophys. Res. **106** (2001).

[9] O. Muñoz, H. Volten, J.F. de Haan, W. Vassen, and J.W. Hovenier. Experimental determination of scattering matrices of randomly oriented fly ash and clay particles at 442 and 633 nm. J. Geophys. Res. **106** (2001)

Scattering of light by Gaussian-random-ellipsoid particles

K. Muinonen*,[1,2] and T. Pieniluoma[1]

[1] *Department of Physics, P.O. box 64, FI-00014 University of Helsinki, Finland.*
[2] *Finnish Geodetic Institute, P.O. box 15, FI-02431 Masala, Finland.*

We introduce the stochastic geometry of a Gaussian random ellipsoid (GE) and, with the discrete-dipole approximation, carry out preliminary computations for light scattering by wavelength-scale GE particles. We compare the scattering characteristics of GE particles to those of perfect ellipsoids.

INTRODUCTION

Natural small particles may exhibit irregular shapes with preferential elongation or flattening. Here the shapes of such irregular small particles are modeled using the stochastic geometry of what we call a Gaussian random ellipsoid (GE). GE is a natural extension for the Gaussian random sphere (GS; e.g. [1, 2]) and GE transforms to GS in the limit of vanishing elongation and flattening.

Scattering properties for GE particles are studied here with the discrete-dipole approximation. DDA is a flexible method for numerical solution of scattering by irregular particles (e.g. [3]). We utilize the Amsterdam DDA code by Yurkin et al. [4]. In what follows, we introduce the stochastic geometry for GE. We then proceed to present the first DDA computations for scattering by GE particles.

GAUSSIAN RANDOM ELLIPSOID

In GE, lognormal height statistics are imposed on a base ellipsoid along the local normal direction. As compared to GS, GE introduces two additional shape parameters: the axial ratio $b : a$ or, equivalently, the elongation $(a - b) : a$; and $c : b$ or the flattening $(b - c) : b$.

The ellipsoidal base geometry raises fundamental issues concerning the homogeneity of the superimposed statistics. In GS, the great-circle distance utilized in the correlation of two radial distances can be interpreted in two ways: first, the distance can be taken literally as the great-circle angle between the two points; second, it can be unambiguously mapped to the Cartesian distance for the two points on the base sphere. In a corresponding way for GE, the distance between two points on the base ellipsoid can be measured along the geodetic line connecting the points or as the Cartesian distance between the points. In the present context, we utilize the Cartesian distance in correlating heights on the base ellipsoid.

Due to the requirement of height variation along the local normal vector, further constraints must be introduced for the mean height corresponding to the mean radial distance in GS. We define the mean height h to coincide with the minimum radius of curvature for the base ellipsoid with semiaxes a, b, and c. This implies that the single center point of GS

*Corresponding author: Karri Muinonen (karri.muinonen@helsinki.fi)

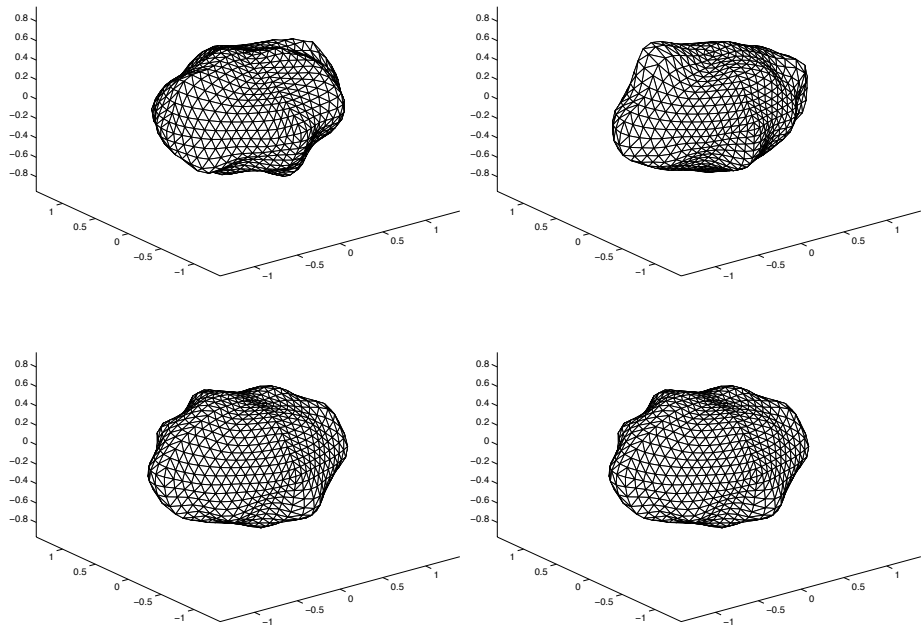

Figure 1. Sample Gaussian ellipsoids with $a : b : c = 1 : 0.7 : 0.6$, $\sigma = 0.05$, and $\ell = 0.2$.

evolves into a surface of center points for GE (note that this surface is not ellipsoidal in shape). In summary, the position of any point on a sample GE can be expressed as

$$\boldsymbol{r}(\vartheta,\phi) \;=\; \boldsymbol{r}_{\rm E}(\vartheta,\phi) + h\left[\exp\left(s(\vartheta,\phi) - \frac{1}{2}\beta^2\right) - 1\right]\boldsymbol{n}(\vartheta,\phi), \qquad (1)$$

where ϑ, ϕ are the polar and azimuthal angles of the spherical coordinate system, $\boldsymbol{r}_{\rm E}(\vartheta,\phi)$ and $\boldsymbol{n}(\vartheta,\phi)$ denote the local position and unit outward normal vectors on the base ellipsoid, respectively, s is the logarithmic height and a Gaussian random variable, and β is the standard deviation of s. The relative variance of heights is $\sigma^2 = \exp(\beta^2) - 1$. Note, in particular, that $\boldsymbol{r}(\vartheta,\phi)$ no longer points in the direction specified by the spherical coordinates ϑ, ϕ.

RESULTS AND DISCUSSION

We compute scattering matrices for GE particles with size parameters $ka = 3$ or $ka = 6$, complex refractive index $m = 1.55 + {\rm i}0.001$, standard deviation $\sigma = 0.05$, correlation length $\ell = 0.2$ in a Gaussian correlation function $C_s(d) = \exp(-\frac{1}{2}\frac{d^2}{\ell^2})$ (d is the Cartesian distance between two points on the base ellipsoid), and axis ratio $a : b : c = 1 : 0.7 : 0.6$ (see Fig. 1 for sample shapes). The scattering characteristics are ensemble-averaged over 100 GE realizations and the scattering characteristics are orientation averaged over 242 different orientations for each realization. The scattering volume is discretized into $32 \times 32 \times 32 =$

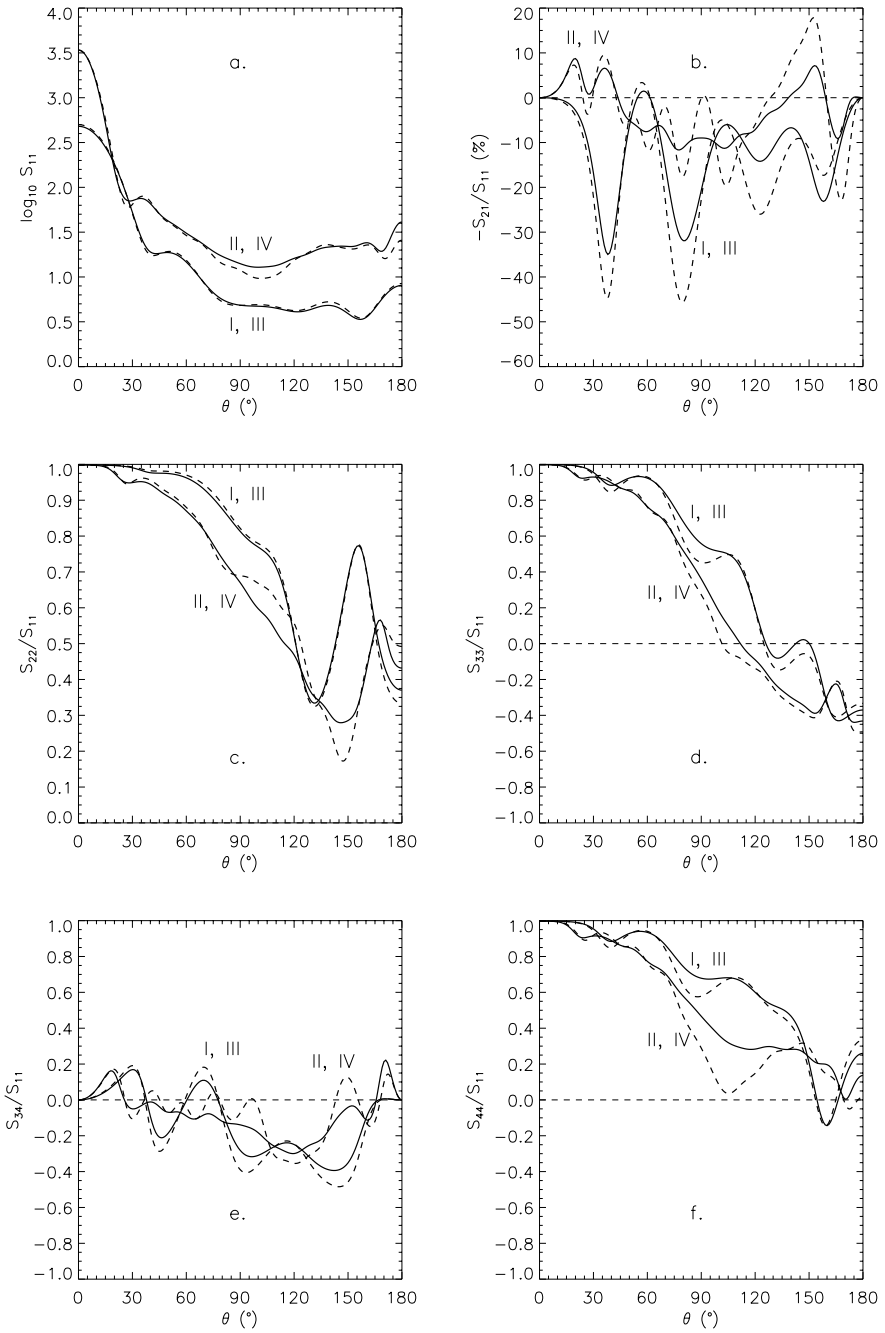

Figure 2. Ensemble-averaged angular scattering characteristics for GE particles with base-ellipsoid axial ratio $a : b : c = 1 : 0.7 : 0.6$ and complex refractive index $m = 1.55+\mathrm{i}0.001$ using Discrete-Dipole Approximation: a. Scattering-matrix element S_{11}; b. Degree of linear polarization $-S_{21}/S_{11}$; c. S_{22}/S_{11}; d. S_{33}/S_{11}; e. S_{34}/S_{11}; f. S_{44}/S_{11}. Four cases are shown: I. GE with $ka = 3$ (solid line); II. GE with $ka = 6$ (solid line); III. base ellipsoid with $ka = 3$ (dashed line); IV. base ellipsoid with $ka = 6$ (dashed line).

32768 cubic cells for $ka = 3$ or into $64 \times 64 \times 64 = 262144$ cells for $ka = 6$, well within the validity criteria of DDA.

Fig. 2 illustrates the results of the scattering computations. The GE particles exhibit overall angular characteristics commonly encountered in scattering experiments for small particles as well as numerical computations for other irregular particles. The scattering-matrix element S_{11} shows the precursor of the forward diffraction pattern as well as increased backward scattering. The increased backward scattering can also be envisaged as a deep minimum next to the backward scattering direction caused by a destructive interference (e.g., [5]). The degree of linear polarization $-S_{21}/S_{11}$ shows clear negative polarization at intermediate scattering angles (cf. [6]) as well as pronounced branches of negative polarization near backscattering. The remaining scattering patterns S_{22}/S_{11}, S_{33}/S_{11}, S_{34}/S_{11}, and S_{44}/S_{11} also resemble those obtained for GS particles.

Comparison to scattering by regular base ellipsoids shows that adding irregularity on the base ellipsoid results in smoothing of all angular patterns. The scattering-matrix elements S_{11} are quite similar for randomly oriented base ellipsoids and Gaussian ellipsoids. Of all the angular patterns, the degree of linear polarization $-S_{21}/S_{11}$ appears to be most sensitive to the surface irregularities.

CONCLUSION

In the future, we will develop a Gaussian random ellipsoid where the correlation is measured along the geodetic line on the ellipsoid. In addition, the Gaussian-ellipsoid geometry can turn useful in physical studies of small solar-system bodies.

The direct problem of light scattering involves the computation of scattering by small particles with varying size, shape, and refractive index or optical properties in general. The inverse problem concerns retrieving particle properties based on observations or laboratory measurements of their scattering and absorption properties. We envisage that the Gaussian random ellipsoid can become a useful tool for irregular small particles in inverse problems.

REFERENCES

[1] K. Muinonen, T. Nousiainen, P. Fast, K. Lumme, and J.I. Peltoniemi. Light scattering by Gaussian random particles: ray optics approximation. JQSRT **55** (1996).

[2] J.I. Peltoniemi, K. Lumme, K. Muinonen, and W.M. Irvine. Scattering of light by stochastically rough particles. Appl. Opt. **28** (1989).

[3] E.S. Zubko, Yu.G. Shkuratov, M. Hart, J. Eversole, and G. Videen, Backscattering and negative polarization of agglomerate particles. Opt. Lett. **28**(17) (2003).

[4] M.A. Yurkin and A.G. Hoekstra. The discrete dipole approximation: an overview and recent developments. JQSRT **106** (2007).

[5] K. Muinonen, J. Tyynelä, E. Zubko, and G. Videen. Coherent backscattering in planetary regoliths. Light Scattering Reviews (in press) (2010).

[6] J. Tyynelä, E. Zubko, K. Muinonen, and G. Videen. Interpretation of single-particle negative polarization at intermediate scattering angles. This volume (2010).

Coherent backscattering by a finite medium of particles

K. Muinonen[1,2] and E. Zubko[1,3]

[1]*Department of Physics, P.O. box 64, FI-00014 University of Helsinki, Finland*
[2]*Finnish Geodetic Institute, P.O. box 15, FI-02431 Masala, Finland*
[3]*Institute of Astronomy, Kharkov National University, 35 Sumskaya St., Kharkov, 61022, Ukraine*

We study coherent backscattering of light by a spherical random medium of spherical particles. Tentatively, the multiple-scattering theory composed of radiative transfer and coherent backscattering (RT-C) reproduces the exact electromagnetic solution available from the superposition T-matrix method for a specific microscopic medium. RT-C has promising future prospects, as it is capable of extending the electromagnetic solutions from microscopic to macroscopic scales.

INTRODUCTION

Atmosphereless solar-system objects exhibit two ubiquitous light-scattering phenomena at small solar phase angles (Sun-object-observer angle α): first, the opposition effect in the intensity of scattered sunlight; and, second, the negative degree of linear polarization $(I_\perp - I_\parallel)/(I_\perp + I_\parallel)$, where $I_\parallel$ and $I_\perp$ denote the intensity components parallel and perpendicular to the scattering plane defined by the Sun, the object, and the observer.

In order to compute multiple scattering by a complex random medium of spherical scatterers, a radiative-transfer coherent-backscattering method (RT-C) has been presented in [1, 2]. In continuation of the studies in [3], we apply RT-C to the computation of the scattering properties for a specific spherical medium of spherical particles already treated using the superposition T-matrix method in [4]. We close by discussing the results and future prospects of RT-C.

RADIATIVE TRANSFER WITH COHERENT BACKSCATTERING

Our RT-C method is based on Monte Carlo ray tracing [1, 2], where coherent backscattering is computed alongside radiative transfer (RT) with the help of the reciprocity relation of electromagnetic scattering in the exact backscattering geometry. Typical for Monte Carlo ray-tracing methods, it is fairly straightforward to extend RT-C to differing geometries of the random medium.

RESULTS AND DISCUSSION

We have carried out multiple-scattering computations for finite, spherical random media of spherical particles using RT-C, concentrating on a specific case studied earlier by Mishchenko et al. [4] using the superposition T-matrix method. The size parameter of the constituent spherical particles is $x = 2$ and the volume density of the medium is $v = 6.25\%$ (this corresponds to the value of 7.3% documented in [4]). Two cases have been studied in detail: first, the complex refractive index of the constituent particles is $m = 1.31$ and the radius of the spherical medium is $kR = 40$, where k is the wave number and R is the radius

*Corresponding author: Karri Muinonen (karri.muinonen@helsinki.fi)

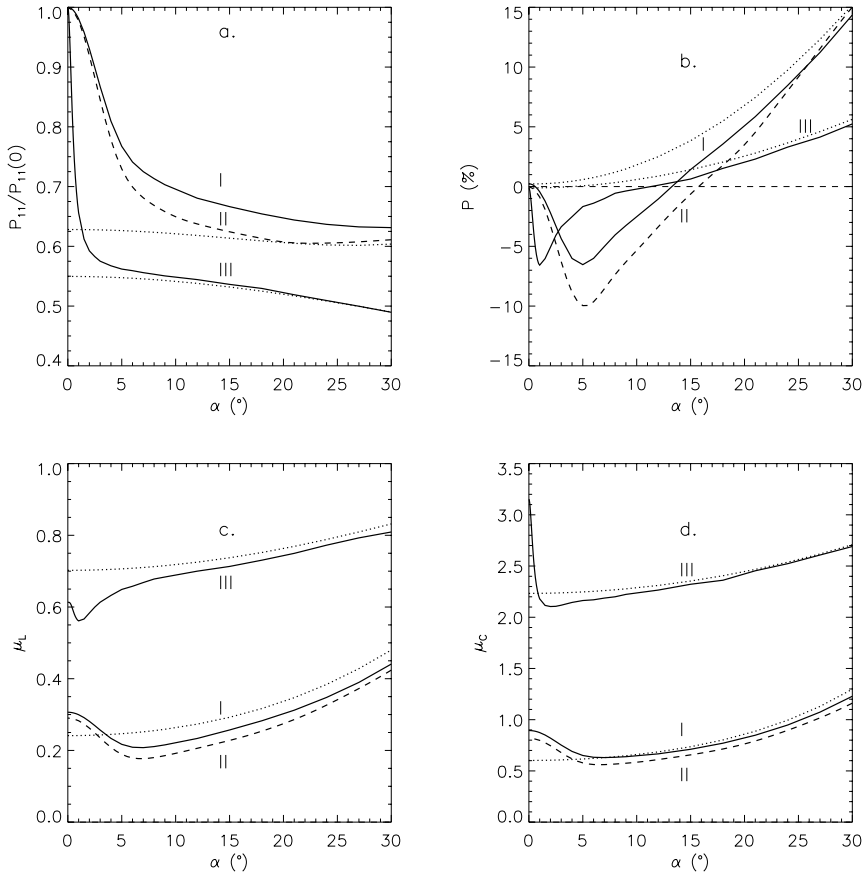

Figure 1. Multiple scattering by spherical media with volume densities $v = 6.25\%$ and varying size parameters kR (k is the wave number) composed of spherical particles with size parameters $x = 2$: a. normalized scattering phase function $P_{11}/P_{11}(0)$; b. degree of linear polarization $P = -P_{21}/P_{11}$; c. linear polarization ratio $\mu_{\rm L}$; and d. circular polarization ratio $\mu_{\rm C}$. Three sets of curves are shown: I. Radiative-transfer coherent-backscattering (RT-C; solid line) and radiative-transfer solutions (RT; dotted line; normalized with the RT-C $P_{11}(0)$ in the denominator) for $kR = 40$ and complex refractive index $m = 1.31$; II. Orientation-averaged superposition T-matrix solution for a single medium with $kR = 40$, $v = 6.25\%$, and $m = 1.31$ (dashed line); and III. RT-C and RT solutions (solid and dotted lines) for $kR \to \infty$ and $m = 1.31 + {\rm i}0.01$.

of the medium; second, $m = 1.31 + \mathrm{i}0.01$ and $kR = 10^7$ (corresponding to $kR \to \infty$). We traced 10^5 rays in the Monte Carlo computations that required several tens of hours of single-processor computing time on a modern work station.

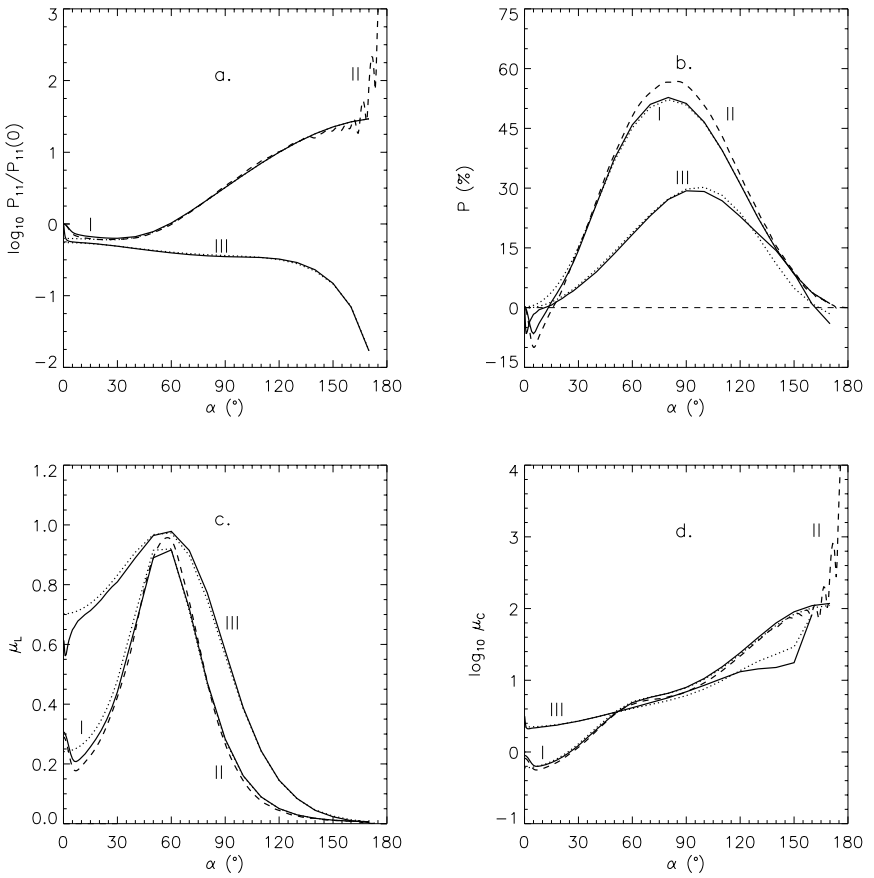

Figure 2. As in Fig. 1 for the full range of phase angles.

Figures 1 and 2 show the RT-C and RT results for the scattering phase matrix element P_{11} (the scattering phase function), degree of linear polarization for incident unpolarized light $P = -P_{21}/P_{11}$, linear polarization ratio $\mu_\mathrm{L} = (P_{11} - P_{22})/(P_{11} + 2P_{21} + P_{22})$, and circular polarization ratio $\mu_\mathrm{C} = (P_{11} + P_{44})/(P_{11} - P_{44})$ as a function of the phase angle α. We note that the results by Mishchenko et al. [4] are based on a single realization of a spherical medium of randomly distributed spherical particles with averaging over orientations.

Overall, RT-C succeeds in reproducing the scattering characteristics of the spherical medium with size parameter $kR = 40$ from zero phase angle to the rise of the diffraction pattern ($\alpha \approx 160°$). This is particularly remarkable as the scattering medium is microscopic in size with a moderate volume density of 6.25%. For $\alpha < 160°$, no other multiple-scattering configurations or interference mechanisms appear to be of significance equal to that of coherent backscattering.

Comparing RT-C and RT shows that, in the present case, coherent backscattering is

significant even for $\alpha > 20^\circ$. Based on additional computations, the angular widths of the coherent-backscattering phenomena are rather insensitive to the volume density because of the forward-scattering tendency of the constituent spheres. It is seen that increasing the size of the medium by more than a factor of 2×10^5 does not cause qualitative differences in the degree of polarization. There are, however, large quantitative differences between all the angular patterns for the media of $kR = 40$ and $kR \to \infty$, showing that there is considerable amount of further development work needed for the superposition T-matrix method. Different RT-C and RT levels for large phase angles $\alpha > 30^\circ$ suggests that further work is needed to improve the numerical accuracy of the Monte-Carlo computations.

There is an extensive amount of future work needed to compare the RT-C and superposition T-matrix methods. Studies can be carried out to find the limits of applicability for RT-C in terms of volume density and medium size. For example, RT-C works for media composed of a single sphere and 500 spheres and it appears mandatory to map the applicability in between. The success of RT-C for finite media of particles calls for a corresponding treatment for compact particles. In this spirit, initial studies were carried out for the so-called exploding particle by Zubko et al. [5] using the discrete-dipole approximation (DDA). DDA can be utilized, in particular, to study the role of the near fields in scattering by aggregates where the spherical particles are in contact with one another.

RT-C is currently being applied to derive lunar single-scattering, volume-density, and surface-roughness characteristics [6]. RT-C can be optimized via parallelization of the Monte Carlo computation. In the longer term, the methods can be extended to the computation of multiple scattering by random media of nonspherical scatterers.

Acknowledgments: We are thankful to M. I. Mishchenko for a constructive review and to J. M. Dlugach for providing us with the superposition T-matrix computations.

REFERENCES

[1] K. Muinonen. Coherent backscattering of light by complex random media of spherical scatterers: Numerical solution. *Waves in Random Media* **14**, 365-388 (2004).

[2] K. Muinonen, J. Tyynelä, E. Zubko, and G. Videen. Coherent backscattering in planetary regoliths. *Light Scattering Reviews*, in press (2010).

[3] K. Lumme, A. Penttilä, and K. Muinonen (2005). Coherent backscattering by aggregates of spherical constituents. In: *Proceedings of the 8th Conference on Electromagnetic and Light Scattering by Nonspherical Particles: Theory, Measurements, and Applications*. F. Moreno, J.J. López-Moreno, O. Muñoz, and A. Molina (eds.). Salobrena, Spain (2005).

[4] M. I. Mishchenko, J. M. Dlugach, L. Liu, V. K. Rosenbush, N. N. Kiselev, and Y. G. Shkuratov. Direct solutions of the Maxwell equations explain opposition phenomena observed for high-albedo solar-system objects. *The Astrophysical Journal* **705**, L118-L122 (2009).

[5] E. Zubko, Y. Shkuratov, M. Mishchenko, and G. Videen. Light scattering in a finite multiparticle system. *JQSRT* **109** (2008).

[6] J. Näränen, H. Parviainen, K. Muinonen, J.-L. Josset, S. Beauvivre, P. Pinet, S. Chevrel, D. Koschny, B. Grieger, and B. Foing. Lunar single-scattering, porosity, and surface-roughness characteristics with SMART-1/AMIE. In: *Electromagnetic and Light Scattering XII* (this volume) (2010).

Interaction of light and fast electrons with metallic nanoparticles

V. Myroshnychenko[*,1], E. Carbó-Argibay[2], J. Rodríguez-Fernandez[2], I. Pastoriza-Santos[2], J. Pérez-Juste[2], L. M. Liz-Marzán[2], and F. J. García de Abajo[1]

[1]*Instituto de Óptica (CSIC), Serrano 121, 28006 Madrid, Spain.*
[2]*Departamento de Quimica Fisica and Unidad Asociada CSIC – Universidade de Vigo; 36310 Vigo, Spain.*

The shape and size of nanoparticles can be tuned through chemical synthesis parameters, which results in a variety of morphologies. The electromagnetic response of highly anisotropic metallic nanoparticles on external stimuli (light and fast electrons) has been modelled using a full 3D boundary element method. A good agreement between numerical calculations and experimental spectra has been obtained.

INTRODUCTION

The last years have witnessed a tremendous increase in research activity on the behavior of electromagnetic fields at nanometer scales. In this context, the collective excitations that are sustained by valence electrons in a nanostructured metal, also known as plasmons, can play a leading role because they can be understood as a hybrid of electromagnetic energy and energy deposited on the metal electron gas. This leads to extreme localization of the electromagnetic field with resonances that happen to be in the visible and near-infrared for metals, such as gold and silver. The localization goes down to regions of a few nanometers, much smaller than the free-space light wavelength, in the range of hundreds of nanometers or a few microns. Accompanying this effect, the electric field undergoes a large enhancement in intensity that is being used for applications as diverse as bio-sensing and information-processing [1].

All of the above is favored by the availability of new techniques of fabrication, and most notably colloidal chemistry and nanolithography. Advances in the understanding of light interaction with nanostructured materials have been produced with strong collaboration between theory and experiment, and new methods of simulation of the electromagnetic field in this context are still needed to cope with the ever increasing complexity of new geometrical designs. The experimental study of the optical response of nanostructured materials relies largely on the ability to address the near field with good resolution in space and energy. Near-field scanning optical microscopy, electron-energy loss spectroscopy, and cathodoluminescence are the most promising techniques in this respect. In this work, the optical response of metallic nanoparticles to external sources (light or fast electrons) is computed numerically using the full 3D boundary element method (BEM-3D).

* Corresponding author: Viktor Myroshnychenko (viktor@io.cfmac.csic.es)

RESULTS AND DISCUSSION

It was recently shown that the shape and size of gold nanoparticles can be tuned through chemical growth in N,N-dimethylformamide (DMF) that results in transition between nearly cylindrical nanorods and perfect octahedrons with a few intermediate morphologies between them, such as rods with close to square cross section and sharp tips at their ends [2]. It is crucial to monitor the evolution of optical response of these nanoparticles. Figure 1 shows a comparison between BEM calculation and experimental optical spectra for selected intermediate stages in the growth evolution. The TEM images of the particles are plotted in the bottom part of Fig. 1. The extinction spectrum of the initial nanorod dispersion displays a longitudinal surface plasmon (SP) mode and weak transverse. During the process, the longitudinal SP mode gradually blue-shifts, while the transverse red-shifts and gets significantly enhanced. Eventually, both bands merge into a single band. Obviously, observed spectral evolution arises from morphological changes of the particles that result in a steady decrease of the particle aspect ratio but also sharpening and formation apexes. A good agreement between numerical calculation (solid curves) and experiment obtained using a Cary 5000 UV-Vis-NIR spectrophotometer (dotted curves) is observed [3-4].

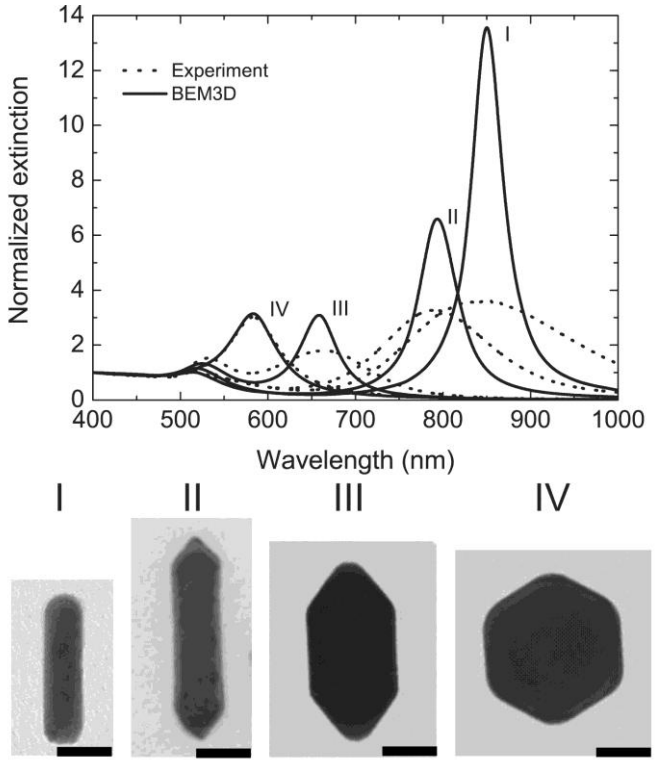

Figure 1. Comparison between measured (dotted curves) and BEM-3D calculations (solid curves) of the optical extinction spectra of gold particles immersed in DMF and obtained at intermediate steps during the growth process from circular nanorods to octahedral particles. The experimental optical spectra are scaled to match the calculated value at 400 nm. TEM images of the particles are shown in the bottom part of the figure. The scale bars equal 25 nm.

Figure 2a shows the calculated optical extinction spectra of an individual Au nanorod (length/diameter, 176/22 nm) [5]. The interaction between the rod and incident light with electric field polarized along (solid curve) and perpendicular (dotted curve) to the rod long axis produces strong light excitation assisted by three respective SP modes (A, C, and D). The mode A is a longitudinal mode excited by parallel polarization and involving an induced dipole dominating along the rod axis, whereas mode D couples to the transversal polarization with an induced dipole perpendicular to that axis. They are dipole-driven SPs. Mode C is a higher-order longitudinal mode. Interestingly, a second-order longitudinal mode B cannot be excited by external light either with electric field polarized along or perpendicular to the rod long axis due to its symmetry; i.e., it has two nodes along the rod, rather than one, as the first-order longitudinal mode. In contrast, the plane wave moving toward the direction of polar angles (30, 40) with polarization given by angles (20, 30) (dashed curve) can excite this mode.

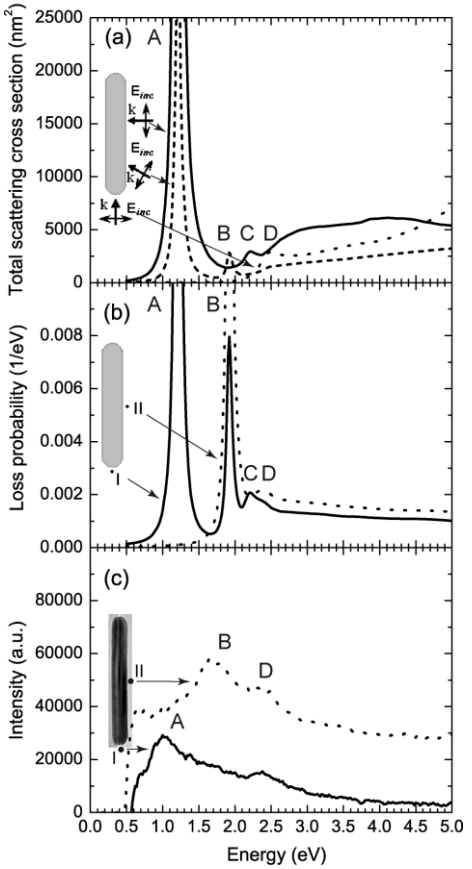

Figure 2. (a) Total scattering cross section as a function of energy for Au nanorod (length/diameter, 176/22 nm). The incident-light electric field is parallel (solid curve) and perpendicular (dotted curve, multiplied by 3 to improve readability) to the rod axis. The dashed curve corresponds to a plane wave moving towards the direction of polar angles (30, 40) with polarization given by angles (20, 30). (b) Calculated electron energy loss probability for locations I (solid curve) and II (dotted curve) of the electron beam relative to the rod under grazing incidence with respect to its surface. The loss probability is given per incoming electron and per electronvolt for a given lost energy. (c) Experimental counterpart of (b).

Figures 2b and 2c show numerical (BEM3D) and experimental (obtained using a scanning transmission electron microscope, FEI Tecnai F20, operated at 200 keV and equipped with a Wien-filter electron monochromator) electron energy loss spectra for an incident electron beam at locations I and II relative to the nanorod, in grazing incidence with respect to the nanoparticle surface. Probing the nanorod with electron beam also leads to the same SP excitations induced by optical illumination. The measured spectral positions of the SP modes (Fig. 2c) are in agreement with those obtained from numerical calculations (Fig. 2a,b). Obviously, the electron beam can excite bright SP modes as optical illumination does.

CONCLUSIONS

We have developed a 3D boundary element method to describe the electromagnetic response of metal nanoparticles with arbitrary morphologies. The method is computationally efficient and presents several advantages with respect to other currently used methods. We have calculated optical and electron energy loss spectra for different metallic nanoparticles and illustrated examples in which theory gives predictive results.

ACKNOWLEDGEMENTS

We would like to acknowledge M.-W. Chu for providing the experimental data. We would also like to acknowledge support of this work by the Spanish Ministry of Science and Innovation (Grants No. MAT2007-66050 and Consolider NanoLight.es) and by the EU (Grants No. NMP4-2006-016881 "SPANS" and NMP4-SL-2008-213669 "ENSEMBLE").

REFERENCES

[1] H. Raether. *Excitation of Plasmons and Interband Transitions by Electrons*. Springer Tracts in Modern Physics (vol. 88), Springer-Verlag: Berlin Heidelberg, Germany (1980).

[2] E. Carbó-Argibay, B. Rodríguez-González, J. Pacifico, I. Pastoriza-Santos, J. Pérez-Juste, and L.M. Liz-Marzán. Chemical sharpening of gold nanorods: The rod-to-octahedron transition. Angew. Chem. Int. Ed. **46** (2007).

[3] V. Myroshnychenko, E. Carbo-Argibay, I. Pastoriza-Santos, J. Perez-Juste, L.M. Liz-Marzan, and F.J. Garcia de Abajo. Modelling the optical response of highly faceted metal nanoparticles with a fully 3D boundary element method. Adv. Mat. **20** (2008).

[4] J. Rodríguez-Fernández, C. Novo, V. Myroshnychenko, A.M. Funston, A. Sánchez-Iglesias, I. Pastoriza-Santos, J. Pérez-Juste, F.J. García de Abajo, L.M. Liz-Marzán, and P. Mulvaney. Spectroscopy, Imaging and Modeling of Individual Gold Decahedra. The Journal of Physical Chemistry C **113**(43) (2009).

[5] M.-W. Chu, V. Myroshnychenko, C. H. Chen, J.-P. Deng, C.-Y. Mou, and F.J. Garcia de Abajo. Probing Bright and Dark Surface-Plasmon Modes in Individual and Coupled Noble Metal Nanoparticles Using an Electron Beam. Nano Letters **9** (2009).

Lunar single-scattering, porosity, and surface-roughness characteristics with SMART-1/AMIE

J. Näränen[1], H. Parviainen[2], K. Muinonen∗, 1, 3, J.-L. Josset[4], S. Beauvivre[5], P. Pinet[6], S. Chevrel[6], D. Koschny[7], B. Grieger[8], and B. Foing[7]

[1]*Finnish Geodetic Institute, P.O. box 15, FI-02431 Masala, Finland.*
[2]*Instituto de Astrofísica de Canarias, Calle Vía Láctea, E-38205 La Laguna (Tenerife), Spain.*
[3]*Department of Physics, P.O. box 64, FI-00014 University of Helsinki, Finland.*
[4]*Space Exploration Institute, Case postale 774, CH-2002 Neuchâtel, Switzerland.*
[5]*Micro-cameras & Space Exploration, Puits-Godet 10a, CH-2000 Neuchâtel, Switzerland.*
[6]*Observatoire Midi-Pyrénées/CNRS/Université Toulouse III, 14, Avenue Edouard Belin, 31400 Toulouse, France.*
[7]*ESA, ESTEC/SCI-S, postbus 299, 2200 AG Noordwijk, The Netherlands.*
[8]*ESA, ESAC/SCI-OS, Apdo. de correos 78, 28691 Villanueva de la Cañada, Madrid, Spain.*

We analyze the single-scattering albedo and phase function, local surface roughness and regolith porosity, and the coherent backscattering, single scattering, and shadowing contributions to the opposition effect for specific lunar mare regions imaged by the AMIE camera onboard the ESA SMART-1 spacecraft.

INTRODUCTION

The Moon exhibits an opposition effect [1, 2], that is, a nonlinear increase of disk-integrated brightness with decreasing solar phase angle, the angle between the Sun and the observer as seen from the object. Whereas the opposition effect is a ubiquitous phenomenon for atmosphereless solar-system objects at large, the lunar opposition effect is of particular significance as we can witness the brightness of the full Moon with our own bare eyes. In the opposition night, the Moon is roughly twice as bright as in the nights just before and after the opposition.

The lunar opposition effect lacks a widely accepted physical explanation. It has been traditionally explained by mutual shadowing among regolith particles (sizes of several tens of microns; shadowing mechanism SM) large compared to the wavelength of incident light: the particles hide their own shadows at exact opposition (see [3]). Recently, the coherent-backscattering mechanism (CBM) has been introduced to explain the opposition effect (e.g., [4, 5, 6]). CBM is a multiple-scattering interference mechanism, where reciprocal waves propagating through the same scatterers in opposite directions always interfere constructively in the backward-scattering direction but with varying interference characteristics in other directions.

In what follows, we extract the effects of the stochastic geometry from the SMART-1 AMIE lunar photometry ([7]) and, simultaneously, obtain the volume-element scattering phase function of the lunar regolith locations studied. The volume-element phase function allows us to constrain the physical properties of the regolith particles.

∗Corresponding author: Karri Muinonen (karri.muinonen@helsinki.fi)

OBSERVATIONS

We include four different lunar mare regions in our study (Fig. 1). Each of these regions covers several hundreds of square kilometers of lunar surface. When selecting the regions, we have required that they have been imaged by AMIE across a wide range of phase angles (α), including the opposition geometry. The phase-angle range covered in total is 0-109°, with incidence and emergence angles (ι and ϵ) ranging within 7-87° and 0-53°, respectively. Overall, 220 images are used for the present study. The pixel scale varies from 288 m down to 29 m during the extended mission phase ended by the SMART-1 spacecraft crashing into the lunar surface. The dataset represents, to our best knowledge, one of the largest phase-angle coverages of specific lunar regions to date. Off-nadir-pointing observations made of these regions allowed for the extensive phase-angle coverage. The clear (or panchromatic) filter was chosen for the present study as it provides the largest field of view and is currently the best-calibrated channel. Large craters and albedo anomalies were excluded from the analysis.

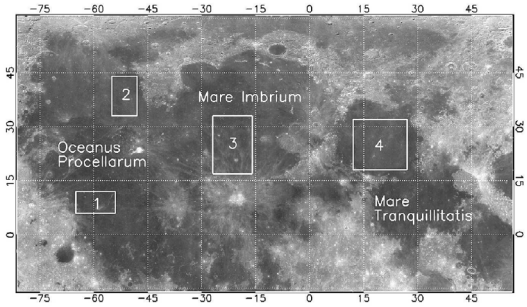

Figure 1. The lunar regions observed by AMIE and analyzed in the present study overlaid on the Clementine albedo map: 1) Oceanus Procellarum, around Reiner Gamma; 2) Oceanus Procellarum, between Mons Rümker and the Mairan crater; 3) Mare Imbrium, north of Copernicus crater; and 4) Mare Serenitatis.

THEORETICAL METHODS

We account for shadowing due to surface roughness and mutual shadowing among the regolith particles with ray-tracing computations for densely packed particulate media with a fractional-Brownian-motion interface with free space. The shadowing modeling allows us to derive the hundred-micron-scale volume-element scattering phase function for the lunar mare regolith. We explain the volume-element phase function by a coherent-backscattering model, where the single scatterers are the submicron-to-micron-scale particle inhomogeneities and/or the smallest particles on the lunar surface. We express the single-scatterer phase function as a sum of three Henyey-Greenstein terms, accounting for increased backward scattering in both narrow and wide angular ranges.

RESULTS AND DISCUSSION

In order to derive the lunar mare volume-element phase function, a best-fit solution to the photometric measurements with phase angles greater than 10° was sought from the computed scattering models using Monte-Carlo minimization techniques. The effects due to different values of packing density v, Hurst exponent H and standard deviation σ in

fractional-Brownian-motion rough surface model were small but noticeable. After the fit, the first-order approximation for the volume-element phase function was obtained by dividing the observational data with the model data (Fig. 2).

The most notable result of the comparison of the photometric measurements and numerical modeling is the inability of SM to explain the intensity surge near the opposition. Even for the most porous media considered in the study, $v = 0.2$, SM cannot explain the behavior of the intensity as a function of decreasing phase angle when $\alpha < 10^\circ$.

The lunar volume-element phase function exhibits a pronounced narrow backscattering enhancement branch that can be assigned to multiple interactions between single scatterers within the volume element. We point out that the related multiple scattering is presently included in what we call the lunar volume-element phase function representing a scattering volume large enough to give rise to coherent-backscattering effects.

In what follows, we present a heuristic scalar coherent-backscattering modeling of the lunar volume-element phase function (see [8]). We fix the radius of the spherical medium at $a = 60$ µm, resulting in a volume roughly equivalent to that of a cubic medium with an edgelength of 100 µm. Fig. 2 shows the best-fit coherent-backscattering model (rms-value of 0.06) with a variation envelope (models with rms-values less than 0.1) among a sequence of models for spherical media of scatterers mimicking the volume element in the lunar surface.

In the modeling, we require that the resulting lunar mare geometric albedos be within $[0.1, 0.2]$ and that the resulting volume-element Bond albedos be within $[0.3, 0.6]$. Such Bond albedos are comparable to the corresponding albedos measured in the laboratory for relevant single particles large compared to the wavelength [9]. The geometric albedos for the mare regions were estimated from the study by [10] and from the characteristics of the AMIE camera.

We obtained acceptable volume-element scattering characteristics using single-scattering albedos $\tilde{\omega} \in [0.7, 0.8]$, extinction mean free paths $k\ell = 60, 90, 120, \ldots, 300$ ($k = 2\pi/\lambda$, where λ is the wavelength), and a triple Henyey-Greenstein single-scattering phase function with total asymmetry parameter $g \approx 0.6$. For the forward and backward-scattering H-G terms, $g_1 = 0.8$ and $g_2 = -0.2$, respectively, with a weight factor of $w_1 = 0.8$ for the former part. For the third H-G term describing narrow backscattering enhancement, $g_3 = -0.9$ with its weight fixed so as to obtain an enhancement by a factor of 1.5 over the value given by the first two H-G terms in the backward-scattering direction.

CONCLUSIONS

Based on the present theoretical modeling of the lunar photometry from SMART-1/AMIE, we conclude that most of the lunar mare opposition effect is caused by coherent backscattering and single scattering within volume elements comparable to lunar particle sizes, with only a small contribution from shadowing effects. We thus suggest that the lunar single scatterers exhibit intensity enhancement towards the backward scattering direction in resemblance to the scattering characteristics experimentally measured and theoretically computed for realistic small particles.

Further interpretations of the lunar volume-element phase function will be the subject of near-future research involving the refinement of the aforedescribed ratioing of the observations and the theoretical model.

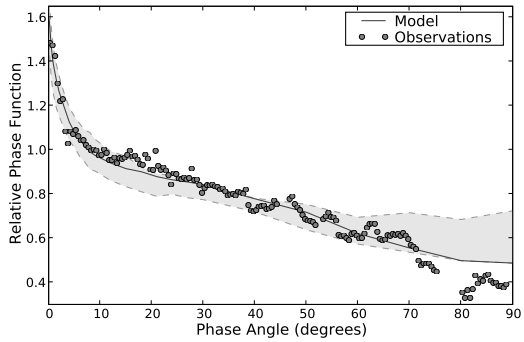

Figure 2. The lunar mare volume-element phase function as obtained from the multiangular AMIE photometry of the mare regions fitted using the fBm-particulate-medium model with $H = 0.4$, $\sigma = 0.06$, and $v = 0.35$ and the corresponding coherent-backscattering modeling. Triple Henyey-Greenstein single-scattering phase functions give rise to coherent-backscattering peaks capable of matching the observations. We show the best-fit coherent-backscattering model as well as a variation envelope resulting from our simulations.

We find that it is possible to derive information about submicron-to-micron-scale surface properties based on multiangular imaging of the target areas. We put forward a novel method where the stochastic surface geometry is derived from the imaging data, whereafter the reduced data allow the derivation of information on the small-scale physical properties.

REFERENCES

[1] N.P. Barabashev. Astron. Nachr **445** (1922).

[2] A. Rougier. Ann, Obs. Strasbourg **205** (1933).

[3] H. Parviainen and K. Muinonen. Bidirectional reflectance of rough particulate media: ray-tracing solution. JQSRT **110** (2009).

[4] Y.G. Shkuratov. Kinematika i Fizika Nebesnykh Tel **4** (1988).

[5] K. Muinonen. Light scattering by inhomogeneous media: backward enchancement and reversal of linear polarization. Ph.D. thesis, University of Helsinki (1990).

[6] M.I. Mishchenko and J.M. Dlugach. Planet. Space Sci. **41** (1993).

[7] P. Pinet, P. Cerroni, J.-L. Josset, S. Beauvivre, S. Chevrel, K. Muinonen, Y. Langevin, M.A. Barucci, M.C. De Sanctis, Y. Shkuratov, V. Shevchenko, P. Plancke, B.A. Hofmann, M. Josset, P. Ehrenfreund, Z. Sodnik, D. Koschny, M. Almeida and B. Foing. The advanced Moon micro-imager experiment (AMIE) on SMART-1: Scientific goals and expected results. Planetary and Space Science **53** (2005).

[8] K. Muinonen, J. Tyynelä, E. Zubko and G. Videen. Coherent backscattering in planetary regoliths. Light Scattering Reviews (in press) (2010).

[9] J. Piironen, K. Muinonen, T. Nousiainen, C. Sasse, S. Roth and J.I. Peltoniemi. Albedo measurements on meteorite particles. Planetary and Space Science **46** (1998).

[10] K. Lumme and W.M. Irvine. AJ **87** (1982).

Scattering of light by mineral-dust particles much larger than the wavelength

T. Nousiainen*,[1], O. Muñoz[2], H. Lindqvist[1], P. Mauno[1], and G. Videen[3]

[1] *Department of Physics, P.O. box 48, FI-00014 University of Helsinki, Finland.*

[2] *Instituto de Astrofísica de Andalucía, CSIC, c/ Camino Bajo de Huétor 50, 18080 Granada, Spain.*

[3] *Army Research Laboratory, 2800 Powder Mill Road,Adelphi, MD 20783, USA.*

We use a modified ray-optics code RODS (Ray Optics with Diffuse and Specular interactions) and laboratory-measured Mueller matrices to study light scattering by dust particles much larger than the wavelength. The rough-surface treatment of the RODS model allows us to reproduce the measured scattering matrices very well, except for the phase function. Surface roughness is found to decrease the asymmetry parameter and increase the single-particle albedo.

INTRODUCTION

Mineral dust is an important component in the Earth's atmosphere, its impacts ranging from direct radiative effects to fertilizing oceans and rain forests, and acting as freezing nuclei for ice clouds. In addition, mineral-dust particles are found in great abundance in, e.g., the Martian atmosphere and regoliths of many Solar-system bodies.

Accurate optical modeling of these particles is very challenging especially when they are larger than the wavelength [1]. One of the complicating factors is the presence of wavelength-scale surface roughness that cannot be explicitly accounted for in traditional ray tracing. Earlier, surface-roughness effects have been studied, e.g., by [2] and [3], using an *ad hoc* Lambertian modification to ray optics. Here we test whether a physically more rigorous RODS model (Ray optics with Diffuse and Specular interactions) introduced by [4] could account for the surface-roughness effects realistically. To this end, a laboratory-measured Mueller matrix of Libyan sand, provided by [3], is used as a reference to which RODS simulations based on the actual, measured size distribution are compared. The Libyan sand sample has an effective radius $r_{\text{eff}} = 125$ μm and effective variance $\nu_{\text{eff}} = 0.15$, guaranteeing that all dust particles are in the ray-optics domain at visible wavelengths.

MODELING APPROACH

The RODS model consists of geometric-optics and diffraction parts. The latter is solved in a Fraunhofer approximation. The geometric-optics part is augmented such that the target shape can be covered with a layer of external scatterers with given single-scattering properties. There are a number of ways the external scatterers can be characterized in the model; here we apply a method where we specify their phase matrix, referred to as an input matrix. In addition, the optical depth of the layer, τ_0, needs to be specified. Here we consider it a free parameter. The single-scattering albedo of the external scatterers, ϖ_0, is set to unity;

*Corresponding author: Timo Nousiainen (timo.nousiainen@helsinki.fi)

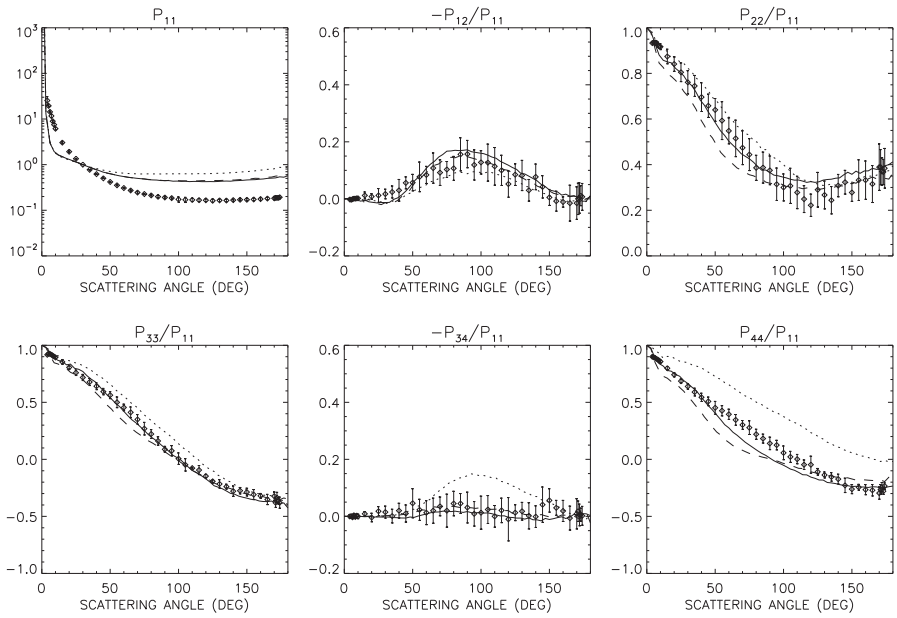

Figure 1. Comparison of simulated and measured Mueller matrices for Libyan sand. The simulated matrices based on different input matrices are plotted with dotted (feldspar), dashed (calcite), and solid (generic clay) lines with $\tau_0 = 1.0$ and $\mathrm{Im}(m) = 3.0 \cdot 10^{-4}$. The measurements are indicated with diamonds and error bars. The P_{11} elements have been renormalized to unity at 30° scattering angle.

we consider the external scatterers to be in the lower part of the resonance domain where even moderately absorbing materials would have high ϖ_0.

Three different input matrices are considered. First, we use a Mueller matrix based on a feldspar sample measured by [5]. Instead of the actual measurements that do not cover the whole scattering-angle range, however, we use the modeled phase matrix based on the $n = 3$ shape distribution of spheroids fitted to the feldspar sample by [6]. In addition, we compile two input matrices from the computations for flaky particles presented in [7]. One is based on calculations for calcite flakes, where the birefringence is fully accounted for. The other is based on the isotropic analog for the calcite flakes and acts here as a proxy for generic clay flakes. The calculations are here integrated over a lognormal size distribution with the geometric mean radius $r_g = 0.35$ μm and the geometric standard deviation $\sigma_g = 1.8$. These two input matrices are motivated by the observation that flake-like particles often cover the surface of large dust particles [7]. All three input matrices represent phase matrices for polydisperse small particles with effective radii between 0.5 and 1.0 μm. The asymmetry parameters associated to the input matrices are $g_0 = 0.725$ for feldspar, $g_0 = 0.808$ for calcite flakes, and $g_0 = 0.815$ for the generic clay.

RESULTS

The simulations are carried out at the wavelength of 633 nm. We use two different optical depths, $\tau_0 = 0.5$ and 1.0, for the layer of external scatterers in addition to a case with no

Table 1. The asymmetry parameter for varying τ_0, $\mathrm{Im}(m)$, and the input matrix.

$\mathrm{Im}(m)$	Asymmetry parameter g						
	$\tau_0 = 0$	$\tau_0 = 0.5$			$\tau_0 = 1.0$		
		Feldspar	Generic clay	Calcite	Feldspar	Generic clay	Calcite
$3 \cdot 10^{-4}$	0.895	0.804	0.830	0.828	0.741	0.782	0.777
$1 \cdot 10^{-4}$	0.801	0.728	0.749	0.747	0.677	0.709	0.706
$3 \cdot 10^{-5}$	0.716	0.653	0.672	0.670	0.611	0.639	0.636

external scatterers. The real part of the refractive index is fixed at 1.55, while the imaginary part is varied between $\mathrm{Im}(m) = 3 \cdot 10^{-4}$ and $3 \cdot 10^{-5}$. The shapes of the model particles are based on the Gaussian random sphere geometry [8] with shape parameters $\sigma = 0.2$ and $\nu = 3.3$ taken from [3].

When the RODS model is run without external scatterers, good fits to the measured Mueller matrix cannot be obtained. When the external scatterers, mimicking the small-scale surface roughness, are introduced, the agreement between simulations and measurements improves drastically. As shown in Figure 1, other elements except the phase function (P_{11}) can be matched very well. The agreements are as good or even better than those attained by [3] using the Lambertian modification, and here we can achieve that by using a physically rigorous model and realistic shapes for model particles.

Different input matrices perform differently and the agreement to measurements depends also on $\mathrm{Im}(m)$ value used, but overall the matrix based on the feldspar sample performs worse than those based on the flaky shapes. Here the Generic clay matrix provides the best fit.

The impact of τ_0, $\mathrm{Im}(m)$, and the input matrices on the asymmetry parameter g and single-particle albedo ϖ are summarized in Tables 1 and 2. Obviously, g increases with increasing $\mathrm{Im}(m)$. Further, g increases with decreasing τ_0. The input matrices also affect g, but their influence is smaller. Not surprisingly, the input matrices with largest asymmetry parameters, g_0, also lead to largest g values for the whole particles. It is noteworthy, however, that the g values for layered particles can be smaller than the g_0 value of the external scatterers or the g value for unlayered particles, signifying the impact of multiple scattering on g.

Likewise, ϖ increases with decreasing $\mathrm{Im}(m)$ or increasing τ_0. The latter is partially connected to the fact that the single-scattering albedo of the roughness elements, ϖ_0, has been set to unity. Still, even if the surface elements were composed of the same material as the host particles, their smaller size parameters would make their single-scattering albedos higher than that of the host particle. This signifies the potential impact of surface roughness on the single-particle albedo of large dust particles.

CONCLUSIONS

The RODS method seems a promising way of modeling the optical properties of dust particles large compared to the wavelength. In particular, all phase matrix elements of the reference Libyan sand sample except the phase function can be reproduced very well based

Table 2. As Table 1 but for the single-particle albedo.

$\mathrm{Im}(m)$	Single-particle albedo ϖ						
	$\tau_0 = 0$	$\tau_0 = 0.5$			$\tau_0 = 1.0$		
		Feldspar	Generic clay	Calcite	Feldspar	Generic clay	Calcite
$3 \cdot 10^{-4}$	0.639	0.668	0.659	0.660	0.691	0.676	0.677
$1 \cdot 10^{-4}$	0.777	0.789	0.786	0.786	0.799	0.793	0.793
$3 \cdot 10^{-5}$	0.905	0.907	0.906	0.906	0.909	0.908	0.908

on realistic model shapes. The problems with the phase function seem to be concentrated on the forward angles, implying that the size distribution of the sample may be in error, or else the surface roughness also affects the diffraction part of the phase function in ways that cannot be realistically accounted for with the present method.

Such amounts of surface roughness that allow good fits between the measurements and simulations ($\tau_0 \approx 1.0$) affect both the asymmetry parameter and the single-particle albedo quite considerably and systematically. This implies that large-particle contributions based on smooth model particles might lead to systematic errors in radiative-transfer applications such as dust radiative-forcing calculations or remote sensing.

REFERENCES

[1] T. Nousiainen. Optical modeling of mineral dust particles: A review. JQSRT **110** (2009).

[2] T. Nousiainen, K. Muinonen, and P. Räisänen. Scattering of light by large Saharan dust particles in a modified ray optics approximation. J. Geophys. Res. **108** (2003).

[3] O. Muñoz, H. Volten, J. Hovenier, T. Nousiainen, K. Muinonen, D. Guirado, F. Moreno, and L. Waters. Scattering matrix of large Saharan dust particles: experiments and computations. J. Geophys. Res. **112** (2007).

[4] K. Muinonen, T. Nousiainen, H. Lindqvist, O. Muñoz, and G. Videen. Light scattering by Gaussian particles with internal inclusions and roughened surfaces using ray optics. JQSRT **110** (2009).

[5] H. Volten, O. Muñoz, J. F. de Haan, W. Vassen, J. W. Hovenier, K. Muinonen, and T. Nousiainen. Scattering matrices of mineral aerosol particles at 441.6 nm and 632.8 nm. J. Geophys. Res. **106** (2001).

[6] T. Nousiainen, M. Kahnert, and B. Veihelmann. Light scattering modeling of small feldspar aerosol particles using polyhedral prisms and spheroids. JQSRT **101** (2006).

[7] T. Nousiainen, E. Zubko, J. V. Niemi, K. Kupiainen, M. Lehtinen, K. Muinonen, and G. Videen. Single-scattering modeling of thin, birefringent mineral dust flakes using the discrete-dipole approximation. J. Geophys. Res. **114** (2009).

[8] K. Muinonen, T. Nousiainen, P. Fast, K. Lumme, and J. I. Peltoniemi. Light scattering by Gaussian random particles: Ray optics approximation. JQSRT **55** (1996).

Light scattering by quasi-spherical ice crystals in tropical cirrus

T. Nousiainen*,[1], H. Lindqvist[1], and G. M. McFarquhar[2]

[1]*Department of Physics, P.O. box 48, FI-00014 University of Helsinki, Finland.*
[2]*University of Illinois, Department of Atmospheric Sciences, 105 S. Gregory Street, Urbana, IL 61801-3070, USA.*

Shape statistics of small, quasi-spherical ice crystals are compiled through analysis of images collected by the Cloud Particle Imager (CPI) in tropical cirrus. Ray-optics simulations are conducted to obtain their single-scattering properties at 550 nm wavelength. Small tropical ice crystals are found to be more spherical than those in midlatitude cirrus and, correspondingly, their asymmetry parameters are higher. The difference is, however, not significantly larger than the variability within tropical cirrus. Sensitivity studies conducted imply that the asymmetry parameter is very sensitive to internal inhomogeneity about which no data currently exist.

INTRODUCTION

Tropospheric ice clouds are important parts of the Earth-atmosphere system. In particular, their scattering, absorption, and emission properties play a major role in distributing the solar and thermal radiative energy within the system. The radiative impact of ice clouds depends on the size-shape distribution of ice crystals, which varies considerably and is still poorly known. The impact of ice crystals smaller than 100 μm in maximum dimension (D) on ice-cloud radiative properties is especially uncertain.

To assess the radiative impact of ice clouds, it is of utmost importance to know the size-shape distributions of ice crystals in real clouds. Such information can be obtained, for example, by flying a Cloud Particle Imager (CPI) through clouds of interest. These measurements have revealed that small ($D < 100$ μm) ice crystals appear to be predominantly irregular and quasi-spherical in shape. However, there has yet to be a study to show whether the characteristics of these small ice crystals vary between different geographical locations. To this end, shapes and single-scattering properties of small ice crystals present in tropical cirrus are derived and compared against those found for midlatitude ice clouds by [1].

DATA

Ice crystal data were collected during the Tropical Warm Pool International Cloud Experiment (TWP-ICE) and during the Aerosol and Chemical Transport In Tropical Convection (ACTIVE) campaign over Darwin, Australia in early 2006. The data used here consist of CPI images of individual ice crystals obtained during three separate days, and cover different types of ice clouds from aged cirrus to freshly formed anvils [2].

*Corresponding author: Timo Nousiainen (timo.nousiainen@helsinki.fi)

Based on Um's [3] analysis of the CPI data collected, it appears that quasi-spherical ice crystals with $D < 100$ µm contributed approximately 79% (26%), 51% (9%) and 57% (14%) to the total number (projected area) for the size distributions measured on 27 January, 29 January and 2 February, respectively. Example images of these ice crystals are shown in Fig. 1. The CPI instrument has a nominal resolution of 2.3 µm, but images of small particles tend to be blurred due to diffraction effects. Accordingly, ice crystals with $D < 20$ µm were excluded from the analysis.

MODELING APPROACH

The shapes of small, quasi-spherical ice crystals were modeled using the Gaussian random sphere geometry [4]. To this end, a statistical shape analysis was performed. About 1600 images were chosen for analysis and ice crystal silhouettes extracted from each image. The covariance function of radius was then computed for the silhouettes. The images used in the analysis were subject to objective and subjective quality criteria and were chosen in as unbiased a way as possible to ascertain representative shape statistics. The methodology was practically identical to that adapted by [1]. The shape statistics were computed separately for each of 17 flight legs that represented different meteorological conditions, temperatures, and varying temporal and spatial proximities to the convection that generated the cloud.

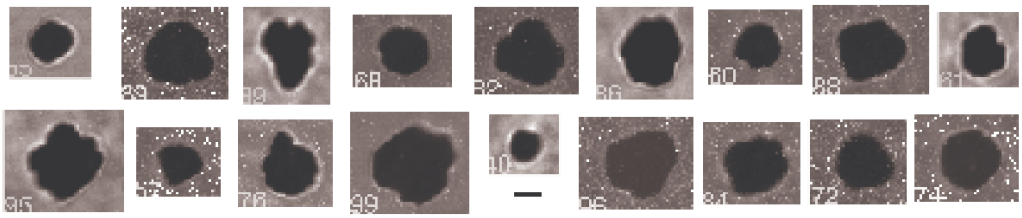

Figure 1. Example CPI images of small, quasi-spherical ice crystals observed in tropical cirrus. The scale bar shown is 11 pixels or about 25 µm long.

The single-scattering properties of the model ice crystals were computed using a modified ray-optics model RODS (Ray Optics with Diffuse and Specular interactions) introduced by [5]. The model consists of the geometric optics and diffraction parts, the latter of which is solved using the Fraunhofer approximation. The geometric optics part is augmented such that the target shape can be filled with internal scatterers, for example soot, sulphate, or air bubbles, with a given mean free-path length δ_0. The single-scattering properties of internal scatterers are given by specifying their scattering phase matrix and the single-scattering albedo. The approach is similar but more flexible than the use of internal Mie spheres adopted by [6].

To assess the impact of internal inhomogeneity on the single-scattering properties of small ice crystals, sensitivity studies with internal scatterers were conducted in addition to simulations of the homogeneous case. The phase matrix of internal scatterers was approximated by a parameterized Henyey-Greenstein phase matrix [5] with specific asymmetry parameter g_0. In the sensitivity study, g_0 and δ_0 were varied. No experimental data is available to constrain the values of these parameters.

RESULTS

The shape analysis revealed that the derived covariance functions of radius closely resemble power-law covariance functions, that is, the weights of the Legendre expansion of the covariance function closely followed a power law. The standard deviation of radius, σ, varied in a range from 0.081 to 0.168, with a number-weighted mean $\langle\sigma\rangle = 0.117$. Likewise, the power law index ν varied from 2.32 to 3.29, with a mean of $\langle\nu\rangle = 2.9$. Incidentally, $\langle\nu\rangle$ is identical to that suggested for the small, quasi-spherical ice crystals in midlatitude cirrus. The mean $\langle\sigma\rangle$, however, is significantly smaller than the value of 0.15 obtained for midlatitudes by [1], and thus deviations from a spherical shape smaller.

To assess whether the power-law covariance function is a good model for the particles, model shapes were generated using both the actual retrieved covariance functions and their power-law fits. Light scattering simulations were then conducted for both sets of particles, while assuming the crystals to be homogeneous. As discussed in [1], the σ values retrieved from silhouettes were multiplied by 1.1 when generating model particles to account for the difference in radius statistics between three-dimensional bodies and their silhouettes; the actual difference depends on the shape, but the aforementioned modification is suitable for the shapes considered here.

Fig. 2 shows the asymmetry parameters obtained for each flight leg for both the original, retrieved covariance functions and their power-law fits. As can be seen, there is some, but not very substantial, variation between flight legs, signifying that the crystal shapes tend to be somewhat different in different conditions or locations. In general, the differences between flight legs are similar to the differences between original shapes and their power-law fits.

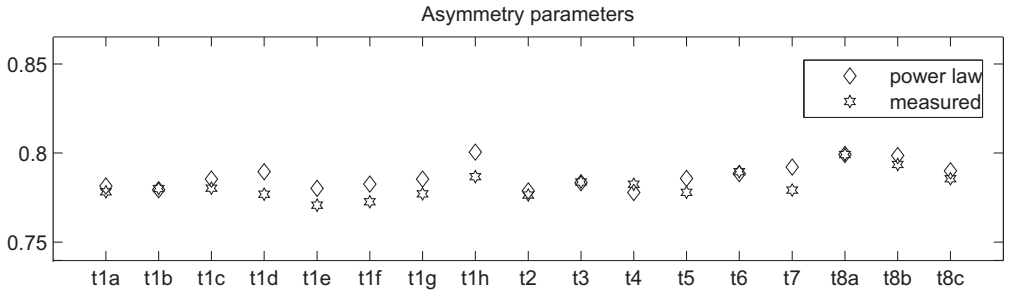

Figure 2. Mean asymmetry parameters obtained for small, quasi-spherical ice crystals observed during each flight leg. The stars depict values obtained for the original, retrieved shape statistics, and diamonds those based on their power-law parameterizations.

The mean shape statistics for the tropical cirrus yields $\langle g\rangle = 0.776$, slightly higher than the corresponding midlatitude value of 0.764 [1]. Thus, the difference between the midlatitude and tropical cases is similar to the internal variability within the tropical cirrus, and the differences are likely to be insignificant for climate.

The sensitivity studies with internal structure revealed that the presence of internal scatterers has a potentially huge impact on scattering. Not surprisingly, a decrease in g_0 or δ_0 decreased g. Internal scatterers cannot, however, increase g over the value obtained for homogeneous crystals, so their possible presence signifies a systematic impact on g. Even when δ_0 was as large as five times the mean crystal radius, g decreased by up to 4 %, de-

pending on g_0. So, even relatively small amounts of internal scatterers caused substantial effects. It is noted, however, that a single micrometer-scale freezing nucleus inside a crystal is unlikely to impact scattering significantly (for a 100 μm crystal, δ_0 would be about 1000 times the crystal size).

Finally, there has been speculation that the CPI might cause the shattering of larger ice crystals so that a fraction of the observed small crystals are merely remnants of shattered particles. To investigate this, the dependence of shape statistics on the number concentration of large ice crystals was examined. Light scattering simulations based on the retrieved statistics showed that the asymmetry parameter varied by less than 0.01 for different large crystal concentrations. Since one of the classes had no large crystals present, it seems unlikely that the results reported here are biased by possible shattering effects. Further, of the 189,905 particles imaged by the CPI during these 3 flights, 98.45 % were the only particle recorded on a frame, suggesting shattering that would generate multiple particles per frame was not an important source of small crystal images.

CONCLUSIONS

A statistical shape analysis of CPI images of small, quasi-spherical ice crystals observed in tropical cirrus reveals that these crystals are closer to spherical than the corresponding crystals in midlatitude cirrus studied by [1]. Ray-optics simulations based on the derived model shapes reveal that their asymmetry parameters are larger than for the midlatitude counterparts. The difference of g between midlatitude and tropical cases is, however, similar to the variability within different types of tropical cirrus and unlikely to be significant for climate considerations.

Sensitivity tests conducted for the impact of internal structures on scattering imply that inhomogeneity of small ice crystals could potentially have a major impact on g and even on the radiative impact of the whole cloud. Unfortunately, no data are available on the inhomogeneity of small ice crystals. Considering the potential impacts, obtaining such data would be highly desirable.

REFERENCES

[1] T. Nousiainen and G.M. McFarquhar. Light scattering by quasi-spherical ice crystals. J. Atmos. Sci. **61** (2004).

[2] J. Um and G.M. McFarquhar. Single-scattering properties of aggregates of plates. Q. J. R. Meteorol. Soc. **135** (2009).

[3] J. Um. The microphysical and radiative properties of tropical cirrus from the 2006 Tropical Warm Pool International Cloud Experiment (TWP-ICE), PhD Thesis, University of Illinois at Urbana-Champaign (2009).

[4] K. Muinonen, T. Nousiainen, P. Fast, K. Lumme, and J.I. Peltoniemi. Light scattering by Gaussian random particles: Ray optics approximation. JQRST **55** (1996).

[5] K. Muinonen, T. Nousiainen, H. Lindqvist, O. Muñoz, and G. Videen. Light scattering by Gaussian particles with internal inclusions and roughened surfaces using ray optics. JQRST **110** (2009).

[6] A. Macke, M.I. Mishchenko, and B. Cairns. The influence of inclusions on light scattering by large ice particles. J. Geophys. Res. **101** (1996).

Asteroid spin and shape inversion for simulated Gaia photometry

D. Oszkiewicz*[,1], K. Muinonen[1,2], and T. Pieniluoma[1]

[1] *Department of Physics, P.O. box 64, FI-00014 University of Helsinki, Finland.*
[2] *Finnish Geodetic Institute, P.O. box 15, FI-02431 Masala, Finland.*

We present Markov-chain Monte-Carlo methods (MCMC) for the inversion of asteroid spins and shapes in the case of limited numbers of or sparsely distributed observations. We focus on convex optimization of asteroid spin and shape, obtaining realistic shape solutions, and exploring the regime of possible spin solutions. The asteroid shape is modeled as a triangulated surface with or without smoothing using bicubic splines. We apply the methods to simulated photometric data for the Gaia mission. We compare the inversion results obtained to the spin and shape originally used to generate the simulated photometric data.

INTRODUCTION

Gaia is an astrometric space mission of the European Space Agency (ESA), and a successor to the ESA Hipparcos mission. While determining and cataloging astrometric positions and movements of about one billion stars, Gaia will observe some hundreds of thousands of asteroids [1]. Photometric data of asteroids will consist of single brightness values ranging over a time interval of five years. This results in a maximum of about one hundred brightness values at varying observing geometries.

Here we apply Markov-chain Monte-Carlo methods [2] to simulated asteroid data in order to obtain spins and shapes of the simulated asteroids (for conventional convex inverse methods, see [3] and [4]). The inverted and original shape and spin solutions are compared to validate the applicability of the methods to the Gaia data.

MCMC METHODS

We have developed three inverse methods for three different purposes:

- In initial convex mapping, we explore the phase space using multiple chains in an optimization mode, accepting gradually improving solutions;
- In convex optimization, we start from the best solution from initial mapping, and gradually move toward the best-fit solution.
- In MCMC convex inversion, we explore the phase space in the neighborhood of the best-fit solution.

We make use of general convex shapes described using a large but finite number of triangles with or without smoothing using bicubic splines. In MCMC convex inversion, the

*Corresponding author: Dagmara Anna Oszkiewicz (dagmara.oszkiewicz@helsinki.fi)

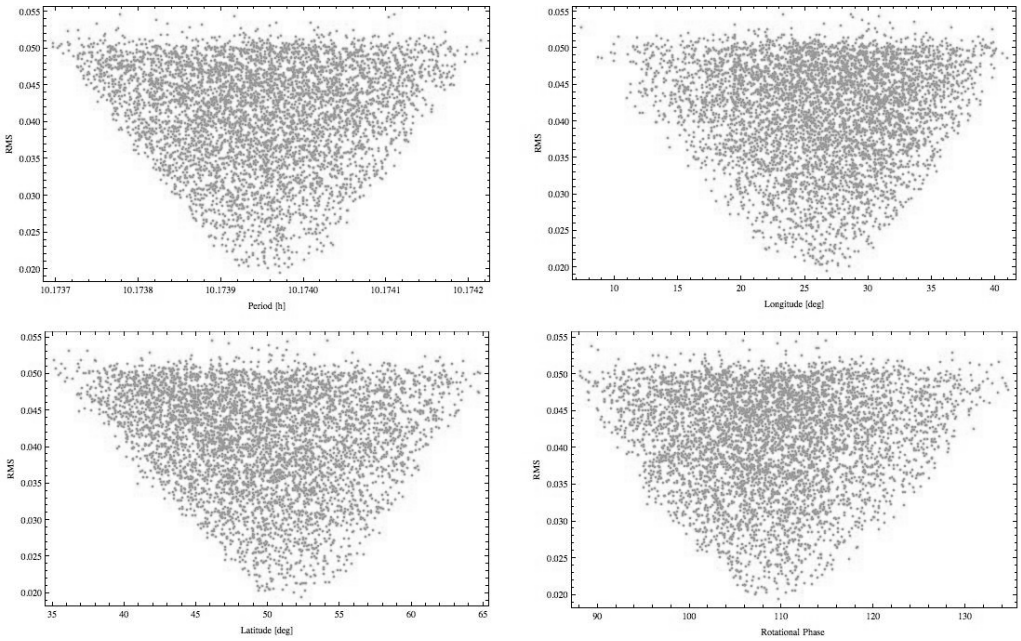

Figure 1. Rotational period and pole distributions as obtained from MCMC convex inversion. Original shape parameters: rotation period 10.17395622 (h), ecliptic longitude of rotational pole 25.02 (°), ecliptic latitude of rotational pole 62.89 (°), and rotational phase 110.1 (°).

convex shape solutions are directly sampled. There are four parameters for the spin characteristics: the rotational period, the ecliptic longitude and latitude of the rotational pole, and the rotational phase of the object at a given time. The $3N$ Cartesian coordinates of the N triangle nodes constitute the free shape parameters. Altogether, there are $3 + 3N$ free parameters [2]. In MCMC convex inversion, the inversion parameters are sampled according to the Metropolis-Hastings algorithm [5]. The accepted shapes and spins generate a sequence, a Markov chain. The proposed spin and shape parameters are accepted or rejected depending on the a posteriori probability density values corresponding to the proposed and current parameters. If the proposed parameters provide a better fit to the data than the current, they are always accepted. If the fit is worse, the candidate is accepted with a certain probability.

RESULTS

We have applied the three inversion methods to the simulated Gaia data. The data was generated for a Gaussian sample sphere mimicking an asteroid. The observing geometries were those simulated for asteroid Vesta for the five-year mission duration [6]. The data for Vesta amounts to 69 brightness values. The accuracy of the simulated data was 0.01 mag. The possible shapes, the rotational period, the ecliptic longitude and latitude of the rotational pole are presented in Figs. 1 and 2. In order to validate the inversion methods, we compare

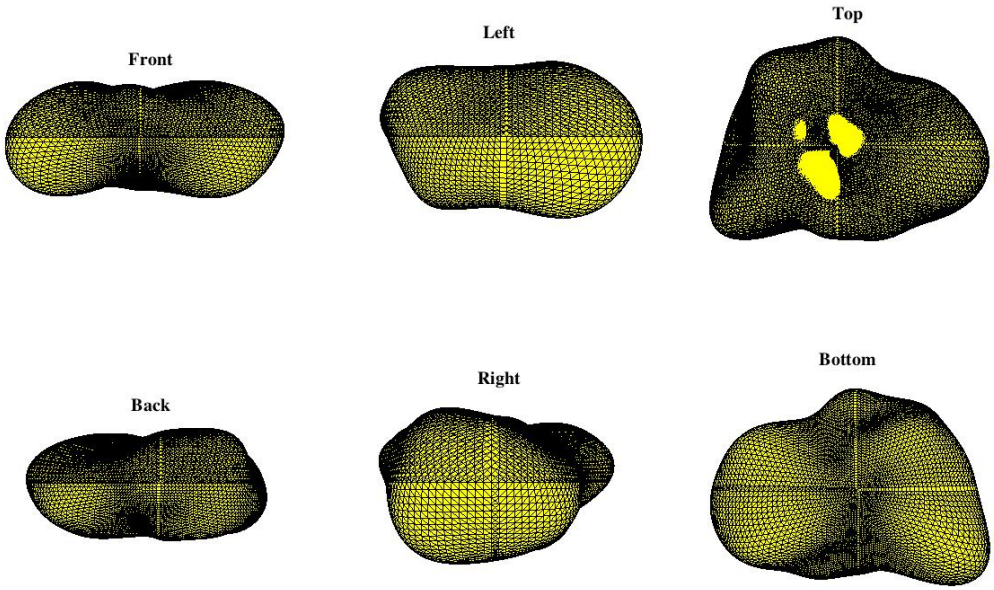

(a) Original shape

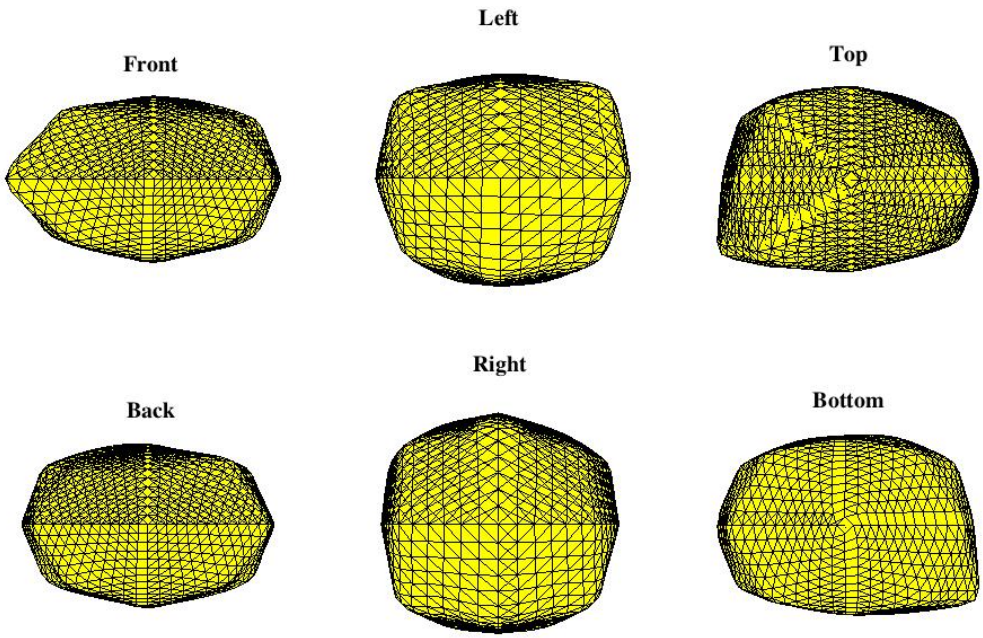

(b) Inverted shape

Figure 2. Original shape together with the one obtained with convex optimization. The best fit resulted in an rms-value of 0.02. In inversion, three triangle rows were utilized per octant.

the results to the original shape and spin values. The distributions for the pole orientation in Fig. 1 and shape in Fig. 2 are in agreement with the pole and shape of the original shape. With simulated Gaia data, we are thus able to obtain overall shape of the object, but not the local shape details.

CONCLUSIONS

We have applied convex stochastic optimization and MCMC inversion methods to derive asteroid spins and shapes using simulated Gaia photometry. The original and inverted shapes are overall in good agreement. The local features are not reflected in the inverted shape. MCMC asteroid lightcurve inversion methods can potentially be applied to the forecoming asteroid photometric observations by the Gaia mission [6] or the lightcurves stored in Standard Asteroid Photometric Catalogue (http://asteroid.astro.helsinki.fi/).

ACKNOWLEDGMENTS

Research supported, in part, by EC Contract No. MRTN-CT-2006-033481 (ELSA).

REFERENCES

[1] A. Cellino, M. Delbò, V. Zappalà, A. Dell'Oro, and P. Tanga. Rotational properties of asteroids from Gaia disk-integrated photometry: A "genetic" algorithm. *Adv. Space Res.* **38** (2006).

[2] K. Muinonen and D. Oszkiewicz. Markov-Chain Monte-Carlo inversion of asteroid photometric lightcurves. In: *11th Electromagnetic and Light Scattering Conference* (2008).

[3] J. Torppa, M. Kaasalainen, T. Michalowski, T. Kwiatkowski, A. Kryszczynska, P. Denchev, and R. Kowalski. Shapes and rotational properties of thirty asteroids from photometric data. Icarus **164** (2003).

[4] M. Kaasalainen, J. Torppa, and K. Muinonen. Optimization methods for asteroid lightcurve inversion. II. The complete inverse problem. Icarus **153** (2001).

[5] W.R. Gilks, S. Richardson, and D.J. Spiegelhalter. *Markov Chain Monte Carlo in Practice*. Chapman and Hall/CRC (1996).

[6] J. Torppa and K. Muinonen. Statistical inversion of Gaia photometry for asteroid spins and shapes. In: *Three-Dimensional Universe with Gaia*. C. Turon, K.S. O'Flaherty, and M.A.C. Perryman (eds.). ESA Special Publications SP-576, ESA Publications Division, ESTEC, The Netherlands (2005).

Soft X-Ray Fluorescence from Particulate Media

H. Parviainen[1], J. Näränen[2], and K. Muinonen[*,2,3]

[1] *Instituto de Astrofísica de Canarias, Calle Vía Láctea, E38205 La Laguna (Tenerife), Spain.*

[2] *Finnish Geodetic Institute, P.O. box 15, FI-02431 Masala, Finland.*

[3] *Department of Physics, P.O. box 64, FI-00014 University of Helsinki, Finland*

We introduce a Monte Carlo ray-tracing code for soft X-ray fluorescence in particulate media. We use the code to investigate the effects on absolute fluorescence line intensities and relative line ratios due to the medium porosity, incident spectrum, and particle size distribution as a function of observation geometry. In particular, we assess the differences between the results given by the simulations and by the analytical fundamental parameters equation.

INTRODUCTION

Soft X-ray fluorescence spectroscopy is a well-established method for elemental analysis of solid matter in laboratory conditions. The measured samples can be prepared for optimal usage, and the brightness and the spectrum of the X-ray source can be controlled to a great accuracy. However, when applied to remote observations of planetary surfaces by space probes, difficulties arise.

The first set of difficulties are due to the fact that the main source for the X-rays, the Sun, is highly variable and unpredictable. The shape and intensity of the X-ray spectrum varies in short timescales, and must be measured simultaneously with the actual fluorescence observations.

The second set of difficulties are inherent to the measured target, i.e., the planetary surface. The surfaces of terrestrial planets and most asteroids are rough, and mostly covered by regolith. The absolute fluorescence line intensities are sensitive to the surface properties such as the particle size distribution, particle packing density, and large-scale surface fluctuations. Furthermore, the effects on absolute line intensities are directly reflected on the ratios of the fluorescence lines, which are used in the elemental analysis of the medium.

Therefore, in order to do elemental analysis using remote X-ray fluorescence observations, it is necessary to know the expected magnitude of the volume and rough-surface effects for the used observation geometries. This knowledge will allow for a realistic assessment of the applicability of the simplified analytical models, such as the fundamental parameters equation (FPE), and will help to constrain the errors when using these analytical models to infer elemental abundances from the observation data. Secondly, a realistic model for the fluorescence output could be used in the future to deduce the regolith properties from the observational data, i.e., fluorescence observations in varying observation geometries can yield information of the surface structure.

Laboratory measurements of the effects on soft X-ray fluorescence due to varying particle size distribution and observation geometry has been carried out by Näränen et al. [1, 2]. An excellent introduction to the theory is given by Clark and Trombka [3], and in-depth reviews of the history of remote soft X-ray observations are given in [2, 1].

*Corresponding author: Karri Muinonen (muinonen@cc.helsinki.fi)

SOFT X-RAY FLUORESCENCE SIMULATION

The simulation code is written in Fortran2003 and uses OpenMP for threading. The simulation data is stored using the netCDF-format, a machine-independent scientific data format, and readable using the standard netCDF tools. The xraylib-package [4] is used for the photoionization coefficient data, as well as for the other atomic data. The analysis of the simulation data is carried out using Python and SciPy.

The particulate media generation is carried out with a dropping-based packing method, described in [5]. Briefly, 5×10^6 spherical particles with radii following the given size distribution are packed into a given packing density inside a rectangular container of edge width w. The edge width is much greater than the mean particle size in order to make the scale of the inhomogeneities produced by the porosity small compared to the spatial extent of the packing.

We model macroscale surface roughness of several mean particle diameters and greater using two-dimensional random fields as described in [6]. The packing is intersected with a random field following Gaussian correlation (Gc) or fractional-Brownian-motion statistics (fBm), and the particles above the random field are removed. The random fields used are functions of two parameters: the standard deviation of heights σ and a model-specific parameter describing the horizontal roughness statistics. The fBm-fields are parametrized by the Hurst exponent H and Gc-fields by the correlation length ℓ.

Fluorescence ray tracing

The X-ray fluorescence ray tracing follows closely the standard ray-tracing principles. A small departure from the basic ray-tracing techniques is taken by calculating the first-order fluorescence signal from all fluorescence lines simultaneously.

For a ray R with radiance I, energy E, position vector $\mathbf{P}$, and direction vector $\hat{\mathbf{D}}$, we compute the mean free path γ from the total extinction coefficient μ_t. The simulation for a single ray begins by searching for the first medium-ray intersection point for the incident ray. Next, a random path length s is drawn from the exponential distribution $s \sim \exp^{-\gamma}$, and the ray is traced to a new position $\mathbf{P} = \mathbf{P} + s_{in}\hat{\mathbf{D}}$, where s_{in} is the distance traveled inside the particles.

Now, the first-order fluorescence signal for fluorescence line l emerging from the point $\mathbf{P}$ inside the medium to a given direction is

$$I_{\mathrm{f,l}} = \frac{I}{4\pi} F_\mathrm{l} f_\mathrm{f} f_\mathrm{e,l} \exp^{-s_\mathrm{out}\mu_\mathrm{t}}, \tag{1}$$

where F_l is the fluorescence yield of the line, f_f and $f_\mathrm{e,l}$ are ratios calculated from the photoionization coefficients, s_out is the distance traveled inside the particles from $\mathbf{P}$, and obtained by tracing a ray until it exits the media. The variables F_l, $f_\mathrm{e,l}$, and μ_t are vectors, and can be precomputed into a lookup table for efficiency.

RESULTS

Absolute line intensities

First we consider the absolute fluorescence line intensities from simple one-element media. We investigate simulated Fe and Ca Kα-line fluorescent signal as a function of varying par-

ticle size distribution models, mean particle sizes, medium packing densities, and incident spectra. We chose two particle size distribution models, monodisperse (constant radius) and uniform, parametrized by the mean particle size (r = 5, 10, 50, 100, and 250 μm). We used two spectrum models, a 9 keV line source and a continuous Ti-tube spectrum. The Ti-tube spectrum was chosen to match closely to the spectrum of the Ti-tube source used in the laboratory measurements by Näränen et. al [1, 2]. Finally, we selected three packing densities ($\rho = 0.20, 0.35, 0.50$).

In Fig. 1 we show the absolute Fe Kα-line intensities for the Ti-tube spectrum, uniform size distribution, three packing densities, and five mean particle radii, together with the results from FPE modelling. The main results are:

- Deviations from the FPE results can be large. Media with low ρ and large r can produce half of the FPE signal for certain observation geometries.
- The mean radius r is one of the most important factors affecting the strength of the absolute line intensities. The effect of changing r is most notable at the transition region where r is close to the mean free path γ.
- The role of the size distribution is small, especially outside the transition region ($r << \gamma$ or $r >> \gamma$). This is because the fluorescence takes place increasingly at the surfaces of single particles for $r >> \gamma$, and for $r << \gamma$ the radiation travels through many particles before ionization.
- Large r values yield a linear trend for $\theta_e > 15°$, and a nonlinear brightening is visible at small θ_e. The nonlinear brightening becomes more pronounced with decreasing ρ, and the curves are nearly linear for the whole θ_e-space for large r and large ρ.

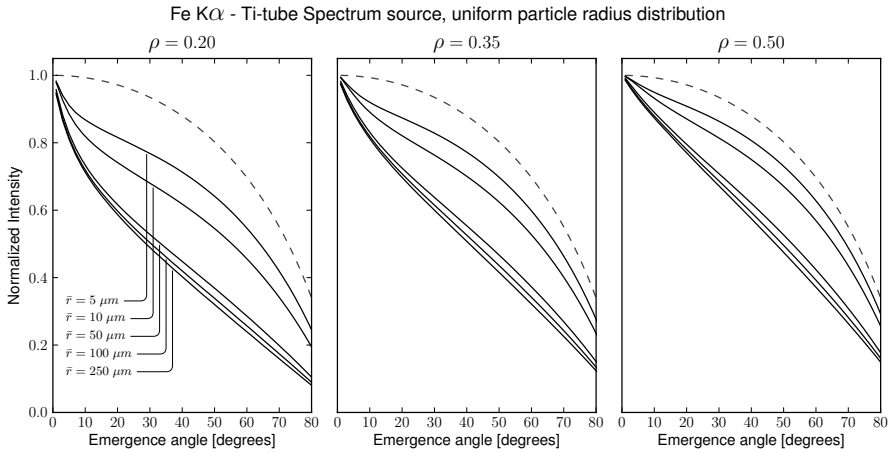

Figure 1. Fe Kα-line intensities as a function of θ_e for $\theta_i = 0°$, Ti-tube source, uniform size distribution, three ρ's, and r's. The results by FPE are shown as dotted line.

Fluorescence line ratios

Next, we focus on the relative line ratios. We use olivine basalt composition listed in Näränen et al. [2] with total molar density of 0.13398 mol/cm^3. We pay special attention to the differences between the simulations and the FPE model, and extend the simulations to include the whole (θ_e,ϕ_e) hemisphere for different values of θ_i.

In Fig. 2 we show the relative differences between the simulated Fe Kα/ Ca Kα line ratios and the FPE-model for the olivine basalt material over the hemisphere for five r values, three ρ values, and $\theta_{\mathrm{i}} = 25°$. The main points are

- In the case of Fig. 2, increasing r and decreasing ρ lead to harder line ratios than expected from FPE modeling.
- Nevertheless, the behavior of the line ratios depend strongly on the incident spectrum. Especially, particulate media can also show softer line ratios than expected.
- The softening relative to FPE is observed for small ϕ_{e} and large θ_{e}. Increasing ϕ_{e} and decreasing θ_{e} harden the line ratios.

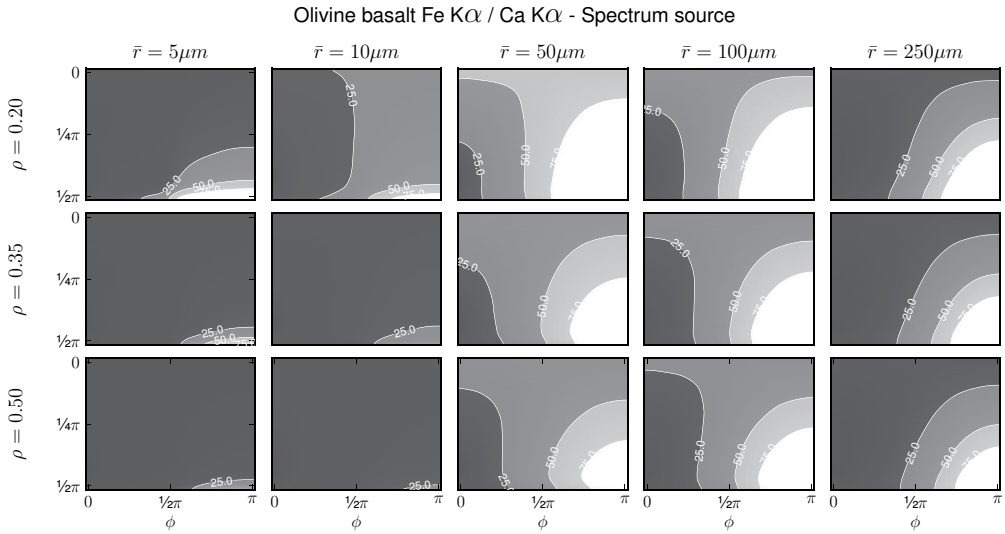

Figure 2. The relative difference between the simulated line ratios and the FPE-model. Dark gray corresponds to $< 25\%$ difference, white to $> 75\%$ difference.

REFERENCES

[1] J. Näränen, H. Parviainen, K. Muinonen, J. Carpenter, K. Nygård, and M. Peura. Laboratory studies into the effect of regolith on planetary X-ray fluorescence spectroscopy. Icarus **198** (2008).

[2] J. Näränen, J. Carpenter, H. Parviainen, K. Muinonen, G. Fraser, M. Peura, and A. Kallonen. Regolith effect in planetary X-ray fluorescence spectroscopy: Laboratory studies at 1.7-6.4 keV. Advances in Space Research **44**(3) (2009).

[3] P.E. Clark and J.I. Trombka. Remote X-ray spectrometry for NEAR and future missions: Modeling and analyzing X-ray production from source to surface. JGR **102** (1997).

[4] A. Brunetti, M. Sanchez del Rio, B. Golosio, A. Simionovici, and A. Somogyi. Spectrochimica Acta Part B: Atomic Spectroscopy. **59**(10--11) (2004).

[5] H. Parviainen and K. Muinonen. Bidirectional reflectance of rough particulate media: Ray-tracing solution. JQSRT **110** (2009).

[6] H. Parviainen and K. Muinonen. Rough-surface shadowing of self-affine random rough surfaces. JQSRT **106** (2007).

Reflectance spectra of meteorites

M. Paton[*,1], K. Muinonen[1,3], L. J. Pesonen[1], V. Kuosmanen[2], T. Kohout[1], J. Laitinen[2], and M. Lehtinen[1]

[1]*Department of Physics, University of Helsinki, P.O. Box 64, FI-00014, Finland.*
[2]*Geological Survey of Finland, P.O. Box 96, FI-02151, Finland.*
[3]*Finnish Geodetic Institute, P.O. Box 15, FI-02431, Finland.*

A spectrometer at the Geological Survey of Finland was used to obtain 33 high-quality reflectance spectra of 26 individual meteorites. Principal Component Analysis was applied to the spectra to explore grouping strategies for meteorite classification. Initial investigations of surface roughness effects on the reflectance spectra features were made.

INTRODUCTION

Spectral photometry is a powerful tool for establishing links between meteorites and their parent bodies (asteroids, comets, the Moon, Mars). The primary information used to interpret asteroid reflectance spectra comes from absorption bands that are diagnostic of the cosmically significant minerals pyroxene and olivine. Then there are secondary effects that can alter the size of the bands and the slope of the continuum. These effects are primarily due to particle size, surface roughness, and temperature which are poorly characterized in the literature. These effects are important because our knowledge of the physical condition of the surface of bodies such as asteroids and comets is limited. Understanding how light scattering changes the features in the reflectance spectra is then useful for interpreting spectra. A lot of effort has gone into characterizing and modeling the effect of particle size on the reflectance spectra with some success. The reason for this is because most asteroids over 100 m in size are thought to be covered by a layer of impact generated particles. However, there has been little characterization of the meteorite samples in terms of their solid surface roughness.

METHOD

A spectrometer at the Finnish Geological Survey was used to obtain 33 reflectance spectra from 26 meteorites representing undifferentiated (C, H, L, LL and E) to differentiated meteorites. To account for inhomogeneity of the surface composition, reflectance spectra were obtained from ten different locations on the surface and then the average was calculated. To explore light scattering effects, spectra were taken from a matt (sanded) and polished surface for one meteorite (Wellman). From another meteorite (Alfianello) we obtained a spectrum from a natural surface and a spectrum from a sawn surface. To compare solid surfaces to powdered samples, we retrieved 163 reflectance spectra of meteorite samples from NASA's Planetary Data System [1]. This dataset also includes meteorite groups not represented by our measurements.

* Corresponding author: Mark Paton (mark.paton@helsinki.fi)

A Principal Component Analysis (PCA) was applied to the combined data sets to explore the distribution of the reflectance spectra structure over the meteorite groups. PCA is a relatively simple mathematical procedure for reorganising a data set so that the information can be described by fewer variables. The technique has been used to explore the distribution of asteroid taxonomic classes [2].

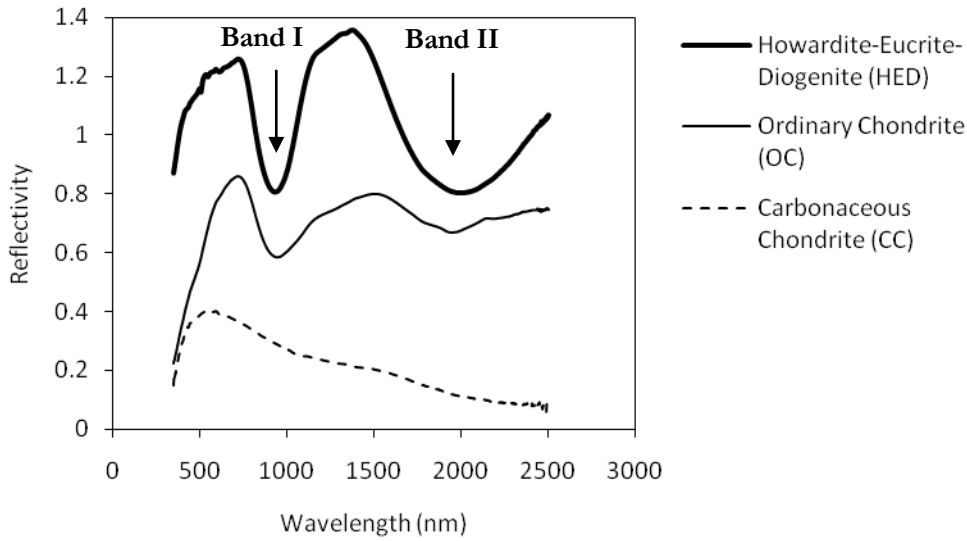

Figure 1. Reflectance spectra obtained by the Geological Survey of Finland. The chart shows examples of spectra for achondrites (HEDs) and chondrites (ordinary and carbonaceous). The spectra have been offset along the y-axis for clarity. Notice how the spectra vary in their structure. This is important for interpreting the PCA results in Fig. 2.

We followed the method of [3] to parameterise the reflectance spectra in principal component space. The slope was removed by this method to account for uncertainties in space weathering and observational uncertainties. Space weathering is not of a concern here but we followed this technique to account for observational uncertainties, such as the phase angle. The spectrum was first normalised and then a slope was least squares fitted and forced to go through unity. The spectrum was then divided by the slope.

RESULTS

The result of a PCA on the meteorite reflectance spectra is shown in Fig. 2. The distribution of the meteorite groups in principal component space can be explained by examining the eigenvectors shown in Fig. 3. Eigenvector 1 has strong loadings close to the locations in wavelength space corresponding to the absorption bands at ~1000 nm and ~2000 nm that are diagnostic of the mineral pyroxene. In Figure 2, the carbonaceous chondrites cluster to the right of the diagram as they have relatively flat spectra. The HEDs then cluster to the left as they have relatively deep absorption bands. Eigenvector 3 has a strong loading close to the location of the bands found at ~1000 nm that are diagnostic of both pyroxene and olivine. The spread along the y-axis for the ordinary chondrites could be explained by the presence of

olivine and pyroxene in these meteorites whose relative ratio of abundance varies over the ordinary chondrite group. Eigenvector 2 is shown for completion but does not have loadings at wavelengths of interest for this investigation.

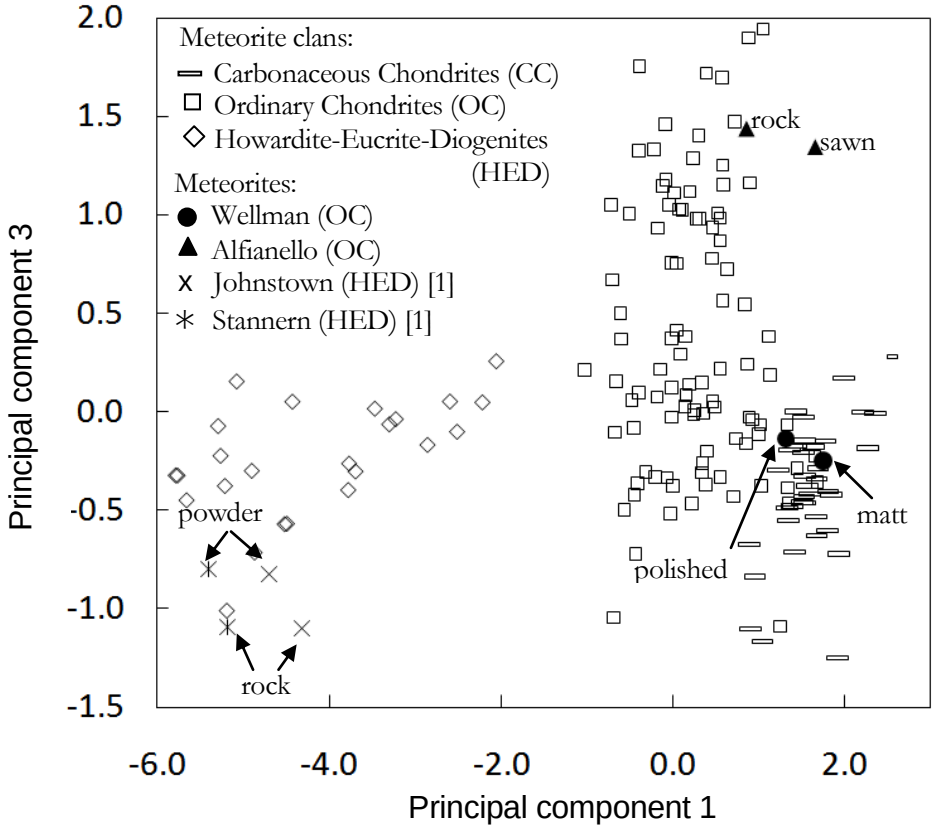

Figure 2. Principal Component Analysis of 196 meteorite reflectance spectra. This includes 33 new measurements from this work plus 163 measurements retrieved from NASA's PDS [1]. The three meteorite clans (groups) are shown. Individual meteorites from these clans are identified with their own symbols and labelled with their surface condition. Wellman and Alfianello are from the spectra obtained from this work.

From measurements by [4], the reflectance spectrum from a rock surface has smaller absorption bands when compared to powdered surfaces. Also an increase in the roughness of the rock surface will increase the band depth. This agrees with measurements made by [1] and shown in Fig. 2. A similar effect occurs with the ordinary chondrites.

In our reflectance spectra, when comparing a matt and a polished surface, the polished surface has deeper absorption bands than found in the reflectance spectrum from the matt surface which suggests that the polished surface is rougher. One explanation suggested in [4] for this contradictory result may be that exposed pore spaces actually increase roughness after polishing. The reflectance spectrum from the rock surface has deeper absorption bands than found in the reflectance spectrum from the sawn surface as would be expected with a rougher surface.

CONCLUSIONS

PCA applied to the reflectance spectra of meteorites successfully separates chondrites and achondrites (HEDs). Meteorites remained inside their specific groups despite changes in the structure of their surface. Future work on understanding surface light scattering effects will help us improve the classification of meteorites using non-destructive methods and help us to further understand the nature of asteroid surfaces.

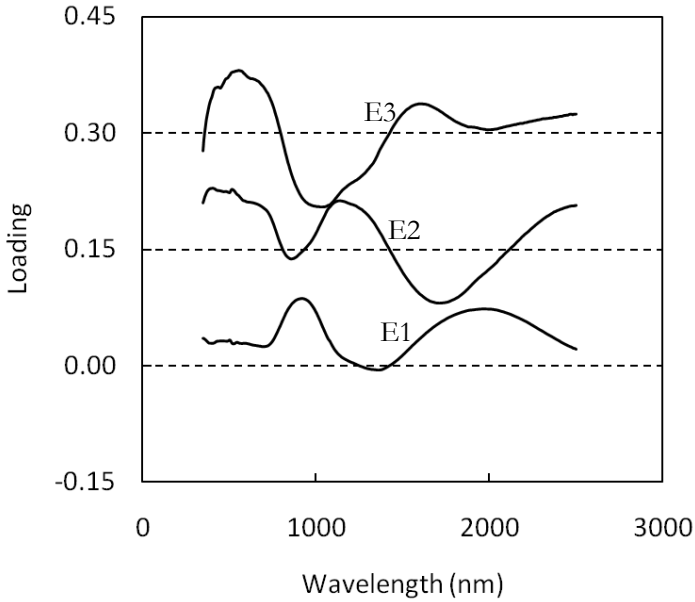

Figure 3. Eigenvectors from PCA of the meteorite reflectance spectra data set. E2 shows that the maximum variation in reflectivity is at around 1000 and 2000 nm while E3 is most strongly correlated to variation in reflectivity around 1200 nm and 1800 nm. E2 and E3 have been offset by 0.15 and 0.3 respectively on the y-axis and the dotted lines are the zero axes.

REFERENCES

[1] M. Gaffey. Meteorite Spectra. EAR-A-3RDR-METEORITE-SPECTRA-V2.0. NASA Planetery Data System (1970).

[2] D. Tholen. Asteroid taxonomy from cluster analysis of photometry. PhD thesis. Univ. of Arizona Press. Tuscon (1984).

[3] S. Bus and R. Binzel. Phase II of the small main-belt asteroid spectroscopic survey the observations. Icarus. **158** (2002).

[4] J. Harloff and G. Arnold. Near-infrared reflectance spectroscopy of bulk analog materials for planetary crust. Planet. Space Sci. **49** (2001).

Measurements of spectral and polarised bidirectional reflectance factor of various natural and artificial land surfaces

J. I. Peltoniemi*, T. Hakala, and J. Suomalainen

Finnish Geodetic Institute, BOX 14, FI 02431 Masala.

Methodology and instrumentation to measure multiple scattering of light from particulate media such as snow, gravel, and sand are discussed. Some results are shown.

INTRODUCTION

Many land surfaces on Earth and other celestial bodies are covered by a particulate medium, i.e., a medium, that is formed by individual particles. Understanding scattering from such surfaces is important for remote sensing, as a boundary condition for Earth radiation and climate models, and for many research purposes.

Models for scattering from the single particles and particulate media are discussed in other presentations of this meeting. All models need validation and stimulation by experimental research. Here, a short discussion of various measurement methods and instruments are given, with special emphasis on field and laboratory gonio-polari-spectro-photometry. Some illustrative sample results are shown.

MEASURABLES AND DEFINITIONS

If the medium is illuminated by a directional beam F_0 from direction (ι, ϕ_0), and observed from direction (ϵ, ϕ) (Fig. 1), the observed intensity $I(\epsilon, \phi) \propto R(\epsilon, \phi, \iota, \phi_0) F_0(\iota, \phi_0)$, where R is the bidirectional reflectance factor (BRF), defined as a ratio against ideal diffuse (Lambertian) reflector. If the incident light is polarized, or if the sensor is sensitive to polarisation, or if the results are used in multiple-scattering calculations, polarisation must be taken into account. Optically complete description of polarisation is given by defining the observables using the Stokes vectors $\mathbf{I} = [I, Q, U, V]$, where I is the intensity (radiance), Q is the $0°$–$90°$linearly polarised component, U is the $45°$–$135°$linearly polarised component, and V is the circularly polarised component. BRF is then defined as a 4×4 matrix. Further define degrees of linear polarisation, $P = -Q/I$ or $P_{\rm lin} = \sqrt{Q^2 + U^2}/I$.

In field measurements, the situation is further complicated by diffuse light coming from the sky and environment. To recover the BRF matrix from the measurements, the incoming direct and diffuse light must be measured separately.

MEASUREMENT INSTRUMENTS

The BRF for a medium can be measured by several systems. If the medium is homogeneous over large enough area, one can scan over the area from one point [1, 2]. Also a wide-angle-lens camera can be used. Small surface areas are better measured by moving the sensor head around the target using a goniometer. Typically such instruments consist of a moving arm

*Corresponding author: Jouni Peltoniemi (jouni.peltoniemi@fgi.fi)

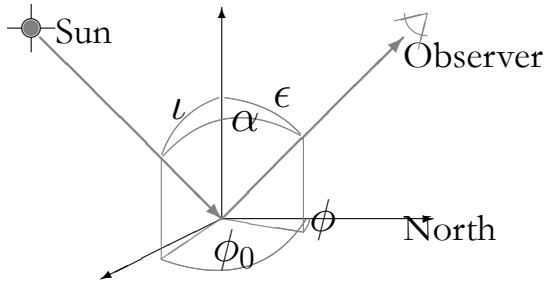

Figure 1. Definition of the angles used in surface reflectance work: ϵ and ι are the zenith angles of the emergent (Observer) and incident (solar) radiation respectively, ϕ and ϕ_0 are the corresponding azimuths.

or rail holding the sensor or optical head[3, 4, 5, 6]. Alternatively all directions are measured simultaneously using light cable construction. To measure large heterogeneous surfaces, one option is to fly the camera over the surface using satellite or air plane. Until recently, this has been an expensive technique for research purposes only, but now new advanced unmanned aerial vehicles (UAV) can carry light cameras economically and accurately, making many new opportunities possible. Spectral properties are measured either using selected filters in the camera, or more completely with a spectrometer. Polarisation can be measured using polarising filters or prisms.

An important issue is to calibrate the measurement system. Most uncertainties and errors are related to deficient calibration. To overcome uncertainties in absolute calibration, most measurements are taken relative to a known reference standard, usually Spectralon. For field use, also larger white or grey sheets are used.

Figure 2. Left: FIGIFIGO measuring snow, foreground left the Spectralon reference panel, right the sky monitoring pyranometer. Right: Microdrone md4-200.

Finnish Geodetic Institute field gonio-spectro-polari-photo-meter (FIGIFIGO) is a light-weight portable instrument to measure the BRF of land surfaces inside and outside (see Fig. 2). It has one moving arm holding the fore optics and fine-pointing system. The main sensor is an ASD FieldSpec Pro FR spectrometer. Footprint is about 10 cm in diameter. Optionally, polarisation can be measured using wide band calcite polariser in four positions to give the Stokes I, Q, and U parameters[7]. Two small UAVs, Microdrone md4-200 and md4-1000, have been equipped with calibrated cameras to measure BRF of larger land surfaces. These are flown in preprogrammed tracks over and around selected target areas, and BRF map is then produced[8].

SAMPLE RESULTS

Over 200 samples have been measured using FIGIFIGO, its predecessors, and the UAV system[9, 10]. Here, two cases are shown: moist snow measured in Sodankylä spring 2009, and grey gravel from Sjökulla aerial image test site, measured summer 2008. A 3-D BRF plot shows how different the cases are: snow is a strong forward scatterer and gravel a backward scatterer (Fig. 3). The reflection spectra taken in four directions in the principal plane show that the spectral shape varies as a function of the observation angle, but all characteristic features remain. The steepness of the spectral features depends on grain size. The degree of linear polarisation is depicted in the principal plane as a function of the observation zenith angle in three wavelengths, indicating how the polarisation depends on the scattering angle (Fig. 4) with maximum in far forward. The polarisation spectrum gives a small surprise with the increase between 600 and 900 nm where BRF is flat.

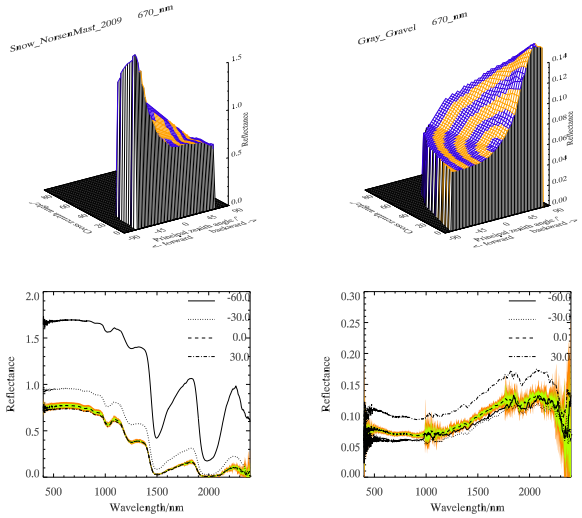

Figure 3. Top: BRF plot of the sample. Bottom: the reflection spectra of the samples in four zenith angles (ϵ) in the principal plane. The targets are snow (left) and grey gravel (right). The zenith angle of incidence (ι) were about 55°.

CONCLUSIONS

Reflectances of many particulate, solid and vegetated surfaces have been measured. Differences between targets are large. Most information is available from the spectrum. Many features are so strong that basic identification is possible even from poor data, but for accurate quantitative analysis careful measurements must be taken, and directional effects taken into account. The directional effects (BRF shape) in general are rather difficult to exploit, because they depend on so many things, and often the angular range remains too narrow. The polarisation poses still many challenges and has unexplained features. New research is needed before full utilisation. Polarisation is a very strong function of the scattering angles, and must be measured angularily.

One must notice that in real nature, every sample is individual, and one cannot generalise results so easily. The surfaces are very heterogeneous, and all parameters, topography, composition, flora and fauna vary in all possible scales. Also, the temporal variations are large, as no target exposed to weather can be assumed to be invariant over any significant

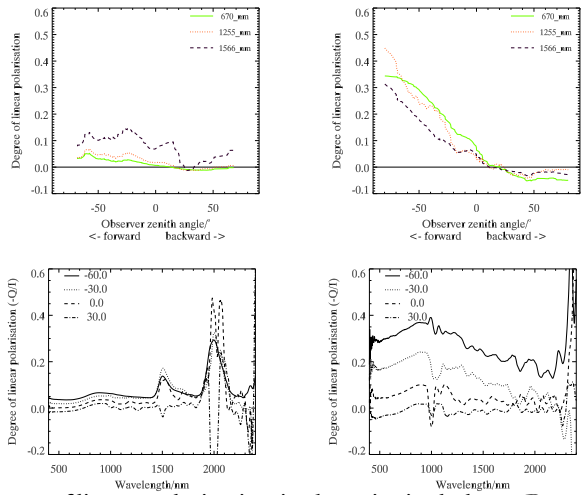

Figure 4. Top: Degree of linear polarisation in the principal plane. Bottom: the polarisation spectra of the samples in four directions in the principal plane.

time scale. The measurements presented here and in the database, are all from carefully selected or artificially made targets, to make interpretation easier. Results have been valuable for modelling, aerial observations, and developing remote-sensing processes. Measurements continue with new targets and improving techniques.

REFERENCES

[1] C.J. Bruegge et al. PARABOLA III: A sphere-scanning radiometer for field determination of surface anisotropic reflectance functions. Rem. Sens. Rev. **19**(1–4) (2000).

[2] S.R. Hudson et al. Spectral bidirectional reflectance of Antarctic snow: Measurements and parameterization. J. Geophys. Res. **111**(D18106) (2006).

[3] S.R. Sandmeier and K. I. Itten. A field goniometer system (FIGOS) for acquisition of hyperspectral BRDF data. IEEE T. on Geosci. and Remote Sensing **37** (1999).

[4] B. Hosgood et al. Goniometers. In: *Encyclopedia of Electronics Engineering*. J. Webster (ed.). Vol. 8, John Wiley, New York (2000).

[5] T.H. Painter, B. Paden, and J. Dozier. Automated spectro-goniometer: A spherical robot for the field measurement of the directional reflectance of snow. Review of Scientific Instruments **74**(12) (2003).

[6] C.S. Bourgeois et al. IAC ETH goniospectrometer: A tool for hyperspectral HDRF measurements. J. Atm. Ocean Tech. **23**(4) (2006).

[7] J. Suomalainen et al. Polarised multiangular reflectance measurements using Finnish Geodetic Institute field goniospectrometer. Sensors **9**(5) (2009).

[8] T. Hakala, J. Suomalainen, and J.I. Peltoniemi. Acquisition of bidirectional reflectance factor dataset using a micro unmanned aerial vehicle and a consumer camera. Remote Sensing **3**(2) (2010).

[9] J. Peltoniemi et al. Bidirectional reflectance spectrometry of gravel at the Sjökulla test field. ISPRS Journal of Photogrammetry and Remote Sensing **62**(6) (2007).

[10] J. Peltoniemi et al. Polarised bidirectional reflectance factor measurements from snow, soil and gravel. JQSRT **110** (2009).

Specular gloss simulations of media with small-scale roughness

A. Penttilä* and K. Lumme

Department of Physics, University of Helsinki, P.O. box 64, FI-00014 Finland.

We study the effect of microroughness on the simulated specular reflection (i.e., gloss). We use the discrete-dipole approximation and compare the results to the Bennet–Porteus approximation. This study is originally applied to print toners for paper industry, but the results are general and apply to all other surfaces with small-scale roughness.

INTRODUCTION

In paper industry, one important feature in digital printing revealing a good image quality is the print gloss. Roughness of paper, determined on a macroscale, is usually exhibiting a good correlation with gloss[1]. Attempts to correlate microroughness properties with gloss has been presented in several reports (e.g. [2, 3]). Despite several studies, the impact of the toner substrate surface roughness is lacking.

The surface of paper printed with toners consists of close-packed toner particles. Individual toners are quite cylindrical with diameters of about 8 µm and thicknesses of about 2–3 µm. The toner surface can be measured with the atomic force microscope (AFM, in tapping mode). Images obtained with AFM show that the surface standard deviation is typically about 21 nm with AFM image size of 3×3 µm and 31 nm with 10×10 µm. Therefore, the study of the effect of toner surface roughness on specular reflection (gloss) can be generalized to a generic case of surface with roughness in scales smaller than the wavelength.

Suitable methods for analysing the effect of the small-scale roughness on light scattering have been lacking. Recently, computational methods, e.g., the discrete-dipole approximation (DDA; see, e.g., [4]), have become relevant due to the increased resources of modern computing clusters. The accuracy of DDA is fairly good compared to exact wave-optical methods[5], and thus DDA can be used to check the validity of other approximations.

METHODS FOR ANALYZING THE SPECULAR REFLECTION

Reflected light from rough surfaces is a sum of coherent scattering, or specular reflection, and incoherent or diffuse scattering. With a Gaussian rough surface with surface standard deviation σ and correlation length τ, both smaller than the wavelength λ, the specular part can be estimated to some extent with analytical approximations. The exact specular component from a smooth surface can be estimated with the Fresnel reflection coefficient and the effect of surface σ can be added with the Bennet–Porteus (B–P) factor[6]. More detailed approximations include the Muinonen–Smythe–Kirchhoff (MSK) approximation[7] for coherent scattering near the specular direction along the principle plane, and the Beckmann–Kirchhoff (B–K) model[8] for coherent scattering off from the principal plane. The results from comparison with the DDA method show that the abovementioned MSK and

*Corresponding author: Antti Penttilä (Antti.I.Penttila@helsinki.fi)

B–K approximations can be quite good in some cases but, especially with non-zenith incoming light, the results off the principal plane with the B–K approximation are not accurate enough (results not shown here).

The Bennet–Porteus (B–P) approximation for gloss G is

$$\mathrm{G}(\sigma) \propto \exp\left(-(4\,\pi\,\sigma\cos(\theta)/\lambda)^2\right), \tag{1}$$

where σ is the surface standard deviation, θ the incoming angle, and λ the wavelength. The proportionality of G and the B–P factor is such that for perfectly smooth surface the B–P factor is one and the gloss value is given by the normalized Fresnel coefficient of the surface. The B–P approximation is very simple to calculate, and thus it is interesting to study its accuracy.

SIMULATION OF GLOSS

We can model the rough surface of cylindrical slab with random height field. We assume the height field to be Gaussian with Matérn (auto)correlation function. The formula of the Matérn correlation function is

$$\mathrm{C}(d) = (2\sqrt{\kappa}\frac{d}{\tau})^{\kappa}\; K_{\kappa}(2\sqrt{\kappa}\frac{d}{\tau})\;\left(2^{\kappa-1}\,\Gamma(\kappa)\right)^{-1}, \tag{2}$$

where K_κ is the modified Bessel function of the second kind and Γ is the gamma function. The parameters are τ which is the correlation length and κ which controls the smoothness of the surface. Actually, κ controls up to which order the surface will have continuous derivatives. Special cases of Matérn are when $\kappa \to \infty$ when it approaches the Gaussian correlation function, and $\kappa = 1/2$ when it is equal to the exponential correlation function.

We have used four different values for κ to study the effect of the correlation structure of the surface on gloss, $\kappa = 1/2, 1, 2$, and $\kappa \to \infty$. For the correlation length τ, we have used three values: $\tau = 250$, 500, and 1000 nm. The most interesting surface parameter is the surface σ and its effect on gloss. We used σ values from 0 nm to 40 nm with 10 nm steps in our simulated surfaces. An example of realizations of the modeled rough cylinders are shown in Fig. 1.

Figure 1. Three realizations of the surface model. All the surfaces have $\tau = 500$ nm and $\sigma = 20$ nm. The leftmost surface has $\kappa = 1/2$ (exponential correlation), the middle $\kappa = 1$, and the rightmost has $\kappa \to \infty$ (Gaussian correlation).

Gloss measurements and DDA

The DDA method produces a map of the reflected intensity from the model surfaces with a given incoming angle. The most interesting part of the reflection in our case is the area around the specular direction. The behavior of the gloss peak can clearly be seen from the

DDA simulation results as in Fig. 2a. However, when comparing the simulated results to the measurements, some data reduction must be done to mimic the measuring configuration, e.g., the TAPPI T 480 standard or similar [9]. In the measurements, the device that captures the reflected flux has some finite acceptance area from where it integrates the flux. With simulated data, we have several options for extracting the gloss value. We can either take the peak value in the exact specular direction or we can integrate over a small area around the specular direction. This integration can be done one-dimensionally (1-D) along the principal plane or, more generally, in two-dimensionally (2-D) on the spherical surface.

The measured gloss values are not the absolute values of the flux, instead the values are compared to the gloss value of the standardized smooth black glass plate [9] with gloss value G of 100 GU (gloss units). If the material refractive index n, especially its imaginary part, that we are interested in is not known, the absolute calibration to black glass is impossible. The relative scale where we standardize the DDA results to the gloss from a smooth cylinder having the same n that we use for the material is sufficient to study the validity of the B–P factor. We found out that all the different methods to extract gloss values (i.e., peak value, 1-D or 2-D integration) will produce about the same outcome when standardized. Therefore, we choose to calculate the 1-D integral along the principal plane with $\pm 4^\circ$ from the specular direction, because its evaluation is more convenient than the 2-D integral. We used 20° zenith angle for incoming light.

RESULTS FROM GLOSS ANALYSIS

The surface model with Matérn correlation function C is parameterized with the smoothness parameter κ and correlation length parameter τ. We have used very absorbing material with $n = 1.54 + \mathrm{i}1$ for more prominent surface effects, but we also studied the case $\mathrm{Im}n = 0.015$. The dipole representation of the cylindrical slab has 320 dipoles for the cylinder diameter of 8 µm and 20 dipoles for depth, resulting about 2×10^6 dipoles for the DDA grid, of which about 1.6×10^6 are occupied by the material.

The effect of four different κ's is shown in Fig. 2b. In overall, it seems that the effect of σ in the B–P approximation behaves quite reasonably but overestimates the gloss systematically. The smoothest C, where $\kappa \to \infty$ and the correlation is Gaussian, as in the original derivation of the B–P factor, is closest to the B–P approximation. As the κ has smaller values and the C changes toward the exponential correlation, the difference to the B–P approximation gets larger.

The effect of the correlation length τ is presented in Fig. 2c. All the values of τ give similar shapes to the gloss as a function of σ, but larger τ give more gloss in better agreement with the B–P approximation. This result is in disconjunction with the theoretical basis of the B–P approximation where it is required that $\tau \ll \lambda$, so it seems that this requirement is not that important. If the imaginary part is small, all the surface effects become less pronounced as seen in Fig. 2d.

In conclusion, we note that the B–P approximates quite well the overall shape of the dependence between the small-scale surface deviations and the specular reflection. However, the B–P factor does not take into account the refractive index or the correlation type or length. If more detailed analysis is needed, DDA is a suitable method.

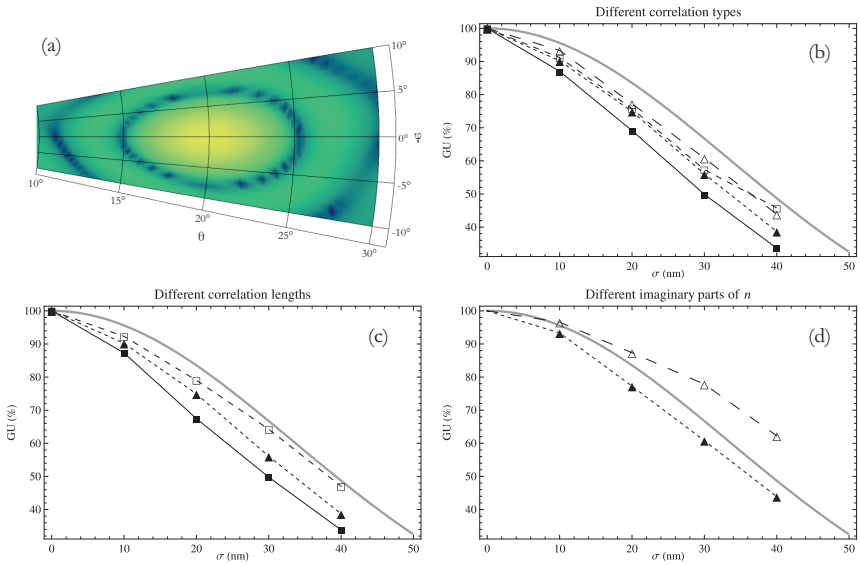

Figure 2. (a) Scattering pattern around the specular direction ($\varphi = 0°, \theta = 20°$) simulated with DDA. Brighter yellow and green areas have higher intensity. (b)–(d) Gloss as a function of surface σ. The gray line shows the B–P approximation. (b) The symbols ■, ▲, □, △ correspond to $\kappa = 1/2, 1, 2$, and $\kappa \to \infty$; $\tau = 500$ nm and $n = 1.54 + \mathrm{i}1$. (c) The symbols ■, ▲, □ correspond to $\tau = 250, 500$ and 1000 nm; $\kappa = 1$ and $n = 1.54 + \mathrm{i}1$. (d) The symbols ▲, △ correspond to $\mathrm{Im}n = 1, 0.015$, $\kappa \to \infty$, $\tau = 500$ nm, and $\mathrm{Re}n = 1.54$.

REFERENCES

[1] M.A. MacGregor. A review of the topographical causes of gloss variation and the effect on perceived print quality. In: *Proceedings of the Hansol Research Symposium*. Seoul (2000).

[2] M.-C. Béland and J.M. Bennett. Effect of local microroughness on the gloss uniformity of printed paper surfaces. Applied Optics **39**(16) (2000).

[3] R. Xu, P.D. Fleming, and A. Pekarovicova. The effect of inkjet paper roughness on print gloss. J. Imaging Sci. and Techn. **49**(16) (2005).

[4] B.T. Draine and P.J. Flatau. The discrete dipole approximation for scattering calculations. J. of Opt. Soc. of Am. A **11** (1994).

[5] A. Penttilä, E. Zubko, K. Lumme et al. Comparison between discrete dipole and exact techniques. JQSRT **106** (2007).

[6] J.O. Porteus. Relation between the height distribution of a rough surface and the reflectance at normal incidence. J. of Opt. Soc. of Am. **53** (1963).

[7] K. Muinonen. Sirontaa ympyrälevyistä Kirchhoff-tyyppisissä approksimaatioissa. In: *Uudistuva paperi - päällystys ja pintakäsittely* (in Finnish). TEKES, Helsinki (1996).

[8] P. Beckmann and A. Spizzichino. *The scattering of electromagnetic waves from rough surfaces*. Pergamon, New York (1963).

[9] J. Vaarasalo. Optical properties of paper. In: *Pulp and paper testing*. Fapet (1999).

[10] M. Juuti, H. Tuononen, A. Penttilä, K. Myller, K. Lumme, and K.-E. Peiponen. Spectral properties and surface uniformity of black glass gloss references. Optical Engineering **48**(3) (2009).

Cubature orientation-averaging scheme

A. Penttilä* and K. Lumme

Department of Physics, University of Helsinki, P.O. box 64, FI-00014 Finland.

We propose the so-called cubature-on-the-sphere orientation-averaging scheme to be used in scattering computations. The cubature points are optimally arranged on the sphere to produce non-biased and fast convergence in scattering problems requiring numerical orientation averaging. Cubature clearly outperforms the conventional regular grid of sample points on the sphere.

INTRODUCTION

A common setup in scattering problems is to compute the orientation-averaged properties of the target. In many cases, we are interested to interpret and compare the scattering simulation results against observational data from a large ensemble of particles in random orientation. Therefore, we need to simulate particles with with different sizes and in different orientations. Usually, the orientation distribution can be considered to be evenly distributed over all Euler angles ($\alpha, \beta,$ and γ).

There are computational methods that can perform the orientation averaging analytically, such as the T-matrix method for individual particles [1] or for cluster of spheres [2]. However, even with the T-matrix method the fixed orientation version of the code has some benefits, as Okada [3] has pointed out. The fixed-orientation superposition T-matrix code (F-ST) consumes less memory and can therefore be used for larger size parameters. Also, if accurate results can be achieved with a modest number or orientation angles, the F-ST can be even faster than the analytical orientation-averaging version (A-ST) for large problems. Another set of codes, where combining the fixed-orientation computations into averaged results is a must, are the volume-integral codes, e.g., the popular discrete-dipole approximation codes (DDA; e.g., [4, 5]).

The task in numerical orientation averaging is, in short, to compute the Mueller scattering matrix for a given set of Euler angles $(\alpha_i, \beta_i, \gamma_i)$ and then average the result over i. In many methods (e.g., in T matrix and DDA), the third angle γ can be sampled efficiently for given (α_i, β_i) by computing the result in several scattering planes. Therefore, the choice of orientation-averaging points reduces to the problem of selecting the (α_i, β_i) points on the sphere.

CUBATURE ON THE SPHERE

Currently, the standard method for selecting the (α_i, β_i) points on the sphere is to produce a regular grid by evenly distributing $\cos\alpha$ in $[0, \pi]$ and β in $[0, 2\pi]$. While there is nothing particularly wrong with this method, it is not the most efficient one. Because the Mueller

*Corresponding author: Antti Penttilä (Antti.I.Penttila@helsinki.fi)

matrix computation for every (α_i, β_i) can be very resource consuming, it would be beneficial to optimize the averaging (i.e., integration) as well as possible.

This optimization has been studied by Xu and Khlebtsov [6] and by Okada [3]. Xu and Khlebtsov state that using either Simpson rule or Gaussian quadrature will improve the accuracy in numerical orientation averaging. Okada proposes the quasi-Monte-Carlo (QMC) method for the same purpose. Both of these will improve the results compared to the standard regular grid on the sphere, but they leave space for improvements. The Simpson rule or Gaussian quadrature are only one-dimensional schemes which must be separately applied for α and β and then combined to a grid $\{\alpha_i\} \times \{\beta_i\}$. This will introduce again certain regularity to the point pattern on the sphere. The QMC points will not have a regular pattern on the sphere, but there is no guarantee that this is the optimal solution. Generally, for two-dimensional problem the optimal solution is a two-dimensional quadrature.

The term *cubature* is used for quadrature integration schemes in more than one dimension. For integration over spherical coordinates we need a cubature on the sphere. Fortunately, there exists some nice results on this subject, e.g., from Womersley and Sloan [7, 8]. They derive different sets of cubature-on-the-sphere points for slightly different minimization criteria, but the main point is that all the sets are very close to optimal and that, in all the sets, the cubature points are very evenly distributed on the sphere but without regular structure. In Fig. 1, we show the points in the regular grid and in the minimum-norm cubature (MN) having the same size.

The spherical cubature points and weights cannot be analytically solved for an arbitrary number of points; instead, they need to be computed using numerical optimization. Therefore it is most convenient that Womersley has a library of cubature-on-the-sphere points with tabulated sets to be downloaded*.

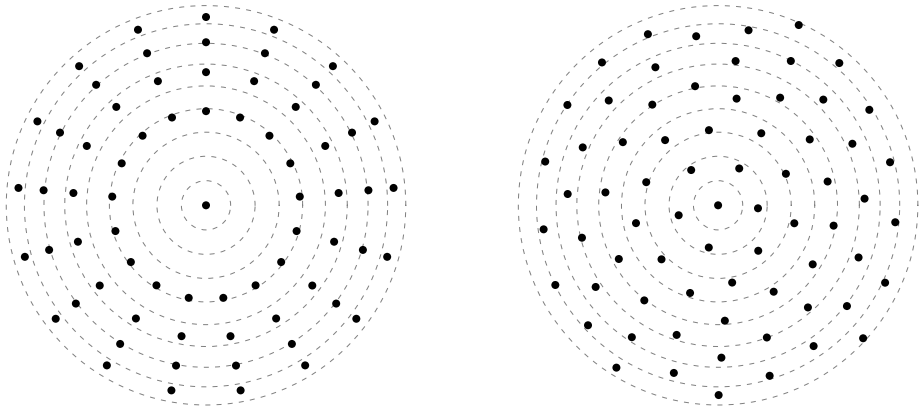

Figure 1. Upper hemispheres of regular grid points (in the left) and MN cubature points (in the right) in Lambertian projections. The regular grid has 69 points in the upper hemisphere and the MN cubature 70 points.

*Interpolation and Cubature on the Sphere in WWW at http://web.maths.unsw.edu.au/∼rsw/Sphere/

TEST WITH CUBATURE

We have been using cubature averaging with the F-ST code and with the DDA code ADDA already for various scattering computations and have been satisfied with its performance. In this section, we present a small example using both the regular grids and MN cubatures with various sizes. We use the same 4-sphere and 50-sphere aggregates that were used in a recent article about the accuracy and performance of different DDA codes [9]. For both geometries, we consider equal-volume-sphere size parameters of 3.80 and 5.11 and refractive indices of $1.5 + i0.001$. The geometries are shown in Fig. 2.

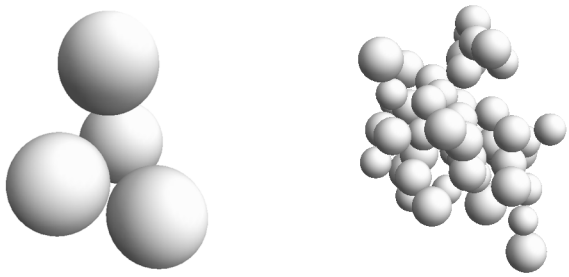

Figure 2. The two geometries used in testing the cubature. On the left, a 4-sphere cluster and, on the right, a 50-sphere cluster.

We run the computations using the F-ST code with regular grids having 23, 38, 80, 138, and 255 (α_i, β_i) points on the sphere (k points for α and $2(k-2)+1$ for β), and with the MN cubature having 25, 36, 81, 144, and 256 points. Both methods use 61 scattering planes (angle γ). The mean absolute relative error (MARE) for the intensity ($\Delta\theta = 1^\circ$, θ is the scattering angle),

$$\mathrm{MARE}(I) = \frac{1}{181}\sum_{j=0}^{180}\frac{|I_A(j\Delta\theta) - I(j\Delta\theta)|}{I_A(j\Delta\theta)}, \tag{1}$$

and the mean absolute error (MAE) for the linear-polarization ratio,

$$\mathrm{MAE}(P) = \frac{1}{181}\sum_{j=0}^{180}|P_A(j\Delta\theta) - P(j\Delta\theta)|, \tag{2}$$

are calculated for all the cases. With I_A and P_A we denote the accurate values of intensity and linear polarization ratio (in percents) using the analytical averaging, and with I and P the corresponding values using numerical orientation averaging. The results are quite similar for both geometries and for both sizes, so we present the averaged behavior of MARE and MAE over all the cases in Fig. 3.

It is evident that the MN cubature outperforms the regular grid points when the size of the cubature exceeds 40–50 points. The improvement with the same number of orientation points is about 3.5-fold (error using grid divided by error using cubature) for intensity and about 4.5-fold for polarization ratio.

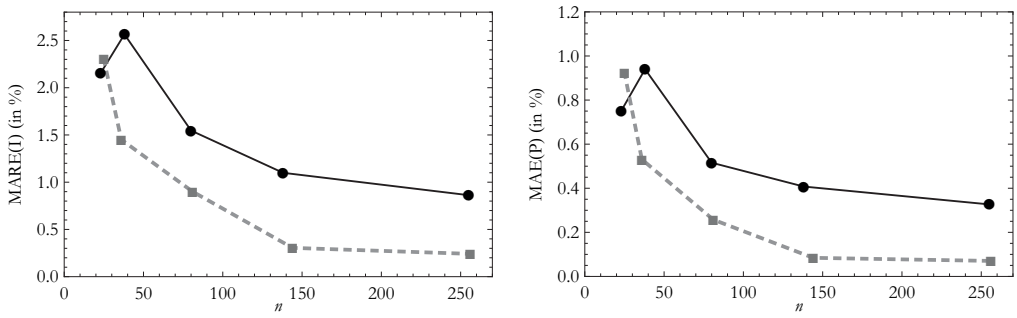

Figure 3. The average error for intensity and linear polarization ratio using regular grid and MN cubature points in orientation averaging. The number of (α_i, β_i) points is n, and the black solid line is for the regular grid and the grey dashed line for the cubature.

CONCLUSIONS

We conclude that the cubature orientation averaging scheme has better accuracy than the common method of regular grid. We recommend that the cubature points should be included as an option for orientation averaging for the popular DDA codes such as DDSCAT and ADDA.

REFERENCES

[1] M.I. Mishchenko and L.D. Travis. Capabilities and limitations of a current FORTRAN implementation of the T-matrix method for randomly oriented, rotationally symmetric scatterers. JQSRT **60** (1998).

[2] D.W. Mackowski and M.I. Mishchenko. Calculation of the T-matrix and the scattering matrix for ensembles of spheres. JOSA A **13** (1996).

[3] Y. Okada, I. Mann, T. Mukai, and M. Köhler. Extended calculation of polarization and intensity of fractal aggregates based on rigorous method for light scattering simulations with numerical orientation averaging. JQSRT **109** (2008).

[4] B.T. Draine and P.J. Flatau. The discrete dipole approximation for scattering calculations. JOSA A **11** (1994).

[5] M.A. Yurkin, V.P. Maltsev, and A.G. Hoekstra. The discrete dipole approximation for simulation of light scattering by particles much larger than the wavelength. JQSRT **106** (2007).

[6] Y. Xu and N.G. Khlebtsov. Orientation-averaged radiative properties of an arbitrary configuration of scatterers. JQSRT **79**–**80** 2003.

[7] I.H. Sloan and R.S. Womersley. Extremal systems of points and numerical integration on the sphere. Advances in Computational Mathematics **21** (2004).

[8] R.S. Womersley and I.H. Sloan. How good can polynomial interpolation on the sphere be? Advances in Computational Mathematics **14**(3) (2001).

[9] A. Penttilä, E. Zubko, K. Lumme, K. Muinonen, M.A. Yurkin, B. Draine, J. Rahola, A.G. Hoekstra, and Y. Shkuratov. Comparison between discrete dipole and exact techniques. JQSRT **106** (2007).

Electromagnetic wave scattering from particles of arbitrary shapes using the *Sh*-matrix technique

D. Petrov[*,1], Yu. Shkuratov[1], and G. Videen[2]

[1] *Astronomical Institute of Kharkov V.N. Karazin National University, 35 Sumskaya St, Kharkov, 61022, Ukraine.*
[2] *Army Research Laboratory AMSRD-ARL-CI-EM, 2800 Powder Mill Road Adelphi Maryland 20783 USA.*

A general analytical solution of the light scattered from arbitrarily shaped particles that are represented by an expansion of a series of trigonometric functions and associated Legendre polynomials is considered. We focus here on the Gaussian random particles calculating the *Sh*-matrix elements; the *Sh*-matrix approach is a variety of the *T*-matrix formulation.

INTRODUCTION

The most fundamental characteristic that determines scattering of electromagnetic waves from physical objects is particle shape. Within the last few decades, there have been many studies of light scattering of electromagnetic waves as a function of particle shape, and significant progress has been achieved in the development of different algorithms and techniques in electromagnetic wave scattering [e.g., 1]. Our approach allows a simplification and unification of the morphological description of particles. We combine this particle description with a *T*-matrix formulation to calculate the light-scattering from such particles using the *Sh*-matrix that can often provide an analytical solution. The *Sh*-matrix technique [2] has been applied to study light scattering of particles with different shapes. The simplified *Sh* matrix depends only on particle morphology and is found by performing surface integrals. Size and refractive index dependence are incorporated through analytical operations on the *Sh* matrix to produce the *T* matrix. We here present the particle generation technique and provide several examples of light scattering calculations using the *Sh*-matrix method. We focus on Gaussian-random-sphere particles.

THEORY

Let us consider a particle whose shape is described by a single-valued continuous function $R(\theta,\varphi)$, where θ and φ are the polar and azimuth angles, respectively, in a spherical coordinate system with the center located within the particle. In our approach we expand $R(\theta,\varphi)$ in a Laplace series

$$R(\theta,\varphi)=\sum_{l=0}^{\infty}\sum_{m=0}^{l}P_l^m(\cos\theta)\left(a_{lm}\cos m\varphi+b_{lm}\sin m\varphi\right), \qquad (1)$$

* Corresponding author: Dmitry Petrov (petrov@astron.kharkov.ua)

where the expansion coefficients a_{lm} and b_{lm} determine the particle shape. The spherical harmonics $P_l^m(\cos\theta)\cos m\varphi$ and $P_l^m(\cos\theta)\sin m\varphi$ are a complete set of orthonormal functions, and hence the set forms an orthonormal basis of the Hilbert space of square-integrable functions. On the unit sphere, any square-integrable function can be expanded as a linear combination of the functions.

To apply the expansion in practice, the upper limit of the outer summation in (1) should be truncated to finite *N*. The coefficients a_{lm} and b_{lm} can be found, analytically, if the function $R(\theta,\varphi)$ is known. However, there is another way to find the coefficients using discrete values of the function $R(\theta_i,\varphi_j)$. Let us consider the values at $2N^2$ points: $R_{ij}=R(\theta_i,\varphi_j),\ i=1\ldots N;\ j=1\ldots 2N$. By substituting $R(\theta_i,\varphi_j)$ into Eq. (1) with finite upper limit we obtain a system of linear equations, where a_{lm} and b_{lm} are unknown. Solution of this system gives us a representation of the particle shape as a simple and easily calculated expansion into a series expansion over trigonometric functions and associated Legendre's polynomials. Such an approach does not require an explicit form of the function $R(\theta,\varphi)$: it is sufficient to designate its values at $2N^2$ points. For example, one can generate numerically a group of radii radiating more-or-less isotropically from the center of the spherical coordinate system. The radii can be considered as a skeleton of a model particle. The length distribution of the radii and orientation of each are arbitrary depending on the particle. Thus, our approach can include regular particles (e.g., spheroids, ellipsoids and cubes) as well as particles with random shapes, like the Gaussian random particles [3]. To find the light-scattering solution, we introduce the so-called *Sh* matrix, which depends on the object shape only. The elements of the *T* matrix [1] can be expressed in terms of *Sh*-matrix elements. For example, the elements $RgJ^{11}_{mnm'n'}$ and $J^{11}_{mnm'n'}$ can be expressed using the *Sh* matrix as follows [2]:

$$RgJ^{11}_{mnm'n'}(X,m_0)=X^{n+n'+2}(m_0)^{n'}\sum_{k_1=0}^{\infty}\frac{(X\cdot m_0)^{2k_1}}{k_1!\Gamma\left(n'+k_1+\frac{3}{2}\right)}\sum_{k_2=0}^{\infty}\frac{(X)^{2k_2}}{k_2!\Gamma\left(n+k_2+\frac{3}{2}\right)}\cdot RgSh^{11}_{mnm'n',k_1+k_2}, \quad (2)$$

$$J^{11}_{mnm'n'}(X,m_0)=X^{-n+n'+1}(m_0)^{n'}\sum_{k_1=0}^{\infty}\frac{(X\cdot m_0)^{2k_1}}{k_1!\Gamma\left(n'+k_1+\frac{3}{2}\right)}\sum_{k_2=0}^{\infty}\frac{(X)^{2k_2}}{k_2!\Gamma\left(-n+k_2+\frac{1}{2}\right)}\cdot Sh^{11}_{mnm'n',k_1+k_2}, \quad (3)$$

where $X=2\pi r/\lambda$ is the size parameter, *r* is the size of the major axis of a particle, λ is the wavelength of incident light; m_0 is the refractive index of the particle, *Sh* and *RgSh* are the shape matrices or just *Sh*-matrix elements. We have found explicitly the elements for any particle whose shape can be represented by the expansion (1). Thus we suggest an analytical solution for a very wide class of particle shapes.

CALCULATIONS AND DISCUSSION

The current implementation of the algorithm for computing the expansion coefficients and particle scattering properties is written in the C++ language and for proper operation re-

quires the Intel Math Kernel Library not older than 9.1. This code allows us to calculate the expansion coefficients for different particles, e.g., ellipsoids, parallelepiped-like particles, and Gaussian random spheres. The latter particles can be described through the spherical harmonics and the associated Legendre polynomials in the manner [3]

$$R(\theta,\varphi)=\frac{C\exp\left(\sum_{l=0}^{N}\sum_{m=0}^{l}P_l^m(\cos\theta)\left(A_{lm}\cos m\varphi+B_{lm}\sin m\varphi\right)\right)}{\sqrt{1+\sigma^2}}, \tag{5}$$

where the coefficients A_{lm} and B_{lm} are independent Gaussian random variables with zero mean and equal variances:

$$\beta_{lm}^2=\left(2-\delta_{m0}\right)\frac{(l-m)!}{(l+m)!}c_l\beta^2, \tag{6}$$

$$\beta^2=\ln\left(1+\sigma^2\right), \tag{7}$$

$$c_l=(2l+1)\exp(-\kappa)i_l(\kappa), \tag{8}$$

$$\kappa=\frac{1}{4}\left(\sin\frac{\Gamma}{2}\right)^{-2}, \tag{9}$$

where C is a constant, σ^2 is the radii variance, Γ is the correlation angle, and $i_l(\kappa)$ are the modified spherical Bessel functions. This method allows one to generate irregular particles. The value Γ should be entered in degrees and cannot be smaller than 3°.

In Figs. 1 and 2, we show orientation-averaged calculated phase dependences of intensity and polarization degree for Gaussian random spheres at different m_0 and Γ using the *Sh*-matrix method.

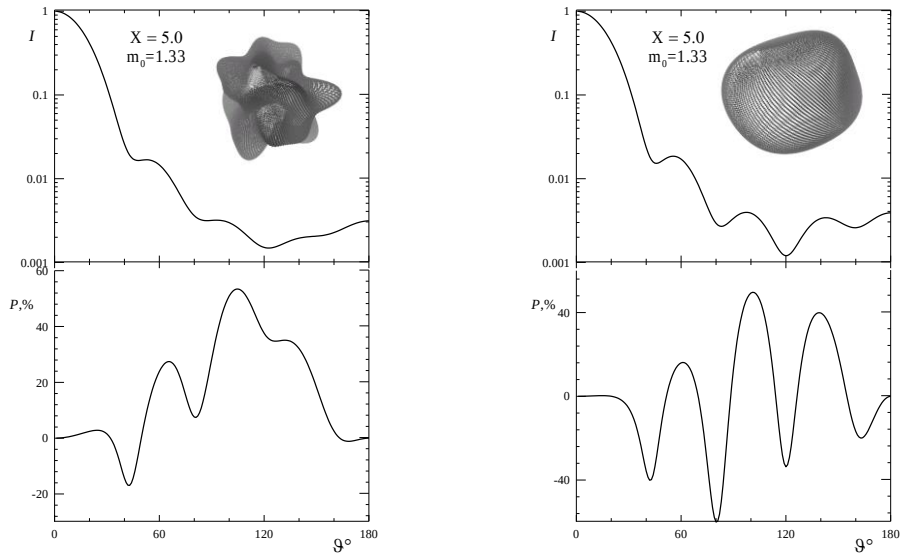

Figure 1. Phase curves of intensity and polarization degree for a Gaussian random sphere having $X = 5$, $m_0 = 1.33$, $\sigma = 0.3$, $\Gamma = 10°$ (left panel), and $\Gamma = 50°$ (right panel).

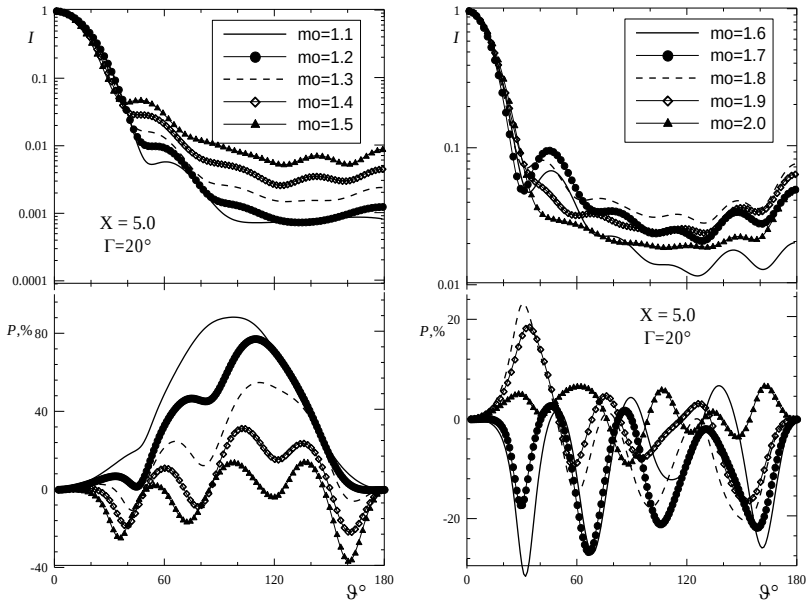

Figure 2. Phase curves of intensity and polarization degree for a Gaussian random sphere having $\sigma = 0.3$ and $\Gamma = 20^o$ at different m_0.

Acknowledgments: This work was supported by the Army Medical Research Institute of Chemical Defense (Lucille Lumley, PhD) under the auspices of the U.S. Army Research Office Scientific Services Program administered by Battelle (Delivery Order 0378, Contract No. W911NF-07-D-0001).

REFERENCES

[1] M.I. Mishchenko, L.D. Travis, and A.A.Lacis. *Scattering, absorption, and emission of light by small particles*. Cambridge: Cambridge University Press (2002).

[2] D. Petrov, E. Synelnyk, Y. Shkuratov, and G. Videen. The *T*-matrix technique for calculations of scattering properties of ensembles of randomly oriented particles with different size. JQSRT **102** (2006).

[3] K. Muinonen. Light scattering by Gaussian random particles: Rayleigh and Rayleigh-Gans approximations JQSRT **55** (1996).

Alteration of skin light-scattering and absorption properties by application of sunscreen nanoparticles: a Monte Carlo study

A. P. Popov[1,2], A. V. Priezzhev[*,2], J. Lademann[3], and R. Myllylä[1]

[1]*Optoelectronics and Measurement Techniques Laboratory, Department of Electrical and Information Engineering, University of Oulu, Oulu, P.O. Box 4500, FI-90014, Finland.*
[2]*Physics Department and International Laser Center, M. V. Lomonosov Moscow State University, Leninskie Gory, 119992 Moscow, Russia.*
[3]*Center of Experimental and Applied Cutaneous Physiology, Department of Dermatology, Universitätsmedizin-Charité Berlin, D-10117 Berlin, Germany.*

We report about alteration of optical properties of the superficial layer of human skin at two UV range wavelengths (310 and 400 nm) by application of 35–200 nm –sized particles of titanium dioxide (TiO_2), silicon (Si) and zinc oxide (ZnO). The study, based on combination of the Mie theory and Monte Carlo simulations, reveals the optimal sizes of the nanoparticles minimizing the transmittance of the layer for the considered wavelengths.

INTRODUCTION

Skin located on the body surface is in direct contact with the environment. It protects the inner cells and tissues from such types of hazards as mechanical, chemical, thermal, optical, etc. The skin thickness depends on the body region and varies between 1.5 and 4 mm. The comprising layers are epidermis, dermis and a layer of subcutaneous fat. The uppermost part of epidermis is known for its dead cells without nuclei and is referred to as stratum corneum or horny layer. The data about stratum corneum thickness differ in different sources: 6 – 40 μm on such common sites as the abdomen, flexor forearm, thigh, and back; however, on the palms of hands and soles of feet it is 5–10 times thicker.

Ultraviolet (UV) radiation, being a part of the solar spectrum, covers a range of 100 – 400 nm and it is usually divided into three sub-ranges: UVC (100 – 280 nm), UVB (280 – 315 nm) and UVA (315 – 400 nm). UVC is completely absorbed by the atmospheric ozone layer located at a height of 18 – 40 km above the sea level. UVB and UVA penetrate the atmosphere and affect humans. The UVB fraction is responsible for sunburn and increases the risk of basal cell and squamous cell carcinoma due to direct DNA damage. The UVA fraction causes sun tanning, photoaging, and provokes malignant melanoma by indirect DNA damage (via free radical generation). Moderate sun tanning can prevent sunburn due to increased production of melanin, a natural UV protector.

Improvement of UV protecting functions of the stratum corneum is achieved with chemical and physical compounds of sunscreens [1], i.e. light-absorbing organic chemical substances and light-scattering and light-absorbing TiO_2 and ZnO nanoparticles [2-3].

* Corresponding author: Alexander Priezzhev (avp2@mail.ru)

Recently, Si nanoparticles were suggested for use in sunscreens [4]. In order to suppress the generation of free radicals by the particles in the presence of UV light, they are covered [5] with silica and alumina. Nanoparticles have a tendency to form aggregates and agglomerates in emulsions resulting in changes of their optical properties that are hard to estimate. Nevertheless, in recent years new methods were designed to produce particles with diameters of 25 nm, deviation of 15 – 20% from the mean value and agglomeration-free.

In this paper, we theoretically investigate how optical properties of skin in the UV spectral range can be modified to reduce the light transmittance by imbedding TiO_2, ZnO, and Si nanoparticels. Performed calculations are based on the Mie theory and Monte Carlo simulations.

MATERIALS AND METHODS

According to our earlier study [6], nanoparticles in sunscreens even after multiple applications are located mostly within the uppermost part (1 – 2 μm from the surface) of the stratum corneum. A mathematical model for Monte Carlo simulations developed by us is represented by an infinitely wide plane layer mimicking stratum corneum (20-μm-thick) containing nanoparticles in its uppermost part (1-μm-thick). Particle diameters were varied between 35 and 200 nm; however, all of them were of the same size for each calculation. Light scattering in this upper part is described by a linear combination (hybrid) of Mie and Henyey-Greenstein phase functions describing scattering by spherical nanoparticles and cells. For the wavelengths used in the simulations, the scattering (μ_s) and absorption (μ_a) coefficients of the stratum corneum (without nanoparticles) are the following: 1) for 310 nm light: μ_s = 240 mm^{-1}, μ_a = 60 mm^{-1}; 2) for 400 nm light: μ_s = 200 mm^{-1}, μ_a = 23 mm^{-1}; refractive index is equal to n = 1.53 and anisotropy factor g = 0.9 are the same for the both wavelengths. The above-mentioned wavelengths were chosen because the 310 nm value corresponds to the erythemal peak and 400 nm is at the end of the UV spectrum. Total thickness of stratum corneum was 20 μm.

Optical properties of nanoparticles were accounted for according to [7, 8]. Free software MieTab 7.23 was utilized to calculate scattering and absorption cross-sections and a g-factor of the particles. Using the obtained values, scattering and absorption coefficients of particle suspensions with a volume fraction of particles of 1 % were further calculated according to the earlier obtained formulas [9, 10].

In all simulations, one million photons were launched into the medium. This amount ensured sufficient statistical precision of the calculations with an error not exceeding 3 %. Based on the amount of photons absorbed, reflected and transmitted through the stratum corneum (depending on the particle size and material) the optimal particle sizes minimizing the light transmittance were calculated.

RESULTS

As an example, calculated transmittance curves for TiO_2 and Si particles for the considered wavelengths are depicted in Fig. 1. For the shorter wavelength (310 nm) the attenuation ef-

fect of both types of particles is comparable, while for the longer one (400 nm) the Si particles clearly outperform TiO_2. The sizes of the most attenuating particles are the following: 56 and 70 nm for Si (for 310 and 400 nm light, respectively) and 62 and 122 nm for TiO_2 particles (for 310 and 400 nm light, respectively). The mechanisms behind these affects are the absorption of the UV radiation of the shorter wavelength for both types of particles; scattering for TiO_2 and absorption and, to a lesser extent, scattering for Si nanoparticles.

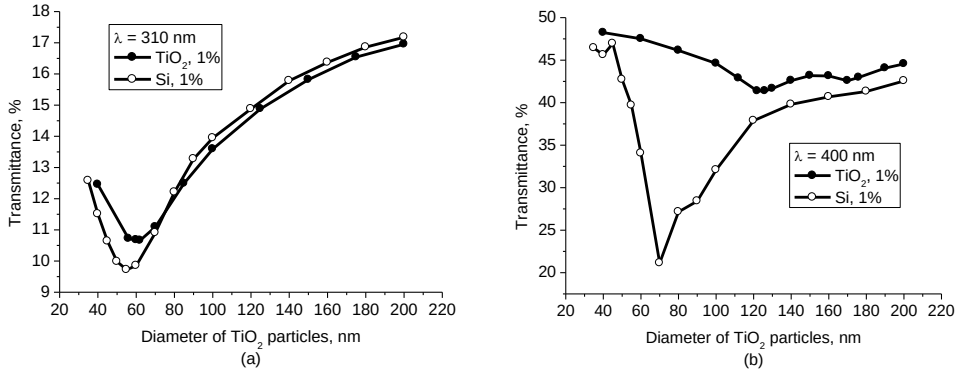

Figure 1. Transmittance of 310- (a) and 400-nm (b) light through the whole stratum corneum in presence of TiO_2 and Si nanoparticles of different sizes within its uppermost 1-μm-thick part.

Comparing the TiO_2 and Si nanoparticels as UV protectors we show that the Si particles are considerably more effective for attenuation of the longer wavelength (400 nm) radiation, while for 310 nm light the efficacy of the particles of both types are more or less at the same level. Results are compared to those for the ZnO particles.

REFERENCES

[1] U. Jacobi, H.-J. Weigmann, M. Baumann, A.-I. Reiche, W. Sterry, and J. Lademann. Lateral spreading of topically applied UV filter substances investigated by tape stripping. Skin Pharmacol. Physiol. **17** (2004).

[2] J. Lademann, H.-J. Weigmann, C. Rickmeyer, H. Barthelmes, H. Schaefer, G. Mueller, and W. Sterry. Penetration of titanium dioxide microparticles in a sunscreen formulation into the horny layer and the follicular orifice. Skin Pharmacol. Appl. Skin Physiol. **12** (1999).

[3] J. Lademann, S. Schanzer, U. Jacobi, H. Schaefer, F. Pflücker, H. Driller, J. Beck, M. Meinke, A. Roggan, and W. Sterry. Synergy effects between organic and inorganic UV filters in sunscreens. J. Biomed. Opt. **10** (2005).

[4] A.I. Rybaltovsky, V.N. Bagratashvili, A.I. Belogorokhov, V.V. Koltashev, V.G. Plotnichenko, A.P. Popov, A.V. Priezzhev, A.A. Ishchenko, A.A. Sviridova, K.V. Zaitseva,

and I.A. Tutorsky. Spectral features of water-emulsion composite media containing silicon nanoparticles. Optics and Spectroscopy **101** (2006).

[5] J. Lademann, H.-J. Weigmann, H. Schaefer, G. Mueller, and W. Sterry. Investigation of the stability of coated titanium microparticles used in sunscreens. Skin Pharmacol. Appl. Skin Physiol. **13** (2000).

[6] A.P. Popov, A.V. Priezzhev, J. Lademann, and R. Myllylä. TiO2 nanoparticles as an effective UV-B radiation skin-protective compound in sunscreens. J. Phys. D: Appl. Phys. **38** (2005).

[7] E.D. Palik. *Handbook of Optical Constants of Solids*. Academic Press, Orlando (1985).

[8] S.M. Al-Hilli and M. Willander. Optical properties of zinc oxide nano-particles embedded in dielectric medium for UV region: Numerical simulation. J. Nanoparticle Research **8** (2006).

[9] A.P. Popov, A.V. Priezzhev, J. Lademann, and R. Myllylä. The effect of nanometer particles of titanium oxide on the protective properties of skin in the UV region. J. Opt. Technol. **73** (2006).

[10] A.P. Popov, A.V. Priezzhev, J. Lademann, and R. Myllylä. Effect of multiple scattering of light by titanium dioxide nanoparticles implanted into a superficial skin layer on radiation transmission in different wavelength ranges. Quantum. Electron. **37** (2007).

Polarizing efficiency of nonspherical scatterers of different structure

M. S. Prokopjeva*[,1], V. B. Il'in[1,2,3], V. G. Farafonov[2], and A. A. Vinokurov[2,3]

[1] *St. Petersburg University, Universitetskij pr. 28, St. Petersburg, 198504 Russia.*
[2] *State Univ. of Aerospace Instrumentation, Bol. Morskaya 67, St. Petersburg, 190000 Russia.*
[3] *Pulkovo Observatory, Pulkovskoe chaussee 65/1, St. Petersburg, 196140 Russia.*

By comparing porous multilayered spheroids and homogeneous ones with effective permittivity, we find that the ratio of the linear polarization degree of transmitted radiation to optical thickness of a medium containing partly aligned nonspherical inhomogeneous particles can strongly depend on their structure. We consider this effect in some detail and note that it occurs for any nonspherical scatterers with inclusions as well.

INTRODUCTION

The optical properties of homogeneous nonspherical particles have been extensively modeled in the past 25 years (see, e.g., [1, 2]). In contrast, inhomogeneous nonspherical scatterers have been studied rather seldomly. Exceptions are fractal aggregates (see [3] and references therein) and particles with randomly distributed small inclusions for which effective medium approximations provide acceptable results (see, e.g., [4]).

In this paper we consider the linear polarization of radiation passing through an ensemble of partly aligned nonspherical inhomogeneous (porous) spheroids of different structure. Sect. 2 describes our models of inhomogeneous scatterers and computational methods used. Sect. 3 presents results of calculations and their discussion.

MODELS AND METHODS

We compare the optical properties of porous spheroids of three kinds (see Fig. 1):

Model I — Scatterers with randomly distributed tiny inclusions approximated by homogeneous particles with the refractive index given by an effective medium theory (EMT).

Model II — Scatterers with randomly distributed large inclusions modeled by applying the standard discrete-dipole approximation (DDA) approach.

Model III — Scatterers with many cyclically repeating layers considered according to [5]. Note that when the number of layers becomes large, the scattering characteristics tends to depend only on the material volume fractions and tends to be independent of the order and number of layers. The optical properties of multilayered particles were obtained by the generalized separation of variables method (SVM) with a spherical basis [6].

Thus, the *general parameters* are the spheroid *aspect ratio* a/b (and the type: prolate/oblate), *size parameter* $x_{\rm V} = 2\pi r_{\rm V}/\lambda$, where $r_{\rm V}$ is the radius of a sphere whose volume is equal to that of the spheroid and λ the wavelength, *orientation angle* α between the particle symmetry axis and the incident radiation wavevector, *porosity* $\mathcal{P}$ being a fraction of the particle volume filled by material with a *refractive index* m.

*Corresponding author: Marina Prokopjeva (marina.prokopjeva@pobox.spbu.ru)

Additional parameters are, for the model II, the *halfwidth of cubic inclusions* r (in units of the interdipole distance) and, for the model III, the *number of layers* L, *aspect ratios* of the external boundaries $(a/b)_i$, *volume fractions* $V_i/V_{\rm tot}$ ($V_{\rm tot}$ is the particle volume) and *refractive indices* m_i of the layers ($i = 1, 2, ..., L$).

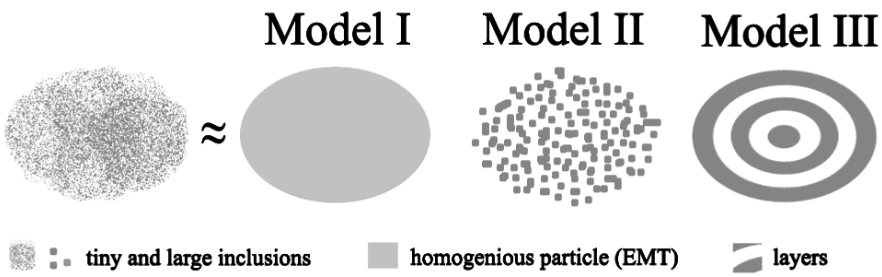

Figure 1. Cross-sections of three model spheroids considered.

NUMERICAL RESULTS AND DISCUSSION

We consider extinction and linear polarization of radiation passing through a medium populated by single size porous spheroids in a picket-fence orientation.

Dimensionless extinction cross-sections of spheroids are calculated for two kinds of incident plane wave polarizations: $Q_{\rm ext}^{\rm TE}$, $Q_{\rm ext}^{\rm TM}$. For an unpolarized radiation, the *extinction and polarization cross-sections* of the particles are $Q_{\rm ext} = (Q_{\rm ext}^{\rm TM} + Q_{\rm ext}^{\rm TE})/2$ and $Q_{\rm pol} = (Q_{\rm ext}^{\rm TM} - Q_{\rm ext}^{\rm TE})/2$, respectively.

We compare the *polarizing efficiency* $P = |Q_{\rm pol}|/Q_{\rm ext}$ (equals to the ratio of the linear polarization degree of transmitted radiation to optical thickness p/τ) calculated for spheroids of the same parameters a/b, $x_{\rm V}$, α, $\mathcal{P}$ and m, but of different structure (the models I--III).

We find that the ratio $Q_{\rm pol}/Q_{\rm ext}$ for porous layered spheroids (model III) systematically differs from that for the corresponding spheroids with an effective permittivity (model I) (see the left panel of Fig. 2), i.e., the *polarizing efficiency of inhomogeneous spheroids may essentially depend on their structure*.

The strength of this effect is more clearly illustrated in the right panel of Fig. 2, where we plot the ratio of polarizing efficiences for the models III and I as $P/P_{\rm emt}$. Note that this ratio exceeds 1.5 for *all particle sizes* and can be as large as 2--5.

The effect depends weakly on the orientation of both the prolate and oblate spheroids but is strongly affected by the particle porosity $\mathcal{P}$ and composition for $\mathcal{P} > 70\%$ (see Fig. 3).

It should be especially important for interpretation of the interstellar extinction and polarization phenomena within the existing porous models of cosmic dust grains. That is why we use refractive index values typical of astronomical silicate, ice, and amorphous carbon in the visual region. The left panel of Fig. 4 gives the ratio of the polarization degree of transmitted radiation to optical thickness p/τ for spheroids of different aspect ratio a/b and porosity $\mathcal{P}$. Note that if an observed value of p/τ was earlier fitted by using homogeneous (model I) spheroids of a ratio a/b, now this value can be obtained for porous particles of essentially lower a/b.

According to [5], the mathematical model of multilayered particles can be useful in prac-

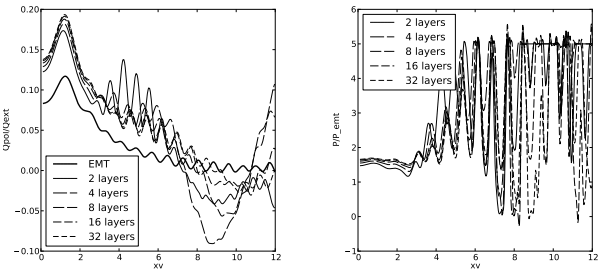

Figure 2. *Left panel:* Extinction cross-section ratio $Q_{\rm pol}/Q_{\rm ext}$ as a function of the size parameter $x_{\rm V}$ for the model I (homogeneous) and different types of model III (layered with $L = 2, 4, 8, 16, 32$) porous icy prolate spheroids. *Right panel:* Polarizing efficiency for the porous layered (model III) spheroids P normalized to that for the corrsponding homogeneous (model I) particles $P_{\rm emt}$. Other parameters are $m = 1.3$, $\alpha = 45°$, $\mathcal{P}$=50%, $(a/b)_i = 1.4$ and $V_i/V_{\rm tot} = L^{-1}$ for $i = 1, 2, ..., L$.

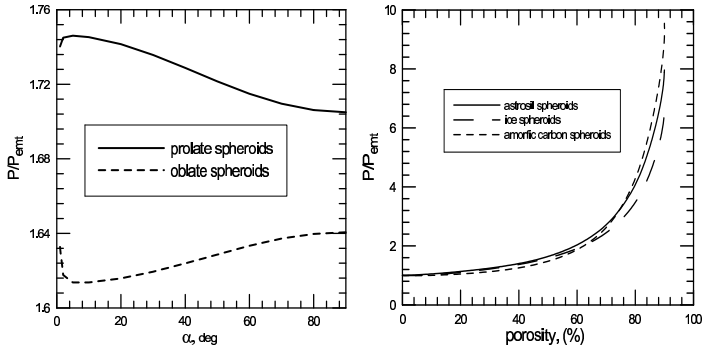

Figure 3. Ratio of the polarizing efficiencies for layered (model III) and homogeneous (model I) spheroids $P/P_{\rm emt}$ as a function of particle parameters. *Left panel:* Different orientation of porous prolate and oblate spheroids ($m = 1.7 - 0.03i$, $x_{\rm V} = 1$, $\mathcal{P}$=50%). *Right panel:* Prolate spheroids of different porosity and composition ($m = 1.3$, $1.7 - 0.03i$ and $1.98 - 0.23i$ for ice, astrosil, and amorphous carbon, respectively, $x_{\rm V} = 3$, $\alpha = 90°$). Other parameters are $L = 20$, $(a/b)_i = 1.5$ and $V_i/V_{\rm tot} = L^{-1}$ for $i = 1, 2, ..., L$.

tice. We confirm this statement by comparing the polarizing efficiency of porous multilayered (model III) and homogeneous (model I) spheroids and (quasi)spheroids with inclusions of different size (model II --- see the right panel of Fig. 4). One can see that the ratio p/τ for scatterers with small inclusions ($r = 0$ and 1) is close to the EMT ratio, while the values of p/τ obtained for the case of larger inclusions ($r = 2$ and 3) tend to those given by the multilayered model; i.e., by comparing two simple computational models III and I, one can reveal possible particle structure effects for scatterers with inclusions.

To conclude, we have found that the ratio of the linear polarization degree of transmitted radiation to optical thickness of a medium containing partly aligned nonspherical porous spheroids can strongly depend on their structure, i.e., distribution of materials inside the scatterers. The effect is especially evident for highly porous particles, but should occur for any nonspherical scatterers with large inclusions when refractive indices of the matrix and

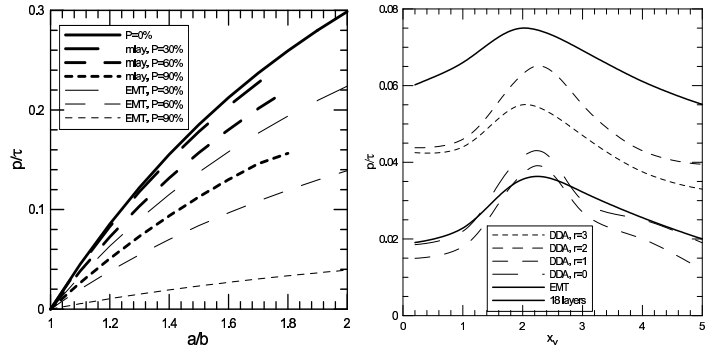

Figure 4. Polarizing efficiency p/τ for structurally different porous oblate spheroids. *Left panel:* Comparison of the models III and I for different aspect ratios a/b and porosity $\mathcal{P}$ ($m = 1.7 - 0.03i$, $x_{\rm V} = 1$). *Right panel:* Comparison of the models III, I, and different models II for size parameters $x_{\rm V} < 5$ ($a/b = 1.4$, $\mathcal{P}$= 90%, layers and inclusions of two materials with $m_1 = 1.7 - 0.03i$ and $m_2 = 1.98 - 0.23i$). Other parameters are $\alpha = 90°$, $L = 18$, $(a/b)_i = a/b$ and $V_i/V_{\rm tot} = L^{-1}$ for $i = 1, 2, ..., L$.

inclusion materials essentially differ. So, the results are general and should have different applications besides interstellar extinction and polarization interpretation mentioned.

Acknowledgements: The work was supported by the grants RFFI 10-02-00593, NTP 2.1.1/665 and NSh 1318.2008.2.

REFERENCES

[1] W.J. Wiscombe and A. Mugnai. Single scattering from nonspherical Chebyshev particles: a compendium of calculations. NASA Ref. Publ. **1157** (1986).

[2] K. Schmidt, J. Wauer, T. Rother, and T. Trautmann. Scattering database for spheroidal particles. Appl. Opt. **48** (2009).

[3] Z. Naeimi and M. Miri. Optical properties of fractal aggregates of nanoparticles: effects of particle size polydispersity. Phys. Rev. B **80** (2009).

[4] P. Chýlek, G. Videen, D.J.W. Geldart, S. Dobbie, and H.C.S. Tso. Effective medium approximation for heterogeneous particles. In: *Light scattering by nonspherical particles*. M.I. Mishchenko, J.W. Hovenier, and L.D. Travis (eds.). Acad. Press (2000).

[5] N.V. Voshchinnikov, V.B. Il'in, and T. Henning. Modelling the optical properties of composite and porous interstellar grains. Astron. Astrophys. **429** (2005).

[6] A.A. Vinokurov, V.G. Farafonov, and V.B. Il'in. Separation of variables method for multilayered nonspherical particles. J. Quant. Spectr. Rad. Transf. **110** (2009).

Monitoring of pathogen carrying air-borne *Camellia sinensis* dust particles by light scattering

S. Roy[*,1], R. Mahatta[1], N. Barua[2], A. K. Buragohain[2], and G. A. Ahmed[1]

[1]*Optoelectronics and Photonics Research laboratory, Department of Physics, Tezpur University, Tezpur -784028, Assam, India.*
[2]*Department of Molecular Biology and Biotechnology, Tezpur University, Tezpur -784028, Assam, India.*

In order to investigate if *Camellia sinensis* dust particles are a possible carrier of the species *Mycobacterium* a biotechnical procedure was used and to verify the possibility of monitoring this dust, a laser-based setup was designed and fabricated and experiments were carried out. *Mycobacterium smegmatis* mc² 155 was used as a model organism to study the effect on *Camellia sinensis* dust particles.

INTRODUCTION

Light scattering [1] is an important tool for the optical characterization of small particles suspended in air or when dispersed in a medium. The study of the angular scattering dependence of such particulate matter helps in the investigation of the nature of the scattering particle and to understand the radiative transfer through a medium containing the scatterer [2,3]. A number of different experimental setups have been made in the past to investigate the scattering behavior of small particles [4].

Tea is an indispensable beverage used all over the world and is mainly brewed from the leaves of the plant species *Camellia sinensis*. *Camellia sinensis* is grown in many tropical regions of the world. During the processing stage from raw leaves to commercially packaged tea, tea dust is released into the atmosphere as an effluent. Such organic dust has the possibility of acting as a carrier for asthmatic triggers and also a carrier for pathogens [5]. It has been reported that tuberculosis, which is caused by the pathogen *Mycobacterium tuberculosis* is also prevalent in such tea gardens, the reasons being given as low socio-economic status, overcrowding of residential area and low literacy. *Mycobacterium tuberculosis* is non-motile and can live up to a few weeks in a dry state. The bacteria range from 0.2 to 0.4 microns in size.

This paper reports the work done in Assam in India, where tea is grown in large gardens and processed on a very large scale, to investigate if air-borne *Camellia-sinensis* dust particles are a possible carrier of *Mycobacterium* pathogens and if monitoring of such non-spherical particles can be done by light scattering techniques. An original laboratory light-scattering instrument, which could be used to measure the volume scattering of *Camellia sinensis* air-borne nonspherical dust was designed and fabricated.

* Corresponding author: Sanchita Roy (rsanchita1@gmail.com)

EXPERIMENTAL DETAILS

Light scattering setup

The setup was designed to study the light scattering characteristics of small particles. The essential components of the setup (Fig. 1) are a laser source, controlled sample holders, a photomultiplier tube (H 5784-20, Hamamatsu, Japan), data acquisition system (Vinytics, PCI-9812) and associated instrumentation. The scattered light intensity is sensed by the photomultiplier tube. The system uses three He-Ne laser sources used alternatively for three different wavelengths of 632 nm, 594 nm and 543 nm respectively, for studying the scattering properties as a function of scattering angle. The system can measure scattered light signals from an angle of 10º to 170º in steps of 5º for θ, and from 0º to 50º in steps of 10º for φ to account for recording the volume scattering. The setup is covered by a black metallic enclosure to cutoff electromagnetic noise and the beam stops are used at strategic points to minimize the intensity of stray reflections.

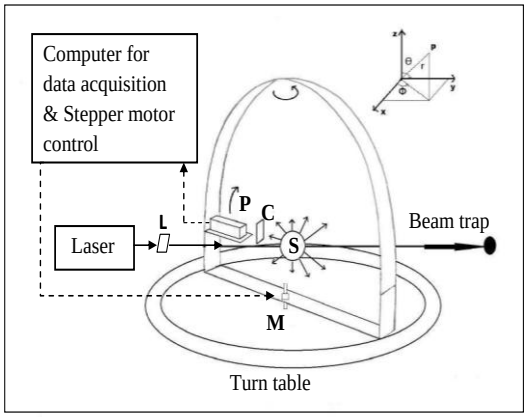

Figure 1. Schematic diagram of the scattering setup. P – Photomultiplier tube; L-Polarizer; C – Analyzer; S – Sample; M – Stepper motor

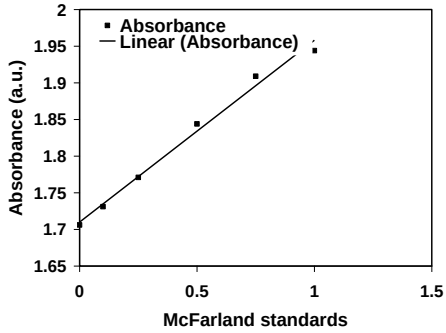

Figure 2. Absorbance of *Camellia sinensis* dust particles at 600 nm

Sample preparation and Antimycobacterial Assay of Camellia sinensis dust

The samples of *Camellia sinensis* dust particles were collected from areas around tea factories (Nonoi Tea estate and Hatikhuli Tea estate situated in Assam, India). Using scanning electron micrograph images the size distribution of these particles was calculated and the results were extrapolated for the population of dust particles. These dust particles are non-spherical and have a large size distribution that is nearly Gaussian. The interaction of *Camellia sinensis* dust, when exposed to *Mycobacterium* species, was studied by using the Agar Well Diffusion Method [6]. In order to maintain safe laboratory procedures, the non-pathogenic species *Mycobacterium smegmatis* which has all the characteristic properties of the pathogenic species *Mycobacterium tuberculosis* was used for the investigations. The strain *Mycobacterium smegmatis* mc² 155 was cultured in Mueller Hinton Broth 2 media at 37° C for 18 hours. The bacterial cells were suspended in a saline solution (0.85 % NaCl) and the McFarland standard of the cells were

adjusted to a turbidity of 0.5 (approximately10^8 CFU/ml). The suspension was inoculated in Mueller Hinton Agar media and four wells (6 mm) were punched. 50 µl of the sterile organic tea dust of two concentrations i.e., 20 mg/ml and 50 mg/ml, dissolved in 1 % (v/v) DMSO were added to the wells. Growth of the bacterial cells was not affected by 1 % DMSO as shown by our control experiments. 1 % DMSO was used as negative control and Streptomycin was used as an antibiotic control. The plates were incubated at 37° C for 18 h. The experiments were conducted in triplicate. An attempt was made to differentiate sterile tea (*Camellia sinensis* (L) Kuntze.) dust from *Mycobacterium smegmatis* contaminated tea dust by investigating the absorbance at 600nm by the sterile tea dust and tea dust inoculated with *Mycobacterium smegmatis* culture at different concentrations. A 16 hour *Mycobacterium smegmatis* culture was harvested by centrifugation at 3000 rpm, washed twice with sterile Phosphate buffer Saline(PBS) pH 7.4, and resuspended in PBS (pH 7.4). The suspension was further diluted and mixed properly in PBS (pH 7.4) containing 20 mg/ml of the tea dust to achieve McFarland standards of 0.1, 0.25, 0.5, 0.75 and 1.0 corresponding to approximately 0.3×10^8 CFU/mL, 0.75×10^8 CFU/mL, 1.5×10^8 CFU/mL, 2.25×10^8 CFU/mL respectively. The absorbance of the samples was measured at 600nm (Cecil Aquarius Spectrophotometer, Sl. No.146 -276). The plot between the McFarland Standards and Absorbance at 600 nm presented in Fig. 2. indicates that the absorbance of the tea dust increases with the increase in bacterial load on the tea dust.

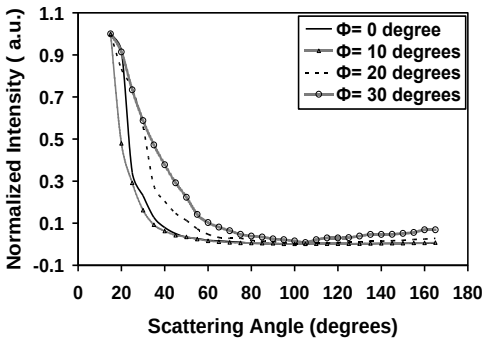

Figure 3. Scattering Intensity profile of uncontaminated *Camellia sinensis* dust particles at 594 nm.

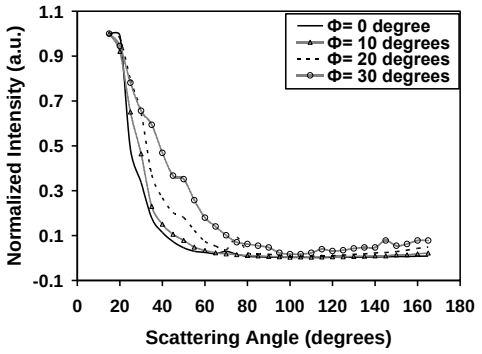

Figure 4. Scattering Intensity profile of *Mycobacterium* contaminated *Camellia sinensis* dust particles at 594 nm.

RESULTS

We have studied the light scattering from *Camellia-sinensis* dust particles at 543 nm, 594 nm and 632 nm laser wavelengths respectively. Scanning electron micrograph images were taken to observe the morphology of the particles. UV-vis absorption spectroscopy was performed to obtain the absorption spectra. The choice of 543 nm, 594 nm and 632 nm as probe wavelengths was employed because UV-vis absorption spectra had shown negligible non-resonant absorption at these particular wavelengths. It was observed that the tea dust particles did not exhibit any antimycobacterial activity and might act as a potent carrier. It was also observed that the light scattering behavior of *Mycobacterium* contaminated *Camellia sinensis* dust particles

significantly vary for the three different laser wavelengths. The scattering results for *Mycobacterium* contaminated and uncontaminated dust sample shows marked difference for $\theta=0^o$, $\theta=10^o$, $\theta=20^o$ and $\theta=30^o$ (Fig. 3 and 4) at wavelength of 594 nm. Preliminary results are shown for the light-scattering behavior of tea dust particles. These will be described in more detail in the presentation.

CONCLUSIONS

In this paper we report the design and fabrication of a low-cost, light-weight and miniaturized light-scattering instrument. The light-scattering behavior of both *Mycobacterium* contaminated and uncontaminated *Camellia sinensis* dust particles has been studied as a function of scattering angle. The instrument has proven itself to be efficient for performing light-scattering experiments on small particulate matter, so extensive investigations will be further carried out on other small particles, aerosols and hydrosols.

ACKNOWLEDGEMENTS

The corresponding author wishes to thank Department of Science and Technology, Ministry of Science and Technology, Government of India for the project grant (sanction no. SR/WOS-A/PS-20/2007 dated 04/08/2008) under the Women Scientist-A Scheme.

REFERENCES

[1] C.F. Bohren and D.R. Huffman. *Absorption and Scattering of Light by Small Particles*. John Wiley & Sons Inc, New York (1983).

[2] M.I. Mishchenko, J.W. Hovenier, and L.D. Travis. *Light Scattering by Nonspherical Particles: Theory, Measurements, and Applications*. San Diego, CA: Academic (2000).

[3] P.H. Kaye. Spatial light-scattering analysis as a means of characterizing and classifying non spherical particles. Meas. Sci. Technol. **9** (1998).

[4] J.W. Hovenier, H. Volten, O. Munõz, W.J. Van Der Zande, and L.B.F.M. Waters. Laboratory studies of scattering matrices for randomly oriented particles: potentials, problems and prospectives. J. Quantitative Spectroscopy and Radiative Transfer **79-80** (2003).

[5] E. Zuskin, E.N. Sachachter, B. Kanceljak, T.J. Whitek Jr., and E. Fein. Organic dust disease of airways. International Archives of Occupational and Environmental Health. **65** (1993).

[6] C. Perez, M. Paul, and P. Bazerque. Antibiotic assay by agar well diffusion method. Acta Biol Med Exp. **15** (1990).

Atmospheric halos provide means to estimate shapes and orientations of airborne ice crystals

J. Ruoskanen*

Finnish Defence Forces Technical Research Centre, Electronics- and information technology division, P.O. box 10, FI-11311 Riihimaki, Finland.

The shapes of ice crystals in tropospheric clouds have been examined with various techniques. An efficient addition to the methods is provided by halo phenomena arising from reflection and refraction of sun light in airborne ice crystals. This paper describes the extent to which conclusions of ice crystal properties can be drawn based on analysis of visible halos. The associations of ice-crystal orientations and shapes with halo forms can be examined with a Monte-Carlo simulation algorithm using geometrical optics.

INTRODUCTION

The problem of determining microphysical properties of cirrus and cirrostratus clouds has received scientific interest due to the role of upper tropospheric clouds in Earth's radiation budget and climate. The issue has been approached from many different angles. Ice-crystal nucleation has been extensively examined and numerous laboratory experiments have been conducted. The ice-crystal content of cirrus clouds has been studied with spaceborne and ground-based remote-sensing methods with frequencies ranging from millimeter waves up to visible light [1]. Also various ice crystal probes and cloud-particle imagers have been flown in aircrafts [2]. Understanding the conditions of the upper troposphere is a demanding task and despite all the results achieved so far, inconsistencies between theories and practical measurements arise constantly [3].

Atmospheric halos offer an additional tool for determination of ice-crystal properties in tropospheric clouds. By looking at the halos visible in a cloud under examination, one can make fairly accurate estimates of the orientations and shapes of the ice crystals, since there exists a well established association between halos and ice crystal orientations [4]. Furthermore, some attributes of a halo display give insight into aspect ratio of ice crystals as well as to possible imperfectness of certain crystal faces. A few authors have dealt with halo phenomena in this context, but their approaches have not exploited the full potential of atmospheric halos as one element in determining the microphysical properties of tropospheric clouds. In this paper some methods for halo - ice crystal associations are described.

COMPUTER SIMULATIONS OF HALOS

Reflection and refraction of sunlight by hexagonal ice crystals (Ice Ih, see Fig. 1) gives rise to about 35 halo forms, and when sometimes these hexagons have also pyramidal $\{10\bar{1}1\}$ faces, a group of about 25 additional halo forms are possible. Earlier scholars used pencil and paper as well as clever geometrical techniques to solve the light ray paths responsible

*Jukka Ruoskanen (jukka.ruoskanen@mil.fi)

for different halo forms and to derive their appearence at different sun elevations. Now we can harness the computer to do all these calculations. The size parameters of halo-making ice crystals are large enough to justify the use of a geometrical-optics-based Monte-Carlo algorithm for simulations of halo phenomena.

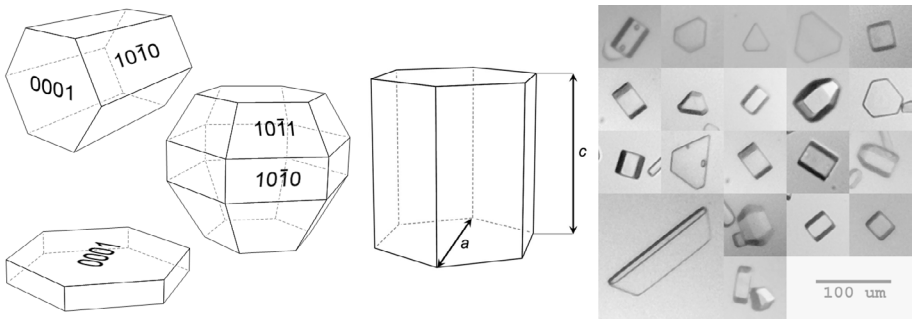

Figure 1. Hexagonal column-, plate- and pyramidal ice crystal on the left. The aspect ratio is the ratio of the length of the prism in c-axis direction to the width in a-axis direction. On the right, examples of real crystals collected in diamond dust near ground.

In a halo-simulation program [5], a ray from the sun's disk is traced through an ice crystal according to the laws of geometrical optics until it leaves the crystal and creates a pixel of light, a halo point, on a celestial sphere. Ice crystals are defined for the computer as an intersection of half-spaces. At each face the light is split into reflected and refracted components, whose intensities are governed by Fresnel equations. These intensities are interpreted as probabilities based on which the decision of plotting is made. After one cycle a new ray is taken under consideration and the process is repeated for as many rays as needed, even millions. Each variable controlling crystal dimensions, shape and orientation can be set to vary according to uniform or normal distribution with a desired standard deviation. Monte-Carlo halo simulation procedure was first implemented by Greenler and Mallman [6], and further elaborated by Pattloch and Tränkle [7].

Faint halos and the sometimes encountered lack of halos in high clouds [8] is a clear indication of the presence of poor halo makers. The program can be expanded to handle also non-convex polyhedra, such as rosettes, capped columns or twinned plates. Also internal impurities, face deficiencies and air bubbles can be modelled. These modifications may be needed in order to evaluate the degradation in halos when the ice crystals are not perfect.

WHAT CAN BE LEARNED BY LOOKING AT A HALO DISPLAY?

Halo displays can be seen regularly – over 100 days a year in most locations worldwide. Typical displays include only a few halo forms, which come from the group of about ten most common ones. Compared to ordinary halos complex displays provide more versatile features from which ice crystal properties can be deduced, but they occur less often. The properties of ice crystals that can be seen from halos are the following:

Main axis orientation. The orientation of the crystal main axis is readily seen; plate crystal halos, such as parhelia and circumzenith arc, arise from crystals with their c-axis vertical, and

column crystal halos, such as 22° tangent arcs, arise from crystals with their c-axis horizontal. In cases of circular halos, the crystals do not have a preferred orientation but are more or less randomly oriented. Birefringence of ice provides another method to determine the main axis direction, since the deviation of the extraordinary component reaches a maximum when the light path is perpendicular to the main (optical) axis of the crystal [9]. The angular separation of the two components is, however, very small. This poses a challenge for detection of this separation, especially since the exact location of the inner edge of a halo is not easy to see.

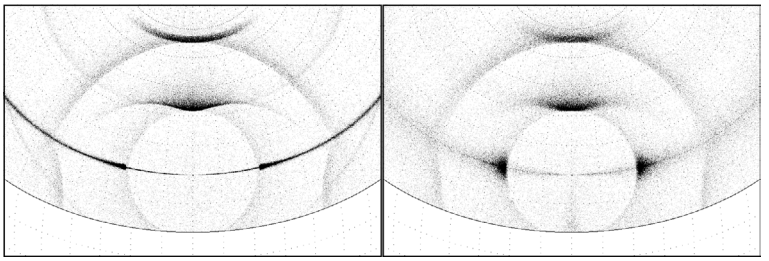

Figure 2. Two simulations showing the effect of different crystal tilts. The standard deviations of normally distributed tilts for plate crystal populations were 3° (left) and 6° (right), and for column populations 0.3° and 3°, respectively. It should be noted that the outer halo touching the circumzenith arc is not a 46° halo, but rather a combination of infralateral and supralateral arcs.

Tilting angles of the crystals. Well developed halos are a sign of very small tilting angles of the main axis of crystals. In some good-quality displays, the crystal tilts of the order of just a few tenths of a degree are needed to attain a good match between a halo photograph and a simulation. The appearence of halos is sensitive to the tilting angle; an increase of a few degrees can result in a considerable change in the halos (Fig 2). This parameter can be fairly accurately estimated by comparing photographs with a simulation, thus opening an interesting possibility for comparison between halo observations and e.g. lidar measurements.

Crystal aspect ratios. The orientations of ice crystals in the air are partially dictated by their aspect ratio and cross section in a plane perpendicular to the main axis. The intensity profiles of halos and their respective definitions give indications of the shape of ice crystals that made the halos. Different aspect ratios and profiles have an effect on relative surface areas of crystal faces, which has a direct impact on the probabilities of occurence of halo-making raypaths. In addition, some raypaths may become more favoured than others when the crystal dimensions change and in some cases part of the raypaths may be completely shut off. These effects are most prominent in pyramid crystal halos and halos with a raypath involving internal reflections, i.e. less frequently seen halos, see Fig 3.

CONCLUSION

Atmospheric halos provide a tool to estimate airborne ice-crystal properties. When halos are seen, the information that can be extracted from their appearence can be combined with the data obtained with other means. Ice crystal - halo associations can be modelled with a Monte-Carlo-simulation algorithm using geometrical optics. With the aid of computer

simulations a good match between observed halos and the model can be obtained, giving values for the shapes and orientations of ice crystals responsible for the halos. There is no direct way to figure out the crystal sizes from the halos, but for that one may use optical phenomena produced by the diffraction, e.g. coronae, which are practically always seen when particles come between the sun and the observer.

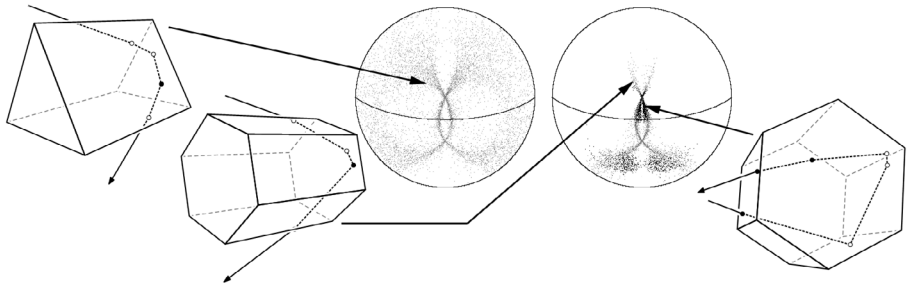

Figure 3. An example of the effect of crystal shape on the formation of halos. Simulations showing two components of diffuse anthelic arcs with a regular hexagonal column (right) and a triangular one (left). With a triangular column the component B spreads wider than with a regular hexagon, since within the crystal there is more room for the raypath. The raypath of the A component (black dots) includes internal reflections from adjacent faces of the hexagon, which is the reason it is completely missing from the leftmost simulation since it can not be formed at all when the crystal profile is triangular.

REFERENCES

[1] G.G. Mace, T.A. Ackerman, P. Minnis, and D.F. Young. Cirrus layer microphysical properties derived from surface-based millimeter radar and infrared interferometer data. J. Geophys. Res. **103** (1998).

[2] G.M. McFarquhar and A.J. Heymsfield. Microphysical characteristics of three anvils sampled during the Central Equatorial Pacific Experiment (CEPEX). J. Atmos. Sci. **53** (1996).

[3] E.J. Jensen, L. Pfister, T.-P. Bui, P. Lawson, and D. Baumgardner. Ice nucleation and cloud microphysical properties in tropical tropopause layer cirrus. Atmos. Chem. Phys. **10** (2010).

[4] W. Tape and J. Moilanen. Atmospheric Halos and the Search for Angle x. American Geophysical Union (2006).

[5] J. Ruoskanen. HaloPoint 2.0 – Software for simulating halo phenomena. *http://www.kolumbus.fi/jukka.ruoskanen/halopoint2.html*

[6] R.G. Greenler and A.J. Mallman. Circumscribed halos. Science **176** (1972).

[7] F. Pattloch and E. Tränkle. Monte Carlo simulation and analysis of halo phenomena. J. Opt. Soc. Am. A **1** (1984).

[8] M.I. Mishchenko and A. Macke. How big should hexagonal ice crystals be to produce halos? Appl. Opt. **38** (1999).

[9] G.P. Können. Polarization and intensity distributions of refraction halos. J. Opt. Soc. Am. **73** (1983).

Measurement of block-diagonal scattering matrix

S. Savenkov[*,1], R. Muttiah[2] , E. Oberemok[1], and A. Klimov[1]

[1] *Radiophysics Department, Kiev Taras Shevchenko University, Kiev, 01 033 Ukraine.*
[2] *Alan Plummer Associates, Inc., 1320 S. University Dr. #300, Fort Worth, Texas 76107, USA.*

The problem of measurement of the block-diagonal scattering matrix is addressed. It has been shown that non-zero elements of the scattering matrix with block-diagonal structure can be measured using only two polarizations of input radiation. Optimal pairs of these polarizations are derived. Utilization of the optimal input polarization results in half the measurement time and a decrease in measurement errors of approximately 30%.

INTRODUCTION

The block-diagonal scattering matrix of the form

$$\mathbf{M} = \begin{pmatrix} m_{11} & m_{12} & 0 & 0 \\ m_{21} & m_{22} & 0 & 0 \\ 0 & 0 & m_{33} & m_{34} \\ 0 & 0 & m_{43} & m_{44} \end{pmatrix}, \tag{1}$$

plays a key role in many light-scattering problems. The structure of **M** in Eq. (1) can be the result of symmetry of a single particle or a collection of particles in multiple scattering [1,2] and by the illumination-observation geometry for backward [3] and forward [4,5] scattering.

Scattering matrix **M** was used in the study of the optical characteristics of oceanic water [6,7]; of an ensemble of identical, but randomly oriented fractal particles [8]; of dense spherical particle suspensions in multiple-scattering case [9]; of the multiple scattering of light by an ice cloud consisting of nonspherical ice crystals [10]; of polydisperse, randomly oriented ice crystals modeled by finite circular cylinders with different size distributions [11]; for characterizing cylindrically shaped radially inhomogeneous particles [12]; small spherical particles (diameters range from 0.2 to 1.5 μm) sparsely seeded on a surface of crystalline silicon *c*-Si wafer [13]; for measurements of the complex refractive index of isotropic materials as matrices of isotropic and ideal metal mirror reflections [14]; in developing a symmetric three-term product decomposition of a Mueller-Jones matrix [15]; in the very general and important cases of (i) randomly oriented particles with a plane of symmetry [16] and (ii) with equal numbers of particles and their mirror particles [17].

Non-zero elements of the matrix **M** can be considered as the corresponding incomplete scattering matrices. Our main concern here is the utilization of this fact in the experimental

* Corresponding author: Sergey N. Savenkov (sns@univ.kiev.ua)

determination of non-zero elements of matrix **M** to decrease the error and time of measurements.

MEASUREMENT OF BLOCK-DIAGONAL SCATTERING MATRIX

The most appropriate measurement strategy of the block-diagonal scattering matrix **M** in Eq. (1) is the so-called time-sequential measurement strategy [18]. The measurement equation [18] of the time-sequential strategy takes the form

$$\begin{pmatrix} m_{11}r_1^1 + m_{12}r_2^1 & m_{11}r_1^2 + m_{12}r_2^2 & m_{11}r_1^3 + m_{12}r_2^3 & \cdot & \cdot & \cdot & m_{43}r_3^4 + m_{44}r_4^4 \end{pmatrix}^T = \begin{pmatrix} s_1^1 & s_1^2 & s_1^3 & s_1^4 & \cdot & \cdot & s_4^4 \end{pmatrix}^T. \quad (2)$$

Here r_i^k, s_i^k are the *i*-th parameters of the *k*-th Stokes vectors of input and output radiation. From Eq. (2) it can be deduced that the non-zero matrix elements can be measured by using only two input polarizations. In other words, Eq. (2) can be reduced to two independent subsystems of equations relative to the non-zero elements of **M** with the following characteristics matrices

$$\mathbf{V}_1 = \begin{pmatrix} r_1^1 & r_2^1 \\ r_1^2 & r_2^2 \end{pmatrix}, \quad \text{and} \quad \mathbf{V}_2 = \begin{pmatrix} r_3^1 & r_4^1 \\ r_3^2 & r_4^2 \end{pmatrix}. \quad (3)$$

It can be seen that the rows of the characteristics matrices $\mathbf{V}_1$ and $\mathbf{V}_2$ are formed by Stokes parameters of two polarizations of input radiation. The most important question resulting from Eq. (3) is what two polarizations should one use to measure the non-zero elements of the matrix **M**?

CHOICE OF INPUT POLARIZATIONS

If the values of parameters r_i^k, s_i^k in Eq. (2) are known accurately, i.e. without measurement errors, then the answer to this question is as follows: any two polarizations giving $\det(\mathbf{V}_1) \neq 0$ and $\det(\mathbf{V}_2) \neq 0$. However, this is not the case in the presence of measurement errors. In this case we use the condition number method [19]. Evidently, the connection between the matrices in Eq. (3) dictates that the values of Stokes parameters of input polarizations r_i^k should minimize the condition numbers of both characteristics matrices $\mathbf{V}_1$ and $\mathbf{V}_2$ in Eq.(3) simultaneously. This can be realized by minimization of the condition number of the product of the matrices $\mathbf{V}_1\mathbf{V}_2=\mathbf{V}$. In this case the condition number is a function of four variables: two azimuths and two ellipticities of two input polarizations.

Analysis shows that the minimal value of condition number is $cond(\mathbf{V}) = 2$, which corresponds to $cond(\mathbf{V}_1)\big|_{\min} = cond(\mathbf{V}_2)\big|_{\min} = 3.18$, and this solution is not unique. Graphical-

ly the dependences of the condition number $cond(\mathbf{V})$ on values of ellipticities $\varepsilon_{1,2}$ and azimuths $\theta_{1,2}$ of input polarizations are presented in Fig.1.

Dependences presented in Fig.1 correspond to the following pair of optimal input polarizations $\varepsilon_1 = 14.7°$, $\varepsilon_2 = 37.6°$, $\theta_1 = 79.8°$, $\theta_2 = -42.5°$. The explicit form of the characteristics matrices Eq.(3) in this case are

$$\mathbf{V}_1 = \begin{pmatrix} 1 & -0.8164 \\ 1 & 0.0218 \end{pmatrix}; \quad \mathbf{V}_2 = \begin{pmatrix} 0.3043 & 0.4907 \\ -0.2539 & 0.9670 \end{pmatrix}. \tag{4}$$

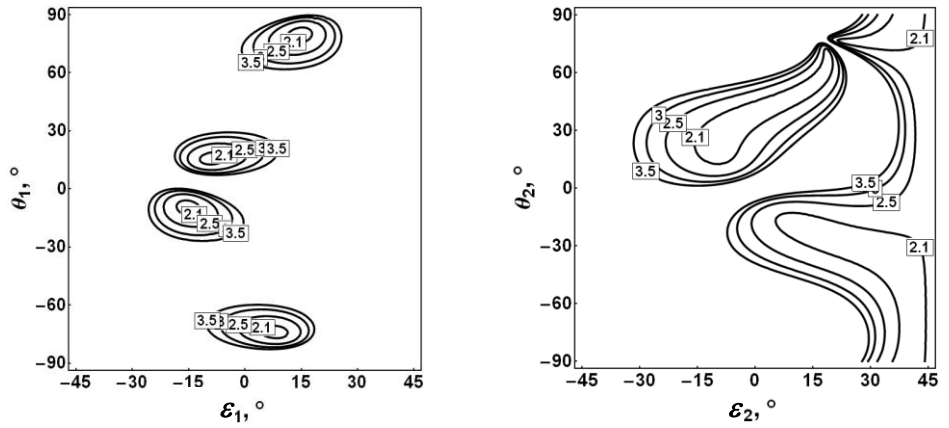

(**a**) (**b**)

Fig.1. Dependences of condition number $cond(\mathbf{V})$ on values of ellipticities $\varepsilon_{1,2}$ and azimuths $\theta_{1,2}$ for first (**a**) and second (**b**) polarization of input radiation (other polarizations in both cases is fixed and optimal).

CONCLUSIONS

We have demonstrated that non-zero elements of the block-diagonal scattering matrix **M** can be measured using only two polarizations of input radiation (see Fig. 1) and derived optimal pairs of these polarizations. Note that in practice the measurements with two input polarizations should be foreshadowed by calibration measurements with four input polarizations, which determine whether the scattering matrix has exactly block-diagonal form. If it is the case, then the utilization of derived optimal input polarizations in Fig. 1 results in half the measurement time and approximately a 30 % decrease of measurement errors, with all else being equal.

REFERENCES

[1] H.C . van de Hulst. *Light Scattering by Small Particles*. Wiley, New York (1957).

[2] M.I. Mishchenko and L.D. Travis. Polarization and depolarization of light. In: *Light Scattering from Microstructures*. F. Moreno and F. González (eds.). Springer-Verlag (2000).

[3] E. Zubko, Y.G. Shkuratov, and G. Videen. Coherent backscattering effect for non-zero elements of Mueller matrix of discrete media at different illumination-observation geometries. J. Quant. Spectrosc. Radiat. Transfer **89** (2004).

[4] S.N. Savenkov, R.S. Muttiah, K.E. Yushtin, and S.A. Volchkov. Mueller-matrix model of an inhomogeneous, linear, birefringent medium: single scattering case. J. Quant. Spectrosc. Radiat. Transfer **106** (2007).

[5] S.N. Savenkov, V.I. Grygoruk, S.M. Ranjan, Y.A. Oberemok, K.E. Yushtin, and V.V. Yakubchak. Effective dichroism in forward scattering by inhomogeneous birefringent medium. J. Quant. Spectrosc. Radiat. Transfer **110** (2008).

[6] K. J. Voss and E. S. Fry. Measurement of the Mueller matrix for ocean water. Appl. Optics **23** (1984).

[7] A.A. Kokhanovsky. Parameterization of the Mueller matrix of oceanic waters. J. Geophys. Res. **108** (2003).

[8] A.A. Kokhanovsky. Optical properties of irregularly shaped particles. J. Phys. D: Appl. Phys. **36** (2003).

[9] B. Kaplan, G. Ledanois, and B. Drevillon. Mueller matrix of dense polystyrene latex sphere suspensions: measurements and Monte Carlo simulation. Appl. Opt. **40** (2001).

[10] R. Lawless, Y. Xie, P. Yang, G.W. Kattawar, and I. Laszlo. Polarization and effective Mueller matrix for multiple scattering of light by nonspherical ice crystals. Opt. Express **14** (2006).

[11] L. Xu, J. Ding, and A. Cheng. Scattering matrix of infrared radiation by ice finite circular cylinders. Appl. Optics **41** (2002).

[12] S. Manickavasagam and P. Menguc. Scattering-matrix elements of coated infinite-length cylinders. Appl. Optics **37** (1998).

[13] B. Kaplan and B. Drevillon. Mueller matrix measurements of small spherical particles deposited on a *c*-Si wafer. Appl. Optics **41** (2002).

[14] L. Deibler and M. Smith. Measurement of the complex refractive index of isotropic materials with Mueller matrix polarimetry. Appl. Optics **40** (2001).

[15] R. Ossikovski. Interpretation of nondepolarizing Mueller matrices based on singular-value decomposition. J. Opt. Soc. Am. A **25** (2008).

[16] J. Hovenier and C. van der Mee. Basic relationships for matrices describing scattering by small particles. In: *Light Scattering by Nonspherical Particles*. M. Mishchenko, J. Hovenier, and L. Travis (eds.). Academic Press, NY (2000).

[17] M.I. Mishchenko, L.D. Travis, and A.A Lacis. *Multiple scattering of light by particles*. Cambridge Univ. Press, Cambridge (2006).

[18] R.A. Chipman. Polarimetry. In: *Handbook of Optics*. Vol. II, McGraw Hill (1995).

[19] R. Horn and Ch. Johnson. *Matrix Analysis*. Cambridge Univ. Press, London (1986).

Numerical study of diffraction effects in light scattering by multiple cylindrical scatterers

J. Schäfer* and A. Kienle

Institut für Lasertechnologien in der Medizin und Meßtechnik an der Universität Ulm, Helmholtzstraße 12, 89081 Ulm, Germany.

We compared Maxwell and radiative transfer theories for light scattering by multiple cylindrical scatterers and observed forward diffraction peaks in the Maxwell solutions. We examined diffraction by dielectric homogeneous obstacles of finite thickness and depicted differences to the scalar diffraction theory for a single slit. We show that for the interpretation of the diffraction effects in our multiple cylinder model the single slit diffraction approximation can be applied.

INTRODUCTION

The application of light has a high potential in medical diagnosis and therapy. For the development of effective methods, a theoretical investigation of the interaction of light with biological tissue is essential. Currently, in most cases, the radiative transfer equation (RTE) is used for this purpose. Nevertheless, this approach neglects effects originating from the wave nature of light, such as interference or diffraction. While general restrictions of the applicability of the RTE are known [1], the task of quantitatively examining these restrictions for special cases still remains. For these examinations it is necessary to compare the RTE results with solutions of the Maxwell equations.

In a recent publication, we examined the coupling between solutions of the RTE and Maxwell theory for the scattering by multiple cylinders arranged in a finite area [2]. Due to the finiteness of the area, diffraction effects occur in the Maxwell solutions that are not present in the RTE results. In this contribution we will further investigate these diffraction effects and highlight some ways to eliminate these effects in order to better compare the two theories.

RESULTS

Cylindrical scatterers in a finite area

In a recent publication, we presented a comparison between RTE and Maxwell theory for the solutions of the light scattering by multiple cylinders [2]. At first, similar results are shown here. The RTE has been solved using a Monte Carlo method [3], where the analytical Maxwell solution for a single cylinder has been used to specify the scattering properties in the RTE. For the Maxwell solutions an analytical multiple cylinder theory has been applied [4]. Our simulation models consisted of infinitely long parallel cylinders having a diameter of $d = 2$ µm and a refractive index of $1.33 + 0i$. The cylinders have been randomly distributed over an area $A = 10 \times 10$ µm^2 with an outer medium refractive index $n_m = 1.52$. We note that the parameters were chosen to model tubules in human dentin. The light is incident

*Corresponding author: Jan Schäfer (jan.schaefer@ilm.uni-ulm.de)

perpendicular to the cylinder axes, having a vacuum wavelength of $\lambda = 633$ nm. Different cylinder densities have been examined. For the Maxwell solution, results of 50 different runs of randomly oriented cylinders have been averaged for each density in order to suppress speckles.

The calculated results for both theories are shown in Fig. 1. A good agreement between Maxwell and RTE results for scattering angles higher than 20 degrees can be observed. For higher concentrations, the differences increase due to dependent scattering effects which cannot be accounted for in radiative transfer theory. Furthermore, a large deviation for small angles can be seen as shown at the right-hand side of Fig. 1. As we argued in [2], these differences are mainly caused by diffraction effects due to the finite size of our model. These effects are immanent to the Maxwell solution but cannot be observed in the RTE results.

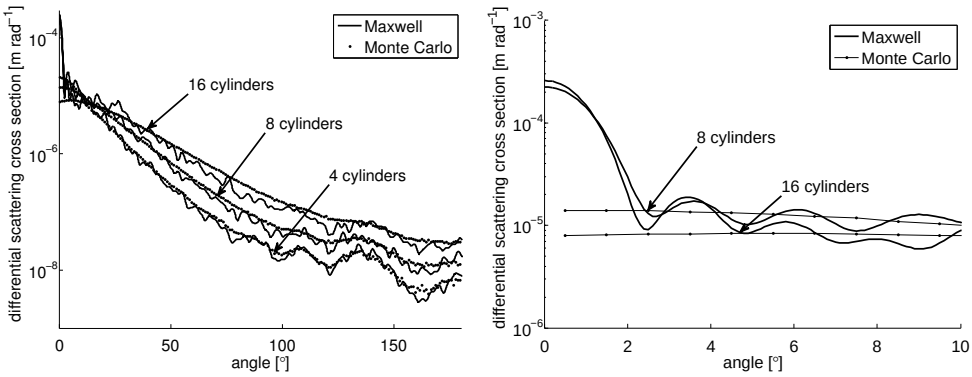

Figure 1. Left: Comparison between the Maxwell and RTE results for three different cylinder densities. Right: In the forward direction huge deviations between the Maxwell and RTE results can be observed, caused by diffraction effects of the finite scattering area.

Diffraction calculations

In this section we will discuss some fundamental issues concerning diffraction and use our Maxwell solver codes to further investigate the observed diffraction effects. For multiple cylinder problems we used the analytical method described in [4], for arbitrary structures we used a self-developed finite-difference time-domain (FDTD) [5] simulation program.

Diffraction occurs when light encounters a small obstacle or opening. The light waves that pass the object form a diffraction pattern which can be observed in the far field. Usually a scalar diffraction theory is used, where it is assumed that the obstacle is infinitely thin and perfectly absorbing. The diffraction by a single cylinder can be approximated as diffraction by an (inverse) slit where the width of the slit is given by the cylinder diameter. For slit diffraction (and also for inverse-slit diffraction as is stated by Babinet's theorem) a very simple formula exists [6]:

$$I(\theta) = I(0)\left(\frac{\sin\beta}{\beta}\right)^2, \tag{1}$$

$$\beta = \left(\frac{kb}{2}\right)\sin\theta, \tag{2}$$

where b is the width of the slit and $k = \frac{2\pi n_m}{\lambda}$ is the wavenumber in the outer medium. We also used this formula for the calculation of the diffraction by multiple cylinders, assuming

that the collection of all cylinders forms a thin obstacle of the same width as the illuminated side of the finite area. We could show that the peaks of the scattering function in forward direction resemble the peaks calculated by the slit-diffraction theory (see reference [2]). The question remains if the slit-diffraction approximation is applicable for dielectric obstacles of finite thickness. On the left-hand side of Fig. 2 we compare the slit diffraction results for a 10 µm slit with the FDTD simulations output for diffraction by dielectric obstacles of finite thickness. For rectangular obstacles, a deviation from the slit diffraction results is observed even if we assume a perfectly absorbing material (perfectly electric conductor - PEC [5]). If we reduce the thickness of the rectangular obstacle, the results converge to the slit solution, also for dielectric materials. On the right-hand side of Fig. 2 the results for a broader slit of 50 µm are also depicted. In summary we can state that the slit diffraction is not applicable if we treat rectangular obstacles of finite thickness. While the period length of the minima and maxima does not change much, a location shift of the minima and maxima is observed. The location is also dependent on the (complex) refractive index of the dielectric media.

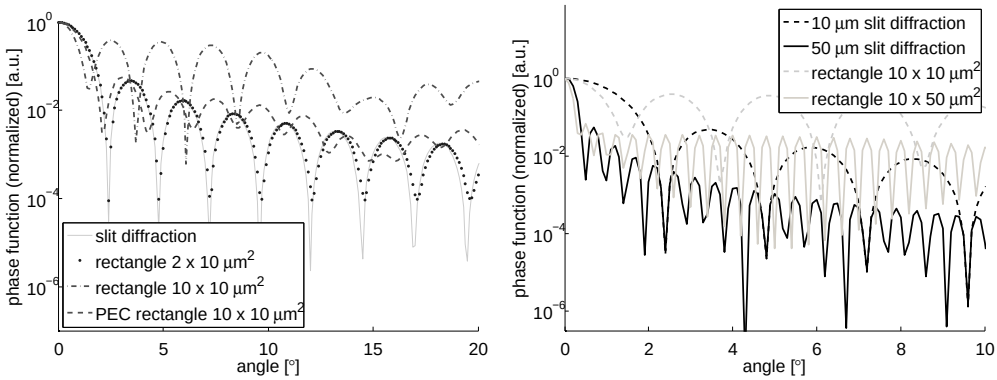

Figure 2. Left: Diffraction by a slit compared to diffraction by different rectangular obstacles. Right: Diffraction by a slit and a rectangular obstacle of various width.

Comparison of diffraction calculations with multiple cylinder scattering results

Based on the diffraction results of the previous section we would not assume that the slit diffraction theory is applicable to our multiple cylinder model, since we are dealing with dielectric cylinders arranged in a finite area. We would rather expect that the diffraction of our model resembles the diffraction pattern by a rectangular profile of the same size as the finite area. In Fig. 3 we compare the diffraction by different obstacles with sizes of $A = 10 \times 10$ µm^2 and $A = 10 \times 50$ µm^2. It can be seen that the multiple cylinder results differ from the results obtained from diffraction by the rectangular obstacle having the same size as the area occupied by the cylinders. On the other hand, the slit diffraction gives a good approximation for the location and period of the minima and maxima in the diffraction pattern of the multiple cylinder solution, especially when the cylinders are considered to be perfectly absorbing. Also, we examined an ordered structure of a grid of 4×4 and 4×20 cylinders with a grid length of 2.5 µm, respectively. For the ordered structure the slit diffraction solution fits even better.

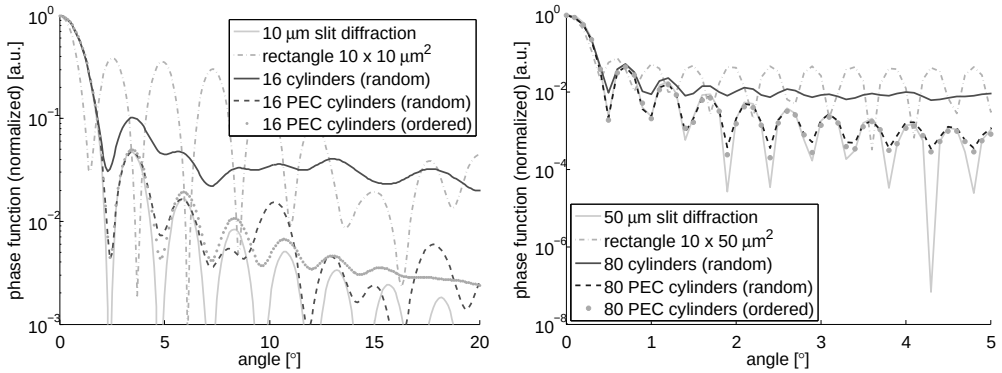

Figure 3. Left: Comparison of diffraction results for the case of $A = 10 \times 10\ \mu\text{m}^2$. Right: Comparison of diffraction results for the case of $A = 10 \times 50\ \mu\text{m}^2$. The broader side is illuminated.

CONCLUSION

We presented a comparison between Maxwell and RTE solutions and depicted the occurrence of forward diffraction peaks in the Maxwell results. We confirmed that in general it is not possible to use the single-slit diffraction approximation to explain diffraction by dielectric obstacles of finite thickness. On the other hand, we could show that this approximation indeed seems to give suitable results for the diffraction of multiple cylinders distributed in a finite area.

To do a better comparison of the Maxwell and RTE solutions, as applied to an infinite expanse of random cylinders, these diffraction effects have to be suppressed since they cannot be explained by means of radiative transfer theory. With our calculations we could qualitatively explain the cause of these effects, but we are not able to quantitatively subtract these effects from our Maxwell results. To get rid of these effects, we have to distribute the cylinders in an infinite (or very broad) slab and use a spatially limited (e.g. focused) source. The Monte Carlo solution of the RTE can easily be extended for performing these calculations. Our FDTD solution offers possibilities to perform such investigations in the Maxwell regime.

REFERENCES

[1] M. I. Mishchenko, L. D. Travis, and A. A. Lacis. *Multiple scattering of light by particles: radiative transfer and coherent backscattering*. Cambridge University Press (2006).

[2] J. Schäfer and A. Kienle. Scattering of light by multiple dielectric cylinders: comparison of radiative transfer and Maxwell theory. Opt. Lett. **33** (2008).

[3] A. Kienle, F. K. Forster, and R. Hibst. Anisotropy of light propagation in biological tissue. Opt. Lett. **29** (2004).

[4] S.-C. Lee. Dependent scattering of an obliquely incident plane wave by a collection of parallel cylinders. J. Appl. Phys. **68** (1990).

[5] A. Taflove and S. C. Hagness. *Computational electrodynamics: the finite difference time-domain method*. Artech House (1995).

[6] E. Hecht. *Optik*. Oldenbourg Verlag (2005).

Iterative solvers for T-matrix and Discrete-Sources Methods

V. Schmidt*,[1], R. Schuh[1], and T. Wriedt[2]

[1] *University of Bremen, Badgasteiner Str. 3, 28359 Bremen, Germany.*
[2] *Institute für Werkstofftechnik, Badgasteiner Str. 3, 28359 Bremen, Germany.*

The different iterative approaches (GMRES, MINRES, BiCGStab, BiCGStab(2)) to solve linear systems in scattering problems based on surface-integral-equation methods (Discrete-Sources Method, T-matrix) are compared. The case where the kernel matrix is relatively small but ill-conditioned is considered. Different preconditioning techniques (diagonal, block-diagonal preconditioning matrix) are also compared.

INTRODUCTION

The numerical simulation of light scattering by small particles is a modern and effective approach to investigate many physical processes. During the centennial history, a lot of numerical methods have been developed and extended. Most of them require or imply to solve the linear system problem.

Solving the linear system can be subjected to numerical difficulties because of the ill-conditionality of the kernel matrix and the finite-precision arithmetic in computers. The iterative methods help to reduce the influence of this factor and to decrease the required time to estimate the solution. The extremely large, sparse, ill-conditioned kernel matrix is the case where the iterative methods are mostly preferable. Therefore, they are used in volume-integral-equation methods like DDA (discrete-dipole approximation). Preconditioning techniques also allow to strongly improve the convergence of iterative processes.

Here, different iterative methods and preconditioning techniques for the Discrete-Sources Method (DSM) and the T-matrix Method labeled as surface-integral-equation methods are compared. Cases with relative small but highly ill-conditioned kernel matrices are considered.

MATHEMATICAL STATEMENT OF THE SCATTERING PROBLEM

Let us consider scattering in an isotropic homogeneous medium R^3 of an electromagnetic wave by a local homogeneous penetrable obstacle D_i with the smooth boundary ∂D. We assume the time dependence to be $\exp(j\omega t)$. Scattering is described by the electromagnetic fields $\{\mathbf{E}_{e,i}, \mathbf{H}_{e,i}\}$ satisfying the Maxwell equations

$$\begin{array}{rcll} \nabla \times \mathbf{H}_{e,i} = & jk\varepsilon_{e,i}\mathbf{E}_{e,i}, & & \\ \nabla \times \mathbf{E}_{e,i} = & -jk\mu_{e,i}\mathbf{H}_{e,i}, & \text{in } D_{e,i}, & D_e := R^3/\bar{D}_i, \end{array} \tag{1}$$

the boundary conditions enforced on the particle surface

$$\begin{array}{rcll} \mathbf{n}_p \times (\mathbf{E}_i(P) - \mathbf{E}_e(P)) = & \mathbf{n}_p \times \mathbf{E}^0(P), & & \\ \mathbf{n}_p \times (\mathbf{H}_i(P) - \mathbf{H}_e(P)) = & \mathbf{n}_p \times \mathbf{H}^0(P), & P \in \partial D, & \end{array} \tag{2}$$

and the Silver-Muller radiation condition at infinity,

$$\lim_{r\to\infty} \left(\sqrt{\varepsilon_e}\mathbf{E}_e \times \frac{\mathbf{r}}{r} - \sqrt{\mu_e}\mathbf{H}_e \right) = 0, \qquad r = |M| \to \infty, \tag{3}$$

*Corresponding author: Vladimir Schmidt (vschmidt@iwt.uni-bremen.de)

where $\{\mathbf{E}^0, \mathbf{H}^0\}$ is an exciting field, $\mathbf{n}_p$ is the unit outward normal to ∂D , index e belongs to the external domain D_e and i to the domain inside the particle D_i, $\varepsilon_{e,i}$ is the permittivity, and $\mu_{e,i}$ is the permeability of media. This boundary value scattering problem is well-known to have an unique solution.

T-matrix Method

The T-matrix approach is a modern and effective numerical tool for exactly solving the scattering problem for particles of arbitrary shape. It was proposed by Waterman [1] and extensively reviewed by Mishchenko et al. [2]. The further extension of the method is called the Null-Field Method with Discrete Sources (NFM-DS) [3].

In the terms of NFM-DS the internal electromagnetic field is expanded by a suitable basis of vector wave functions, e.g. in an isotropic medium regular vector spherical wave functions are used

$$\mathbf{E}_i(\mathbf{r}) = \sum_{n=1}^{\infty} \sum_{m=-n}^{n} \left[p_{mn} \mathbf{RgM}(k_s \mathbf{r}) + q_{mn} \mathbf{RgN}(k_s \mathbf{r}) \right], \quad k_i = \sqrt{\varepsilon_i \mu_i}. \tag{4}$$

The electromagnetic fields outside the circumscribed sphere are expanded into a series of spherical vector wave functions

$$\mathbf{E}_e(\mathbf{r}) = \sum_{n=1}^{\infty} \sum_{m=-n}^{n} \left[a_{mn} \mathbf{M}(k_s \mathbf{r}) + b_{mn} \mathbf{N}(k_s \mathbf{r}) \right], \quad k_s = \sqrt{\varepsilon_s \mu_s}, \tag{5}$$

$$\mathbf{E}_s(\mathbf{r}) = \sum_{n=1}^{\infty} \sum_{m=-n}^{n} \left[f_{mn} \mathbf{RgM}_i(k_s \mathbf{r}) + g_{mn} \mathbf{RgN}_i(k_s \mathbf{r}) \right], \tag{6}$$

where k_s is the wave number of the isotropic surrounding medium, and a_{mn}, b_{mn} and f_{mn}, g_{mn} are the expansion coefficients of the incident and scattered fields, respectively. Considering the null-field equations (2) and the expansions (4-6), the transition matrix $\mathbf{T}$ can be obtained from the following linear system:

$$\mathbf{T} \cdot \mathbf{Q}^{31} = -\mathbf{Q}^{11}, \quad \begin{pmatrix} f_{mn} \\ g_{mn} \end{pmatrix} = \mathbf{T} \begin{pmatrix} a_{mn} \\ b_{mn} \end{pmatrix}, \tag{7}$$

where the matrices $\mathbf{Q}^{31}$, $\mathbf{Q}^{11}$ include surface integrals over the particle surface. In real simulations, the matrix size depends on the expansion order $1 \le n \le N_{rank}$ in (4-6) and is typically less than 10000.

Discrete Sources Method

In the frame of DSM, an approximate solution of the scattering problem is constructed as a finite linear combination of the field of dipoles and multipoles $\{z_n\}_{n=1}^{N}$ deposited in a supplementary domain ω_0. Detailed review can be found in the book by Wriedt et al. [4]. In the case of a P-polarized incident plane wave and an axially symmetric particle, the approximate solution can be presented in the form

$$\begin{pmatrix} \mathbf{E}_{e,i}^{N} \\ \mathbf{H}_{e,i}^{N} \end{pmatrix} = \sum_{m=0}^{M} \sum_{n=1}^{N_{e,i}^{m}} \left\{ p_{mn}^{e,i} D_1 \mathbf{A}_{mn}^{1,e,i} + q_{mn}^{e,i} D_2 \mathbf{A}_{mn}^{2,e,i} \right\} + \sum_{n=1}^{N_{e,i}^{0}} r_n^{e,i} D_1 \mathbf{A}_n^{3,e,i} \tag{8}$$

with vector differential operators D_1, D_2, the vector potentials in a cylindrical coordinate system $\mathbf{A}_{mn}^{1,e,i}$, $\mathbf{A}_{mn}^{2,e,i}$, $\mathbf{A}_{n}^{3,e,i}$, and the amplitudes of the corresponding multipoles $p_{mn}^{e,i}$, $q_{mn}^{e,i}$, $r_n^{e,i}$.

The unknown amplitudes of the discrete sources are to be determined from the boundary conditions (2). To solve this problem, the Generalized Point-Matching Technique is used. The matching of the approximate solution and the external excitation over the particle surface is replaced by the matching over particle generatrix $\{\eta_n\}_{n=1}^{L}$ for each Fourier harmonic m separately. As a consequence, the unknown vector of amplitudes $\mathbf{p}_m = \{p_{mn}^{e,i}, q_{mn}^{e,i}\}_{n=1}^{N_{e,i}^m}$ can be found as a pseudosolution of an over-determined system of linear equations:

$$\mathbf{B}_m \mathbf{p}_m = \mathbf{q}_m, \qquad m = 0, ..., M, \tag{9}$$

where $\mathbf{B}_m$ is a rectangular matrix of dimension $4L \times 2(N_i^m + N_e^m)$. Similarly, the amplitudes $\mathbf{p}_{-1} = \{r_n^{e,i}\}_{n=1}^{N_{e,i}}$ corresponding to the vertical electric or magnetic dipoles can be found.

Solving this problem we transform (directly or formally) the equation (9) to its 'equivalent' normal form ($n = m$) (10) through multiplication by the conjugate transpose matrix,

$$A_m \mathbf{p}_m = \hat{b}_m, \quad A_m = \mathbf{B}_m^T \mathbf{B}_m, \quad \hat{b}_m = \mathbf{B}_m^T \mathbf{q}_m. \tag{10}$$

Here A_m is a Hermitian, non-singular, positive definite matrix with the dimension $2(N_i^m + N_e^m) \times 2(N_i^m + N_e^m)$. Usually, the matrix size lies in the range between 500 and 5000.

ITERATIVE SOLVERS

Krylov subspace

Many powerful and effective methods are Krylov subspace projection methods. These methods were initiated in the early 1950s with the introduction of the conjugate gradients methods [5]. For a given non-singular matrix A, an approximate solution is constructed in the so-called Krylov subspace

$$x_k \in x_0 + K^k(A; r_0), \quad K^k(A; r_0) = span\{r_0, Ar_0, \ldots, A^{k-1} r_0\},$$

where $r_0 = b - Ax_0$ is an initial residual, x_0 is a given initial solution, and k is the iteration step. Because of the non-singularity of A, the vectors $r_0, Ar_0, \ldots, A^{k-1} r_0$ are linearly independent and the Krylov subspace is a k-dimensional space. This means that the dimensionality of the subspace will increase by 1 up to n per iteration. The Krylov subspace methods should give the exact solution after at least n iterations, but they give a suitable approximate solution much earlier. By the criteria on 'optimality', these methods fall in three different classes:

The Ritz-Galerkin approach — Construct the $x_k \in x_0 + K^k(A, r_0)$ for which the residual $r_k = b - Ax_k$ is orthogonal to the current subspace $r_k \perp K^k(A, r_0)$. The commonly used methods for symmetric (Hermitian) matrices are CG, SYMMLQ, for non-symmetric matrices are FOM, CGNE, CGNR.

The minimum residual approach — Construct the $x_k \in x_0 + K^k(A, r_0)$ for which the Euclidian norm $\|b - Ax_k\|_2$ is minimal over the current subspace. The commonly used algorithms of the current group are GMRES, RGMRES, FGMRES, GMRESR and version of GMRES for symmetric (Hermitian) matrices MINRES.

The Petrov-Galerkin approach — Construct the $x_k \in x_0 + K^k(A, r_0)$ for which the residual r_k is orthogonal to some other suitable k-dimensional subspace. If we select $L^k =$

$K^k(A^T, s^0)$ for some vector s^0, then we obtain the BiCG and QMR methods and their further modifications CGS, BiCGStab, BiCGStab(l) and TFQMR, respectively.

Based on preliminary simulations, for further comparisons, the following methods RGMRES(m), BiCGStab, BiCGStab(l) (PIM library [6]) and MINRES were chosen.

Preconditioning techniques

One of the advantages of the iterative methods is the availability of preconditioning techniques. The convergence of an iterative process and the accumulation of round-off errors strongly depend on the condition number $\kappa(A) = \max \|\lambda_i\| / / \min \|\lambda_i\|$, where λ_i is the i-th eigenvalue of the matrix A. By multiplication (left- and/or right-sided) by some other matrix K, we can change the condition number and therefore improve the iterative process.

Because the calculation of well-known preconditioners (*ILU*, *ILUT*, *IC*, polynomial preconditioner) for ill-conditioned dense matrices could be numerically difficult and unstable, diagonal matrix preconditioners $D = diag\{d_{11}, d_{22}, \ldots, d_{nn}\}$ with different filling rules as well as two-diagonal preconditioners are chosen. To keep the Hermitian symmetry of the matrix A, we used the left and right preconditioning $\hat{A} = D^{1/2} A D^{1/2}$, $P = D^{1/2}$.

In Fig. 1, the iterative behavior of the scattering computation using the DSM method is plotted. The scatterer is a prolate spheroidal particle with size parameter $kR = 50$, aspect ratio $e = 10$, and refractive index $m_r = 1.6$. As a measure of the quality of the solution, the discrepancy of the surface fields ($\|\mathbf{n}_p \times (\mathbf{E}_i - \mathbf{E}_e - \mathbf{E}^0)\| / \|\mathbf{E}^0\|$) is used.

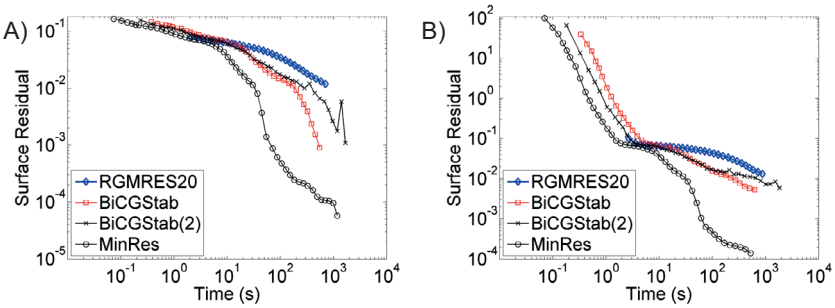

Figure 1. The iterative behaviour of scattering computation using iterative solvers (a) without preconditioning techniques and (b) with a block-diagonal preconditioning matrix.

Acknowledgments: We acknowledge support by Deutsche Forschungsgemeinschaft (DFG).

REFERENCES

[1] P.C. Waterman. Symmetry, unitary and geometry in electromagnetic scattering. Phys. Rev. D **3** (1971).

[2] M.I. Mishchenko, G. Videen, N.G. Khlebtsov, T. Wriedt, and N.T. Zakharova. Comprehensive T-matrix reference database: A 2006-07 update. JQRST **109** (2008).

[3] T. Wriedt. Review of the null-field method with discrete sources. JQSRT **106** (2007).

[4] T. Wriedt. *Generalized Multipole Techniques for Electromagnetic and Light Scattering*. Elsevier, Amsterdam (1999).

[5] Y. Saad. *Iterative Methods for Sparse Linear Systems*. Second edition (2000)

[6] R.D. da Cunha and T. Hopkins. The Parallel Iterative Methods (PIM) package for the solution of systems of linear equations on parallel computers. Applied Numerical Mathematics **19** (1995).

Dust models for cometary grains to explain optical polarization

A. K. Sen* and H. S. Das

Department of Physics, Assam University, Silchar 788011, India.

The observed optical polarizations for comets have been explained in the past by assuming the cometary grains to be compact spheres, such that Mie theory could be applied to simulate the observed polarizations. However, from a realistic point of view, recently other shapes like spheroids and aggregates of monomers have been considered for cometary grains. For this purpose, *T*-matrix or DDA based light scattering techniques have mostly been used to simulate the observed polarizations. Such polarizations, as observed by the authors for comets Halley and Austin, have been explained earlier using Mie theory to understand the composition and size distribution of cometary grains. Recently, the authors have used *T*-matrix technique and aggregate grain model to explain the polarizations of comets like Hale-Bopp, Levy, and Hyakutake. The simulated polarization values, with the aggregate model, were found to match the observed values much better as compared to compact spherical or spheroidal models. However, difficulties have been noted in a simple aggregate model of grains and some possibilities are discussed here.

INTRODUCTION

Comets are known to exhibit high amount of polarization, caused due to scattering of sunlight by dust grains present in the coma of comets. The polarizations observed through ground based or space borne telescopes largely depend on the scattering angle. As the scattering angle becomes very high (> 160 degrees), almost all the comets exhibit negative polarization. It has been found that the observed cometary polarization data can be explained fairly well by assuming the grains to be Mie spheres with a specific dust size distribution and compositions characterized by complex refractive indices. Following this procedure, the authors had in the past explained the observed polarization values of various comets with reasonable accuracy [1-3]. For this calculation, a power-law grain size distribution was assumed from space-craft observations [4] and the complex refractive index was used as a free parameter for modeling. This procedure of fitting the observed polarization data using Mie theory, for various sizes and compositions, was applied to several comets and it was found that the grains of the comets increase in their sizes as they grow dynamically older with successive revolutions around the Sun [3].

ASPHERICAL GRAINS AS COMPARED TO THE SPHERICAL GRAINS IN COMETS

It seems quite reasonable to expect that the naturally-occurring cometary grains cannot be ideal compact spheres, as required by Mie theory. However, until recently, cometary scientists have been using such Mie particles to explain the observed polarization data, as it is more convenient and direct, with a fewer number of free parameters required for modeling.

* Corresponding author: Asoke Kumar Sen (asokesen@yahoo.com)

In an attempt to explain the observed polarization data of comet Levy (1990XX), we noticed that the polarization can be simulated more accurately if we assume the grains to be prolate (with aspect ratio of 0.48) rather than Mie's ideal spheres [5]. This model calculation also successfully reproduced the observed negative polarization values for comet Levy, which was earlier not possible for similar comets [6]. A Chi-square minimization technique was followed for model fitting. We considered particles with different sizes and compositions, and a *T*-matrix based scattering code was executed. It was found that the sum of squares of difference between the observed and calculated values of polarization becomes minimum if we assume that the grains are prolate instead of spheres. And there was complete uniqueness in the model fitting of data. Thus, one could conclude that the cometary grains are more likely to be prolates rather than spheres (at least for comet Levy).

THE AGGREGATES OF MONOMERS AS THE GRAINS OF THE COMETS

With the fact that the prolate grains gave a better fit to the observed polarization data, as was seen for comet Levy, we extended these calculations to other comets, for which fits using Mie theory were already available. But no significant progress could be made.

It has been long believed that cometary grains are fluffy aggregates [7]. Xing and Hanner [8] carried out calculations with porous aggregates using DDA techniques for comets and got good results. Assuming an individual cometary grain to be an aggregate of several monomers, we performed calculations by superposition *T*-matrix method [9]. To begin with, one can assume that all the monomers are of same size and composition. Aggregates are built by using either Ballistic Particle Cluster Aggregate (BPCA) or Ballistic Cluster Cluster Aggregate (BCCA) method [10]. BPCA is more compact than BCCA. We took several test cases of aggregate grains containing 32 and 1024 monomers (with BPCA and BCCA structures) and it was observed that, as we increase the number of monomers, the calculated polarization values are not very sensitive to the structure or the size of the aggregate. However, the polarization value depends strongly on the radius of the monomers. Since we considered 32 to 1024 monomers in our calculations with monomer radii between 0.10 to 0.13 μm, the effective aggregate size considered was within the range of 0.1 to 1.3 μm (see [11] and references therein). With the polarization data of comet Levy at 0.485 μm [12], a theoretical fit was made by choosing *N* (number of monomers)=128 and initially taking a refractive index value close to that of olivine (1.771, 0.108; linearly interpolated value of the refractive index: details in [13]) . The monomer radius *a* was also varied within the range of 0.10 to 0.13 μm. A chi-square minimization technique was applied for obtaining the best fit. By this technique, we could fit the observed data with a refractive index of (1.783, 0.052) and $a = 0.12$ μm very well and the fit was better than that with prolates obtained earlier [5].

With the success for comet Levy, a similar approach was followed for comet Hale Bopp [13]. Lasue & Levasseur-Regourd [14] used aggregate dust model to study Hale Bopp. The comet exhibited high polarization and grains were believed to be rich in silicates. Data from various authors at $\lambda = 0.485$ μm and 0.684 μm were considered for modeling. Monomer radius *a* was varied within a range of 0.10–0.18 μm. To begin with, calculations were done by taking the refractive index for amorphous olivine, pyroxene, and carbonaceous materials, but none of them could produce good fit to the observed data well. It was observed that the

data can be fitted with two different values of monomer radius *a,* at two different values of wavelength, however, the size parameters remained the same as 1.56.

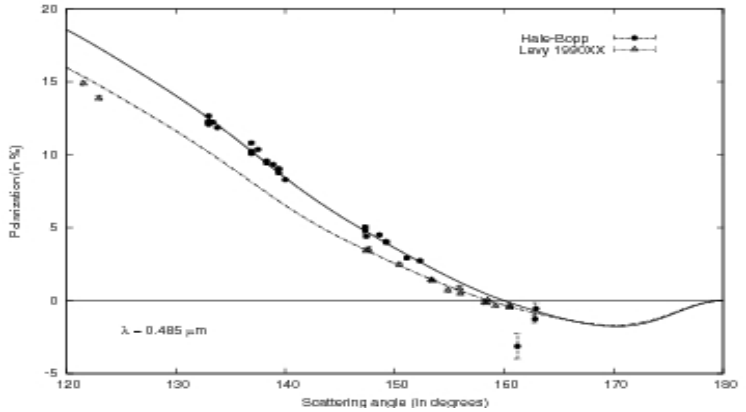

Figure 1. The polarization characteristics of comets Levy and Hale Bopp at 0.485 μm are compared .The solid curves represent simulated polarization values using aggregate model.

At wavelength 0.485 μm, the simulated value of *a* was 0.12 μm, which was the same as that obtained for Levy, but with a different refractive index value (1.778, 0.059). For Levy, the corresponding value was (1.783, 0.052). However, at 0.684 μm, the best fit value of *a* was 0.17 μm, with the refractive index value (1.755, 0.080). Figure 1 shows the observed polarization values of comets Levy and Hale Bopp, along with the theoretical scattering angle versus polarization curve simulated assuming the aggregate model of grains.

More recently, by applying the similar technique, the polarization data of comet Hyakutake at three distinct wavelengths 0.365 μm, 0.485 μm, and 0.684 μm were fitted by assuming an aggregate model of grains by the authors [15]. It was again found that the monomer radius had to be varied to obtain the best fit at different wavelengths, but the size parameter almost remained the same. Since this represents an unrealistic situation, it can be indicative of a situation which is more complex than just having one single aggregate composed of one single size of monomers with identical composition. A grain model containing compact spheroids and aggregates together may be able to explain the situation better. The work on this is under progress.

CONCLUSIONS

Any model for cometary grain, in addition to explaining the observed polarization, should also explain in general all the observed dust features: the scattered intensity, especially back-scattering enhancement, polarimetric color as a function of wavelength, etc. However, in the present case, we are limiting ourselves to polarization data only, which have been observed only at certain specific wavelengths and phase angle ranges. With these limitations and based on our analysis above one can conclude that: i) Cometary polarization can be best explained by the aggregate model of dust, as compared to other shapes like Mie spheres and spheroids (prolate, oblate etc.); ii) The polarization values are not very sensitive to the structure or size of the aggregate. Instead, size of a monomer plays an important role; iii) It is interesting to note that the three different comets Levy, Hale Bopp and Hyakutake

require almost the same monomer size at same wavelength to simulate the observed polarization curve; iv) At different wavelengths, the best fit conditions can be obtained by varying the monomer radius but the size parameter almost remains the same; v) Other grain models containing compact spheroids and aggregates together [16] may explain the situation in a better way.

REFERENCES

[1] A.K. Sen, M.R. Deshpande, U.C. Joshi, N.K. Rao, and A.V. Raveendran. Polarimetry of comet P/Halley: properties of dust. A&A **242** (1991).

[2] A.K. Sen, U.C.Joshi, and M.R. Deshpande. Polarimetric properties of comet Austin. MNRAS **253** (1991).

[3] H.S. Das, A.K. Sen, and C.L. Kaul. The polarimetric effects of cometary dusts and possible effect of grain aging by sun. A&A **423** (2004).

[4] E.P. Mazets et al. Comet Halley dust environment from SP-2 detector measurements. Nature **321** (1986).

[5] H.S. Das and A.K. Sen. Polarimetric studies of comet Levy 1990. A&A **459** (2006).

[6] D.X. Kerola and S.M. Larson. Analysis of Coma Dust Optical Properties in Comet C/1995 O1 (Hale-Bopp). II. Effects of Polarization. Icarus **149** (2001).

[7] J.M. Greenberg and J.L. Hage. From interstellar dust to comets - A unification of observational constraints. ApJ **361** (1990).

[8] Z. Xing and M.S. Hanner. Light scattering by aggregate particles. A&A **324** (1997).

[9] D.W. Mackowski and M.I. Mishchenko. Calculation of the T matrix and the scattering matrix for ensembles of spheres. Journal Opt. Soc. America A **13** (1996).

[10] P. Meaki. Effects of cluster trajectories on cluster-cluster aggregation: A comparison of linear and Brownian trajectories in two- and three-dimensional simulations. Phys. Rev. A **29** (1984).

[11] H.S. Das, S.R. Das, T. Paul, and A.K. Sen. Aggregate model of cometary dust: An application to comet Levy 1990XX. MNRAS **389** (2008).

[12] G.P. Chernova, N.N. Kiselev, and K. Jockers. Polarimetric characteristics of dust particles as observed in 13 comets – Comparisons with asteroids. Icarus **103** (1993).

[13] H.S. Das, S.R. Das, and A.K. Sen. Aggregate dust model to describe polarization properties of comet Hale-Bopp. MNRAS **390** (2008).

[14] J. Lasue and A.C. Levasseur-Regourd. Porous irregular aggregates of sub-micron sized grains to reproduce cometary dust light scattering observations. JQSRT **100** (2006).

[15] H.S. Das, A. Suklabaidya, S.D. Majumder, and A.K. Sen. Aggregate dust model to study the polarization properties of comet C/1996 B2 Hyakutake. Res. Astron. Astrophys. **10**(4) (2010).

[16] J. Lasue, A.C. Levasseur-Regourd, E. Hadamcik, and G. Alcouffe. Cometary dust properties retrieved from polarization observations: Application to C/1995 O1 Hale Bopp and 1P/Halley. Icarus **199** (2009).

Novel approach for modeling optical properties of systems containing large number of metal nanoparticles

A. Shcherbakov[*,1,2] , A. Tishchenko[1,2], and S. Goreinov[3]

[1]*Laboratory Hubert Curien, University Jean Monnet, 18 Rue du Professeur Benoit Lauras, Saint-Etienne, 42000 France.*
[2] *Laboratory of Nanooptics and Femtosecond Electronics, Moscow Institute of Physics and Technology, 9 Institutsky, Dolgoprudny, 141701 Russia.*
[3] *Institute of Numerical Mathematics of Russian Academy of Sciences, 8 Gubkina, Moscow, 119333 Russia.*

We propose a novel method for optical properties calculation of very large and complex-shaped systems of metal nanoparticles having size of the order of 10 nm. The method is based on the volume integral equation that describes the electromagnetic scattering. In the numerical algorithm, the generalized minimal residual method is used to enlarge the domain of the applicability of the method.

INTRODUCTION

With the development of fabrication of complex nanostructured composite media [1] there have been intensively elaborated several approaches for modeling their optical properties. Approaches that appear to be the most useful in applications and analysis of experiments can be divided into two types. The first type includes effective medium approximations [2]. The second type includes different techniques of exact electromagnetic analysis of scattering structures [3]. Both of them exhibit evident disadvantages. Notably, the effective medium theory cannot take into account additional structuring of a medium. By applying an exact approach one shortly reaches the limit of calculation resources while attempting to analyze structures with growing complexity.

In this work we propose a method that represents a combination of the two mentioned approaches. It gives the possibility to calculate the light scattering on systems containing thousands of metal nanoparticles with radii of dozens of nanometers and sufficiently low volume density with the restrictions being imposed by the use of quasistatic (dipole) approximation and the assumption that the field from one particle to another comes in the form of a spherical wave.

DESCRIPTION OF THE METHOD

The numerical derivation of the method is close to the procedure used in volume integral equation methods [3] and is based on the generalized source method (GSM) written in the

* Corresponding author: Alexey Shcherbakov (alex.shcherbakov@phystech.edu)

form developed earlier [4]. The volume integral equation that gives the solution of the Helmholtz equation writes:

$$\mathbf{A} = \mu_0 \mathbf{J} * G_s = \int_{V'} \mu_0 \mathbf{J}(\mathbf{r}') G_s(\mathbf{r} - \mathbf{r}') dV', \quad (1)$$

where G_s is the scalar free-space Green's function of the Helmholtz equation. The GSM implies the use of "generalized" sources which reflect the difference in spatial permittivity distribution of a given problem and some basis value ε_s:

$$\mathbf{J}_{gen} = -i\omega(\varepsilon - \varepsilon_s)\mathbf{E} \quad (2)$$

The standard discretization procedure of Eq. (1) consists in partition of a scattering volume into a number of spatial cells each characterized by some constant value of permittivity ε_i with index i giving the cell number. Then one obtains an algebraic equation which is usually solved by the conjugate gradient method or its variations.

We also use the spatial partitioning of the scattering volume into cells, the size of which is small with respect to the wavelength of incident radiation. However, we suppose that these cells contain both the host material and metal inclusions which implies for some effective permittivity $\varepsilon_{i\,eff}$. Since the quasi-static approximation is quite acceptable in this case, we use the well-known relation [2]

$$\varepsilon_{i\,eff} = \varepsilon_s \left(1 + f_i \frac{\varepsilon_m - \varepsilon_s}{\varepsilon_m + 2\varepsilon_s} \right) \quad (3)$$

where ε_m is the dielectric permittivity of metal nanoparticles and f_i is the volume density of metal inclusions. Note that both these values can vary from one cell to another.

So, after the mentioned discretization subject to formula (3) we arrive to the system of algebraic equations that can be written in form:

$$\vec{E} = \vec{E}_0 + \mathrm{DA}\vec{E}. \quad (4)$$

Here the vectors $\vec{E}_0$ and $\vec{E}$ stand for the components of incident and scattered field in all spatial cells, diagonal matrix **D** contains factors with effective permittivities and matrix **A** contains geometric factors depending on relative spatial positions of all cells. Note that the diagonal of matrix A is chosen to be zero to avoid the appearance of nonphysical field singularities.

Frequently, linear systems like (4) are solved by the conjugate gradient method. However, it often reveals poor convergence rate and, to overcome this drawback, we use the generalized minimal residual method (GMRES). With the use of GMRES, the capabilities of the

method allow considering very large systems partitioned into about 100×100×100 cells by the use of PC.

EXAMPLE AND DISCUSSION

As an example, we calculated the effective refractive index of the transparent medium (refractive index 1) consisting of silica particles of radii 100 nm covered by a layer of silver nanoparticles of radii 10 nm with volume density about 0.2 (Fig. 1).

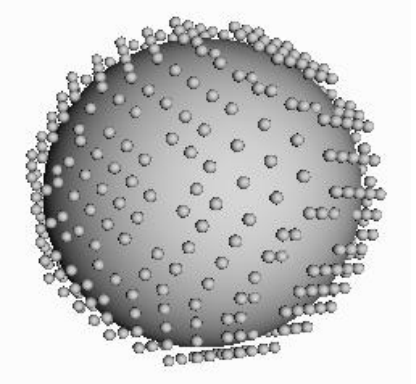

Figure 1. Scatterer that represents a silica particle of radius 100 nm covered by a layer of silver nanoparticles of radii 10 nm.

It is supposed that such "particles" (silica with a core of silver impurities) are located far enough one from another so that re-scattering can be neglected. Such systems appear, for example, in the process of growth of metal covers on dielectric nanoparticles [1]. The spectrum of the refractive index modification in comparison with transparent host medium is depicted in Fig. 2. For the calculation we used the formula

$$n_{eff} - n_2 = 2\pi N R^3 n_2 \frac{(\varepsilon_1 - \varepsilon_2)}{(2\varepsilon_2 + \varepsilon_1)} \tag{5}$$

where n_{eff} is the effective index of the inhomogeneous medium; n_2 is the refractive index of the host material (and ε_2 is the corresponding permittivity); N is the volume density of metal spheres with permittivity ε_1 and R is the effective radius of a single sphere corresponding to its extinction cross-section.

The present method is especially useful beyond effective medium approximations when it is necessary to introduce some additional structure in the system under consideration. Together with the powerful numerical technique, it provides facilities for modeling optical behavior of a wide class of nanostructured media.

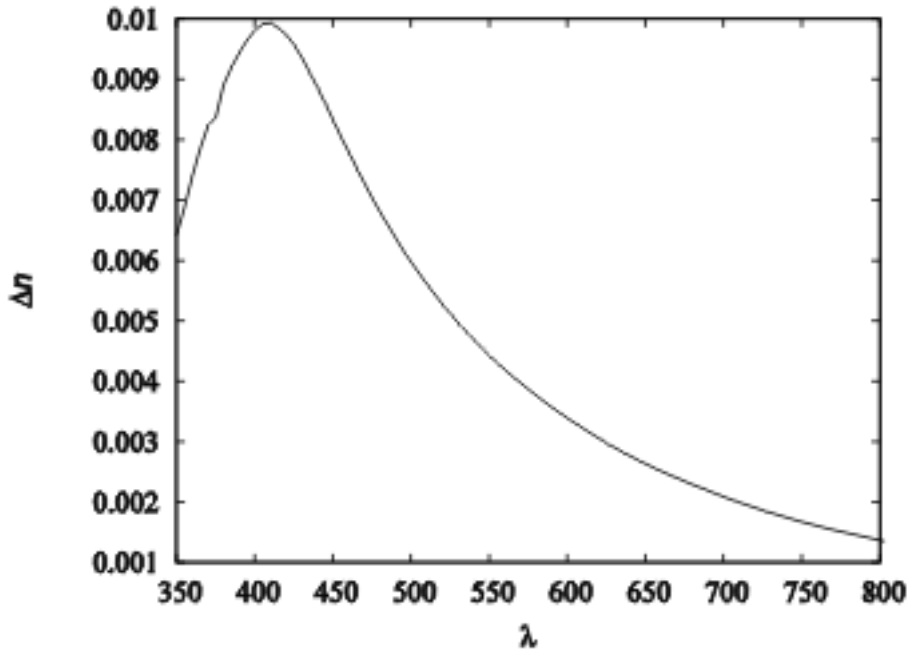

Figure 2. Spectral dependence of the change in the effective refractive index.

ACKNOWLEDGEMENTS

This work was supported in part by the Russian Foundation for Basic Research (grants No. 09-07-00285 and 09-07-12144-ofi_m) and the Russian Federal Agency of Education (contract No. 02.740.11.5058). Alexey Shcherbakov held a fellowship from the region Rhone-Alpes (MIRA).

REFERENCES

[1] C. Burda, X. Chen, R. Narayanan, and M.A. El-Sayed. Chemistry and properties of nanocrystals of different shape. Chem. Rev. **105** (2005).

[2] T.C. Choy. *Effective medium theory. Principles and Applications*. Oxford University Press, New York (1999).

[3] F.M. Kahnert. Numerical methods in electromagnetic scattering theory. J. Quant. Spec. Rad. Trans. **79-80** (2003).

[4] I.M. Akhmedzhanov, A.V. Tishchenko, and A.A. Shcherbakov. Modeling the light scattering by nanoparticles of complex shape using the generalized source method. Opt. Spec. **105** (2008).

Why the opposition spikes of regolith-like media are usually sharp and do not show rounding off

Yu. Shkuratov[*,1], V. Psarev[1], D. Stankevich[1], A. Ovcharenko[1], and G. Videen[2]

[1]*Astronomical Institute of Kharkov V.N. Karazin National University, 35 Sumskaya Str. Kharkov, 61022, Ukraine.*
[2]*Research Laboratory AMSRD-ARL-CI-EM, 2800 Powder Mill Road Adelphi Maryland 20783 USA.*

For particulate surfaces the slope of photometric phase curves must be zero at zero phase angle, otherwise the Maxwell equations are violated. In experiments such surfaces usually reveal sharp opposition spikes; however, we found samples that show tendency to have rounded phase functions. We also show that blocking of reciprocal trajectories at coherent backscattering could influence the rounding.

INTRODUCTION

The brightness phase curves at small phase angles near opposition were measured for a great number of different particulate surfaces, including planetary regoliths and laboratory samples consisting of irregular particles with sizes greater than the wavelength [1]. The shadow-hiding effect and contribution of single scattering are leading factors forming such phase dependencies for dark particulate surfaces. For rather bright surfaces the effect of coherent backscattering enhancement manifests itself against the background of the shadow-hiding effect weakened by incoherent multiple scattering. A fundamental property of measured backscattering curves of powdered surfaces is that almost all of them do not reveal rounding at small phase angles. We might anticipate the behavior for the shadowing effect, when electromagnetic wave diffraction and the angular size of the light source can be ignored; however, coherent backscattering models [e.g. 2,3] predict the rounding, otherwise the Maxwell equations are violated. Thus, theory predicts concave curves, while experiment shows convex curves at small phase angles. This contradiction between experimental and theoretical results has been noted in different papers [e.g. 4]. We discuss possible reasons of the discrepancy.

LABORATORY MEASUREMENTS AT VERY SMALL PHASE ANGLES

An obvious explanation of the contradiction could be that in all mentioned astrophysical and laboratory measurements the minimum phase angles are too large to reveal the peak flattening. However, photometric observations of Kuiper belt objects at phase angles <1° do not show the rounding [5]. Photometrical laboratory measurements of rather bright powders also do not show such a peak flattening [1,6,7], though they were carried out at very small phase angles. For instance, in case of measurements [6] the minimum angle was 0.01°, however, the

* Corresponding author: Yurij Shkuratov (shkuratov@vk.kh.ua)

flattening was not found. To improve this parameter we reconstructed our small-phase-angle photometer, lengthening the distance between the sample place and the detector. We also decreased the light source and detector apertures up to 0.001º. This enables us to reach the minimum phase angle equals 0.002º. Figure 1 shows photometric measurements of MgO smoke deposits on a smooth substrate. The phase function appears to have a slight bend towards zero slope at these small phase angles, though we do not yet observe explicit flattening. Note, that the MgO sample is a very complicated surface consisting of particles < 1 μm.

Another example is more prominent. Figure 2 shows photometric measurements of MgO smoke deposits and blue water-color crusts, which were measured with another laboratory photometer [8]. The MgO deposits demonstrate a sharp opposition spike that is very typical for bright regolith-like surfaces. The water-color crusts with albedo 25% show the tendency to have a rounded response that we expect from the wave-based models, but which are not commonly observed. This, perhaps, relates to the crust structure that is very dense and the crust surface that is smoother than in case of MgO deposits. Thus, the problem of flattening near opposition is not as dramatic as noted in [4]. The questions, however, are why the rounding of photometric curves is so rare and why, if the phase curve is nevertheless concave, the rounding effect is so weak.

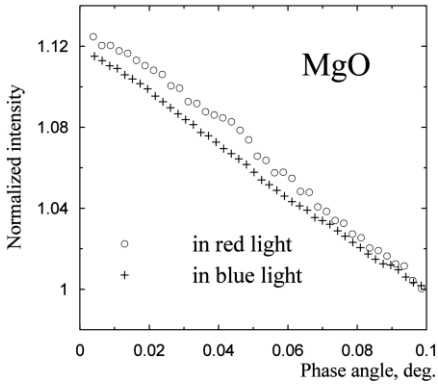

Figure 1. Phase function for MgO smoke deposits at λ=0.66 and 0.47 μm measured with the modified laboratory photometer [6].

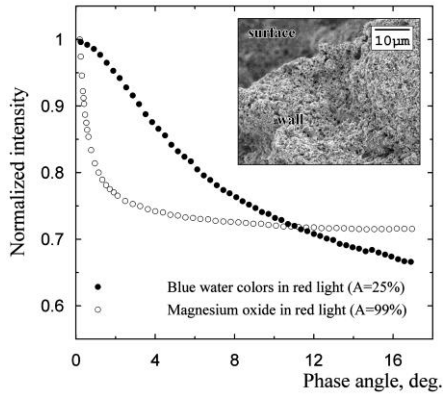

Figure 2. Phase function for MgO deposits on a substrate of smoke from burned Mg at λ=0.63 μm measured with the laboratory photometer described in [8]. The inset shows an electron micrograph of a fracture in the water-color crust.

TRAJECTORY BLOCKING IN COHERENT BACKSCATTERING

The shadow-hiding effect accompanying single scattering may sharpen concave phase curves produced by the coherent backscatter. The same can be observed at higher scattering orders. Indeed, shadowing could influence the coherent backscatter by blocking reciprocal components of coherent backscattering. We illustrate this in Fig. 3, which shows how one of the complementary trajectories can be blocked in the second scattering order.

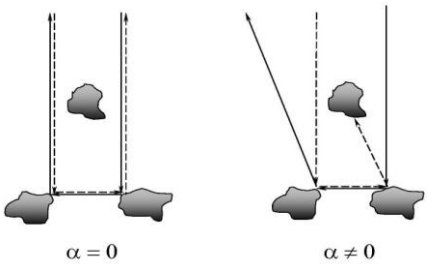

Figure 3. Blocking of a complementary trajectory of coherent backscattering.

We carried out a computer ray-tracing [9] that allows us to estimate the number of complementary trajectories with and without blocking of one of the reciprocal components for different orders of scattering. We studied a particulate medium with packing density near 0.3. Figure 4 shows that high scattering orders have peaks in the number of successful trajectories, when both complementary ways are open and may interfere. This influences coherent backscattering, making the phase functions sharper near opposition.

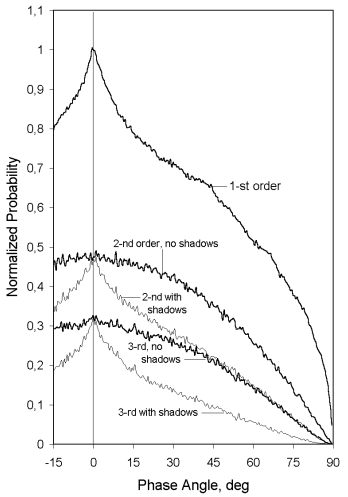

Figure 4. Phase functions of the normalized number of complementary trajectories with and without accounting for the shadowing in second and third orders of scattering, computed using ray-tracing [9]. The first scattering order presents the "classical" shadow effect.

Obviously, we cannot expect that the shadowing effect is valid for a system consisting of small particles. However, such a particle (Fig. 2) instead of actual shadowing may produce a small electromagnetic phase shift influencing the interference. Recent computations carried out by K. Lumme [10] with the *T*-matrix method have shown that some particulate systems, e.g., a cylinder particulate layer, may have convex phase functions. This suggests either unknown factors in forming the coherent backscattering or a manifestation of the blocking mechanism that is automatically taken into account in the *T*-matrix calculations.

CONCLUSION

Our experiments show that the discrepancy between laboratory measurements and theoretical calculation results are not dramatic. We have experimental examples of rather bright particulate surfaces that have phase curves whose slope could approach zero at small phase angles. While the Maxwell equations require zero slope in the exact backscattering direction, measured peaks are sharper than expected. Our simulations suggest that a blocking mechanism of one of the reciprocal components can increase the sharpness of the backscattering peak. This mechanism is valid for all orders of scattering. In case of small particles the blocking may produce an electromagnetic phase shift that also can destroy the constructive interference of reciprocal trajectories.

REFERENCES

[1] Y. Shkuratov, A. Ovcharenko, E. Zubko et al. The opposition effect and negative polarization of structurally simulated planetary regoliths. Icarus **159** (2002).

[2] Y. Shkuratov. Diffractional model of the brightness surge of complex structure surfaces. Kin. Phys. Cel. Bodies **4** (1988).

[3] V. Tishkovets and M. Mishchenko. Approximate calculation of coherent backscattering for semi-infinite discrete random media. JQSRT **110** (2009).

[4] B. Hapke and R. Nelson. Comments on "Approximate calculation of coherent backscattering for semi-infinite discrete random media" by V. P. Tishkovets and M. I. Mishchenko. JQSRT **111** (2010).

[5] I.N. Belskaya, A.M. Barucci, and Yu.G. Shkuratov. Opposition effect of Kuiper belt objects: preliminary estimation. The Earth, Moon, and Planets **92** (2003).

[6] V. Psarev, A. Ovcharenko, Y. Shkuratov, I. Belskaya, and G. Videen. Photometry of surfaces with complicated structure at extremely small phase angles. JQSRT **106** (2007).

[7] J. Piatek, B. Hapke, R. Nelson, W. Smythe, and A. Hale. Scattering properties of planetary regolith analogs. Icarus **171** (2004).

[8] A.A. Ovcharenko, S.Yu. Bondarenko, E.S. Zubko, Yu.G. Shkuratov, G. Videen, and R. Nelson. Particle size effect on the opposition spike and negative polarization. JQSRT **101** (2006).

[9] D. Stankevich, L. Istomina, Yu. Shkuratov, and G. Videen. The coherent backscattering effects in a random medium as calculated using a ray tracing technique for large non-transparent spheres. JQSRT **106** (2007).

[10] K. Lumme. Light scattering by dust particles in the solar system with assessments of both direct and inverse problems. Proceedings of the ELS'XII in Helsinki (2010).

Optical characterization of individual bio-aerosols

V. Sivaprakasam[1], J.W. Lou[2], M. Currie[1], J. Czege[2], and J. D. Eversole[*,1]

[1]*Naval Research Laboratory, 4555 Overlook Ave. S.W., Washington, DC 20375, USA.*
[2]*Global Defense Technology & Systems Inc., (at Naval Research Laboratory) 4555 Overlook Ave. S.W., Washington, DC 20375 USA.*

Our group at the US Naval Research Laboratory has experimentally investigated the optical properties of aerosol particles of biological composition, both ambient and laboratory-generated, for several years. This paper provides an update on recent laser-induced fluorescence results as well as a description of a new experiment to study angle-dependent Mueller matrix scattering elements starting this fall.

INTRODUCTION

The measurement method that has provided the most significant discrimination capability so far has been laser-induced fluorescence [1-6]. We are currently near completion of a 3-year program to develop mode-locked laser excitation, having pulse widths in the 0.5 ps range, and to evaluate its application to bio-aerosol classification. Comparison has been made of a custom-designed mode-locked fiber laser to commercially available Q-switched lasers in terms of the fluorescence and scattering cross sections for a variety of different aerosol particle compositions. The result shows that saturation and/or photo-bleaching effects are negligible for the fluence levels used for either laser type. Reasonable agreement of the two laser excitation sources was obtained. A potentially more significant result arises from the fact that such extremely short pulses create sufficiently high photon densities to make 2-photon transition pumping feasible. We have observed 2-photon excitation of UV emission with visible wavelength excitation. Measurements were made on different biological materials, each over a range of relevant particle sizes that yield quantitative 2-photon excitation/emission cross sections for bacterial samples for the first time.

In continuing efforts to develop optical measurement techniques that are applicable to a broader range of particle compositions than only those that exhibit fluorescence, we have recently gained approval to investigate feasibility of measuring selected Mueller matrix elements from single aerosol particles. If polarimetric scattering signatures of individual biological aerosol particles as a function of both scattering angles and incident wavelength could be obtained, it may be possible to correlate these signature patterns to the structure and composition of the particles, providing a basis for classification, and discrimination among different particle types.

* Corresponding author: Jay D. Eversole (jay.eversole@nrl.navy.mil)

MODE-LOCKED LASER 2-PHOTON EMISSION RESULTS

A previously fabricated apparatus for measuring fluorescent emission in multiple discrete spectral bands using commercially available Nd:YAG lasers frequency summed to the UV wavelengths of 266 and 355 nm was modified to accommodate a newly developed Yb-doped fiber laser. By switching between these two alternative sources, data could be efficiently acquired on the same aerosol sample flowing through the interrogation chamber, and comparison of the Nd:YAG and Yb-fiber excitation data could be evaluated. Two experiments were performed in which: (1) the mode-locked fiber laser was frequency-quadrupled to 262 nm, and (2) the same laser fundamental was frequency-doubled to 524 nm. Comparison of the two types of UV laser sources in the first case showed that there was reasonable agreement in the fluorescence intensity obtained from a variety of aerosol sample materials once differences in the incident excitation intensity was taken into account. For the second arrangement, using the 524 nm laser operating at 41 MHz, the aerosol particles transit the focal thickness of the beam (55 micron) in about 18 microseconds and receive an effective fluence of 463 mJ/cm^2. The PMT gate width was set to sufficient time to integrate the entire signal. Figure 1, below, shows a scatter plot of fluorescent emission from particles of two different compositions: (a) *Bacillus atrophaeous* spore (BG) and (b) *Yersinia rohdei* (YR) and for two distinct particles sizes for each sample, as labeled. The data points are values of individual particles, and the x and y axes are the emission intensities in 80 nm-wide spectral bands centered at 350 and 435 nm respectively. Particles of kaolin (green dots), a non-fluorescent material, were included in both plots as a reference. One can see that the emission from the biological particles can be as much as an order of magnitude higher than the kaolin particles of similar size. Scatter of the data for the biological particles results predominantly from spatial variation of the particle trajectories in the excitation beam.

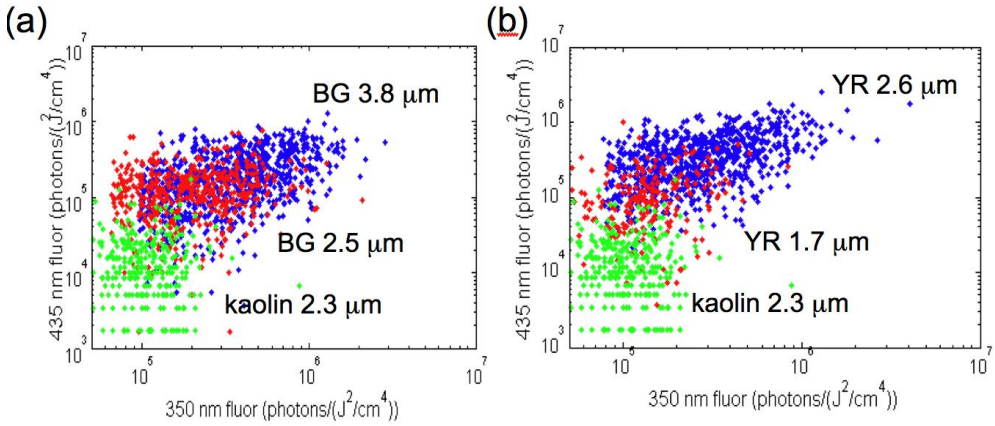

Figure 1. Shows a scatter-plot of 524 nm laser-induced emission from (a) *Bacillus* (BG) spore, and (b) *Yersinia rohdei* (YR) particles for a smaller (red) and larger (blue) particle size for each sample.

APPROACH FOR SINGLE PARTICLE POLARIMETRIC MEASUREMENT

A novel, highly parallel, detection scheme has been proposed that is a radical departure from previous, conventional approaches to the measurement of polarized scattering data. Successful demonstration of this new, rapid measurement approach will enable, for the first time, polarimetric characterization of individual free-flowing aerosol particles. Combining this experimental capability with state-of-the-art computational scattering models also creates, for the first time, an opportunity to use modern multivariate data analysis and pattern recognition methods to establish correlations between scattering data features and basic particle morphology and composition. Such quasi-empirical analytical approaches could lead to the use of scattering measurements to rapidly classify bioaerosol particles of interest.

Conventional methods for the measurement of polarized scattering involve using a single wavelength with a single detector scanned over many discrete angles. These traditional techniques have confirmed the potential utility of polarized scattering measurements for discriminating particles based on their size, shape and/or composition differences [7-8]. However, practical implementation of polarimetric scattering techniques for analysis of aerosol particles is not possible with such labor-intensive and time-consuming approaches.

A recently developed approach [9] in polarized scattering permits very rapid, multiple-angle and multiple wavelength elastic scatter measurements to be performed on ensembles of particles (organisms) suspended in solution. The approach is based on using an array of optical fibers, an imaging spectrometer and a focal plane array to instantaneously create a two-dimensional snapshot of scattering data as a function of both wavelength and scattering angle. In principle, all the parameters needed for inversion analysis of the particles' size, shape and composition can be measured simultaneously. Our plan to modify this multiple angle, multiple wavelength experimental method to be able to interrogate individual aerosol particles has been approved, and this effort will begin this fall. Preliminary calculations predict that single-particle measurements are feasible by modifying the new approach to incorporate currently available supercontinuum light sources, and intensified CCD arrays.

Planned initial studies will be conducted on known (nonspherical) particles in suspension and validated with models based on T-matrix, discrete dipole approximation (DDA) or other established computational scattering methods for ensembles of particles, averaged over all orientations. These selected samples will be studied to determine which scattering matrix parameters contribute the greatest degree of discrimination, as well as establish a predictive computational model framework for conducting sensitivity analyses.

The next step will be to extend the technique to interrogate individual aerosol particles. We will start with engineered particles of known geometry and composition, and validate orientation-dependent models using experimental measurements. To date, we are aware of only one prior, but recent, study of polarimetric scattering from a homogeneous aerosol sample (incorporating ensemble orientational averaging) [10]. If successful, our proposed study will collect polarized scattering measurements from individual, freely-suspended aerosol particles. Collecting data on different matrix parameters for both polar and azimuthal angles simultaneously will hopefully lead to discovery of appropriate combinations of measured parameters that will decouple the influence of the particle orientation, and permit particle classification on the basis of its general shape and composition into broad categories.

Recent modeling studies have shown that the depolarization ratio at near backscattering angles are strongly dependent on the particles' aspect ratio, while the periodicity of the backscatter is a strong function of the incident wavelength [11]. This feature has not yet been exploited experimentally, and may be especially relevant for biological particles such as *Bacillus* spores.

Ultimately, a basic understanding of the connection between particle size, shape and composition, and its polarimetric two-dimensional angular scattering profile as a function of wavelength could lead to enhanced capabilities for real-time bioaerosol agent detection.

REFERENCES

[1] R.G. Pinnick, S.C. Hill, P. Nachman, J.D. Pendleton, G.L. Fernandez, M.W. Mayo, and J.G. Bruno. Fluorescent particle counter for detecting airborne bacteria and other biological particles. Aerosol Sci. Tech**. 23**(4) (1995).

[2] M. Seaver, J.D. Eversole, J.J. Hardgrove, W.K. Cary Jr., and D.C. Roselle. Size and fluorescence measurements for field detection of biological aerosols. Aerosol Sci. Tech. **30**(2) (1999).

[3] F.L. Reyes, T.H. Jeys, N. R. Newbury, C.A. Primmerman, G.S. Rowe, and A. Sanchez. Bio-aerosol fluorescence sensor. Field Anal. Chem. and Technol. **3**(4-5) (1999).

[4] Y-L Pan, J. Hartings, R.G. Pinnick, S.C. Hills, J. Halverson, and R.K. Chang. Single particle fluorescence spectrometer for ambient aerosols. Aerosol Sci. Tech. **37**(8) (2003).

[5] P.H. Kaye, J.E. Barton, E. Hirst, and J.M. Clark. Simultaneous light scattering and intrinsic fluorescence measurement for the classification of airborne particles. Appl. Opt. **39**(21) (2000).

[6] V. Sivaprakasam, A. Huston, C. Scotto, and J. Eversole. Multiple UV wavelength excitation of bioaerosols. Optics Express **12**(19) (2004).

[7] B.V. Bronk, S.D. Druger, Jozsef Czege, and W.P. Van DeMerwe. Measuring Diameters of Rod Shaped Bacteria in Vivo with Polarized Light Scattering. Biophysical J. **69** (1995).

[8] W.S. Bickel, J.F. Davidson, D.R. Huffman, and R. Kilkson. Application of polarization effects in light scattering: A new biophysical tool. In: *Proceedings of the National Academy of Sciences of the Unites States of America* **73**(2) (1976).

[9] Czeke and B.V. Bronk. Process and apparatus for measurements of Mueller matrix parameters of polarized light scattering. International Patent application PCT/US2006/03846 (2006).

[10] J.M. Richardson and J.C. Aldridge. The standoff aerosol active signature testbed (SAAST) at MIT Lincoln Laboratory. In: *Chemical and Biological Standoff Detection III (Proc. SPIE 5995)* (2005).

[11] D.D. Duncan and M.E. Thomas. Particle shape as revealed by spectral depolarization. Applied Optics **46**(24) (2007).

Modeling radar backscattering from melting snowflakes at C-band using DDA and TMM

J. Tyynelä*[,1], J. Leinonen[2], D. Moisseev[1], and T. Nousiainen[1]

[1]*Department of Physics, University of Helsinki, P.O. box 14, FI-00014 Helsinki, Finland.*
[2]*Finnish Meteorological Institute, P.O. box 503, FI-00101 Helsinki, Finland.*

We model radar backscattering in the C-band from fluffy snowflakes at early stages of melting using both the discrete-dipole approximation (DDA) and the T-matrix method (TMM). DDA approximates the particle as a cubic lattice of dipoles, while TMM is an exact method for nonspherical particles. To simulate falling snowflakes at early melting, the particles are modeled as oriented oblate spheroids and have melted only at the bottom part. We use two different dipole distributions for DDA; random single dipoles and dipole groups consisting of $4\times4\times4$ dipoles. We find that even a very fluffy particle shows resonance features for most radar parameters. Using the Maxwell-Garnett effective medium approximation in TMM computations seems to match DDA well for all sizes studied. Small amount of inhomogeneously distributed water has a negligible effect on most radar parameters for both DDA and TMM. Only the specific differential phase K_{DP} shows clear deviation between DDA and TMM. Using dipole groups instead of single dipoles to approximate a fluffy snowflake seems to effect K_{DP} the most.

INTRODUCTION

Uncertainty in modeling of scattering properties of wet snow particles is one of the major error sources in melting layer modeling [1]. Typically, wet snow particles are modeled using spherical or spheroidal shapes with a dielectric constant defined by an effective-medium approximation [2]. It is, however, known that melting hydrometeors represent non-homogeneous scatterers. Mitra et al. [3] have presented results of wind-tunnel observations of snow-melting behavior. Based on those observations, several melting stages were identified. In this study, we analyze scattering properties of the melting snow particles at the initial stages of melting. At this stage, small water droplets, with diameters of tens of microns, are formed at the periphery of a snow flake. These droplets are mainly concentrated at the lower part of the particle. This results in an inhomogeneous distribution of water in the particle. Given the sensitivity of dual-polarization radar observations on the shape and dielectric properties of hydrometeors, it is important to analyze whether such particle inhomogeneities cause observable radar signatures.

In our previous study [4], we modeled radar backscattering from simple shapes, like spheres, spheroids, and clusters of spheres. We used four different water contents for the coated spheres and the clusters. We used both DDA and TMM for modeling. The results showed that DDA agreed well with the exact solutions for homogeneous particles but, for water-coated particles, the grid should be large enough in order to preserve skin depth. Using effective-medium approximations in the Rayleigh approximation produced significant errors when compared to the results for the clusters of spheres. It was also noted that using the

*Corresponding author: Jani Tyynelä (jktyynel@mappi.helsinki.fi)

filtered coupled dipole (FCD) as polarizability in the DDA modeling effectively doubled the accuracy for water particles. We have adopted FCD in our DDA computations.

MODELING

For the modeling, we use an oblate, spheroidal shape to represent falling snowflakes. The outer shape is used as a spheroidal surface envelope for the fluffy interior, which is composed of an array of discrete ice dipoles in uniform random positions. We use two different dipole distributions; random single dipoles (case 1) and dipoles that are clumped into $4 \times 4 \times 4$ groups (case 2) in order to check how the skin depth is affected. The total number of dipoles is practically the same for these two cases. To simulate the early melting process, the ice dipoles near the bottom surface of the particle are changed to water randomly using Gaussian statistics. We have prohibited any melting above the equator of the particle. In Fig. 1, we show example particles for case 1 (left panel) and for case 2 (right panel).

Scattering computations are conducted using the DDA code by [5] and the TMM code by [6]. For the latter, the Maxwell-Garnett effective-medium approximation is used to obtain the corresponding refractive indices. In the computations, we use diameters $D = 1.0-50.0$ mm and two different water contents (relative to mass): 0 %, and 1 %. The aspect ratio is 0.6, which is a typical value observed for snowflakes [7]. We model in the C-band (5.6 GHz), so the corresponding equal-volume-sphere size parameters vary between 0.05 and 2.5. We used size-dependent density for the snowflakes $\rho = 0.15D^{-1}$ (D in mm) according to [1]. Particles are horizontally oriented, so the incident direction is normal to the rotational axis. The scattering matrices are averaged over the horizontal orientation, around the symmetry axis. In addition, we average over two incident polarizations, parallel and perpendicular to the symmetry axis.

We plot the horizontal reflectivity $Z_h = C(k,m)n_0|S_{11}|^2$, the differential reflectivity $Z_{DR} = |S_{22}|^2/|S_{11}|^2$, the argument of the copolarized correlation coefficient $\delta_{hv} = arg(S_{22}S_{11}^*)$, and the specific differential phase $K_{DP} = -\frac{2\pi}{k}n_0 Re[S_{22}(\mathbf{n},\mathbf{n})+S_{11}(\mathbf{n},\mathbf{n})]$ as a function of size (k is the wavenumber, n_0 the number density, $C(k,m)$ a constant factor, and $\mathbf{S}$ the amplitude scattering matrix in the backscattering-alignment convention). See, e.g., [8] for more detailed definitions.

RESULTS

Figs. 2–3 show Z_h (top left panel), Z_{DR} (top right panel), δ_{hv} (bottom left panel), and K_{DP} (bottom right panel) for both TMM and the DDA cases.

Fig. 2 shows the radar parameters for the 0 % water content case. For Z_h, there seems to be a 1 –2 dB systematic difference between DDA and TMM. It is not yet clear, where the difference originates from. There is a strong resonance peak at $D = 38.0$ mm, which can also be seen for both DDA cases. This indicates that even a very fluffy particle preserves some resonance features typical for symmetric solid particles. Z_{DR} and δ_{hv} show some variation between the DDA cases, but these are negligible. Both parameters show signs of the resonance peak. For K_{DP}, both DDA cases differ from TMM, with case 2 showing larger, and case 1 smaller, values than TMM.

Fig. 3 shows the radar parameters for the 1 % water content case. Relatively small

amount of water has a negligible effect, when compared to the dry case. Overall, TMM computations together with the Maxwell-Garnett effective medium approximation matches DDA well for all sizes studied. Small amount of inhomogeneously distributed water has a negligible effect on most radar parameters for both DDA and TMM. Only K_{DP} shows clear deviation between DDA and TMM. Using dipole groups instead of single dipoles to approximate a fluffy snowflake seems to effect K_{DP} the most.

In the future, we will continue this study using larger water contents, and also study the effect of canting, i.e., deviations from the horizontal orientation due to air drag, on radar parameters.

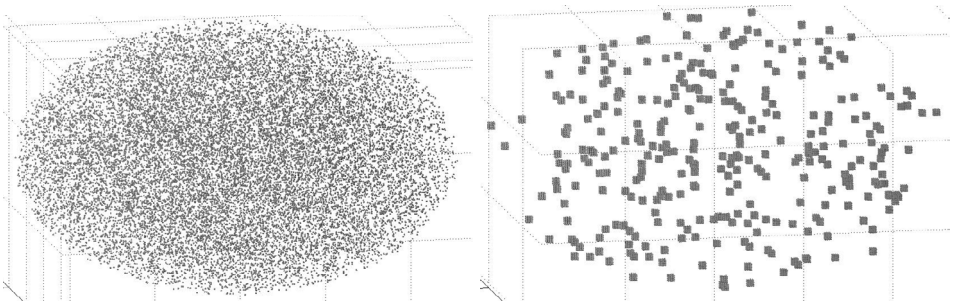

Figure 1. Sample shapes for the modeled particles with the density $\rho = 0.04$ and aspect ratio 0.6. The single dipole case is on the left and the dipole group case on the right.

REFERENCES

[1] F. Fabry and W. Szyrmer. Modeling of the melting layer. Part II. Electromagnetic. J. Atmos. Sci. **56** (1999).

[2] R. Meneghini and L. Liao. Effective dielectric constants of mixed-phase hydrometeors. J. Atmos. Ocean. Tech. **17** (2000).

[3] S.K. Mitra, O. Vohl, M. Ahr, and H.R. Pruppacher. A wind tunnel and theoretical study of the melting behavior of atmospheric ice particles. IV: Experiment and theory for snowflakes. J. Atmos. Sci. **47** (1990).

[4] J. Tyynelä, T. Nousiainen, S. Göke, and K. Muinonen. Modeling C-band single scattering properties of hydrometeors using discrete-dipole approximation and T-matrix method. JQSRT **110** (2009).

[5] M.A. Yurkin, V.P. Maltsev, and A.G. Hoekstra. The discrete dipole approximation for simulation of light scattering by particles much larger than the wavelength. JQSRT **106** (2007).

[6] M.I. Mishchenko. Calculation of the amplitude matrix for a nonspherical particle in a fixed orientation. Appl. Opt. **39** (2000).

[7] S.Y. Matrosov, A.J. Heymsfield, and Z. Wang. Dual-frequency radar ratio of nonspherical atmospheric hydrometeors. Geophys. Res. Lett. **32** (2005).

[8] K. Aydin. Centimeter and millimeter wave scattering from nonspherical hydrometeors. In: *Light scattering by nonspherical particles*, Academic Press (2000).

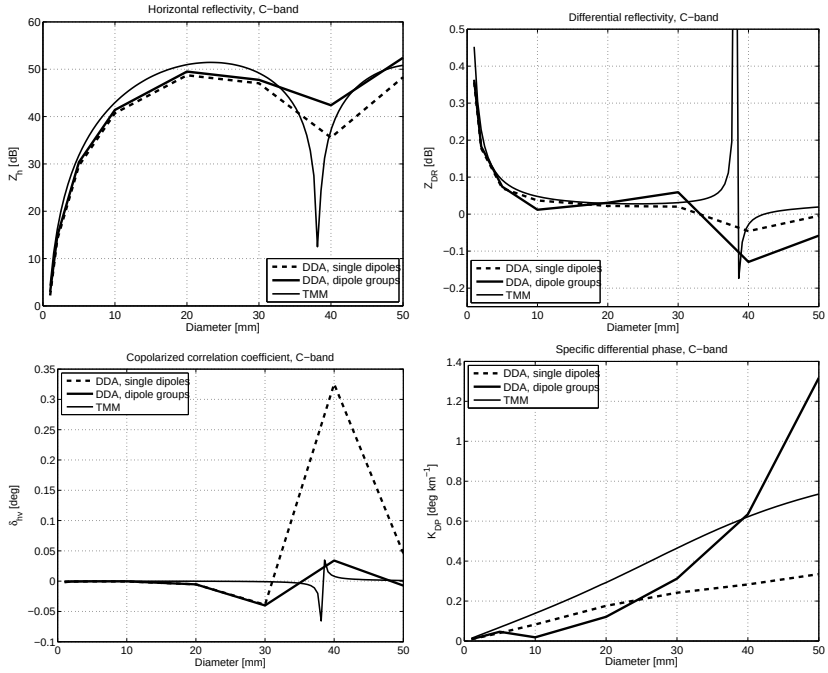

Figure 2. Z_h, Z_{DR}, δ_{hv}, and K_{DP} as a function of particle diameter in millimeters for the 0 % water content case. TMM computations are in thin solid lines, the DDA case for single dipoles is in thick dashed line, and the DDA case for the dipole groups is in thick solid line.

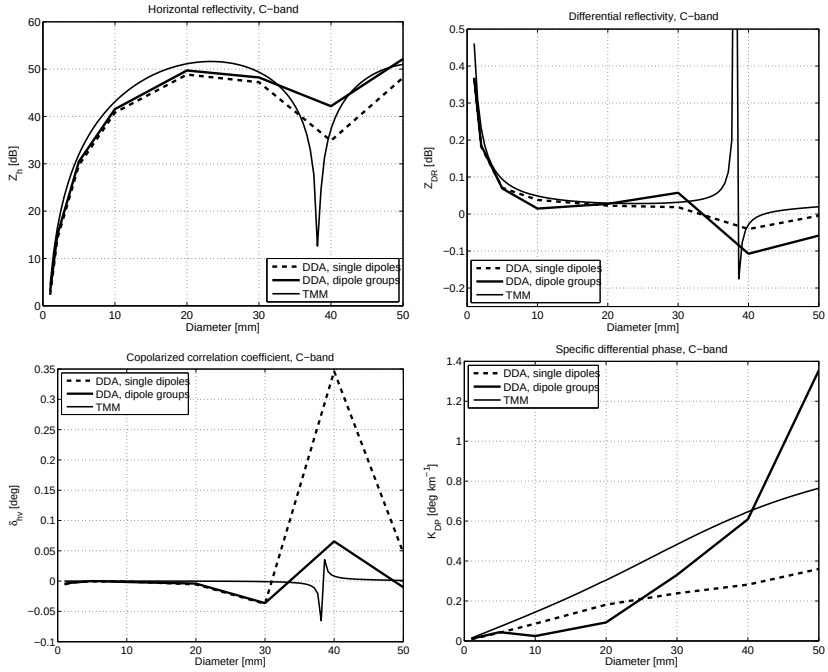

Figure 3. Same as in Fig. 2, but for the 1 % water content case.

Interpretation of single-particle negative polarization at intermediate scattering angles

J. Tyynelä*[,1], E. Zubko[1,2], K. Muinonen[1,3], and G. Videen[4]

[1]*Department of Physics, University of Helsinki, P.O. box 14, FI-00014 Helsinki, Finland.*
[2]*Astronomical Institute of Kharkov National University, 35 Sumskaya Street, Kharkov, Ukraine.*
[3]*Finnish Geodetic Institute, P.O. box 15, FI-02431 Masala, Finland.*
[4]*Army Res. Lab., AMSRD-ARL-CI-ES, 2800 Powder Mill Road, Adelphi, Maryland 20783, U.S.A.*

We study how the internal field structure of irregular particles affects the far-field scattering characteristics by modifying the internal fields of the dipole groups that have the greatest contribution. We concentrate on the longitudinal component, i.e., the internal field component parallel to the incident wave vector. We use the discrete-dipole approximation to discretize the internal field and omit the longitudinal component from the dipoles that have the highest energy density above a preset cutoff value. We conclude that only a relatively small number of core dipoles, about 5 % of all dipoles, contribute to the non-Rayleigh-type negative polarization at intermediate scattering angles. These core dipole groups are located at the forward part of the particles. The number of core dipoles in the group becomes greater as particle asphericity increases. We find that the interference between the core dipole groups, which was studied previously for spherical particles, is preserved to a large extent for non-spherical particles. We also find that the longitudinal component has little effect on both the degree of negative polarization and the depolarization ratio near backscattering.

INTRODUCTION

Single scattering from irregular mineral particles produces negative polarization and shows a decrease in positive polarization at intermediate scattering angles [1, 2, 3]. Multiple scattering between different parts of the scattering system can also decrease the positive polarization, but no mechanism has been hypothesized for it to produce negative polarization at these scattering angles. We feel that this feature most likely has a single-scattering mechanism, as we have seen similar polarization characteristics in numerical simulations of large agglomerated debris particles. In this manuscript, we provide evidence that concentrated regions of the longitudinal component of the electric field inside scatterers are responsible for these features.

We consider single dielectric particles that are comparable to the wavelength in size. For spherical particles the incident wave always 'refracts' into the particle and produces an odd parity with respect to the central scattering plane for the longitudinal component [4]. For non-spherical particles, the refraction is distorted by the irregular surface. Refraction also can focus the incident wave on to certain parts of the particle interior. The curved surface acts like a source of internal waves, whose resulting interference can result in concentrated areas, known as hot spots [5]. We define dipoles that are located at these areas as core dipoles, and all other dipoles as non-core dipoles. In this manuscript we show that these hot spots cause a decrease in linear polarization at intermediate scattering angles. This effect is more prominent for symmetric particles, like spheres.

*Corresponding author: Jani Tyynelä (jktyynel@mappi.helsinki.fi)

In our previous studies [6, 7], we have argued that the negative polarization occurring at intermediate scattering angles for wavelength-scale spherical particles arises from constructive interference in the scattering plane between two maxima of the longitudinal component that are separated by distances on the order of half a wavelength. There is always destructive interference between the waves that form these maxima in the case where the incident field is polarized perpendicular to the scattering plane (TE) and, hence, zero contribution from the longitudinal component. However, for the parallel incident field (TM), the contribution generally varies between destructive and constructive interference depending on the scattering angle. Near the 90° scattering angle, the partial electromagnetic waves originated from these maxima interfere constructively and, so, their contribution to the scattered field is additionally amplified. We stress that the longitudinal component always produces negative polarization of light scattered at 90°. This means that non-Rayleigh-type polarization characteristics arising from the longitudinal component must be related to interference inside the scatterer.

In this study, we identify regions inside the scatterers, defined as the core dipoles, that are the primary contributors to linear polarization characteristics at intermediate scattering angles, and study the effect when we omit the longitudinal component for core dipoles, non-core dipoles, and the same number of randomly chosen dipoles. We choose the brightest core dipoles based on a 30 % cutoff value from the total longitudinal energy density of all dipoles. Based on our studies, this seems to represent the most contributing dipoles. We also study the effect of interference between the waves scattered internally from the core dipoles by computing the total electric field in the YZ-plane from all dipoles along the X-axis. We also compute the total electric field from all dipoles in the XZ- and XY-planes to reveal phase differences between the maxima. We do this for both X- and Y-polarized incident fields. It should be noted that this procedure is purely a mathematical tool and not something that could be observed or measured.

MODELING

For the Gaussian-random-sphere particles, we use circumscribing-sphere size parameter $x_{cs} = 12.0$, refractive indices $m = 1.5 + \mathrm{i}0.01$, and $m = 1.5 + \mathrm{i}0.1$, the standard deviation of relative radius $\rho = 0.245$, and the power-law index of the covariance function $\nu = 4$. For the agglomerated debris particles, we use the same size and refractive indices as for the Gaussian-random-sphere particles. For all the studied particles we use ensemble averaging for the shapes using 20 different realizations of shape for each case. For the computations we use the DDA code developed by Zubko [8]. In the DDA computations we use a $64 \times 64 \times 64$ -dipole grid for the sample shapes.

RESULTS

In Fig. 1, we present the results from numerical computations using DDA averaged over 20 samples. We show the degree of polarization $P = (I_\perp - I_\parallel)/(I_\perp + I_\parallel)$ using a 30 % cutoff value for the Gaussian and debris particles. For the Gaussian particles, the effect of omitting the core dipoles is comparable to omitting the non-core dipoles in magnitude. Here we also see deviations from the exact solution at intermediate scattering angles when omitting random dipoles. Notice also that omitting the core dipoles has little effect on

the negative polarization at forward scattering and backscattering directions. For the debris particles, omitting non-core dipoles has a stronger effect than omitting the core dipoles. We also studied more highly absorbing particles (not shown here), and found that increasing absorption weakens the effect of omitting for both Gaussian and debris particles. This indicates that the contribution from the longitudinal component to linear polarization at intermediate scattering angles is weakest for absorbing, highly irregular particles. We also used 10, 50, 70, and 90 % cutoff values in our studies, and found similar effects than for the 30 % cutoff case shown here.

In Fig. 2, we show the contributions of the internal longitudinal components on the far-field scattering intensities at 90°. For all particles, when the incident field is polarized parallel to the scattering plane (panels at the top), there is a very bright amplified area at the forward part of the particle. The area is symmetric for the sphere, becomes distorted for the Gaussian-random-sphere particle, and even divides into several areas for the debris particle. When the incident field is polarized perpendicular to the scattering plane (panels at the bottom), there is only weak amplification for all particles. In the X-polarized incident field case for the sphere (top panel on the left), the whole bright area is in phase, which can be seen as enhancement in the curve above the panel. For the Y-polarized case (bottom panel on the left), the two weak maxima have opposite phase, which can be seen as cancellation in the curve above the panel. For the X-polarized incident field case for the Gaussian particle (top panel in the middle), the bright areas are generally in phase, while for the Y-polarized case (bottom panel in the middle), there is significant cancellation. In the X-polarized case for the debris particle (top panel on the right), there are actually two bright areas, which also can be seen in the curve above the panel. However, these bright areas have opposite phases, which is seen as partial cancellation in the curve to the right from the panel. This also produces cancellation for the X-polarized incident wave. For the Y-polarized case (bottom panel on the right), the contribution of the three maxima near the front part of the particle almost completely cancel due to destructive interference. This can be seen in the curve above this panel. Overall, it is evident that the greatest contribution to negative polarization comes from the incident field polarized parallel to the scattering plane. The contribution appears to be weakened for the perpendicular incident field.

REFERENCES

[1] E. Zubko, Yu.G. Shkuratov, G. Videen, and N. Kiselev. DDA simulations of light scattering by small irregular particles with various structure. JQSRT **101** (2006).

[2] O. Muñoz, H. Volten, J.F. de Haan, W. Vassen, and J. Hovenier. Experimental determination of scattering matrices of randomly oriented fly ash and clay particles at 442 and 633 nm. J. Geophys. Res. **106** (2001).

[3] H. Volten , O. Muñoz, J.F. de Haan, W. Vassen, J. Hovenier, K. Muinonen, and T. Nousiainen. Scattering matrices of mineral aerosol particles at 441.6 nm and 632.8 nm. J. Geophys. Res. **106** (2001).

[4] K.F. Ren. Symmetry relations in generalized Lorentz-Mie theory. JOSA A **11** (1994).

[5] J.F. Owen, R. K. Chang, and P. W. Barber. Internal electric field distributions of a dielectric cylinder at resonance wavelengths. Opt. Lett. **6** (1981).

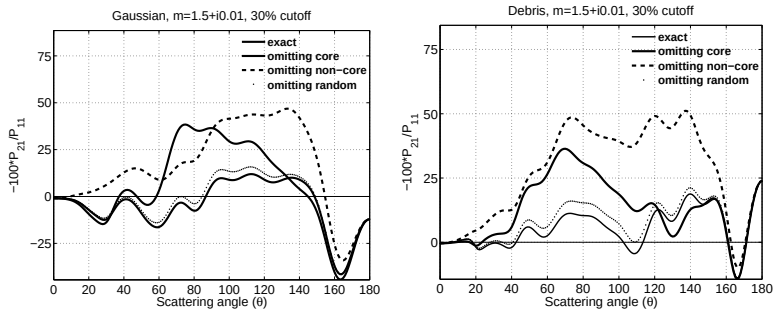

Figure 1. The degree of linear polarization for the Gaussian-random-sphere and debris particles with the exact solution (thin line), and when omitting the longitudinal component from core dipoles (thick line), non-core dipoles (dashed line), and random dipoles (dotted line). The longitudinal energy density cutoff value is 30%. The size parameter is $x_{cs} = 12$, the refractive index is $m = 1.5 + \mathrm{i}0.01$, and the standard deviation of radius for the Gaussian-random-sphere particle is $\rho = 0.245$. Notice that the results are only averaged over 20 samples.

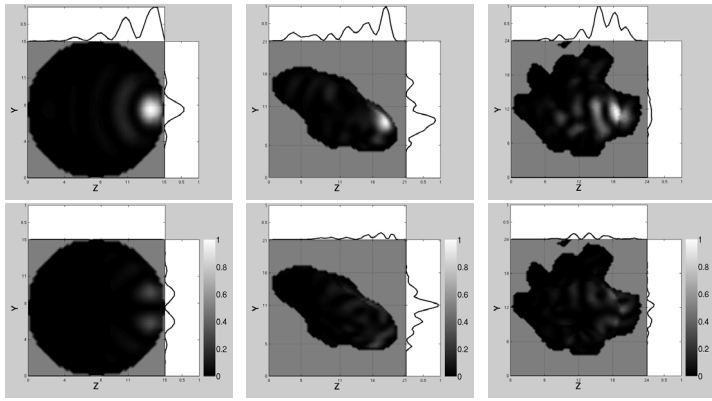

Figure 2. The far-field contribution of the longitudinal intensity component at 90° scattering angle for the spherical (panels on the left), Gaussian-random-sphere (panels in the middle), and agglomerated debris particle (panels on the right) in fixed orientation in the $Y - Z$ plane. The mapping is not a cross-section, but shows results integrated over the X dimension. On the top panels are the cases with the incident field X-polarized, and on the bottom panels Y-polarized. At the top of each panel, we show the intensity contributions integrated along both the X- and Y-axes of the particle. Similarly, at the right of each panel, we show the intensity contributions integrated along the X- and Z-axes. The refractive index is $m = 1.5 + \mathrm{i}0.01$. The incident wave is propagating from left to right.

[6] J. Tyynelä et al. Interrelating angular scattering characteristics to internal electric fields for wavelength-scale spherical particles. JQSRT **106** (2007).

[7] K. Muinonen, E. Zubko, J. Tyynelä, Yu.G. Shkuratov, and G. Videen. Light scattering by Gaussian random particles with discrete-dipole approximation. JQSRT **106** (2007).

[8] E. Zubko, Yu.G. Shkuratov, M. Hart, J. Eversole, and G. Videen. Backscattering and negative polarization of agglomerate particles. Opt. Lett. **28** (2003).

Light scattering by ice particles in the Earth's atmosphere and related laboratory measurements

Z. Ulanowski*, P. H. Kaye, E. Hirst, and R. S. Greenaway

Centre for Atmospheric and Instrumentation Research, University of Hertfordshire, Hatfield AL10 9AB, United Kingdom.

The microphysical properties of ice crystals, such as size, shape, concavity and roughness, are important in the context of radiative properties of ice and mixed phase clouds. Limitations of current cloud probes to measure such properties can be circumvented by acquiring light-scattering patterns instead of particle images. Recent *in situ* cloud data from the SID-3 probe is shown which is consistent with ice particles with rough surfaces being dominant.

INTRODUCTION

Cloud feedbacks remain the largest source of uncertainty in climate models. In particular, uncertainties exist concerning the radiative forcing of clouds containing ice crystals, most notably cirrus. Indeed, whether cirrus clouds warm or cool the Earth's surface depends on ice crystal morphology. Reducing this uncertainty requires detailed *in situ* characterization of cloud particles, so that the scattering properties of the clouds can be correctly represented in models. Also, detailed knowledge of the scattering properties of various cloud particle types is needed for accurate retrieval of cloud microphysical properties from remote sensing. One of the main barriers to achieving these goals is the inability of cloud probes to determine the contribution of small ice crystals (that is crystals smaller than about 50 μm) to the total distribution. This is due to crystal breakup on the inlets of these probes [1] and their inability to resolve the geometric structure of small ice crystals because of the conflicting demands of high optical resolution and large sample volume [2,3].

In addition to size and shape, two other important properties of ice particles, surface roughness and concavity, are known to profoundly affect radiative properties of ice clouds, e.g. the asymmetry parameter g [4,5,6]. The measured g of smooth and rough ice analogues is typically 0.8 and 0.63, respectively, at visible wavelengths [7]. This means that, in simple terms, the rough ice particles in this example might back-reflect nearly twice as much solar radiation as their smooth counterparts. Since the longwave g is not expected to vary by as much, the overall radiative forcing of cirrus might shift towards negative values, an issue of great importance in the context of climate change. However, little *in situ* data on ice roughness exists: mainly indirect evidence, e.g. the absence of atmospheric halos [6,8] or the shape of phase functions [9]. As for the concavity of ice particles, it is thought to occur frequently but is seldom quantified, mainly due to cloud probe limitations [10]. Here, we examine the recovery of size, shape, concavity, and roughness of ice particles from scattering data, so as to bypass the optical resolution limitations of cloud probes.

* Corresponding author: Joseph Z. Ulanowski (z.ulanowski@herts.ac.uk)

ICE PARTICLE CHARACTERIZATION USING SCATTERING PATTERNS

Particle size, shape and concavity

Several light scattering cloud probes, jointly known as Small Ice Detectors (SID) have been developed over the last decade at the University of Hertfordshire. Successive models obtain scattering patterns with progressively higher angular resolution. The earlier designs rely on multi-element detectors measuring mainly the azimuthal scattering. The first one, SID-1, was intended to discriminate between water droplets and ice crystals by determining their sphericity, and relies on six photomultipliers arranged symmetrically around the azimuth [11]. This instrument was superseded by SID-2 probes, containing between 24 and 28 detector elements arranged azimuthally in an annulus [12]. Despite their simplicity, azimuthal scattering patterns can also provide the size, concavity, and aspect ratio of prismatic ice crystals [13] through comparison with the Ray Tracing with Diffraction on Facets (RTDF) scattering model [14]. Some particle information is retained even in the azimuthal frequency spectrum, as shown by the recovery of the size and aspect ratio of prismatic ice crystals [15] although, not surprisingly, such frequency analysis is limited to cases when some *a priori* information on particle shape exists, and even then some ambiguity can remain [13,16].

High-resolution two-dimensional (2D) scattering patterns offer high potential for detailed particle characterization [17]. The latest SID probes, collectively known as SID-3, use intensified CCD cameras to capture 2D patterns. It is possible to recover the shape of small ice particles by comparing such patterns to the RTDF scattering model [18]. In the next section we examine the application of 2D patterns to ice particle roughness.

Particle roughness

An indication that ice roughness can be quantified from 2D scattering is provided by experimental patterns from ice analogue crystals with smooth and rough surfaces, which show distinct differences: while the former have sharp, well-defined bright arcs and spots, the latter have much more random, "speckly" appearance, but with greater azimuthal symmetry [7]. The first *in situ* cloud data using the SID-3 probe was obtained during the UK Met Office CONSTRAIN campaign in Scotland in February 2010. Fig. 1 shows a random selection of particles observed in cirrus and mixed phase clouds. Comparison with laboratory ice analogue data, also shown in Fig. 1, demonstrates qualitatively that the image texture of the majority of the *in situ* patterns is consistent with the presence of significant roughness.

Image texture can be quantified using statistical measures, such as the grey-level co-occurrence matrix (GLCM), which deals with the spatial relationships of pairs of grey values of images pixels. In the past, GLCM was applied to retrieving surface roughness from laser speckle images of surfaces [19]. Here, four features of GLCM were chosen: contrast, correlation, energy, and homogeneity, in addition to image entropy. They were calculated for 2D patterns from cirrus and mixed phase cloud particles as well as smooth and rough ice analogues, and correlated with a subjective measure of speckle pattern. Energy had the strongest correlation with the subjective speckle pattern: -0.7. A combined contrast-energy-homogeneity feature had correlation similar in magnitude with opposite sign, but showed slightly larger difference for test patterns of smooth and rough analogues. Interestingly, the

GLCM energy shows good correlation with surface roughness and is most robust with respect to variation of "*the setup configuration, the position, and the orientation of the surface to be measured*" in the context of laser speckle [19]. Distributions of the statistical features for a random sample of 500 patterns from CONSTRAIN are shown in Fig. 2. Like for the qualitative comparison in Fig. 1, the properties of most of the patterns were consistent with the presence of significant particle roughness, at levels exceeding that found in the moderately rough analogue crystal used as a reference. The spread of roughness was slightly wider in cirrus.

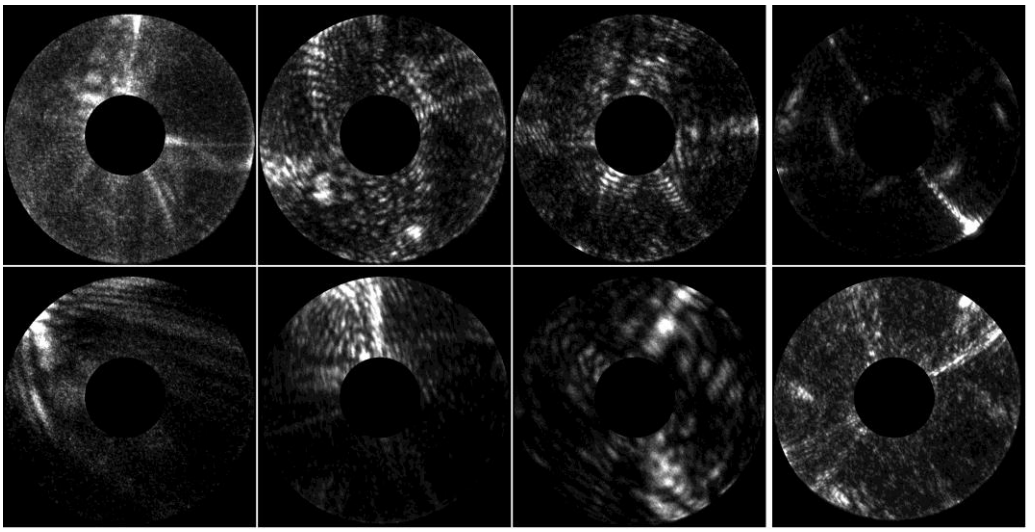

Figure 1. Six randomly selected SID-3 patterns from ice particles seen during CONSTRAIN cirrus (top) and mixed phase (bottom) flights, compared to patterns from ice-analogue rosettes with smooth (top right) and moderately rough surfaces (bottom right).

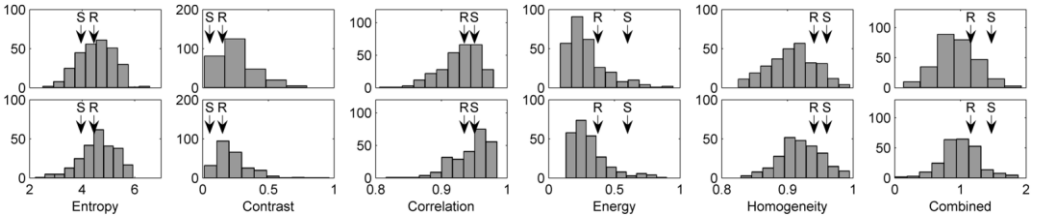

Figure 2. Frequency distributions of statistical features of 2D patterns from cirrus (top row) and mixed phase (lower row) flights. Arrows show values for the smooth (S) and moderately rough (R) ice analogues from Fig. 1. The "combined" feature is (energy + homogeneity – contrast). Note that all but entropy and contrast are anticorrelated with roughness.

REFERENCES

[1] P.R. Field, A.J. Heymsfield, and A. Bansemer. Shattering and particle interarrival times measured by optical array probes in ice clouds. JTECH **23** (2006).

[2] Z. Ulanowski, P. Connolly, M. Flynn et al. Using ice crystal analogues to validate cloud ice parameter retrievals from the CPI ice spectrometer. In *Proc. 14 Int. Conf. Clouds Precip.* http://strc.herts.ac.uk/ls/ICCP14_poster_P2.8.29.pdf (2004).

[3] P.J. Connolly, M.J. Flynn, Z. Ulanowski et al. Calibration of 2-D imaging probes using calibration beads and ice crystal analogues. JTECH **24** (2007).

[4] Q. Fu. A new parameterization of an asymmetry parameter of cirrus clouds for climate models. J. Atmos. Sci. **64** (2007).

[5] P. Yang, Z. Zhang, G.W. Kattawar et al. Effect of cavities on the optical properties of bullet rosettes. Appl. Meteor. Climate **47** (2008).

[6] P. Yang, G.W. Kattawar, G. Hong, P. Minnis, and Y. Hu. Uncertainties associated with the surface texture of ice particles in satellite-based retrieval of cirrus. IEEE Trans. Geosci. Remote Sens. **46** (2008).

[7] Z. Ulanowski, E. Hesse, P.H. Kaye, and A.J. Baran Light scattering by complex ice-analogue crystals. JQSRT **100** (2006).

[8] Z. Ulanowski. Ice analog halos. Appl. Opt. **44** (2005).

[9] V. Shcherbakov, J.-F. Gayet, O. Jourdan, J. Ström, and A Minikin. Light scattering by single ice crystals of cirrus clouds. Geophys. Res. Lett. **33** (2006).

[10] C.G. Schmitt and A.J. Heymsfield. On the occurrence of hollow bullet rosette- and column-shaped ice crystals in midlatitude cirrus. J. Atm. Sci. **64** (2007).

[11] E. Hirst, P.H. Kaye, R.S. Greenaway et al. Discrimination of micrometre-sized ice and super-cooled droplets in mixed-phase cloud**.** Atm. Env. **35** (2001).

[12] R. Cotton, S. Osborne, Z. Ulanowski et al. The ability of the Small Ice Detector (SID-2) to characterise cloud particle and aerosol morphologies obtained during flights of the FAAM BAe-146 research aircraft. JTECH **27** (2009).

[13] C. Stopford. Ice crystal identification using two-dimensional light scattering patterns. PhD thesis, University of Hertfordshire (2010).

[14] A.J.M. Clarke, E. Hesse, Z. Ulanowski, and P. H. Kaye. A 3D implementation of ray tracing combined with diffraction on facets. JQSRT **100** (2006).

[15] Z. Ulanowski, C. Stopford, E. Hesse, P.H. Kaye, E. Hirst, and M. Schnaiter. Characterization of small ice crystals using frequency analysis of azimuthal scattering patterns. In *Proc. 10 Int. Conf. on EM & Light Scatt.* (2007).

[16] C. Stopford, Z. Ulanowski, E. Hesse, P.H. Kaye, E. Hirst, M. Schnaiter, and D. McCall. Initial investigation into using Fourier spectra as a means of classifying ice crystal shapes. In *Proc. 11 Int. Conf. EM & Light Scatt.* (2008).

[17] P.H. Kaye, K. Aptowicz, R.K. Chang, V. Foot, and G. Videen. Angularly resolved elastic scattering from airborne particles. In *Optics of Biological Particles*.. A. Hoekstra et al. (eds.). Springer (2007).

[18] P.H. Kaye, E. Hirst, R.S. Greenaway et al. Classifying atmospheric ice crystals by spatial light scattering. Opt. Lett. **33** (2008).

[19] R.S. Lu, G.Y. Tian, D. Gledhill, and S. Ward. Grinding surface roughness measurement based on the co-occurrence matrix of speckle pattern texture. Appl. Opt. **45** (2006).

A novel implementation of a microwave analog to light-scattering measurement setup

R. Vaillon[*,1], J.-M. Geffrin[2], O. Merchiers[1], C. Eyraud[2], P. Sabouroux[2], and B. Lacroix[1]

[1]*Université de Lyon, CNRS, INSA-Lyon, UCBL, CETHIL, UMR5008, F-69621, Villeurbanne, France.*
[2]*Institut Fresnel, Aix-Marseille Univ., Ecole Centrale Marseille, CNRS, Domaine Univ. St-Jérôme, 13397 Marseille, France.*

We report on a novel implementation of the well-known and established method to test approximate light-scattering codes using the so-called microwave analogy principles for fully controlled complex-shaped particles. The set-up allows making broadband ([2-20] GHz) 3D measurements of the full amplitude scattering matrix (amplitude and phase of the elements). An insight into the most relevant results obtained to date for a 74 sphere aggregate is provided.

INTRODUCTION

The Scale Invariance Rule (SIR) states that a dimensionless amplitude scattering matrix can be defined for an arbitrary fixed particle embedded in an infinite, homogeneous, linear, isotropic, and non-absorbing medium[1]. This represents the underlying condition to carry out microwave analog to light-scattering experiments which involve the simultaneous scaling of particle size and wavelength by the same factor, keeping the size parameter constant, and using materials that have the same complex refractive index in the microwave region as in the optical domain. Application of this method has been successfully proven to provide reliable experimental data for the assessment of light-scattering codes (see details and a review by B.Å.S. Gustafson[2], with a particular emphasis on the University of Florida's set-up).

Still some improvements could be envisaged at several levels: the use of larger wavelengths to make the building of fully controlled complex-shaped particles even easier; the realization of 3D measurements, viz. when the emitter and the receiver displacement courses are not necessarily in the same plane; the determination of both amplitude and phase of all elements of the amplitude scattering matrix for a non-spherical particle. In the following, a novel implementation of a microwave analog to light-scattering measurement setup is presented which accounts for these possible extensions. The next section is dedicated to a short description of the microwave scattering facility as well as of the procedure to build a fully controlled aggregate of few centimeters in size. Then, the methodology to perform a proper assessment of scattering codes is summarized, followed by the delivery of sample results.

* Corresponding author: Rodolphe Vaillon (Rodolphe.Vaillon@insa-lyon.fr)

EXPERIMENTAL METHODS AND SET-UPS

The microwave scattering facility

The main features of the experimental set-up developed by members of the Institut Fresnel in the anechoic chamber of the 'Centre Commun de Ressources Microondes'[3] are the following (see Fig. 1): broadband measurements (2 to 20 GHz, i.e. λ_0 = 1.5 to 15 cm); the course of the receiver antenna in the azimuthal plane is of 260°; possible location of the emitter antenna out of the azimuthal plane with a 180° vertical excursion (3D measurements); analysis of all polarization cases by rotating the linearly polarized antennas; drift compensation[4] and noise characterization and reduction to permit cross-polarization scattering measurements for centimeter-sized targets; and investigation of target orientation from axial rotations around the vertical axis (see [5-6] for details).

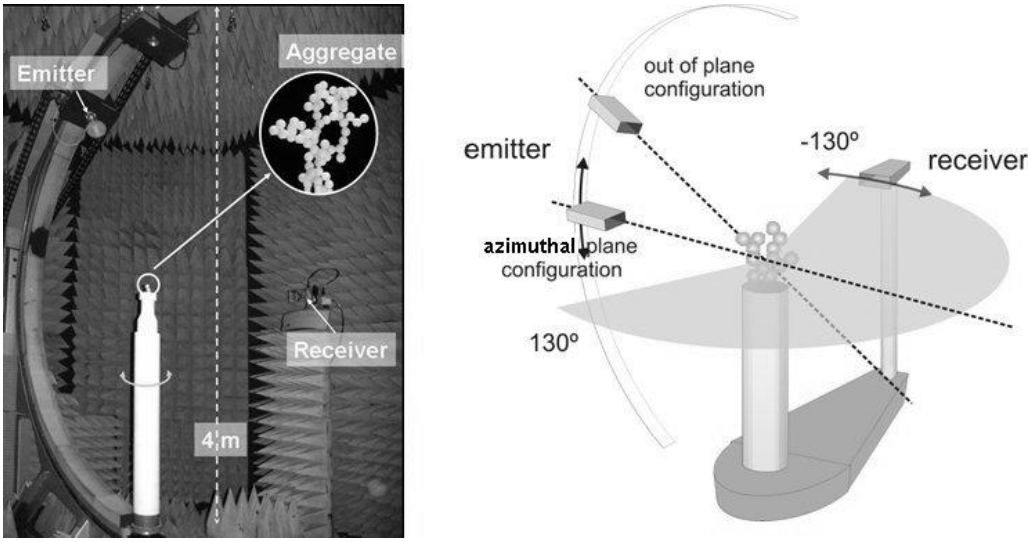

Figure 1. Picture of the facility (left) and azimuthal ("in plane configuration") and "out of plane configuration" for the location of the emitter antenna (right).

Building of a fully controlled aggregate

The tested fractal aggregate depicted on Fig. 1 is the analog of a micrometric particle composed of 74 spherical monomers with tens of nanometers in diameter. It was obtained by realization of the following steps (see Fig. 2): computational generation of the position of each individual sphere from pre-specified fractal parameters (fractal dimension 1.7, prefactor 2); building of the analog aggregate by using a micro-milling machine as three-dimensional positioning system and by glueing each sphere (5 mm in diameter) one after the other; positioning of the resulting aggregate onto a polystyrene support (transparent to microwaves) which itself is put at the top of the pole in the microwave facility. Permittivity in the microwave range of the material constituting the spheres (polyacetal) was determined by using the 'Epsimu' laboratory facility[7]. Some other encouraging tests have also been made using stereo-photolithography to design the targets offering thus new possibilities.

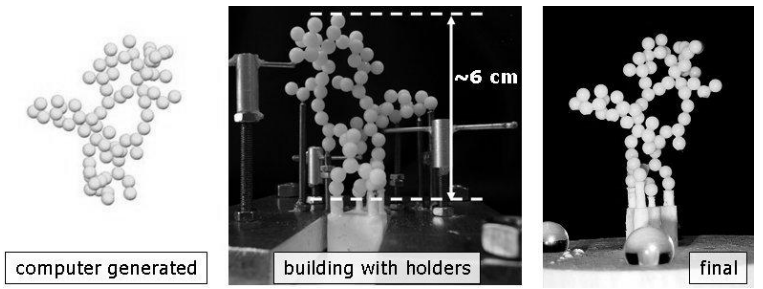

Figure 2. Steps for the preparation of the analog 74-sphere fractal aggregate.

ASSESSMENT OF LIGHT SCATTERING CODES: METHODOLOGY, DATABASE AND SAMPLE RESULTS

The aforementioned setups allow the building of a database containing the measurements of all amplitude-scattering-matrix elements (amplitude and phase) for this aggregate. To make the comparison with light-scattering codes easy and fully coherent, several pre-processing operations have to be performed[6]: a calibration method must be applied to both measured and simulated data to ensure that the exact same normalization technique is employed (amplitude of the incident field equal to unity and phase null at the centre of the target). As the convention used in the experimental set-up for the polarization components is not the common Bohren and Huffman one (referring to the scattering plane), all experimental data were converted into the usual frame to define incident and scattered polarization orientations. Thus, direct comparison with simulated data is made fully possible as well as it is ensured that off-diagonal (S3 and S4) elements contain solely cross-polarization information.

The resulting database is freely and publicly accessible at the web page http://www.fresnel.fr/3Ddirect/database.php, where downloads of the coordinates of the aggregate's spheres, the experimental results and the simulations obtained with Mackowski's T-matrix code are made possible after a registration process. Sample results are provided in Fig. 3. One can observe the high quality of measurement data, particularly for the cross-polarization term S_4, where amplitude minima are satisfactorily resolved. Simulations compare very well with the experiments, both in amplitude and phase of the elements. Additional experimental results and comparisons with other numerical methods can be found in [6].

CONCLUSION

The novel implementation of a microwave analog to light-scattering measurement setup introduced in this paper allows 3D measurements of the full amplitude scattering matrix for fully controlled targets, so as to constitute databases for the assessment of approximate light-scattering codes and also for inversion purposes. We believe that this facility can still be improved to perform full 3D measurements around the object and with application to particles even more complex in geometry and composition.

Acknowledgments: The authors would like to thank the ANR (Agence Nationale de la Recherche, France) for its financial support to the project "SOOT" #ANR-06-BLAN-0349-03.

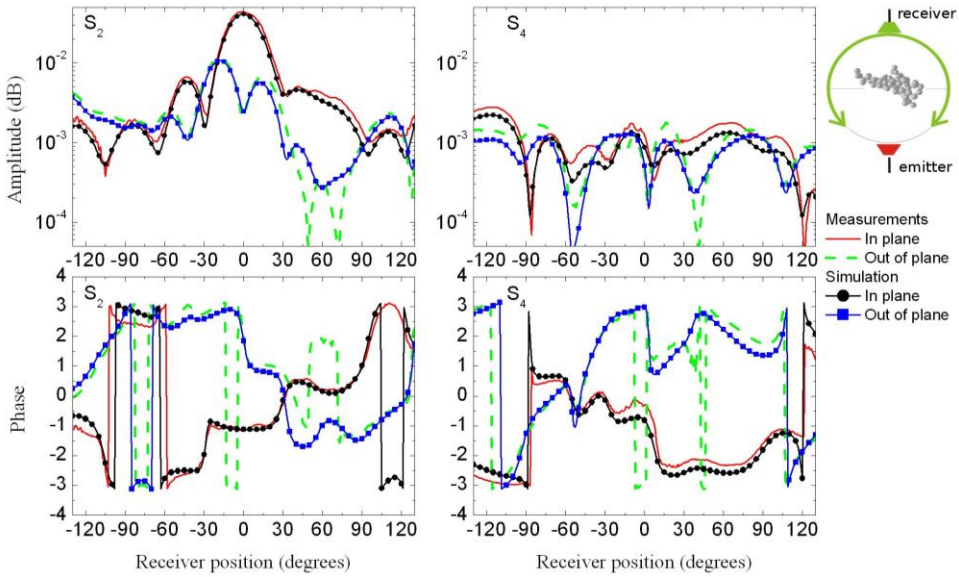

Figure 3. Measurements and Mackowski's T-Matrix simulations of the amplitude and phase of S_2 and S_4 at 18 GHz. The out of plane configuration corresponds to a position of the emitter at 60° from the vertical axis.

REFERENCES

[1] M.I. Mishchenko. Scale invariance rule in electromagnetic scattering. J. Quant. Spectrosc. Radiat. Transf. **101** (2006).

[2] B.Å.S. Gustafson. Microwave analog to light-scattering measurements. In: *Light scattering by nonspherical particles*. M.I. Mishchenko, J.W. Hovenier, and L.D. Travis (eds.). Academic Press (2000).

[3] C. Eyraud, J.-M. Geffrin, P. Sabouroux, P.C. Chaumet, H. Tortel, H. Giovannini, and A. Litman. Validation of a 3D bistatic microwave scattering measurement setup. Radio Sci. **43** (2008).

[4] C. Eyraud, J.-M. Geffrin, A. Litman, P. Sabouroux, and H. Giovannini. Drift correction for scattering measurements. Appl. Phys. Lett. **89** (2006).

[5] O. Merchiers, J.-M. Geffrin, R. Vaillon, P. Sabouroux, and B. Lacroix. Microwave analog to light scattering measurements on a fully characterized complex aggregate. Appl. Phys. Lett. **94** (2009).

[6] O. Merchiers, C. Eyraud, J.-M. Geffrin, R. Vaillon, B. Stout, P. Sabouroux, and B. Lacroix. Microwave measurements of the full amplitude scattering matrix of a complex aggregate: a database for the assessment of light scattering codes. Optics Express **18**, (2010).

[7] P. Sabouroux and P. Boschi. Rev. Electr. Electron. **10** (2005).

Opposition effect of the Moon from ground-based and space observations

Yu. I. Velikodsky[*,1], V. G. Kaydash[1], Yu. G. Shkuratov[1], N. V. Opanasenko[1], V. V. Korokhin[1], and G. Videen[2]

[1] *Institute of Astronomy, Kharkiv National University, Sumskaya 35, Kharkiv, 61022, Ukraine.*
[2] *Space Science Institute, Silver Spring Maryland 20905 USA.*

We study phase ratio images of the lunar nearside at low phase angles (1.6° and 2.7°) using ground-based telescope observations. The ratio appears highest for highlands of intermediate albedo, while bright craters have lower values. An average phase curve obtained with ground-based and spacecraft photometry of the Moon at phase angles 0.25–73° is presented.

INTRODUCTION

The brightness opposition effect (BOE) is a rapid increase of surface brightness seen when the phase angle α approaches zero. There are two mechanisms governing the BOE of planetary regoliths: the shadow-hiding effect and coherent backscattering enhancement [e.g. 1,2]. The relative contribution of each mechanism depends on α, albedo, and surface structure. Coherent backscattering can be significant only if the surface is rather bright. The BOE is observed for many atmosphereless celestial bodies including the Moon at α below 5–10° [1]. There are so far discrepant data about the role of coherent backscattering in the formation of the lunar BOE. Low-phase-angle observations of the Moon are difficult. Absolute photometry has low accuracy [3], spacecraft data are scarce, and ground-based observations cannot be carried out at α<1° because of the lunar eclipse. Relative lunar photometry can be performed by dividing one image obtained at α_1 by another image acquired at a generally larger α_2. This method can be very effective and was applied to select Clementine [4] and SMART-1 [5] data. Similar phase ratio technique was applied to Earth-based telescope data [6,7]. We use this method to produce a phase ratio (1.6°/2.7°) image of the lunar disk.

OBSERVATIONS

During a two-month campaign in 2006, we carried out quasi-simultaneous imaging photometry of the Moon and the Sun using a 15-cm refractor at Maidanak Observatory (Uzbekistan) [3,8]. We have presented results of absolute photometry [3], in particular, phase dependencies at α = 1.6 … 73° for several lunar areas acquired at 603 nm. We also obtained a series of lunar images near opposition suitable for phase-ratio analysis. The series covers the range of α = 1.6 … 3.1° (hereafter, α values correspond to the lunar disk centre). During the observations near opposition the photometric equator, the direction from the sub-observer point to

* Corresponding author: Yuri I. Velikodsky (dslpp@astron.kharkov.ua)

sub-solar one, was continuously rotated around 180°, and the direction of the phase-angle trend over the lunar disk was also rotated. Using this rotation we may separate the phase-angle trend from the albedo distribution on the lunar disk. Below we present results of processing the opposition series of lunar images at 603 nm.

PHASE RATIOS

A phase-ratio image is the quotient of coregistered brightness images of the same scene acquired at different phase angles. Before calculation of the phase-ratio image, the brightness images should be corrected for the global limb-terminator darkening using a disk function. We here apply Akimov's theoretical disk function [1,9]

$$D(\alpha,\beta,\gamma)=(\cos\beta)^{\frac{\alpha}{\pi-\alpha}}\frac{\cos\frac{\alpha}{2}}{\cos\gamma}\cos\left(\frac{\pi}{\pi-\alpha}\left(\gamma-\frac{\alpha}{2}\right)\right), \quad (1)$$

where β and γ are the photometric latitude and longitude, respectively. The observed brightness (radiance factor) divided by a disk function (e.g., Eq. (1)) is called the equigonal albedo A_{eq} because it corresponds to the mirror geometry of observation/illumination when the incidence and emergence angles are equals to $\alpha/2$ [e.g., 10].

The ratio of equigonal albedo images obtained at 1.6° and 2.7° is shown in Fig. 1. One can see that the phase ratio is lower for maria than for highlands, though the difference is small (≤1%). Meanwhile, bright craters (e.g., Tycho and Copernicus) are clearly visible as dark spots; these are areas having smaller phase-function slopes. Both mare and highland craters have phase ratios about 5% lower than their neighbourhood. This is an unexpected result, as the craters are rather bright and we could anticipate a manifestation of the coherent backscattering effect resulting in BOE increasing at so small α. Thus, either the albedo is not high enough to provide the coherent spike or it is too narrow to be revealed at 1.6° … 2.7°. The global brightness trend on the image relates to the variations of α over the lunar disk.

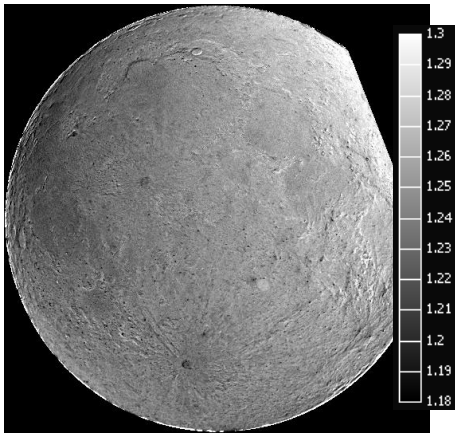

Figure 1. Phase ratios 1.6°/2.7°.

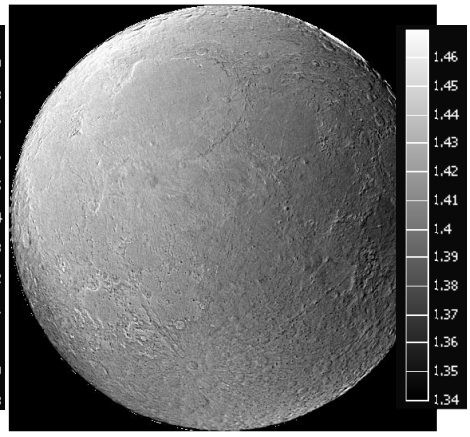

Figure 2. Phase ratio 2.59°/−2.59°.

Figure 2 shows the phase ratio (2.59°/−2.59°) of equigonal albedo images obtained before and after opposition. Albedo variations in Fig. 2 are almost suppressed, but due to variations of α over the lunar disk (in limits of 0.5°) a gradient of phase ratio is seen very well.

RELATIVE PHOTOMETRY

The global trends seen in Figs. 1 and 2 allow us to estimate the lunar phase function at small α. We clipped the edges of the equigonal albedo images to avoid errors of the disk function (1) near the limb and terminator. Then, applying the least-squares method we fit an equigonal albedo distribution at a fixed α and simultaneously relative phase dependence (the values in the range of α = 1.4° … 3.2° with step 0.1°) using whole series of lunar images. In Fig. 3 the relative phase dependence is shown together with data of absolute photometry of the Sinus Medii area (latitude 0°35', longitude −1°17') at large α [3] and with data of relative photometry (averaged different lunar types) of Clementine [4] and SMART-1 [5] for very small α. All equigonal albedo data were fitted (Fig. 3) by the expression [3]:

$$A_{eq}(\alpha) = a_1 e^{-\mu_1 \alpha} + a_2 e^{-\mu_2 \alpha} + a_3 e^{-\mu_3 \alpha}, \qquad (2)$$

where a_1=0.0244, μ_1=30.1, a_2=0.0384, μ_2=5.55, a_3=0.0842, μ_3=0.633 with α measured in radians. Simultaneously, normalizing factors for the three sequences of phase function relative values were fitted to convert these values to absolute equigonal albedo of Sinus Medii at 603 nm [3]. Figure 3 shows that the lunar BOE is very prominent; its amplitude is almost 40% in the range of α = 0.25° … 5.0°. At α = 0.5° … 2.0° the phase function of the Moon is almost linear. It appears that the main factor determining the lunar BOE is the shadow-hiding effect. At α<0.25° a slight tendency to flatten the phase curve is revealed; this relates to the angular size of the solar disk.

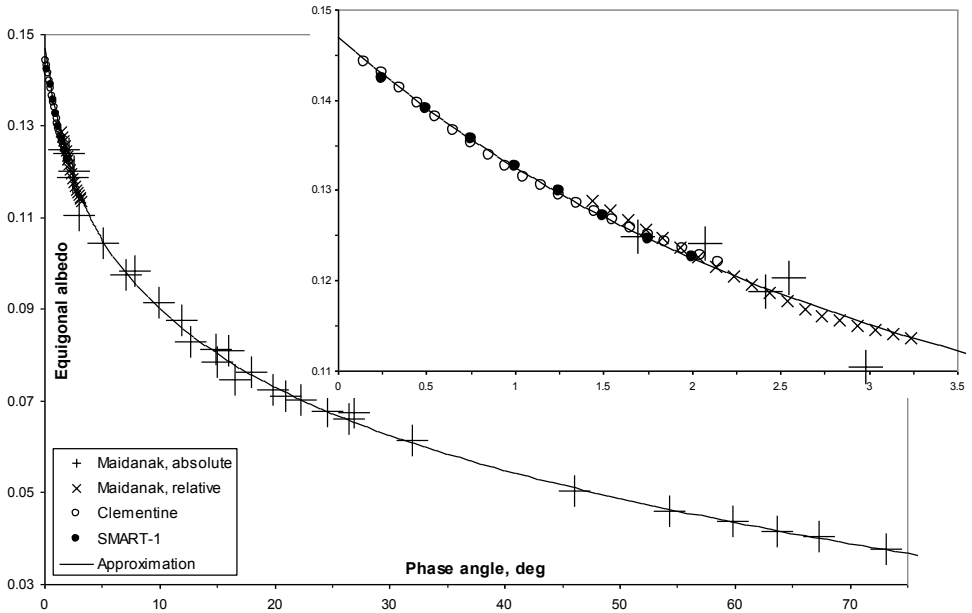

Figure 3. Phase dependence of lunar equigonal albedo.

CONCLUSIONS

The phase dependencies averaged over different areas of the lunar surface, obtained by ground-based, Clementine and SMART-1 observations, are in agreement with each other and compose the integrated phase curve of absolute equigonal albedo. The integrated dependence at $\alpha = 0.25° \ldots 75°$ can be described by the smooth function in Eq. (2), which has neither inflection nor corner points, suggesting a single mechanism of the BOE formation. The phase ratio (1.6°/2.7°) is slightly lower for maria than for highlands, which can be related to greater roughness of the highland surface. Bright craters have smaller phase-function slopes. This is unexpected, as the craters should manifest themselves in coherent backscattering. This suggests that either the albedo is yet not high enough or the spike is too narrow to be revealed at 1.6° … 2.7°. The latter is consistent with the regolith of bright young craters being immature and, hence, consisting of larger particles, resulting in a narrower coherent peak.

REFERENCES

[1] Yu. G. Shkuratov, M. A. Kreslavsky, A. A. Ovcharenko, D. G. Stankevich, E.S. Zubko, C. Pieters, and G. Arnold. Opposition Effect from Clementine Data and Mechanisms of Backscatter. Icarus **141** (1999).

[2] B. Hapke. *Theory of Reflectance and Emittance Spectroscopy*. Cambridge Univ. Press (1993).

[3] Yu.I. Velikodsky, N.V. Opanasenko, L.A. Akimov, V.V. Korokhin, Yu.G. Shkuratov, and V.G. Kaydash. Kharkiv Absolute Photometry of the Moon. LPSC 41th 1760 (2010).

[4] M.A. Kreslavsky, Yu.G. Shkuratov, Yu. Velikodsky, V.G. Kaydash, D.G. Stankevich, and C.M. Pieters. Photometric Properties of the Lunar Surface Derived from Clementine Observations. J. Geophys. Res. **105**(E8) (2000).

[5] V. Kaydash, M. Kreslavsky, Yu. Shkuratov, S. Gerasimenko, P. Pinet, S. Chevrel, J.-L. Josset, S. Beauvivre, and B. Foing. The Opposition Effect of the Moon from SMART-1 AMIE Data. LPSC 39th 1195 (2008).

[6] R. L. Wildey. The Moon in Heiligenschein. Science **200** (1978).

[7] V. G. Kaidash, S. Yu. Gerasimenko, Yu. G. Shkuratov, N. V. Opanasenko, Yu. I. Velikodskii, and V. V. Korokhin. Photometric Function Variations Observed on the Near Side of the Moon: Mapping. Solar System Res. **43**(2) (2009).

[8] Yu. I. Velikodsky, N. V. Opanasenko, L. A. Akimov, V. V. Korokhin, and Yu. G. Shkuratov. Absolute Photometry of the Lunar Surface. In: *48-th Vernadsky-Brown Microsymp.* Moscow (2008).

[9] L. A. Akimov. Reflection of Light by the Moon. 1. Kinemat. Fiz. Nebesykh Tel **4**(1) (in Russian) (1988).

[10] V.V. Korokhin, Yu.I. Velikodsky, Yu.G. Shkuratov, and U. Mall. The Phase Dependence of Brightness and Color of the Lunar Surface: a Study Based on Integral Photometric Data. Solar System Res. **41**(1) (2007).

A single scattering study using aggregates of spheres in random orientation

R. Vilaplana*[,1], R. Luna[1], and D. Guirado[2]

[1]*Centro de Tecnologías Físicas: Acústica, Materiales y Astrofísica, Universidad Politécnica de Valencia, Spain.*
[2]*Instituto de Astrofísica de Andalucía (CSIC), Granada, Spain.*

The particle shape influences the efficiencies of scattering (Q_{sca}) curves versus size parameter (X) and consequently on the overall single scattering properties of a sample of particles in random orientation. In order to show how the influence of the shape works, a model consisting of aggregates of different numbers of spheres has been used to fit laboratory measurements of fly ashes.

INTRODUCTION

Single scattering properties of a distribution of particles in random orientation depend on different parameters such as refractive index, size, shape, internal structure, as well as the degree of fluffiness of the particles. The measurements carried out in the scattering laboratory [1] and those obtained from astronomical observations [2] provide information on the overall scattering properties of a sample formed by small particles in random orientation. Individually identifying or "untangling" the way in which each parameter is affecting the overall scattering properties is difficult since these parameters have a collective influence on the measurements. In order to better understand how the single scattering properties observed are affected by these parameters, a lot of research has been carried out [3-7]; however, some questions remain open. The problem of single scattering by a distribution of small particles in random orientation can be approached by different techniques. We chose the DDA (Discrete Dipole Approximation). Despite it is not suitable for performing calculations for particles bigger than the wavelength of the incident light, on the current computers, in a reasonable time (days), it has the potential to reproduce any particle shape. We can fix all parameters of the model except for one and then vary it to study the response of the system. In this work, we present an attempt to fit a set of scattering laboratory measurements [1] by modeling it with a distribution of different aggregates of spheres. Nevertheless, our main goal is not to exactly fit the laboratory measurements, but to show how the particle shape is influencing Qsca; and therefore, the way it is determining the size average of the elements of the scattering matrix.

MODEL

We have modeled the system by using Eq. (1), which gives the scattering matrix as a function of the scattering angle θ, for a certain wavelength λ, under the assumption of independent scattering

* Corresponding author: Rosario Vilaplana (rovilap@fis.upv.es.)

$$Fij(\lambda,\theta) = \int_{r_1}^{r_2} F^{ij}(\lambda,\theta,r)n(r)dr\,. \quad (1)$$

In Eq. (1), *n(r)* is the size distribution as a function of the radius, r_1 and r_2 correspond to the smallest and largest particles in the distribution respectively, and $F^{ij}(\lambda,\theta,r)$ is one of the elements of the scattering matrix for a single particle of radius *r*.

CALCULATIONS

As mentioned, we have compared our calculations with laboratory measurements of fly ashes. The peculiar shapes of the particles involved in these measurements [1] have motivated the used model. Upper side in Fig. 1 show what these shapes are like. Regarding the eight aggregates of spheres shown in this image, the four on the left are made of a smaller number of spheres than those on the right. The shape average was performed by considering all these aggregates and a single sphere, with the same weight. Calculations corresponding to all aggregates have been carried out by DDA, and those for the single sphere have been also performed by Mie theory, for a wavelength of 0.633 μm in all cases. The value of the refractive index used was 1.5+0.001i, as given in [1]. The size distribution function n(r) was chosen a power law with negative exponent equal to -1.8, r_1=0.1 μm and r_2=1.0 μm. We have divided this range into 35 radii equally spaced intervals. The truncation of the size distribution to these values was a consequence of the computational limitations with the DDA code. The calculations were averaged over 2000 orientations to mimic the random orientation, and the number of dipoles was chosen so that the accuracy condition $|mkd| < 0.5$ was fulfilled [8].

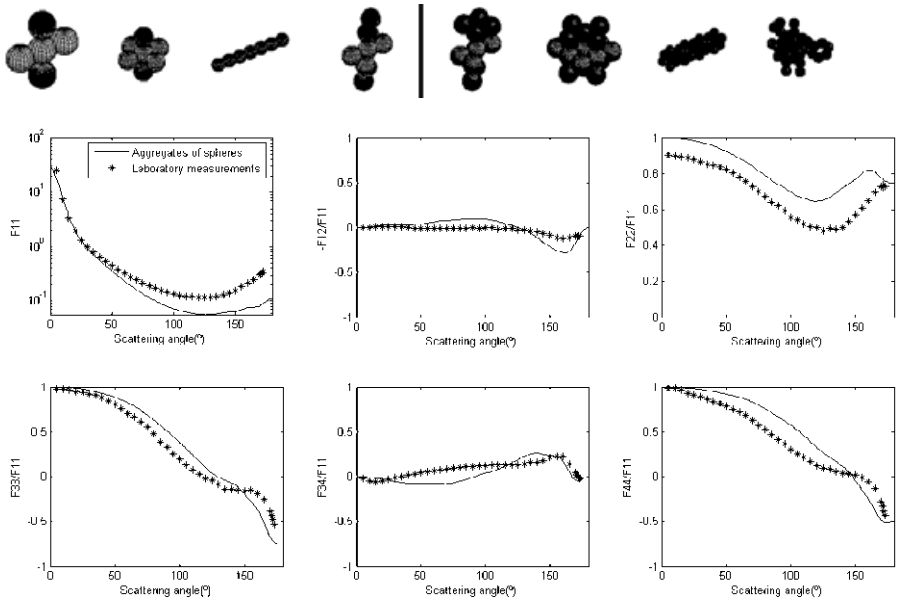

Figure 1. Eight aggregates made of 5, 7, 7-linear, 9, 14, 19, 25 and 36 spheres (top) and a comparison of laboratory measurements of fly ashes with our size and shape averages from 0.1 to 1.0 μm considering the eight aggregates and a single sphere equally weighted (bottom).

RESULTS AND DISCUSSION

In Fig. 1 (bottom), we show the comparison of our results with the laboratory measurements, size and shape averaged, considering the eight aggregates of spheres shown on the upper side of this figure, plus a single sphere. In Fig. 2, we can see the overlapped images of the size averaged results for each of the aggregates of spheres (blue and green lines) and for a single sphere (dashed black line). From Fig. 2, it comes out that the contribution of the aggregates of less number of spheres (≤9) is necessary to approach the laboratory measurements (see in Fig. 2 the blue and green lines). On the other hand, we note that the real size distribution, as given in the reference [1], has constituents with X larger than 10.

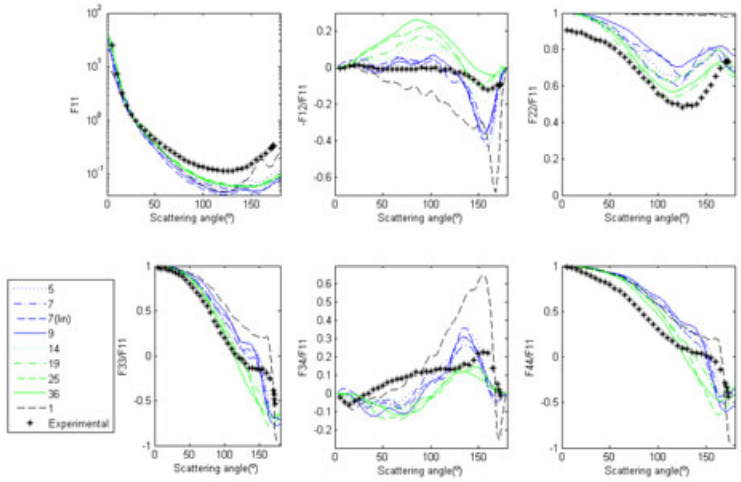

Figure 2. Comparison of laboratory measurements of single scattering matrix elements of fly ashes with our size averages from 0.1 to 1.0 μm for each one of the aggregates of spheres (blue and green lines) and for a single sphere (dashed black line).

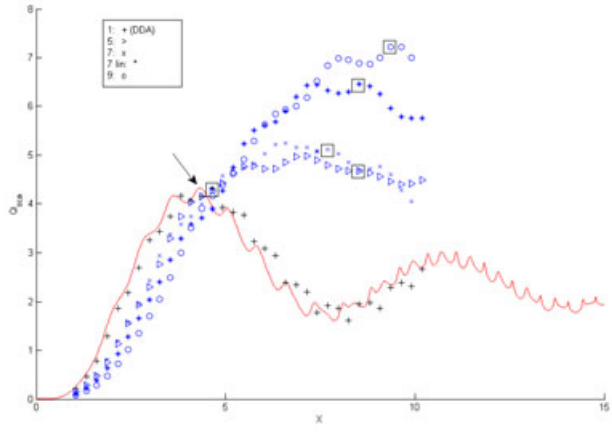

Figure 3. Q_{sca} versus X for the aggregates with a number of spheres ≤ 9 (5: **×**, 7: **>**, 7-linear: ***** and 9: **o**) and a single sphere (DDA: **+** and Mie: solid red line). The square on Q_{sca} curve of aggregates with number of spheres of 1, 5, 7, 7-lin and 9 are considered in the "same" state of oscillation to that marked by an arrow on the Q_{sca} curve of the single sphere (red line).

In Fig. 1, we see a not perfect fit of the results of DDA to the measurements, the calculations
stopping at r_2=1.0 μm. In particular, the deviation of the calculated values from the measurements points to a Rayleigh-like behaviour. From Fig. 2, we infer that the more spheres the aggregates are made of, the more the calculated values resemble Rayleigh features of the scattering matrix elements as functions of the scattering angle. This is suggesting us an explanation for the unperfected fitting: when aggregates are made of a large number of spheres, the curve of Q_{sca} as a function of X changes so that we are skipping some of its main features by cutting our size distribution at r_2=1.0 μm. In order to prove this, we present on Fig. 3 the Q_{sca} curves for the four aggregates with a number of spheres ≤ 9 till X=10, along with the Q_{sca} curve of the single sphere, calculated till X=15. A progressive displacement to the right and rising of the Q_{sca} curves is observed when the number of spheres of the aggregates increases. Due to this displacement, some of the features of Q_{sca} that correspond to r > 1.0 μm are lost in our calculations, and this effect becomes more important as the number of spheres of the aggregates increases. The result is a Rayleigh-like behaviour because only the first oscillation of the curve of Q_{sca} is been considered for the size distribution.

REFERENCES

[1] O. Muñoz, H. Volten, J.F. Haan, W. Vassen, and J.W. Hovenier. Experimental determination of scattering matrices of randomly oriented fly ash and clay particles at 441.6 nm and 632.8 nm. J. Geophys. Res. **106** (2001).

[2] L. Kolokolova, H. Kimura, N. Kiselev, and V. Rosenbush. Two different evolutionary types of comets proved by polarimetric and infrared properties of their dust. Astron. Astrophys. **463** (2007).

[3] H. Kimura, L. Kolokolova, and I. Mann. Light scattering by cometary dust numerically simulated with aggregate particles consisting of identical spheres. Astron. Astrophys. **449** (2006).

[4] T. Nousiainen. Optical modeling of mineral dust particles: A review. J. Quant. Spectrosc. Radiat. Transf. **110** (2009).

[5] R. Vilaplana, F. Moreno, and A. Molina. Study of the sensitivity of size-averaged scattering matrix elements of non-spherical particles to changes in shape, porosity and refractive index. J. Quant. Spectrosc. Radiat. Transf. **100** (2006).

[6] F. Moreno, O. Muñoz, D. Guirado, and R. Vilaplana. Comet dust as a size distribution of irregularly shaped, compact particles. J. Quant. Spectrosc. Radiat. Transf. **106** (2007).

[7] Y. Shen, B.T. Draine, and E.T. Johnson. Modeling porous dust grains with ballistic aggregates. II. Light scattering properties. Astron. Astrophys. **696** (2009).

[8] B.T. Draine, P.J. Flatau. Discrete-dipole approximation for scattering calculations. J. Opt. Soc. Am. A. **11** (1994).

A Python library for computing light scattering by multilayered non-spherical particles

A. A. Vinokurov*[,1,2], V. B. Il'in[1,2,3], and V. G. Farafonov[1]

[1] *State Univ. of Aerospace Instrumentation, Bol. Morskaya 67, St. Petersburg, 190000 Russia.*
[2] *Pulkovo Observatory, Pulkovskoe chaussee 65/1, St. Petersburg, 196140 Russia.*
[3] *St. Petersburg University, Universitetskij pr. 28, St. Petersburg, 198504 Russia.*

We present a new library of routines for computing light scattering by axially symmetric particles with multiple layers. The library is written in Python and relies on the modern scientific framework SciPy. The tool is based on the generalized separation of variables method with a spherical basis. We discuss capabilities of the code and present results of extensive computations giving insight in the dependence of optical properties on the scatterer size and structure. We also share some experience of Python/SciPy usage.

INTRODUCTION

FORTRAN and C++ are traditionally used for computations in light scattering. They provide very fast codes, but using them is known to require development skills from researchers. A programming language that is more convenient to develop with and at the same time allowing as fast computations as with traditional languages is Python (*http://python.org*). This modern powerful scripting language is used in a wide variety of application domains. Its major advantages are cross-platform compatibility, open source, very clear and readable syntax, large amount of standard and third-party libraries for different tasks. Python code is very easy to develop, maintain and scale.

Python has recently become widely used in scientific applications mostly because of development of SciPy. SciPy (*http://scipy.org*) is a Python library for scientific computations, including modules for linear algebra, special functions, multiprecision arithmetic, symbolic mathematics and many others. Using Python allows researches to utilize standard functions for most of the tasks and focus on the algorithm implementation. SciPy also provides MATLAB-like environment for interactive computations and rich data visualization tools. As Python/SciPy nowadays are widely used in various fields of science there are a lot of packages for astronomy, biology, geosciences, chemistry, etc. Using SciPy makes integration with these packages quite easy.

The speed of SciPy-based code is comparable with that of MATLAB codes. However, Python provides facilities for integration with FORTRAN and C++ that allow one to have the speed of the low level languages, while keeping the code simplicity of Python.

GENERALIZED SEPARATION OF VARIABLES METHOD

To solve the light scattering problem we generalize the separation of variables method [1], that is most suitable for layered particles among the methods using field expansion [2].

We consider a particle with L layers embedded in a homogeneous medium. Each layer surface $\partial\Gamma^{(i)}$ is axisymmetric with the symmetry axis coinciding with z-axis. An incident

*Corresponding author: Alexander A. Vinokurov (alexander.a.vinokurov@gmail.com)

plane wave propagates at the angle α to the z-axis. The electromagnetic fields in each of the domains $\Gamma^{(i)}$ satisfy the boundary conditions

$$\vec{E}^{(i)}(\vec{r}) \times \vec{n}^{(i)}(\vec{r}) = \vec{E}^{(i+1)}(\vec{r}) \times \vec{n}^{(i)}(\vec{r}), \quad \vec{r} \in \partial\Gamma^{(i)}, \quad i = 1, \ldots, L, \tag{1}$$

where $\vec{n}^{(i)}$ is an outward normal to the layer surface $\partial\Gamma^{(i)}$. The field in $\Gamma^{(1)}$ is a sum of the incident and scattered fields $\vec{E}^{(1)} = \vec{E}^{\text{inc}} + \vec{E}^{\text{sca}}$.

All fields are expanded in terms of spherical wave functions. The expansions are substituted in the boundary conditions (1). Multiplication of these conditions by the angular part of different index wave functions and integration over the corresponding surface $\partial\Gamma^{(i)}$ yield a system of linear algebraic equations relative to the expansion coefficients $\vec{x}^{(i)}$

$$P_i^{(i)}\vec{x}^{(i)} = P_{i+1}^{(i)}\vec{x}^{(i+1)}, \quad i = 1, \ldots, L,$$

where $P_j^{(i)}$ are some infinite matrices (see for details [3]), $\vec{x}^{(1)} = (\vec{x}^{\text{inc}}, \vec{x}^{\text{sca}})^{\text{T}}$. The expansion coefficients of the incident field $\vec{x}^{\text{inc}}$ are known. The unknown coefficients of the scattered field expansion can be found from a smaller system [1]

$$P_1^{(1)}\vec{x}^{(1)} = P_2^{(1)} \prod_{i=2}^{L} \left[(P_i^{(i)})^{-1} P_{i+1}^{(i)} \right] \vec{x}^{(L+1)}.$$

TOOL IMPLEMENTATION AND TESTING

The algorithm was implemented as a Python code. SciPy routines were used for linear algebra and for computing values of spherical functions. For massive computations Python's standard data storage and plotting methods were effectively used. The most resource-hungry part (computation of elements of matrices $P_j^{(i)}$) was implemented as a FORTRAN77 module and imported with *f2py*. The use of object oriented programming allowed efficient code reuse and more scalable design. With Python we achieved a significantly more clear and smaller code than with FORTRAN77 (1700 versus 2600 lines of code) and richer functionality, while preserving the same speed as with FORTRAN.

The new tool was compared with available codes based on the extended boundary condition [4], null-field [5], and DDA [6] methods. For example, see Fig. 1, where normalized intensity of multilayered prolate spheroids (F_{11}/g) computed with different techniques is plotted. Here g is the cross section of equivolume sphere. The computations have shown that our results perfectly match with those given by the other codes for particles with a relatively small number of layers and provide more accurate results for particles with a large number of layers.

Fig. 1 shows that our code is highly effective for multilayered particles, providing reliable results for small scatterers with several hundreds of layers and for large scatterers ($x_{\text{V}} = 30$) with up to 4 layers. Relative difference between the scattering and extinction cross sections $\delta = |C_{\text{sca}} - C_{\text{ext}}|/(C_{\text{sca}} + C_{\text{ext}})$ was utilized as an accuracy measure.

NUMERICAL RESULTS

Using the code we have performed extensive computations to analyze the impact of particle size, shape and structure on different optical properties. A detailed graphical library of computational results is presented at the Database of Optical Properties (DOP) at *http://www.astro.spbu.ru/DOP/8-GLIB/op3*.

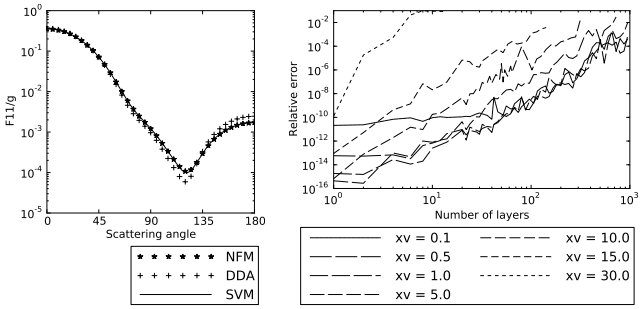

Figure 1. Results validation for multilayered particles. In left, comparison with NFM and DDA, and in right, relative error vs. the number of layers. The particle layers are equivolume prolate spheroids with aspect ratio $a/b = 1.4$, the materials are ice ($m = 1.3$) and vacuum ($m = 1$) repeating cyclically. The incident wave propagation angles are $\alpha = 0°$ (left) and $45°$ (right), effective size parameters $x_{\mathrm{V}} = 3$ (left) and from 0.1 to 30 (right), number of layers $L = 8$ (left) and from 1 to 1000 (right).

Fig. 2 illustrates comparison of intensity and degree of linear polarization of porous scatterers approximated by 2- and 16-layered particles and homogeneous particles having the refractive index derived from the effective medium theory. These results extend the well-known work [7] where dependence of the scattering matrix elements on homogeneous particle size and orientation was discussed in detail. One can see that *the main effect of scatterer structure is appearance of strong polarization maxima and minima in a very wide range of the scattering angle values*. This and other revealed effects of scatterer structure are discussed in detail in [3].

Acknowledgements: The work was supported by the grants RFFI 10-02-00593a, NTP 2.1.1/665 and NSh 1318.2008.2.

REFERENCES

[1] A.A. Vinokurov, V.G. Farafonov, and V.B. Il'in. Separation of variables method for multilayered nonspherical particles. J. Quant. Spectr. Rad. Transf. **110** (2009).

[2] V.B. Il'in, V.G. Farafonov, and A.A. Vinokurov. Theoretical and computational aspects of the SVM, EBCM, and PMM methods in light scattering by small particles. Abstr. ELS12 Conf. (2010).

[3] A.A. Vinokurov, V.B. Il'in, and V.G. Farafonov. On optical properties of nonspherical inhomogeneous particles. Opt. Spectr. (submitted) (2010).

[4] V.G. Farafonov, V.B. Il'in, and M.S. Prokopjeva. Light scattering by multilayered nonspherical particles: a set of methods. J. Quant. Spectr. Rad. Transf. **79**–**80** (2003).

[5] A. Doicu, Y.A. Eremin, and T. Wriedt. *Light scattering by systems of particles*. Springer (2006).

[6] B.T. Draine and P.J. Flatau. User guide to the Discrete Dipole Approximation code. Preprint arXiv.1002.1505v1 (2010)

[7] M.I. Mishchenko and L.D. Travis. Light scattering by polydispessions of randomly oriented spheroids with sizes comparable to wavelength of observation. Appl. Opt. **33** (1994).

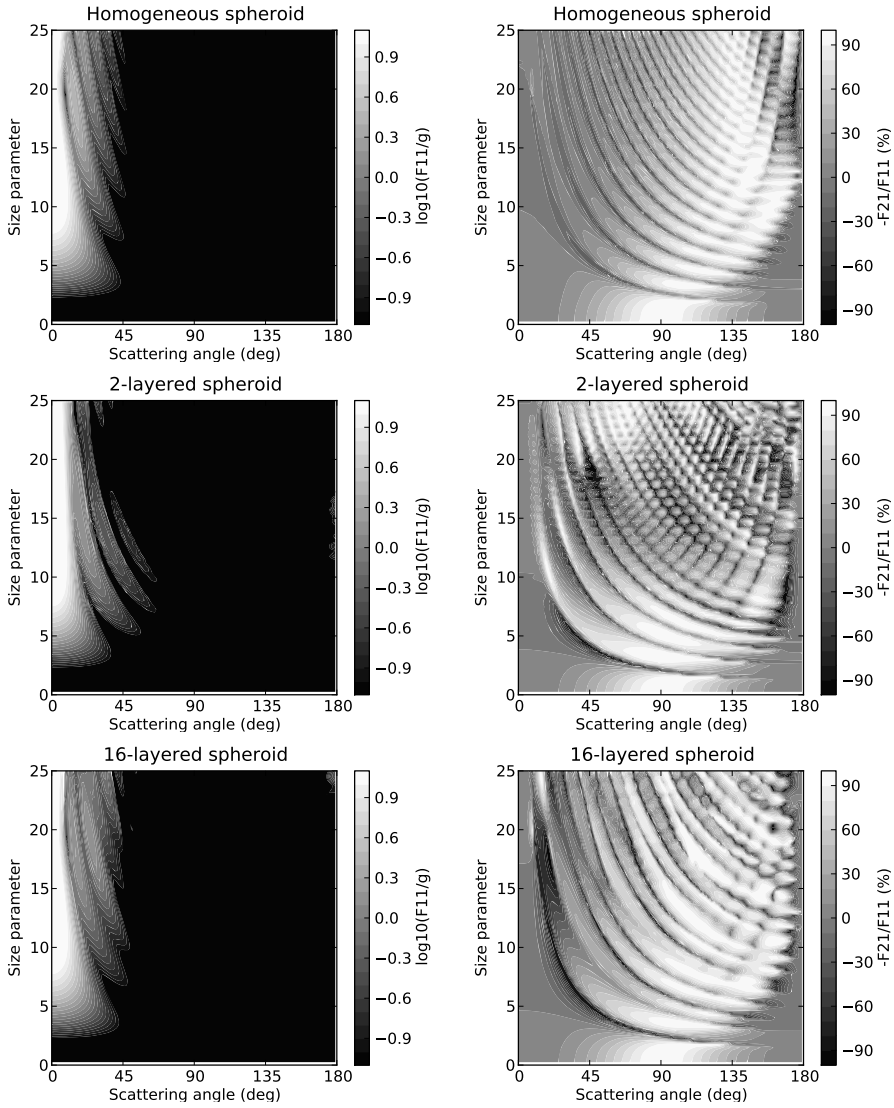

Figure 2. Normalized intensity and the degree of linear polarization vs the scattering angle and effective size parameter for homogeneous and layered prolate spheroids. The particle symmetry axis is parallel to the incident beam ($\alpha = 0°$). The particle layers are equivolume spheroids with aspect ratio $a/b = 1.4$, the materials are ice ($m = 1.3$) and vacuum ($m = 1$) repeating cyclically.

Light scattering by interstellar dust: Assessments of related direct and inverse problems

A. N. Witt*

Department of Physics & Astronomy, University of Toledo, Toledo, OH 43606, USA.

This summary provides a gateway to the literature on light scattering by interstellar dust.

INTRODUCTION

About half of the atoms heavier than helium in the interstellar medium (ISM) of the Milky Way Galaxy are in the form of interstellar dust, amounting to about 1% of the mass of the ISM. The most profound effect produced by interstellar dust is interstellar extinction of star light, resulting in an optical depth at visual wavelengths of about unity for a path length of about 3×10^{21} cm [1]. Consequently, with a diameter of the galactic disk near 1×10^{23} cm, the extinction by dust causes most parts of our Galaxy to be unobservable at optical wavelengths.

Interstellar extinction is caused both by absorption and scattering by solid grains exhibiting a wide size distribution ranging from a few 10^{-7} cm to a few 10^{-4} cm, with scattering by the larger grains being the dominant contribution to the extinction at most ultraviolet/visible/near-infrared wavelengths [2−4]. The study of the scattering properties of interstellar dust provides important constraints on the size distribution of the grains as well as critical information for astrophysical problems in which dust scattering is involved.

DIRECT PROBLEM: OPTICAL PROPERTIES OF SMALL PARTICLES

The early work by Mie [5] and the slow acceptance of the existence of interstellar dust by the astronomical community in the 1930's [1−4] allowed a rapid convergence of theory and observation [6,7], once the presence of dust particles in the diffuse interstellar medium of the Milky Way galaxy was established [8]. The monographs by van de Hulst [9] and Bohren & Huffman [10] provided the basis for the computation of the optical properties of interstellar grains, following Mie's [5] theory for homogeneous spherical particles. Although polarimetric observations have established the mostly non-spherical shape of interstellar grains, and although techniques for the computation of the optical properties of inhomogeneous, non-spherical particles have been developed (see Voshchinnikov [11] for a recent review), Mie's theory for spherical grains is still considered an adequate approximation for most applications, given the persistent uncertainties involving the chemical nature, physical structure, optical constants, and size distribution of interstellar dust [12]. These uncertainties will persist as long as remote sensing is the exclusive method for the study of the properties of interstellar grains. When needed, techniques such as the T-matrix method [13] or the discrete dipole approximation [14] are available for the computation of optical properties of

*Adolf N. Witt (Adolf.Witt@utoledo.edu)

non-spherical particles or particles of arbitrary shape and mixed composition, respectively. The most comprehensive resource on the theory of scattering by non-spherical particles currently available is the monograph by Borghese, Denti, and Saija [15]. Special computational tools have been developed for the determination of scattering properties of spherical particles with very large size parameters [16,17].

INDIRECT PROBLEM: SCATTERING PROPERTIES OF COSMIC DUST

Four classes of astrophysical systems exist in which scattering by interstellar grains can be observed and used as a basis for the empirical determination of their scattering properties. These are, in decreasing order of the angular extent, the sky as a whole, which contains the diffuse galactic light (DGL) produced by the general galactic dust distribution [18−20], illuminated by the interstellar radiation field (ISRF) due to all stars, followed by individual interstellar clouds illuminated externally [21] by the ISRF, then reflection nebulae [22−25], where individual clouds are illuminated by single or multiple embedded stars, and finally scattered light halos surrounding distant point sources, seen at both X-rays and optical light [26−28]. In all instances, appropriately designed radiative transfer models [17,22] are the essential tools that produce the link between observations and the scattering properties of the grains. The information typically derived are the dust albedo and the asymmetry of the scattering phase function as functions of wavelength, critical information about the sizes of grains, and finally information about the spatial distribution of the dust particles. The dust albedo, at most UV/visible/near-IR wavelengths, is $\sim 0.6 - 0.7$ and the phase function asymmetry parameter $g =< \cos\alpha >\sim 0.6 - 0.8$, indicating that interstellar scattering is dominated by highly reflective, strongly-forward scattering grains. The reduction of the dust albedo around the wavelength of the far-UV extinction feature at 2175 Å [25] shows that this feature is produced by absorbing nanoparticles. Similarly, the decline of the albedo at the shortest far-UV wavelengths [29] indicates the growing absorption contribution by the smallest interstellar grains. High-albedo scattering at near-IR wavelengths identifies astronomical environments where micron-sized grains dominate the scattering [30,31].

ASTRONOMICAL APPLICATIONS

The empirically determined scattering properties of interstellar dust are commonly used to constrain models of interstellar grains [32,33]. They also are critical input parameters for models designed to compute the dust attenuation in externally observed dusty galaxies, in which the dust-scattered radiation becomes a significant part of the total spectral energy distribution seen by a distant observer [34]. Finally, in addition to scattering, interstellar dust exhibits optical photoluminescence when exposed to ultraviolet observation. Knowledge of the wavelength dependence of the scattering properties is essential in order to separate the photoluminescence component from the scattered light component [35,36].

REFERENCES

[1] R.J. Trumpler. Spectrophotometric Measures of Interstellar Light Absorption. P. A. S. P. **42** (1930).

[2] O. Struve. On the Interpretation of the Surface Brightness of Diffuse Galactic Nebulae. ApJ **85** (1937).

[3] J.L. Greenstein and L.G. Henyey. The Ratio of Interstellar Absorption to Reddening. ApJ **93** (1941).

[4] L.G. Henyey and J.L. Greenstein. Diffuse Radiation in the Galaxy. ApJ **93** (1941).

[5] G. Mie. Beitraege zur Optik trueber Medien, speciell kolloidaler Metalloesungen. Ann. Phys. **25** (1908).

[6] C. Schalen. Untersuchungen ueber Dunkelnebel. Medd. Astron. Observ. Upsala **58** (1933).

[7] C. Schalen. Ueber Probleme der Interstellaren Absorption. Medd. Astron. Observ. Upsala **64** (1936).

[8] J.H. Oort and H.C. van de Hulst. Gas and Smoke in Interstellar Space. B. A. N. **10** (1946).

[9] H.C. van de Hulst. *Light Scattering by Small Particles*. New York: John Wiley & Sons, Publ. (1957).

[10] C.F. Bohren and D.R. Huffman. *Absorption and Scattering of Light by Small Particles*. New York: John Wiley & Sons, Publ. (1983).

[11] N.V. Voshchinnikov. Optics of Cosmic Dust I. Astroph. Space Phys. Rev. **12** Part 3 (2004).

[12] J.S. Mathis, W. Rumpl, and K.H. Nordsieck. The Size Distribution of Interstellar Grains. ApJ **217** (1977).

[13] H.K. Das, N.V. Voshchinnikov, and V.B. Il'in. Interstellar Extinction and Polarization — A Spheroidal Dust Grain Approach Perspective. MNRAS (in press) (2010).

[14] B.T. Draine and P.J. Flatau. Users Guide for the Discrete Dipole Approximation Code DDSCAT 7.1. http://arxiv.org/abs/1002.1505 (2010).

[15] F. Borghese, P. Denti, and R. Saija. *Scattering from Model Nonspherical Particles*. Berlin: Springer (2007).

[16] W.J. Wiscombe. Mie Scattering Calculations: Advances in Technique and Fast Vector-Speed Computer Codes. NCAR Tech. Note TN-140+STR, Boulder, NCAR (1979).

[17] S. Wolf and N.V. Voshchinnikov. Mie Scattering by Ensembles of Particles with very large Size Parameters. CmpPhC **162** (2004).

[18] P.A. Bastiaansen and H.C. van de Hulst. Models for Interpreting the Diffuse Galactic Light. A&A **61** (1977).

[19] J.S. Mathis. The Interpretation of the Diffuse Galactic Light. ApJ **186** (1973).

[20] A.N. Witt, B.C. Friedmann, and T.P. Sasseen. Radiative Transfer Analysis of Far-Ultraviolet Background Observations obtained with the Far Ultaviolet Space Telescope. ApJ **481** (1997).

[21] A.N. Witt, M.V. Oliveri, and R.E. Schild. The Scattering Properties and Density Distribution of Dust in a Small Interstellar Cloud. AJ **99** (1990).

[22] W. Rush. Albedo of Particles in Reflection Nebulae. AJ **80** (1975).

[23] J.S. Mathis, B.A. Whitney, and K. Wood. Can Reflection from Grains Diagnose the Albedo? ApJ **574** (2002).

[24] A.N. Witt et al. Ultraviolet Imaging Telescope Images of the Reflection Nebula NGC 7023: Derivation of Ultraviolet Scattering Properties of Dust Grains. ApJ **395** L5 (1992).

[25] D. Calzetti, R.C. Bohlin, K.D. Gordon, A.N. Witt, and L. Bianchi. Scattering Properties of the Dust in the Reflection Nebula IC 435. ApJ **446** L97 (1995).

[26] A.N. Witt, R.K. Smith, and E. Dwek. X-Ray Halos and Large Grains in the Diffuse Interstellar Medium. ApJ **550** L201 (2001).

[27] A. Socrates and B.T. Draine. Brilliant Pebbles: A Method for Detection of Very Large Interstellar Grains. ApJ **702** L77 (2009).

[28] N.J. Turner, K. Grogan, and J.B. Breckinridge. Probing Interstellar Dust with Space-Based Coronographs. ApJS **177** (2008).

[29] A.N. Witt et al. Voyager 2 Observations of NGC 7023: Dust Scattering Shortward of 1600 A. ApJ **410** (1993).

[30] A.N. Witt, R.S. Lindell, D.L. Block, and Rh. Evans. K′-Band Observations of the Evil Eye Galaxy: Are the Optical and Near-Infrared Albedos Identical? ApJ **427** (1994).

[31] J. Steinacker, L. Pagani, A. Bacmann, and S. Guieu. Direct Evidence of Dust Growth in L183 from MIR Light Scattering. arxiv0912.0145 (2009).

[32] B.T. Draine. Scattering by Interstellar Grains. I. Optical and Ultraviolet. ApJ **598** (2003).

[33] B.T. Draine. Scattering by Interstellar Grains. II. X-Rays. ApJ **598** (2003).

[34] D. Pierini, K.D. Gordon, A.N. Witt, and G.J. Madsen. Dust Attenuation in Late-Type Galaxies. I. Effects on Bulge and Disk Components. ApJ **617** (2004).

[35] A.N. Witt and T.A. Boroson. Spectroscopy of Extended Red Emission in Reflection Nebulae. ApJ **355** (1990).

[36] A.N. Witt, S. Mandel, P.H. Sell, T. Dixon, and U.P. Vijh. Extended Red Emission in High Galactic Latitude interstellar Clouds. ApJ **679** (2008).

The relationship between grain shape and interstellar polarization

N. V. Voshchinnikov* and I. S. Yakovlev

Astronomy Department and Sobolev Astronomical Institute, St. Petersburg University, Universitetskii prosp., 28, St. Petersburg, 198504 Russia.

We analyze the effects of grain shape and orientation on the parameters of the interstellar linear-polarization curve. The consideration is performed for partially aligned prolate and oblate spheroidal particles with aspect ratios a/b varying from 1.1 to 10.

LINEAR POLARIZATION: OBSERVATIONS

The phenomenon of interstellar linear polarization is caused by the linear dichroism of the interstellar medium due to the presence of non-spherical oriented grains. Non-spherical particles produce differing extinction of light depending on the orientation of the electric vector of incident radiation relative to the particle axis. The spectral dependence of polarization in the visible part of the spectrum $P(\lambda)$ is described by the Serkowski empirical formula (see, e.g., [1])

$$P(\lambda)/P_{\max} = \exp[-K \ln^2(\lambda_{\max}/\lambda)], \quad (1)$$

where K is the coefficient, $P_{\max}$ the maximum degree of polarization, and $\lambda_{\max}$ the wavelength corresponding to it. From the analysis of observational data for several hundred stars, it has been found that the upper limit on the ratio of $P_{\max}$ to the colour excess $E(\mathrm{B-V})$ is [1]

$$P_{\max}/E(\mathrm{B-V}) \lesssim 9\%/\mathrm{mag}\,. \quad (2)$$

This ratio determines the polarizing efficiency of the interstellar medium towards a particular star.

A relation has been established between the total-to-selective extinction ratio R_{V} and $\lambda_{\max}$ ($R_{\mathrm{V}} = (5.6 \pm 0.3)\,\lambda_{\max}$, $\lambda_{\max}$ in μm) and regional variations of R_{V} and $\lambda_{\max}$ (see Fig. 4.13 in [2]). The increase of R_{V} and $\lambda_{\max}$ is usually attributed to the growth of grain size, although both parameters also depend on the degree and direction of grain alignment [3].

In [3], an anticorrelation has been noted between the observed polarizing efficiency and $\lambda_{\max}$, i.e., a larger value of $\lambda_{\max}$ corresponds to a smaller value of $P_{\max}/E(\mathrm{B-V})$. Using the model of infinite cylinders, this fact has been interpreted as the decrease of the angle between the line of sight and the magnetic field direction Ω.

To test this hypothesis, we have used recent data of Efimov [4], who fitted the multi-wavelength polarimetric observations for 105 stars. We have chosen 76 stars located in the galactic plane ($|b| \lesssim 20^\circ$) with distances $D \lesssim 1$ kpc. The observed values of $P_{\max}/E(\mathrm{B-V})$

*Corresponding author: Nikolai Voshchinnikov (nvv@astro.spbu.ru)

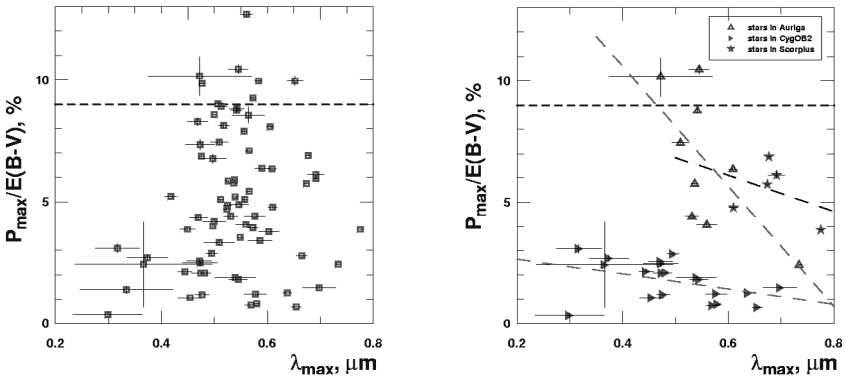

Figure 1. Polarizing efficiency of the interstellar medium as a function of wavelength, where interstellar linear polarization is maximized. Data are shown for 76 stars located within 1000 pc (left) and, separately, for stars in Auriga, Cygnus, and Scorpius (right). The horizontal line is the observational upper limit as given by Eq. 2. Dashed lines are linear fits. Data were taken from [4].

versus $\lambda_{\max}$ (we have used the Whittet fit from [4]) are plotted in Fig. 1 (left panel). It can be seen that there is no correlation. However, for stars more or less closely located on the sky, a systematic trend toward smaller polarizing efficiency for larger $\lambda_{\max}$ is obvious (right panel of Fig. 1).

To interpret the observations, one needs to utilize a model of rotating partially aligned non-spherical grains. Such a model was recently developed and applied in the simultaneous interpretation of the observed interstellar extinction and polarization curves for certain stars [5, 6]. The shape of the grains in the spheroidal model is characterized by one parameter: the ratio of the major and minor semi-axes a/b. Note that previous modelling of interstellar polarization with spheroids has included non-rotating particles with $a/b \lesssim 2$ (see [7, 8, 9]).

SPHEROIDAL MODEL OF INTERSTELLAR DUST

We use the model of homogeneous spheroids with a power-law size distribution ($n(r_V) \propto r_V^{-q}$) with imperfect Davis-Greenstein (IDG) orientation (see [5, 6] for details). Spheroids are characterized by their type (prolate or oblate), the aspect ratio a/b, and size parameter r_V (radius of a sphere whose volume is equal to that of a non-spherical particle). For a given wavelength λ, the extinction and polarization cross sections $\langle C_{\rm ext}\rangle_\lambda$ and $\langle C_{\rm pol}\rangle_\lambda$ are obtained by averaging of the cross sections over the size distribution and grain orientations. The direction of grain orientation is described by the angle Ω (angle between the line of sight and the magnetic field direction, $0^\circ \le \Omega \le 90^\circ$). The value $\Omega = 90^\circ$ corresponds to the case when the particle rotation plane contains the light propagation vector $\mathbf{k}$, which gives the maximum degree of linear polarization. For $\Omega = 0^\circ$, the light falls perpendicular to the particle rotation plane and from symmetry reasons the net degree of polarization produced is zero.

The IDG mechanism is described by the function $f(\xi, \beta)$ depending on the alignment parameter ξ and the precession angle β

$$f(\xi, \beta) = \frac{\xi \sin\beta}{(\xi^2 \cos^2\beta + \sin^2\beta)^{3/2}}. \qquad (3)$$

The parameter ξ depends on the particle size r_V, the imaginary part of the grain magnetic susceptibility χ'', gas density $n_{\rm H}$, the strength of magnetic field B, and temperatures of dust $T_{\rm d}$ and gas $T_{\rm g}$,

$$\xi^2 = \frac{r_V + \delta_0(T_{\rm d}/T_{\rm g})}{r_V + \delta_0}\,, \qquad \delta_0 = 8.23 \times 10^{23} \frac{\varkappa B^2}{n_{\rm H} T_{\rm g}^{1/2} T_{\rm d}}\ [\mu{\rm m}]. \tag{4}$$

Our model has the following main parameters: the minimum and maximum grain radii $r_{V,\rm min}$ and $r_{V,\rm max}$, the power index q, and the degree (δ_0) and direction (Ω) of grain alignment.

RESULTS AND DISCUSSION

We made calculations for polydisperse ensembles of spheroids consisting of astronomical silicate (astrosil [10]) and amorphous carbon (AC-Be [11]). The size-distribution parameters were chosen so as to give the ratio $R_{\rm V} \approx 3.1 - 3.2$ for particles with $a/b \approx 1$. This occurs if $r_{V,\rm min} = 0.010\mu$m, $r_{V,\rm max} = 0.25$ μm, and $q = 2.5$ for particles from astrosil and $r_{V,\rm min} = 0.001$ μm, $r_{V,\rm max} = 0.25$ μm, and $q = 4.0$ for particles from AC-Be. Some results are plotted in Figs. 2 and 3. They show the polarizing efficiency $P_{\rm max}/E({\rm B-V})$ as a function of the angle Ω and the degree of alignment δ_0. The colour excess $E({\rm B-V})$ was found by averaging over the B and V filter passbands taken from [12].

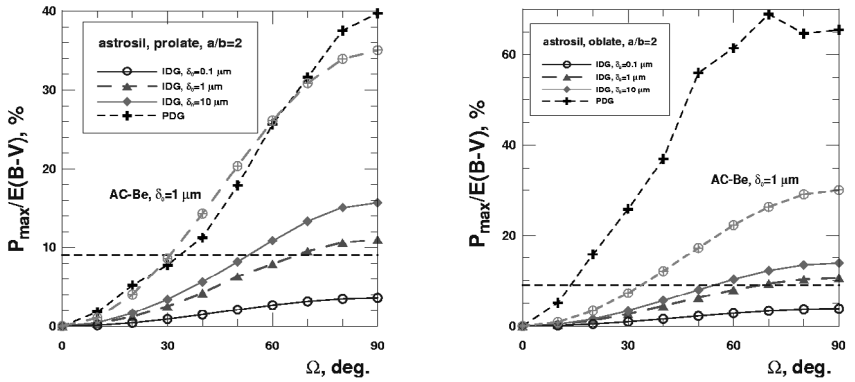

Figure 2. Polarizing efficiency dependence on angle between the line of sight and the magnetic field. The results are plotted for prolate (left) and oblate (right) spheroids from astrosil with imperfect (IDG) and perfect (PDG) Davis-Greenstein orientation. The horizontal line shows the observational upper limit as given by Eq. 2.

As expected, the polarizing efficiency grows with increasing Ω, δ_0, and a/b (Figs. 2 and3). At the same time, a difference is seen between the polarizing properties of the prolate and oblate spheroids. Partially aligned oblate particles only slightly polarize transmitted radiation if $\Omega \lesssim 40^\circ - 50^\circ$ (Fig. 2, right panel). This is true for silicate and carbon particles. If the aspect ratios of prolate and oblate particles are the same, then similar polarization can be reached if the degree of alignment for oblate particles is higher than that for prolate particles.

Note that $\lambda_{\rm max}$ is mainly determined by grain size and shape and weakly depend on the alignment parameters. The resulting relationships will be applied in detailed comparison of

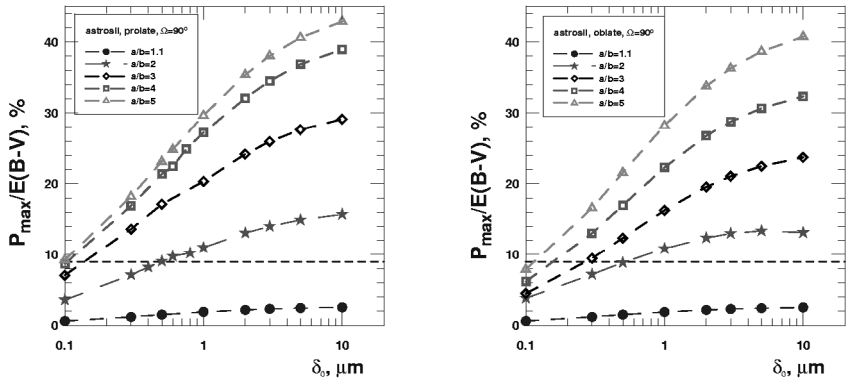

Figure 3. Polarizing efficiency dependence on the degree of alignment. The results are plotted for prolate (left) and oblate (right) spheroids from astrosil with IDG orientation. The horizontal line shows the observational upper limit as given by Eq. 2.

the theory with observations.

Acknowledgments: The work was partly supported by the grants RFBR 07-02-00831, RFBR 10-02-00593a, NTP 2.1.1/665 and NSh 1318.2008.2.

REFERENCES

[1] K. Serkowski, D.S. Mathewson and V.L. Ford. Wavelength dependence of interstellar polarization and ratio of total to selective ratio. ApJ **196** (1975).

[2] D.C.B. Whittet. *Dust in the Galactic Environments*. Institute of Physics Publishing, Bristol (2nd ed.) (2003).

[3] N.V. Voshchinnikov. Determination of dust properties and magnetic fields from polarimetric and photometric observations of stars. Astron. Nachr. **310** (1989).

[4] Yu.S. Efimov. Interstellar polarization: new approximation. Bull. CrAO **105** (2009).

[5] N.V. Voshchinnikov and H.K. Das. Modelling interstellar extinction and polarization with spheroidal grains. JQSRT **109** (2008).

[6] H.K. Das, N.V. Voshchinnikov, and V.B. Il'in. Interstellar extinction and polarization — A spheroidal dust grain approach perspective. MNRAS **404** (2010).

[7] P.G. Martin. *Cosmic Dust*. Oxford Univ. Press, Oxford (1978).

[8] C. Rogers and P.G. Martin. On the shape of interstellar grains. ApJ **228** (1979).

[9] B.T. Draine and A.A. Fraisse. Polarized far-infrared and submillimeter emission from interstellar dust. ApJ **696** (2009).

[10] B.T. Draine. Scattering by interstellar dust grains. II. X-rays. ApJ **598** (2003).

[11] V.G. Zubko, V. Menella, L. Colangeli, and E. Bussoletti. Optical constants of cosmic carbon analogue grains - I. Simulation of clustering by a modified continous distribution of ellipsoids. MNRAS **282** (1996).

[12] V. Straizys. *Multicolor Stellar Photometry*. Pachart Publ. House, Tucson (1992).

Differentiating between sintered and non-sintered aggregates

T. Wriedt[*,1], J. Wilkens[2], and J. Hellmers[2]

[1]*Institut für Werkstofftechnik, Badgasteinerstr. 3, 28359 Bremen, Germany.*
[2]*University of Bremen, FB4, PO Box 330440, 28334 Bremen, Germany.*

Through light-scattering simulation we investigate whether measurement of the extinction spectrum can be used to characterize the morphology of sintered aggregates and whether we can distinguish between sintered and non-sintered aggregates.

INTRODUCTION

Methods for the quantitative assessment of the sintering morphology of aggregates are of recent interest in aerosol science. If aggregates are sintered, mechanical stability is improved. Additionally with conducting aggregates electrical conductivity is improved.

There are various experimental methods to characterize the state of sintering of aggregates that are based on impaction experiments [1]. If an aggregate hits a plane it will break into a number of subcomponents depending on whether the primary particles are sintered together or not. In this way one can distinguish soft and hard aggregates. An optical method for characterization would be of advantage because it is noninstrusive and could be used in process control.

Optical methods for the characterization of aggregates of nanoparticles commonly involve scattering measurements at multiple wavelengths. Using light-scattering simulation we investigate whether spectrally resolved scattering can be used to differentiate between sintered and non-sintered titania (TiO_2) aggregates.

SINTERING

In order to generate aggregates of spheres on the computer, a Diffusion Limited Aggregation (DLA) algorithm has been used [2]. The algorithm starts with a fixed particle in the origin of the coordinate system. Additional particles are then positioned individually on a starting radius and then start a so-called random walk to model Brownian motion. If a particle hits the first particle or the growing cluster it will stick and a new particle will start is walk. In this way realistic aggregates consisting of 24 primary particles are produced.

Next some sintering method is needed to produce sintered aggregates on the computer. The morphological transformation of an aggregate during sintering is driven by minimization of the free energy of the aggregate by surface reduction. To model this process we use a

* Corresponding author: Thomas Wriedt (thw@iwt.uni-bremen.de)

phenomenological method. This phenomenological method is based on the Metaball algorithm [3]. In the Metaball algorithm all primary particles are replaced by a potential function positioned at the centre of the every particle. The strength of the potential field decreases with the distance to the centre of the particles. The potential functions of neighboring primary particles overlap. Next a threshold is introduced in such a way that volume will be generated if the total potential field is higher than this threshold. The exact value of the threshold is chosen such that the generated boundary resembles a sintered aggregate. Additionally some small amount of shrinkage is introduced such that the total volume of the sintered aggregate is kept constant. To characterize the degree of sintering by a suitable parameter the ratio of the surface area of the sintered to the surface area of the non-sintered aggregate is used A/A_0.

For the sample computation we use the following parameters, radius of primary particles r = 25 nm, fractal dimension D_f = 1.8, number of primary particles N = 24. Fig. 1a gives the shape of a non-sintered DLA aggregate. An exemplary figure of the three dimensional shape of a sintered aggregate is shown in Fig. 1b. This aggregate has an intermediate sinter parameter A/A_0 = 0.86.

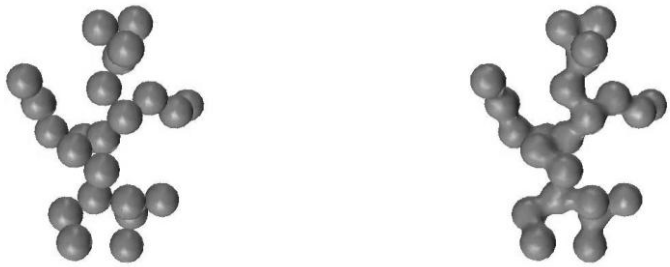

Figure 1. a) Shape of DLA aggregate, r = 25 nm, D_f = 1.8, N = 24. **b)** Shape of sintered aggregate with sinter parameter A/A_0 = 0.86.

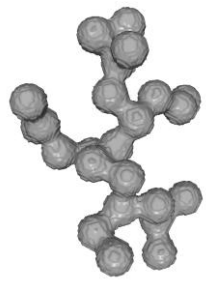

Figure 2. DDSCAT shape data of sintered aggregate of Fig. 1b.

LIGHT SCATTERING COMPUTATION

Next we present some computational results of the extinction spectra of sintered and non-sintered aggregates. For the aggregate material we use titania. The refractive index of titania used for the scattering computations is plotted in Fig. 3.

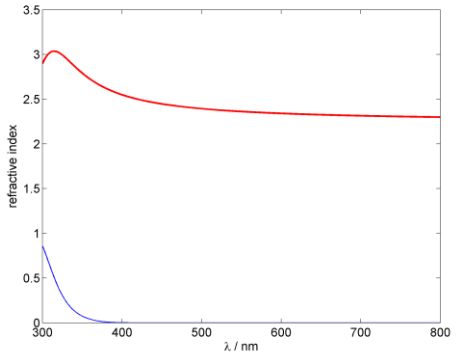

Figure 3. Refractive index of titania. Real part: red, imaginary part: blue.

To compute light scattering, DDSCAT has been applied. For the discretization a grid spacing of 3nm has been used. The input DDSCAT shape data used for the sintered aggregate is visualized in Fig 2. DDSCAT has been validated by comparing to results computed via the NFM-DS [4] for an aggregate of titania spheres. In Fig. 4 the orientationally averaged scattering efficiency of the sample aggregate with two degrees of sintering is plotted. One can see that depending on the degree of sintering the maximum is shifted to shorter wavelength.

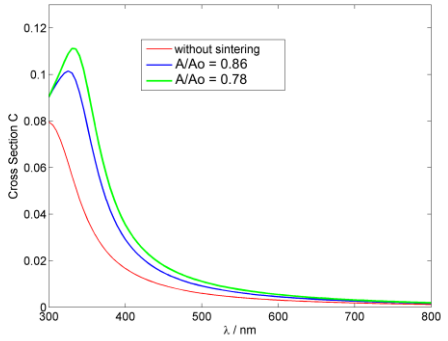

Figure 4. Computed extinction cross section for a non-sintered and a sintered aggregate with sinter parameters A/A_0 = 0.86 and 0.78.

In Figure 5 the position of this maximum is plotted versus the sintering parameter A/A_0. One can see that there is an almost linear relation between the position of this maximum and the sintering parameter.

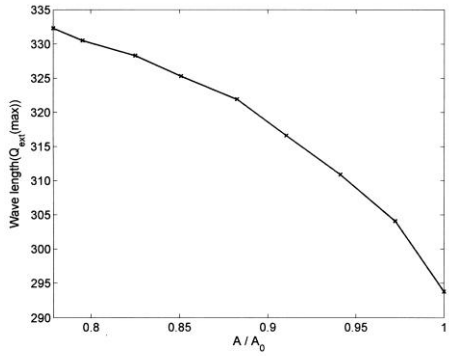

Figure 5. Position of maximum in computed extinction cross section versus sintering parameter.

CONCLUSION

Using light-scattering simulation the spectral extinction of sintered and non-sintered aggregates of titania has been investigated. There is a shift in the extinction curves such that we hope to be able to develop a spectral method for characterization of the state of sintering of aggregates.

REFERENCES

[1] M. Seipenbusch, P. Toneva, W. Peukert, and A. P. Weber. Impact fragmentation of metal nanoparticle agglomerates. Part. Part. Syst. Charact. **24** (2007).

[2] N. Riefler, S. di Stasio, and T. Wriedt. Structural analysis of clusters using configurational and orientational averaging in light scattering analysis. JQSRT **89** (2004).

[3] B. G. Graves. The magic of metaballs. Computer Graphics World **16** (1993).

[4] T. Wriedt and R. Schuh. Decompositioning method to compute scattering by complex shaped particles using a multiple scattering *T*-matrix approach. JQSRT **109** (2008).

Light scattering simulations with the discrete dipole approximation

M. A. Yurkin*

Institute of Chemical Kinetics and Combustion SB RAS, Institutskaya 3, 630090, Novosibirsk, Russia.
Novosibirsk State University, Pirogova 2, 630090, Novosibirsk, Russia.

The discrete dipole approximation (DDA) is reviewed, discussing both theoretical and numerical aspects. Existing applications and capabilities of the method are shown, as well as its place among other methods of light scattering simulation. Finally, remaining challenges are pointed out.

INTRODUCTION

DDA is a general method to compute scattering and absorption of electromagnetic waves by particles of arbitrary geometry and composition. The Maxwell equations are solved in the frequency domain employing volume discretization. Initially DDA was proposed by Purcell and Pennypacker (PP) [1], who replaced the scatterer by a set of dipoles. These dipoles interact with each other and the incident field, giving rise to a system of linear equations, which is solved to obtain dipole polarizations. All measured scattering quantities can be obtained from these polarizations. This approach was further developed and popularized by Draine and coworkers (see e.g. [2]) and others.

Due to its conceptual simplicity and public availability of efficient computer implementations, DDA has gained popularity in many practical applications. An extensive review of DDA, including both theoretical and computational aspects, was recently performed by Yurkin and Hoekstra [3]. This paper is based on this review but also includes a discussion of the most recent advances and challenges in this field. Due to space limitations, I discuss only those references that were not discussed in the review.

THEORETICAL FORMULATION AND NUMERICAL CONSIDERATIONS

Considering a physical picture of the point dipoles, "the DDA equations" can be derived, one of the equivalent forms of which is the following:

$$\mathbf{P}_i = \overline{\boldsymbol{\alpha}}_i \left(\mathbf{E}_i^{\mathrm{inc}} + \sum_{j \neq i} \overline{\mathbf{G}}_{ij} \mathbf{P}_j \right), \qquad (1)$$

* Maxim A. Yurkin (yurkin@gmail.com)

where $\mathbf{P}_i$ and $\overline{\boldsymbol{\alpha}}_i$ are the polarization vector and polarizability tensor of the i-th dipole , $\mathbf{E}_i^{\text{inc}}$ is the incident field at the center of this dipole, and $\overline{\mathbf{G}}_{ij}$ is the Green's tensor describing the interaction between any two dipoles. Material properties (e.g. any distribution of the refractive index in the scatterer) are fully contained in the values of $\overline{\boldsymbol{\alpha}}_i$. DDA (and Eq. (1) in particular) can be derived from the integral equation for the electric field, which is discretized by dividing the scatterer into small cubical subvolumes. This gives more mathematical insight into the approximation, pointing at ways to improve the method.

The original PP formulation is based on the expressions for $\overline{\boldsymbol{\alpha}}_i$ and $\overline{\mathbf{G}}_{ij}$, obtained in the limit of point (infinitely small) dipoles separated by finite distances. All formulations of DDA thereafter modify expressions for $\overline{\boldsymbol{\alpha}}_i$ and/or $\overline{\mathbf{G}}_{ij}$. Here I mention only a few of them: 1) the lattice dispersion relation (LDR) is the most widely used DDA formulation, which adds corrections to the polarizability of the order of dipole size parameter squared; 2) filtered coupled dipoles (FCD) and the integration of Green's tensor (IGT) are rather recent formulations, which modify expression for $\overline{\mathbf{G}}_{ij}$ based on the sampling theorem and integration of the Green's tensor over the cubical subvolume, respectively.

More generally, DDA belongs to a broad range of method of moments, applied to the volume integral equation for the electric fields, which are actively discussed in the electrical engineering community. Unfortunately, the latter is almost independent from the ELS community, making it hard to compare DDA with similar methods.

The main numerical challenge is the solution of a system of linear equations in Eq. (1), the total number of which is three times the number of dipoles. The important advantage of DDA is that this system can be solved in $O(N \ln N)$ operations, which allows one to consider scatterers described by up to a *billion* dipoles on a modern supercomputer. This surprising speed is due to 1) using an iterative solver, which usually converges after much fewer than N iterations (N_{it}); 2) using FFT to compute the convolution-like matrix-vector product in $O(N \ln N)$ operations. The latter employs the special structure of DDA interaction matrix resulting from translation invariance of $\overline{\mathbf{G}}_{ij}$ and placing dipoles on a regular rectangular lattice. The regular dipole grid is, however, a significant limitation in terms of possible DDA improvements. In particular, dipole sizes and locations cannot be varied individually to better describe particle shape. This limitation is removed by a fast multipole method (FMM), an alternative to FFT acceleration, which potentially has the same order of operations. However, the FMM is not likely to be implemented in any production DDA code in the near future due to its complexity.

The overall time of a DDA simulation is largely determined by N_{it}, which increases with size and refractive index of the scatterer and depends on the choice of iterative solver and DDA formulation. Although it is almost impossible to predict N_{it} *a priori* for a particular scattering problem, existing benchmark studies may help to estimate this quantity and to choose a suitable iterative solver. Moreover, N_{it} only slightly depends on the number of dipoles; hence, refining discretization for a fixed scattering problem implies predictable costs of computer resources.

APPLICATIONS AND COMPARISON WITH OTHER METHODS

Being suitable for scatterers in a wide range of size and refractive index and with any internal structure, DDA has found numerous applications in different fields of science. Originally, the driving application was remote sensing in astrophysics [1,2] (interstellar and interplanetary dust, surfaces of atmosphereless Solar system bodies, etc.) and planetary atmospheres (e.g., mineral aerosols [4] and hydrometeors). Applications involving biological cells (from bacteria to human blood cells [5]) have pushed DDA to supercomputers and size parameters above 100 (for index-matching scatterers).

Another class of applications, requiring supercomputers, involves particles near plane interfaces (e.g. silver nanospheres on a dielectric substrate, covered by a thin liquid layer) and porous layers or rough surfaces (e.g. paper coatings and paint pigments). The complexity of these problems is caused by direct discretizations of the large part of the plane medium. In some cases the latter can be avoided using a different expression for $\overline{\mathbf{G}}_{ij}$, based on the electric field of a point dipole in the presence of the plane interface. However, this has certain drawbacks in terms of fast evaluation of the matrix-vector product and the only code, featuring this improvement, is not publicly available [6].

Probably the most frequent application of DDA nowadays is simulating optical properties of metal nanoparticles [7]. In this field DDA is often considered as a "black box" that is supposed to always produce correct numerical results. However, gold and silver (especially in the IR range) are far from the well-proven range of DDA applicability ($|m-1|<2$). This may cause large simulation times and low accuracy, which should be carefully considered in applications [8]. Moreover, the choice of DDA formulation is more important, since e.g. the FCD may largely outperform the LDR in certain cases.

The reverse of the DDA wide applicability range in terms of scatterer morphology is its very limited ability to employ particle symmetries. Therefore, DDA may be not the best option for axisymmetric homogeneous scatterers, for which surface-based methods, such as extended boundary condition (a.k.a. null-field or T-matrix) or discrete sources methods, are more suitable. However, for very large scatterers (e.g. red blood cells) the latter methods may have poor accuracy or fail completely, leaving DDA as a preferable option [5].

Homogeneous asymmetric scatterers generally require similar computation times for the DDA and surface-based methods for fixed particle orientation. The latter are faster for simulation of orientation-averaged scattering properties. For general inhomogeneous scatterers the finite difference time domain method is the only viable alternative to DDA. The relative performance of these two methods is mostly determined by the refractive index. In particular, DDA is faster for index-matching particles.

The increase of DDA applicability to scatterers much larger than the incident wavelength allowed breaching the gap between "rigorous" and geometrical optics methods [4]. The agreement between the two methods in the intermediate size range is good, although it was shown only for orientation-averaged integral scattering quantities.

CONCLUSION

DDA is the method of choice for many light scattering applications, featuring a solid theoretical base, a large volume of benchmark data, and efficient publicly available computer codes. However, a number of challenges still remain: 1) theoretical improvements of the DDA formulation, especially for large refractive indices; 2) numerical improvements, in particular different iterative solvers and/or preconditioners; 3) implementation of existing ideas in the publicly available codes. The latter ideas include, e.g., weighted discretization and Green's tensor for particles near the plane interface.

ACKNOWLEDGMENTS

I would like to thank Alfons Hoekstra for introducing me to the beautiful world of DDA and for many fruitful discussions we had on this subject. I also thank Evgenij Zubko for his comments. This research is supported by the Russian Government "Research and educational personnel of innovative Russia" (contract P2497).

REFERENCES

[1] E.M. Purcell and C.R. Pennypacker. Scattering and adsorption of light by nonspherical dielectric grains. Astrophys. J. **186** (1973).

[2] B.T. Draine and P.J. Flatau. Discrete-dipole approximation for scattering calculations. J. Opt. Soc. Am. A **11** (1994).

[3] M.A. Yurkin and A.G. Hoekstra. The discrete dipole approximation: an overview and recent developments. J. Quant. Spectrosc. Radiat. Transfer **106** (2007).

[4] L. Bi, P. Yang, G.W. Kattawar, and R. Kahn. Modeling optical properties of mineral aerosol particles by using nonsymmetric hexahedra. Appl. Opt. **49** (2010).

[5] K.V. Gilev, E. Eremina, M.A. Yurkin, and V.P. Maltsev. Comparison of the discrete dipole approximation and the discrete source method for simulation of light scattering by red blood cells. Opt. Express **18** (2010).

[6] E. Bae, H. Zhang, and E.D. Hirleman. Application of the discrete dipole approximation for dipoles embedded in film. J. Opt. Soc. Am. A **25** (2008).

[7] C. Ungureanu, R.G. Rayavarapu, S. Manohar, and T.G. van Leeuwen. Discrete dipole approximation simulations of gold nanorod optical properties: Choice of input parameters and comparison with experiment. J. Appl. Phys. **105** (2009).

[8] M.A. Yurkin, D. de Kanter, and A.G. Hoekstra. Accuracy of the discrete dipole approximation for simulation of optical properties of gold nanoparticles. J. Nanophoton. **4** (2010).

Electromagnetic scattering by an inhomogeneous circular cylinder using fast convergent series expansions

G. P. Zouros* and G. D. Tsogkas

School of Electrical and Computer Engineering, National Technical University of Athens, 15780, Zographou, Athens, Greece.

In this paper we examine the scattering of a TM plane wave by an infinite circular cylinder having inhomogeneous optical properties e.g. ρ–varying permittivity $\epsilon(\rho)$. The method is based on constructing the volume integral equation and then expanding the unknown functions in Dini's series, which have the characteristic of being fast convergent. Numerical results are given for the various values of the parameters.

INTRODUCTION

Electromagnetic scattering problems of main interest are those which present structures having irregular optical properties. In [1], a circular cylinder with inhomogeneous cladding is examined using electric and magnetic current distributions while in [2], scattering from inhomogeneous bodies using a new boundary method is presented.

In the present work we study the scattering of a TM plane wave by a circular infinite dielectric cylinder of radius a with varying permittivity $\epsilon(\rho)$. The geometry of the scatterer is shown in Fig. 1.

In nonhomogeneous media, Helmholtz equation has the extra term [3] $\nabla[2\,\nabla n(\vec{r}) \cdot \vec{E}(\vec{r})/n(\vec{r})]$, with $n(\vec{r})$ being the refraction index of the medium. By selecting a slow varying profile for $n(\vec{r})$, the term can be omitted and therefore, this concession leads to the well known homogeneous Helmholtz equation. Then we try to solve it by constructing the volume integral equation.

E-WAVE POLARIZATION

Formulation of the problem

By applying the surface equivalence theorem [4] to the configuration of Fig. 1 and then, by making use of the reaction theorem [4], one can arrive at the desired integral equation

$$E_z(\vec{\rho}) = E_z^{\text{inc}}(\vec{\rho}) + j\frac{k_1^2}{\omega\mu_1}\iint_S \left[\frac{k_2^2(\rho')}{k_1^2} - 1\right] E_z(\vec{\rho}')G(\vec{\rho};\vec{\rho}')\,d\alpha' \tag{1}$$

In order to come to (1), both permeabilities of the two regions, as shown in Fig. 1, should be equal, otherwise another integral term in (1) should be placed which complicates the problem. Because of the infinite length along z axis, volume integral has been replaced by a surface one. In (1) S is the surface of inhomogeneity, $k_{1,2}$ is the wavenumber of outer and inner region respectively, $G(\vec{\rho};\vec{\rho}')$ is the free space cylindrical Green's function [4] while $E_z(\vec{\rho})$ is the unknown field. If $\vec{\rho} \in S$ then $E_z(\vec{\rho})$ represents the stationary field inside the cylinder; if $\vec{\rho} \notin S$ then $E_z(\vec{\rho})$ represents the total field outside the cylinder.

*Corresponding author: Grigorios P. Zouros (zouros@mail.ntua.gr)

Expansion of the fields

The incident plane wave illuminates the cylinder normally on the z axis and is impinging with an incident angle of zero degrees. Therefore is has the form [5]

$$E_z^{\text{inc}}(\vec{\rho}) = \sum_{m=0}^{\infty} \varepsilon_m \, j^{-m} J_m(k_1\rho)\cos(m\varphi) \tag{2}$$

where ρ and φ are the polar coordinates with respect to xOy, J_m is the cylindrical Bessel function of the first kind and ε_m is the Neumann factor ($\varepsilon_0 = 1$, $\varepsilon_n = 2,\ n \geq 1$). The unknown field is expressed in the form

$$E_z(\vec{\rho}) = \sum_{m=0}^{\infty} R_m(\rho)\cos(m\varphi) \tag{3}$$

where $R_m(\rho)$ is the unknown radial function to be evaluated. Then, by substituting (2) and (3) into (1) and applying orthogonality relations for cosines, we arrive at the following integral equation

$$\begin{aligned} R_m(\rho) =& \varepsilon_m \, j^{-m} J_m(k_1\rho) \\ &+ \frac{k_1^2 \pi \varepsilon_m (3-\varepsilon_m)}{4j} \int_0^a \left[\frac{\epsilon_2(\rho')}{\epsilon_1} - 1\right] R_m(\rho') J_m(k_1\rho^<) H_m(k_1\rho^>) \rho' \, d\rho' \end{aligned} \tag{4}$$

where H_m is the Hankel function of the second kind while $\rho^< = \min(\rho, \rho')$ and $\rho^> = \max(\rho, \rho')$.

Expansion in Dini's series

We expand the radial functions in (4) in Dini's series as follows

$$\left[\frac{\epsilon_2(\rho)}{\epsilon_1(\rho)} - 1\right] R_m(\rho) = \sum_{\ell=1}^{\infty} A_{m\ell} J_m\left(\frac{\gamma_{m\ell}}{a}\rho\right), \tag{5}$$

$$R_m(\rho) = \sum_{\ell=1}^{\infty} B_{m\ell} J_m\left(\frac{\gamma_{m\ell}}{a}\rho\right), \text{ and } J_m(k_1\rho) = \sum_{\ell=1}^{\infty} C_{m\ell} J_m\left(\frac{\gamma_{m\ell}}{a}\rho\right). \tag{6}$$

In (5)–(6), $\gamma_{m\ell}$ is the ℓ–th root for every different value of m of the equation [6]

$$\gamma_{m\ell} J_m'(\gamma_{m\ell}) + t_m J_m(\gamma_{m\ell}) = 0 \tag{7}$$

In (7), t_m is an arbitrary parameter (complex number in general) and J_m' is the derivative of Bessel function with respect to its argument.

Solution of the problem

Substituting Dini's series expansions (5)–(6) into (4), putting position vector $\vec{\rho}$ inside the inhomogeneity and using the well known integral of two Bessel functions and a power function [6] as well as Bessel Wronskian relations, one can calculate the unknown coefficients $B_{m\ell}$ of function $R_m(\rho)$ for the internal field by solving the linear systems of equations

$$B_{m\ell} - \sum_{q=1}^{\infty} \left\{ \varepsilon_m \, j^{-m} C_{m\ell} M_{mq} + \frac{(k_1 a)^2}{2} \frac{\varepsilon_m(3-\varepsilon_m)}{N_{m\ell}\left[\gamma_{m\ell}^2 - (k_1 a)^2\right]} G_{m\ell q} \right\} B_{mq} = \varepsilon_m \, j^{-m} C_{m\ell} \tag{8}$$

for $\ell = 1, 2, 3, \ldots$ and for every different value of $m = 0, 1, 2, \ldots$.
In (8), $C_{m\ell}$, $N_{m\ell}$ and M_{mq} are known analytical expressions while $G_{m\ell q}$ is defined by the integral over the inhomogeneity $G_{m\ell q} = \int_0^a \left[k_2^2(\rho)/k_1^2 - 1\right] J_m(\gamma_{mq}\rho/a) J_m(\gamma_{m\ell}\rho/a)\rho\, d\rho$ and is evaluated numerically for every different permittivity profile $\epsilon_2(\rho)$.

The scattered far field

By putting the position vector $\vec{\rho}$ outside the inhomogeneity and carrying out the calculations in (4), we obtain the unknown function $R_m(\rho)$ when $\rho > a$

$$R_m(\rho) = \varepsilon_m\, j^{-m} J_m(k_1\rho) + \frac{k_1^2\pi\varepsilon_m(3-\varepsilon_m)}{4j} H_m(k_1\rho) \sum_{\ell=1}^{\infty} C_{m\ell} \sum_{q=1}^{\infty} G_{m\ell q} B_{mq} \qquad (9)$$

Using now the asymptotic expansion for the Hankel function in (9), we can calculate the cross section [4] by $\sigma_b = \lim_{\rho\to\infty} \left(2\pi\rho\, |E_z^{\text{sc}}|^2/|E_z^{\text{inc}}|^2\right)$ and therefore obtain

$$k_1\sigma_b = \frac{(k_1 a)^4}{4}\pi \sum_{m=0}^{\infty} \varepsilon_m\, (3-\varepsilon_m)\, j^m \cos(m\phi) \sum_{\ell=1}^{\infty} C_{m\ell} \sum_{q=1}^{\infty} G_{m\ell q} B_{mq} \qquad (10)$$

Acceleration of convergence

It is apparent from (10) that, in order to calculate $k_1\sigma_b$, the coefficients B_{mq} of the internal field are required. Carrying out asymptotic analysis for B_{mq} reveals that $B_{mq} = O(q^{-3/2})$ for arbitrary values of t_m while, by putting in t_m a special value, it emerges that $B_{mq} = O(q^{-7/2})$. Therefore the series in (10) are optimized and converge faster. The aforementioned special value is obtained from (9) and is [7] $-aR'_m(a)/R_m(a)$ with $R'_m(a)$ being the derivative of (9) with respect to ρ at $\rho = a$.

NUMERICAL RESULTS AND DISCUSSION

In Table 1, the values of back and forward scattering cross section are given for various values of $k_1 a$ and for $\epsilon_2(\rho)/\epsilon_1 = 2.45 + 0.5\sin(\pi\rho/a + 0.5)$. We have also compared and verified some results of our method to a high degree of accuracy with the analytical procedure presented in [2].

In Fig. 2, the bistatic scattering cross section is plotted for observation angles from 0° to 180°. This is done for two different permittivity profiles, linear and sinusoidal, and for various values of $k_1 a$. The results are symmetric about $\varphi = 180^\circ$ as it is imposed by the geometry of the scatterer. We also observe the high sensitivity of $k_1\sigma$ to the change of observation angle φ.

In Fig. 3, we depict the behaviour of convergence for the sum versus q in (10) using the optimum and an arbitrary value for t_m. The desired accuracy is achieved with much less terms, when we use the optimum values for t_m in (7) for finding the roots $\gamma_{m\ell}$.

It is noticed that we have verified analytically the known solution, when permittivity profile is constant [4] for arbitrary values of t_m. Finally, this method can be expanded for permittivity profiles which depend on both ρ and φ.

Acknowledgments: This work was supported by the Program of Basic Research PEBE 2007 of NTUA.

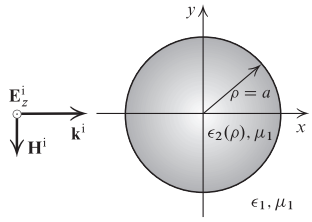

Figure 1: The geometry of the scatterer.

Table 1: Values of back and forward scattering cross section for $\epsilon_2(\rho)/\epsilon_1 = 2.54 + 0.5\sin(\pi\rho/a + 0.5)$ and comparison with others.

$k_1 a$	$k_1\sigma_{\mathrm{b}}$ $(\varphi = 180^\circ)$	$k_1\sigma_{\mathrm{f}}$ $(\varphi = 0^\circ)$
3.4π	17.585	4.3927
3.6π	36.495	8.6822
3.8π	48.287	1.2574

Comparison: $|E_z^{\mathrm{sc}}|$ at $\rho/a = 2, \varphi = 0^\circ$ for $\epsilon_2(\rho)/\epsilon_1 = 1 + \beta(\rho/a)^2$

$k_1 a$	β	This paper	[2]
1.4π	1.2	1.88669509	1.88669443
2.4π	1	2.445371720	2.445359179

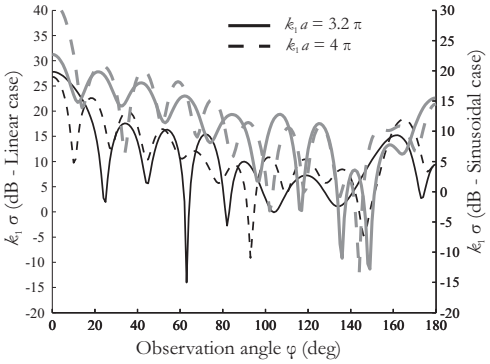

Figure 2: Normalized cross section in dB $[10\log(k_1\sigma)]$. Linear case (black lines): $\epsilon_2(\rho)/\epsilon_1 = 2.54 + \rho/a$. Sinusoidal case (gray lines): $\epsilon_2(\rho)/\epsilon_1 = 2.54 + 0.5\sin(\pi\rho/a + 0.5)$.

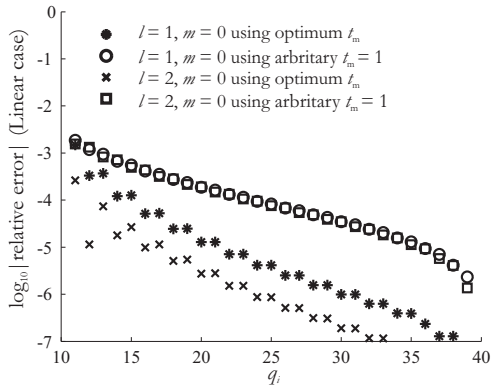

Figure 3: $\log_{10}|\sum_{q=1}^{q_{\max}} G_{m\ell q}B_{mq} - \sum_{q=1}^{q_i} G_{m\ell q}B_{mq}/\sum_{q=1}^{q_{\max}} G_{m\ell q}B_{mq}|$ in (10) for $\epsilon_2(\rho)/\epsilon_1 = 2.54 + \rho/a$ and for $k_1 a = 4\pi$.

REFERENCES

[1] C. A. Valagiannopoulos. Arbitrary Currents on Circular Cylinder with Inhomogeneous Cladding and RCS Optimization. J. of Electromagn. Waves and Appl. **21**(5) (2007).

[2] S. Yu. Reutskiy and B. Tirozzi. A New Boundary Method for Electromagnetic Scattering from Inhomogeneous Bodies. JQSRT **72** (2002).

[3] M. S. Sodha and A. K. Ghatak. *Inhomogeneous Optical Waveguides*. Plenum Press, New York (1977).

[4] C. A. Balanis. *Advanced Engineering Electromagnetics*. John Wiley and Sons (1989).

[5] J. A. Stratton. *Electromagnetic Theory*. McGraw-Hill, New York (1941).

[6] G. N. Watson. *A Treatise on the Theory of Bessel Functions*. Cambridge University Press (1995).

[7] G. C. Kokkorakis, J. G. Fikioris, and G. Fikioris. Field Induced in Inhomogeneous Spheres by External Sources. J. Acoust. Soc. Am. **112**(4) (2002).

The Umov effect applied to single particles

E. Zubko[*,1,2], G. Videen[3], Yu. Shkuratov[2], K. Muinonen[1,4], and T. Yamamoto[5]

[1]*Department of Physics, P.O. box 64, FI-00014 University of Helsinki, Finland.*
[2]*Institute of Astronomy, Kharkov National University, 35 Sumskaya St., Kharkov, 61022, Ukraine.*
[3]*Space Science Institute, 4750 Walnut Street, Suite 205, Boulder, CO 80301 USA.*
[4]*Finnish Geodetic Institute, P.O. box 15, FI-02431 Masala, Finland.*
[5]*Institute of Low Temperature Science, Hokkaido University, Kita-ku North 19 West 8, Sapporo 060-0819, Japan.*

We study the Umov effect as applied to single irregularly shaped particles comparable with wavelength. For these particles an inverse correlation between geometric albedo and maximum of positive polarization at large phase angles does exist; however, it takes a form different from what was found for planetary regoliths. The difference is substantially caused by contribution of relatively small particles with $x < 14$.

INTRODUCTION

The Umov effect refers to the inverse correlation between geometric albedo (albedo_G) and the amplitude of the maximum of linear polarization (P_{max}) of sunlight scattered from rough surfaces. It is being exploited in astronomical studies of the Solar system objects, such as asteroids, atmosphereless planets, and moons. This correlation is valid over a wide range of albedo (e.g., [1]), including relatively dark objects, like the Moon, whose average albedo is about 12%. For such dark surfaces, one expects a relatively small contribution of multiple scattering between constituent particles and a greater role of the first scattering order than for brighter objects. Therefore, one can extrapolate that if a dark regolith shows the Umov effect, then single constituent particles forming that regolith should show the effect, too.

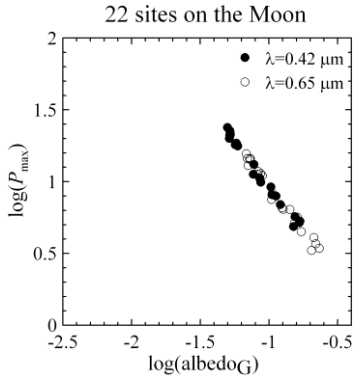

Figure 1. Diagram $\log(P_{max})$ vs. $\log(\text{albedo}_G)$ for 22 sites on the Moon [1].

* Corresponding author: Evgenij Zubko (ezubko@rambler.ru)

One unknown is the mathematical relationship the Umov effect takes in the case of single dust particles comparable with the wavelength. In the case of a regolith, a linear relation exists between $\log(P_{max})$ and $\log(\text{albedo}_G)$. Figure 1 shows such a diagram for 22 various sites of the Moon (data adopted from [1]).

TECHNIQUE AND DETAILS OF CALCULATION

We compute light-scattering properties of irregularly shaped particles using the discrete dipole approximation (DDA) (e.g. [2]), and we use the algorithm developed by Zubko et al. [3]. We consider agglomerated debris particles, whose generation is described in [3]. These irregular particles are fluffy in nature, having a material density of approximately 25 % of the volume of a circumscribing sphere. Note that such features are thought to be quite relevant for a model of cosmic dust and regolith particles. We consider light-scattering properties that are well averaged over sample shapes; in each case, at least 500 shapes have been considered. In many cases this number is significantly larger to make the results statistically reliable. Detail on averaging can be found in [3]. We consider homogeneous materials having one of 15 different refractive indices m, representative of materials in cometary dust and regoliths of atmosphereless celestial bodies: $m = 1.2 + 0i$, $1.313 + 0i$, $1.313 + 0.1i$, $1.4 + 0i$, $1.5 + 0i$, $1.5 + 0.02i$, $1.5 + 0.1i$, $1.6 + 0.0005i$, $1.6 + 0.01i$, $1.6 + 0.02i$, $1.6 + 0.05i$, $1.6 + 0.1i$, $1.7 + 0i$, $1.7 + 0.1i$, and $1.758 + 0.0844i$. We classify all these materials into two groups for convenience: highly absorbing ($\text{Im}(m) > 0.02$) and weakly absorbing ($\text{Im}(m) \le 0.02$) materials. Another parameter important for light scattering is the size parameter $x = 2\pi r/\lambda$, where r is the radius of the circumscribing sphere and λ is the wavelength of the incident radiation. Through this study, the size parameter x has been varied from 2 to 40.

RESULTS AND DISCUSSION

The definition of albedo for single particles is different from that of regoliths. Indeed, the geometric albedo does not specify absorption or scattering efficiency: $\text{albedo}_G = (S_{11}\pi)/(k^2 G)$, where S_{11} is the total intensity Mueller matrix element at backscattering, k is the wavenumber, and G is the geometric cross-section of the particle. Instead, it describes only the efficiency of backscattering. The use of single-scattering albedo seems a more reasonable choice for analysis, since it includes the total scattering and not that at an arbitrary angle. In [3] it was shown that the amplitude of positive polarization was inversely correlated with single-scattering albedo over a wider range of $\text{Im}(m)$ than the geometric albedo. However, the use of the single-scattering albedo meets an obvious difficulty when non- or weakly absorbing particles are considered. Indeed, for $\text{Im}(m) = 0$, the single-scattering albedo equals to unity throughout the entire range of size parameter x; whereas, the amplitude of positive polarization dramatically varies over x.

In the upper row of Fig. 2, the diagrams of P_{max} versus the single-scattering albedo are shown; whereas, the bottom row displays similar diagrams for the case of the geometric al-

bedo. The subscripts "S" and "G" designate single-scattering and geometric albedos, respectively. In both cases, the left panel corresponds to highly absorbing materials; whereas, the right panel corresponds to weakly absorbing materials. Arrowed lines show the dependence on the size parameter x. As one can see from Fig. 2, there exists a much stronger inverse correlation of P_{max} with the geometric than the single-scattering albedo, especially for weakly absorbing particles (right bottom panel). In all cases, the relationship depends on the particle size, and only for weakly absorbing particles does there appear to be a functional dependence on P_{max} with albedo$_G$. No functional dependence appears between P_{max} with albedo$_S$; thus, we consider and discuss only the inverse correlation of P_{max} with albedo$_G$.

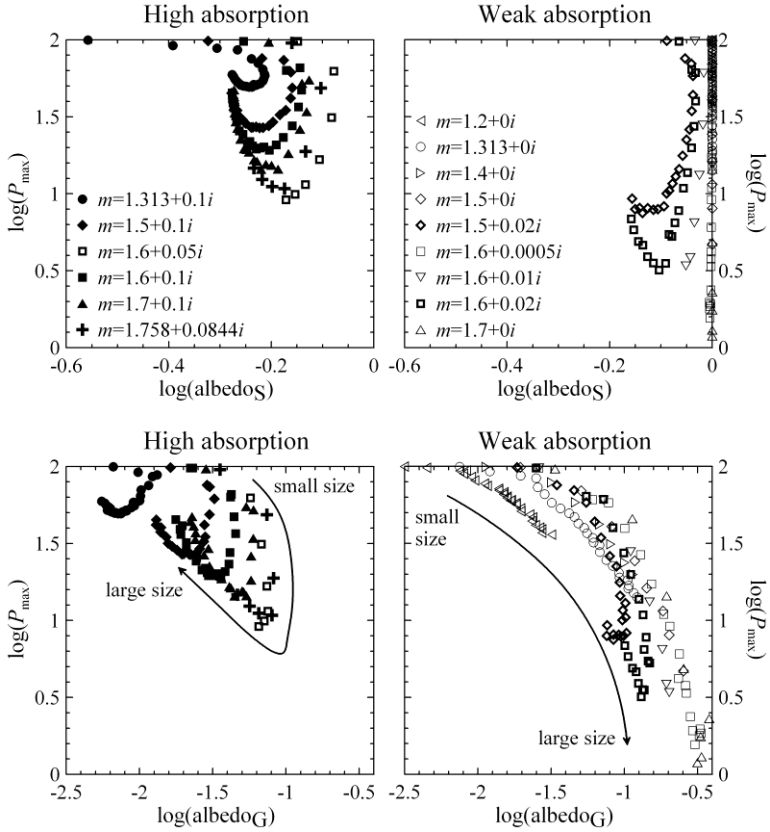

Figure 2. Diagrams log(P_{max}) vs. log(albedo$_S$) (upper row) and log(P_{max}) vs. log(albedo$_G$) (bottom row) for agglomerated debris particles.

When we consider highly absorbing particles, an inflection is clearly seen in the bottom left panel in Fig. 2. One also can be found in the bottom right panel for the cases of m = 1.5 + 0.02i and m = 1.6 + 0.02i. These inflection points depend on the real part of refractive index Re(m); for instance, at Im(m) = 0.1, when varying Re(m) from 1.313 to 1.7, the size parameter of the inflection decreases from about x = 18 to 10. The inflection strongly depends also on Im(m). For example, at Re(m) = 1.6, when varying Im(m) from 0.02 to 0.1 only, its size parameter is decreased from x = 16 to 10. A detection of this inflection point on the P_{max} – albedo$_G$ diagram could be used to retrieve properties of target particles. Such a possi-

bility is especially intriguing for cometary dust particles that are thought to be highly absorbing.

The inverse correlation between $\log(P_{max})$ and $\log(\text{albedo}_G)$ in Fig. 2 is obviously nonlinear. For highly absorbing particles, a minimum appears when the particles are approximately $x = 14$. For larger particles, the relationship is nearly linear. In Fig. 3 we show the combined results of highly and weakly absorbing particles $x > 14$ in the left panel. In the right panel we show just the particles having $x = 14$. In this case, the trend for highly absorbing particles can be distinguished from that for weakly absorbing particles.

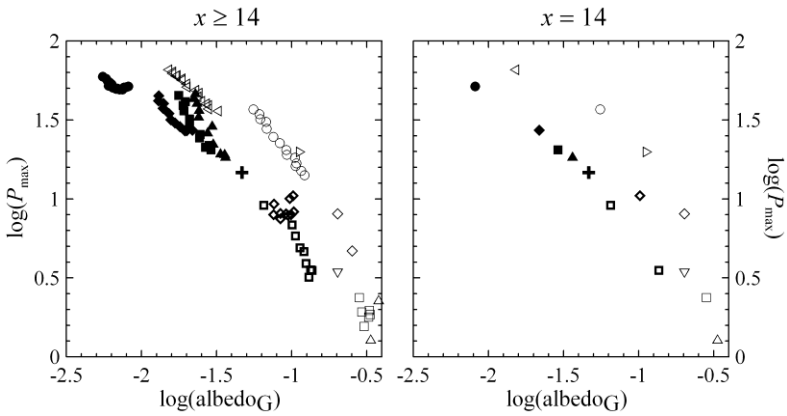

Figure 3. Diagrams $\log(P_{max})$ vs. $\log(\text{albedo}_G)$ for agglomerated debris particles.

Finally, we note that variations of the refractive index m cause the trend line to move on the $\log(P_{max})$ – log (albedo_G) diagrams; whereas, the scatter from this trend line due to variations of the size parameter x are relatively small (compare left and right panels in Fig. 3). This result can potentially assist in characterizing particle composition.

REFERENCES

[1] Yu.G. Shkuratov and N.V. Opanasenko. Polarimetric and photometric properties of the Moon: Telescopic observations and laboratory simulations: 2. The positive polarization. Icarus **99** (1992).

[2] B.T. Draine and P.J. Flatau. Discrete-dipole approximation for scattering calculations. JOSA A **11** (1994).

[3] E. Zubko, H. Kimura, Yu.G. Shkuratov, K. Muinonen, T. Yamamoto, H. Okamoto, and G. Videen. Effect of absorption on light scattering by agglomerated debris particles. JQSRT **110** (2009).

Interpretation of spectro-polarimetry of comet 17P/Holmes during outburst in 2007

E. Zubko[*,1,2], R. Furusho[3], K. S. Kawabata[4], T. Yamamoto[5], K. Muinonen[1,6], and G. Videen[7]

[1]*Department of Physics, University of Helsinki, P.O. box 64, FI-00014 Finland.*
[2]*Institute of Astronomy, Kharkov National University, 35 Sumskaya St., Kharkov, 61022, Ukraine.*
[3]*National Astronomical Observatory of Japan, 2-21-1, Osawa, Mitaka, Tokyo 181-8588, Japan.*
[4]*Hiroshima Astrophysical Science Center, Hiroshima University, 1-3-1 Kagamiyama, Higashi-Hiroshima, 739-8526, Japan.*
[5]*Institute of Low Temperature Science, Hokkaido University, Kita-ku North 19 West 8, Sapporo 060-0819, Japan.*
[6]*Finnish Geodetic Institute, P.O. box 15, FI-02431 Masala, Finland.*
[7]*Space Science Institute, 4750 Walnut Street, Suite 205, Boulder, CO 80301 USA.*

Spectro-polarimetry of comet 17P/Holmes carried out a day after its outburst in October 24, 2007 shows a strong dependence of negative polarization on wavelength λ: while λ increases from 0.5 to 0.9 μm the polarization falls from –0.6% to almost 0. Ten days after the outburst, polarization was found to be approximately -1% for all λ. We found such behavior to be consistent with highly absorbing (e.g., m=1.5+0.1i) agglomerated debris particles that obey a power-law size distribution and have a small-size limit near 0.6 μm.

INTRODUCTION

The outburst of comet 17P/Holmes occurred on October 24, 2007 and, within two days, the apparent total brightness of the comet increased by 630,000 [1]. In this manuscript we present and interpret spectro-polarimetric observations carried out by the "Kanata" group of Hiroshima University. Using the 1.5 m Kanata telescope and spectro-polarimeter operating at a wavelength range of 0.5–0.9 μm [2], comet 17P/Holmes was observed on October 25 (15:15 UT), October 27 (16:24 UT), and November 3 (15:17 UT), during which the phase angle α went from 16.6° on October 25, to 16.1° on October 27, and 14.3° on November 3.

The average linear polarization was measured using a slit with angular length of 17.3 and width of 3.4 arcsecs, corresponding to a projected area of 20500×4000 km^2. The slit was centered on the photometric nucleus of the comet (i.e., the brightest point of halo) and oriented along a north-south direction. Taking into account that even for the earliest observation on October 25, the diameter of the dust halo exceeded 90 arcsecs [3], one can conclude that the measured polarization results primarily from the inner part of the coma.

* Corresponding author: Evgenij Zubko (ezubko@rambler.ru)

Fig. 1 shows spectral profiles of linear polarization of comet 17P/Holmes. At all wavelengths and dates, the degree of linear polarization P is negative. Note that the negative linear polarization at small phase angles is widely observed for comets (e.g., [4]). Interestingly, during the earliest observation, the negative polarization reveals a dependence on wavelength λ: an increase of wavelength from 0.5 to 0.9 μm results in a decrease of the amplitude of negative polarization from 0.6% to almost zero. On October 27, the dependence of polarization on wavelength is weaker than that on October 25. And on November 3, the amplitude of the negative polarization is almost independent of wavelength as polarization P remains approximately -1% throughout the wavelength range. As for dust color, it was red in appearance on October 25 and became redder in later observations. Note, that these findings are qualitatively consistent with other spectro-polarimetric observations of comet 17P/Holmes [5,[6]; whereas, the diversities between them could be explained by different observation conditions.

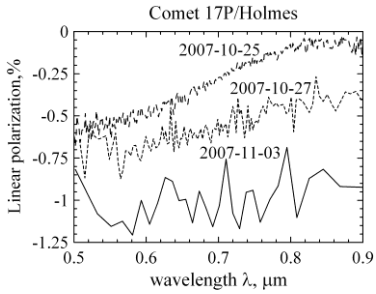

Figure 1. Degree of linear polarization as a function of wavelength for comet 17P/Holmes.

INTERPRETATION OF SPECTRO-POLARIMETRY OF COMET 17P/HOLMES

We model the cometary particles as agglomerated debris [7] and use the discrete dipole approximation (DDA) to calculate their scattering. The particles are non-extremely porous and consist of small irregular constituents. Both features can be seen in images of cometary dust collected in the stratosphere (e.g., [8]). We examine homogeneous agglomerated debris with many different refractive indices m chosen to represent likely cometary materials: water ice, Mg-rich silicates, and organic. We characterize the particles in terms of the size parameter $x = 2\pi r/\lambda$, where r is the radius of the circumscribing sphere for an agglomerated debris particle.

One possible explanation of the spectral behavior of linear polarization of comet 17P/Holmes on October 25 can be ascertained from Fig. 2. We see that the evolution of $P_{\min}$ with x is qualitatively the same despite the significant difference between the amplitudes of negative polarization produced by highly and weakly absorbing particles. Our results can be summarized as follows. Negative polarization does not exist for small x (< 4–6). The negative polarization appears at $x \sim 5$ and grows rapidly. The amplitude of the negative polarization reaches its maximum at $x \sim 8$–10, and then slowly decreases toward zero. For convenience, we denote the size parameter at which the negative polarization appears as x_{app}; whereas, the size parameter of the maximal amplitude of negative polarization we designate as

x_{max}. In the case of highly absorbing particles, we can observe a disappearance of negative polarization at $x \sim 30$.

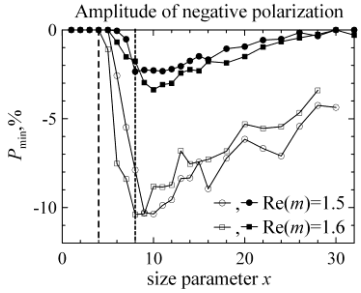

Figure 2. Dependence of amplitude of the negative polarization P_{min} on size parameter x. Open symbols show Im(m) = 0.02; whereas, closed symbols show Im(m) = 0.1.

In our simulations, the ratio of x_{max} to x_{app} remains approximately 2, i.e., $x_{max} = 2\ x_{app}$. This relationship holds for Re(m) = 1.5 – 1.6, with slight deviation for Re(m) = 1.313 and Re(m) = 1.7. The relationship is almost independent of Im(m) in the range of values 0–0.1. Therefore, a particle can produce a significant negative polarization at short wavelengths, while at longer wavelengths, it may produce no negative polarization at all. For instance, in Fig. 2, one can see that all particles with $x = 8$ produce noticeable negative polarization; whereas, at $x = 4$, none of the particles do. Note that the dramatic change in polarization on October 25 occurs within the range of λ from 0.5 to 0.9 μm. This may suggest that there is an abundance of particles having a corresponding size $r \approx 0.6$ μm; such particles have $x \approx 4$ at $\lambda = 0.9$ μm and $x \approx 8$ at $\lambda = 0.5$ μm. Furthermore, because cometary particles follow a power-law size distribution (e.g., [9]), the abundance of particles with $r \approx 0.6$ μm can be obtained only if the distribution of particles has a bottom limit around 0.6 μm. Therefore, one can conclude that, in the inner part of the dust halo of comet 17P/Holmes, particles smaller than 0.6 μm do not appear in considerable concentrations on October 25, 2007.

So far, we have only considered particles with a fixed size. To simulate light scattering in the dust halo of comet 17P/Holmes, we consider a cloud of independently scattering agglomerated debris particles that follow the size distribution r^a ($1.5 < a < 3.5$ [9]). Fig. 3 shows the degree of linear polarization at small phase angles corresponding to $m = 1.5 + 0.1i$ for this distribution. The left panel corresponds to a power-law index $a = 3.5$ and the right panel to $a = 1.5$. In each panel, the solid line shows the case of incident light at $\lambda = 0.9$ μm; whereas, the dotted line shows the case for an incident wavelength $\lambda = 0.45$ μm.

As one can see in Fig. 3, a size distribution characterized by power index $a = 3.5$, with a lower size limit of 0.6 μm, provides a significantly more prominent negative polarization branch at $\lambda = 0.45$ μm than at $\lambda = 0.9$ μm; whereas, with $a = 1.5$, the negative polarization shows little wavelength dependence. We would like to stress that this wavelength dependence appears for all refractive indices considered in this study, with the primary differences in the refractive index being reflected in the magnitude of the negative polarization. For instance, in the case of weakly absorbing particles, the total amplitude of negative polarization is approximately 6–7%, which is significantly larger than the observed values. Such weakly absorbing particles are blue in appearance, which is contrary to observations.

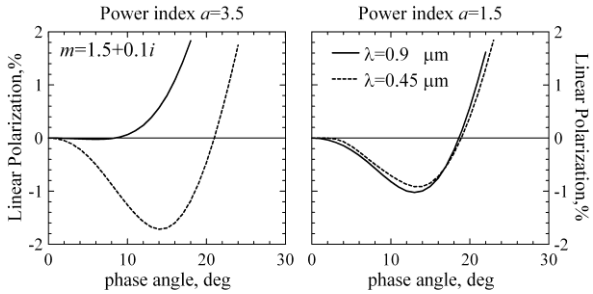

Figure 3. Dependence of the linear polarization degree on the phase angle for agglomerated debris particles averaged over size at two different wavelengths of the incident light.

Highly absorbing particles, however, are red in appearance for all considered Re(*m*) and *a*. Moreover, at Re(*m*) = 1.5–1.6, these particles produce a negative polarization branch whose amplitude is comparable to that observed for comet 17P/Holmes. The evolution in spectral behavior of linear polarization observed for comet 17P/Holmes between October 25 and November 3 can be attributed to a change in the power index *a* from 3.5 to 1.5. Such an alteration of power index is consistent with a decrease of the relative contribution of smaller particles with time.

REFERENCES

[1] D.W.E. Green. Comet 17P/Holmes. IAU Circ. **8886** (2007).

[2] M. Watanabe, H. Nakaya, T. Yamamuro et al. TRISPEC: A Simultaneous Optical and Near-Infrared Imager, Spectrograph, and Polarimeter. PASP **117** (2005).

[3] Z. Sekanina. Exploding comet 17P/Holmes. Int Comet Quart **30** (2008).

[4] A.C. Levasseur-Regourd and E. Hadamcik. Light scattering by irregular dust particles in the solar system: observations and interpretation by laboratory measurements. JQSRT **79-80** (2003).

[5] U.C. Joshi, S. Ganesh, and K.S. Baliyan. Optical polarimetry and photometry of comet 17P/Holmes. Mon. Not. R. Astron. Soc. **402** (2010).

[6] V. Rosenbush, N. Kiselev, L. Kolokolova, S. Velichko, F. Velichko, K. Antoniuk, and S. Kolesnikov. Polarization properties of odd comet 17P/Holmes. JQSRT **110** (2009).

[7] E. Zubko, H. Kimura, Yu.G. Shkuratov, K. Muinonen, T. Yamamoto, H. Okamoto, and G. Videen. Effect of absorption on light scattering by agglomerated debris particles. JQSRT **110** (2009).

[8] Z.R. Dai and J.P. Bradley. Iron-nickel sulfides in anhydrous interplanetary dust particles. Geochimica et Cosmochimica Acta **65** (2001).

[9] E.P. Mazets, R.L. Aptekar, S.V. Golenetskii et al. Comet Halley Dust Environment from SP-2 Detector Measurements. Nature **321** (1986).

AUTHOR INDEX

	Mo	**Tu**
9:00	session 1.1 Solar-system particles I	session 2.1 T-matrix method
	Lumme, Dlugach, Kolokolova	**Petrov**, Mackowski(2), Kyurkchan[Smirnova](2), Kyurkchan(3), Schmidt
10:30	coffee	coffee
11:00	session 1.2 Discrete-dipole approximation	session 2.2 Interstellar and circumstellar particles
	Yurkin, Zubko, Vilaplana, Wriedt, Tyynelä	**Witt**, Iati, Voshchinnikov, **Min**
12:30	lunch	lunch
14:00	session 1.3 Experimental measurements I	session 2.3 Experimental measurements II
	Munoz, Hadamcik, **Peltoniemi** Paton	**Berg**, Krieger, Loke[Nieminen](2), Vaillon, Munoz(2)
15:30	coffee	coffee
16:00-17:30	session 1.4 Solar-system particles II	session 2.4 Atmospheric particles I
	Muinonen(2), Shkuratov[Videen], Velikodsky Mikrenska, Nousiainen, Savenkov	**Mishchenko**, Kahnert, Francis, Lindqvist, Merikallio
	19-20 Helsinki City Reception, Helsinki City Hall	

program version June 15

We	Th	Fr
	session 4.1 Demos, 9:00-10:00	session 5.1 Atmospheric particles II
	Penttilä(2), Muinonen[Pieniluoma], Gogoi, Vinokurov, Hellmers	**Ulanowski**, Borovoi, Hovenier, Kiselev, Mauno
		coffee
session 3.1 SVM, DSM, DDA, and other methods		session 5.2 Cometary particles
Il'in, Eremin, Grishina, Loiko, Penttilä	Free time, possibility to visit Stockholm	**Levasseur-Regourd,** Guirado, Sen, Mackowski, Zubko(2)
lunch		lunch, 12:30-13:15
session 3.2 From nanoparticles to Special Relativity		session 5.3, 13:15-14:30 Discussion JQSRT Young Scientist Award
Censor, Loke, Myroshnychenko, Shcherbakov, Zouros, Schäfer	session 4.2 15:30-17:00 Posters 17:00-18:00 JQSRT & cocktails 18:00-18:30 Halo-presentation	
coffee	Berdnik, Loiko, Deau, Dlugach(2), Gogoi, Kyurkchan, Lindqvist(2), Francoeur, Moussaoui, Näränen, Nousiainen(2), Oszkiewicz, Parviainen, Prokopyeva, Ruoskanen, Benghorieb, Tyynelä(2), Cellino, Vinokurov, Hellmers	
session 3.3 Biological particles		
Eremina, Sivaprakasam[Eversole] , Ahmed, Roy, Popov[Priezzhev]		
18:30 SOC meeting 20-Conference Dinner	20-Dinner	